

# **From Nuclei to Compact Stars**



# Contents

<b>1. Topics</b>	<b>1415</b>
<b>2. Participants</b>	<b>1417</b>
2.1. ICRA <span>Net</span> participants . . . . .	1417
2.2. Past collaborators . . . . .	1417
2.3. On going collaborations . . . . .	1417
2.4. Ph.D. Students . . . . .	1418
<b>3. Brief Description of the Research Activities</b>	<b>1419</b>
3.1. Nuclear and Atomic Astrophysics . . . . .	1420
3.2. White Dwarf Physics and Astrophysics . . . . .	1424
3.3. Neutron Star Physics and Astrophysics . . . . .	1427
3.4. Neutron Star Physics with Gamma Ray Bursts . . . . .	1429
3.5. Emission-Radiation Mechanisms of White Dwarfs and Neutron Stars . . . . .	1432
3.6. Exact Solutions of the Einstein-Maxwell equations in Astrophysics . . . . .	1432
3.7. Critical fields and Non Linear Electrodynamics Effects in Neutron Stars and Black Holes . . . . .	1433
<b>4. Publications (before 2012)</b>	<b>1435</b>
4.1. Refereed Journals . . . . .	1435
4.2. Conference Proceedings . . . . .	1436
<b>5. Publications 2012</b>	<b>1439</b>
5.1. Refereed Journals . . . . .	1439
5.2. Conference Proceedings . . . . .	1440
<b>6. Attended Meetings and Conferences</b>	<b>1443</b>
<b>7. APPENDICES</b>	<b>1445</b>
<b>A. Nuclear and Atomic Astrophysics</b>	<b>1447</b>
A.1. On gravitationally and electro-dynamically bound massive nuclear density cores . . . . .	1447
A.1.1. Introduction . . . . .	1447

A.1.2.	The relativistic Thomas-Fermi equation and the beta equilibrium condition . . . . .	1449
A.1.3.	The ultra-relativistic analytic solutions . . . . .	1451
A.1.4.	New results derived from the analytic solutions . . . . .	1455
A.1.5.	Estimates of gravitational effects in a Newtonian approximation . . . . .	1456
A.1.6.	Possible applications to neutron stars . . . . .	1457
A.1.7.	Conclusions . . . . .	1458
A.2.	On the relativistic Thomas-Fermi treatment of compressed atoms and compressed nuclear matter cores of stellar dimensions . . . . .	1461
A.2.1.	Introduction . . . . .	1461
A.2.2.	The Thomas-Fermi model for compressed atoms: the Feynman-Metropolis-Teller treatment . . . . .	1463
A.2.3.	The relativistic generalization of the Feynman-Metropolis-Teller treatment . . . . .	1467
A.2.4.	Comparison and contrast with approximate treatments . . . . .	1472
A.2.5.	Application to nuclear matter cores of stellar dimensions . . . . .	1477
A.2.6.	Compressional energy of nuclear matter cores of stellar dimensions . . . . .	1483
A.2.7.	Conclusions . . . . .	1485
A.3.	The relativistic Feynman-Metropolis-Teller equation of state at finite temperatures . . . . .	1494
A.3.1.	Introduction . . . . .	1494
A.3.2.	The Relativistic Feynman Metropolis Teller (FMT) Treatment . . . . .	1494
A.3.3.	The extension to finite temperatures . . . . .	1496
A.3.4.	The equation of state . . . . .	1498
A.3.5.	Conclusions . . . . .	1498
A.4.	On Magnetic Fields in Rotating Nuclear Matter Cores of Stellar Dimensions . . . . .	1500
A.4.1.	Introduction . . . . .	1500
A.4.2.	The Relativistic Thomas-Fermi equation . . . . .	1501
A.4.3.	The ultra-relativistic analytic solutions . . . . .	1503
A.4.4.	Rotating Nuclear Matter Cores of Stellar Dimensions in Classical Electrodynamics . . . . .	1503
A.4.5.	Conclusions . . . . .	1506
<b>B.</b>	<b>White Dwarfs Physics and Astrophysics</b>	<b>1509</b>
B.1.	The relativistic Feynman-Metropolis-Teller theory for white dwarfs in general relativity . . . . .	1509
B.1.1.	Introduction . . . . .	1509
B.1.2.	The Equation of State . . . . .	1513
B.1.3.	General relativistic equations of equilibrium . . . . .	1527
B.1.4.	Mass and radius of general relativistic stable white dwarfs	1531

---

B.1.5. Conclusions . . . . .	1538
B.2. On general relativistic uniformly rotating white dwarfs . . . . .	1540
B.2.1. Introduction . . . . .	1540
B.2.2. Spacetime geometry and Hartle's formalism . . . . .	1542
B.2.3. Limits on the stability of rotating white dwarfs . . . . .	1542
B.2.4. WD structure and stability boundaries . . . . .	1547
B.2.5. The maximum mass . . . . .	1550
B.2.6. The minimum rotation period . . . . .	1551
B.2.7. Occurrence of secular axisymmetric instability . . . . .	1553
B.2.8. Spin-up and spin-down evolution . . . . .	1556
B.2.9. Astrophysical implications . . . . .	1557
B.2.10. Concluding remarks . . . . .	1559
B.2.11. Supplementary information . . . . .	1560
B.3. SGRs and AXPs as rotation powered massive white dwarfs . . . . .	1570
B.3.1. Introduction . . . . .	1570
B.3.2. SGRs and AXPs within the white dwarf model . . . . .	1571
B.3.3. SGRs and AXPs within the magnetar model . . . . .	1575
B.3.4. Observations of massive fast rotating highly magnetized white dwarfs . . . . .	1580
B.3.5. Rotational instability of white dwarfs . . . . .	1581
B.3.6. Glitches and outbursts in SGRs and AXPs . . . . .	1583
B.3.7. Magnetosphere emission from white dwarfs . . . . .	1584
B.3.8. The connection with supernova remnants . . . . .	1587
B.3.9. On the fiducial neutron star and white dwarf parame- ters in light of recent theoretical progress . . . . .	1589
B.3.10. Conclusions and remarks . . . . .	1590
B.4. SGR 0418+5729 and Swift J1822.3-1606 as massive fast rotating highly magnetized white dwarfs . . . . .	1593
B.4.1. Introduction . . . . .	1593
B.4.2. Rotation powered white dwarfs . . . . .	1595
B.4.3. Structure and stability of rotating white dwarfs . . . . .	1595
B.4.4. SGR 0418+5729 . . . . .	1597
B.4.5. Swift J1822.3-1606 . . . . .	1603
B.4.6. Concluding Remarks . . . . .	1606
B.5. White Dwarf Mergers as Progenitors of SGRs and AXPs: the case of 4U 0142+61 . . . . .	1608
B.6. Finite temperature effects on the mass-radius relation of white dwarfs . . . . .	1616
<b>C. Neutron Stars Physics and Astrophysics</b>	<b>1619</b>
C.1. The self-consistent general relativistic solution for a system of degenerate neutrons, protons and electrons in $\beta$ -equilibrium . . . . .	1619
C.1.1. Introduction . . . . .	1619

---

C.1.2.	The impossibility of a solution with local charge neutrality . . . . .	1621
C.1.3.	The solution with global charge neutrality . . . . .	1624
C.1.4.	Numerical integration of the equilibrium equations . . . . .	1624
C.1.5.	Conclusions . . . . .	1628
C.2.	The Klein first integrals in an equilibrium system with electromagnetic, weak, strong and gravitational interactions . . . . .	1630
C.2.1.	Introduction . . . . .	1630
C.2.2.	The Constitutive General Relativistic Equations . . . . .	1631
C.2.3.	The Thermodynamic Laws and the Field Equations in the Spherically Symmetric Case . . . . .	1634
C.2.4.	Constancy of the Klein potentials and $\beta$ -equilibrium . . . . .	1637
C.2.5.	Concluding Remarks . . . . .	1639
C.3.	On the constitutive equations of a self-gravitating system of neutrons, protons and electrons in $\beta$ -equilibrium at finite temperatures . . . . .	1641
C.3.1.	Introduction . . . . .	1641
C.3.2.	Einstein-Maxwell-Thomas-Fermi equations in the degenerate case . . . . .	1642
C.3.3.	Newtonian limit . . . . .	1645
C.3.4.	Introducing strong interactions . . . . .	1648
C.3.5.	Finite temperature effects . . . . .	1651
C.3.6.	Concluding Remarks . . . . .	1656
C.4.	Neutron star equilibrium configurations within a fully relativistic theory with strong, weak, electromagnetic, and gravitational interactions . . . . .	1661
C.4.1.	Introduction . . . . .	1661
C.4.2.	The Constitutive Relativistic Equations . . . . .	1662
C.4.3.	Neutron star structure . . . . .	1673
C.4.4.	Observational constraints on the mass-radius relation . . . . .	1675
C.4.5.	Comparison with the traditional TOV treatment . . . . .	1676
C.4.6.	Concluding Remarks . . . . .	1677
C.5.	On uniformly rotating globally neutral neutron stars . . . . .	1693
<b>D.</b>	<b>Neutron Stars Physics with Gamma-Ray Bursts</b>	<b>1697</b>
D.1.	Cooling of young neutron stars in GRB associated to Supernova	1697
D.1.1.	Introduction . . . . .	1697
D.1.2.	Cooling of Young, Hot Neutron Stars . . . . .	1698
D.1.3.	Late X-Ray Emission in GRBs associated to Supernovae: URCA's . . . . .	1702
D.1.4.	Neo-Neutron Star Luminosity and the URCA's . . . . .	1703
D.1.5.	Discussion and Conclusions . . . . .	1707
D.2.	Gravitational Waves versus Electromagnetic Emission in Gamma-Ray Bursts . . . . .	1709

<b>E. Exact Solutions of the Einstein-Maxwell equations in Astrophysics</b>	<b>1717</b>
E.1. On the relativistic precession and oscillation frequencies of test particles around rapidly rotating compact stars . . . . .	1717
E.1.1. Introduction . . . . .	1717
E.1.3. Orbital Motion Frequencies on the Equatorial Plane . . . . .	1722
E.1.4. Accuracy of Ryan’s Analytic Formulas . . . . .	1734
E.1.5. Accuracy of PRS solution . . . . .	1737
E.1.6. The Relativistic Precision Model . . . . .	1739
E.1.7. Concluding Remarks . . . . .	1742
E.1.8. Supplementary information . . . . .	1745
<b>Bibliography</b>	<b>1749</b>



# 1. Topics

- Nuclear and Atomic Astrophysics.
- White Dwarfs Physics and Astrophysics.
- Neutron Stars Physics and Astrophysics.
- Emission-Radiation Mechanisms of White Dwarfs and Neutron Stars.
- Critical fields and Non Linear Electrodynamics Effects in Neutron Stars and Black Holes.
- Exact Solutions of the Einstein-Maxwell equations in Astrophysics.



## 2. Participants

### 2.1. ICRA Net participants

- D. Arnett (Steward Observatory, University of Arizona, USA)
- D. Bini (Istituto Nazionale per l'Applicazione del Calcolo, Italy)
- H. Kleinert (Free University of Berlin , Germany)
- V. Popov (ITEP, Moscow, Russia)
- M. Rotondo (ICRA Net, University of Rome, Italy)
- Jorge A. Rueda (ICRA Net, University of Rome, Italy)
- R. Ruffini (ICRA Net, University of Rome, Italy)
- S.-S. Xue (ICRA Net, University of Rome, Italy)

### 2.2. Past collaborators

- W. Greiner (Institut für Theoretical Physics Johann Wolfgang Goethe-Universität, Frankfurt am Main )
- D. Pugliese (School of Mathematical Sciences, Queen Mary, University of London, United Kingdom)
- L. Stella (Rome Astronomical Observatory, Italy)

### 2.3. On going collaborations

- M. Malheiro (Instituto Tecnológico de Aeronáutica, Brazil)
- R. Negreiros (Universidade Federal de Fluminense, Brazil)
- L. Pachón (Universidad de Antioquia, Colombia)
- C. Valenzuela (Universidad del Valle, Colombia)

## **2.4. Ph.D. Students**

- R. Belvedere (ICRANet, University of Rome, Italy)
- K. Boshkayev (ICRANet, University of Rome, Italy)
- D. Cáceres (ICRANet, University of Rome, Italy)
- F. Gomes de Oliveira (ICRANet, University of Rome, Italy and Université de Nice Sophia-Antipolis, France)
- S. Martins de Carvalho (ICRANet, University of Rome, Italy and Université de Nice Sophia-Antipolis, France)
- J. Pereira (ICRANet, University of Rome, Italy and Université de Nice Sophia-Antipolis, France)
- Y. Wu (ICRANet, University of Rome, Italy and Université de Nice Sophia-Antipolis, France)

### 3. Brief Description of the Research Activities

The study of white dwarfs and neutron stars requires the interplay between nuclear and atomic physics together with relativistic field theories e.g. general relativity, quantum electrodynamics, quantum chromodynamics, as well as particle physics. In addition to the Physics, the study of astrophysical scenarios characterized by the presence of a compact star has also started to be focus of extensive research within our group. The works done and currently being developed within our group can be divided into the following topics:

1. Nuclear and Atomic Astrophysics
2. White Dwarfs Physics and Astrophysics
3. Neutron Stars Physics and Astrophysics
4. Emission-Radiation Mechanisms of White Dwarfs and Neutron Stars
5. Neutron Star Physics and Astrophysics with Gamma Ray Bursts
6. Critical fields and Non Linear Electrodynamics Effects in Neutron Stars and Black Holes
7. Exact Electrovacuum Solutions of the Einstein-Maxwell equations in Astrophysics

The last four topics have been added with respect to the 2011 Scientific Report and some others show the activity being carried out on topics related to the observation and analysis of astrophysical phenomena related with white dwarfs and neutron stars.

The above research topics are the natural continuation of the doctoral works of M. Rotondo and Jorge A. Rueda, which have been followed by the ones of R. Belvedere, K. Boshkayev, D. Pugliese, and currently by S. Martins de Carvalho, J. Pereira, and Y. Wu. Some astrophysical applications of the theory of white dwarfs and neutron stars are also addressed by some of the aforementioned people and is, in particular, one of the main topics of the Ph. D. research works of D. Cáceres and F. Gomes de Oliveira.

Below we shall describe every topic and discuss in detail the main research works we have been pushing forward in the last years along the previous research areas.

### 3.1. Nuclear and Atomic Astrophysics

By Nuclear and Atomic Astrophysics we mean the study of nuclear and atomic physics related to astrophysical systems like white dwarfs and neutron stars. We focus on the properties of nuclear matter under extreme conditions of density and pressure found in these objects. The equation of state of the matter in compact star interiors is studied in detail taking into account all the interactions between the constituents within a full relativistic framework. The aim is to have a unified approach for nuclei, for superheavy nuclei up to atomic numbers of the order of  $10^5$ – $10^6$ , and for what we have called “nuclear matter cores of stellar dimensions”, which are

- characterized by atomic number of the order of  $10^{57}$ ;
- composed by a degenerate fluid of neutrons, protons and electrons in  $\beta$ -equilibrium;
- globally neutral configurations;
- expected to be kept at nuclear density by self gravity.

It is known that the Thomas-Fermi model has been extensively applied in atomic physics, also has been applied extensively in atomic physics in its relativistic form as well as in the study of atoms with heavy nuclei (see Gombás (1949) for instance). Similarly there have been considerations of relativistic Thomas-Fermi model for quark stars pointing out the existence of critical electric fields on their surfaces Alcock et al. (1986). Similar results have also been obtained in the transition at very high densities, from the normal nuclear matter phase in the core to the color-flavor-locked phase of quark matter in the inner core of hybrid stars Alford et al. (2001). However, no example exists to the application of the electromagnetic Thomas-Fermi model to white dwarfs and neutron stars.

The analysis of superheavy nuclei has historically represented a major field of research, developed by Prof. V. Popov and Prof. W. Greiner and their schools. This same problem was studied in the context of the relativistic Thomas-Fermi equation also by R. Ruffini and L. Stella, already in the '80s. The recent approach was started with the Ph.D. Thesis of M. Rotondo and has shown the possibility to extrapolate this treatment of superheavy nuclei to the case of nuclear matter cores of stellar dimensions (see App. A.3). The very unexpected result has been that also around these massive cores there is the distinct possibility of having an electromagnetic field close to the critical value

$$E_c = \frac{m_e^2 c^3}{e \hbar},$$

although localized in a very narrow shell of the order of the electron Compton wavelength (see Fig. 3.1).

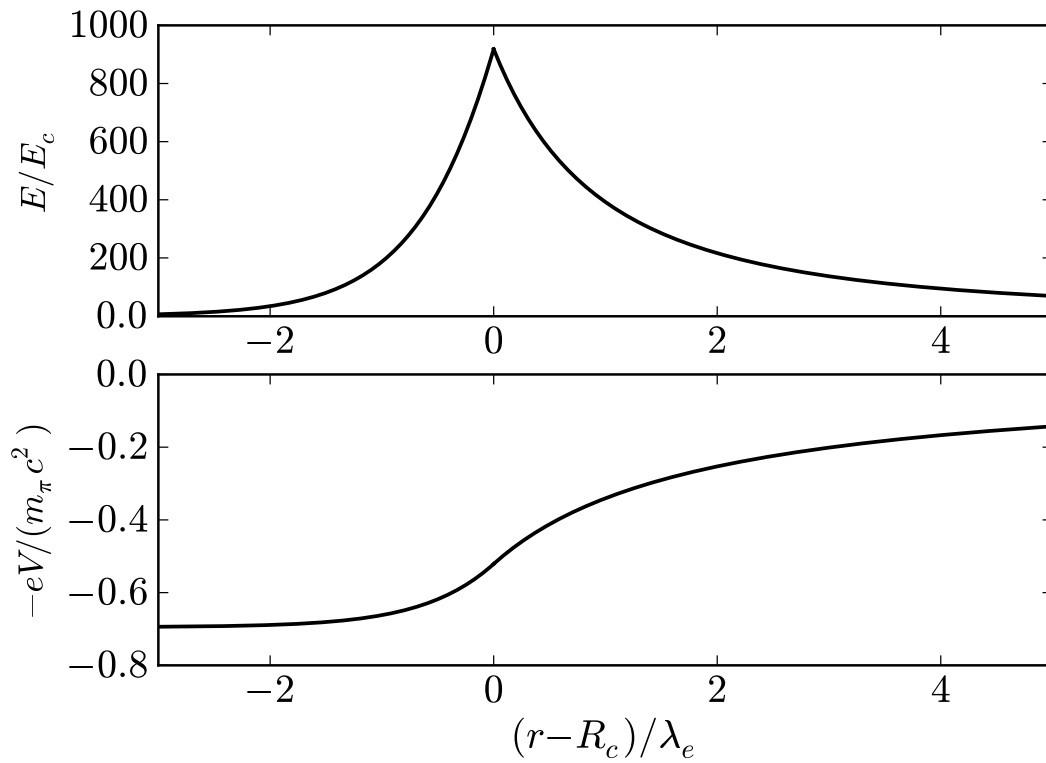


**Figure 3.1.:** Upper panel: electric field around the surface of a nuclear matter core of stellar dimensions in units of the critical field  $E_c$ . Lower panel: corresponding sharp increasing of the electron Coulomb potential  $-eV$ . Here  $R_c$  denotes the core radius and  $\lambda_e = \hbar/(m_e c)$  is the electron Compton wavelength.

The welcome result was that all the analytic work developed by Prof. V. Popov and the Russian school can be applied using scaling laws satisfied by the relativistic Thomas-Fermi equation to the case of nuclear matter cores of stellar dimensions, if the  $\beta$ -equilibrium condition is properly taken into account. This has been the result obtained and published by Ruffini, Rotondo and Xue already in 2007. Since then, a large variety of problems has emerged, which have seen the direct participation of ICRANet Professors, Ph. D. students, post-docs, as well as collaborators worldwide including Prof. V. W. Greiner, Prof. Popov, and Prof. G. 't Hooft.

One of the crucial issues to be debated is the stability of such cores under the competing effects of self-gravity and Coulomb repulsion. It has been demonstrated their stability against nuclear fission, as opposed to the case of heavy nuclei, see App. A.1 . In particular, on the basis of Newtonian gravitational energy considerations it has been found the existence of a possible new island of stability for mass numbers  $A > A_R = 0.039 \left(\frac{N_p}{A}\right)^{1/2} \left(\frac{m_{\text{Planck}}}{m_n}\right)^3$ , where  $N_p$  is the number of protons,  $A$  is the total number of baryons,  $m_n$  is the neutron mass and  $m_{\text{Planck}} = (\hbar c/G)^{1/2}$  is the Planck mass. The equilibrium against Coulomb repulsion originates now from the combined effect of the screening of the relativistic electrons, of the surface tension due to strong interactions, and of the gravitational interaction of these massive cores.

By enforcing the condition of  $\beta$ -equilibrium, it has been also obtained a generalization to the relation between the mass number  $A$  and atomic number  $N_p$  which encompasses phenomenological expressions (see App. A.1 for details).

All these considerations have been made for an isolated core with constant proton density whose boundary has been sharply defined by a step function. No external forces are exerted. Consequently, the Fermi energy of the electrons has been assumed to be equal to zero.

Different aspects concerning these macroscopic systems have been also considered. For instance, the analysis of the electron distribution around such cores in both the case of global charge neutrality and the case of not global charge neutrality has been presented by R. Ruffini, M. Rotondo and S.-S. Xue in *Neutral nuclear core versus super charged one*, Proc. 11th Marcel Grossmann Meeting, 2008.

The assumption of a sharp proton density profile has been relaxed and, consequently, a smooth surface modeled by a Woods-Saxon-like proton distribution has been introduced in *The Extended Nuclear Matter Model with Smooth Transition Surface* by Jorge A. Rueda H., B. Patricelli, M. Rotondo, R. Ruffini, S.-S. Xue, , Proc. 3rd Stueckelberg Workshop on Relativistic Field Theories, 2008. The presence of overcritical electric fields close to their surface has been confirmed also in this more general case.

The existence of the scaling laws of the ultrarelativistic Thomas-Fermi equation (see App. A.1) has led to the very exciting possibility of having macro-

scopic configurations of nuclear matter in  $\beta$ -equilibrium exhibiting strong electric fields on their surfaces. In order to go one step further towards a more realistic description of macroscopic configurations as white dwarfs and neutron stars, further improvements and extensions must be applied to the starting model.

It is therefore interesting, in order to approach both the complex problem of a neutron star core and its interface with the neutron star crust and the problem of the equilibrium of gas in a white dwarf taking into account all possible global electromagnetic interactions between the nucleus and the relativistic electrons, to extend the model to the compressed case in which the Fermi energy of electrons turns to be positive.

The analysis of globally neutral and compressed configurations composed by a nucleus made of relativistic degenerate neutrons and protons surrounded by relativistic degenerate electrons in  $\beta$ -equilibrium has been recently accomplished. This work has generalized the Feynman-Metropolis-Teller treatment of compressed atoms to relativistic regimes, and the concept of compressed nuclear matter cores of stellar dimensions has been introduced (see App. A.2 for details).

In the relativistic generalization of the Feynman-Metropolis-Teller approach, the equation to be integrated is the relativistic Thomas-Fermi equation. The integration of this equation does not admit any regular solution for a point-like nucleus and both the nuclear radius and the nuclear composition have necessarily to be taken into account. This introduces a fundamental difference from the non-relativistic Thomas-Fermi model where a point-like nucleus was adopted.

Due to the introduction of the concept of Wigner-Seitz cells, the study of degenerate compressed matter in white dwarfs can be addressed. This problem presents, still today, open issues of great interest such as the equilibrium of the electron gas and the associated nuclear component, taking into account the electromagnetic, the gravitational and the weak interactions formulated in a correct special and general relativistic framework.

A complete analysis of the properties of such configurations as a function of the compression can be duly done through the relativistic generalization of the Feynman-Metropolis-Teller approach (see App. A.2 for details).

It has been then possible to derive a consistent equation of state for compressed matter which generalizes both the uniform free-electron fluid approximation, adopted for instance by Chandrasekhar (1931b) in his famous treatment of white dwarfs, and the well-known work of Salpeter (1961a) which describes the electrodynamic and relativistic effects by a sequence of approximations. Apart from taking into account all possible electromagnetic and special relativistic corrections to the equation of state of white dwarf matter, the new equation of state that incorporates the  $\beta$ -equilibrium condition, leads to a self-consistent calculation of the onset for inverse  $\beta$ -decay as function of the Fermi energy of electrons or the density of the system. This is

very important for the analysis of the stability of white dwarfs against gravitational collapse (see below and App. B.1).

The extension of the above works to the case of finite temperatures is part of the Ph. D. work of S. Martins de Carvalho. The generalization of the relativistic Feynman-Metropolis-Teller treatment to the case  $T \neq 0$  has been already accomplished, see App. A.3.

A related topic of current interest concerns the case of rotating nuclear matter cores of stellar dimensions. The induced magnetic field by electric field rotation has been recently obtained (see App. A.4). Such analysis has been done in the framework of classical electrodynamics under the assumption of uniform rigid rotation of the macroscopic nuclear cores in the non-compressed case. For rotation periods of the order of  $\sim 10$  ms, overcritical magnetic fields has been obtained near the surface of the configuration.

In neutron star cores, nuclear matter is under very extreme conditions of density and pressure. The importance of the strong interactions between nucleons at such extreme pressures it has been known for years (see e.g. Cameron (1970); Shapiro and Teukolsky (1983)). However, due to the absence of a complete theory of the strong interactions, and due to the impossibility of performing terrestrial experiments with similar extreme pressure-density conditions, the equation of state of nuclear matter at densities larger than the nuclear saturation density  $\sim 2.7 \times 10^{14}$  g/cm<sup>3</sup>, is still today unknown. The construction of nuclear equations of state combined with a fully consistent formulation of the equations of equilibrium in general relativity both for white dwarfs and neutron stars is an active topic of research within our group. In the recent past, some Ph. D. Theses have been devoted to this topic e.g. starting from the Ph. D. works of M. Rotondo and Jorge A. Rueda and later followed by the ones of R. Belvedere, K. Boshkayev, D. Pugliese, and currently by S. Martins de Carvalho and Y. Wu.

## 3.2. White Dwarf Physics and Astrophysics

A branch of research which is currently under continuous evolution corresponds to the extension to the case of general relativity, all the previous theory about the Thomas-Fermi model and the relativistic Thomas-Fermi model, applied initially to the study of heavy nuclei, superheavy nuclei as well as to the theoretical hypothesis of nuclear matter cores of stellar dimensions. The aim is to construct a self-consistent theory of self-gravitating systems obeying relativistic quantum statistics, electromagnetic, weak and strong interactions in the framework of general relativity, from which it is possible to study the properties of compact objects e.g. white dwarfs and neutron stars.

The recent generalization of the Feynman-Metropolis-Teller treatment to relativistic regimes, which led to a new equation of state of white dwarf matter (see App. A.2), has been recently used to construct equilibrium configura-

tions of white dwarfs in general relativity (see App. B.1).

The description of the inverse  $\beta$ -decay within the relativistic Feynman-Metropolis-Teller equation of state in conjunction with general relativity, leads to a self-consistent calculation of the critical mass of white dwarfs (see App. B.1 for details). The numerical value of the mass, of the radius, and of the critical mass of white dwarfs turn to be smaller with respect to the ones obtained with approximate equations of state (see e.g. Hamada and Salpeter (1961)). Therefore, the analysis of compressed atoms following the relativistic Feynman-Metropolis-Teller treatment has important consequences in the determination of the mass-radius relation of white dwarfs, leading to the possibility of a direct confrontation of these results with observations, in view of the current great interest for the cosmological implications of the type Ia supernovae.

The generalization of the above general relativistic theory of white dwarfs to the case of rotation is the thesis work of K. Boshkayev, see App. B.2 for details. The entire family of uniformly rotating stable white dwarfs has been already obtained by studying the mass-shedding, the inverse  $\beta$ -decay, pycnonuclear reactions, as well as the axisymmetric instabilities. Both the maximum mass and the minimum(maximum) rotation period(frequency) have been obtained for selected nuclear compositions. This work is relevant for the evolution of massive white dwarfs, type Ia supernovae, and for the description of Soft-Gamma-Ray Repeaters (SGRs) and the Anomalous X-Ray Pulsars (AXPs) as rotation powered white dwarfs, as shown in App. B.3.

SGRs and AXPs are a class of compact objects that show interesting observational properties: rotational periods in the range  $P \sim (2-12)$  s, a narrow range with respect to the wide range of ordinary pulsars  $P \sim (0.001-10)$  s; spin-down rates  $\dot{P} \sim (10^{-13}-10^{-10})$ , larger than ordinary pulsars  $\dot{P} \sim 10^{-15}$ ; strong outburst of energies  $\sim (10^{41}-10^{43})$  erg, and for the case of SGRs, giant flares of even large energies  $\sim (10^{44}-10^{47})$  erg, not observed in ordinary pulsars.

The recent observation of SGR 0418+5729 with a rotational period of  $P = 9.08$  s, an upper limit of the first time derivative of the rotational period  $\dot{P} < 6.0 \times 10^{-15}$ , and an X-ray luminosity of  $L_X = 6.2 \times 10^{31}$  erg/s, promises to be an authentic Rosetta Stone, a powerful discriminant for alternative models of SGRs and AXPs. The loss of rotational energy of a neutron star with this spin-down rate  $\dot{P}$  cannot explain the X-ray luminosity of SGR 0418+5729, excluding the possibility of identifying this source as an ordinary spin-down powered pulsar. The inferred upper limit of the surface magnetic field of SGR 0418+5729  $B < 7.5 \times 10^{12}$  G, describing it as a neutron star within the magnetic braking scenario, is well below the critical field challenging the power mechanism based on magnetic field decay purported in the magnetar scenario.

We have shown that the observed upper limit on the spin-down rate of SGR 0418+5729 is, instead, perfectly in line with a model based on a massive

fast rotating highly magnetized white dwarf of mass  $M = 1.4M_{\odot}$ , radius  $R = 10^3$  km, and moment of inertia  $I \approx 10^{49}$  g cm<sup>2</sup>. We analyze the energetics of all SGRs and AXPs including their outburst activities and show that they can be well explained through the change of rotational energy of the white dwarf associated to the observed sudden changes of the rotational period, the glitches. All SGRs and AXPs can be interpreted as rotating white dwarfs that generate their energetics from the rotational energy and therefore there is no need to invoke the magnetic field decay of the magnetar model. Details can be found in App. B.3. The above calculation of the range of minimum rotation periods of massive WDs,  $0.3 \lesssim P_{min} \lesssim 2.2$  seconds, depending on the nuclear composition (see App. B.2), implies the rotational stability of SGRs and AXPs. The relatively long minimum period of <sup>56</sup>Fe RWDs  $\sim 2.2$  seconds, implies that RWDs describing SGRs and AXPs have to be composed of nuclear compositions lighter than <sup>56</sup>Fe, e.g. <sup>12</sup>C or <sup>16</sup>O.

We have analyzed within the white dwarf model of SGRs and AXPs, SGR 0418+5729 and Swift J1822.3-1606 the so-called *low magnetic field magnetars*, see App. B.3. The request of the rotational stability of the white dwarf gives bounds for the mass, radius, moment of inertia and magnetic field, through the analysis of constant rotation period sequences of general relativistic uniformly rotating degenerate white dwarf configurations. We have also analyzed the emission properties of these two objects in the optical band. Concerning the emission in the high-energy bands, e.g. X and Gamma rays, it is part of the Ph. D. work of D. Cáceres.

We are in addition considering the possible progenitors of these massive fast rotating highly magnetized white dwarfs (see App. B.4). Recent Smoothed Particle Hydrodynamics (SPH) simulations of white dwarfs (WDs) mergers (Garcia-Berro et al. 2012) indicate that the outcomes of these binaries are WDs with the above properties, and thus they can be progenitors of SGRs and AXPs. We applied these considerations to the specific case of 4U 0142+61. The request of the rotational stability of the resulting white dwarf gives bounds for the mass, radius, moment of inertia and magnetic field, through the analysis of constant rotation period sequences of general relativistic uniformly rotating degenerate white dwarf configurations. Assuming a carbon composition, we find that the mass and radius of 4U 0142+61 must be in the range  $1.16\text{--}1.39 M_{\odot}$  and  $0.0014\text{--}0.0086 R_{\odot}$ . We performed SPH simulations of  $0.8+1.0 M_{\odot}$  WD mergers that lead to a final WD of  $1.3M_{\odot}$ , in agreement with the above limits. From our SPH simulations we obtained also the radius, moment of inertia, magnetic field, and inclination angle of the magnetic moment with respect to the rotation axis of the white dwarf. We followed the subsequent cooling evolution of the newly formed white dwarf and show that its emission properties fully explain the current observed infrared, optical, and ultraviolet emissions. This leads to a prediction of the current age of the white dwarf since the merger process. From the fit of the IR, optical, and UV spectrum we find a surface temperature and radius of

the white dwarf  $T \sim 1.45 \times 10^5$  K, and  $R_{wd} \sim 0.0056R_{\odot} \simeq 3.9 \times 10^8$  cm, in full agreement with the derived bounds for the white dwarf stability. The observed infrared excess is explained by the presence of a surrounding hot disk of dust material created during the merger process. The disk has inner and outer radii,  $R_{in} \simeq 0.8R_{\odot}$  and  $R_{out} \simeq R_{\odot}$ , and inner and outer temperatures  $T_{in} \simeq 2.4 \times 10^3$  K and  $T_{out} \simeq 2 \times 10^3$  K. Details can be found in App. B.4.

### 3.3. Neutron Star Physics and Astrophysics

In the earliest description of neutron stars in the works of Tolman (1939) and Oppenheimer and Volkoff (1939) only a gas of neutrons was considered and the equations of equilibrium (hereafter TOV equations) were written in the Schwarzschild metric. They considered the model of a degenerate gas of neutrons to hold from the center to the border, with the density monotonically decreasing away from the center.

In the intervening years, more realistic neutron star models have been presented challenging the original considerations of Tolman (1939) and Oppenheimer and Volkoff (1939). The TOV equations considered the existence of neutrons all the way to the surface of the star. The presence of neutrons, protons and electrons in  $\beta$ -equilibrium were instead introduced by Harrison et al. (1965). Still more important, the neutron stars have been shown to be composed of two sharply different components: the core at nuclear and supra-nuclear densities consisting of degenerate neutrons, protons and electrons in  $\beta$ -equilibrium and a crust of white dwarf like material, namely a nuclei lattice in a background of degenerate electrons (see Harrison et al. (1965); Baym et al. (1971a) for details). Further works describing the nuclear interactions were later introduced. Clearly all these considerations departed profoundly from the Oppenheimer and Volkoff (1939) assumption.

The matching between the core and the crust is still today an open issue in neutron star physics. In order to handle with this interesting problem, a step-by-step procedure is needed. In such a case, the neutron, proton, and electron fluid is confined within the core radius due to the compression exerted by the crust component of the neutron star.

Most of the effort have been given to the construction of self-consistent solutions of the equations of equilibrium for neutron stars in general relativity taking into account the traditionally neglected electromagnetic interaction. In nearly all the scientific literature on neutron stars, a “local approach”, where the equation of state of neutron star matter is constructed ignoring global gravitational and Coulombian effects by assuming not only flat space but also local charge neutrality, has been traditionally used. The gravitational effects are then taken into account by embedding such an equation of state into the TOV equations of hydrostatic equilibrium.

We have introduced a new approach which thanks to the existence of scal-

ing laws can apply to compressed atoms as well as to massive nuclear matter cores of stellar dimensions. This approach on the compressed atom has already given a new contribution in the study of white dwarfs. It represents the first self-consistent calculation taking into due account the electromagnetic contribution in a relativistic treatment of the Thomas-Fermi equation, within global formulation of the equilibrium of white dwarfs in general relativity.

The application of the above results to the case of neutron stars is much more complex and it has been approached stepwise. As a first step we have considered the application of this novel approach to the case of a system of neutrons, protons, and electrons in  $\beta$ -equilibrium at zero temperatures within general relativity (see App. C.1). The crucial role of the generalized Fermi energy of particles, for short Klein potentials, and their constancy on the entire equilibrium configuration has been outlined. Such a solution, although does not represent a realistic model for a neutron star, contains all the essential physics of the phenomenon of gravito-polarization in neutron star interiors: the existence of an electric potential and consequently an electric field over the entire configuration has been there evidenced.

We have there proved, for the case of this simplified example where strong interactions are neglected, that the traditional approach of describing the system imposing the condition of local charge neutrality and solving the corresponding TOV equations is conceptually inconsistent. We have then substitute the condition of local charge neutrality with the condition of global charge neutrality and derived the correct equations within the Einstein-Maxwell-Thomas-Fermi system. The boundary conditions are also different from a traditional Cauchy data with the values of the functions and first derivatives at the center into a boundary condition at the center and delicate eigenvalue problem at the boundary determining the condition of charge neutrality at the border (see App. C.1). The conceptual differences and the alternative mathematical equations of the two approaches, the ones imposing local versus global charge neutrality, lead to the presence of additional electrodynamic global structures. However, in this specific simple example, they do not give significant quantitative differences in the mass-radius relation for the equilibrium configurations. A very different situation occurs when strong interactions are also taken into account.

The next step has been to introduce self-consistently the strong interactions in the construction of the equilibrium configurations. We have indeed recently generalized the Einstein-Maxwell-Thomas-Fermi equations to the case of strong interactions, see App. C.2 for details. There the major aim has been to prove the constancy of the Klein potentials in the case in which the nuclear interactions are described by a Lagrangian including in addition to the gravitational, electromagnetic, and weak interactions, also the presence of  $\sigma$ ,  $\omega$ , and  $\rho$  virtual mesons that mediate the nuclear interactions.

We have also extended to finite temperatures the theoretical treatment of

gravito-polarization for a system of neutrons, protons and electrons in  $\beta$ -equilibrium, taking into account strong interactions modeled through the exchange of  $\sigma$ ,  $\omega$  and  $\rho$  virtual mesons (see App. C.3 for details). The crucial role of the Klein potentials of particles is outlined as well as the condition of isothermality of Tolman. We have shown that, the gravito-polarization effect although energetically much weaker than the corresponding gravitational and thermal effects, do survive in the case of finite temperatures. Their role, when strong interactions are considered, is of fundamental astrophysical importance.

Many interesting aspects of the physics and astrophysics of neutron stars are the research topic of the Ph. D. thesis of R. Belvedere and were part of the Ph. D. thesis of D. Pugliese. The construction of realistic neutron star with core and crust satisfying global (but not local) charge neutrality has been already accomplished (see App. C.4). The solutions lead to a new structure of the star: a positively charged core at supranuclear densities surrounded by an electronic distribution of thickness  $\sim \hbar/(m_e c) \sim 10^2 \hbar/(m_\pi c)$  of opposite charge, as well as a neutral crust at lower densities. Inside the core there is a Coulomb potential well of depth  $\sim m_\pi c^2/e$ . The constancy of the Klein potentials in the transition from the core to the crust, impose the presence of an overcritical electric field  $\sim (m_\pi/m_e)^2 E_c$ . For each central density, an entire family of core-crust interface boundaries can be constructed, each of them reaching the neutrality point at a different electron density at the edge of the crust. This leads consequently to crusts with masses and thickness smaller than the ones obtained from the traditional TOV treatment, resulting in a novel neutron star mass-radius relation.

The analysis of the properties of the core-crust interface, such as its surface and Coulomb energies, are being studied by Y. Wu, as part of his Ph. D. thesis. In particular, a generalization of the Bohr-Wheeler equilibrium condition for a macroscopic giant nucleus, as a neutron star, has been obtained. It has been shown that globally neutral neutron stars are stable against fission and that the optimal density for stability at the edge of the crust of the star is around  $\sim 10\rho_{\text{drip}}$ , where  $\rho_{\text{drip}} = 4.3 \times 10^{11} \text{ g cm}^{-3}$  is the so-called neutron-drip density.

The formulation and solution of the equilibrium equations of rotating neutron stars as well as their numerical integration are part of the Ph. D. thesis of K. Boshkayev and R. Belvedere (see App. C.5).

### 3.4. Neutron Star Physics with Gamma Ray Bursts

The progenitors and emission mechanisms leading to the most energetic radiation observed in astrophysics, the Gamma Ray Bursts (GRBs), are studied. Focus is given to the termed GRB-Supernova connection and to Short GRBs. The binary progenitors of these systems are studied in detail with particular

emphasis on the role played by neutron stars.

It is understood that the Supernovae (SNe) associated to Gamma Ray Bursts (GRBs) are of type Ib/c. However, the temporal coincidence of the GRB and the SN represents still a major enigma of Relativistic Astrophysics. A novel concept has been recently proposed for explaining the temporal coincidence of some Gamma Ray Bursts (GRBs) with an associated Supernova (SN) in terms of the gravitational collapse of a neutron star to a Black Hole (BH), induced by a type Ib/c SN explosion (see Rueda and Ruffini (2012b) and report of activities of the GRB group). There, based on the pioneer idea of Ruffini et al. (2008a), the specific case of a close (orbital period  $< 1$  h) binary system composed of an evolved star with a neutron star companion has been considered. We have computed in (Rueda and Ruffini, 2012b) the accretion rate onto the neutron star of the material expelled from the explosion of the core progenitor as a type Ib/c SN, and give the explicit expression of the accreted mass as a function of the nature of the components and binary parameters. We showed that the NS can reach, in a few seconds, the critical mass and consequently gravitationally collapses to a Black Hole. This gravitational collapse process leads to the emission of the GRB.

We have recently applied in (Izzo et al., 2012a) the above considerations to the case of GRB 090618 (see also report of activities of the GRB group), for which there is evidence of a SN  $\sim 10$  days after the GRB occurrence. We compute the progenitor binary parameters: the mass of the neutron star companion,  $M_{\text{NS}}$ , and the mass of the SN core progenitor,  $M_{\text{core}}$ , are in the following mass ranges:  $1.8 \lesssim M_{\text{NS}}/M_{\odot} \lesssim 2.1$  and  $3 \leq M_{\text{core}}/M_{\odot} \leq 8$ . We have also discussed in (Rueda and Ruffini, 2012b; Izzo et al., 2012a) the complementarity of these considerations to alternative processes explaining long and short GRBs.

It is clear that after the occurrence of the SN and the GRB emission, the outcome is represented, respectively, by a NS and a BH. A possible strong evidence of the NS formation is represented by the observation of a characteristic late ( $t = 10^8$ – $10^9$  s) X-ray emission that has been interpreted as originated by the young ( $t \sim 1$  minute–(10–100) years), hot ( $T \sim 10^7$ – $10^8$  K) NS, which we have called neo-NS (see Negreiros et al. (2012) and App. D.1, for details). This has been indeed observed in GRB 090618 (Izzo et al., 2012b) and also in GRB 101023 (Penacchioni et al., 2012). If the NS and the BH are gravitationally bound they give origin to a new kind of binary system, which can lead itself to the merging of the NS and the BH and consequently to a new process of gravitational collapse of the NS into the BH. In this case the system could originate a yet additional process of GRB emission and possibly a predominant emission in gravitational waves.

The traditional study of neutron star cooling has been generally applied to quite old objects as the Crab Pulsar (957 years) or the Central Compact Object in Cassiopeia A (330 years) with an observed surface temperature  $\sim 10^6$  K. However, as we just mentioned in GRB-SN systems there is possible evi-

dence of the cooling of neutron stars with surface temperatures  $\sim 10^7$ – $10^8$  K. The traditional thermal processes taking place in the neutron star crust might be enhanced by the extreme high temperature conditions of neo-neutron star and therefore the study of the thermal behavior especially of the crust of neo-neutron stars deserve the appropriate attention. This issue is part of the Ph. D. thesis of S. Martins de Carvalho. The influence of possible fallback accretion after the SN explosion is part of the Ph. D. thesis work of F. Gomes de Oliveira.

We now turn to the so-called short GRBs. The progress obtained from the Fermi-GBM and Konus-Wind satellites has been used to identify through the analysis of GRB 090227B (Muccino et al., 2012) the new class of genuinely short GRBs: short bursts with the same inner engine of the long GRBs but endowed with a severely low value of the baryon load,  $B \equiv M_B c^2 / E_{tot}^{GRB} \lesssim 5 \times 10^{-5}$ , where  $M_B$  is the mass of the baryons engulfed by the expanding ultrarelativistic  $e^+e^-$  plasma of energy  $E_{tot}^{GRB}$ . The emission from these GRBs mainly consists in a first emission, the peak GRB (P-GRB), followed by a softer emission squeezed on the first one. The typical separation between the two components is expected to be shorter than 1–10 ms.

A special case is GRB 090227B. From the 16 ms time-binned light curves a significant thermal emission in the first 96 ms, which has been identified with the P-GRB, has been found Muccino et al. (2012). The subsequent emission is identified with the extended afterglow. The P-GRB of 090227B has the highest temperature ever observed,  $k_B T = 517$  keV, where  $k_B$  is the Boltzmann constant. Other properties of the GRB have been computed, e.g. the total energy emitted  $E_{tot}^{GRB}$ , Baryon load  $B$ , Lorentz factor at transparency  $\Gamma_{tr}$ , cosmological redshift  $z$ , intrinsic duration of the GRB emission  $\Delta t$ , and average density of the CircumBurst Medium (CBM)  $\langle n_{CBM} \rangle$ ; we refer to Muccino et al. (2012) for further details.

These quantitative results lead to the conclusion that the progenitor of GRB 090227B is a neutron star binary: (1) the natal kicks velocities imparted to a neutron star binary at birth can be even larger than  $200 \text{ km s}^{-1}$  and therefore a binary system can runaway to the halo of its host galaxy, clearly pointing to a very low average number density of the CBM; (2) the very large total energy, which we can indeed infer in view of the absence of beaming, and the very short time scale of emission point again to a neutron star binary; (3) as we shall show below the very small value of the baryon load is strikingly consistent with two neutron stars having small crusts, in line with the recent neutron star theory Belvedere et al. (2012). This first identification of a genuinely short GRB has allowed us to compute for the first time the total energy release in form of gravitational waves from a neutron star binary merger that leads to the emission of a GRB (see Rueda and Ruffini (2012a) and App. D.2).

We refer for further details on the concept of induced gravitational collapse, the distinction between long and short GRBs, as well as the GRB-SN connection, to the report of the GRB group.

### **3.5. Emission-Radiation Mechanisms of White Dwarfs and Neutron Stars**

In this new topic, we are studying the possible emission mechanisms of white dwarfs and neutron stars. We are thus interested in the radiation generated in the magnetospheres of magnetized white dwarfs and neutron stars. Both energetics and spectrum of different radiation mechanisms operating in the magnetosphere of compact objects are analyzed and applied to the observations of white dwarfs and neutron star pulsars, Soft Gamma-Ray Repeaters (SGRs), X-ray pulsars (ordinary and anomalous), and other similar systems. This is one of the main fields of the Ph. D. work of D. Cáceres.

There are some preliminary results regarding the high-energy emission in X and Gamma rays from magnetized white dwarfs. It comes out that a massive ( $M \sim M_{\odot}$ ), fast rotating ( $P \sim 1$  s), highly magnetized ( $B \sim 10^8$  G), can emit persistent high-energy emission as a by-product of the pair-creation process in the magnetosphere. The positrons bombard the polar caps of the magnetosphere producing an X-ray emission with luminosities of the order of  $10^{35}$  erg s<sup>-1</sup>. This is in line with what observed in SGRs and AXPs and similar mechanisms are also at work in ordinary pulsars. We are currently preparing a manuscript with the first application of this work to some SGRs and AXPs.

### **3.6. Exact Solutions of the Einstein-Maxwell equations in Astrophysics**

We analyze the ability of analytic exact solutions of the Einstein-Maxwell equations to describe the exterior spacetime of compact stars like white dwarfs and neutron stars. The problem of matching between interior and exterior spacetimes is addressed in detail. The effect of the quadrupole moment on the properties of the spacetime is also investigated. Particular attention is given to the application of exact solutions in astrophysics, e.g. the dynamics of particles around compact stars and its relevance in astrophysical systems like X ray binaries.

Thus, whether analytic exact vacuum(electrovacuum) solutions of the Einstein(Einstein-Maxwell) field equations can accurately describe or not the exterior spacetime of compact stars remains still an interesting open question. As an attempt to establish their level of accuracy, the radii of the Innermost Stable Circular Orbits (ISCOs) of test particles given by analytic exterior spacetime geometries have been compared with the ones given by numerical solutions for neutron stars obeying a realistic equation of state. It has been so shown that the six-parametric solution of Pachón, Rueda, and Sanabria (2006) (hereafter PRS) is more accurate to describe the neutron star ISCO radii than

other analytic models.

In this line, Pachón et al. (2012) have recently proposed an additional test of accuracy for analytic exterior geometries based on the comparison of orbital frequencies of neutral test particles. The Keplerian, frame-dragging, as well as the precession and oscillation frequencies of the radial and vertical motions of neutral test particles for the Kerr and PRS geometries have been computed in (Pachón et al., 2012). Then, they were compared with the numerical values obtained by Morsink and Stella (1999) for realistic neutron stars. Contrary to what previously stated in the literature, it has been identified the role of high-order multipole moments such as the mass quadrupole and current octupole in the determination of the orbital frequencies, especially in the rapid rotation regime. These results are relevant to cast a separatrix between black holes and neutron star signatures as well as probe the nuclear matter equation of state and neutron star parameters from the Quasi-Periodic Oscillations (QPOs) observed in Low Mass X-Ray Binaries. We refer to (Pachón et al., 2012) and App. E.1, for further details.

### **3.7. Critical fields and Non Linear Electrodynamics Effects in Neutron Stars and Black Holes**

We turn now to a more theoretical topic: the effects of non-linear electrodynamics minimally coupled to gravity. We construct new analytic and numeric solutions to the Einstein-Maxwell equations representing black holes or the exterior field of a compact star. Some astrophysical applications are studied in detail e.g. the magnetosphere of a neutron star or the extractable energy of black holes and its role in the emission of Gamma Ray Bursts. This is part of the Ph. D. thesis of J. Pereira.



## 4. Publications (before 2012)

### 4.1. Refereed Journals

1. Jorge A. Rueda, R. Ruffini, and S.-S. Xue, *The Klein first integrals in an equilibrium system with electromagnetic, weak, strong and gravitational interactions*, Nuclear Physics A **872**, 286 (2011).
2. M. Rotondo, Jorge A. Rueda, R. Ruffini, S.-S. Xue, *Relativistic Feynman-Metropolis-Teller theory for white dwarfs in general relativity*, Phys. Rev. D **84**, 084007 (2011).
3. M. Rotondo, Jorge A. Rueda, R. Ruffini, S.-S. Xue, *The self-consistent general relativistic solution for a system of degenerate neutrons, protons and electrons in  $\beta$ -equilibrium*, Phys. Lett. B **701**, 667 (2011).
4. M. Rotondo, Jorge A. Rueda, R. Ruffini, S.-S. Xue, *Relativistic Thomas-Fermi treatment of compressed atoms and compressed nuclear matter cores of stellar dimensions*, Phys. Rev. C **83**, 045805 (2011).
5. M. Rotondo, R. Ruffini, S.-S. Xue, and V. S. Popov, *On Gravitationally and Electrodynamically Bound Nuclear Matter Cores of Stellar Dimensions*, Int. J. Mod. Phys. D **20**, 1995 (2011).
6. Jorge A. Rueda, R. Ruffini, *Towards a Relativistic Thomas-Fermi Theory of White Dwarfs and Neutron Stars*, Int. J. Mod. Phys. E **20**, 141 (2011).
7. K. Boshkayev, Jorge A. Rueda, R. Ruffini, *On the Maximum Mass of General Relativistic Uniformly Rotating White Dwarfs*, Int. J. Mod. Phys. E **20**, 136 (2011).
8. Jorge A. Rueda, M. Rotondo, R. Ruffini, S.-S. Xue, *On Compressed Nuclear Matter: from Nuclei to Neutron Stars*, Int. J. Mod. Phys. D **20**, 1789 (2011).
9. K. Boshkayev, Jorge A. Rueda, R. Ruffini, *On the Maximum Mass of General Relativistic Uniformly Rotating White Dwarfs*, Int. J. Mod. Phys. E **20**, 136 (2011).
10. Jorge A. Rueda, Michael Rotondo, Remo Ruffini, She-Sheng Xue, *A self-consistent approach to neutron stars*, J. Korean Phys. Soc. **57**, 560 (2010).

11. R. Ruffini, M. Rotondo and S.-S. Xue, *Electrodynamics for Nuclear Matter in Bulk*, Int. J. Mod. Phys. D **16**, 1 (2007).
12. R. Ruffini and L. Stella, *Some comments on the relativistic Thomas-Fermi model and the Vallarta-Rosen equation*, Phys. Lett. B **102**, 442 (1981).
13. J. Ferreira, R. Ruffini and L. Stella, *On the relativistic Thomas-Fermi model*, Phys. Lett. B **91**, 314 (1980).

## 4.2. Conference Proceedings

1. M. Malheiro, Jorge A. Rueda, R. Ruffini, *SGRs and AXPs: White Dwarf Pulsars versus Magnetars*, Proc. "The X-ray Universe 2011", Germany (2011).
2. R. Belvedere, Jorge A. Rueda, R. Ruffini, *Mass, Radius and Moment Of Inertia of Neutron Stars*, Proc. 2nd Ferrara Workshop on "X-ray Astrophysics up to 511 keV", Italy (2011).
3. S. Martins de Carvalho, C. Argüelles, Jorge A. Rueda, R. Ruffini, *SGRs and AXPs: White Dwarf Pulsars versus Magnetars*, Proc. "The X-ray Universe 2011", Germany (2011).
4. Jorge A. Rueda, M. Rotondo, R. Ruffini, and S.-S. Xue, *On the relativistic Feynman-Metropolis-Teller equation of state and general relativistic white-dwarfs*, Proceedings of Science, PoS(Texas2010), 269 (2011).
5. D. Pugliese, Jorge A. Rueda, R. Ruffini, and S.-S. Xue, *A general relativistic Thomas-Fermi treatment of neutron star cores*, Proceedings of Science, PoS(Texas 2010), 271 (2011).
6. R. Belvedere, *On the structure of the crust of neutron stars*, Proceedings of Science, PoS(Texas 2010), 270 (2011).
7. K. Boshkayev, *On the Stability of Rotating Nuclear Matter Cores of Stellar Dimensions*, Proceedings of Science, PoS(Texas 2010), 275 (2011).
8. K. Boshkayev, Jorge A. Rueda, and R. Ruffini, *On the minimum rotational period of fast rotating white dwarfs*, Proc. Erasmus Mundus IRAP PhD Workshop "From Nuclei to White Dwarfs to Neutron Stars", Eds. A. Mezzacappa, World Scientific (2011).
9. Jorge A. Rueda, D. Pugliese, M. Rotondo, R. Ruffini, S.-S. Xue, *A general relativistic Thomas-Fermi treatment of neutron stars cores I. The case of non-interacting particles*, Proc. 2nd Galileo-Xu Guangqi Meeting, Italy (2010).

10. Jorge A. Rueda, D. Pugliese, M. Rotondo, R. Ruffini, S.-S. Xue, *A general relativistic Thomas-Fermi treatment of neutron stars cores II. Generalized Fermi energies and beta equilibrium in the strongly interacting case*, Proc. 2nd Galileo-Xu Guangqi Meeting, Italy (2010).
11. K. Boshkayev, M. Rotondo, and R. Ruffini, *On Magnetic Fields in Rotating Nuclear Matter Cores of Stellar Dimensions*, Proc. 2nd Galileo-Xu Guangqi Meeting, Italy (2010).
12. R. Mohammadi, Jorge A. Rueda, R. Ruffini, and S.-S. Xue, *The solution of the Thomas-Fermi equation in the presence of strong magnetic fields*, Proc. 2nd Galileo-Xu Guangqi Meeting, Italy (2010).
13. Jorge A. Rueda, R. Ruffini, S.-S. Xue, *On the electrostatic structure of neutron stars*, AIP Conf. Proc. 1205, 143 (2010).
14. Jorge A. Rueda H., B. Patricelli, M. Rotondo, R. Ruffini, S.-S. Xue, *The Extended Nuclear Matter Model with Smooth Transition Surface*, Proc. 3rd Stueckelberg Workshop on Relativistic Field Theories, Italy (2008).
15. B. Patricelli, J. A. Rueda H., R. Ruffini *On the Crust of Neutron Stars*, Proc. 3rd Stueckelberg Workshop on Relativistic Field Theories, Pescara, Italy (2008).
16. R. Ruffini, M. Rotondo and S.-S. Xue, *Neutral nuclear core vs super charged one*, Proc. 11th Marcel Grossmann Meeting, Eds. R. Jantzen, H. Kleinert, R. Ruffini, World Scientific, Singapore (2008).
17. B. Patricelli, M. Rotondo and R. Ruffini, *On the Charge to Mass Ratio of Neutron Cores and Heavy Nuclei*, AIP Conf. Proc. **966**, 143 (2008).
18. M. Rotondo, R. Ruffini and S.-S. Xue, *On the Electrodynamical properties of Nuclear matter in bulk*, AIP Conf. Proc. **966**, 147 (2008).
19. B. Patricelli, M. Rotondo, J. A. Rueda H. and R. Ruffini, *The Electrodynamics of the Core and the Crust components in Neutron Stars*, AIP Conf. Proc. **1059**, 68 (2008).
20. R. Ruffini, *The Role of Thomas-Fermi approach in Neutron Star Matter*, Proceedings of the 9<sup>th</sup> International Conference "Path Integrals-New trends and perspectives", Eds. W. Janke and A. Pelster, World Scientific, Singapore (2008).
21. R. Ruffini, M. Rotondo, S.-S. Xue, *The Thomas-Fermi Approach and Gamma-Ray Bursts*, AIP Conf. Proc. **1053**, 243 (2008).

22. Jorge A. Rueda, B. Patricelli, M. Rotondo, R. Ruffini, and S. S. Xue, *The Extended Nuclear Matter Model with Smooth Transition Surface*, Proc. 3rd Stueckelberg Workshop on Relativistic Field Theories, Italy (2008).

# 5. Publications 2012

## 5.1. Refereed Journals

1. R. Belvedere, K. Boshkayev, Jorge A. Rueda, R. Ruffini, *On globally neutral uniformly rotating neutron stars*, to be submitted.
2. Jorge A. Rueda, G. Aznar-Siguán, K. Boshkayev, E. García-Berro, L. Izzo, P. Lorén-Aguilar, R. Ruffini, *White Dwarf Binaries as the Progenitors of SGRs and AXPs: the case of 4U 0142+61*, to be submitted.
3. K. Boshkayev, L. Izzo, Jorge A. Rueda, R. Ruffini, *SGR 0418+5729 and Swift J1822.3-1606 as massive fast rotating highly magnetic white dwarfs*, to be submitted.
4. J. Pereira, H. Mosquera-Cuesta, Jorge A. Rueda, R. Ruffini, *The mass-formula of black holes in general relativity minimally coupled to non-linear electrodynamics*, to be submitted.
5. R. Mohammadi, Jorge A. Rueda, R. Ruffini, S-S. Xue, *The relativistic Thomas-Fermi equation in presence of strong magnetic fields*, to be submitted.
6. S. Martins de Carvalho, Jorge A. Rueda, R. Ruffini, *The relativistic Feynman-Metropolis-Teller equation of state at finite temperatures*, to be submitted.
7. S. Martins de Carvalho, Jorge A. Rueda, R. Ruffini, *On the mass-radius relation of general relativistic white dwarfs at finite temperatures*, to be submitted.
8. Jorge A. Rueda, R. Ruffini, *Gravitational waves versus electromagnetic emission in Gamma-Ray Bursts*, to be submitted; arXiv:1205.6915.
9. K. Boshkayev, Jorge A. Rueda, R. Ruffini, I. Siutsou, *On general relativistic uniformly rotating white dwarfs*, *Astroph. J.* (2012), in press; arXiv:1204.2070.
10. Jorge A. Rueda, R. Ruffini, *On the general relativistic Thomas-Fermi theory of white dwarfs and neutron stars*, *Il Nuovo Cimento C* (2012); in press.
11. Jorge A. Rueda, R. Ruffini, *On the Einstein-Maxwell-Thomas-Fermi equations for white dwarfs and neutron stars*, *Int. J. Mod. Phys. D* (2012); in press.

12. Jorge A. Rueda, R. Ruffini, *From nuclei to white dwarfs to neutron stars*, Int. J. Mod. Phys. D (2012); in press.
13. Jorge A. Rueda, R. Ruffini, *Fundamental interactions in neutron stars*, Int. J. Mod. Phys. D (2012), in press.
14. L. Izzo, Jorge A. Rueda, R. Ruffini, *GRB 090618: a Candidate of a Neutron Star Gravitational Collapse to a Black Hole Induced by a Type Ib/c Supernova*, A&A, 548, L5 (2012).
15. Jorge A. Rueda, R. Ruffini, *On the Induced Gravitational Collapse of a Neutron Star to a Black Hole by a Type Ib/c Supernova*, Astroph. J **758**, L7 (2012).
16. L. A. Pachón, Jorge A. Rueda, C. Valenzuela, *On the relativistic precession and oscillation frequencies of test particles around rapidly rotating compact stars*, Astroph. J. **756**, 82 (2012).
17. M. Malheiro, Jorge A. Rueda, R. Ruffini, *SGRs and AXPs as rotation-powered massive white dwarfs*, Publ. Astron. Soc. Japan **64**, 56 (2012).
18. R. Belvedere, D. Pugliese, Jorge A. Rueda, R. Ruffini, S.-S. Xue, *Neutron star equilibrium configurations within a fully relativistic theory with strong, weak, electromagnetic, and gravitational interactions*, Nucl. Phys. A **883**, 1 (2012).
19. R. Negreiros, C. L. Bianco, Jorge A. Rueda, R. Ruffini, *Cooling of young neutron stars in GRB associated to supernovae*, A&A **540**, A12 (2012).

## 5.2. Conference Proceedings

1. R. Belvedere, Jorge A. Rueda, R. Ruffini, S.-S. Xue *Neutron star equilibrium configurations within a fully relativistic theory with strong, weak, electromagnetic, and gravitational interactions*, Current Issues on Relativistic Astrophysics, South Korea (2012).
2. K. Boshkayev, Jorge A. Rueda, R. Ruffini, *SGRs and AXPs AXPs as Massive Fast Rotating Highly Magnetized White Dwarfs*, Current Issues on Relativistic Astrophysics, South Korea (2012).
3. S. Martins de Carvalho, Jorge A. Rueda, R. Ruffini, *On the relativistic Feynman-Metropolis-Teller equation of state at finite temperatures and low-mass white dwarfs*, Current Issues on Relativistic Astrophysics, South Korea (2012).
4. Jorge A. Rueda, R. Ruffini, *Fundamental interactions in neutron stars*, 13th Marcel Grossmann Meeting, Sweden (2012).

5. S. Martins de Carvalho, Jorge A. Rueda, R. Ruffini, *On the relativistic Feynman-Metropolis-Teller equation of state at finite temperatures and low-mass white dwarfs*, 13th Marcel Grossmann Meeting, Sweden (2012).
6. K. Boshkayev, Jorge A. Rueda, R. Ruffini, *SGRs and AXPs as Massive Fast Rotating Highly Magnetized White Dwarfs: Bounds on the Mass, Moment of Inertia and Magnetic Fields*, 13th Marcel Grossmann Meeting, Sweden (2012).
7. K. Boshkayev, Jorge A. Rueda, R. Ruffini, *On General Relativistic Uniformly Rotating White Dwarfs*, 13th Marcel Grossmann Meeting, Sweden (2012).
8. R. Belvedere, Jorge A. Rueda, R. Ruffini, S.-S. Xue *Neutron star equilibrium configurations within a fully relativistic theory with strong, weak, electromagnetic, and gravitational interactions*, 13th Marcel Grossmann Meeting, Sweden (2012).
9. Jorge A. Rueda, *SGRs and AXPs as massive fast rotating highly magnetized white dwarfs*, 39th COSPAR Scientific Assembly, India (2012).
10. K. Boshkayev, *Fast Rotating White Dwarfs as Precursors of Type Ia supernovae and Millisecond Pulsars*, 39th COSPAR Scientific Assembly, India (2012).
11. R. Belvedere, Jorge A. Rueda, R. Ruffini, *Moment of inertia, radii, surface emission from a new theoretical understanding of Neutron Stars*, 39th COSPAR Scientific Assembly, India (2012).
12. K. Boshkayev, Jorge A. Rueda, R. Ruffini, *Rotating white dwarfs and their stability*, CompStar: the physics and astrophysics of compact stars, Tahiti (2012).
13. R. Belvedere, Jorge A. Rueda, R. Ruffini, *Neutron star equilibrium configurations within a fully relativistic theory with strong, weak, electromagnetic, and gravitational interactions*, CompStar: the physics and astrophysics of compact stars, Tahiti (2012).
14. K. Boshkayev, Jorge A. Rueda, R. Ruffini, *Stability of Rotating Nuclear Matter Cores of Stellar Dimensions*, CompStar: Equation of State for Compact Star Interiors and Supernovae, Croatia (2012).
15. R. Belvedere, Jorge A. Rueda, R. Ruffini, *Neutron star equilibrium configurations*, CompStar: Equation of State for Compact Star Interiors and Supernovae, Croatia (2012).

16. M. Rotondo, Jorge A. Rueda, R. Ruffini, S.-S. Xue, *On Degenerate Compressed Atoms and Compressed Nuclear Matter Cores of Stellar Dimensions*, Int. J. Mod. Phys. Conf. S. **12**, 203 (2012).
17. K. Boshkayev, M. Rotondo, R. Ruffini, *On Magnetic Fields in Rotating Nuclear Matter Cores of Stellar Dimensions*, Int. J. Mod. Phys.: Conf. S. **12**, 58 (2012).
18. Jorge A. Rueda, R. Ruffini, S.-S. Xue, *Electrostatic Configurations Crossover Neutron Star Core*, Proc. 12th Marcel Grossmann Meeting, 1042 (2012).
19. Jorge A. Rueda, M. Rotondo, R. Ruffini, S.-S. Xue, *A New Family of Neutron Star Models: Global Neutrality versus Local Neutrality*, Proc. 12th Marcel Grossmann Meeting, 1039 (2012).
20. M. Rotondo, Jorge A. Rueda, R. Ruffini, S.-S. Xue, *From Compressed Atoms to Compressed Massive Nuclear Density Cores*, Proc. 12th Marcel Grossmann Meeting, 1036 (2012).

## 6. Attended Meetings and Conferences

1. 3rd Colombian Meeting of Astronomy and Astrophysics, November 5–9, 2012 Bucaramanga (Colombia).
2. Current Issues on Relativistic Astrophysics, November 5–6, 2012 Seoul (South Korea).
3. CompStar: Equation of State for Compact Star Interiors and Supernovae, September 24–28, 2012 Zadar (Croatia).
4. IRAP Ph. D. Erasmus Mundus School, September 3–21, 2012 Nice (France).
5. CompStar: the physics and astrophysics of compact stars, June 4–8, 2012 Tahiti (French Polynesia).
6. 39th COSPAR Scientific Assembly, July 14–22, 2012 Mysore (India).
7. 13th Marcel Grossmann Meeting, July 1–7, 2012 Stockholm (Sweden).



## 7. APPENDICES



# A. Nuclear and Atomic Astrophysics

## A.1. On gravitationally and electrodynamically bound massive nuclear density cores

### A.1.1. Introduction

Models involving  $e^+e^-$  plasmas of total energy  $\leq 10^{55}$  ergs originating from a vacuum polarization process during the formation of a black hole are being studied to explain a variety of ultra-relativistic astrophysics events (Ruffini et al., 2010b; Cherubini et al., 2009; Aksenov et al., 2007). The formation of such a Kerr-Newman black hole with overcritical electromagnetic fields can only occur during the process of gravitational collapse, e.g., of two coalescing neutron stars. Accordingly in this article we consider new electrodynamical properties of massive nuclear density cores which have been neglected in the astrophysics literature. This issue has been overlooked in the traditional description of neutron stars by considering only neutrons (Oppenheimer and Volkoff, 1939) or by imposing *ab initio* local charge neutrality, i.e., local identity of the densities of protons and electrons  $n_p = n_e$ , thus bypassing the description of any possible electrodynamical effect (Harrison et al., 1965; Baym et al., 1971a).

The model we consider here generalizes the relativistic Thomas-Fermi treatment for neutral atoms with heavy nuclei (Pieper and Greiner, 1969; Müller et al., 1972; Greenberg and Greiner, 1982; Popov, 1971b; Zeldovich and Popov, 1972; Migdal et al., 1976). The study of neutral atoms with nuclei of mass number  $A \sim 10^2$ – $10^6$  is a classic problem of theoretical physics (Zeldovich and Popov, 1972; Ruffini et al., 2010b). Special attention has been given to a possible vacuum polarization process and the creation of  $e^+e^-$  pairs (Pieper and Greiner, 1969; Zeldovich and Popov, 1972; Ruffini et al., 2010b) as well as to the study of nuclear stability against Coulomb repulsion (Greenberg and Greiner, 1982). The existence of electric fields larger than the critical value  $E_c = m_e^2 c^3 / (e\hbar)$  near their surfaces (Popov, 1971b) has also been shown. We have generalized these models by enforcing the beta equilibrium conditions (Ruffini et al., 2007b).

We have then extrapolated those results by numerical integration to the case of massive nuclear density cores of mass  $\approx 1M_\odot$  and radius  $R_c \approx 10$  km

(Ruffini et al., 2007b). Such a massive nuclear density core is a globally neutral system of  $N_n$  neutrons,  $N_p$  protons and  $N_e$  electrons in beta equilibrium at nuclear density having mass numbers  $A \sim (m_{\text{Planck}}/m_n)^3$  where  $m_n$  ( $m_e$ ) is the neutron (electron) mass and  $m_{\text{Planck}} = (\hbar c/G)^{1/2}$  (Ruffini et al., 2007b). As in the nuclear model (Migdal et al., 1976), the proton distribution is here assumed to be constant up to the core radius  $R_c$ . We have obtained configurations with global charge neutrality  $N_p = N_e$  but  $n_p \neq n_e$ , in contrast with the local condition  $n_p = n_e$  traditionally assumed in astrophysics. As a result electric fields of critical value are confirmed to exist, near the surface, also in the case of massive nuclear density cores in analogy to the case of heavy nuclei.

Recently a new dimensionless form of the relativistic Thomas-Fermi treatment for a nuclear density core has been obtained which reveals the existence of new scaling laws for this model.

In this article we present a unified treatment extending from heavy nuclei to massive nuclear density cores by using an explicit analytic solitonic solution of the new dimensionless form of the relativistic Thomas-Fermi equation. We confirm the existence of and give an analytic expression for the overcritical electric field near the surface of massive nuclear density cores already obtained in (Ruffini et al., 2007b) by numerical integration. Furthermore there are a variety of new results made possible by the new analytic formulation. First we give an explicit expression for the Coulomb energy of such cores, demonstrating their stability against nuclear fission, as opposed to the case of heavy nuclei. Secondly on the basis of Newtonian gravitational energy considerations we propose the existence of a possible new island of stability for mass numbers  $A > A_R = 0.039 \left(\frac{N_p}{A}\right)^{1/2} \left(\frac{m_{\text{Planck}}}{m_n}\right)^3$ . The equilibrium against Coulomb repulsion originates now from the combined effect of the screening of the relativistic electrons, of the surface tension due to strong interactions and of the gravitational interaction of the massive dense cores. By enforcing the condition of beta equilibrium, we also obtain a generalized relation between the mass number  $A$  and atomic number  $N_p$  which encompasses previous phenomenological expressions.

All the above solutions have been obtained assuming the electron Fermi energy to be equal to zero. The necessity and the methodology of extending these results to the case of compressed atoms along the lines of the Feynman-Metropolis-Teller treatment (Feynman et al., 1949), corresponding to positive values of the Fermi energy of electrons, are outlined here. We also motivate the clear necessity and the general methodology of justifying the above results using a self-consistent general relativistic treatment of the system. These ideas will be pursued in detail elsewhere.

### A.1.2. The relativistic Thomas-Fermi equation and the beta equilibrium condition

It has been known since the classic work of Fermi (Fermi, 1950) that the phenomenological drop model of the nucleus gives excellent results for a variety of properties including the isobaric behavior and nuclear fission. In addition to the masses of the baryonic components and the asymmetry energy and pairing term, the mass formula contains terms estimating the surface tension energy of the nucleus (Fermi, 1950)

$$\varepsilon_s = 17.5 \cdot A^{2/3} \text{ MeV}, \quad (\text{A.1.1})$$

and the Coulomb energy (Fermi, 1950)

$$\varepsilon_c = \frac{3\alpha N_p^2}{5R_c}, \quad (\text{A.1.2})$$

where  $R_c = r_0 A^{1/3}$ ,  $r_0 = 1.5 \cdot 10^{-13}$  cm and the numerical factors are derived by fitting the observational data. From the extremization of the mass formula the following relation between  $A$  and  $N_p$  is obtained (Fermi, 1950)

$$N_p \simeq \left[ \frac{2}{A} + \frac{3}{200} \frac{1}{A^{1/3}} \right]^{-1}, \quad (\text{A.1.3})$$

which in the limit of small  $A$  gives

$$N_p \simeq \frac{A}{2}. \quad (\text{A.1.4})$$

The analysis of the stability of the nucleus against finite deformation leads to a stability condition against fission given by the equality of the surface energy term to the Coulomb energy. This leads to the condition (Fermi, 1950)

$$\frac{N_p^2}{A} < 45. \quad (\text{A.1.5})$$

A novel situation occurs when super-heavy nuclei ( $A > \tilde{A} \sim 10^4$ ) are examined (Ferreirinho et al., 1980; Ruffini et al., 2007b). The distribution of electrons penetrates inside the nucleus: a much smaller effective net charge of the nucleus occurs due to the screening of relativistic electrons (Migdal et al., 1976; Ferreira et al., 1980). In Ruffini and Stella (1981) a definition of an effective nuclear charge due to the penetration of the electrons was presented. A treatment based on the relativistic Thomas-Fermi model has been developed in order to describe the penetration of the electrons and their effective screening of the positive nuclear charge. In particular, by assuming

$N_p \simeq A/2$ , Pieper and Greiner (1969); Müller et al. (1972); Greenberg and Greiner (1982) and Popov (1971b); Zeldovich and Popov (1972); Migdal et al. (1976) in a series of papers were able to solve the non-linear Thomas-Fermi equation. It was demonstrated in Migdal et al. (1976) that the effective positive nuclear charge is confined to a small layer of thickness  $\sim \hbar/\sqrt{\alpha}m_\pi c$  where  $m_\pi$  is the pion mass and as usual  $\alpha = e^2/\hbar c$ . Correspondingly electric fields of strength much larger than the critical value  $E_c$  for vacuum polarization at the surface of the core are created. However, the creation of electron-positron pairs due to the vacuum polarization process does not occur because of the Pauli blocking by the degenerate electrons Ruffini et al. (2010b).

Here we generalize the work of Pieper and Greiner (1969); Müller et al. (1972); Greenberg and Greiner (1982) and Popov (1971b); Zeldovich and Popov (1972); Migdal et al. (1976). We have relaxed the condition  $N_p \simeq A/2$  adopted by Popov and Greiner as well as the condition  $N_p \simeq [2/A + 3/200A^{1/3}]^{-1}$  adopted by Ferreira et al. (1980). Instead we explicitly impose the beta decay equilibrium between neutrons, protons and electrons. We then extrapolate such model to the case  $A \approx (m_{\text{Planck}}/m_n)^3 \sim 10^{57}$ . A supercritical field still exists in a shell of thickness  $\sim \hbar/\sqrt{\alpha}m_\pi c$  at the core surface, and a charged lepton-baryonic core is surrounded by an oppositely charged leptonic component. Such massive nuclear density cores, including the leptonic component, are globally neutral.

As usual we assume that the protons are distributed at constant density  $n_p$  within a radius

$$R_c = \Delta \frac{\hbar}{m_\pi c} N_p^{1/3}, \quad (\text{A.1.6})$$

where  $\Delta$  is a parameter such that  $\Delta \approx 1$  ( $\Delta < 1$ ) corresponds to nuclear (supranuclear) densities when applied to ordinary nuclei. The overall Coulomb potential satisfies the Poisson equation

$$\nabla^2 V(r) = -4\pi e [n_p(r) - n_e(r)], \quad (\text{A.1.7})$$

with the boundary conditions  $V(\infty) = 0$  (due to the global charge neutrality of the system) and finiteness of  $V(0)$ . The density  $n_e(r)$  of the electrons of charge  $-e$  is determined by the Fermi energy condition on their Fermi momentum  $P_e^F$ ; we assume here

$$E_e^F = [(P_e^F c)^2 + m_e^2 c^4]^{1/2} - m_e c^2 - eV(r) = 0, \quad (\text{A.1.8})$$

which leads to

$$n_e(r) = \frac{(P_e^F)^3}{3\pi^2 \hbar^3} = \frac{1}{3\pi^2 \hbar^3 c^3} \left[ e^2 V^2(r) + 2m_e c^2 eV(r) \right]^{3/2}. \quad (\text{A.1.9})$$

By introducing  $x = r/[\hbar/m_\pi c]$ ,  $x_c = R_c/[\hbar/m_\pi c]$  and  $\chi/r = eV(r)/c\hbar$ , the relativistic Thomas-Fermi equation takes the form

$$\frac{1}{3x} \frac{d^2\chi(x)}{dx^2} = -\frac{\alpha}{\Delta^3} \theta(x_c - x) + \frac{4\alpha}{9\pi} \left[ \frac{\chi^2(x)}{x^2} + 2 \frac{m_e \chi}{m_\pi x} \right]^{3/2}, \quad (\text{A.1.10})$$

where  $\chi(0) = 0, \chi(\infty) = 0$ . The neutron density  $n_n(r)$  is determined by the Fermi energy condition on their Fermi momentum  $P_n^F$  imposed by beta decay equilibrium

$$\begin{aligned} E_n^F &= [(P_n^F c)^2 + m_n^2 c^4]^{1/2} - m_n c^2 \\ &= [(P_p^F c)^2 + m_p^2 c^4]^{1/2} - m_p c^2 + eV(r), \end{aligned} \quad (\text{A.1.11})$$

which in turn is related to the proton and electron densities by Eqs. (A.1.7), (A.1.9) and (A.1.10). These equations have been integrated numerically (see Ruffini et al. (2007b)).

### A.1.3. The ultra-relativistic analytic solutions

In the ultrarelativistic limit, the relativistic Thomas-Fermi equation admits an analytic solution. Introducing the new function  $\phi$  defined by  $\phi = \frac{4^{1/3}}{(9\pi)^{1/3}} \Delta \frac{\chi}{x}$  and the new variables  $\hat{x} = (12/\pi)^{1/6} \sqrt{\alpha} \Delta^{-1} x$ ,  $\xi = \hat{x} - \hat{x}_c$ , where  $\hat{x}_c = (12/\pi)^{1/6} \sqrt{\alpha} \Delta^{-1} x_c$ , then Eq. (A.1.10) becomes

$$\frac{d^2 \hat{\phi}(\xi)}{d\xi^2} = -\theta(-\xi) + \hat{\phi}(\xi)^3, \quad (\text{A.1.12})$$

where  $\hat{\phi}(\xi) = \phi(\xi + \hat{x}_c)$ . The boundary conditions on  $\hat{\phi}$  are:  $\hat{\phi}(\xi) \rightarrow 1$  as  $\xi \rightarrow -\hat{x}_c \ll 0$  (at the massive nuclear density core center) and  $\hat{\phi}(\xi) \rightarrow 0$  as  $\xi \rightarrow \infty$ . The function  $\hat{\phi}$  and its first derivative  $\hat{\phi}'$  must be continuous at the surface  $\xi = 0$  of the massive nuclear density core. Equation (A.1.12) admits an exact solution

$$\hat{\phi}(\xi) = \begin{cases} 1 - 3 \left[ 1 + 2^{-1/2} \sinh(a - \sqrt{3}\xi) \right]^{-1}, & \xi < 0, \\ \frac{\sqrt{2}}{(\xi + b)}, & \xi > 0, \end{cases} \quad (\text{A.1.13})$$

where the integration constants  $a$  and  $b$  have the values  $a = \text{arcsinh}(11\sqrt{2}) \approx 3.439$ ,  $b = (4/3)\sqrt{2} \approx 1.886$ . Next we evaluate the Coulomb potential energy

function

$$eV(\xi) = \left(\frac{9\pi}{4}\right)^{1/3} \frac{1}{\Delta} m_\pi c^2 \hat{\phi}(\xi), \quad (\text{A.1.14})$$

and by differentiation, the electric field

$$E(\xi) = - \left(\frac{3^5\pi}{4}\right)^{1/6} \frac{\sqrt{\alpha} m_\pi^2 c^3}{\Delta^2 e\hbar} \hat{\phi}'(\xi). \quad (\text{A.1.15})$$

Details are given in Figs. A.1 and A.2.

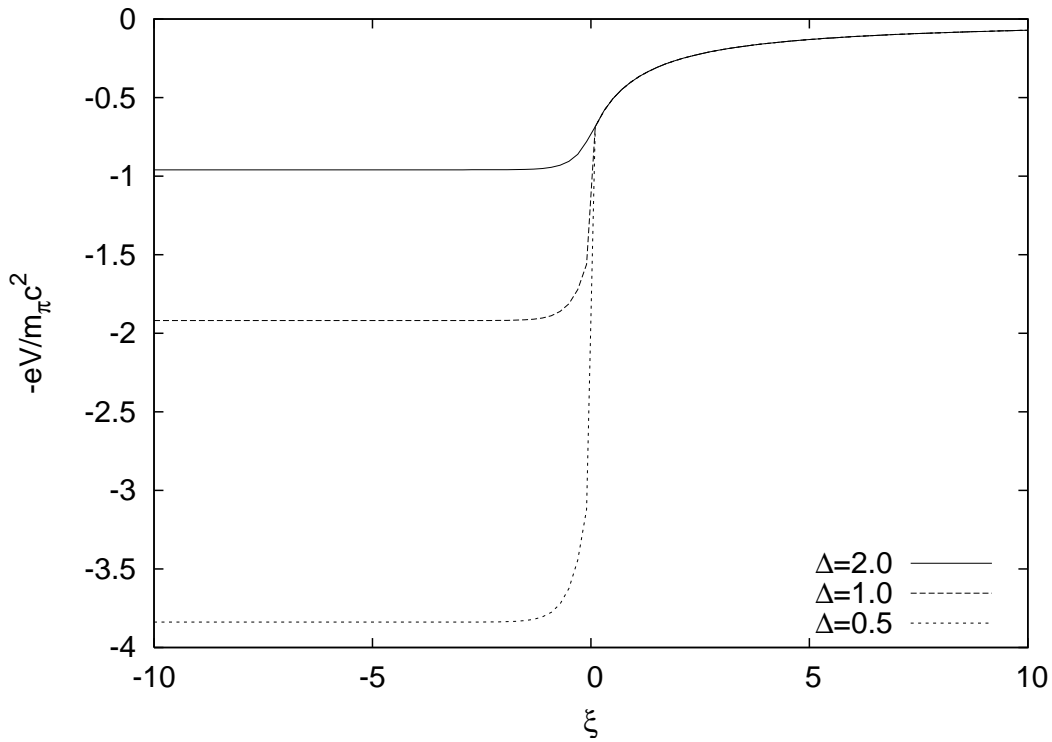


**Figure A.1.:** The electron Coulomb potential energy  $-eV$ , in units of pion mass  $m_\pi$  is plotted as a function of the radial coordinate  $\xi = \hat{x} - \hat{x}_c$ , for selected values of the density parameter  $\Delta$ .

We now estimate three crucial quantities:

1) the Coulomb potential at the center of the configuration,

$$eV(0) \approx \left(\frac{9\pi}{4}\right)^{1/3} \frac{1}{\Delta} m_\pi c^2, \quad (\text{A.1.16})$$

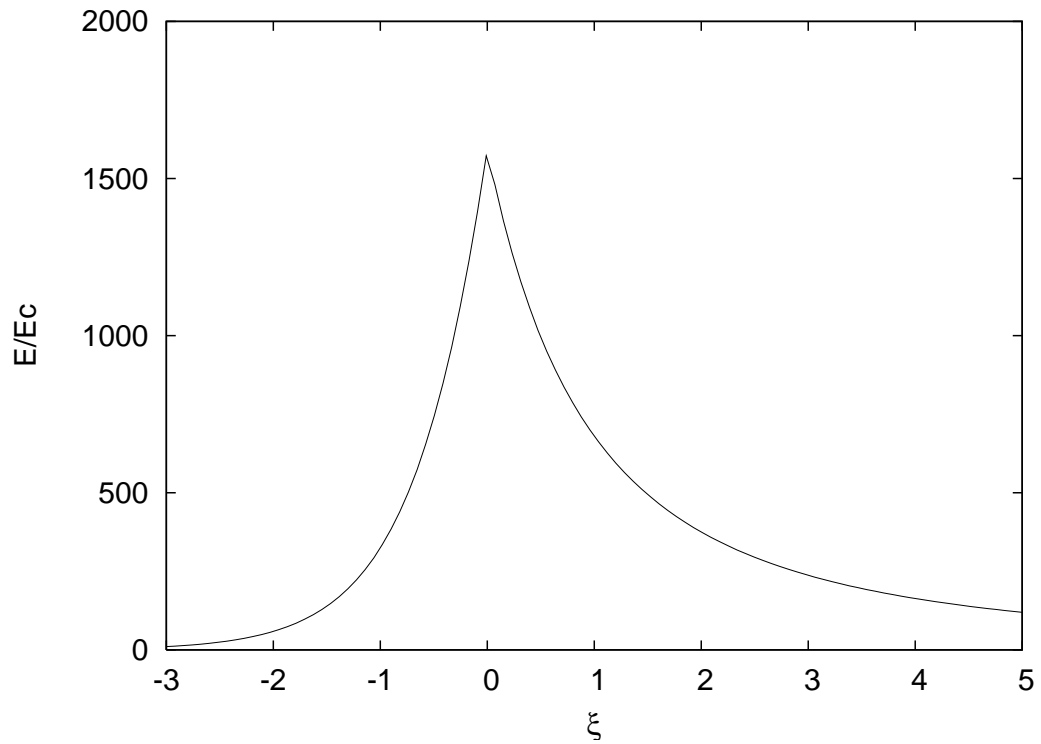


**Figure A.2.:** The electric field is plotted in units of the critical field  $E_c$  as a function of the radial coordinate  $\xi$  for  $\Delta=2$ , showing a sharp peak at the core radius.

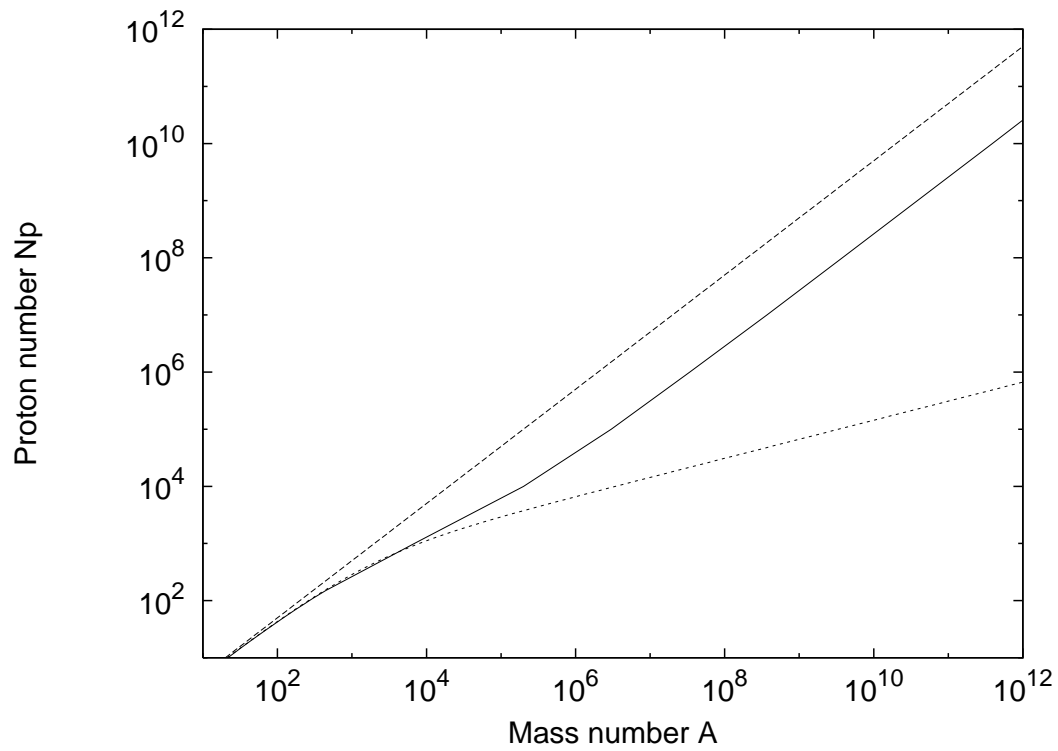


**Figure A.3.:** The  $A$ - $N_p$  relation at nuclear density (solid line) obtained from first principles compared with the phenomenological expressions given by  $N_p \simeq A/2$  (dashed line) and Eq. (A.1.3) (dotted line). The asymptotic value, for  $A \rightarrow (m_{\text{Planck}}/m_n)^3$ , is  $N_p \approx 0.0046A$ .

2) the electric field at the surface of the core

$$E_{\max} \approx 0.95\sqrt{\alpha}\frac{1}{\Delta^2}\frac{m_\pi^2 c^3}{e\hbar} = 0.95\frac{\sqrt{\alpha}}{\Delta^2}\left(\frac{m_\pi}{m_e}\right)^2 E_c. \quad (\text{A.1.17})$$

3) the Coulomb electrostatic energy of the core

$$\mathcal{E}_{\text{em}} = \int \frac{E^2}{8\pi} d^3r \approx 0.15\frac{3\hbar c(3\pi)^{1/2}}{4\Delta\sqrt{\alpha}}A^{2/3}\frac{m_\pi c}{\hbar}\left(\frac{N_p}{A}\right)^{2/3}. \quad (\text{A.1.18})$$

These three quantities are functions only of the pion mass  $m_\pi$ , the density parameter  $\Delta$  and of the fine structure constant  $\alpha$ . Their formulas apply over the entire range from superheavy nuclei with  $N_p \sim 10^3$  all the way up to massive cores with  $N_p \approx (m_{\text{Planck}}/m_n)^3$ .

#### A.1.4. New results derived from the analytic solutions

Starting from the analytic solutions of the previous section we obtain the following new results.

**a)** Using the solution (A.1.13), we have obtained a new generalized relation between  $A$  and  $N_p$  for any value of  $A$ . In the limit of small  $A$  this result agrees well with the phenomenological relations given by Eqs. (A.1.3) and (A.1.4), as is clearly shown in Fig. A.3. It appears that the explicit evaluation of the beta equilibrium, in contrast with the previously adopted Eqs.(3,4), leads to an effect comparable in magnitude and qualitatively similar to the asymmetry energy in the phenomenological liquid drop model.

**b)** The charge-to-mass ratio of the effective charge  $Q$  at the core surface to the core mass  $M$  is given by

$$\frac{Q}{\sqrt{GM}} \approx \frac{E_{\max}R_c^2}{\sqrt{G}m_n A} \approx \frac{m_{\text{Planck}}}{m_n}\left(\frac{1}{N_p}\right)^{1/3}\frac{N_p}{A}. \quad (\text{A.1.19})$$

For superheavy nuclei with  $N_p \approx 10^3$ , the charge-to-mass ratio for the nucleus is

$$\frac{Q}{\sqrt{GM}} > \frac{1}{20}\frac{m_{\text{Planck}}}{m_n} \sim 10^{18}. \quad (\text{A.1.20})$$

Gravitation obviously plays no role in the stabilization of these nuclei.

Instead for massive nuclear density cores where  $N_p \approx (m_{\text{Planck}}/m_n)^3$ , the ratio  $Q/\sqrt{GM}$  given by Eq. (A.1.19) is simply

$$\frac{Q}{\sqrt{GM}} \approx \frac{N_p}{A}, \quad (\text{A.1.21})$$

which is approximately 0.0046 (see Fig. A.3). It is well-known that the charge-to-mass ratio (A.1.21) smaller than 1 evidences the equilibrium of self-gravitating mass-charge system both in Newtonian gravity and general relativity (see, e.g., Chandrasekhar (1992)).

c) For a massive core at nuclear density the criterion of stability against fission ( $\mathcal{E}_{em} < 2\mathcal{E}_s$ ) is satisfied. In order to see this we use Eqs. (A.1.1) and (A.1.18)

$$\frac{\mathcal{E}_{em}}{2\mathcal{E}_s} \approx 0.15 \frac{3}{8} \sqrt{\frac{3\pi}{\alpha}} \frac{1}{\Delta} \left( \frac{N_p}{A} \right)^{2/3} \frac{m_\pi c^2}{17.5 \text{ MeV}} \sim 0.1 < 1. \quad (\text{A.1.22})$$

### A.1.5. Estimates of gravitational effects in a Newtonian approximation

In order to investigate the possible effects of gravitation on these massive neutron density cores we proceed to some qualitative and quantitative estimates based on the Newtonian approximation.

a) The *maximum* Coulomb energy per proton is given by Eq. (A.1.16) where the potential is evaluated at the center of the core. The Newtonian gravitational potential energy per proton (of mass  $m_p$ ) in the field of a massive nuclear density core with  $A \approx (m_{\text{Planck}}/m_n)^3$  is given by

$$\mathcal{E}_g = -G \frac{M m_p}{R_c} = -\frac{1}{\Delta} \frac{m_{\text{Planck}}}{m_n} \frac{m_\pi c^2}{N_p^{1/3}} \simeq -\frac{m_\pi c^2}{\Delta} \left( \frac{A}{N_p} \right)^{1/3}. \quad (\text{A.1.23})$$

Since  $A/N_p \sim 0.0046$  (see Fig. A.3) for any value of  $\Delta$ , the gravitational energy is larger in magnitude than and opposite in sign to the Coulomb potential energy per proton of Eq. (A.1.16) so the system should be gravitationally stable.

b) There is yet a more accurate derivation of the gravitational stability based on the analytic solution of the Thomas-Fermi equation Eq. (A.1.12). The Coulomb energy  $\mathcal{E}_{em}$  given by (A.1.18) is mainly distributed within a thin shell of width  $\delta R_c \approx \hbar \Delta / (\sqrt{\alpha} m_\pi c)$  and proton number  $\delta N_p = n_p 4\pi R_c^2 \delta R_c$  at the surface. To ensure the stability of the system, the attractive gravitational energy of the thin proton shell

$$\mathcal{E}_{gr} \approx -3 \frac{G}{\Delta} \frac{A^{4/3}}{\sqrt{\alpha}} \left( \frac{N_p}{A} \right)^{1/3} m_n^2 \frac{m_\pi c}{\hbar} \quad (\text{A.1.24})$$

must be larger than the repulsive Coulomb energy (A.1.18). For small  $A$ , the gravitational energy is always negligible. However, since the gravitational energy increases proportionally to  $A^{4/3}$  while the Coulomb energy only increases proportionally to  $A^{2/3}$ , the two must eventually cross, which occurs at

$$A_R = 0.039 \left( \frac{N_p}{A} \right)^{1/2} \left( \frac{m_{\text{Planck}}}{m_n} \right)^3. \quad (\text{A.1.25})$$

This establishes a *lower* limit for the mass number  $A_R$  necessary for the existence of an island of stability for massive nuclear density cores. The *upper* limit of the island of stability will be determined by general relativistic effects.

c) Having established the role of gravity in stabilizing the Coulomb interaction of the massive nuclear density core, we outline the importance of the strong interactions in determining its surface. We find for the neutron pressure at the surface:

$$P_n = \frac{9}{40} \left( \frac{3}{2\pi} \right)^{1/3} \left( \frac{m_\pi}{m_n} \right) \frac{m_\pi c^2}{(\hbar/m_\pi c)^3} \left( \frac{A}{N_p} \right)^{5/3} \frac{1}{\Delta^5}, \quad (\text{A.1.26})$$

and for the surface tension, as extrapolated from nuclear scattering experiments,

$$P_s = - \left( \frac{0.13}{4\pi} \right) \frac{m_\pi c^2}{(\hbar/m_\pi c)^3} \left( \frac{A}{N_p} \right)^{2/3} \frac{1}{\Delta^2}. \quad (\text{A.1.27})$$

We then obtain

$$\frac{|P_s|}{P_n} = 0.39 \cdot \Delta^3 \left( \frac{N_p}{A} \right) = 0.24 \cdot \frac{\rho_{\text{nucl}}}{\rho_{\text{surf}}}, \quad (\text{A.1.28})$$

where  $\rho_{\text{nucl}} = 3m_n A / 4\pi R_c^3$ . The relative importance of the nuclear pressure and nuclear tension is a very sensitive function of the density  $\rho_{\text{surf}}$  at the surface.

It is important to emphasize a major difference between nuclei and the massive nuclear density cores treated in this article: the gravitational binding energy in these massive nuclear density cores is instead  $\varepsilon_{\text{gr}} \approx GM_\odot m_n / R_c \approx 0.1 m_n c^2 \approx 93.8 \text{ MeV}$ . In other words it is much bigger than the nuclear energy in ordinary nuclei  $\varepsilon_{\text{nuclear}} \approx \hbar^2 / m_n r_0^2 \approx 28.8 \text{ MeV}$ .

### A.1.6. Possible applications to neutron stars

All the above considerations have been made for an isolated massive core at constant density whose boundary has been sharply defined by a step func-

tion. No external forces are exerted. Consequently due to the global charge neutrality, the Fermi energy of the electrons has been assumed to be equal to zero. In the earliest description of neutron stars in the work of Oppenheimer and Volkoff (1939) only a gas of neutrons was considered and the equation of equilibrium was written in the Schwarzschild metric. They considered the model of a degenerate gas of neutrons to hold from the center to the border, with the density monotonically decreasing away from the center.

In the intervening years a more realistic model has been presented challenging the original considerations of Tolman (1939); Oppenheimer and Volkoff (1939). Their TOV equations considered the existence of neutrons all the way to the surface of the star. The presence of neutrons, protons and electrons in beta equilibrium were instead introduced in Harrison et al. (1965). Still more important the neutron stars have been shown to be composed of two sharply different components: the core at nuclear and/or supra-nuclear density consisting of neutrons, protons and electrons and a crust of white dwarf like material, namely of degenerate electrons in a nuclei lattice (Harrison et al., 1965; Baym et al., 1971a). The pressure and the density of the core are mainly due to the baryons while the pressure of the crust is mainly due to the electrons with the density due to the nuclei and possibly with some free neutrons due to neutron drip (see e.g. Baym et al. (1971a)). Further works describing the nuclear interactions were later introduced (see e.g. Haensel et al. (2007)). Clearly all these considerations departed profoundly from the TOV approximation. The matching between the core component and the crust is the major unsolved problem. To this issue this article introduces some preliminary results in a simplified model which has the advantage to present explicit analytic solutions.

In all the above treatments in order to close the system of equations the condition of local charge neutrality  $n_e = n_p$  was adopted without a proof. The considerations of massive neutron density cores presented in this article offer an alternative to the local charge neutrality condition  $n_e = n_p$ . In a specific example which can be solved also analytically such condition is substituted by the Thomas-Fermi relativistic equations implying  $n_e \neq n_p$  and an overall charge neutral system ( $N_e = N_p$ ). The condition of global charge neutrality as opposed to the local one, leads to the existence of overcritical electric fields at the core surface which may be relevant in the description of neutron stars.

### A.1.7. Conclusions

We have first generalized the treatment of heavy nuclei by enforcing the condition of beta equilibrium in the relativistic Thomas-Fermi equation, avoiding the imposition of  $N_p \simeq A/2$  between  $N_p$  and  $A$  traditionally assumed in the literature. In doing so we have obtained (see Fig. A.3) an  $A - N_p$  relation which extends the ones adopted in the literature. Using the existence

of scaling laws for the system of equations considered, we extend the results obtained for heavy nuclei to the case of massive nuclear density cores. The novelty in this article is to show how both the considerations of heavy nuclei and of systems of macroscopic astrophysical dimensions can take advantage from a rigorous and analytic solution of the Thomas-Fermi relativistic equations and the beta equilibrium conditions. This task is achieved by obtaining explicit analytic solutions fulfilling precise boundary conditions and using the scaling laws introduced in this article.

Indeed the Thomas-Fermi treatment has been considered also in the context of quark stars with a charge and a density distribution analogous to the one of massive nuclear density cores we consider in this article Itoh (1970); Witten (1984); Alcock et al. (1986); Kettner et al. (1995); Usov (1998). There are however a variety of differences both in the boundary conditions adopted and in the solution obtained. In the present article we show that we can indeed obtain overcritical electric fields at nuclear density on macroscopic scales of  $R_c \approx 10$  Km and  $M \approx 1M_\odot$  for existing field theories involving only neutrons, protons and electrons and their fundamental interactions and no quarks present. We obtain explicit analytic solutions of the relativistic Thomas-Fermi equations, self-consistently solved with the condition of beta equilibrium. Such analytic solutions allow to give explicit expressions for the Coulomb energy, surface energy and Newtonian gravitational energy of such massive nuclear density cores.

These cores are stable against fission (see Eq. (A.1.22)), the surface tension determines the sharpness of their boundary (see Eq. (A.1.28)) and the gravitational interaction, at Newtonian level, balances the Coulomb repulsion for mass numbers larger than the critical value given by Eq. (A.1.25).

As a by-product of these results, we also conclude that the arguments often quoted concerning limits on the electric fields of an astrophysical system based on a free test particle (the dust approximation) considering only the gravitational and electric interactions

$$(E_{\max})_{\text{dust}} \approx \frac{m_e m_n c^3}{e \hbar} \frac{m_n}{m_{\text{Planck}}}, \quad (\text{A.1.29})$$

$$\left( \frac{Q}{\sqrt{GM}} \right)_{\text{dust}} \approx \sqrt{G} \frac{m_e}{e} = \frac{1}{\sqrt{\alpha}} \frac{m_e}{m_{\text{Planck}}}, \quad (\text{A.1.30})$$

appear to be inapplicable for  $A \sim (m_{\text{Planck}}/m_n)^3$ . Here nuclear densities are reached and the roles of *all* fundamental interactions, including weak and strong interactions in addition to the electromagnetic and gravitational ones and including as well quantum statistics, have to be taken into account through the relativistic Thomas-Fermi model. Eqs. (A.1.29) and (A.1.30) are

replaced by Eqs. (A.1.17) and (A.1.21),

$$E_{\max} \approx \frac{0.95\sqrt{\alpha} m_{\text{Planck}}}{\Delta^2 m_e} \left(\frac{m_\pi}{m_n}\right)^2 (E_{\max})_{\text{dust}}, \quad (\text{A.1.31})$$

$$\frac{Q}{\sqrt{GM}} \approx \frac{N_p}{A} \sqrt{\alpha} \frac{m_{\text{Planck}}}{m_e} \left(\frac{Q}{\sqrt{GM}}\right)_{\text{dust}}. \quad (\text{A.1.32})$$

## **A.2. On the relativistic Thomas-Fermi treatment of compressed atoms and compressed nuclear matter cores of stellar dimensions**

### **A.2.1. Introduction**

In a classic article Baym et al. (1971a) presented the problem of matching, in a neutron star, a liquid core, composed of  $N_n$  neutrons,  $N_p$  protons and  $N_e$  electrons, to the crust taking into account the electro-dynamical and surface tension effects. After discussing the different aspects of the problem they concluded: *The details of this picture requires further elaboration; this is a situation for which the Thomas-Fermi method is useful.* This statement, in first instance, may appear surprising: the Thomas-Fermi model has been extensively applied in atomic physics (see e.g. Gombás (1949); March (1957); Lundqvist and March (1983)), also has been applied extensively in atomic physics in its relativistic form (see e.g. Ferreira et al. (1980); Ruffini and Stella (1981)) as well as in the study of atoms with heavy nuclei in the classic works of Migdal et al. (1976, 1977). Similarly there have been considerations of relativistic Thomas-Fermi model for quark stars pointing out the existence of critical electric fields on their surfaces (see e.g. Alcock et al. (1986); Usov (1998)). Similar results have also been obtained by Alford et al. (2001) in the transition at very high densities, from the normal nuclear matter phase in the core to the color-flavor-locked phase of quark matter in the inner core of hybrid stars. No example exists of the application of the electromagnetic Thomas-Fermi model for neutron stars. This problem can indeed be approached with merit by studying the simplified but rigorous concept of a nuclear matter core of stellar dimensions which fulfills the relativistic Thomas-Fermi equation as discussed by Ruffini et al. (2007b), by Rotondo et al. (2011e) and by Popov (2010). As we will see this work leads to the prediction of the existence of a critical electric field at the interface between the core and the crust of a neutron star.

In Ruffini et al. (2007b) and Rotondo et al. (2011e) it is described a degenerate system of  $N_n$  neutrons,  $N_p$  protons and  $N_e$  electrons constrained to a constant density distribution for the protons and it is solved the corresponding relativistic Thomas-Fermi equation and derived for the neutrons the distribution following the implementation of the beta equilibrium condition. This generalizes e.g. the works of Migdal et al. (1976, 1977); Popov (1971b,a) and Pieper and Greiner (1969); Greenberg and Greiner (1982) by eliminating the constraint  $N_p \approx A/2$ , clearly not valid for heavy nuclei, and enforcing self-consistently in a new relativistic Thomas-Fermi equation the condition of beta equilibrium. Using then the existence of scaling laws we have extended in Rotondo et al. (2011e) the results from heavy nuclei to the case of nuclear matter cores of stellar dimensions. In both these treatments we had assumed

the Fermi energy of the electrons  $E_e^F = 0$ . The aim of this article is to proceed with this dual approach and to consider first the case of compressed atoms and then, using the existence of scaling laws, the compressed nuclear matter cores of stellar dimensions with a positive value of their electron Fermi energies.

It is well known that Salpeter has been among the first to study the behavior of matter under extremely high pressures by considering a Wigner-Seitz cell of radius  $R_{WS}$  (Salpeter, 1961a). Salpeter assumed as a starting point the nucleus point-like and a uniform distribution of electrons within a Wigner-Seitz cell, and then considered corrections to the above model due to the inhomogeneity of electron distribution. The first correction corresponds to the inclusion of the lattice energy  $E_C = -(9N_p^2\alpha)/(10R_{WS})$ , which results from the point-like nucleus-electron Coulomb interaction and, from the electron-electron Coulomb interaction inside the cell of radius  $R_{WS}$ . The second correction is given by a series-expansion of the electron Fermi energy about the average electron density  $n_e$  of the uniform approximation. The electron density is then assumed equals to  $n_e[1 + \epsilon(r)]$  with  $\epsilon(r)$  considered as infinitesimal. The Coulomb potential energy is assumed to be the one of the point-like nucleus with the uniform distribution of electrons of density  $n_e$  thus the correction given by  $\epsilon(r)$  is neglected on the Coulomb potential. The electron distribution is then calculated at first-order by expanding the relativistic electron kinetic energy about its value given by the uniform approximation considering as infinitesimal the ratio  $eV/E_e^F$  between the Coulomb potential energy  $eV$  and the electron Fermi energy  $E_e^F = \sqrt{[cP_e^F(r)]^2 + m_e^2c^4} - m_e c^2 - eV$ . The inclusion of each additional Coulomb correction results in a decreasing of the pressure of the cell  $P_S$  by comparison to the uniform one.

It is quite difficult to assess the self-consistency of all the recalled different approximations adopted by Salpeter. In order to validate and also to see the possible limits of the Salpeter approach, we consider the relativistic generalization of the Feynman, Metropolis, Teller treatment (Feynman et al., 1949) which takes automatically and globally into account all electromagnetic and special relativistic contributions. We show explicitly how this new treatment leads in the case of atoms to electron distributions markedly different from the ones often adopted in the literature of constant electron density distributions. At the same time it allows to overcome some of the difficulties in current treatments.

Similarly the point-like description of the nucleus often adopted in literature is confirmed to be unacceptable in the framework of a relativistic treatment.

In Sec. A.2.2 we first recall the non-relativistic treatment of the compressed atom by Feynman, Metropolis and Teller. In Sec. A.2.3 we generalize that treatment to the relativistic regime by integrating the relativistic Thomas-Fermi equation, imposing also the condition of beta equilibrium. In Sec. A.2.4

we first compare the new treatment with the one corresponding to a uniform electron distribution often used in the literature and to the Salpeter treatment. We also compare and contrast the results of the relativistic and the non-relativistic treatment.

In Sec. A.2.5, using the same scaling laws adopted by Ruffini et al. (2007b) and Rotondo et al. (2011e) we turn to the case of nuclear matter cores of stellar dimensions with mass numbers  $A \approx (m_{\text{Planck}}/m_n)^3 \sim 10^{57}$  or  $M_{\text{core}} \sim M_{\odot}$  where  $m_n$  is the neutron mass and  $m_{\text{Planck}} = (\hbar c/G)^{1/2}$  is the Planck mass. Such a configuration presents global but not local charge neutrality. Analytic solutions for the ultra-relativistic limit are obtained. In particular we find:

1) explicit analytic expressions for the electrostatic field and the Coulomb potential energy,

2) an entire range of possible Fermi energies for the electrons between zero and a maximum value  $(E_e^F)_{\text{max}}$ , reached when  $R_{WS} = R_c$ , which can be expressed analytically,

3) the explicit analytic expression of the ratio between the proton number  $N_p$  and the mass number  $A$  when  $R_{WS} = R_c$ .

We turn then in Sec. A.2.6 to the study of the compressional energy of the nuclear matter cores of stellar dimensions for selected values of the electron Fermi energy. We show that the solution with  $E_e^F = 0$  presents the largest value of the electro-dynamical structure.

We finally summarize the conclusions in Sec. A.2.7.

## A.2.2. The Thomas-Fermi model for compressed atoms: the Feynman-Metropolis-Teller treatment

### The classical Thomas-Fermi model

The Thomas-Fermi model assumes that the electrons of an atom constitute a fully degenerate gas of fermions confined in a spherical region by the Coulomb potential of a point-like nucleus of charge  $+eN_p$ . Feynman, Metropolis and Teller have shown that this model can be used to derive the equation of state of matter at high pressures by considering a Thomas-Fermi model confined in a Wigner-Seitz cell of radius  $R_{WS}$  (Feynman et al., 1949).

We recall that the condition of equilibrium of the electrons in an atom, in the non-relativistic limit, is expressed by

$$\frac{(P_e^F)^2}{2m_e} - eV = E_e^F, \quad (\text{A.2.1})$$

where  $m_e$  is the electron mass,  $V$  is the electrostatic potential and  $E_e^F$  is their constant Fermi energy.

The electrostatic potential fulfills, for  $r > 0$ , the Poisson equation

$$\nabla^2 V = 4\pi e n_e, \quad (\text{A.2.2})$$

where the electron number density  $n_e$  is related to the Fermi momentum  $P_e^F$  by

$$n_e = \frac{(P_e^F)^3}{3\pi^2 \hbar^3}. \quad (\text{A.2.3})$$

For neutral atoms and ions  $n_e$  vanishes at the boundary so the electron Fermi energy is, respectively, zero or negative. In the case of compressed atoms  $n_e$  does not vanish at the boundary while the Coulomb potential energy  $eV$  does. Consequently  $E_e^F$  is positive.

Defining

$$eV(r) + E_e^F = e^2 N_p \frac{\phi(r)}{r}, \quad (\text{A.2.4})$$

and introducing the new dimensionless radial coordinate  $\eta$  as

$$r = b\eta \quad \text{with} \quad b = \frac{(3\pi)^{2/3}}{2^{7/3}} \frac{1}{N_p^{1/3}} \frac{\hbar^2}{m_e e^2} = \frac{\sigma}{N_p^{1/3}} r_{Bohr}, \quad (\text{A.2.5})$$

where  $\sigma = (3\pi)^{2/3} / 2^{7/3} \approx 0.88$ ,  $r_{Bohr} = \hbar^2 / (m_e e^2)$  is the Bohr radius, we obtain the following expression for the electron number density

$$n_e(\eta) = \frac{N_p}{4\pi b^3} \left( \frac{\phi(\eta)}{\eta} \right)^{3/2}, \quad (\text{A.2.6})$$

and then Eq. (A.2.2) can be written in the form

$$\frac{d^2 \phi(\eta)}{d\eta^2} = \frac{\phi(\eta)^{3/2}}{\eta^{1/2}}, \quad (\text{A.2.7})$$

which is the classic Thomas-Fermi equation. A first boundary condition for this equation follows from the point-like structure of the nucleus

$$\phi(0) = 1. \quad (\text{A.2.8})$$

A second boundary condition comes from the conservation of the number of electrons  $N_e = \int_0^{R_{WS}} 4\pi n_e(r) r^2 dr$

$$1 - \frac{N_e}{N_p} = \phi(\eta_0) - \eta_0 \phi'(\eta_0), \quad (\text{A.2.9})$$

where  $\eta_0 = R_{WS}/b$  defines the radius  $R_{WS}$  of the Wigner-Seitz cell. In the case

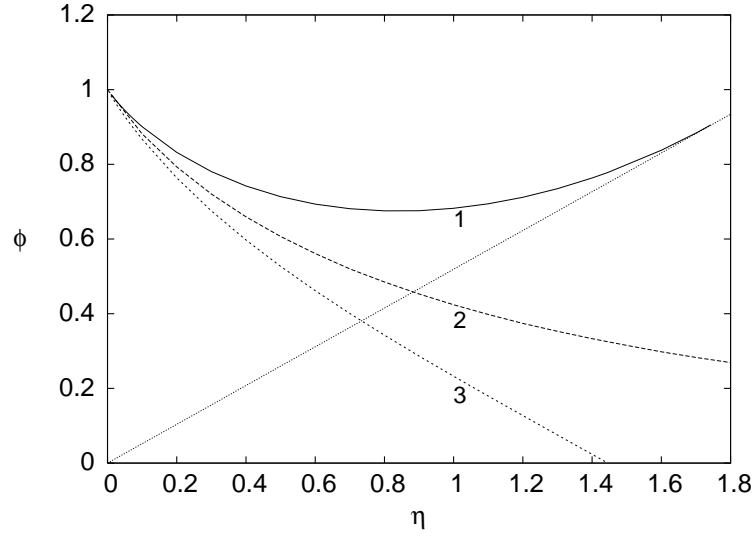


**Figure A.4.:** Physically relevant solutions of the Thomas-Fermi Equation (A.2.7) with the boundary conditions (A.2.8) and (A.2.9). The curve 1 refers to a neutral compressed atom. The curve 2 refers to a neutral free atom. The curve 3 refers to a positive ion. The dotted straight line is the tangent to the curve 1 at the point  $(\eta_0, \phi(\eta_0))$  corresponding to overall charge neutrality (see Eq. (A.2.9)).

of compressed atoms  $N_e = N_p$  so the Coulomb potential energy  $eV$  vanishes at the boundary  $R_{WS}$ . As a result, using Eqs. (A.2.1) and (A.2.3), the Fermi energy of electrons satisfies the universal relation

$$\frac{\sigma r_{Bohr}}{e^2} \frac{E_e^F}{N_p^{4/3}} = \frac{\phi(\eta_0)}{\eta_0}, \quad (\text{A.2.10})$$

while the Wigner-Seitz cell radius  $R_{WS}$  satisfies the universal relation

$$\frac{R_{WS}}{\sigma r_{Bohr} N_p^{-1/3}} = \eta_0. \quad (\text{A.2.11})$$

Therefore in the classic treatment  $\eta_0$  can approach zero and consequently the range of the possible values of the Fermi energy extends from zero to infinity.

The results are summarized in Figs. A.4 and A.5.

### The Thomas-Fermi-Dirac model

Dirac has introduced modifications to the original Thomas-Fermi theory to include effects of the exchange interaction (Dirac, 1930). In this case the con-

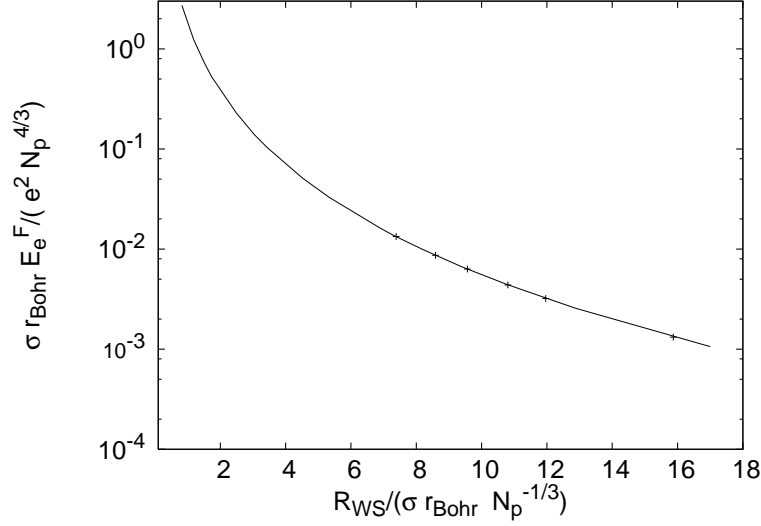


**Figure A.5.:** The electron Fermi energy  $E_e^F$ , in units of  $e^2 N_p^{4/3} / (\sigma r_{Bohr})$  is plotted as a function of the Wigner-Seitz cell radius  $R_{WS}$ , in units of  $\sigma r_{Bohr} N_p^{-1/3}$  (see Eqs. (A.2.10), (A.2.11)). Points refer to the numerical integrations of the Thomas-Fermi equation (A.2.7) performed originally by Feynman, Metropolis and Teller in Feynman et al. (1949).

dition of equilibrium of the electrons in the atom is generalized as follows

$$\frac{(P_e^F)^2}{2m_e} - eV - \frac{e^2}{\pi\hbar} P_e^F = E_e^F. \quad (\text{A.2.12})$$

The electron number density is now connected to the Coulomb potential energy by

$$n_e = \frac{1}{3\pi^5} \frac{1}{r_{Bohr}^3} \left[ 1 + \sqrt{1 + 2\pi^2 \frac{r_{Bohr}}{e^2} (eV + E_e^F)} \right]^3. \quad (\text{A.2.13})$$

Defining

$$\frac{1}{2\pi^2} \frac{e^2}{r_{Bohr}} + eV(r) + E_e^F = e^2 N_p \frac{\chi(r)}{r}, \quad (\text{A.2.14})$$

the Eq. (A.2.2) can be written in dimensionless form as

$$\frac{d^2\phi(\eta)}{d\eta^2} = \eta \left[ d + \left( \frac{\phi(\eta)}{\eta} \right)^{1/2} \right]^3, \quad (\text{A.2.15})$$

where  $d = (3/(32\pi^2))^{1/3}(1/N_p)^{2/3}$ . The boundary condition for Eq. (A.2.15) are  $\phi(0) = 1$  and  $\eta_0\phi'(\eta_0) = \phi(\eta_0)$ .

### A.2.3. The relativistic generalization of the Feynman-Metropolis-Teller treatment

#### The relativistic Thomas-Fermi model for atoms

In the relativistic generalization of the Thomas-Fermi equation the point-like approximation of the nucleus must be abandoned (Ferreirinho et al., 1980; Ruffini and Stella, 1981) since the relativistic equilibrium condition

$$E_e^F = \sqrt{(P_e^F c)^2 + m_e^2 c^4} - m_e c^2 - eV(r), \quad (\text{A.2.16})$$

which generalizes the Eq. (A.2.1), would lead to a non-integrable expression for the electron density near the origin. Consequently we adopt an extended nucleus. Traditionally the radius of an extended nucleus is given by the phenomenological relation  $R_c = r_0 A^{1/3}$  where  $A$  is the number of nucleons and  $r_0 = 1.2 \times 10^{-13}$  cm. Further it is possible to show from the extremization of the semi-empirical Weizsacker mass-formula that the relation between  $A$  and  $N_p$  is given by (see e.g. Segré (1977) and Ferreirinho et al. (1980))

$$N_p \approx \left[ \frac{2}{A} + \frac{2a_C}{a_A} \frac{1}{A^{1/3}} \right]^{-1} \approx \left[ \frac{2}{A} + \frac{3}{200} \frac{1}{A^{1/3}} \right]^{-1}, \quad (\text{A.2.17})$$

where  $a_C \approx 0.71$  MeV,  $a_A \approx 93.15$  MeV are the Coulomb and the asymmetry coefficients respectively. In the limit of small  $A$  Eq. (A.2.17) gives

$$N_p \approx \frac{A}{2}. \quad (\text{A.2.18})$$

In Rotondo et al. (2011e) we have relaxed the condition  $N_p \approx A/2$  adopted e.g. in Migdal et al. (1977) as well as the condition  $N_p \approx [2/A + 3/(200A^{1/3})]^{-1}$  adopted e.g. in Ferreirinho et al. (1980); Ruffini and Stella (1981) by imposing explicitly the beta decay equilibrium between neutron, protons and electrons.

In particular, following the previous treatments (see e.g. Rotondo et al. (2011e)), we have assumed a constant distribution of protons confined in a

radius  $R_c$  defined by

$$R_c = \Delta \frac{\hbar}{m_\pi c} N_p^{1/3}, \quad (\text{A.2.19})$$

where  $m_\pi$  is the pion mass and  $\Delta$  is a parameter such that  $\Delta \approx 1$  ( $\Delta < 1$ ) corresponds to nuclear (supranuclear) densities when applied to ordinary nuclei. Consequently, the proton density can be written as

$$n_p(r) = \frac{N_p}{\frac{4}{3}\pi R_c^3} \theta(R_c - r) = \frac{3}{4\pi} \frac{m_\pi^3 c^3}{\hbar^3} \frac{1}{\Delta^3} \theta(R_c - r), \quad (\text{A.2.20})$$

where  $\theta(x)$  is the Heaviside function which by definition is given by

$$\theta(x) = \begin{cases} 0, & x < 0, \\ 1, & x > 0. \end{cases} \quad (\text{A.2.21})$$

The electron density is given by

$$n_e(r) = \frac{(P_e^F)^3}{3\pi^2 \hbar^3} = \frac{1}{3\pi^2 \hbar^3 c^3} \left[ e^2 V^2(r) + 2m_e c^2 e V(r) \right]^{3/2}, \quad (\text{A.2.22})$$

where  $V$  is the Coulomb potential.

The overall Coulomb potential satisfies the Poisson equation

$$\nabla^2 V(r) = -4\pi e [n_p(r) - n_e(r)], \quad (\text{A.2.23})$$

with the boundary conditions  $V(\infty) = 0$  (due to global charge neutrality) and finiteness of  $V(0)$ .

Using Eqs. (A.2.4), (A.2.5) and replacing the particle densities (A.2.20) and (A.2.22) into the Poisson equation (A.2.23) we obtain the relativistic Thomas-Fermi equation

$$\frac{d^2 \phi(\eta)}{d\eta^2} = -\frac{3\eta}{\eta_c^3} \theta(\eta_c - \eta) + \frac{\phi^{3/2}}{\eta^{1/2}} \left[ 1 + \left( \frac{N_p}{N_p^{crit}} \right)^{4/3} \frac{\phi}{\eta} \right]^{3/2}, \quad (\text{A.2.24})$$

where  $\phi(0) = 0$ ,  $\phi(\infty) = 0$  and  $\eta_c = R_c/b$ . The critical number of protons  $N_p^{crit}$  is defined by

$$N_p^{crit} = \sqrt{\frac{3\pi}{4}} \alpha^{-3/2}, \quad (\text{A.2.25})$$

where, as usual,  $\alpha = e^2/(\hbar c)$ .

It is interesting that by introducing the new dimensionless variable

$$x = \frac{r}{\lambda_\pi} = \frac{b}{\lambda_\pi} \eta, \quad (\text{A.2.26})$$

and the function

$$\chi = \alpha N_p \phi, \quad (\text{A.2.27})$$

where  $\lambda_\pi = \hbar/(m_\pi c)$ , Eq. (A.2.24) assumes a canonical form, the master relativistic Thomas-Fermi equation (see Ruffini (2008a))

$$\frac{1}{3x} \frac{d^2 \chi(x)}{dx^2} = -\frac{\alpha}{\Delta^3} \theta(x_c - x) + \frac{4\alpha}{9\pi} \left[ \frac{\chi^2(x)}{x^2} + 2 \frac{m_e \chi}{m_\pi x} \right]^{3/2}, \quad (\text{A.2.28})$$

where  $x_c = R_c/\lambda_\pi$  with the boundary conditions  $\chi(0) = 0$ ,  $\chi(\infty) = 0$ . The neutron density  $n_n(r)$ , related to the neutron Fermi momentum  $P_n^F = (3\pi^2 \hbar^3 n_n)^{1/3}$ , is determined, as in the previous case Rotondo et al. (2011e), by imposing the condition of beta equilibrium

$$\begin{aligned} E_n^F &= \sqrt{(P_n^F c)^2 + m_n^2 c^4} - m_n c^2 \\ &= \sqrt{(P_p^F c)^2 + m_p^2 c^4} - m_p c^2 + eV(r), \end{aligned} \quad (\text{A.2.29})$$

which in turn is related to the proton density  $n_p$  and the electron density by Eqs. (A.2.22), (A.2.23). Integrating numerically these equations we have obtained a new generalized relation between  $A$  and  $N_p$  for any value of  $A$ . In the limit of small  $A$  this result agrees with the phenomenological relations given by Eqs. (A.2.17, A.2.18), as is clearly shown in Fig. (A.6).

### The relativistic Thomas-Fermi model for compressed atoms

We turn now to the case of compressed atoms in which the electron Fermi energy is positive. The relativistic generalization of the equilibrium condition (A.2.1) now reads

$$E_e^F = \sqrt{(P_e^F c)^2 + m_e^2 c^4} - m_e c^2 - eV(r) > 0. \quad (\text{A.2.30})$$

Adopting an extended-nucleus with a radius given by Eq. (A.2.19) and a proton density given by Eq. (A.2.20) the Poisson equation (A.2.23), with the fol-

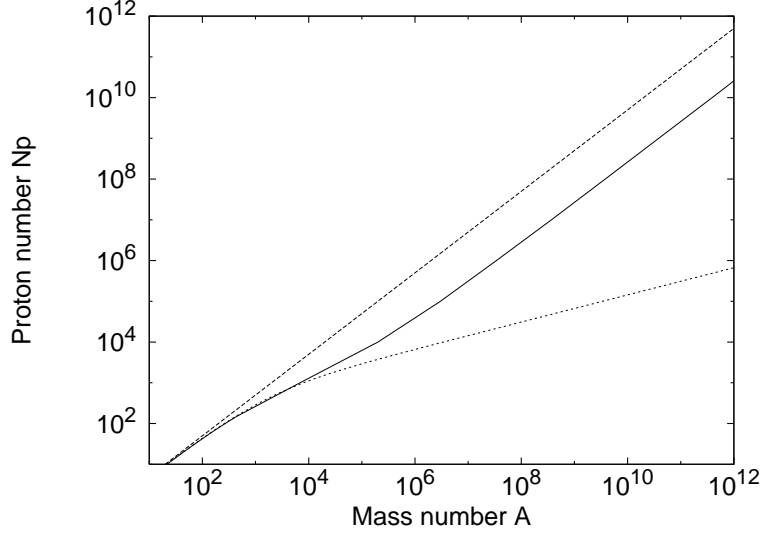


**Figure A.6.:** The  $A$ - $N_p$  relation at nuclear density (solid line) obtained from first principles compared with the phenomenological expressions given by  $N_p \approx A/2$  (dashed line) and Eq. (A.2.17) (dotted line). The asymptotic value, for  $A \rightarrow (m_{\text{Planck}}/m_n)^3$ , is  $N_p \approx 0.0046A$ .

lowing electron density

$$n_e(r) = \frac{(P_e^F)^3}{3\pi^2\hbar^3} = \frac{1}{3\pi^2\hbar^3 c^3} \left[ e^2 \hat{V}^2(r) + 2m_e c^2 e \hat{V}(r) \right]^{3/2}, \quad (\text{A.2.31})$$

gives again the master relativistic Thomas-Fermi equation (A.2.28) where  $\chi/r = e\hat{V}(r)/(c\hbar)$  and  $e\hat{V} = eV + E_e^F$ .

In this case Eq. (A.2.28) has to be integrated with the boundary conditions  $\chi(0) = 0$ ,  $\chi(x_{WS}) = x_{WS}\chi'(x_{WS})$ ,  $x_{WS} = R_{WS}/\lambda_\pi$ . Using Eqs. (A.2.4), (A.2.26) and (A.2.27) we obtain the electron Fermi energy in the form

$$E_e^F = m_\pi c^2 \frac{\chi(x_{WS})}{x_{WS}}. \quad (\text{A.2.32})$$

The neutron density  $n_n(r)$ , related to the neutron Fermi momentum  $P_n^F = (3\pi^2\hbar^3 n_n)^{1/3}$ , is determined by imposing the condition of beta equilibrium

$$\begin{aligned} E_n^F &= \sqrt{(P_n^F c)^2 + m_n^2 c^4} - m_n c^2 \\ &= \sqrt{(P_p^F c)^2 + m_p^2 c^4} - m_p c^2 + eV(r) + E_e^F. \end{aligned} \quad (\text{A.2.33})$$

Using this approach, it is then possible to determine the beta equilibrium nuclide as a function of the density of the system. Infact, electrons and pro-

tons can be converted to neutrons in inverse beta decay  $p + e^- \rightarrow n + \nu_e$  if the condition  $E_n^F < \sqrt{(P_p^F c)^2 + m_p^2 c^4} - m_p c^2 + eV(r) + E_e^F$  holds. The condition of equilibrium (A.2.33) is crucial, for example, in the construction of a self-consistent equation of state of high energy density matter present in white dwarfs and neutron star crusts. In the case of zero electron Fermi energy the generalized  $A - N_p$  relation of Fig. (A.6) is obtained.

### The relativistic Thomas-Fermi-Dirac model for compressed atoms

We now take into account the exchange corrections to the relativistic Thomas-Fermi equation (A.2.28). In this case we have (see Migdal et al. (1977) for instance)

$$E_e^F = \sqrt{(cP_e^F)^2 + m_e^2 c^4} - m_e c^2 - eV - \frac{\alpha}{\pi} cP_e^F = \text{constant}. \quad (\text{A.2.34})$$

Introducing the function  $\chi(r)$  as before

$$E_e^F + eV = e\hat{V} = \hbar c \frac{\chi}{r}, \quad (\text{A.2.35})$$

we obtain the electron number density

$$n_e = \frac{1}{3\pi^2 \hbar^3 c^3} \left\{ \gamma (m_e c^2 + e\hat{V}) + [(e\hat{V})^2 + 2m_e c^2 e\hat{V}]^{1/2} \right. \\ \left. \times \left[ \frac{(1 + \gamma^2)(m_e c^2 + e\hat{V})^2 - m_e^2 c^4}{(m_e c^2 + e\hat{V})^2 - m_e^2 c^4} \right]^{1/2} \right\}^3, \quad (\text{A.2.36})$$

where  $\gamma = (\alpha/\pi)/(1 - \alpha^2/\pi^2)$ .

If we take the approximation  $1 + \gamma^2 \approx 1$  the above equation becomes

$$n_e = \frac{1}{3\pi^2 \hbar^3 c^3} \left\{ \gamma (m_e c^2 + e\hat{V}) + [(e\hat{V})^2 + 2m_e c^2 e\hat{V}]^{1/2} \right\}^3. \quad (\text{A.2.37})$$

The second term on the right-hand-side of Eq. (A.2.37) has the same form of the electron density given by the relativistic Thomas-Fermi approach without the exchange correction (A.2.31) and therefore the first term shows the explicit contribution of the exchange term to the electron density.

Using the full expression of the electron density given by Eq. (A.2.36) we

obtain the relativistic Thomas-Fermi-Dirac equation

$$\begin{aligned} \frac{1}{3x} \frac{d^2\chi(x)}{dx^2} = & -\frac{\alpha}{\Delta^3} \theta(x_c - x) + \frac{4\alpha}{9\pi} \left\{ \gamma \left( \frac{m_e}{m_\pi} + \frac{\chi}{x} \right) + \left[ \left( \frac{\chi}{x} \right)^2 + 2 \frac{m_e}{m_\pi} \frac{\chi}{x} \right]^{1/2} \right. \\ & \times \left. \left[ \frac{(1 + \gamma^2)(m_e/m_\pi + \chi/x)^2 - (m_e/m_\pi)^2}{(m_e/m_\pi + \chi/x)^2 - (m_e/m_\pi)^2} \right]^{1/2} \right\}^3, \end{aligned} \quad (\text{A.2.38})$$

which by applying the approximation  $1 + \gamma^2 \approx 1$  becomes

$$\frac{1}{3x} \frac{d^2\chi(x)}{dx^2} = -\frac{\alpha}{\Delta^3} \theta(x_c - x) + \frac{4\alpha}{9\pi} \left\{ \gamma \left( \frac{m_e}{m_\pi} + \frac{\chi}{x} \right) + \left[ \left( \frac{\chi}{x} \right)^2 + 2 \frac{m_e}{m_\pi} \frac{\chi}{x} \right]^{1/2} \right\}^3. \quad (\text{A.2.39})$$

The boundary conditions for Eq. (A.2.38) are  $\chi(0) = 0$  and  $\chi(x_{WS}) = x_{WS}\chi'(x_{WS})$ . The neutron density can be obtained as before by using the beta equilibrium condition (A.2.33) with the electron Fermi energy given by Eq. (A.2.34).

In Fig. A.7 we show the results of the numerical integration of the relativistic Thomas-Fermi equation (A.2.28) and of the relativistic Thomas-Fermi-Dirac equation (A.2.38) for helium, carbon and iron. In particular, we show the electron Fermi energy multiplied by  $N_p^{-4/3}$  as a function of the ratio  $R_{WS}/R_c$  between the Wigner-Seitz cell radius  $R_{WS}$  and the nucleus radius  $R_c$  given by Eq. (A.2.19).

The effects of the exchange term are appreciable only in the low density (low compression) region, i.e. when  $R_{WS} \gg R_c$  (see Fig. A.7). We can then conclude in total generality that the correction given by the Thomas-Fermi-Dirac exchange term is, small in the non-relativistic low compression (low density) regime, and negligible in the relativistic high compression (high density) regime.

#### A.2.4. Comparison and contrast with approximate treatments

There exists in the literature a variety of semi-qualitative approximations adopted in order to describe the electron component of a compressed atom (see e.g. Bürvenich et al. (2007) for applications of the uniform approximation and e.g. Chabrier and Potekhin (1998); Potekhin et al. (2009); Douchin and Haensel (2001); Haensel and Zdunik (1990a,b), for applications of the Salpeter approximate treatment).

We shall see how the relativistic treatment of the Thomas-Fermi equation affects the current analysis of compressed atoms in the literature by introducing qualitative and quantitative differences which deserve attention.

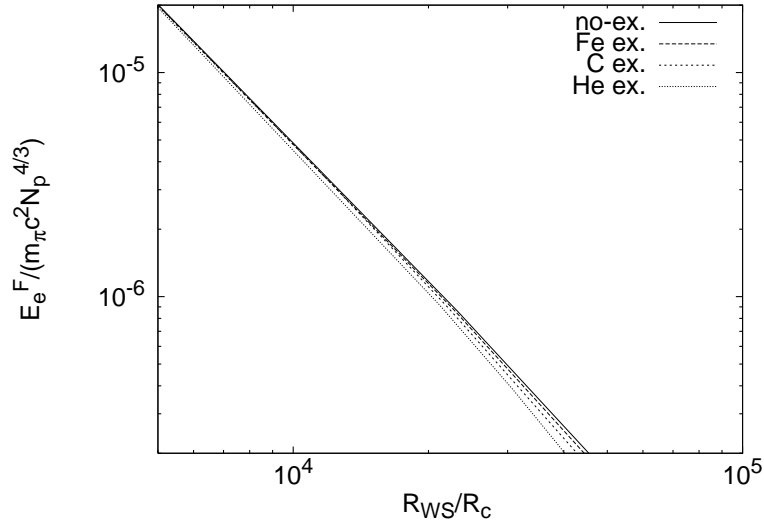


**Figure A.7.:** The electron Fermi energy in units of  $m_{\pi}c^2N_p^{4/3}$  is plotted for helium, carbon and iron, as a function of the ratio  $R_{WS}/R_c$  in the relativistic Feynman-Metropolis-Teller (FMT) treatment with and without the exchange effects. Here  $R_{WS}$  denotes the Wigner-Seitz cell radius and  $R_c$  is the nucleus radius as given by Eq. (A.2.19). It is clear that the exchange terms are appreciable only in the low density region and are negligible as  $R_{WS} \rightarrow R_c$ .

### Relativistic FMT treatment vs. relativistic uniform approximation

One of the most used approximations in the treatment of the electron distribution in compressed atoms is the one in which, for a given nuclear charge  $+eN_p$ , the Wigner-Seitz cell radius  $R_{WS}$  is defined by

$$N_p = \frac{4\pi}{3}R_{WS}^3n_e, \quad (\text{A.2.40})$$

where  $n_e = (P_e^F)^3/(3\pi^2\hbar^3)$ . The Eq. (A.2.40) ensures the global neutrality of the Wigner-Seitz cell of radius  $R_{WS}$  assuming a uniform distribution of electrons inside the cell.

We shall first compare the Feynman-Metropolis-Teller treatment, previously introduced, with the uniform approximation for the electron distribution. In view of the results of the preceding section, hereafter we shall consider the non-relativistic and the relativistic formulation of the Feynman-Metropolis-Teller treatment with no Thomas-Fermi-Dirac exchange correction.

In Fig. A.8 we have plotted the electron number density obtained from Eq. (A.2.31) where the Coulomb potential is related to the function  $\chi$ , which is obtained from numerical integration of the relativistic Thomas-Fermi equa-

tion (A.2.28) for different compressions for helium and iron. We have normalized the electron density to the average electron number density  $n_0 = 3N_e/(4\pi R_{WS}^3) = 3N_p/(4\pi R_{WS}^3)$  as given by Eq. (A.2.40).

We can see in Fig. A.8 how our treatment, based on the numerical integration of the relativistic Thomas-Fermi equation (A.2.28) and imposing the condition of beta equilibrium (A.2.33), leads to electron density distributions markedly different from the constant electron density approximation.

From Eqs. (A.2.30), (A.2.40) and taking into account the global neutrality condition of the Wigner-Seitz cell  $eV(R_{WS}) = 0$ , the electron Fermi energy in the uniform approximation can be written as

$$E_e^F \simeq \left[ -\frac{m_e}{m_\pi} + \sqrt{\left(\frac{m_e}{m_\pi}\right)^2 + \left(\frac{9\pi}{4}\right)^{2/3} \frac{N_p^{2/3}}{x_{WS}^2}} \right] m_\pi c^2. \quad (\text{A.2.41})$$

We show in Fig. A.9 the electron Fermi energy as a function of the average electron density  $n_0 = 3N_e/(4\pi R_{WS}^3) = 3N_p/(4\pi R_{WS}^3)$  in units of the nuclear density  $n_{nuc} = 3A/(4\pi\Delta^3 N_p \lambda_\pi^3)$ . For selected compositions we show the results for the relativistic Feynman-Metropolis-Teller treatment, based on the numerical integration of the relativistic Thomas-Fermi equation (A.2.28), and for the relativistic uniform approximation.

As clearly shown in Fig. A.8 and summarized in Fig. A.9 the relativistic treatment leads to results strongly dependent at low compression from the nuclear composition. The corresponding value of the electron Fermi energy derived from a uniform approximation overevaluates the true electron Fermi energy (see Fig. A.9). In the limit of high compression the relativistic curves asymptotically approach the uniform one (see also Fig. A.8).

The uniform approximation becomes exact in the limit when the electron Fermi energy acquires its maximum value as given by

$$(E_e^F)_{max} \simeq \left[ -\frac{m_e}{m_\pi} + \sqrt{\left(\frac{m_e}{m_\pi}\right)^2 + \left(\frac{3\pi^2}{2}\right)^{2/3} \left(\frac{N_p}{A}\right)^{2/3}} \right] m_\pi c^2, \quad (\text{A.2.42})$$

which is attained when  $R_{WS}$  coincides with the nuclear radius  $R_c$ . Here, the maximum electron Fermi energy (A.2.42) is obtained by replacing in Eq. (A.2.41) the value of the normalized Wigner-Seitz cell radius  $x_{WS} = x_c = R_c/\lambda_\pi \approx [(3/2)\pi]^{1/3} A^{1/3}$ .

### Relativistic FMT treatment vs. Salpeter approximate treatment

Corrections to the uniform distribution were also studied by Salpeter (1961a) and his approximations are largely applied in physics (see e.g. Chabrier and Potekhin (1998); Potekhin et al. (2009)) and astrophysics (see e.g. Douchin

and Haensel (2001); Haensel and Zdunik (1990a,b)).

Keeping the point-like nucleus assumption, Salpeter (1961a) studied the corrections to the above models due to the inhomogeneity of the electron distribution inside the Wigner-Seitz cell. He expressed an analytic formula for the total energy of a Wigner-Seitz cell based on Coulomb corrections to the uniform distribution of electrons. The first correction corresponds to the inclusion of the lattice energy  $E_C = -(9N_p^2\alpha)/(10R_{WS})$ , which results from the point-like nucleus-electron Coulomb interaction and, from the electron-electron Coulomb interaction inside the cell of radius  $R_{WS}$ . The second correction is given by a series-expansion of the electron Fermi energy about the average electron density  $n_e$  given by Eq. (A.2.40) the uniform approximation  $n_e = 3N_p/(4\pi R_{WS}^3)$ . The electron density is then assumed equals to  $n_e[1 + \epsilon(r)]$  with  $\epsilon(r)$  considered as infinitesimal. The Coulomb potential energy is assumed to be the one of the point-like nucleus with the uniform distribution of electrons of density  $n_e$ , thus the correction given by  $\epsilon(r)$  is neglected on the Coulomb potential. The electron distribution is then calculated at first-order by expanding the relativistic electron kinetic energy

$$\begin{aligned}\epsilon_k &= \sqrt{[cP_e^F(r)]^2 + m_e^2c^4} - m_e c^2 \\ &= \sqrt{(3\pi^2 n_e)^{2/3}[1 + \epsilon(r)]^{2/3} + m_e^2c^4} - m_e c^2,\end{aligned}\quad (\text{A.2.43})$$

about its value given by the uniform approximation

$$\epsilon_k^{\text{unif}} = \sqrt{(3\pi^2 n_e)^{2/3} + m_e^2c^4} - m_e c^2,\quad (\text{A.2.44})$$

considering as infinitesimal the ratio  $eV/E_e^F$  between the Coulomb potential energy  $eV$  and the electron Fermi energy  $E_e^F = \sqrt{[cP_e^F(r)]^2 + m_e^2c^4} - m_e c^2 - eV$ .

The effect of the Dirac electron-exchange correction (Dirac, 1930) on the equation of state was also considered by Salpeter (1961a). However, adopting the general approach of Migdal et al. (1977), these effects are negligible in the relativistic regime (see Subsec. A.2.3).

The inclusion of each additional Coulomb correction results in a decreasing of the pressure of the cell  $P_S$ . However, despite to be very interesting in identifying piecewise contributions to the total pressure, the validity of the Salpeter approach needs a verification by a more general treatment. For instance, the failure of the Salpeter formulas can be seen at densities of the order of  $\sim 10^2 - 10^3 \text{ g cm}^{-3}$  for nuclei with large  $N_p$ , as in the case of iron, where the pressure becomes negative (see Table (A.1)). Therefore, the problem of solving the relativistic Thomas-Fermi equation within the Feynman, Metropolis, Teller approach becomes a necessity, since this approach gives all the possible Coulomb and relativistic contributions automatically and correctly.

**Table A.1.:** Pressure for iron as a function of the density  $\rho$  in the uniform approximation ( $P$ ), in the Salpeter approximation ( $P_S$ ) and in the relativistic Feynman-Metropolis-Teller approach ( $P_{FMTrel}$ ). Here  $x_S = P_{e,S}^F/(m_e c)$ ,  $x_{FMTrel} = P_e^F/(m_e c)$  are respectively the normalized Salpeter Fermi momentum and the relativistic Feynman-Metropolis-Teller Fermi momentum.

$\rho$ (g/cm <sup>3</sup> )	$x_S$	$x_{FMTrel}$	$P$ (bar)	$P_S$ (bar)	$P_{FMTrel}$ (bar)
$2.63 \times 10^2$	0.05	0.0400	$2.9907 \times 10^{10}$	$-1.8800 \times 10^8$	$9.9100 \times 10^9$
$2.10 \times 10^3$	0.10	0.0857	$9.5458 \times 10^{11}$	$4.4590 \times 10^{11}$	$5.4840 \times 10^{11}$
$1.68 \times 10^4$	0.20	0.1893	$3.0227 \times 10^{13}$	$2.2090 \times 10^{13}$	$2.2971 \times 10^{13}$
$5.66 \times 10^4$	0.30	0.2888	$2.2568 \times 10^{14}$	$1.8456 \times 10^{14}$	$1.8710 \times 10^{14}$
$1.35 \times 10^5$	0.40	0.3887	$9.2964 \times 10^{14}$	$8.0010 \times 10^{14}$	$8.0790 \times 10^{14}$
$2.63 \times 10^5$	0.50	0.4876	$2.7598 \times 10^{15}$	$2.4400 \times 10^{15}$	$2.4400 \times 10^{15}$
$4.53 \times 10^5$	0.60	0.5921	$6.6536 \times 10^{15}$	$6.0040 \times 10^{15}$	$6.0678 \times 10^{15}$
$7.19 \times 10^5$	0.70	0.6820	$1.3890 \times 10^{16}$	$1.2693 \times 10^{16}$	$1.2810 \times 10^{16}$
$1.08 \times 10^6$	0.80	0.7888	$2.6097 \times 10^{16}$	$2.4060 \times 10^{16}$	$2.4442 \times 10^{16}$
$2.10 \times 10^6$	1.00	0.9853	$7.3639 \times 10^{16}$	$6.8647 \times 10^{16}$	$6.8786 \times 10^{16}$
$3.63 \times 10^6$	1.20	1.1833	$1.6902 \times 10^{17}$	$1.5900 \times 10^{17}$	$1.5900 \times 10^{17}$
$5.77 \times 10^6$	1.40	1.3827	$3.3708 \times 10^{17}$	$3.1844 \times 10^{17}$	$3.1898 \times 10^{17}$
$8.62 \times 10^6$	1.6	1.5810	$6.0754 \times 10^{17}$	$5.7588 \times 10^{17}$	$5.7620 \times 10^{17}$
$1.23 \times 10^7$	1.80	1.7790	$1.0148 \times 10^{18}$	$9.6522 \times 10^{17}$	$9.6592 \times 10^{17}$
$1.68 \times 10^7$	2.0	1.9770	$1.5981 \times 10^{18}$	$1.5213 \times 10^{18}$	$1.5182 \times 10^{18}$
$3.27 \times 10^7$	2.50	2.4670	$4.1247 \times 10^{18}$	$3.9375 \times 10^{18}$	$3.9101 \times 10^{18}$
$5.66 \times 10^7$	3.00	2.965	$8.8468 \times 10^{18}$	$8.4593 \times 10^{18}$	$8.4262 \times 10^{18}$
$1.35 \times 10^8$	4.00	3.956	$2.9013 \times 10^{19}$	$2.7829 \times 10^{19}$	$2.7764 \times 10^{19}$
$2.63 \times 10^8$	5.00	4.939	$7.2160 \times 10^{19}$	$6.9166 \times 10^{19}$	$6.9062 \times 10^{19}$
$8.85 \times 10^8$	7.50	7.423	$3.7254 \times 10^{20}$	$3.5700 \times 10^{20}$	$3.5700 \times 10^{20}$

### Relativistic FMT treatment vs. non-relativistic FMT treatment

We now compare and contrast the Fermi energy, given by Eq. (A.2.32), of a compressed atom in the non-relativistic and the relativistic limit (see Fig. A.10).

There are major differences:

1) The electron Fermi energy in the relativistic treatment is strongly dependent on the nuclear composition, while the non-relativistic treatment presents a universal behavior in the units of Fig. A.10. In the limit of low densities the relativistic curves approach the universal non-relativistic curve. In the non-relativistic treatment the ratio  $E_e^F / (m_\pi c^2 N_p^{4/3})$  does not depend on the number of protons  $N_p$  if the Wigner-Seitz cell radius  $R_{WS}$  is multiplied by  $N_p^{1/3}$  (see Eqs. (A.2.10), (A.2.11)). This universality is lost in the relativistic treatment since there is no way to eliminate the dependence of the electron Fermi energy on the nuclear composition (see Eq. (A.2.28)).

2) The relativistic treatment leads to values of the electron Fermi energy consistently smaller than the ones of the non-relativistic treatment.

3) While in the non-relativistic treatment the electron Fermi energy can reach, by compression, infinite values as  $R_{WS} \rightarrow 0$ , in the relativistic treatment it reaches a perfectly finite value given by Eq. (A.2.42) attained when  $R_{WS}$  coincides with the nuclear radius  $R_c$ .

It is clear then, from above considerations, the relativistic treatment of the Thomas-Fermi equation introduces significant differences from the current approximations in the literature: a) the uniform electron distribution (Bürvenich et al., 2007), b) the approximate perturbative solutions departing from the uniform distribution (Salpeter, 1961a) and c) the non-relativistic treatment (Feynman et al., 1949). We have recently applied these results of the relativistic Feynman, Metropolis, Teller treatment of a compressed atom to the study of white dwarfs and their consequences on the determination of their masses, radii and critical mass (Rotondo et al., 2011b).

### A.2.5. Application to nuclear matter cores of stellar dimensions

We turn now to nuclear matter cores of stellar dimensions of  $A \simeq (m_{\text{Planck}}/m_n)^3 \sim 10^{57}$  or  $M_{\text{core}} \sim M_\odot$ .

Following the treatment presented in Rotondo et al. (2011e), we use the existence of scaling laws and proceed to the ultra-relativistic limit of Eqs. (A.2.20), (A.2.28), (A.2.31), (A.2.33). For positive values of the electron Fermi energy  $E_e^F$ , we introduce the new function  $\phi = 4^{1/3}(9\pi)^{-1/3}\chi\Delta/x$  and the new variable  $\hat{x} = kx$  where  $k = (12/\pi)^{1/6}\sqrt{\alpha}\Delta^{-1}$ , as well as the variable  $\xi = \hat{x} - \hat{x}_c$  in order to describe better the region around the core radius.

Eq. (A.2.28) becomes

$$\frac{d^2\hat{\phi}(\xi)}{d\xi^2} = -\theta(-\xi) + \hat{\phi}(\xi)^3, \quad (\text{A.2.45})$$

where  $\hat{\phi}(\xi) = \phi(\xi + \hat{x}_c)$  and the curvature term  $2\hat{\phi}'(\xi)/(\xi + \hat{x}_c)$  has been neglected.

The Coulomb potential energy is given by

$$eV(\xi) = \left(\frac{9\pi}{4}\right)^{1/3} \frac{1}{\Delta} m_\pi c^2 \hat{\phi}(\xi) - E_e^F, \quad (\text{A.2.46})$$

corresponding to the electric field

$$E(\xi) = - \left(\frac{3^5\pi}{4}\right)^{1/6} \frac{\sqrt{\alpha} m_\pi^2 c^3}{\Delta^2 e\hbar} \hat{\phi}'(\xi), \quad (\text{A.2.47})$$

and the electron number-density

$$n_e(\xi) = \frac{1}{3\pi^2\hbar^3 c^3} \left(\frac{9\pi}{4}\right) \frac{1}{\Delta^3} (m_\pi c^2)^3 \hat{\phi}^3(\xi). \quad (\text{A.2.48})$$

In the core center we must have  $n_e = n_p$ . From Eqs. (A.2.20) and (A.2.48) we then have that, for  $\xi = -\hat{x}_c$ ,  $\hat{\phi}(-\hat{x}_c) = 1$ .

In order to consider a compressed nuclear density core of stellar dimensions, we then introduce a Wigner-Seitz cell determining the outer boundary of the electron distribution which, in the new radial coordinate  $\xi$  is characterized by  $\xi^{WS}$ . In view of the global charge neutrality of the system the electric field goes to zero at  $\xi = \xi^{WS}$ . This implies, from Eq. (A.2.47),  $\hat{\phi}'(\xi^{WS}) = 0$ .

We now turn to the determination of the Fermi energy of the electrons in this compressed core. The function  $\hat{\phi}$  and its first derivative  $\hat{\phi}'$  must be continuous at the surface  $\xi = 0$  of the nuclear density core.

This boundary-value problem can be solved analytically and indeed Eq. (A.2.45) has the first integral,

$$2[\hat{\phi}'(\xi)]^2 = \begin{cases} \hat{\phi}^4(\xi) - 4\hat{\phi}(\xi) + 3, & \xi < 0, \\ \hat{\phi}^4(\xi) - \hat{\phi}^4(\xi^{WS}), & \xi > 0, \end{cases} \quad (\text{A.2.49})$$

with boundary conditions at  $\xi = 0$ :

$$\begin{aligned} \hat{\phi}(0) &= \frac{\hat{\phi}^4(\xi^{WS}) + 3}{4}, \\ \hat{\phi}'(0) &= -\sqrt{\frac{\hat{\phi}^4(0) - \hat{\phi}^4(\xi^{WS})}{2}}. \end{aligned} \quad (\text{A.2.50})$$

Having fulfilled the continuity condition we integrate Eq. (A.2.49) obtaining for  $\xi \leq 0$

$$\hat{\phi}(\xi) = 1 - 3 \left[ 1 + 2^{-1/2} \sinh(a - \sqrt{3}\xi) \right]^{-1}, \quad (\text{A.2.51})$$

where the integration constant  $a$  has the value

$$\sinh(a) = \sqrt{2} \left( \frac{11 + \hat{\phi}^4(\xi^{WS})}{1 - \hat{\phi}^4(\xi^{WS})} \right). \quad (\text{A.2.52})$$

In the interval  $0 \leq \xi \leq \xi^{WS}$ , the field  $\hat{\phi}(\xi)$  is implicitly given by

$$F \left( \arccos \frac{\hat{\phi}(\xi^{WS})}{\hat{\phi}(\xi)}, \frac{1}{\sqrt{2}} \right) = \hat{\phi}(\xi^{WS})(\xi - \xi^{WS}), \quad (\text{A.2.53})$$

where  $F(\varphi, k)$  is the elliptic function of the first kind, and  $F(0, k) \equiv 0$ . For  $F(\varphi, k) = u$ , the inverse function  $\varphi = F^{-1}(u, k) = \text{am}(u, k)$  is the well known Jacobi amplitude. In terms of it, we can express the solution (A.2.53) for  $\xi > 0$  as,

$$\hat{\phi}(\xi) = \hat{\phi}(\xi^{WS}) \left\{ \cos \left[ \text{am} \left( \hat{\phi}(\xi^{WS})(\xi - \xi^{WS}), \frac{1}{\sqrt{2}} \right) \right] \right\}^{-1}. \quad (\text{A.2.54})$$

In the present case of  $E_e^F > 0$  the ultra-relativistic approximation is indeed always valid up to  $\xi = \xi^{WS}$  for high compression factors, i.e. for  $R_{WS} \simeq R_c$ . In the case  $E_e^F = 0$ ,  $\xi^{WS} \rightarrow \infty$ , there is a breakdown of the ultra-relativistic approximation when  $\xi \rightarrow \xi^{WS}$ .

Details are given in Figs. A.11, A.12, A.13.

We can now estimate two crucial quantities of the solutions: the Coulomb potential at the center of the configuration and the electric field at the surface of the core

$$eV(0) \simeq \left( \frac{9\pi}{4} \right)^{1/3} \frac{1}{\Delta} m_\pi c^2 - E_e^F, \quad (\text{A.2.55})$$

$$E_{\max} \simeq 2.4 \frac{\sqrt{\alpha}}{\Delta^2} \left( \frac{m_\pi}{m_e} \right)^2 E_c |\hat{\phi}'(0)|, \quad (\text{A.2.56})$$

where  $E_c = m_e^2 c^3 / (e\hbar)$  is the critical electric field for vacuum polarization. These functions depend on the value  $\hat{\phi}(\xi^{WS})$  via Eqs. (A.2.49)–(A.2.53). At the boundary  $\xi = \xi^{WS}$ , due to the global charge neutrality, both the electric field  $E(\xi^{WS})$  and the Coulomb potential  $eV(\xi^{WS})$  vanish. From Eq. (A.2.46),

we determine the value of  $\hat{\phi}(\xi)$  at  $\xi = \xi^{WS}$

$$\hat{\phi}(\xi^{WS}) = \Delta \left( \frac{4}{9\pi} \right)^{1/3} \frac{E_e^F}{m_\pi c^2}, \quad (\text{A.2.57})$$

as a function of the electron Fermi energies  $E_e^F$ . From the above Eq. (A.2.57), one can see that there exists a solution, characterized by the value of electron Fermi energy

$$\frac{(E_e^F)_{max}}{m_\pi c^2} = \frac{1}{\Delta} \left( \frac{9\pi}{4} \right)^{1/3}, \quad (\text{A.2.58})$$

such that  $\hat{\phi}(\xi^{WS}) = 1$ . From Eq. (A.2.53) and  $\xi = 0$ , we also have

$$\xi^{WS}(\hat{\phi}(\xi^{WS})) = \left\{ \frac{1}{\hat{\phi}(0)} F \left[ \arccos \left( 4 - \frac{3}{\hat{\phi}(0)} \right), \frac{1}{\sqrt{2}} \right] \right\}. \quad (\text{A.2.59})$$

For  $\hat{\phi}(\xi^{WS}) = 1$ , from Eq. (A.2.50) follows  $\hat{\phi}(0) = 1$  hence Eq. (A.2.59) becomes

$$\xi^{WS}(\hat{\phi}(0)) = F \left[ 0, \frac{1}{\sqrt{2}} \right]. \quad (\text{A.2.60})$$

It is well known that if the inverse Jacobi amplitude  $F[0, 1/\sqrt{2}]$  is zero, then

$$\xi^{WS}(\hat{\phi}(\xi^{WS}) = \hat{\phi}(0) = 1) = 0. \quad (\text{A.2.61})$$

Indeed from  $\hat{\phi}(\xi^{WS}) = 1$  follows  $\hat{\phi}(0) = 1$  and  $\xi^{WS} = 0$ . When  $\xi^{WS} = 0$  from Eq. (A.2.50) follows  $\hat{\phi}'(0) = 0$  and, using Eq. (A.2.56),  $E_{max} = 0$ . In other words for the value of  $E_e^F$  fulfilling Eq. (A.2.57) no electric field exists on the boundary of the core and from Eq. (A.2.48) and Eqs. (A.2.19, A.2.20) it follows that indeed this is the solution fulfilling both global  $N_e = N_p$  and local  $n_e = n_p$  charge neutrality. In this special case, starting from Eq. (A.2.33) and  $A = N_p + N_n$ , we obtain

$$(E_e^F)_{max}^{3/2} = \frac{\frac{9\pi}{4}(\hbar c)^3 \frac{A}{R_c^3} - (E_e^F)_{max}^3}{2^{3/2} \left[ \left( \frac{9\pi}{4}(\hbar c)^3 \frac{A}{R_c^3} - (E_e^F)_{max}^3 \right)^{2/3} + m_n^2 c^4 \right]^{3/4}}. \quad (\text{A.2.62})$$

In the ultra-relativistic approximation  $(E_e^F)_{max}^3 / \frac{9\pi}{4}(\hbar c)^3 \frac{A}{R_c^3} \ll 1$  so Eq. (A.2.62)

can be approximated to

$$(E_e^F)_{max} = 2^{1/3} \frac{m_n}{m_\pi} \gamma \left[ -1 + \sqrt{1 + \frac{\beta}{2\gamma^3}} \right]^{2/3} m_\pi c^2, \quad (\text{A.2.63})$$

where

$$\beta = \frac{9\pi}{4} \left( \frac{\hbar}{m_n c} \right)^3 \frac{A}{R_c^3}, \quad \gamma = \sqrt{1 + \beta^{2/3}}. \quad (\text{A.2.64})$$

The corresponding limiting value to the  $N_p/A$  ratio is obtained as follows

$$\frac{N_p}{A} = \frac{2\gamma^3}{\beta} \left[ -1 + \sqrt{1 + \frac{\beta}{2\gamma^3}} \right]^2. \quad (\text{A.2.65})$$

Inserting Eqs. (A.2.63), (A.2.64) in Eq. (A.2.65) one obtains the ultra-relativistic limit of Eq. (A.2.42), since the electron Fermi energy, in view of the scaling laws introduced in Rotondo et al. (2011e), is independent of the value of  $A$  and depends only on the density of the core.

The  $N_p$ -independence in the limiting case of maximum electron Fermi energy attained when  $R_{WS} = R_c$ , in which the ultra-relativistic treatment approaches the uniform one, and the  $N_p$ -dependence for smaller compressions  $R_{WS} > R_c$  can be understood as follows. Let see the solution to the ultra-relativistic equation (A.2.45) for small  $\xi > 0$ . Analogously to the Feynman-Metropolis-Teller approach to the non-relativistic Thomas-Fermi equation, we solve the ultra-relativistic equation (A.2.45) for small  $\xi$ . Expanding  $\hat{\phi}(\xi)$  about  $\xi = 0$  in a semi convergent power series,

$$\frac{\hat{\phi}(\xi)}{\hat{\phi}(0)} = 1 + \sum_{n=2}^{\infty} a_n \xi^{n/2} \quad (\text{A.2.66})$$

and substituting it into the ultra-relativistic equation (A.2.45), we have

$$\sum_{k=3}^{\infty} a_k \frac{k(k-2)}{4} \xi^{(k-4)/2} = \phi^2(0) \exp \left[ 3 \ln \left( 1 + \sum_{n=2}^{\infty} a_n \xi^{n/2} \right) \right]. \quad (\text{A.2.67})$$

This leads to a recursive determination of the coefficients:

$$\begin{aligned} a_3 &= 0, \quad a_4 = \phi^2(0)/2, \quad a_5 = 0, \quad a_6 = \phi^2(0)a_2/2, \quad a_7 = 0, \\ a_8 &= \phi^2(0)(1 - a_2^2)/8, \dots, \end{aligned} \quad (\text{A.2.68})$$

with  $a_2 = \hat{\phi}'(0)/\hat{\phi}(0)$  determined by the initial slope, namely, the boundary

condition  $\hat{\phi}'(0)$  and  $\hat{\phi}(0)$  in Eq. (A.2.50):

$$\hat{\phi}(0) = \frac{\hat{\phi}^4(\xi^{WS}) + 3}{4}, \quad \hat{\phi}'(0) = -\sqrt{\frac{\hat{\phi}^4(0) - \hat{\phi}^4(\xi^{WS})}{2}} \quad (\text{A.2.69})$$

Thus the series solution (A.2.66) is uniquely determined by the boundary value  $\hat{\phi}(\xi^{WS})$  at the Wigner-Seitz cell radius.

Now we consider the solution up to the leading orders

$$\begin{aligned} \hat{\phi}(\xi) &= \hat{\phi}(0) + \hat{\phi}'(0)\xi + \frac{1}{2}\hat{\phi}''(0)\xi^2 + \frac{1}{2}\hat{\phi}'''(0)a_2\xi^3 \\ &+ \frac{1}{8}\hat{\phi}^{(4)}(0)(1 - a_2^2)\xi^4 + \dots \end{aligned} \quad (\text{A.2.70})$$

Using Eq. (A.2.70), the electron Fermi energy (A.2.57) becomes

$$\begin{aligned} E_e^F &= (E_e^F)_{max} \left[ 1 + a_2\xi^{WS} + \frac{1}{2}\hat{\phi}''(0)(\xi^{WS})^2 + \frac{1}{2}\hat{\phi}''(0)a_2(\xi^{WS})^3 \right. \\ &\left. + \frac{1}{8}\hat{\phi}^{(4)}(0)(1 - a_2^2)(\xi^{WS})^4 + \dots \right] \hat{\phi}(0), \end{aligned} \quad (\text{A.2.71})$$

where  $(E_e^F)_{max} = (9\pi/4)^{1/3}\Delta^{-1}$  is the maximum Fermi energy which is attained when the Wigner-Seitz cell radius equals the nucleus radius  $R_c$  (see Eq. A.2.58). For  $\hat{\phi}(\xi^{WS}) < 1$ , we approximately have  $\hat{\phi}(0) = 3/4$ ,  $\hat{\phi}'(0) = -(3/4)^2/\sqrt{2}$  and the initial slope  $a_2 = \hat{\phi}'(0)/\hat{\phi}(0) = -(3/4)/\sqrt{2}$ . Therefore Eq. (A.2.71) becomes

$$\begin{aligned} E_e^F &\approx (E_e^F)_{max} \left[ 1 - \frac{3}{4\sqrt{2}}\xi^{WS} + \frac{1}{2}\left(\frac{3}{4}\right)^2(\xi^{WS})^2 - \frac{1}{2^{3/2}}\left(\frac{3}{4}\right)^3(\xi^{WS})^3 \right. \\ &\left. + \frac{1}{8}\left(\frac{3}{4}\right)^2\left(\frac{41}{32}\right)(\xi^{WS})^4 + \dots \right]. \end{aligned} \quad (\text{A.2.72})$$

By the definition of the coordinate  $\xi$ , we know all terms except the first term in the square bracket depend on the values of  $N_p$ . In the limit of maximum compression when the electron Fermi energy acquires its maximum value, namely when  $\xi^{WS} = 0$ , the electron Fermi energy (A.2.72) is the same as the one obtained from the uniform approximation which is independent of  $N_p$ . For smaller compressions, namely for  $\xi^{WS} > 0$  the electron Fermi energy deviates from the one given by the uniform approximation becoming  $N_p$ -dependent.

In Fig. A.14 we plot the Fermi energy of electrons, in units of the pion rest energy, as a function of the dimensionless parameter  $\xi^{WS}$  and, as  $\xi^{WS} \rightarrow 0$ , the limiting value given by Eq. (A.2.63) is clearly displayed.

In Alcock et al. (1986), in order to study the electro-dynamical properties of strange stars, the ultra-relativistic Thomas-Fermi equation was numerically solved in the case of bare strange stars as well as in the case of strange stars with a crust (see e.g. curves (a) and (b) in Fig. 6 of Alcock et al. (1986)). In Fig. 6 of Alcock et al. (1986) was plotted what they called the Coulomb potential energy, which we will denote as  $V_{\text{Alcock}}$ . The potential  $V_{\text{Alcock}}$  was plotted for different values of the electron Fermi momentum at the edge of the crust. Actually, such potential  $V_{\text{Alcock}}$  is not the Coulomb potential  $eV$  but it coincides with our function  $e\hat{V} = eV + E_e^F$ . Namely, the potential  $V_{\text{Alcock}}$  corresponds to the Coulomb potential shifted by the the Fermi energy of the electrons. We then have from Eq. (A.2.46)

$$e\hat{V}(\xi) = \left(\frac{9\pi}{4}\right)^{1/3} \frac{1}{\Delta} m_{\pi} c^2 \hat{\phi}(\xi) = V_{\text{Alcock}}. \quad (\text{A.2.73})$$

This explains why in Alcock et al. (1986), for different values of the Fermi momentum at the crust the depth of the potential  $V_{\text{Alcock}}$  remains unchanged. Instead, the correct behavior of the Coulomb potential is quite different and, indeed, its depth decreases with increasing of compression as can be seen in Fig. A.11.

### A.2.6. Compressional energy of nuclear matter cores of stellar dimensions

We turn now to the compressional energy of these family of compressed nuclear matter cores of stellar dimensions each characterized by a different Fermi energy of the electrons. The kinematic energy-spectra of complete degenerate electrons, protons and neutrons are

$$\epsilon^i(p) = \sqrt{(pc)^2 + m_i^2 c^4}, \quad p \leq P_i^F, \quad i = e, p, n. \quad (\text{A.2.74})$$

So the compressional energy of the system is given by

$$\mathcal{E} = \mathcal{E}_B + \mathcal{E}_e + \mathcal{E}_{\text{em}}, \quad \mathcal{E}_B = \mathcal{E}_p + \mathcal{E}_n, \quad (\text{A.2.75})$$

$$\mathcal{E}_i = 2 \int_i \frac{d^3 r d^3 p}{(2\pi\hbar)^3} \epsilon^i(p), \quad i = e, p, n, \quad \mathcal{E}_{\text{em}} = \int \frac{E^2}{8\pi} d^3 r. \quad (\text{A.2.76})$$

Using the analytic solution (A.2.54) we calculate the energy difference between two systems,  $I$  and  $II$ ,

$$\Delta\mathcal{E} = \mathcal{E}(E_e^F(II)) - \mathcal{E}(E_e^F(I)), \quad (\text{A.2.77})$$

with  $E_e^F(II) > E_e^F(I) \geq 0$ , at fixed  $A$  and  $R_c$ .

We first consider the infinitesimal variation of the total energy  $\delta\mathcal{E}_{\text{tot}}$  with

respect to the infinitesimal variation of the electron Fermi energy  $\delta E_e^F$

$$\delta \mathcal{E} = \left[ \frac{\partial \mathcal{E}}{\partial N_p} \right]_{VWS} \left[ \frac{\partial N_p}{\partial E_e^F} \right] \delta E_e^F + \left[ \frac{\partial \mathcal{E}}{\partial VWS} \right]_{N_p} \left[ \frac{\partial VWS}{\partial E_e^F} \right] \delta E_e^F. \quad (\text{A.2.78})$$

For the first term of this relation we have

$$\left[ \frac{\partial \mathcal{E}}{\partial N_p} \right]_{VWS} = \left[ \frac{\partial \mathcal{E}_p}{\partial N_p} + \frac{\partial \mathcal{E}_n}{\partial N_p} + \frac{\partial \mathcal{E}_e}{\partial N_p} + \frac{\partial \mathcal{E}_{em}}{\partial N_p} \right]_{VWS} \simeq \left[ E_p^F - E_n^F + E_e^F + \frac{\partial \mathcal{E}_{em}}{\partial N_p} \right]_{VWS}, \quad (\text{A.2.79})$$

where the general definition of chemical potential  $\partial \epsilon_i / \partial n_i = \partial \mathcal{E}_i / \partial N_i$  is used ( $i = e, p, n$ ) neglecting the mass defect  $m_n - m_p - m_e$ . Further using the condition of the beta-equilibrium (A.2.33) we have

$$\left[ \frac{\partial \mathcal{E}}{\partial N_p} \right]_{VWS} = \left[ \frac{\partial \mathcal{E}_{em}}{\partial N_p} \right]_{VWS}. \quad (\text{A.2.80})$$

For the second term of the Eq. (A.2.78) we have

$$\left[ \frac{\partial \mathcal{E}}{\partial VWS} \right]_{N_p} = \left[ \frac{\partial \mathcal{E}_p}{\partial VWS} + \frac{\partial \mathcal{E}_n}{\partial VWS} + \frac{\partial \mathcal{E}_e}{\partial VWS} + \frac{\partial \mathcal{E}_{em}}{\partial VWS} \right]_{N_p} = \left[ \frac{\partial \mathcal{E}_e}{\partial VWS} \right]_{N_p} + \left[ \frac{\partial \mathcal{E}_{em}}{\partial VWS} \right]_{N_p}, \quad (\text{A.2.81})$$

since in the process of increasing the electron Fermi energy namely, by decreasing the radius of the Wigner-Seitz cell, the system by definition maintains the same number of baryons  $A$  and the same core radius  $R_c$ .

Now  $\delta \mathcal{E}$  reads

$$\delta \mathcal{E} = \left\{ \left[ \frac{\partial \mathcal{E}_e}{\partial VWS} \right]_{N_p} \frac{\partial VWS}{\partial E_e^F} + \left[ \frac{\partial \mathcal{E}_{em}}{\partial VWS} \right]_{N_p} \frac{\partial VWS}{\partial E_e^F} + \left[ \frac{\partial \mathcal{E}_{em}}{\partial N_p} \right]_{VWS} \frac{\partial N_p}{\partial E_e^F} \right\} \delta E_e^F, \quad (\text{A.2.82})$$

so only the electromagnetic energy and the electron energy give non-null contributions.

From this equation it follows that

$$\Delta \mathcal{E} = \Delta \mathcal{E}_{em} + \Delta \mathcal{E}_e, \quad (\text{A.2.83})$$

where  $\Delta \mathcal{E}_{em} = \mathcal{E}_{em}(E_e^F(II)) - \mathcal{E}_{em}(E_e^F(I))$  and  $\Delta \mathcal{E}_e = \mathcal{E}_e(E_e^F(II)) - \mathcal{E}_e(E_e^F(I))$ .

In the particular case in which  $E_e^F(II) = (E_e^F)_{max}$  and  $E_e^F(I) = 0$  we obtain

$$\Delta \mathcal{E} \simeq 0.75 \frac{3^{5/3}}{2} \left( \frac{\pi}{4} \right)^{1/3} \frac{1}{\Delta \sqrt{\alpha}} \left( \frac{\pi}{12} \right)^{1/6} N_p^{2/3} m_\pi c^2, \quad (\text{A.2.84})$$

which is positive.

The compressional energy of a nuclear matter core of stellar dimensions increases with its electron Fermi energy as expected.

### A.2.7. Conclusions

The results presented in this article are in the realm of theoretical physics of nuclear physics and of atomic physics and give special attention to relativistic effects. They generalize to the relativistic regimes classical results obtained by Feynman, Metropolis and Teller (Feynman et al., 1949) and, by the introduction of scaling laws, they generalize the classical results obtained by Migdal et al. (1976, 1977); Rotondo et al. (2011e) in heavy nuclei to massive cores of  $\sim M_{\odot}$ . As such they find their justification. They acquire also special meaning in astrophysics: the considerations contained in Secs. I–IV lead to a consistent treatment of white dwarfs and the ones in Secs. V and VI lead to a deeper understanding of neutron star physics.

We have generalized to the relativistic regime the classic work of Feynman, Metropolis and Teller by solving the relativistic Thomas-Fermi equation in a Wigner-Seitz cell corresponding to a compressed atom. The integration of this equation does not admit regular solutions for a point-like nucleus and both the nuclear radius and the nuclear composition have necessarily to be taken into account (Ferreirinho et al., 1980; Ruffini and Stella, 1981). This introduces a fundamental difference from the non-relativistic Thomas-Fermi model where a point-like nucleus is traditionally adopted.

As in previous works by Ferreira et al. (1980), Ruffini and Stella (1981) and Rotondo et al. (2011e), the protons in the nuclei have been assumed to be at constant density, the electron distribution has been derived by the relativistic Thomas-Fermi equation and the neutron component by the beta equilibrium between neutrons, protons and electrons.

We have examined, for completeness, the relativistic generalization of the Thomas-Fermi-Dirac equation by taking into due account the exchange terms (Dirac, 1930), adopting the general approach of Migdal et al. (1977), and shown that these effects, generally small, can be neglected in the relativistic treatment.

There are marked differences between the relativistic and the non-relativistic treatments.

The first is that the existence of a finite size nucleus introduces a limit to the compressibility: the dimension of the Wigner-Seitz cell can never be smaller than the nuclear size. Consequently the electron Fermi energy which in the non-relativistic approach can reach arbitrarily large values, reaches in the present case a perfectly finite value: an expression for this finite value of the electron Fermi energy has been given in analytic form. There are in the literature many papers adopting a relativistic treatment for the electrons, with a point-like approximation for the nucleus, which are clearly inconsistent (see e.g. Chabrier and Potekhin (1998) and Potekhin et al. (2009)).

The second is the clear difference of the electron distribution as a function of the radius and of the nuclear composition as contrasted to the uniform approximation (see Fig. A.8 of Sec. A.2.4), often adopted in the literature (see

e.g. Bürvenich et al. (2007)). Therefore the validity of inferences based on a uniform approximation should be duly verified both in the relativistic and in the non-relativistic regime.

The third is that the relativistic Feynman-Metropolis-Teller treatment allows to treat precisely the electro-dynamical interaction within a compressed atom with all the relativistic corrections. This allows to validate and in some cases overcome the difficulties of treatments describing the electro-dynamical effect by a sequence of successive approximations. This is the case of validation of the Salpeter approach at high densities and the overcome of negative pressures at low densities. The new treatment evidences a softening of the dependence of the electron Fermi energy on the compression factor, as well as a gradual decrease of the exchange terms in proceeding from the non-relativistic to the fully relativistic regimes. It is then possible to derive, as shown in Table A.1 of Sec. A.2.4, a consistent equation of state for compressed matter.

The equation of state obtained in Table A.1 of Sec. A.2.4 has been recently applied to the study of the general relativistic white-dwarf equilibrium configurations by Rotondo et al. (2011b). The contribution of quantum statistics, weak and electromagnetic interactions here considered have been further generalized there by considering the contribution of the general relativistic equilibrium of white dwarf matter. This is expressed by the simple formula  $\sqrt{g_{00}}\mu_{ws} = \text{constant}$ , which links the chemical potential of the Wigner-Seitz cell  $\mu_{ws}$  with the general relativistic gravitational potential  $g_{00}$  at each point of the configuration. The configuration outside each Wigner-Seitz cell is strictly neutral and therefore no global electric field is necessary to warranty the equilibrium of the white dwarf. These equations modify the ones used by Chandrasekhar by taking into due account the Coulomb interaction between the nuclei and the electrons as well as inverse beta decay. They also generalize the work of Salpeter by considering a unified self-consistent approach to the Coulomb interaction in each Wigner-Seitz cell. The consequences on the numerical value of the Chandrasekhar-Landau mass limit have been then presented as well as on the mass-radius relation of white dwarfs (Rotondo et al., 2011b). This leads to the possibility of a direct confrontation of these results with observations, in view of the current great interest for the cosmological implications of the type Ia supernovae (Phillips, 1993; Riess et al., 1998; Perlmutter et al., 1999; Riess et al., 2004) and in the case of low mass white dwarf companion of the Pulsar PSRJ1141-6545 (Kramer, 2010) as well as the role of white dwarfs in novae.

In Secs. V and VI we have then extrapolated these results to the case of nuclear matter cores of stellar dimensions for  $A \approx (m_{\text{Planck}}/m_n)^3 \sim 10^{57}$  or  $M_{\text{core}} \sim M_{\odot}$ . The aim here is to explore the possibility of obtaining for these systems a self-consistent solution presenting global and not local charge neutrality. The results generalize the considerations presented in the previous article by Rotondo et al. (2011e) corresponding to a nuclear matter core of stel-

lar dimensions with null Fermi energy of the electrons. The ultra-relativistic approximation allows to obtain analytic expressions for the fields in the case of positive electron Fermi energies. An entire family of configurations exist with values of the Fermi energy of the electrons ranging from zero to a maximum value  $(E_e^F)_{max}$  which is reached when the Wigner-Seitz cell coincides with the core radius. The configuration with  $E_e^F = (E_e^F)_{max}$  corresponds to the configuration with  $N_p = N_e$  and  $n_p = n_e$ : for this limiting value of the Fermi energy the system fulfills both the global and the local charge neutrality and, correspondingly, no electro-dynamical structure is present in the core. The other configurations present generally overcritical electric fields close to their surface. The configuration with  $E_e^F = 0$  has the maximum value of the electric field at the core surface, well above the critical value  $E_c$  (see Fig. A.11, Fig. A.12 and Fig. A.13 of Section A.2.5). All these cores with overcritical electric fields are stable against the vacuum polarization process due to the Pauli blocking by the degenerate electrons (see e.g. Ruffini et al. (2010b)). We have also compared and contrasted our treatment of the relativistic Thomas-Fermi solutions to the corresponding one addressed in the framework of strange stars by Alcock et al. (1986), pointing out in these treatments some inconsistency in the definition of the Coulomb potential. We have finally compared the compressional energy of configurations with selected values of the electron Fermi energy.

The above problem is theoretically well defined, represents a necessary step in order to approach the more complex problem of a neutron star core and its interface with the neutron star crust.

Neutron stars are composed of two sharply different components: the liquid core at nuclear and/or supra-nuclear density consisting of neutrons, protons and electrons and a crust of degenerate electrons in a lattice of nuclei (see e.g. Baym et al. (1971a)) and Harrison et al. (1965)) and possibly of free neutrons due to neutron drip when this process occurs (see e.g. Baym et al. (1971a)). Consequently, the boundary conditions for the electrons at the surface of the neutron star core will have generally a positive value of the electron Fermi energy in order to take into account the compressional effects of the neutron star crust on the core. The case of zero electron Fermi energy corresponds to the limiting case of absence of the crust.

In a set of interesting papers Glendenning (1992); Glendenning and Pei (1995); Christiansen and Glendenning (1997); Glendenning and Schaffner-Bielich (1999); Christiansen et al. (2000); Glendenning (2001) have relaxed the local charge neutrality condition for the description of the mixed phases in hybrid stars. In such configurations the global charge neutrality condition, as opposed to the local one, is applied to the limited regions where mixed phases occur while in the pure phases the local charge neutrality condition still holds. We have generalized Glendenning's considerations by looking to a violation of the local charge neutrality condition on the entire configuration, still keeping its overall charge neutrality. This effect cannot occur locally, and

requires a global description of the equilibrium configuration. To exemplified this novel approach we have considered in Rotondo et al. (2011d) the simplest, nontrivial, self-gravitating system of degenerate neutrons, protons and electrons in beta equilibrium in the framework of relativistic quantum statistics and the Einstein-Maxwell equations. The impossibility of imposing the condition of local charge neutrality on such systems is proved in complete generality. The crucial role of the constancy of the generalized electron Fermi energy is emphasized and consequently the coupled system of the general relativistic Thomas-Fermi equations and the Einstein-Maxwell equations is solved. We then give an explicit solution corresponding to a violation of the local charge neutrality condition on the entire star, still fulfilling the global charge neutrality when electromagnetic, weak and general relativistic effects are taken into account.

The results presented in the second part of this article on nuclear matter cores of stellar dimensions evidence the possibility of having the existence of critical electromagnetic fields at the core surface.

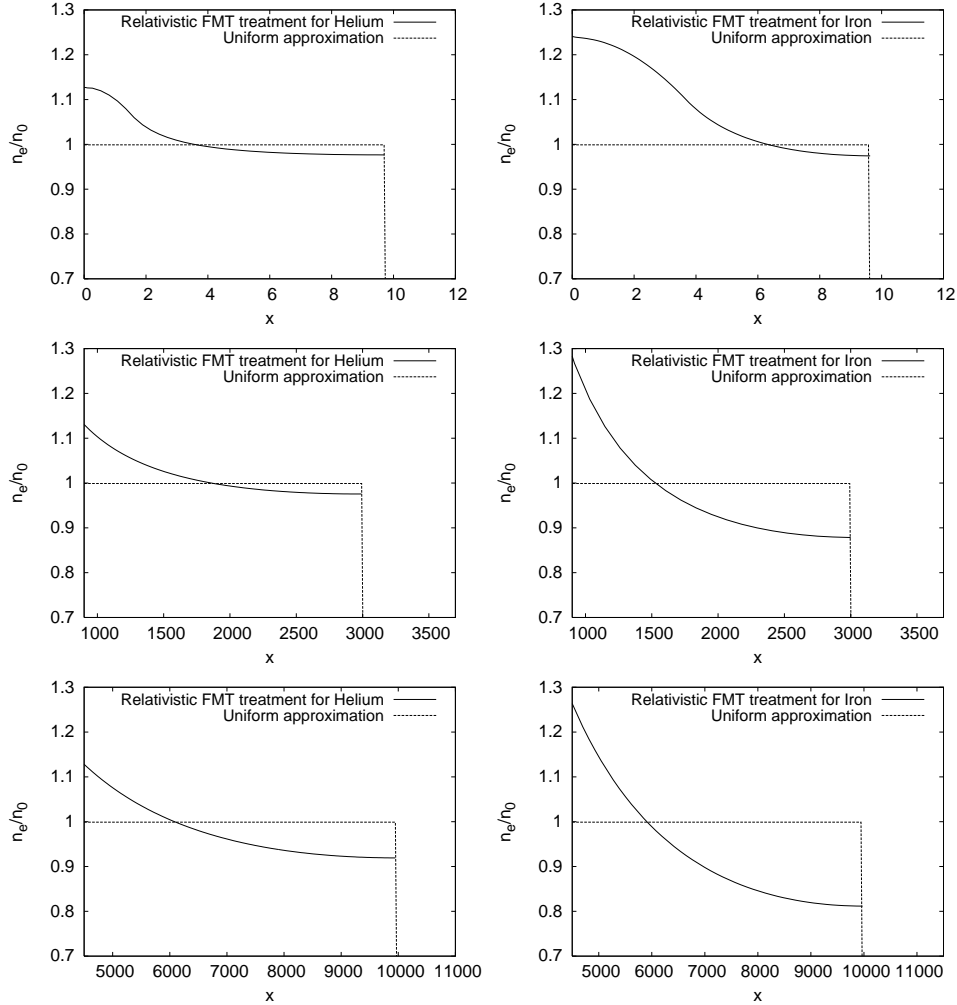


**Figure A.8.:** The electron number density  $n_e$  in units of the average electron number density  $n_0 = 3N_e/(4\pi R_{WS}^3)$  is plotted as a function of the dimensionless radial coordinate  $x = r/\lambda_\pi$  for the selected compressions  $x_{WS} = 9.7$  (upper panels),  $x_{WS} = 3 \times 10^3$  (middle panels) and  $x_{WS} = 10^4$  (bottom panels), in both the relativistic Feynman, Metropolis, Teller approach and the uniform approximation respectively for helium (panels on the left) and iron (panels on the right).

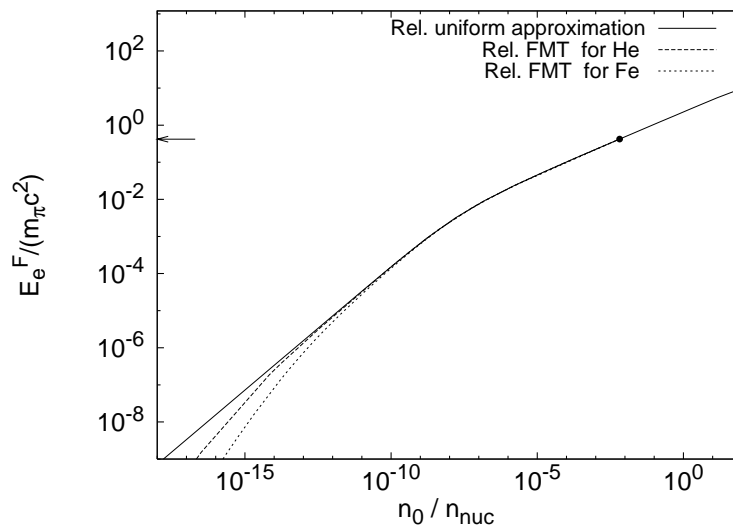


**Figure A.9.:** The electron Fermi energy  $E_e^F$  in units of the pion rest energy is plotted as a function of the average electron density  $n_0 = 3N_e / (4\pi R_{WS}^3)$  in units of the nuclear density  $n_{nuc} = 3A / (4\pi \Delta^3 N_p \lambda_\pi^3)$  for a uniform approximation (solid line), compared and contrasted to the ones obtained considering the relativistic Feynman, Metropolis, Teller approach. The arrow and the dot indicate the value of the maximum electron Fermi energy as given by Eq. (A.2.42), consistent with the finite size of the nucleus.

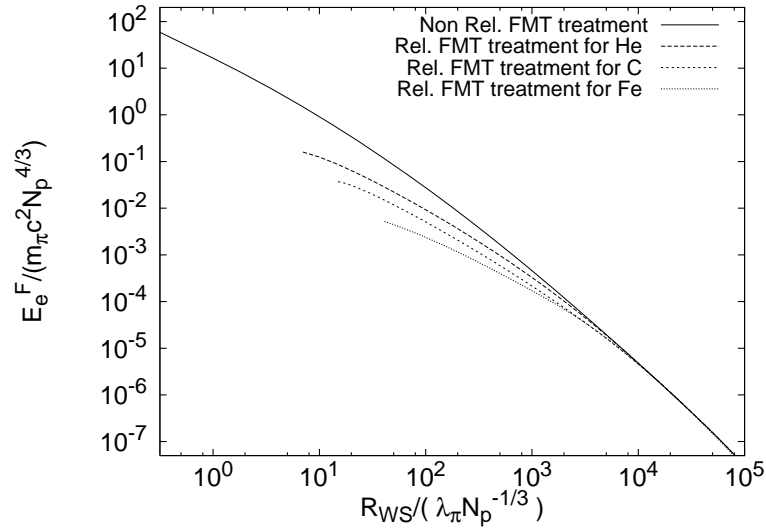


**Figure A.10.:** The electron Fermi energies in units of  $m_{\pi}c^2N_p^{4/3}$  for helium, carbon and iron are plotted as a function of the ratio  $R_{WS}/(\lambda_{\pi}N_p^{-1/3})$  respectively in the non-relativistic and in the relativistic Feynman-Metropolis-Teller (FMT) treatment. The dimensionless quantities have been chosen in order to obtain an universal curve in the non relativistic treatment following Eqs. (A.2.10) and (A.2.11). The relativistic treatment leads to results of the electron Fermi energy dependent on the nuclear composition and systematically smaller than the non-relativistic ones. The electron Fermi energy can attain arbitrary large values, in the non relativistic treatment, as the point-like nucleus is approached.

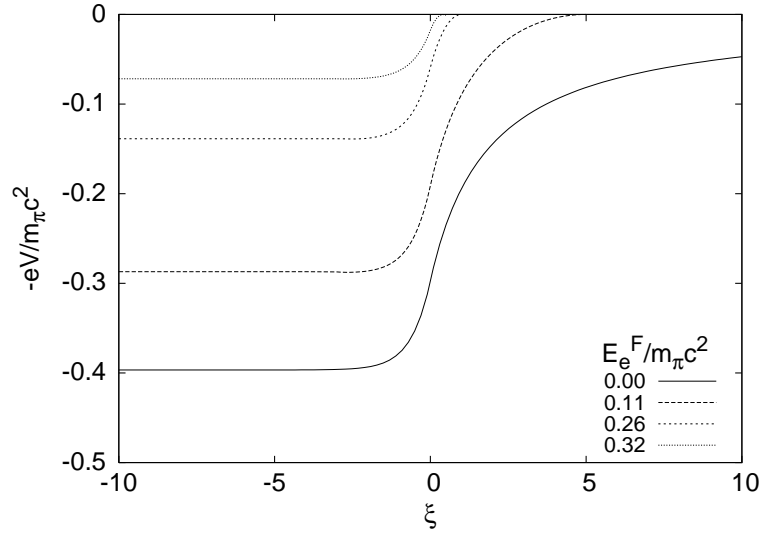


**Figure A.11.:** The electron Coulomb potential energies in units of the pion rest energy in a nuclear matter core of stellar dimensions with  $A \simeq 10^{57}$  or  $M_{core} \sim M_{\odot}$  and  $R_c \approx 10^6$  cm, are plotted as a function of the dimensionless variable  $\xi$ , for different values of the electron Fermi energy also in units of the pion rest energy. The solid line corresponds to the case of null electron Fermi energy. By increasing the value of the electron Fermi energy the electron Coulomb potential energy depth is reduced.

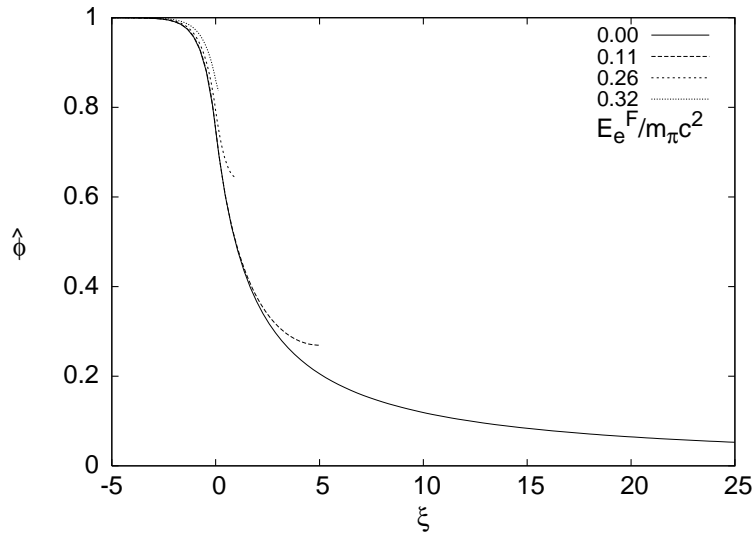


**Figure A.12.:** Solutions of the ultra-relativistic Thomas-Fermi equation (A.2.45) for different values of the Wigner-Seitz cell radius  $R_{WS}$  and correspondingly of the electron Fermi energy in units of the pion rest energy as in Fig. A.11, near the core surface. The solid line corresponds to the case of null electron Fermi energy.

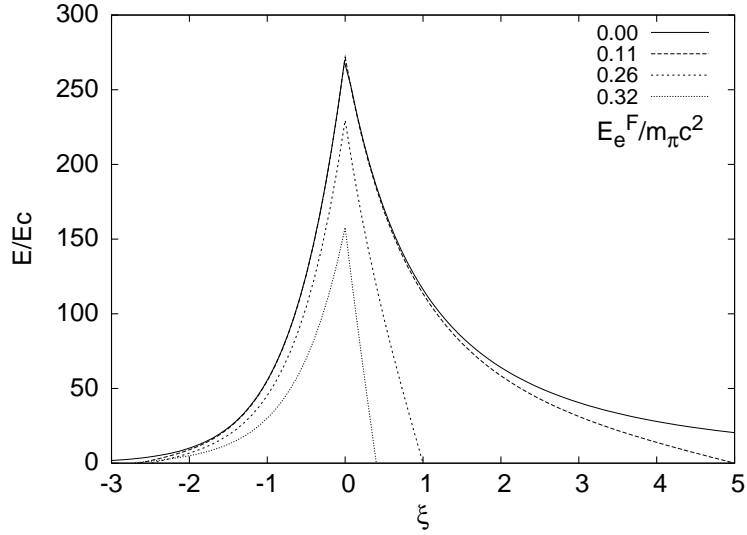


**Figure A.13.:** The electric field in units of the critical field for vacuum polarization  $E_c = m_e^2 c^3 / (e\hbar)$  is plotted as a function of the coordinate  $\xi$ , for different values of the electron Fermi energy in units of the pion rest energy. The solid line corresponds to the case of null electron Fermi energy. To an increase of the value of the electron Fermi energy it is found a reduction of the peak of the electric field.

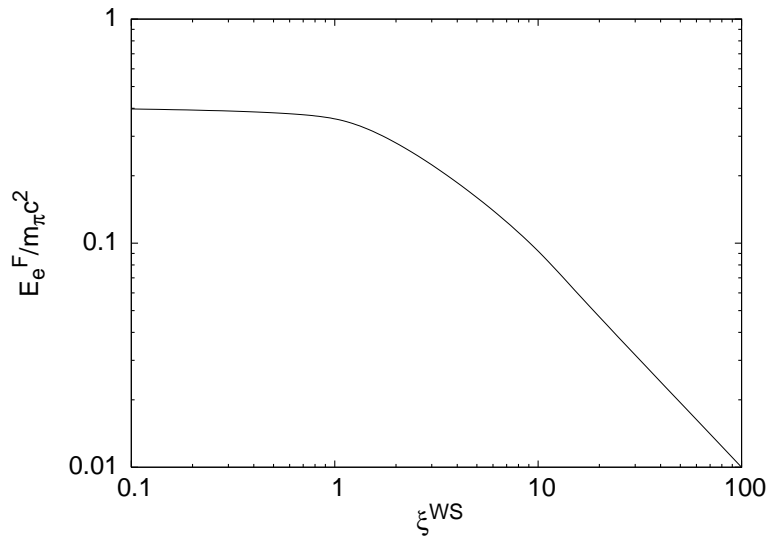


**Figure A.14.:** The Fermi energy of electrons in units of the pion rest energy is plotted for different Wigner-Seitz cell dimensions (i.e for different compressions)  $\xi^{WS}$  in the ultra-relativistic approximation. In the limit  $\xi^{WS} \rightarrow 0$  the electron Fermi energy approaches asymptotically the value  $(E_e^F)_{max}$  given by Eq. (A.2.63).

## A.3. The relativistic Feynman-Metropolis-Teller equation of state at finite temperatures

### A.3.1. Introduction

The Feynman-Metropolis-Teller (FMT) treatment considering a classic non-relativistic Thomas-Fermi model confined in a Wigner-Seitz cell has been recently generalized to relativistic regimes (Rotondo et al., 2011c) and applied to the description of non-rotating white dwarfs in general relativity Rotondo et al. (2011b). This approach improves all previous treatments of white dwarfs in the following aspects: 1) in order to guarantee self-consistency with a relativistic treatment of the electrons, the point-like assumption of the nucleus is abandoned introducing a finite sized nucleus; 2) the Coulomb interaction energy is fully calculated without any approximation by solving numerically the relativistic Thomas-Fermi equation for each given nuclear composition; 3) the energy-density of the system is calculated taking into account the contributions of the nuclei, of the Coulomb interactions as well as of the relativistic electrons, this latter neglected in all previous treatments and which is particularly important at high-densities and light nuclear compositions e.g.  ${}^4\text{He}$  and  ${}^{12}\text{C}$ ; 4) the  $\beta$ -equilibrium between neutrons, protons and electrons is also taken into account leading to a self-consistent calculation of the threshold density for triggering the inverse  $\beta$ -decay of a given nucleus; 5) the structure of the star is obtained by integrating the general relativity equations of equilibrium; 6) due to the points 4) and 5) we are able to determine if the instability point leading to a maximum stable mass of the non-rotating white dwarf is induced by the inverse  $\beta$ -decay or by general relativistic effects. This procedure takes into account many additional theoretical features and generalize the Chandrasekhar-Landau (Chandrasekhar, 1931b; Landau, 1932) and the work of Hamada and Salpeter (1961).

The main goal of this work is study the effects of finite temperatures on the equation of state (EOS). We first recall the construction of the EOS for matter composed of ions and relativistic electrons at zero temperatures following the recent relativistic Feynman-Metropolis-Teller treatment by Rotondo et al. (2011c) and extended such a treatment to the case of finite temperatures. The new EOS takes into account self-consistently the relativistic, Coulomb, thermal effects and beta equilibrium in a wide range of densities relevant for both white dwarfs and neutron star crusts.

### A.3.2. The Relativistic Feynman Metropolis Teller (FMT) Treatment

In the relativistic generalization of the Thomas-Fermi equation the point-like approximation of the nucleus must be abandoned. The relativistic equilib-

rium condition of compressed atoms for the degenerate case is expressed by

$$E_e^F = \sqrt{c^2(P_e^F)^2 + m_e^2c^4} - m_e^2c^2 - eV(r) = \text{constant} > 0, \quad (\text{A.3.1})$$

where  $V$  denotes the Coulomb potential,  $P_e^F$  is the electron Fermi momentum and  $E_e^F$  denotes the Fermi energy of electrons. The equation above would lead to a non-integrable expression for the electron density near the origin. Then we assume a constant distribution of protons confined in a radius  $R_c$  defined by:

$$R_c = \Delta\lambda_\pi Z^{\frac{1}{3}}, \quad (\text{A.3.2})$$

where  $\lambda_\pi = \hbar/(m_\pi c)$  and  $Z$  is the number of protons.

If we have nuclear density,  $\Delta \approx (r_0/\lambda_\pi)(A/Z)^{1/3}$  with  $r_0 \approx 1.2$  fm and  $A$  is the total number of nucleons. In the case of ordinary nuclei  $\Delta \approx 1$ . The proton density can be written as

$$n_p(r) = \frac{Z}{\frac{4}{3}\pi R_c^3} \Theta(R_c - r), \quad (\text{A.3.3})$$

where  $\Theta(R_c - r)$  denotes the heavside function centered at  $R_c$  and the electron density can be written as

$$n_e(r) = \frac{(P_e^F)^3}{3\pi^2\hbar^3} = \frac{1}{3\pi^2\hbar^3c^3} [\hat{V}^2(r) + 2m_e c^2 \hat{V}(r)]^{\frac{3}{2}}, \quad (\text{A.3.4})$$

where  $\hat{V} = e\hat{V} + E_e^F$ .

By introducing the dimensionless quantities  $x = r/\lambda_\pi$ ,  $x_c = R_c/\lambda_\pi$ ,  $\chi/r = \hat{V}(r)/(\hbar c)$  and replacing the particle densities into the Poisson Equation we obtain the relativistic Thomas-Fermi Equation

$$\frac{1}{3x} \frac{d^2\chi(x)}{dx^2} = \frac{-\alpha}{\Delta^3} \Theta(x_c - x) + \frac{4\alpha}{9\pi} \left[ \frac{\chi^2(x)}{x^2} + \frac{2m_e}{m_\pi} \frac{\chi(x)}{x} \right]^{\frac{3}{2}}, \quad (\text{A.3.5})$$

where  $x_{ws} = R_{ws}/\lambda_\pi$  and  $R_{ws}$  is the radius of Wigner-Seitz cell. The total energy of the Wigner-Seitz cell can be written as

$$E_{ws} = E_N + E_k + E_C \quad (\text{A.3.6})$$

where

$$E_N = M_N(A, Z)c^2, \quad (\text{A.3.7})$$

being  $M_N(A, Z)$  the nucleus mass. The total kinetic energy is given by

$$E_k = \int_0^{R_{ws}} 4\pi r^2 (\mathcal{E}_e - m_e n_e) dr, \quad (\text{A.3.8})$$

$$\mathcal{E}_e = \frac{2}{(2\pi\hbar)^3} \int_0^{P_e^F} \sqrt{c^2 p^2 + m_e^2 c^4} 4\pi p^2 dp, \quad (\text{A.3.9})$$

and the total Coulomb energy,

$$E_C = \frac{1}{2} \int_{R_C}^{R_{ws}} 4\pi r^2 e [n_p(r) - n_e(r)] V(r) dr. \quad (\text{A.3.10})$$

The total pressure of the Wigner-Seitz cell is given by

$$P_{FMT}^{rel} = P_e [n_e(R_{ws})], \quad (\text{A.3.11})$$

$$P_e = \frac{1}{3} \frac{2}{(2\pi\hbar)^3} \int_0^{P_e^F} \frac{c^2 p^2}{\sqrt{c^2 p^2 + m_e^2 c^4}} 4\pi p^2 dp. \quad (\text{A.3.12})$$

### A.3.3. The extension to finite temperatures

Now we consider the problem of a relativistic and non-degenerate gas of electrons at temperature  $T$  surrounding a degenerate finite sized and positively charged nucleus. The relativistic equilibrium condition is given by  $E_e = \tilde{\mu}_e - eV = \text{constant}$ , where  $\mu_e = Mc^2 + \tilde{\mu}_e$  is the electron chemical potential. We assume the proton density as in the degenerate case and we can write the electron density as

$$n_e = \frac{2}{(2\pi\hbar)^3} \int_0^\infty \frac{4\pi p^2 dp}{\exp\left(\frac{\tilde{E}(p) - \tilde{\mu}_e(p)}{k_B T}\right) + 1}, \quad (\text{A.3.13})$$

where  $\tilde{E}(p) = \sqrt{c^2 p^2 + m_e^2 c^4} - m_e c^2$  and  $k_B$  is the Boltzmann constant.

Using  $\eta = \mu/kT$ ,  $x = \tilde{E}(p)/kT$  and  $\beta = T/(mc^2)$  we can write the electron density in function of the Fermi-Dirac Integral,

$$n_e = \frac{8\pi\sqrt{2}}{(2\pi\hbar)^3} m^3 c^3 \beta^{3/2} [F_{1/2}(\eta, \beta) + \beta F_{3/2}(\eta, \beta)], \quad (\text{A.3.14})$$

where the Fermi-Dirac Integral is given by

$$F_k(\eta, \beta) \equiv \int_0^\infty \frac{t^k \sqrt{1 + (\beta/2)t}}{1 + \exp(t - \eta)} dt. \quad (\text{A.3.15})$$

We are considering the anti-particles also, and in this case the  $\eta = -\mu/KT$ .

The electron number density is given by:

$$n_e = n_{e^-} - n_{e^+} \quad (\text{A.3.16})$$

Using the same dimensionless quantities and replacing the particle densities into the Poisson equation we obtain the Thomas-Fermi equation

$$\begin{aligned} \frac{d^2\chi(x)}{dx^2} = & -4\pi\alpha x \left[ \frac{3}{4\pi\Delta^3} \Theta(x_c - x) \right. \\ & \left. - \frac{\sqrt{2}}{\pi^2} \left( \frac{m_e}{m_\pi} \right)^3 \beta^{3/2} [F_{1/2}(\eta, \beta) + \beta F_{3/2}(\eta, \beta)] \right], \end{aligned} \quad (\text{A.3.17})$$

which must be integrated subjected to the boundary conditions  $\chi(0) = 0$ ,  $\chi(x_{ws}) = x_{ws}\chi'(x_{ws})$ , where  $\eta\beta + 1 = m_\pi/m_e(\chi(x)/x)$ .

For the case with finite temperature both, the nucleons energy and the pressure, take into account the contribution of the internal energy density  $u = \frac{3}{2}n_N k_B T$ , where  $n_N$  is the nucleon number density. Then, the total energy of Wigner-Seitz cell can be written as

$$E_{ws} = E_N + E_k + E_C \quad (\text{A.3.18})$$

where

$$E_N = M_N(A, Z)c^2 + \frac{3}{2}Ak_B T, \quad (\text{A.3.19})$$

being  $M_N(A, Z)$  the nucleus mass. The total kinetic energy is given by

$$E_k = \int_0^{R_{ws}} 4\pi r^2 (\mathcal{E}_e - m_e n_e) dr, \quad (\text{A.3.20})$$

$$\mathcal{E}_{e^-} = c^2 m_e n_e + \frac{8\pi\sqrt{2}}{(2\pi\hbar)^3} m_e^4 c^5 \beta^{5/2} [F_{3/2}(\eta, \beta) + \beta F_{5/2}(\eta, \beta)], \quad (\text{A.3.21})$$

where the total energy density is given by  $\mathcal{E}_e = \mathcal{E}_{e^-} + \mathcal{E}_{e^+}$  and the total Coulomb energy

$$E_C = \frac{1}{2} \int_{R_C}^{R_{ws}} 4\pi r^2 e [n_p(r) - n_e(r)] V(r) dr. \quad (\text{A.3.22})$$

Then, the total pressure is given by

$$P = P_N + P_e = n_N k_B T + \frac{1}{3} \frac{2}{(2\pi\hbar)^3} \int_0^\infty \frac{c^2 p^2}{\tilde{E}(p)} \frac{d^3 p}{\exp\left(\frac{\tilde{E}(p) - \tilde{\mu}_e(p)}{k_B T}\right) + 1}. \quad (\text{A.3.23})$$

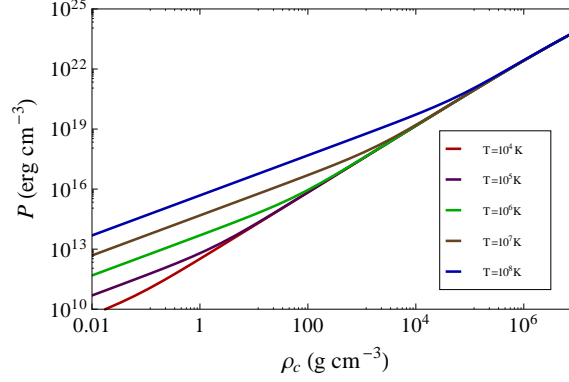


**Figure A.15.:** Total pressure as a function of the mass-density in the case of  $^{12}\text{C}$  for selected temperatures from  $T = 10^4$  K to  $T = 10^8$  K.

where  $P_N$  is the contribution to the pressure by ions and  $P_e = P_{e^-} - P_{e^+}$ .

### A.3.4. The equation of state

We have constructed the EOS for  $^4\text{He}$ ,  $^{12}\text{C}$ ,  $^{16}\text{O}$  and  $^{56}\text{Fe}$  compositions. In Fig. A.15 we show the EOS in the case of  $^{12}\text{C}$  for selected temperatures from  $T = 10^4$  K to  $T = 10^8$  K.

We see that the EOS deviates at low-densities from the degenerate EOS that in practice almost overlaps with the curve  $T = 10^4$  K, i.e. very little difference can be found at these temperatures at any density. The density at which this deviation starts is an increasing function of the temperature as can be seen from Fig. A.15.

### A.3.5. Conclusions

From the behavior of the EOS shown in Fig. A.15, we expect that finite temperatures produce appreciable effects in low-mass white dwarfs  $M < 0.5M_\odot$ , which have central densities  $\rho < 10^6$  g cm $^{-3}$ . At higher densities the differences are very small. White dwarfs may become unstable against the inverse  $\beta$ -decay process  $(Z, A) \rightarrow (Z - 1, A)$  through the capture of energetic electrons (ref). The electron Fermi energy must be larger than the mass difference between the initial nucleus  $(Z, A)$  and the final nucleus  $(Z - 1, A)$  in order to trigger such a process. We denote this threshold energy as  $\epsilon_Z^\beta$ . Usually it is satisfied  $\epsilon_Z^\beta - 1 < \epsilon_Z^\beta$  and therefore the initial nucleus undergoes two successive decays, i.e.  $(Z, A) \rightarrow (Z - 1, A) \rightarrow (Z - 2, A)$ . The electrons in the white dwarf may eventually reach the threshold energy to trigger a given decay at some critical density  $\rho_{crit}^\beta$ . Configurations with  $\rho > \rho_{crit}^\beta$  become unstable. From the fact that, for a given density, the electron density at

the Wigner-Seitz boundary satisfies  $n_e^{relFMT} < n_e^{unif}$  we should expect to see  $\rho_{crit}^{\beta,relFMT} > \rho_{crit}^{\beta,unif}$ . This means that, in order to reach the given threshold energy, the electrons within the relativistic Feynman-Metropolis-Teller approach must be subjected to a larger density with respect to the one given by the uniform approximation, see Rotondo et al. (2011c) and App. A.2 for details. In agreement with the fact that the temperature effects are negligible at high densities, we find that the critical densities for the occurrence of the inverse  $\beta$  decay are the same as the ones presented in (Rotondo et al., 2011c).

## A.4. On Magnetic Fields in Rotating Nuclear Matter Cores of Stellar Dimensions

### A.4.1. Introduction

Neutron stars are mainly detected as pulsars, whose regular pulsations in the radio, X-ray, and optical bands are produced by constant, ordered magnetic fields that are the strongest known in the Universe. However the origin of the magnetic field in the neutron stars is not fully understood, so far. Nevertheless in the literature one may find various hypotheses explaining the formation of the magnetic field (Ginzburg, 1964; Woltjer, 1964; Ruderman, 1972, 1995; Reisenegger, 2001, 2007; Reisenegger et al., 2007). The simplest hypothesis to explain the presence of the strong fields observed in neutron stars is the conservation of the magnetic flux already present in the progenitor stars during the gravitational collapse. This idea is based on the assumption that all stars at all stages of their evolution have some magnetic field, due to electronic currents circulating in their interiors. Thus this argument led to the prediction of the fields  $B \approx 10^{12}$  G in neutron stars a few years before the discovery of pulsars (Ginzburg, 1964; Woltjer, 1964). However, there is no detailed physical picture of such a flux conserving collapse. Thompson and Duncan (1993) put forward the hypothesis that newborn neutron stars are likely to combine vigorous convection and differential rotation making a dynamo process operate in them. They predicted fields up to  $10^{15} - 10^{16}$  G in neutron stars with few millisecond initial periods, and suggested that such fields could explain much of the phenomenology associated with Soft Gamma Repeaters and Anomalous X-ray Pulsars (Thompson and Duncan, 1995, 1996).

Probably, these processes are not mutually exclusive. A strong field might be present in the collapsing star, but later be deformed and perhaps amplified by some combination of convection, differential rotation, and magnetic instabilities (Tayler, 1973; Spruit, 2002). The relative importance of these ingredients depends on the initial field strength and rotation rate of the star. For both mechanisms, the field and its supporting currents are not likely to be confined to the solid crust of the star, but distributed in most of the stellar interior, which is mostly a fluid mixture of neutrons, protons, electrons, and other, more exotic particles.

Unlike aforementioned hypotheses which are based on the assumptions that all stars are magnetized or charged with some net charge different from zero, we explore the system recently considered by Ruffini et al. (2007b). According to that work the system consisting of degenerate neutrons, protons and electrons in beta equilibrium is globally neutral and expected to be kept at nuclear density by self gravity. In what follows these systems are termed as Nuclear Matter Cores of Stellar Dimensions. Despite the global neutrality the charge distribution turned out to be different from zero inside and out-

side (near the surface) the star. The magnitude of the net charge inside and outside the core is equal, but the sign is opposite. Such an effect takes place as a consequence of the beta equilibrium, the penetration of electrons into the core, hence the screening of the core charge and global charge neutrality. As a result of this effect, one may show the presence of an electric field close to the critical value  $E_c = m_e^2 c^3 / e \hbar$  near the surface of the massive cores, although localized in a very narrow shell. Thus in this case the magnetic field of the neutron star may be generated only if it spins like pulsars, even though the progenitor star has not been magnetized or electrically charged.

#### A.4.2. The Relativistic Thomas-Fermi equation

The Thomas-Fermi equation is the exact theory for atoms, molecules and solids as  $Z \rightarrow \infty$  (Lieb and Simon, 1973). The relativistic Thomas-Fermi theory developed for the study of atoms for heavy nuclei with  $Z = 10^6$  (Ferreirinho et al., 1980; Ruffini and Stella, 1981) gives important basic new information on the study of nuclear matter in bulk in the limit of  $A = (m_{Planck}/m_n)^3$  nucleons of mass  $m_n$  and on its electrodynamic properties. The analysis of nuclear matter bulk in neutron stars composed of degenerate gas of neutrons, protons and electrons, has traditionally been approached by implementing microscopically the charge neutrality condition by requiring the electron density  $n_e(r)$  to coincide with the proton density  $n_p(r)$ ,

$$n_e(r) = n_p(r). \quad (\text{A.4.1})$$

It is clear however that especially when conditions close to the gravitational collapse occur, there is an ultra-relativistic component of degenerate electrons whose confinement requires the existence of very strong electromagnetic fields, in order to guarantee the overall charge neutrality of the neutron star. Under these conditions equation (A.4.1) will be necessarily violated.

Using substantially a statistical approach based on the relativistic Thomas-Fermi equation, Ferreira et al. (1980); Ruffini and Stella (1981) have analyzed the electron densities around an extended nucleus in a neutral atom all the way up to  $Z = 6000$ . They have shown the effect of penetration of the electron orbital well inside the nucleus, leading to a screening of the nuclei positive charge and to the concept of an “effective” nuclear charge distribution.

In the work of Ruffini et al. (2007b) and Rotondo et al. (2011e) the relativistic Thomas-Fermi equation has been used to extrapolate the treatment of super heavy nuclei to the case of nuclear matter cores of stellar dimensions. These cores represent the inner part of neutron stars and are characterized by an atomic number of order of  $A = (m_{Planck}/m_n)^3 \approx 10^{57}$ , composed of degenerate  $N_n$  neutrons,  $N_p$  protons and  $N_e$  electrons in beta equilibrium and expected to be kept at nuclear density by self gravity. It has been shown that

near the surface of the massive cores it is possible to have an electric field close to the critical value  $E_c$ , although localized in a very narrow shell of the order of the  $\lambda_e$  electron Compton wavelength. Now let us review the main assumptions and results of those works.

According to Ruffini et al. (2007b) and Rotondo et al. (2011e) the protons are distributed at constant density  $n_p$  within a radius

$$R_c = \Delta \frac{\hbar}{m_\pi c} N_p^{1/3}, \quad (\text{A.4.2})$$

where  $\Delta$  is a parameter such that  $\Delta \approx 1$  ( $\Delta < 1$ ) corresponds to nuclear (supranuclear) densities when applied to ordinary nuclei. The overall Coulomb potential satisfies the Poisson equation

$$\nabla^2 V(r) = -4\pi e [n_p(r) - n_e(r)], \quad (\text{A.4.3})$$

with the boundary conditions  $V(\infty) = 0$  (due to the global charge neutrality of the system) and finiteness of  $V(0)$ . The density  $n_e(r)$  of the electrons of charge  $-e$  is determined by the Fermi energy condition on their Fermi momentum  $P_e^F$ ; we assume here

$$E_e^F = [(P_e^F c)^2 + m_e^2 c^4]^{1/2} - m_e c^2 - eV(r) = 0, \quad (\text{A.4.4})$$

which leads to

$$n_e(r) = \frac{(P_e^F)^3}{3\pi^2 \hbar^3} = \frac{1}{3\pi^2 \hbar^3 c^3} [e^2 V^2(r) + 2m_e c^2 eV(r)]^{3/2}. \quad (\text{A.4.5})$$

Introducing the dimensionless quantities  $x = r/[\hbar/m_\pi c]$ ,  $x_c = R_c/[\hbar/m_\pi c]$  and  $\chi/r = eV(r)/c\hbar$ , the relativistic Thomas-Fermi equation takes the form

$$\frac{1}{3x} \frac{d^2 \chi(x)}{dx^2} = -\frac{\alpha}{\Delta^3} H(x_c - x) + \frac{4\alpha}{9\pi} \left[ \frac{\chi^2(x)}{x^2} + 2 \frac{m_e}{m_\pi} \frac{\chi}{x} \right]^{3/2}, \quad (\text{A.4.6})$$

where  $\alpha = e^2/(\hbar c)$  is the fine structure constant,  $H(x_c - x)$  is the Heaviside step function and the boundary conditions for  $\chi(x)$  are  $\chi(0) = 0, \chi(\infty) = 0$ . The neutron density  $n_n(r)$  is determined by the Fermi energy condition on their Fermi momentum  $P_n^F$  imposed by beta decay equilibrium

$$E_n^F = [(P_n^F c)^2 + m_n^2 c^4]^{1/2} - m_n c^2 = [(P_p^F c)^2 + m_p^2 c^4]^{1/2} - m_p c^2 + eV, \quad (\text{A.4.7})$$

which in turn is related to the proton and electron densities by Eqs. (A.4.3), (A.4.5) and (A.4.6).

### A.4.3. The ultra-relativistic analytic solutions

In the ultrarelativistic limit with the planar approximation the relativistic Thomas-Fermi equation admits an analytic solution. Introducing the new function  $\phi$  defined by  $\phi = 4^{1/3}(9\pi)^{-1/3}\Delta\chi/x$  and the new variables  $\hat{x} = (12/\pi)^{1/6}\sqrt{\alpha}\Delta^{-1}x$ ,  $\xi = \hat{x} - \hat{x}_c$ , where  $\hat{x}_c = (12/\pi)^{1/6}\sqrt{\alpha}\Delta^{-1}x_c$ , Eq. (A.4.6) becomes

$$\frac{d^2\hat{\phi}(\xi)}{d\xi^2} = -H(-\xi) + \hat{\phi}(\xi)^3, \quad (\text{A.4.8})$$

where  $\hat{\phi}(\xi) = \phi(\xi + \hat{x}_c)$ . The boundary conditions on  $\hat{\phi}$  are:  $\hat{\phi}(\xi) \rightarrow 1$  as  $\xi \rightarrow -\hat{x}_c \ll 0$  (at the nuclear matter core center) and  $\hat{\phi}(\xi) \rightarrow 0$  as  $\xi \rightarrow \infty$ . The function  $\hat{\phi}$  and its first derivative  $\hat{\phi}'$  must be continuous at the surface  $\xi = 0$  of the nuclear matter core of stellar dimensions. Hence equation (A.4.8) admits an exact solution

$$\hat{\phi}(\xi) = \begin{cases} 1 - 3 \left[ 1 + 2^{-1/2} \sinh(a - \sqrt{3}\xi) \right]^{-1}, & \xi < 0, \\ \frac{\sqrt{2}}{(\xi + b)}, & \xi > 0, \end{cases} \quad (\text{A.4.9})$$

where the integration constants  $a$  and  $b$  have the values  $a = \text{arccosh}(9\sqrt{3}) \approx 3.439$ ,  $b = (4/3)\sqrt{2} \approx 1.886$ . Next we evaluate the Coulomb potential function

$$V(\xi) = \left( \frac{9\pi}{4} \right)^{1/3} \frac{m_\pi c^2}{\Delta e} \hat{\phi}(\xi), \quad (\text{A.4.10})$$

and by differentiation, the electric field

$$E(\xi) = - \left( \frac{3^5 \pi}{4} \right)^{1/6} \frac{\sqrt{\alpha} m_\pi^2 c^3}{\Delta^2 e \hbar} \hat{\phi}'(\xi). \quad (\text{A.4.11})$$

Details are given in Figs. A.16 and A.17.

### A.4.4. Rotating Nuclear Matter Cores of Stellar Dimensions in Classical Electrodynamics

In section A.4.2 and A.4.3 we have seen that in the massive nuclear density cores the electric charge distribution is different from zero, although it is globally neutral. In this section we investigate the case when this charge distribution is allowed to rotate with the constant angular velocity  $\Omega$  around the axis of symmetry. Thus the magnetic field of the resultant current density is calculated in terms of the charge distribution.

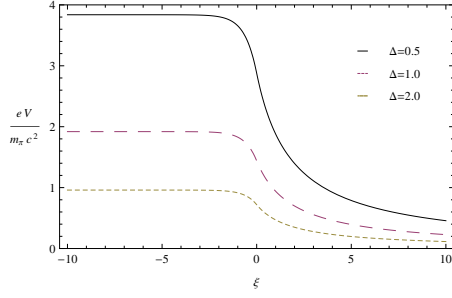


**Figure A.16.:** The electron Coulomb potential energy  $eV$ , in units of pion mass  $m_\pi$  is plotted as a function of the radial coordinate  $\xi = \hat{x} - \hat{x}_c$ , for selected values of the density parameter  $\Delta$ .

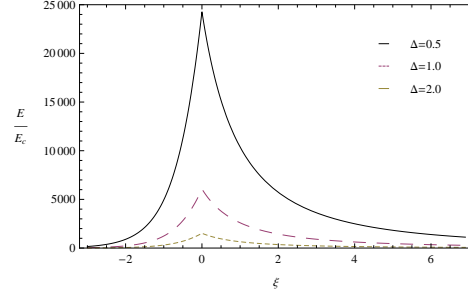


**Figure A.17.:** The electric field is plotted in units of the critical field  $E_c$  as a function of the radial coordinate  $\xi$ , showing a sharp peak at the core radius, for selected values of  $\Delta$ .

Consider a charge distribution moving in a such way that at every point in space the charge density and the current density remain constant. In this case the magnetic field is defined by

$$\mathbf{B}(\mathbf{r}) = \nabla \times \mathbf{A}(\mathbf{r}), \quad \mathbf{A}(\mathbf{r}) = (\boldsymbol{\Omega}/c^2) \times \mathbf{F}(\mathbf{r}), \quad \mathbf{F}(\mathbf{r}) = \frac{1}{4\pi} \int \frac{\mathbf{r}'\rho(\mathbf{r}')d^3\mathbf{r}'}{|\mathbf{r}-\mathbf{r}'|}, \quad (\text{A.4.12})$$

where  $\mathbf{A}$  is the vector potential of the magnetic field,  $\mathbf{F}(\mathbf{r})$  is the "superpotential" in general form. In the case of spherical symmetry,  $\mathbf{F}(\mathbf{r})$  may be taken as radial (see Marsh (1982)). Writing  $\mathbf{F}(\mathbf{r}) = \mathbf{e}_r F(r)$ , where  $\mathbf{e}_r$  is the unit radial vector, one has

$$F(r) = \frac{1}{r^2} \int_0^r r'^2 \frac{d}{dr'} [r'V(r')] dr'. \quad (\text{A.4.13})$$

This expression allows to calculate the magnetic field due to rotation of any spherically symmetric distribution of charge in terms of its electrostatic Coulomb potential. Note that in fact due to rotation the shape of the neutron star must deviate from spherical symmetry. Since we are interested in the estimation of the order of the magnetic field the distortions to the shape of the star can be neglected for simplicity. Thus the magnetic field is defined by

$$\mathbf{B}(\mathbf{r}) = B_r \mathbf{e}_r + B_\theta \mathbf{e}_\theta, \quad B_r = \frac{2\Omega F}{c^2 r} \cos \theta, \quad B_\theta = -\frac{2\Omega}{c^2} \left[ \frac{F}{r} + \frac{r}{2} \frac{d}{dr} \left( \frac{F}{r} \right) \right] \sin \theta, \quad (\text{A.4.14})$$

where  $B_r$  is the radial component and  $B_\theta$  is the angular component of the magnetic field,  $\theta$  is the angle between  $r$  and  $z$  axis, and  $\mathbf{e}_\theta$  is the unit vector along  $\theta$ . Consequently the expression for the magnitude (the absolute value)

of the magnetic field can be written as

$$B(r, \theta) = \frac{\Omega r}{c^2} \sqrt{\left(\frac{2F}{r^2}\right)^2 + \left\{ \frac{4F}{r^2} \frac{d}{dr} \left(\frac{F}{r}\right) + \left[ \frac{d}{dr} \left(\frac{F}{r}\right) \right]^2 \right\} \sin^2 \theta}. \quad (\text{A.4.15})$$

Using the relation between  $r$  and  $\xi$

$$r = R_c + \left(\frac{\pi}{12}\right)^{1/6} \frac{\Delta}{\sqrt{\alpha}} \frac{\hbar}{m_{\pi} c} \xi, \quad (\text{A.4.16})$$

one may estimate the value of the magnetic field. In Figs. A.18, A.19, A.20 and A.21 details are given.

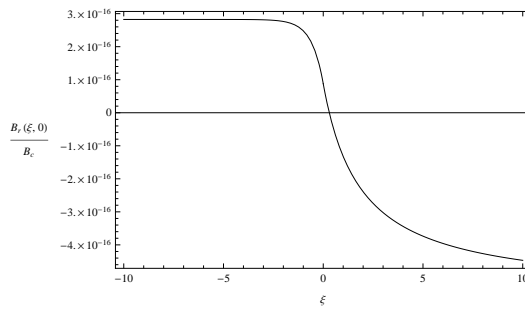


**Figure A.18.:** The radial component of the magnetic field is plotted as a function of the radial coordinate  $\xi$  in units of the critical field  $B_c = m_c^2 c^3 / e \hbar \approx 4.5 \times 10^{13}$  G. Here the period is taken to be  $P = 10$  ms,  $\theta = 0$ ,  $\Delta = 1$  and the radius of the core  $R_c = 10$  km. Note that  $B_r$  is considered at the poles of star, where it has maximum value. Outside the star  $B_r$  has very small negative value and it tends to zero. Because of visualization difficulties it is not seen in the figure.

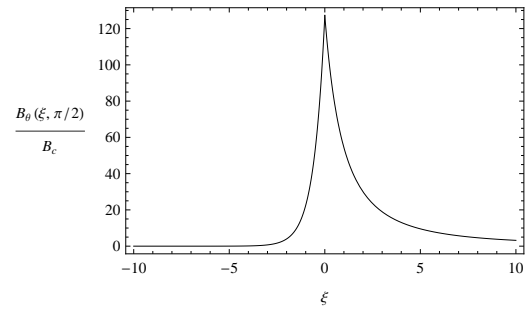


**Figure A.19.:** The angular component of the magnetic field is plotted in units of the  $B_c$ . Here  $P = 10$  ms,  $\theta = \pi/2$ ,  $\Delta = 1$  and  $R_c = 10$  km. Note that  $B_\theta$  is considered at the equator, where it has maximum value. Inside the star it has very small constant negative value. Outside the star first it becomes negative (the value is very small) then it tends to zero. Because of scale problems this behavior is not seen from the figure.

Examining the Fig. A.18 one can see very small value of  $B_r$  which almost does not make a significant contribution to the magnitude of the field, except for the poles of the star. On the contrary,  $B_\theta$  Fig. A.19 has values exceeding the critical magnetic field near the surface of the core although localized in a narrow region between positively and negatively charged shells as expected. Outside the core the magnetic field becomes negative. The magnitude of the

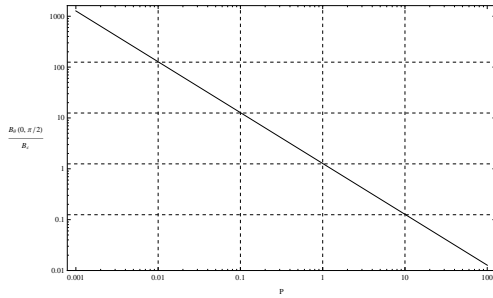


**Figure A.20.:** The magnitude of the magnetic field is plotted as a function of the period of the star  $P$  in the units of the critical field  $B_c$  at the surface of the core  $R_c = 10 \text{ km}$  on the equator in the logarithmic scale.

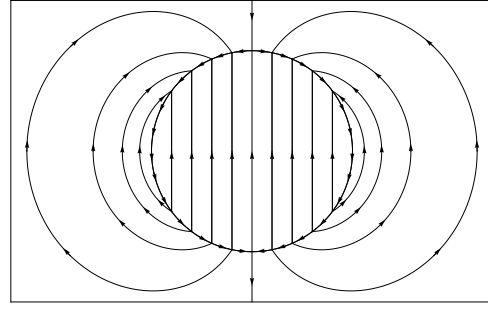


**Figure A.21.:** The magnetic lines of forces. Outside the star the magnetic field looks like a dipole field. Extra lines along the surface of the star indicate overcritical value of the field between positively and negatively charged shells.

field has very small and eventually vanishing values. This effect can not be seen from the figures, because of visualization difficulties.

In Fig. A.20 the magnitude of the magnetic field is presented as a function of the rotational period  $P$  on the surface of the core at the equator. Practically it demonstrates the upper limit of possible values of the magnetic field in the range between  $1 \text{ ms}$  and  $100 \text{ s}$ . Fig. A.21 represents magnetic lines of force inside, outside and on the surface of the star. It turned out that the lines of force of the overcritical magnetic field are oppressed between two shells along the surface of the core.

#### A.4.5. Conclusions

In this paper we have investigated the behavior of the magnetic field induced due to rotation on the basis of the research works considered in Ruffini et al. (2007b) and Rotondo et al. (2011e) using the technique developed by Marsh (1982).

For this purpose considering a rotating neutron star with the period of  $10 \text{ ms}$  we have obtained the magnetic field of order of the critical field near the surface of the star and analyzed the magnetic lines of forces.

According to our results the magnetic fields of the neutron stars could be generated due to the rotation of the star as a whole rigid body. We believe that the generation of the magnetic field due to the rotation is the reason for the formation of the constant magnetic fields at the initial moments of neutron stars birth.

The problem of investigating the magnetic field in general relativity for a self-gravitating system of degenerate fermions in beta equilibrium is beyond

the scope of the present work. We expect to investigate this problem in the nearest future.



# B. White Dwarfs Physics and Astrophysics

## B.1. The relativistic Feynman-Metropolis-Teller theory for white dwarfs in general relativity

### B.1.1. Introduction

The necessity of introducing the Fermi-Dirac statistics in order to overcome some conceptual difficulties in explaining the existence of white dwarfs leading to the concept of degenerate stars was first advanced by (Fowler, 1926) in a classic paper. Following that work, Stoner (1929) introduced the effect of special relativity into the Fowler considerations and he discovered the critical mass of white dwarfs

$$M_{\text{crit}}^{\text{Stoner}} = \frac{15}{16} \sqrt{5\pi} \frac{M_{\text{Pl}}^3}{\mu^2 m_n^2} \approx 3.72 \frac{M_{\text{Pl}}^3}{\mu^2 m_n^2}, \quad (\text{B.1.1})$$

where  $M_{\text{Pl}} = \sqrt{\hbar c/G} \approx 10^{-5}$  g is the Planck mass,  $m_n$  is the neutron mass, and  $\mu = A/Z \approx 2$  is the average molecular weight of matter which shows explicitly the dependence of the critical mass on the chemical composition of the star.

Following the Stoner's work, Chandrasekhar (1931b) pointed out the relevance of describing white dwarfs by using an approach, initiated by Milne (1930), of using the mathematical method of the solutions of the Lane-Emden polytropic equations (Emden, 1907). The same idea of using the Lane-Emden equations taking into account the special relativistic effects to the equilibrium of stellar matter for a degenerate system of fermions, came independently to Landau (1932). Both the Chandrasekhar and Landau treatments were explicit in pointing out the existence of the critical mass

$$M_{\text{crit}}^{\text{Ch-L}} = 2.015 \frac{\sqrt{3\pi}}{2} \frac{M_{\text{Pl}}^3}{\mu^2 m_n^2} \approx 3.09 \frac{M_{\text{Pl}}^3}{\mu^2 m_n^2}, \quad (\text{B.1.2})$$

where the first numerical factor on the right hand side of Eq. (B.1.2) comes from the boundary condition  $-(r^2 du/dr)_{r=R} = 2.015$  (see last entry of Table 7 on Pag. 80 in Emden (1907)) of the  $n = 3$  Lane-Emden polytropic equation.

Namely for  $M > M_{\text{crit}}^{\text{Ch-L}}$ , no equilibrium configuration should exist.

Some of the basic assumptions adopted by Chandrasekhar and Landau in their idealized approach e.g. the treatment of the electron as a free-gas without taking into due account the electromagnetic interactions, as well as the stability of the distribution of the nuclei against the gravitational interaction led to some criticisms by Eddington (1935). It was unfortunate that the absence of interest of E. Fermi on the final evolution of stars did not allow Fermi himself to intervene in these well-posed theoretical problems (Boccaletti and Ruffini, 2010). Indeed, we are showing in this article how the solution of the conceptual problems of the white dwarf models, left open for years, can be duly addressed by considering the relativistic Thomas-Fermi model of the compressed atom (see Subsec. B.1.2 and Sec. B.1.4).

The original work on white dwarfs was motivated by astrophysics and found in astrophysics strong observational support. The issue of the equilibrium of the electron gas and the associated component of nuclei, taking into account the electromagnetic, the gravitational and the weak interactions is a theoretical physics problem, not yet formulated in a correct special and general relativistic context.

One of the earliest alternative approaches to the Chandrasekhar-Landau work was proposed by Salpeter (1961a). He followed an idea originally proposed by Frenkel (1928): to adopt in the study of white dwarfs the concept of a Wigner-Seitz cell. Salpeter introduced to the lattice model of a point-like nucleus surrounded by a uniform cloud of electrons, corrections due to the non-uniformity of the electron distribution (see Subsec. B.1.2 for details). In this way Salpeter (1961a) obtained an analytic formula for the total energy in a Wigner-Seitz cell and derived the corresponding equation of state of matter composed by such cells, pointing out explicitly the relevance of the Coulomb interaction.

The consequences of the Coulomb interactions in the determination of the mass and radius of white dwarfs, was studied in a subsequent paper by Hamada and Salpeter (1961) by using the equation of state constructed in Salpeter (1961a). They found that the critical mass of white dwarfs depends in a nontrivial way on the specific nuclear composition: the critical mass of Chandrasekhar-Landau which depends only on the mass to charge ratio of nuclei  $A/Z$ , now depends also on the proton number  $Z$ .

This fact can be seen from the approximate expression for the critical mass of white dwarfs obtained by Hamada and Salpeter (1961) in the ultrarelativistic limit for the electrons

$$M_{\text{crit}}^{\text{H\&S}} = 2.015 \frac{\sqrt{3\pi}}{2} \frac{1}{\mu_{\text{eff}}^2} \frac{M_{\text{Pl}}^3}{m_n^2}, \quad (\text{B.1.3})$$

where

$$\mu_{\text{eff}} = \mu \left( \frac{P_S}{P_{\text{Ch}}} \right)^{-3/4}, \quad (\text{B.1.4})$$

being  $P_S$  the pressure of the Wigner-Seitz cell obtained by Salpeter (1961a) (see Subsec. B.1.2) and  $P_{\text{Ch}}$  is the pressure of a free-electron fluid used by Chandrasekhar (see Subsec. B.1.2). The ratio  $P_S/P_{\text{Ch}}$  is a function of the number of protons  $Z$  (see Eq. (20) in Salpeter (1961a)) and it satisfies  $P_S/P_{\text{Ch}} < 1$ . Consequently, the effective molecular weight satisfies  $\mu_{\text{eff}} > \mu$  and the critical mass of white dwarfs turns to be smaller than the original one obtained by Chandrasekhar-Landau (see Eq. (B.1.2)).

In the mean time, the problem of the equilibrium gas in a white dwarf taking into account possible global electromagnetic interactions between the nucleus and the electrons was addressed by Olson and Bailyn (1975, 1976). They well summarized the status of the problem: Traditional models for the white dwarf are non-relativistic and electrically neutral. Although an electric field is needed to support the pressureless nuclei against gravitational collapse, the star is treated essentially in terms of only one charge component, where charge neutrality is assumed. Their solution to the problem invokes the breakdown of the local charge neutrality and the presence of an overall electric field as a consequence of treating also the nuclei inside the white dwarf as a fluid. They treated the white dwarf matter through a two-fluid model not enforcing local charge neutrality. The closure equation for the Einstein-Maxwell system of equations was there obtained from a minimization procedure of the mass-energy of the configuration. This work was the first pointing out the relevance of the Einstein-Maxwell equations in the description of an astrophysical system by requiring global and non local charge neutrality. As we will show here, this interesting approach does not apply to the case of white dwarfs. It represents, however, a new development in the study of neutron stars (see e.g. Rotondo et al. (2011d))

An alternative approach to the Salpeter treatment of a compressed atom was reconsidered in gur (2000) by applying for the first time to white dwarfs a relativistic Thomas-Fermi treatment of the compressed atom introducing a finite size nucleus within a phenomenological description (see also Bertone and Ruffini (2000)).

Recently, the study of a compressed atom has been revisited in Rotondo et al. (2011c) by extending the global approach of Feynman et al. (1949) taking into account weak interactions. This treatment takes also into account all the Coulomb contributions duly expressed relativistically without the need of any piecewise description. The relativistic Thomas-Fermi model has been solved by imposing in addition to the electromagnetic interaction also the weak equilibrium between neutrons, protons and electrons self-consistently. This presents some conceptual differences with respect to previous approaches and can be used in order both to validate and to establish their limitations.

In this article we apply the considerations presented in Rotondo et al. (2011c) of a compressed atom in a Wigner-Seitz cell to the description of non-rotating white dwarfs in general relativity. This approach improves all previous treatments in the following aspects:

1. In order to warranty self-consistency with a relativistic treatment of the electrons, the point-like assumption of the nucleus is abandoned introducing a finite sized nucleus (Rotondo et al., 2011c). We assume for the mass as well as for charge to mass ratio of the nucleus their experimental values instead of using phenomenological descriptions based on the semi-empirical mass-formula of Weizsacker (see e.g. gur (2000); Bertone and Ruffini (2000)).
2. The electron-electron and electron-nucleus Coulomb interaction energy is calculated without any approximation by solving numerically the relativistic Thomas-Fermi equation for selected energy-densities of the system and for each given nuclear composition.
3. The energy-density of the system is calculated taking into account the contributions of the nuclei, of the Coulomb interactions as well as of the relativistic electrons; the latter being neglected in all previous treatments. This particular contribution turns to be very important at high-densities and in particular for light nuclear compositions e.g.  ${}^4\text{He}$  and  ${}^{12}\text{C}$ .
4. The  $\beta$ -equilibrium between neutrons, protons, and electrons is also taken into account leading to a self-consistent calculation of the threshold density for triggering the inverse  $\beta$ -decay of a given nucleus.
5. The structure of the white dwarf configurations is obtained by integrating the general relativity equations of equilibrium.
6. Due to 4) and 5) we are able to determine if the instability point leading to a maximum stable mass of the non-rotating white dwarf is induced by the inverse  $\beta$ -decay instability of the composing nuclei or by general relativistic effects.

Paradoxically, after all this procedure which takes into account many additional theoretical features generalizing the Chandrasekhar-Landau and the Hamada and Salpeter works, a most simple equation is found to be fulfilled by the equilibrium configuration in a spherically symmetric metric. Assuming the metric

$$ds^2 = e^{\nu(r)}c^2dt^2 - e^{\lambda(r)}dr^2 - r^2d\theta^2 - r^2\sin^2\theta d\varphi^2, \quad (\text{B.1.5})$$

we demonstrate how the entire system of equations describing the equilibrium of white dwarfs, taking into account the weak, the electromagnetic and

the gravitational interactions as well as quantum statistics all expressed consistently in a general relativistic approach, is simply given by

$$\sqrt{g_{00}}\mu_{\text{ws}} = e^{\nu(r)/2}\mu_{\text{ws}}(r) = \text{constant}, \quad (\text{B.1.6})$$

which links the chemical potential of the Wigner-Seitz cell  $\mu_{\text{ws}}$ , duly solved by considering the relativistic Feynman-Metropolis-Teller model following Rotondo et al. (2011c), to the general relativistic gravitational potential at each point of the configuration. The overall system outside each Wigner-Seitz cell is strictly neutral and no global electric field exists, contrary to the results reported in Olson and Bailyn (1976). The same procedure will apply as well to the case of neutron star crusts.

The article is organized as follows. In Sec. B.1.2 we summarize the most common approaches used for the description of white dwarfs and neutron star crusts: the uniform approximation for the electron fluid (see e.g. Chandrasekhar (1931b)); the often called lattice model assuming a point-like nucleus surrounded by a uniform electron cloud (see e.g. Baym et al. (1971b)); the generalization of the lattice model due to Salpeter (1961a); the Feynman, Metropolis and Teller approach (Feynman et al., 1949) based on the non-relativistic Thomas-Fermi model of compressed atoms and, the relativistic generalization of the Feynman-Metropolis-Teller treatment recently formulated in Rotondo et al. (2011c).

In Sec. B.1.3 we formulate the general relativistic equations of equilibrium of the system and show how, from the self-consistent definition of chemical potential of the Wigner-Seitz cell and the Einstein equations, comes the equilibrium condition given by Eq. (B.1.6). In addition, we obtain the Newtonian and the first-order post-Newtonian equations of equilibrium.

Finally, we show in Sec. B.1.4 the new results of the numerical integration of the general relativistic equations of equilibrium and discuss the corrections to the Stoner critical mass  $M_{\text{crit}}^{\text{Stoner}}$ , to the Chandrasekhar-Landau mass limit  $M_{\text{crit}}^{\text{Ch-L}}$ , as well as to the one of Hamada and Salpeter  $M_{\text{crit}}^{\text{H\&S}}$ , obtained when all interactions are fully taken into account through the relativistic Feynman-Metropolis-Teller equation of state (Rotondo et al., 2011c).

## B.1.2. The Equation of State

There exists a large variety of approaches to model the equation of state of white dwarf matter, each one characterized by a different way of treating or neglecting the Coulomb interaction inside each Wigner-Seitz cell, which we will briefly review here. Particular attention is given to the calculation of the self-consistent chemical potential of the Wigner-Seitz cell  $\mu_{\text{ws}}$ , which plays a very important role in the conservation law (B.1.6) that we will derive in Sec. B.1.3.

### The uniform approximation

In the uniform approximation used by Chandrasekhar (1931b), the electron distribution as well as the nucleons are assumed to be locally constant and therefore the condition of local charge neutrality

$$n_e = \frac{Z}{A_r} n_N, \quad (\text{B.1.7})$$

where  $A_r$  is the average atomic weight of the nucleus, is applied. Here  $n_N$  denotes the nucleon number density and  $Z$  is the number of protons of the nucleus. The electrons are considered as a fully degenerate free-gas and then described by Fermi-Dirac statistics. Thus, their number density  $n_e$  is related to the electron Fermi-momentum  $P_e^F$  by

$$n_e = \frac{(P_e^F)^3}{3\pi^2\hbar^3}, \quad (\text{B.1.8})$$

and the total electron energy-density and electron pressure are given by

$$\begin{aligned} \mathcal{E}_e &= \frac{2}{(2\pi\hbar)^3} \int_0^{P_e^F} \sqrt{c^2p^2 + m_e^2c^4} 4\pi p^2 dp \\ &= \frac{m_e^4c^5}{8\pi^2\hbar^3} [x_e \sqrt{1+x_e^2}(1+2x_e^2) - \text{arcsinh}(x_e)], \quad (\text{B.1.9}) \\ P_e &= \frac{1}{3} \frac{2}{(2\pi\hbar)^3} \int_0^{P_e^F} \frac{c^2p^2}{\sqrt{c^2p^2 + m_e^2c^4}} 4\pi p^2 dp \\ &= \frac{m_e^4c^5}{8\pi^2\hbar^3} [x_e \sqrt{1+x_e^2}(2x_e^2/3 - 1) \\ &\quad + \text{arcsinh}(x_e)], \quad (\text{B.1.10}) \end{aligned}$$

where we have introduced the dimensionless Fermi momentum  $x_e = P_e^F / (m_e c)$  with  $m_e$  the electron rest-mass.

The kinetic energy of nucleons is neglected and therefore the pressure is assumed to be only due to electrons. Thus the equation of state can be written as

$$\mathcal{E}_{\text{unif}} = \mathcal{E}_N + \mathcal{E}_e \approx \frac{A_r}{Z} M_u c^2 n_e + \mathcal{E}_e, \quad (\text{B.1.11})$$

$$P_{\text{unif}} \approx P_e, \quad (\text{B.1.12})$$

where  $M_u = 1.6604 \times 10^{-24}$  g is the unified atomic mass and  $\mathcal{E}_e$  and  $P_e$  are given by Eqs. (B.1.9)–(B.1.10).

Within this approximation, the total self-consistent chemical potential is

given by

$$\mu_{\text{unif}} = A_r M_u c^2 + Z \mu_e, \quad (\text{B.1.13})$$

where

$$\mu_e = \frac{\mathcal{E}_e + P_e}{n_e} = \sqrt{c^2 (P_e^F)^2 + m_e^2 c^4}, \quad (\text{B.1.14})$$

is the electron free-chemical potential.

As a consequence of this effective approach which does not take into any account the Coulomb interaction, it is obtained an effective one-component electron-nucleon fluid approach where the kinetic pressure is given by electrons of mass  $m_e$  and their gravitational contribution is given by an effective mass  $(A_r/Z)M_u$  attached to each electron (see e.g. Landau and Lifshitz (1980)). This is even more evident when the electron contribution to the energy-density in Eq. (B.1.11) is neglected and therefore the energy-density is attributed only to the nuclei. Within this approach followed by Chandrasekhar (1931b), the equation of state reduces to

$$\mathcal{E}_{\text{Ch}} = \frac{A_r}{Z} M_u c^2 n_e, \quad (\text{B.1.15})$$

$$P_{\text{Ch}} = P_{\text{unif}} = P_e. \quad (\text{B.1.16})$$

### The lattice model

The first correction to the above uniform model, corresponds to abandon the assumption of the electron-nucleon fluid through the so-called “lattice” model which introduces the concept of Wigner-Seitz cell: each cell contains a point-like nucleus of charge  $+Ze$  with  $A$  nucleons surrounded by a uniformly distributed cloud of  $Z$  fully-degenerate electrons. The global neutrality of the cell is guaranteed by the condition

$$Z = V_{\text{ws}} n_e = \frac{n_e}{n_{\text{ws}}}, \quad (\text{B.1.17})$$

where  $n_{\text{ws}} = 1/V_{\text{ws}}$  is the Wigner-Seitz cell density and  $V_{\text{ws}} = 4\pi R_{\text{ws}}^3/3$  is the cell volume.

The total energy of the Wigner-Seitz cell is modified by the inclusion of the Coulomb energy, i.e

$$E_L = \mathcal{E}_{\text{unif}} V_{\text{ws}} + E_C, \quad (\text{B.1.18})$$

being

$$E_C = E_{e-N} + E_{e-e} = -\frac{9}{10} \frac{Z^2 e^2}{R_{\text{ws}}}, \quad (\text{B.1.19})$$

where  $\mathcal{E}_{\text{unif}}$  is given by Eq. (B.1.11) and  $E_{e-N}$  and  $E_{e-e}$  are the electron-nucleus

and the electron-electron Coulomb energies

$$\begin{aligned} E_{e-N} &= - \int_0^{R_{ws}} 4\pi r^2 \left( \frac{Ze}{r} \right) en_e dr \\ &= - \frac{3}{2} \frac{Z^2 e^2}{R_{ws}}, \end{aligned} \quad (\text{B.1.20})$$

$$E_{e-e} = \frac{3}{5} \frac{Z^2 e^2}{R_{ws}}. \quad (\text{B.1.21})$$

The self-consistent pressure of the Wigner-Seitz cell is then given by

$$P_L = - \frac{\partial E_L}{\partial V_{ws}} = P_{unif} + \frac{1}{3} \frac{E_C}{V_{ws}}, \quad (\text{B.1.22})$$

where  $P_{unif}$  is given by Eq. (B.1.12). It is worth to recall that the point-like assumption of the nucleus is incompatible with a relativistic treatment of the degenerate electron fluid (see Ferreira et al. (1980); Ruffini and Stella (1981) for details). Such an inconsistency has been traditionally ignored by applying, within a point-like nucleus model, the relativistic formulas (B.1.9) and (B.1.10) and their corresponding ultrarelativistic limits (see e.g. Salpeter (1961a)).

The Wigner-Seitz cell chemical potential is in this case

$$\mu_L = E_L + P_L V_{ws} = \mu_{unif} + \frac{4}{3} E_C. \quad (\text{B.1.23})$$

By comparing Eqs. (B.1.12) and (B.1.22) we can see that the inclusion of the Coulomb interaction results in a decreasing of the pressure of the cell due to the negative lattice energy  $E_C$ . The same conclusion is achieved for the chemical potential from Eqs. (B.1.13) and (B.1.23).

### Salpeter approach

A further development to the lattice model came from Salpeter (1961a) whom studied the corrections due to the non-uniformity of the electron distribution inside a Wigner-Seitz cell.

Following the Chandrasekhar (1931b) approximation, Salpeter also neglects the electron contribution to the energy-density. Thus, the first term in the Salpeter formula for the energy of the cell comes from the nuclei energy (B.1.15). The second contribution is given by the Coulomb energy of the lattice model (B.1.19). The third contribution is obtained as follows: the electron density is assumed as  $n_e[1 + \epsilon(r)]$ , where  $n_e = 3Z/(4\pi R_{ws}^3)$  is the average electron density as given by Eq. (B.1.17), and  $\epsilon(r)$  is considered infinitesimal. The Coulomb potential energy is assumed to be the one of the point-like nucleus surrounded by a uniform distribution of electrons, so the correction

given by  $\epsilon(r)$  on the Coulomb potential is neglected. The electron distribution is then calculated at first-order by expanding the relativistic electron kinetic energy

$$\begin{aligned}\epsilon_k &= \sqrt{[cP_e^F(r)]^2 + m_e^2c^4} - m_e c^2 \\ &= \sqrt{\hbar^2 c^2 (3\pi^2 n_e)^{2/3} [1 + \epsilon(r)]^{2/3} + m_e^2 c^4} \\ &\quad - m_e c^2,\end{aligned}\tag{B.1.24}$$

about its value in the uniform approximation

$$\epsilon_k^{\text{unif}} = \sqrt{\hbar^2 c^2 (3\pi^2 n_e)^{2/3} + m_e^2 c^4} - m_e c^2,\tag{B.1.25}$$

considering as infinitesimal the ratio  $eV/E_e^F$  between the Coulomb potential energy  $eV$  and the electron Fermi energy

$$E_e^F = \sqrt{[cP_e^F(r)]^2 + m_e^2 c^4} - m_e c^2 - eV.\tag{B.1.26}$$

The influence of the Dirac electron-exchange correction (Dirac, 1930) on the equation of state was also considered by Salpeter (1961a). However, adopting the general approach of Migdal et al. (1977), it has been shown that these effects are negligible in the relativistic regime (Rotondo et al., 2011c). We will then consider here only the major correction of the Salpeter treatment.

The total energy of the Wigner-Seitz cell is then given by (see Salpeter (1961a) for details)

$$E_S = E_{\text{Ch}} + E_C + E_S^{TF},\tag{B.1.27}$$

being

$$E_S^{TF} = -\frac{162}{175} \left(\frac{4}{9\pi}\right)^{2/3} \alpha^2 Z^{7/3} \mu_e,\tag{B.1.28}$$

where  $E_{\text{Ch}} = \mathcal{E}_{\text{Ch}} V_{\text{ws}}$ ,  $E_C$  is given by Eq. (B.1.19),  $\mu_e$  is given by Eq. (B.1.14), and  $\alpha = e^2/(\hbar c)$  is the fine structure constant.

Correspondingly, the self-consistent pressure of the Wigner-Seitz cell is

$$P_S = P_L + P_{TF}^S,\tag{B.1.29}$$

where

$$P_{TF}^S = \frac{1}{3} \left(\frac{P_e^F}{\mu_e}\right)^2 \frac{E_S^{TF}}{V_{\text{ws}}}.\tag{B.1.30}$$

The Wigner-Seitz cell chemical potential can be then written as

$$\mu_S = \mu_L + E_{TF}^S \left[ 1 + \frac{1}{3} \left( \frac{P_e^F}{\mu_e} \right)^2 \right]. \quad (\text{B.1.31})$$

From Eqs. (B.1.29) and (B.1.31), we see that the inclusion of each additional Coulomb correction results in a further decreasing of the pressure and of the chemical potential of the cell. The Salpeter approach is very interesting in identifying piecewise Coulomb contribution to the total energy, to the total pressure and, to the Wigner-Seitz chemical potential. However, it does not have the full consistency of the global solutions obtained with the Feynman-Metropolis-Teller approach (Feynman et al., 1949) and its generalization to relativistic regimes (Rotondo et al., 2011c) which we will discuss in detail below.

### The Feynman-Metropolis-Teller treatment

Feynman et al. (1949) showed how to derive the equation of state of matter at high pressures by considering a Thomas-Fermi model confined in a Wigner-Seitz cell of radius  $R_{ws}$ .

The Thomas-Fermi equilibrium condition for degenerate non-relativistic electrons in the cell is expressed by

$$E_e^F = \frac{(P_e^F)^2}{2m_e} - eV = \text{constant} > 0, \quad (\text{B.1.32})$$

where  $V$  denotes the Coulomb potential and  $E_e^F$  denotes the Fermi energy of electrons, which is positive for configurations subjected to external pressure, namely, for compressed cells.

Defining the function  $\phi(r)$  by  $eV(r) + E_e^F = e^2 Z \phi(r) / r$ , and introducing the dimensionless radial coordinate  $\eta$  by  $r = b\eta$ , where  $b = (3\pi)^{2/3} (\lambda_e / \alpha) 2^{-7/3} Z^{-1/3}$ , being  $\lambda_e = \hbar / (m_e c)$  the electron Compton wavelength; the Poisson equation from which the Coulomb potential  $V$  is calculated self-consistently becomes

$$\frac{d^2 \phi(\eta)}{d\eta^2} = \frac{\phi(\eta)^{3/2}}{\eta^{1/2}}. \quad (\text{B.1.33})$$

The boundary conditions for Eq. (B.1.33) follow from the point-like structure of the nucleus  $\phi(0) = 1$  and, from the global neutrality of the Wigner-Seitz cell  $\phi(\eta_0) = \eta_0 d\phi/d\eta|_{\eta=\eta_0}$ , where  $\eta_0$  defines the dimensionless radius of the Wigner-Seitz cell by  $\eta_0 = R_{ws}/b$ .

For each value of the compression, e.g.  $\eta_0$ , it corresponds a value of the electron Fermi energy  $E_e^F$  and a different solution of Eq. (B.1.33), which determines the self-consistent Coulomb potential energy  $eV$  as well as the self-

consistent electron distribution inside the cell through

$$n_e(\eta) = \frac{Z}{4\pi b^3} \left[ \frac{\phi(\eta)}{\eta} \right]^{3/2}. \quad (\text{B.1.34})$$

In the non-relativistic Thomas-Fermi model, the total energy of the Wigner-Seitz cell is given by (see Slater and Krutter (1935); Feynman et al. (1949) for details)

$$E_{\text{ws}} = E_N + E_k^{(e)} + E_C, \quad (\text{B.1.35})$$

being

$$E_N = M_N(Z, A)c^2, \quad (\text{B.1.36})$$

$$\begin{aligned} E_k^{(e)} &= \int_0^{R_{\text{ws}}} 4\pi r^2 \mathcal{E}_e[n_e(r)] dr \\ &= \frac{3Z^2 e^2}{7b} \left[ \frac{4}{5} \eta_0^{1/2} \phi^{5/2}(\eta_0) - \phi'(0) \right], \end{aligned} \quad (\text{B.1.37})$$

$$\begin{aligned} E_C &= E_{e-N} + E_{e-e} \\ &= -\frac{6Z^2 e^2}{7b} \left[ \frac{1}{3} \eta_0^{1/2} \phi^{5/2}(\eta_0) - \phi'(0) \right], \end{aligned} \quad (\text{B.1.38})$$

where  $M_N(Z, A)$  is the nucleus mass,  $\mathcal{E}_e[n_e(r)]$  is given by Eq. (B.1.9) and  $E_{e-N}$  and  $E_{e-e}$  are the electron-nucleus Coulomb energy and the electron-electron Coulomb energy, which are given by

$$E_{e-N} = - \int_0^{R_{\text{ws}}} 4\pi r^2 \left( \frac{Ze}{r} \right) n_e(r) dr, \quad (\text{B.1.39})$$

$$\begin{aligned} E_{e-e} &= \frac{1}{2} \int_0^{R_{\text{ws}}} 4\pi r^2 n_e(\vec{r}) dr \\ &\times \int_0^{R_{\text{ws}}} 4\pi r'^2 \frac{n_e(\vec{r}')}{|\vec{r} - \vec{r}'|} dr'. \end{aligned} \quad (\text{B.1.40})$$

From Eqs. (B.1.37) and (B.1.38) we recover the well-known relation between the total kinetic energy and the total Coulomb energy in the Thomas-Fermi model (Slater and Krutter, 1935; Feynman et al., 1949)

$$E_k^{(e)} = E_k^{\text{unif}}[n_e(R_{\text{ws}})] - \frac{1}{2} E_C, \quad (\text{B.1.41})$$

where  $E_k^{\text{unif}}[n_e(R_{\text{ws}})]$  is the non-relativistic kinetic energy of a uniform electron distribution of density  $n_e(R_{\text{ws}})$ , i.e.

$$E_k^{\text{unif}}[n_e(R_{\text{ws}})] = \frac{3}{5} Z^* \mu_e(R_{\text{ws}}), \quad (\text{B.1.42})$$

with  $Z^*$  defined by

$$Z^* = V_{\text{ws}} n_e(R_{\text{ws}}), \quad (\text{B.1.43})$$

and  $\mu_e(R_{\text{ws}}) = \hbar^2 [3\pi^2 n_e(R_{\text{ws}})]^{2/3} / (2m_e)$ .

The self-consistent pressure of the Wigner-Seitz cell given by the non-relativistic Thomas-Fermi model is (see Slater and Krutter (1935); Feynman et al. (1949) for details)

$$P_{\text{TF}} = \frac{2}{3} \frac{E_k^{\text{unif}}[n_e(R_{\text{ws}})]}{V_{\text{ws}}}. \quad (\text{B.1.44})$$

The pressure of the Thomas-Fermi model (B.1.44) is equal to the pressure of a free-electron distribution of density  $n_e(R_{\text{ws}})$ . Being the electron density inside the cell a decreasing function of the distance from the nucleus, the electron density at the cell boundary,  $n_e(R_{\text{ws}})$ , is smaller than the average electron distribution  $3Z/(4\pi R_{\text{ws}}^3)$ . Then, the pressure given by (B.1.44) is smaller than the one given by the non-relativistic version of Eq. (B.1.10) of the uniform model of Subsec. B.1.2. Such a smaller pressure, although faintfully given by the expression of a free-electron gas, contains in a self-consistent fashion all the Coulomb effects inside the Wigner-Seitz cell.

The chemical potential of the Wigner-Seitz cell of the non-relativistic Thomas-Fermi model can be then written as

$$\mu_{\text{TF}} = M_N(Z, A)c^2 + Z^* \mu_e(R_{\text{ws}}) + \frac{1}{2}E_C, \quad (\text{B.1.45})$$

where we have used Eqs. (B.1.41)–(B.1.43).

Integrating by parts the total number of electrons

$$Z = \int_0^{R_{\text{ws}}} 4\pi r^2 n_e(r) dr = Z^* + I(R_{\text{ws}}), \quad (\text{B.1.46})$$

where

$$I(R_{\text{ws}}) = \int_0^{R_{\text{ws}}} \frac{4\pi}{3} r^3 \frac{\partial n_e(r)}{\partial r} dr, \quad (\text{B.1.47})$$

we can rewrite finally the following semi-analytical expression of the chemical potential (B.1.45) of the cell

$$\begin{aligned} \mu_{\text{TF}} = & M_N(Z, A)c^2 + Z\mu_e^{\text{unif}} \left[ 1 + \frac{I(R_{\text{ws}})}{Z} \right]^{2/3} \\ & + \mu_e^{\text{unif}} I(R_{\text{ws}}) \left[ 1 + \frac{I(R_{\text{ws}})}{Z} \right]^{2/3} + \frac{1}{2}E_C, \end{aligned} \quad (\text{B.1.48})$$

where  $\mu_e^{\text{unif}}$  is the electron free-chemical potential (B.1.14) calculated with the average electron density, namely, the electron chemical potential of the uniform approximation. The function  $I(R_{\text{ws}})$  depends explicitly on the gradient

of the electron density, i.e. on the non-uniformity of the electron distribution.

In the limit of absence of Coulomb interaction both the last term and the function  $I(R_{\text{ws}})$  in Eq. (B.1.48) vanish and therefore in this limit  $\mu_{\text{TF}}$  reduces to

$$\mu_{\text{TF}} \rightarrow \mu_{\text{unif}}, \quad (\text{B.1.49})$$

where  $\mu_{\text{unif}}$  is the chemical potential in the uniform approximation given by Eq. (B.1.13).

### The relativistic Feynman-Metropolis-Teller treatment

We recall now how the above classic Feynman, Metropolis, and Teller treatment of compressed atoms has been recently generalized to relativistic regimes (see Rotondo et al. (2011c) for details). One of the main differences in the relativistic generalization of the Thomas-Fermi equation is that, the point-like approximation of the nucleus, must be abandoned since the relativistic equilibrium condition of compressed atoms

$$E_e^F = \sqrt{c^2(P_e^F)^2 + m_e^2 c^4} - m_e c^2 - eV(r) = \text{constant} > 0, \quad (\text{B.1.50})$$

would lead to a non-integrable expression for the electron density near the origin (see e.g. Ferreira et al. (1980); Ruffini and Stella (1981)).

It is then assumed a constant distribution of protons confined in a radius  $R_c$  defined by

$$R_c = \Delta \lambda_\pi Z^{1/3}, \quad (\text{B.1.51})$$

where  $\lambda_\pi = \hbar/(m_\pi c)$  is the pion Compton wavelength. If the system is at nuclear density  $\Delta \approx (r_0/\lambda_\pi)(A/Z)^{1/3}$  with  $r_0 \approx 1.2$  fm. Thus, in the case of ordinary nuclei (i.e., for  $A/Z \approx 2$ ) we have  $\Delta \approx 1$ . Consequently, the proton density can be written as

$$n_p(r) = \frac{Z}{\frac{4}{3}\pi R_c^3} \theta(r - R_c) = \frac{3}{4\pi} \left( \frac{1}{\Delta \lambda_\pi} \right)^3 \theta(r - R_c), \quad (\text{B.1.52})$$

where  $\theta(r - R_c)$  denotes the Heaviside function centered at  $R_c$ . The electron density can be written as

$$n_e(r) = \frac{(P_e^F)^3}{3\pi^2 \hbar^3} = \frac{1}{3\pi^2 \hbar^3 c^3} \left[ \hat{V}^2(r) + 2m_e c^2 \hat{V}(r) \right]^{3/2}, \quad (\text{B.1.53})$$

where  $\hat{V} = eV + E_e^F$  and we have used Eq. (B.1.50).

The overall Coulomb potential satisfies the Poisson equation

$$\nabla^2 V(r) = -4\pi e [n_p(r) - n_e(r)], \quad (\text{B.1.54})$$

with the boundary conditions  $dV/dr|_{r=R_{\text{ws}}} = 0$  and  $V(R_{\text{ws}}) = 0$  due to the global charge neutrality of the cell.

By introducing the dimensionless quantities  $x = r/\lambda_\pi$ ,  $x_c = R_c/\lambda_\pi$ ,  $\chi/r = \hat{V}(r)/(\hbar c)$  and replacing the particle densities (B.1.52) and (B.1.53) into the Poisson equation (B.1.54), it is obtained the relativistic Thomas-Fermi equation (Ruffini, 2008a)

$$\begin{aligned} \frac{1}{3x} \frac{d^2\chi(x)}{dx^2} &= -\frac{\alpha}{\Delta^3} \theta(x_c - x) \\ &+ \frac{4\alpha}{9\pi} \left[ \frac{\chi^2(x)}{x^2} + 2\frac{m_e}{m_\pi} \frac{\chi(x)}{x} \right]^{3/2}, \end{aligned} \quad (\text{B.1.55})$$

which must be integrated subjected to the boundary conditions  $\chi(0) = 0$ ,  $\chi(x_{\text{ws}}) \geq 0$  and  $d\chi/dx|_{x=x_{\text{ws}}} = \chi(x_{\text{ws}})/x_{\text{ws}}$ , where  $x_{\text{ws}} = R_{\text{ws}}/\lambda_\pi$ .

The neutron density  $n_n(r)$ , related to the neutron Fermi momentum  $P_n^F = (3\pi^2\hbar^3 n_n)^{1/3}$ , is determined by imposing the condition of beta equilibrium

$$\begin{aligned} E_n^F &= \sqrt{c^2(P_n^F)^2 + m_n^2c^4} - m_nc^2 = \sqrt{c^2(P_p^F)^2 + m_p^2c^4} \\ &- m_pc^2 + eV(r) + E_e^F, \end{aligned} \quad (\text{B.1.56})$$

subjected to the baryon number conservation equation

$$A = \int_0^{R_c} 4\pi r^2 [n_p(r) + n_n(r)] dr. \quad (\text{B.1.57})$$

In Fig. B.1 we see how the relativistic generalization of the Feynman-Metropolis-Teller treatment leads to electron density distributions markedly different from the constant electron density approximation. The electron distribution is far from being uniform as a result of the solution of Eq. (B.1.55), which takes into account the electromagnetic interaction between electrons and between the electrons and the finite sized nucleus. Additional details are given in Rotondo et al. (2011c).

Rotondo et al. (2011e) have shown how the solution of the relativistic Thomas-Fermi equation (B.1.55) together with the self-consistent implementation of the  $\beta$ -equilibrium condition (B.1.56) leads, in the case of zero electron Fermi energy ( $E_e^F = 0$ ), to a theoretical prediction of the  $\beta$ -equilibrium line, namely a theoretical  $Z$ - $A$  relation. Within this model the mass to charge ratio  $A/Z$  of nuclei is overestimated, e.g. in the case of  ${}^4\text{He}$  the overestimate is  $\sim 3.8\%$ , for  ${}^{12}\text{C}$   $\sim 7.9\%$ , for  ${}^{16}\text{O}$   $\sim 9.52\%$ , and for  ${}^{56}\text{Fe}$   $\sim 13.2\%$ . These discrepancies are corrected when the model of the nucleus considered above is improved by explicitly including the effects of strong interactions. This model, however, illustrates how a self-consistent calculation of compressed nuclear matter can be done including electromagnetic, weak, strong as well as special relativistic

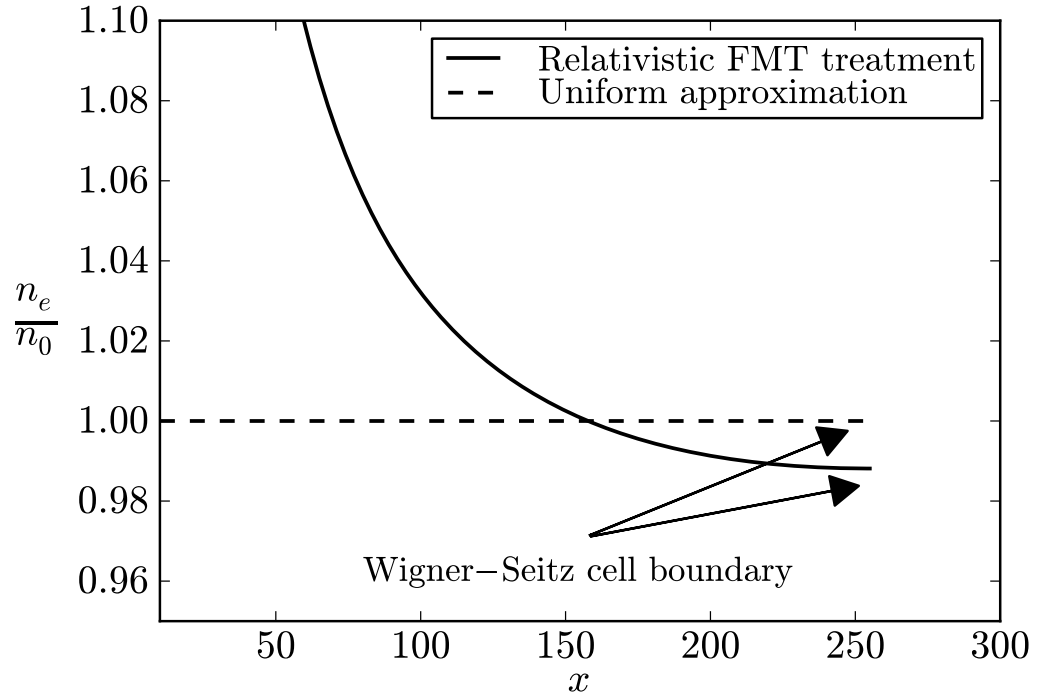


**Figure B.1.:** The electron number density  $n_e$  in units of the average electron number density  $n_0 = 3Z/(4\pi R_{\text{ws}}^3)$  inside a Wigner-Seitz cell of  $^{12}\text{C}$ . The dimensionless radial coordinate is  $x = r/\lambda_\pi$  and Wigner-Seitz cell radius is  $x_{\text{ws}} \approx 255$  corresponding to a density of  $\sim 10^8 \text{ g/cm}^3$ . The solid curve corresponds to the relativistic Feynman-Metropolis-Teller treatment and the dashed curve to the uniform approximation. The electron distribution for different levels of compression as well as for different nuclear compositions can be found in Rotondo et al. (2011c).

tic effects without any approximation. This approach promises to be useful when theoretical predictions are essential, for example in the description of nuclear matter at very high densities, e.g. nuclei close and beyond the neutron drip line.

The densities in white dwarf interiors are not highly enough to require such theoretical predictions. Therefore, in order to ensure the accuracy of our results we use for  $(Z, A)$ , needed to solve the relativistic Thomas-Fermi equation (B.1.55), as well as for the nucleus mass  $M_N(Z, A)$ , their known experimental values. In this way we take into account all the effects of the nuclear interaction.

Thus, the total energy of the Wigner-Seitz cell in the present case can be written as

$$E_{\text{FMT}}^{\text{rel}} = E_N + E_k^{(e)} + E_C, \quad (\text{B.1.58})$$

being

$$E_N = M_N(Z, A)c^2, \quad (\text{B.1.59})$$

$$E_k^{(e)} = \int_0^{R_{\text{ws}}} 4\pi r^2 (\mathcal{E}_e - m_e n_e) dr, \quad (\text{B.1.60})$$

$$E_C = \frac{1}{2} \int_{R_c}^{R_{\text{ws}}} 4\pi r^2 e [n_p(r) - n_e(r)] V(r) dr, \quad (\text{B.1.61})$$

where  $M_N(Z, A) = A_r M_u$  is the experimental nucleus mass, e.g. for  ${}^4\text{He}$ ,  ${}^{12}\text{C}$ ,  ${}^{16}\text{O}$  and  ${}^{56}\text{Fe}$  we have  $A_r = 4.003, 12.01, 16.00$  and  $55.84$  respectively. In Eq. (B.1.61) the integral is evaluated only outside the nucleus (i.e. for  $r > R_c$ ) in order to avoid a double counting with the Coulomb energy of the nucleus already taken into account in the nucleus mass (B.1.59). In order to avoid another double counting we subtract to the electron energy-density  $\mathcal{E}_e$  in Eq. (B.1.60) the rest-energy density  $m_e c^2 n_e$  which is also taken into account in the nucleus mass (B.1.59).

The total pressure of the Wigner-Seitz cell is given by

$$P_{\text{FMT}}^{\text{rel}} = P_e[n_e(R_{\text{ws}})], \quad (\text{B.1.62})$$

where  $P_e[n_e(R_{\text{ws}})]$  is the relativistic pressure (B.1.10) computed with the value of the electron density at the boundary of the cell.

The electron density at the boundary  $R_{\text{ws}}$  in the relativistic Feynman-Metropolis-Teller treatment is smaller with respect to the one given by the uniform density approximation (see Fig. B.1). Thus, the relativistic pressure (B.1.62) gives systematically smaller values with respect to the uniform approximation pressure (B.1.10) as well as with respect to the Salpeter pressure (B.1.29).

In Fig. B.2 we show the ratio between the relativistic Feynman-Metropolis-Teller pressure  $P_{\text{FMT}}^{\text{rel}}$  (B.1.62) and the Chandrasekhar pressure  $P_{\text{Ch}}$  (B.1.10) and the Salpeter pressure  $P_{\text{S}}$  (B.1.29) in the case of  ${}^{12}\text{C}$ . It can be seen how  $P_{\text{FMT}}^{\text{rel}}$  is smaller than  $P_{\text{Ch}}$  for all densities as a consequence of the Coulomb interaction. With respect to the Salpeter case, we have that the ratio  $P_{\text{FMT}}^{\text{rel}}/P_{\text{S}}$  approaches unity from below at large densities as one should expect.

However, at low densities  $\lesssim 10^4\text{--}10^5 \text{ g/cm}^3$ , the ratio becomes larger than unity due to the defect of the Salpeter treatment which, in the low density non-relativistic regime, leads to a drastic decrease of the pressure and even to negative pressures at densities  $\lesssim 10^2 \text{ g/cm}^3$  or higher for heavier nuclear compositions e.g.  ${}^{56}\text{Fe}$  (see Salpeter (1961a); Rotondo et al. (2011c) and Table B.1). This is in contrast with the relativistic Feynman-Metropolis-Teller treatment which matches smoothly the classic Feynman-Metropolis-Teller equation of state in that regime (see Rotondo et al. (2011c) for details).

No analytic expression of the Wigner-Seitz cell chemical potential can be

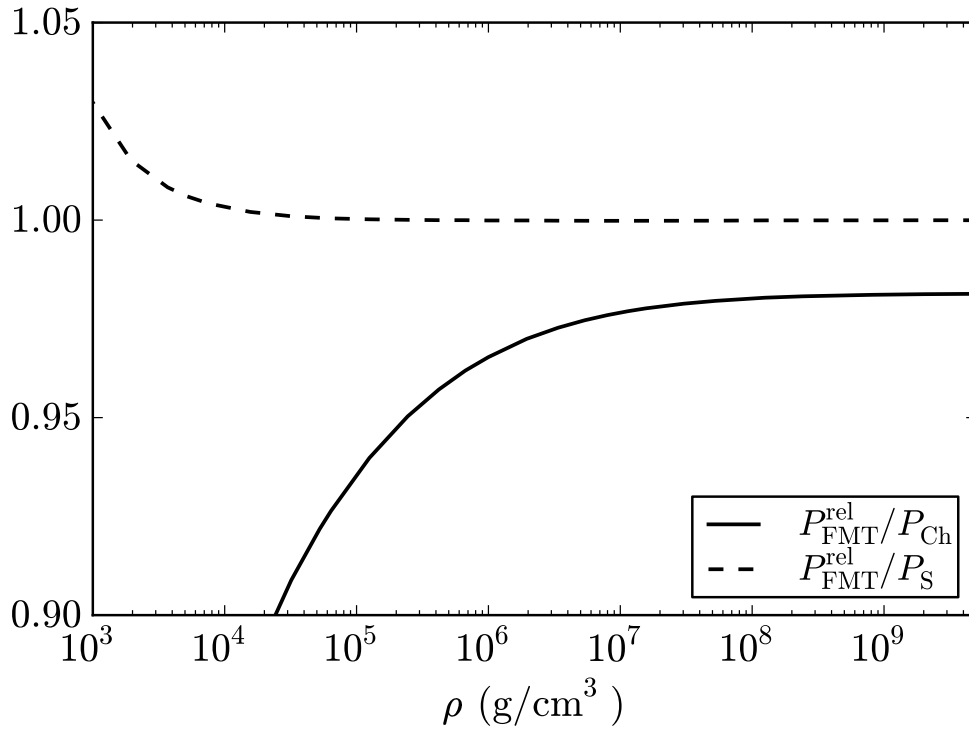


**Figure B.2.:** Ratio of the pressures in the different treatments as a function of the density for  $^{12}\text{C}$  white dwarfs (see Table B.1). The solid curve corresponds to the ratio between the relativistic Feynman-Metropolis-Teller pressure  $P_{\text{FMT}}^{\text{rel}}$  given by Eq. (B.1.62) and the Chandrasekhar pressure  $P_{\text{Ch}}$  given by Eq. (B.1.10). The dashed curve corresponds to the ratio between the relativistic Feynman-Metropolis-Teller pressure  $P_{\text{FMT}}^{\text{rel}}$  given by Eq. (B.1.62) and the Salpeter pressure  $P_{\text{S}}$  given by Eq. (B.1.29).

$\rho$	$P_{\text{Ch}}$	$P_{\text{S}}$	$P_{\text{FMT}}^{\text{rel}}$
10	$1.46731 \times 10^{14}$	$-1.35282 \times 10^{13}$	$4.54920 \times 10^{14}$
40	$1.47872 \times 10^{15}$	$4.60243 \times 10^{14}$	$7.09818 \times 10^{14}$
70	$3.75748 \times 10^{15}$	$1.60860 \times 10^{15}$	$2.05197 \times 10^{15}$
$10^2$	$6.80802 \times 10^{15}$	$3.34940 \times 10^{15}$	$3.90006 \times 10^{15}$
$10^3$	$3.15435 \times 10^{17}$	$2.40646 \times 10^{17}$	$2.44206 \times 10^{17}$
$10^4$	$1.45213 \times 10^{19}$	$1.28976 \times 10^{19}$	$1.28965 \times 10^{19}$
$10^5$	$6.50010 \times 10^{20}$	$6.14494 \times 10^{20}$	$6.13369 \times 10^{20}$
$10^6$	$2.62761 \times 10^{22}$	$2.54932 \times 10^{22}$	$2.54431 \times 10^{22}$
$10^7$	$8.46101 \times 10^{23}$	$8.28899 \times 10^{23}$	$8.27285 \times 10^{23}$
$10^8$	$2.15111 \times 10^{25}$	$2.11375 \times 10^{25}$	$2.10896 \times 10^{25}$
$10^9$	$4.86236 \times 10^{26}$	$4.78170 \times 10^{26}$	$4.76613 \times 10^{26}$
$10^{10}$	$1.05977 \times 10^{28}$	$1.04239 \times 10^{28}$	$1.03668 \times 10^{28}$

**Table B.1.:** Equation of state for  $^{12}\text{C}$  within the different treatments. The pressure in the uniform approximation for  $\mu = 2$  is  $P_{\text{Ch}}$ , the Salpeter pressure is  $P_{\text{S}}$  and the relativistic Feynman-Metropolis-Teller pressure is  $P_{\text{FMT}}^{\text{rel}}$ . The units for the density are  $\text{g}/\text{cm}^3$  and for the pressure  $\text{dyn}/\text{cm}^2$ .

given in this case, so we only write its general expression

$$\mu_{\text{FMT}}^{\text{rel}} = E_{\text{FMT}}^{\text{rel}} + P_{\text{FMT}}^{\text{rel}} V_{\text{ws}}, \quad (\text{B.1.63})$$

where  $E_{\text{FMT}}^{\text{rel}}$  and  $P_{\text{FMT}}^{\text{rel}}$  are given by Eqs. (B.1.58) and (B.1.62) respectively. The above equation, contrary to the non-relativistic formula (B.1.45), in no way can be simplified in terms of its uniform counterparts. However, it is easy to check that, in the limit of no Coulomb interaction  $n_e(R_{\text{ws}}) \rightarrow 3Z/(4\pi R_{\text{ws}}^3)$ ,  $E_C \rightarrow 0$ , and  $E_k \rightarrow \mathcal{E}_{\text{Ch}} V_{\text{ws}}$  and, neglecting the nuclear binding and the proton-neutron mass difference, we finally obtain

$$\mu_{\text{FMT}}^{\text{rel}} \rightarrow \mu_{\text{unif}}, \quad (\text{B.1.64})$$

as it should be expected.

Now we summarize how the equation of state of compressed nuclear matter can be computed in the Salpeter case and in the relativistic Feynman-Metropolis-Teller case, parameterized by the total density of the system:

(i) For a given radius  $R_{\text{ws}}$  of the Wigner-Seitz cell the relativistic Thomas-Fermi equation (B.1.55) is integrated numerically and the density of the configuration is computed as  $\rho = E_{\text{FMT}}^{\text{rel}}/(c^2 V_{\text{ws}})$  where  $E_{\text{FMT}}^{\text{rel}}$  is the energy of the cell given by Eq. (B.1.58).

(ii) For that value of the density, the radius of the Wigner-Seitz cell in the

Salpeter treatment is

$$R_{\text{ws}} = \left( \frac{3A_r M_u}{4\pi\rho} \right)^{1/3}, \quad (\text{B.1.65})$$

where Eq. (B.1.15) has been used. On the contrary, in the relativistic Feynman-Metropolis-Teller treatment no analytic expression relating Wigner-Seitz cell radius and density can be written.

(iii) From this Wigner-Seitz cell radius, or equivalently using the value of the density, the electron density in the Salpeter model is computed from the assumption of uniform electron distribution and the charge neutrality condition, i.e. Eq. (B.1.15). In the relativistic Feynman-Metropolis-Teller treatment, the electron number density at the boundary of the Wigner-Seitz cell is, following Eq. (B.1.53), given by

$$n_e^{\text{relFMT}} = \frac{1}{3\pi^2 \lambda_\pi^3} \left[ \frac{\chi^2(x_{\text{ws}})}{x_{\text{ws}}^2} + 2 \frac{m_e}{m_\pi} \frac{\chi(x_{\text{ws}})}{x_{\text{ws}}} \right]^{3/2}, \quad (\text{B.1.66})$$

where the function  $\chi(x)$  is the solution of the relativistic Thomas-Fermi equation (B.1.55).

(iv) Finally, with the knowledge of the electron density at  $R_{\text{ws}}$ , the pressure can be calculated. In the Salpeter approach it is given by Eq. (B.1.29) while in the relativistic Feynman-Metropolis-Teller case it is given by Eq. (B.1.62).

### B.1.3. General relativistic equations of equilibrium

Outside each Wigner-Seitz cell the system is electrically neutral, thus no overall electric field exists. Therefore, the above equation of state can be used to calculate the structure of the star through the Einstein equations. Introducing the spherically symmetric metric (B.1.5), the Einstein equations can be written in the Tolman-Oppenheimer-Volkoff form Tolman (1939); Oppenheimer and Volkoff (1939)

$$\frac{dv(r)}{dr} = \frac{2G}{c^2} \frac{4\pi r^3 P(r)/c^2 + M(r)}{r^2 \left[ 1 - \frac{2GM(r)}{c^2 r} \right]}, \quad (\text{B.1.67})$$

$$\frac{dM(r)}{dr} = 4\pi r^2 \frac{\mathcal{E}(r)}{c^2}, \quad (\text{B.1.68})$$

$$\frac{dP(r)}{dr} = -\frac{1}{2} \frac{dv(r)}{dr} [\mathcal{E}(r) + P(r)], \quad (\text{B.1.69})$$

where we have introduced the mass enclosed at the distance  $r$  through  $e^{\lambda(r)} = 1 - 2GM(r)/(c^2 r)$ ,  $\mathcal{E}(r)$  is the energy-density and  $P(r)$  is the total pressure.

We turn now to demonstrate how, from Eq. (B.1.69), it follows the general relativistic equation of equilibrium (B.1.6), for the self-consistent Wigner-

Seitz chemical potential  $\mu_{\text{ws}}$ . The first law of thermodynamics for a zero temperature fluid of  $N$  particles, total energy  $E$ , total volume  $V$ , total pressure  $P = -\partial E/\partial V$ , and chemical potential  $\mu = \partial E/\partial N$  reads

$$dE = -PdV + \mu dN, \quad (\text{B.1.70})$$

where the differentials denote arbitrary but simultaneous changes in the variables. Since for a system whose surface energy can be neglected with respect to volume energy, the total energy per particle  $E/N$  depends only on the particle density  $n = N/V$ , we can assume  $E/N$  as an homogeneous function of first-order in the variables  $N$  and  $V$  and hence, it follows the well-known thermodynamic relation

$$E = -PV + \mu N. \quad (\text{B.1.71})$$

In the case of the Wigner-Seitz cells, Eq. (B.1.71) reads

$$E_{\text{ws}} = -P_{\text{ws}} V_{\text{ws}} + \mu_{\text{ws}} N_{\text{ws}}, \quad (\text{B.1.72})$$

where we have introduced the fact that the Wigner-Seitz cells are the building blocks of the configuration and therefore we must put in Eq. (B.1.71)  $N_{\text{ws}} = 1$ . Through the entire article we have used Eq. (B.1.72) to obtain from the knowns energy and pressure, the Wigner-Seitz cell chemical potential (see e.g. Eqs. (B.1.13) and (B.1.23)). From Eqs. (B.1.70) and (B.1.71) we obtain the so-called Gibbs-Duhem relation

$$dP = nd\mu. \quad (\text{B.1.73})$$

In a white dwarf the pressure  $P$  and the chemical potential  $\mu$  are decreasing functions of the distance from the origin. Thus, the differentials in the above equations can be assumed as the gradients of the variables which, in the present spherically symmetric case, become just derivatives with respect to the radial coordinate  $r$ . From Eq. (B.1.73) it follows the relation

$$\frac{dP_{\text{ws}}}{dr} = n_{\text{ws}} \frac{d\mu_{\text{ws}}}{dr}. \quad (\text{B.1.74})$$

From Eqs. (B.1.69), (B.1.72) and (B.1.74) we obtain

$$n_{\text{ws}}(r) \frac{d\mu_{\text{ws}}(r)}{dr} = -\frac{1}{2} \frac{dv(r)}{dr} n_{\text{ws}}(r) \mu_{\text{ws}}(r), \quad (\text{B.1.75})$$

which can be straightforwardly integrated to obtain the first integral

$$e^{v(r)/2} \mu_{\text{ws}}(r) = \text{constant}. \quad (\text{B.1.76})$$

The above equilibrium condition is general and it also applies for non-zero temperature configurations ( see e.g. Klein (1949)). In such a case, it can be

shown that in addition to the equilibrium condition (B.1.76) the temperature of the system satisfies the Tolman isothermality condition  $e^{\nu(r)/2}T(r) = \text{constant}$  Tolman (1930); Tolman and Ehrenfest (1930).

### The weak-field non-relativistic limit

In the weak-field limit we have  $e^{\nu/2} \approx 1 + \Phi$ , where the Newtonian gravitational potential has been defined by  $\Phi(r) = \nu(r)/2$ . In the non-relativistic mechanics limit  $c \rightarrow \infty$ , the chemical potential  $\mu_{\text{ws}} \rightarrow \tilde{\mu}_{\text{ws}} + M_{\text{ws}}c^2$ , where  $\tilde{\mu}_{\text{ws}}$  denotes the non-relativistic free-chemical potential of the Wigner-Seitz cell and  $M_{\text{ws}}$  is the rest-mass of the Wigner-Seitz cell, namely, the rest-mass of the nucleus plus the rest-mass of the electrons. Applying these considerations to Eq. (B.1.76) we obtain

$$e^{\nu/2}\mu_{\text{ws}} \approx M_{\text{ws}}c^2 + \tilde{\mu}_{\text{ws}} + M_{\text{ws}}\Phi = \text{constant}. \quad (\text{B.1.77})$$

Absorbing the Wigner-Seitz rest-mass energy  $M_{\text{ws}}c^2$  in the constant on the right-hand-side we obtain

$$\tilde{\mu}_{\text{ws}} + M_{\text{ws}}\Phi = \text{constant}. \quad (\text{B.1.78})$$

In the weak-field non-relativistic limit, the Einstein equations (B.1.67)–(B.1.69) reduce to

$$\frac{d\Phi(r)}{dr} = \frac{GM(r)}{r^2}, \quad (\text{B.1.79})$$

$$\frac{dM(r)}{dr} = 4\pi r^2 \rho(r), \quad (\text{B.1.80})$$

$$\frac{dP(r)}{dr} = -\frac{GM(r)}{r^2} \rho(r), \quad (\text{B.1.81})$$

where  $\rho(r)$  denotes the rest-mass density. The Eqs. (B.1.79)–(B.1.80) can be combined to obtain the gravitational Poisson equation

$$\frac{d^2\Phi(r)}{dr^2} + \frac{2}{r} \frac{d\Phi(r)}{dr} = 4\pi G\rho(r). \quad (\text{B.1.82})$$

In the uniform approximation (see Subsec. B.1.2), the equilibrium condition given by Eq. (B.1.78) reads

$$\tilde{\mu}_e + \frac{A_r}{Z} M_u \Phi = \text{constant}, \quad (\text{B.1.83})$$

where we have neglected the electron rest-mass with respect to the nucleus rest-mass and we have divided the equation by the total number of electrons  $Z$ . This equilibrium equation is the classical condition of thermodynamic

equilibrium assumed for non-relativistic white dwarf models (see e.g. Landau and Lifshitz (1980) for details).

Introducing the above equilibrium condition (B.1.83) into Eq. (B.1.82), and using the relation between the non-relativistic electron chemical potential and the particle density  $n_e = (2m_e)^{3/2} \tilde{\mu}_e^{3/2} / (3\pi^2 \hbar^3)$ , we obtain

$$\frac{d^2 \tilde{\mu}_e(r)}{dr^2} + \frac{2}{r} \frac{d\tilde{\mu}_e(r)}{dr} = - \frac{2^{7/3} m_e^{3/2} (A_r/Z)^2 m_N^2 G}{3\pi \hbar^3} \tilde{\mu}_e^{3/2}(r), \quad (\text{B.1.84})$$

which is the correct equation governing the equilibrium of white dwarfs within Newtonian gravitational theory (Landau and Lifshitz, 1980). It is remarkable that the equation of equilibrium (B.1.84), obtained from the correct application of the Newtonian limit, does not coincide with the equation given by Chandrasekhar (1931b,a, 1935, 1939), which, as correctly pointed out by Eddington (1935), is a mixture of both relativistic and non-relativistic approaches. Indeed, the consistent relativistic equations should be Eq. (B.1.76). Therefore a dual relativistic and non-relativistic equation of state was used by Chandrasekhar. The pressure on the left-hand-side of Eq. (B.1.81) is taken to be given by relativistic electrons while, the term on the right-hand-side of Eq. (B.1.80) and (B.1.81) (or the source of Eq. (B.1.82)), is taken to be the rest-mass density of the system instead of the total relativistic energy-density. Such a procedure is equivalent to take the chemical potential in Eq. (B.1.78) as a relativistic quantity. As we have seen, this is inconsistent with the weak-field non-relativistic limit of the general relativistic equations.

### The Post-Newtonian limit

Indeed, if one were to treat the problem of white dwarfs approximately without going to the sophistications of general relativity, but including the effects of relativistic mechanics, one should use at least the equations in the post-Newtonian limit. The first-order post-Newtonian expansion of the Einstein equations (B.1.67)–(B.1.69) in powers of  $P/\mathcal{E}$  and  $GM/(c^2 r)$  leads to the equilibrium equations (Ciufolini and Ruffini, 1983)

$$\frac{d\Phi(r)}{dr} = - \frac{1}{\mathcal{E}(r)} \left[ 1 - \frac{P(r)}{\mathcal{E}(r)} \right] \frac{dP(r)}{dr}, \quad (\text{B.1.85})$$

$$\frac{dM(r)}{dr} = 4\pi r^2 \frac{\mathcal{E}(r)}{c^2}, \quad (\text{B.1.86})$$

$$\begin{aligned} \frac{dP(r)}{dr} = & - \frac{GM(r)}{r^2} \frac{\mathcal{E}(r)}{c^2} \left[ 1 + \frac{P(r)}{\mathcal{E}(r)} + \frac{4\pi r^3 P(r)}{M(r)c^2} \right. \\ & \left. + \frac{2GM(r)}{c^2 r} \right], \end{aligned} \quad (\text{B.1.87})$$

where Eq. (B.1.87) is the post-Newtonian version of the Tolman-Oppenheimer-Volkoff equation (B.1.69).

Replacing Eq. (B.1.74) into Eq. (B.1.85) we obtain

$$\left[1 - \frac{P(r)}{\mathcal{E}(r)}\right] \frac{d\mu_{\text{ws}}(r)}{dr} + \frac{\mathcal{E}(r)/c^2}{n_{\text{ws}}(r)} \frac{d\Phi(r)}{dr} = 0. \quad (\text{B.1.88})$$

It is convenient to split the energy-density as  $\mathcal{E} = c^2\rho + U$ , where  $\rho = M_{\text{ws}}n_{\text{ws}}$  is the rest-energy density and  $U$  the internal energy-density. Thus, Eq. (B.1.88) becomes

$$\begin{aligned} \frac{d\mu_{\text{ws}}(r)}{dr} + M_{\text{ws}} \frac{d\Phi(r)}{dr} - \frac{P(r)}{\mathcal{E}(r)} \frac{d\mu_{\text{ws}}(r)}{dr} \\ + \frac{U/c^2}{n_{\text{ws}}(r)} \frac{d\Phi(r)}{dr} = 0, \end{aligned} \quad (\text{B.1.89})$$

which is the differential post-Newtonian version of the equilibrium equation (B.1.76) and where the post-Newtonian corrections of equilibrium can be clearly seen. Applying the non-relativistic limit  $c \rightarrow \infty$  to Eq. (B.1.89):  $P/\mathcal{E} \rightarrow 0$ ,  $U/c^2 \rightarrow 0$ , and  $\mu_{\text{ws}} \rightarrow M_{\text{ws}}c^2 + \tilde{\mu}_{\text{ws}}$ , we recover the Newtonian equation of equilibrium (B.1.78).

## B.1.4. Mass and radius of general relativistic stable white dwarfs

### Inverse $\beta$ -decay instability

It is known that white dwarfs may become unstable against the inverse  $\beta$ -decay process  $(Z, A) \rightarrow (Z - 1, A)$  through the capture of energetic electrons (see e.g. Hund (1936); Landau (1938); Zel'Dovich (1958a); Harrison et al. (1958)). In order to trigger such a process, the electron Fermi energy must be larger than the mass difference between the initial nucleus  $(Z, A)$  and the final nucleus  $(Z - 1, A)$ . We denote this threshold energy as  $\epsilon_Z^\beta$ . Usually it is satisfied  $\epsilon_{Z-1}^\beta < \epsilon_Z^\beta$  and therefore the initial nucleus undergoes two successive decays, i.e.  $(Z, A) \rightarrow (Z - 1, A) \rightarrow (Z - 2, A)$  (see e.g. Salpeter (1961a); Shapiro and Teukolsky (1983)). Some of the possible decay channels in white dwarfs with the corresponding known experimental threshold energies  $\epsilon_Z^\beta$  are listed in Table B.2. The electrons in the white dwarf may eventually reach the threshold energy to trigger a given decay at some critical density  $\rho_{\text{crit}}^\beta$ . Configurations with  $\rho > \rho_{\text{crit}}^\beta$  become unstable (see Harrison et al. (1958); Salpeter (1961a) for details).

Within the uniform approximation, e.g. in the case of the Salpeter equation of state Salpeter (1961a), the critical density for the onset of inverse  $\beta$ -decay

Decay	$\epsilon_Z^\beta$	$\rho_{\text{crit}}^{\beta,\text{relFMT}}$	$\rho_{\text{crit}}^{\beta,\text{unif}}$
${}^4\text{He} \rightarrow {}^3\text{H} + n \rightarrow 4n$	20.596	$1.39 \times 10^{11}$	$1.37 \times 10^{11}$
${}^{12}\text{C} \rightarrow {}^{12}\text{B} \rightarrow {}^{12}\text{Be}$	13.370	$3.97 \times 10^{10}$	$3.88 \times 10^{10}$
${}^{16}\text{O} \rightarrow {}^{16}\text{N} \rightarrow {}^{16}\text{C}$	10.419	$1.94 \times 10^{10}$	$1.89 \times 10^{10}$
${}^{56}\text{Fe} \rightarrow {}^{56}\text{Mn} \rightarrow {}^{56}\text{Cr}$	3.695	$1.18 \times 10^9$	$1.14 \times 10^9$

**Table B.2.:** Onset of inverse beta decay instability for  ${}^4\text{He}$ ,  ${}^{12}\text{C}$ ,  ${}^{16}\text{O}$  and  ${}^{56}\text{Fe}$ . The experimental inverse  $\beta$ -decay energies  $\epsilon_Z^\beta$  are given in MeV and they have been taken from Table 1 of Audi et al. (2003a). The corresponding critical density for the uniform electron density model,  $\rho_{\text{crit}}^{\beta,\text{unif}}$  given by Eq. (B.1.90), is given in  $\text{g}/\text{cm}^3$  as well as the critical density  $\rho_{\text{crit}}^{\beta,\text{relFMT}}$  for the relativistic Feynman-Metropolis-Teller case. The numerical values of  $\epsilon_Z^\beta$  are taken from Audi et al. (2003a), see also Shapiro and Teukolsky (1983)

is given by

$$\rho_{\text{crit}}^{\beta,\text{unif}} = \frac{A_r}{Z} \frac{M_u}{3\pi^2 \hbar^3 c^3} [(\epsilon_Z^\beta)^2 + 2m_e c^2 \epsilon_Z^\beta]^{3/2}, \quad (\text{B.1.90})$$

where Eq. (B.1.15) has been used.

Because the computation of the electron Fermi energy within the relativistic Feynman-Metropolis-Teller approach Rotondo et al. (2011c) involves the numerical integration of the relativistic Thomas-Fermi equation (B.1.55), no analytic expression for  $\rho_{\text{crit}}^\beta$  can be found in this case. The critical density  $\rho_{\text{crit}}^{\beta,\text{relFMT}}$  is then obtained numerically by looking for the density at which the electron Fermi energy (B.1.50) equals  $\epsilon_Z^\beta$ .

In Table B.2 we show, correspondingly to each threshold energy  $\epsilon_Z^\beta$ , the critical density both in the Salpeter case  $\rho_{\text{crit}}^{\beta,\text{unif}}$  given by Eq. (B.1.90) and in the relativistic Feynman-Metropolis-Teller case  $\rho_{\text{crit}}^{\beta,\text{relFMT}}$ . It can be seen that  $\rho_{\text{crit}}^{\beta,\text{relFMT}} > \rho_{\text{crit}}^{\beta,\text{unif}}$  as one should expect from the fact that, for a given density, the electron density at the Wigner-Seitz cell boundary satisfies  $n_e^{\text{relFMT}} < n_e^{\text{unif}}$ . This means that, in order to reach a given energy, the electrons within the relativistic Feynman-Metropolis-Teller approach must be subjected to a larger density with respect to the one given by the approximated Salpeter analytic formula (B.1.90).

### General relativistic instability

The concept of the critical mass has played a major role in the theory of stellar evolution. For Newtonian white dwarfs the critical mass is reached asymptotically at infinite central densities of the object. One of the most important

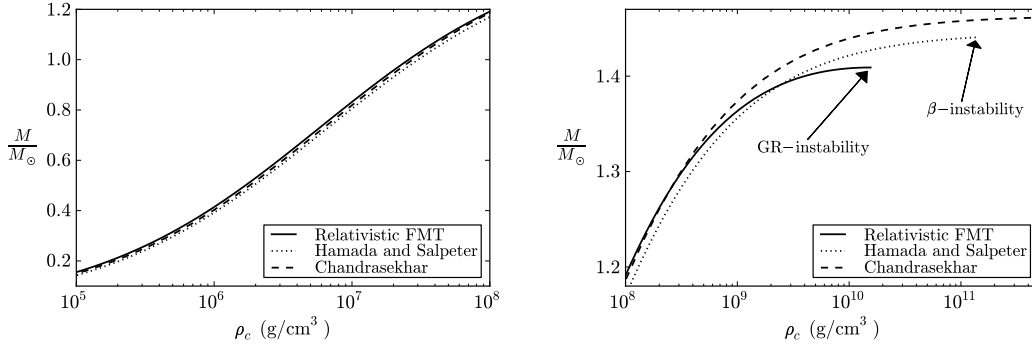


**Figure B.3.:** Mass in solar masses as a function of the central density in the range (left panel)  $10^5$ – $10^8$   $\text{g}/\text{cm}^3$  and in the range (right panel)  $10^8$ – $5 \times 10^{11}$   $\text{g}/\text{cm}^3$  for  ${}^4\text{He}$  white dwarfs. The solid curve corresponds to the present work, the dotted curves are the Newtonian configurations of Hamada and Salpeter and the dashed curve are the Newtonian configurations of Chandrasekhar.

general relativistic effects is to shift this critical point to some finite density  $\rho_{\text{crit}}^{\text{GR}}$ .

This general relativistic effect is an additional source of instability with respect to the already discussed instability due to the onset of inverse  $\beta$ -decay which, contrary to the present general relativistic one, applies also in the Newtonian case by shifting the maximum mass of Newtonian white dwarfs to finite densities (see e.g. Harrison et al. (1958)).

### Numerical results

In Figs. B.3–B.10 we have plotted the mass-central density relation and the mass-radius relation of general relativistic  ${}^4\text{He}$ ,  ${}^{12}\text{C}$ ,  ${}^{16}\text{O}$  and  ${}^{56}\text{Fe}$  white dwarfs. In particular, we show the results for the Newtonian white dwarfs of Hamada and Salpeter (1961), for the Newtonian white dwarfs of Chandrasekhar (1931b) and the general relativistic configurations obtained in this work based on the relativistic Feynman-Metropolis-Teller equation of state (Rotondo et al., 2011c).

Since our approach takes into account self-consistently both  $\beta$ -decay equilibrium and general relativity, we can determine if the critical mass is reached due either to inverse  $\beta$ -decay instability or to the general relativistic instability.

A comparison of the numerical value of the critical mass as given by Stoner (1929), Eq. (B.1.1), by Chandrasekhar (1931b) and Landau (1932), Eq. (B.1.2), by Hamada and Salpeter (1961) and, by the treatment presented here can be found in Table B.3.

From the numerical integrations we have obtained:

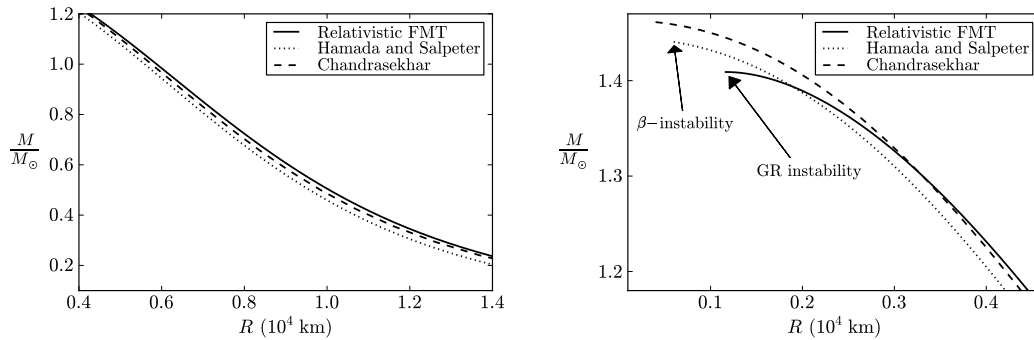


**Figure B.4.:** Mass in solar masses as a function of the radius in units of  $10^4$  km for  ${}^4\text{He}$  white dwarfs. The left and right panels show the configurations for the same range of central densities of the corresponding panels of Fig. B.3. The solid curve corresponds to the present work, the dotted curves are the Newtonian configurations of Hamada and Salpeter and the dashed curve are the Newtonian configurations of Chandrasekhar.

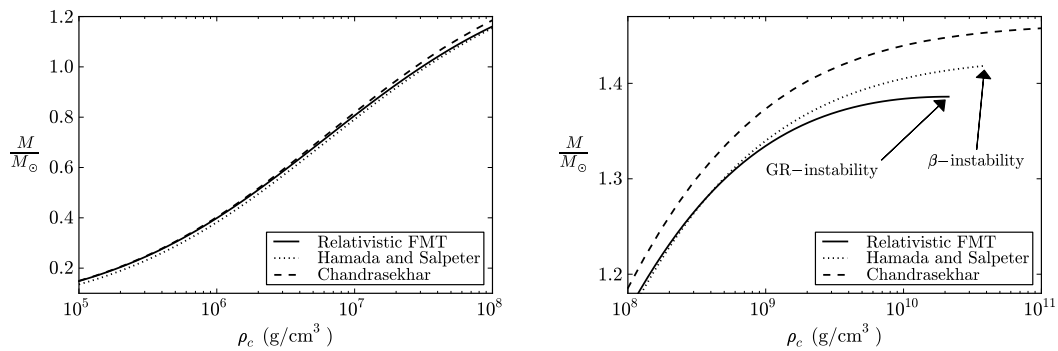


**Figure B.5.:** Mass in solar masses as a function of the central density in the range (left panel)  $10^5$ – $10^8$   $\text{g}/\text{cm}^3$  and in the range (right panel)  $10^8$ – $10^{11}$   $\text{g}/\text{cm}^3$  for  ${}^{12}\text{C}$  white dwarfs. The solid curve corresponds to the present work, the dotted curves are the Newtonian configurations of Hamada and Salpeter and the dashed curve are the Newtonian configurations of Chandrasekhar.

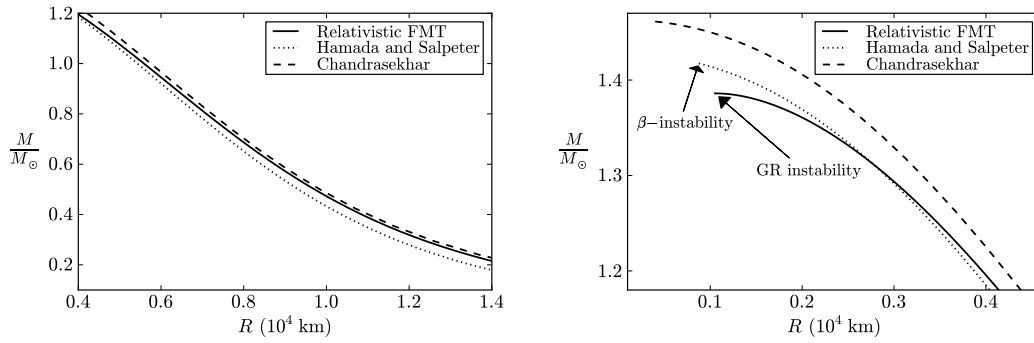


**Figure B.6.:** Mass in solar masses as a function of the radius in units of  $10^4$  km for  $^{12}\text{C}$  white dwarfs. The left and right panels show the configurations for the same range of central densities of the corresponding panels of Fig. B.5. The solid curve corresponds to the present work, the dotted curves are the Newtonian configurations of Hamada and Salpeter and the dashed curve are the Newtonian configurations of Chandrasekhar.

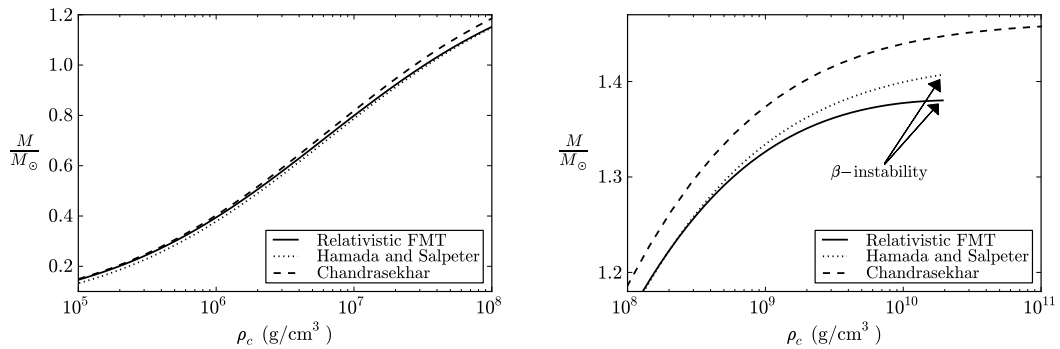


**Figure B.7.:** Mass in solar masses as a function of the central density in the range (left panel)  $10^5$ – $10^8$   $\text{g/cm}^3$  and in the range (right panel)  $10^8$ – $10^{11}$   $\text{g/cm}^3$  for  $^{16}\text{O}$  white dwarfs. The solid curve corresponds to the present work, the dotted curves are the Newtonian configurations of Hamada and Salpeter and the dashed curve are the Newtonian configurations of Chandrasekhar.

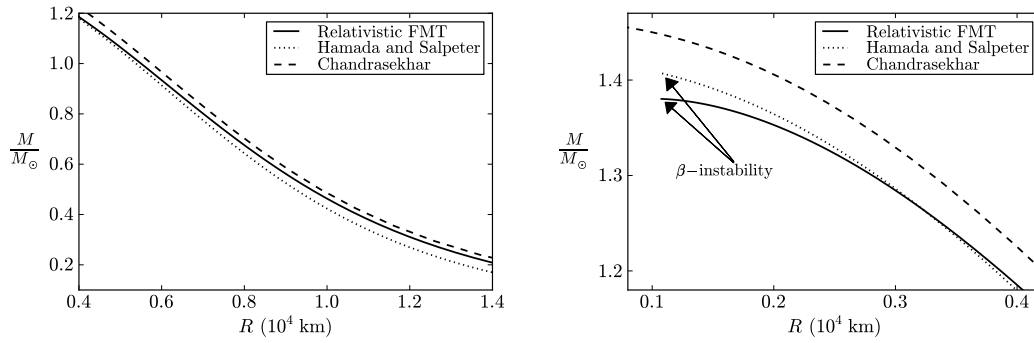


**Figure B.8.:** Mass in solar masses as a function of the radius in units of  $10^4$  km for  $^{16}\text{O}$  white dwarfs. The left and right panels show the configurations for the same range of central densities of the corresponding panels of Fig. B.7. The solid curve corresponds to the present work, the dotted curves are the Newtonian configurations of Hamada and Salpeter and the dashed curve are the Newtonian configurations of Chandrasekhar.

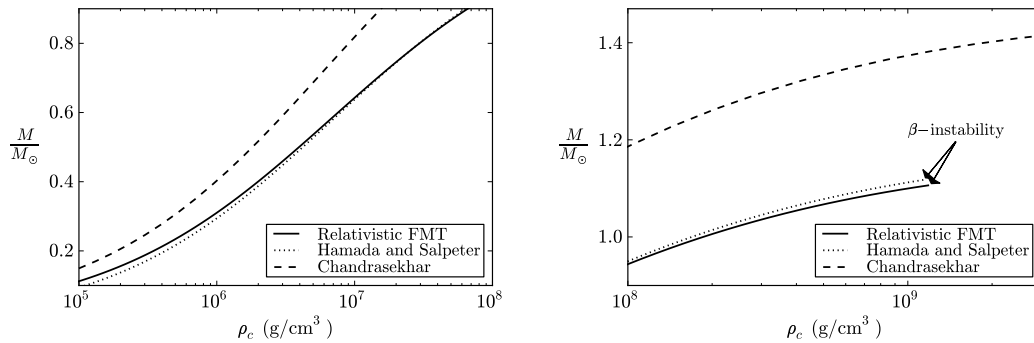


**Figure B.9.:** Mass in solar masses as a function of the central density in the range (left panel)  $10^5$ – $10^8$   $\text{g}/\text{cm}^3$  and in the range (right panel)  $10^8$ – $3 \times 10^9$   $\text{g}/\text{cm}^3$  for  $^{56}\text{Fe}$  white dwarfs. The solid curve corresponds to the present work, the dotted curves are the Newtonian configurations of Hamada and Salpeter and the dashed curve are the Newtonian configurations of Chandrasekhar.

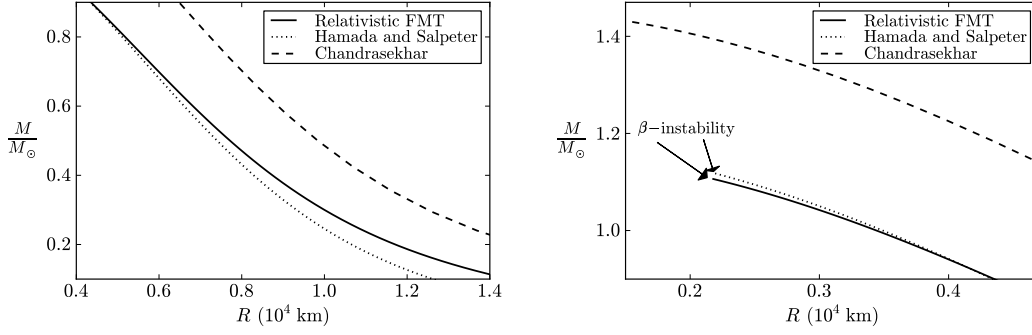


**Figure B.10.:** Mass in solar masses as a function of the radius in units of  $10^4$  km for  $^{56}\text{Fe}$  white dwarfs. The left and right panels show the configurations for the same range of central densities of the corresponding panels of Fig. B.9. The solid curve corresponds to the present work, the dotted curves are the Newtonian configurations of Hamada and Salpeter and the dashed curve are the Newtonian configurations of Chandrasekhar.

1.  $^4\text{He}$  and  $^{12}\text{C}$  white dwarfs satisfy  $\rho_{\text{crit}}^{\text{GR}} < \rho_{\text{crit}}^{\beta}$  (see Figs. B.3–B.6 and Tables B.2 and B.3), so they are unstable with respect to general relativistic effects. The critical density of  $^{12}\text{C}$  white dwarfs is  $\sim 2.12 \times 10^{10} \text{ g/cm}^3$ , to be compared with the value  $2.65 \times 10^{10} \text{ g/cm}^3$  obtained from calculations based on general relativistic corrections to the theory of polytropes (see e.g. Shapiro and Teukolsky (1983)).
2. White dwarfs composed of heavier material than  $^{12}\text{C}$ , e.g.  $^{16}\text{O}$  and  $^{56}\text{Fe}$  are unstable due to inverse  $\beta$ -decay of the nuclei (see Figs. B.7–B.10 and Tables B.2 and B.3). It is worth to notice that the correct evaluation of general relativistic effects and of the combined contribution of the electrons to the energy-density of the system introduce, for  $^{12}\text{C}$  white dwarfs, a critical mass not due to the inverse beta decay. When the contribution of the electrons to the energy-density is neglected (e.g. Chandrasekhar (1931b) and Hamada and Salpeter (1961), see Eq. (B.1.15)) the critical density for Carbon white dwarfs is determined by inverse beta decay irrespective of the effects of general relativity.
3. It can be seen from Figs. B.3–B.10 that the drastic decrease of the Salpeter pressure at low densities (see Salpeter (1961a); Rotonondo et al. (2011c) and Table B.1 for details) produces an underestimate of the mass and the radius of low density (low mass) white dwarfs.
4. The Coulomb effects are much more pronounced in the case of white dwarfs with heavy nuclear compositions e.g.  $^{56}\text{Fe}$  (see Figs. B.9 and B.10).

	$\rho_{\text{crit}}^{\text{H\&S}}$	$M_{\text{crit}}^{\text{H\&S}} / M_{\odot}$	$\rho_{\text{crit}}^{\text{FM Trel}}$	$M_{\text{crit}}^{\text{FM Trel}} / M_{\odot}$
${}^4\text{He}$	$1.37 \times 10^{11}$	1.44064	$1.56 \times 10^{10}$	1.40906
${}^{12}\text{C}$	$3.88 \times 10^{10}$	1.41745	$2.12 \times 10^{10}$	1.38603
${}^{16}\text{O}$	$1.89 \times 10^{10}$	1.40696	$1.94 \times 10^{10}$	1.38024
${}^{56}\text{Fe}$	$1.14 \times 10^9$	1.11765	$1.18 \times 10^9$	1.10618

**Table B.3.:** Critical density and corresponding critical mass for the onset of gravitational collapse of the Newtonian  ${}^4\text{He}$ ,  ${}^{12}\text{C}$ ,  ${}^{16}\text{O}$  and  ${}^{56}\text{Fe}$  white dwarfs of Hamada and Salpeter (1961), based on the Salpeter equation of state (Salpeter, 1961a), and of the corresponding general relativistic configurations obtained in this work based on the relativistic Feynman-Metropolis-Teller equation of state (Rotondo et al., 2011c). Densities are in  $\text{g}/\text{cm}^3$  and masses in solar masses. For the sake of comparison, the critical mass of Stoner (B.1.1) and of the one of Chandrasekhar-Landau (B.1.2) are  $M_{\text{crit}}^{\text{Stoner}} \sim 1.72M_{\odot}$  and  $M_{\text{crit}}^{\text{Ch-L}} \sim 1.45M_{\odot}$ , for the average molecular weight  $\mu = A_r/Z = 2$ .

### B.1.5. Conclusions

We have addressed the theoretical physics aspects of the white dwarf configurations of equilibrium, quite apart from the astrophysical application.

The recently accomplished description of a compressed atom within the global approach of the relativistic Feynman, Metropolis and Teller (Rotondo et al., 2011c) has been here solved within the Wigner-Seitz cell and applied to the construction of white dwarfs in the framework of general relativity. From a theoretical physics point of view, this is the first unified approach of white dwarfs taking into account consistently the gravitational, the weak, the strong and the electromagnetic interactions, and it answers open theoretical physics issues in this matter. No analytic formula for the critical mass of white dwarfs can be derived and, on the contrary, the critical mass can be obtained only through the numerical integration of the general relativistic equations of equilibrium together with the relativistic Feynman-Metropolis-Teller equation of state.

The value of the critical mass and the radius of white dwarfs in our treatment and in the Hamada and Salpeter (1961) treatment becomes a function of the composition of the star. Specific examples have been given in the case of white dwarfs composed of  ${}^4\text{He}$ ,  ${}^{12}\text{C}$ ,  ${}^{16}\text{O}$  and  ${}^{56}\text{Fe}$ . The results of Chandrasekhar, of Hamada and Salpeter and ours have been compared and contrasted (see Table B.3 and Figs. B.3–B.10).

The critical mass is a decreasing function of  $Z$  and Coulomb effects are more important for heavy nuclear compositions. The validity of the Salpeter approximate formulas increases also with  $Z$ , namely for heavy nuclear compositions the numerical values of the masses as well as of the radii of white dwarfs obtained using the Salpeter equation of state are closer to the ones ob-

tained from the full numerical integration of the general relativistic treatment presented here.

Turning now to astrophysics, the critical mass of white dwarfs is today acquiring a renewed interest in view of its central role in the explanation of the supernova phenomena (Phillips, 1993; Riess et al., 1998; Perlmutter et al., 1999; Riess et al., 2004). The central role of the critical mass of white dwarfs as related to supernova was presented by Hoyle and Fowler (1960) explaining the difference between type I and type II Supernova. This field has developed in the intervening years to a topic of high precision research in astrophysics and, very likely, both the relativistic and the Coulomb effects outlined in this article will become topic of active confrontation between theory and observation. For instance, the underestimate of the mass and the radius of low density white dwarfs within the Hamada and Salpeter (1961) treatment (see Figs. B.3–B.10) leads to the possibility of a direct confrontation with observations in the case of low mass white dwarfs e.g. the companion of the Pulsar J1141-6545 (Kramer, 2010).

We have finally obtained a general formula in Eq. (B.1.76) as a “first integral” of the general relativistic equations of equilibrium. This formula relates the chemical potential of the Wigner-Seitz cells, duly obtained from the relativistic Feynman-Metropolis-Teller model (Rotondo et al., 2011c) taking into account weak, nuclear and electromagnetic interactions, to the general relativistic gravitational potential at each point of the configuration. Besides its esthetic value, this is an important tool to examine the radial dependence of the white dwarf properties and it can be also applied to the crust of a neutron star as it approaches to the physical important regime of neutron star cores.

The formalism we have introduced allows in principle to evaluate subtle effects of a nuclear density distribution as a function of the radius and of the Fermi energy of the electrons and of the varying depth of the general relativistic gravitational potential. The theoretical base presented in this article establishes also the correct framework for the formulation of the more general case when finite temperatures and magnetic fields are present. This treatment naturally opens the way to a more precise description of the crust of neutron stars, which will certainly become an active topic of research in view of the recent results by Goriely et al. (2011a,b) on the importance of the Coulomb effects in the r-process nucleosynthesis of the crust material during its post-ejection evolution in the process of gravitational collapse and/or in the merging of neutron star binaries.

## **B.2. On general relativistic uniformly rotating white dwarfs**

### **B.2.1. Introduction**

The relevance of rotation in enhancing the maximum stable mass of a white dwarf (WD) have been discussed for many years both for uniform rotation (see e.g. James, 1964; Anand, 1965; Roxburgh and Durney, 1966; Monaghan, 1966; Geroyannis and Hadjopoulos, 1989) and differential rotation (see e.g. Ostriker and Bodenheimer, 1968; Ostriker and Tassoul, 1969; Tassoul and Ostriker, 1970; Durisen, 1975). Newtonian gravity and post-Newtonian approximation have been mainly used to compute the structure of the star, with the exception of the work of Arutyunyan et al. (1971), where rotating white dwarfs (RWDs) were computed in full General Relativity (GR). From the microscopical point of view, the equation of state (EOS) of cold WD matter has been assumed to be either the one of a microscopically uniform degenerate electron fluid used by Chandrasekhar (1931b) in his classic work, or assumed to have a polytropic form.

However, as shown first by Salpeter (1961a) in the Newtonian case and then by (Rotondo et al., 2011c,b) in General Relativity (GR), a detailed description of the EOS taking into account the effects of the Coulomb interaction are essential for the determination of the maximum stable mass of non-rotating WDs. Specific microphysics of the ion-electron system forming a Coulomb lattice, together with the detail computation of the inverse  $\beta$ -decays and the pycnonuclear reaction rates, play a fundamental role.

A new EOS taking into account the finite size of the nucleus, the Coulomb interactions, and the electroweak equilibrium in a self-consistent relativistic fashion has been recently obtained by Rotondo et al. (2011c). This relativistic Feynman-Metropolis-Teller (RFMT) EOS generalizes both the Chandrasekhar (1931b) and Salpeter (1961a) works in that a full treatment of the Coulomb interaction is given through the solution of a relativistic Thomas-Fermi model. This leads to a more accurate calculation of the energy and pressure of the Wigner-Seitz cells, hence a more accurate EOS. It has been shown how the Salpeter EOS overestimates at high densities and underestimates at low densities the electron pressure. The application of this new EOS to the structure of non-rotating  ${}^4\text{He}$ ,  ${}^{12}\text{C}$ ,  ${}^{16}\text{O}$  and  ${}^{56}\text{Fe}$  was recently done in (Rotondo et al., 2011b). The new mass-radius relations generalize the works of Chandrasekhar (1931b) and Hamada and Salpeter (1961); smaller maximum masses and a larger minimum radii are obtained. Both GR and inverse  $\beta$ -decay can be relevant for the instability of non-rotating WDs depending on the nuclear composition, as we can see from Table B.4, which summarizes some results of Rotondo et al. (2011b).

We here extend the previous results of Rotondo et al. (2011b) for uniformly

Composition	$\rho_{\text{crit}}^{J=0}$ (g/cm <sup>3</sup> )	Instability	$M_{\text{max}}^{J=0}/M_{\odot}$
<sup>4</sup> He	$1.56 \times 10^{10}$	GR	1.40906
<sup>12</sup> C	$2.12 \times 10^{10}$	GR	1.38603
<sup>16</sup> O	$1.94 \times 10^{10}$	inverse $\beta$ -decay	1.38024
<sup>56</sup> Fe	$1.18 \times 10^9$	inverse $\beta$ -decay	1.10618

**Table B.4.:** Critical density and mass for the gravitational collapse of non-rotating <sup>4</sup>He, <sup>12</sup>C, <sup>16</sup>O and <sup>56</sup>Fe WDs in GR obtained by Rotondo et al. (2011b), based on the RFMT EOS Rotondo et al. (2011c). We indicate in the third column if the critical density is due either to inverse  $\beta$ -decay or to general relativistic effects.

RWDs at zero temperatures obeying the RFMT EOS. We use the Hartle’s approach (Hartle, 1967) to solve the Einstein equations accurately up to second order approximation in the angular velocity of the star. We calculate the mass  $M$ , equatorial  $R_{eq}$  and polar  $R_p$  radii, angular momentum  $J$ , eccentricity  $\epsilon$ , and quadrupole moment  $Q$ , as a function of the central density  $\rho_c$  and rotation angular velocity  $\Omega$  of the WD. We construct also RWD models for the Chandrasekhar and Salpeter EOS and compare and contrast the differences with the RFMT ones.

We analyze in detail the stability of RWDs both from the microscopic and macroscopic point of view in Sec. B.2.3. Besides the inverse  $\beta$ -decay instability, we also study the limits to the matter density imposed by zero-temperature pycnonuclear fusion reactions using up-to-date theoretical models (Gasques et al., 2005; Yakovlev et al., 2006). The mass-shedding limit as well as the secular axisymmetric instability boundary are calculated.

The general structure and stability boundaries of <sup>4</sup>He, <sup>12</sup>C, <sup>16</sup>O and <sup>56</sup>Fe WDs are discussed in in Sec. B.2.4. From the maximally rotating models (mass-shedding sequence), we calculate in Sec. B.2.5 the maximum mass of uniformly rotating <sup>4</sup>He, <sup>12</sup>C, <sup>16</sup>O and <sup>56</sup>Fe WDs for the Chandrasekhar, Salpeter, and RFMT EOS, and compare the results with the existing values in the literature. We calculate the minimum(maximum) rotation period(frequency) of a RWD for the above nuclear compositions, taking into account both inverse  $\beta$ -decay and pycnonuclear restrictions to the density; see Sec. B.2.6.

We discuss in Sec. B.2.7 the axisymmetric instabilities found in this work. A comparison of Newtonian and general relativistic WDs presented in App. B.2.11 show that this is indeed a general relativistic effect. Furthermore, we estimate in App. B.2.11 the accuracy of the “slow” rotation approximation (power-series solutions up to order  $\Omega^2$ ) for the determination of the maximally rotating sequence of WDs. In this line, we calculate the rotation to gravitational energy ratio and the deviations from spherical symmetry.

In addition, we construct in Sec. B.2.8 constant rest-mass evolution tracks of RWDs at fixed chemical composition and show that RWDs may experi-

ence both spin-up and spin-down epochs while loosing angular momentum, depending on their initial mass and rotation period.

Finally, in Sec. B.2.9 we outline some astrophysical implications of the results presented in this work, which we summarized in Sec. B.2.10.

### B.2.2. Spacetime geometry and Hartle's formalism

Hartle (1967) described for the first time the structure of rotating objects approximately up to second order terms in the angular velocity of the star  $\Omega$ , within GR. In this "slow" rotation approximation, the solution of the Einstein equations in the exterior vacuum can be written in analytic closed form in terms of the total mass  $M$ , angular momentum  $J$  and quadrupole moment  $Q$  of the star (see App. B.2.11). The interior metric is constructed by solving numerically a system of ordinary differential equations for the perturbation functions (see Hartle, 1967; Hartle and Thorne, 1968, for details).

The spacetime geometry up to order  $\Omega^2$ , with an appropriate choice of coordinates is, in geometrical units  $c = G = 1$ , described by (Hartle, 1967)

$$\begin{aligned}
 ds^2 = & \left\{ e^{v(r)} [1 + 2h_0(r) + 2h_2(r)P_2(\cos \theta)] - \omega^2 r^2 \sin^2 \theta \right\} dt^2 \\
 & + 2\omega r^2 \sin^2 \theta dt d\phi - e^{\lambda(r)} \left[ 1 + 2 \frac{m_0(r) + m_2(r)P_2(\cos \theta)}{r - M^{J=0}(r)} \right] dr^2 \\
 & - r^2 [1 + 2k_2(r)P_2(\cos \theta)] (d\theta^2 + \sin^2 \theta d\phi^2), \quad (\text{B.2.1})
 \end{aligned}$$

where  $P_2(\cos \theta)$  is the Legendre polynomial of second order,  $e^{v(r)}$  and  $e^{\lambda(r)} = [1 - 2M^{J=0}(r)/r]^{-1}$ , and  $M^{J=0}(r)$  are the metric functions and mass of the corresponding static (non-rotating) solution with the same central density as the rotating one. The angular velocity of local inertial frames  $\omega(r)$ , proportional to  $\Omega$ , as well as the functions  $h_0$ ,  $h_2$ ,  $m_0$ ,  $m_2$ ,  $k_2$ , proportional to  $\Omega^2$ , must be calculated from the Einstein equations (see Hartle, 1967; Hartle and Thorne, 1968, for details); their analytic expressions in the vacuum case can be found in App. B.2.11.

The parameters  $M$ ,  $J$  and  $Q$ , are then obtained for a given EOS from the matching procedure between the internal and external solutions at the surface of the rotating star. The total mass is defined by  $M = M^{J \neq 0} = M^{J=0} + \delta M$ , where  $M^{J=0}$  is the mass of a static (non-rotating) WD with the same central density as  $M^{J \neq 0}$ , and  $\delta M$  is the contribution to the mass due to rotation.

### B.2.3. Limits on the stability of rotating white dwarfs

#### The mass-shedding limit

The velocity of particles on the equator of the star cannot exceed the Keplerian velocity of "free" particles, computed at the same location. In this limit,

particles on the star's surface keep bound to the star only due to a balance between gravity and centrifugal forces. The evolution of a star rotating at this Keplerian rate is accompanied by loss of mass, becoming thus unstable (see e.g. Stergioulas, 2003, for details). A procedure to obtain the maximum possible angular velocity of the star before reaching this limit was developed e.g. by Friedman et al. (1986). However, in practice, it is less complicated to compute the mass-shedding (or Keplerian) angular velocity of a rotating star,  $\Omega_K^{J \neq 0}$ , by calculating the orbital angular velocity of a test particle in the external field of the star and corotating with it at its equatorial radius,  $r = R_{eq}$ .

For the Hartle-Thorne external solution, the Keplerian angular velocity can be written as (see e.g. Torok et al. (2008) and App. B.2.11, for details)

$$\Omega_K^{J \neq 0} = \sqrt{G \frac{M}{R_{eq}^3} \left[ 1 - jF_1(R_{eq}) + j^2F_2(R_{eq}) + qF_3(R_{eq}) \right]}, \quad (\text{B.2.2})$$

where  $j = cJ/(GM^2)$  and  $q = c^4Q/(G^2M^3)$  are the dimensionless angular momentum and quadrupole moment, and the functions  $F_i(r)$  are defined in App. B.2.11. Thus, the numerical value of  $\Omega_K^{J \neq 0}$  can be computed by gradually increasing the value of the angular velocity of the star,  $\Omega$ , until it reaches the value  $\Omega_K^{J \neq 0}$  expressed by Eq. (B.2.2).

It is important to analyze the issue of the accuracy of the slow rotation approximations, e.g. accurate up to second order in the rotation expansion parameter, for the description of maximally rotating stars as WDs and neutron stars (NSs). We have performed in App. B.2.11 a scrutiny of the actual physical request made by the slow rotation regime. Based on this analysis, we have checked that the accuracy of the slow rotation approximation increases with the density of the WD, and that the mass-shedding (Keplerian) sequence of RWDs can be accurately described by the  $\Omega^2$  approximation within an error smaller than the one found for rapidly rotating NSs,  $\lesssim 6\%$ .

### The turning-point criterion and secular axisymmetric instability

In a sequence of increasing central density the mass of non-rotating star is limited by the first maximum of the  $M-\rho_c$  curve, i.e. the turning-point given by the maximum mass,  $\partial M/\partial \rho_c = 0$ , marks the secular instability point and it coincides also with the dynamical instability point if the perturbation obeys the same EOS as of the equilibrium configuration (see e.g. Shapiro and Teukolsky, 1983, for details). The situation is, however, much more complicated in the case of rotating stars; the determination of axisymmetric dynamical instability points implies to find the perturbed solutions with zero frequency modes, that is, perturbed configurations whose energy (mass) is the same as the unperturbed (equilibrium) one, at second order. However, Friedman et al. (1988) formulated, based on the works of Sorkin (1981, 1982),

a turning-point method to locate the points where secular instability sets in for uniformly rotating relativistic stars: along a sequence of rotating stars with fixed angular momentum and increasing central density, the onset of secular axisymmetric instability is given by

$$\left( \frac{\partial M(\rho_c, J)}{\partial \rho_c} \right)_J = 0. \quad (\text{B.2.3})$$

Thus, configurations on the right-side of the maximum mass of a  $J$ -constant sequence are secularly unstable. After the secular instability sets in, the configuration evolves quasi-stationarily until it reaches a point of dynamical instability where gravitational collapse should take place (see Stergioulas, 2003, and references therein). The secular instability boundary thus separates stable from unstable stars. It is worth stressing here that the turning-point of a constant  $J$  sequence is a sufficient but not a necessary condition for secular instability and therefore it establishes an absolute upper bound for the mass (at constant  $J$ ). We construct the boundary given by the turning-points of constant angular momentum sequences as given by Eq. (B.2.3). The question whether dynamically unstable RWDs can exist or not on the left-side of the turning-point boundary remains an interesting problem and deserves further attention in view of the very recent results obtained by Takami et al. (2011) for some models of rapidly rotating NSs.

### Inverse $\beta$ -decay instability

It is known that a WD might become unstable against the inverse  $\beta$ -decay process  $(Z, A) \rightarrow (Z - 1, A)$  through the capture of energetic electrons. In order to trigger such a process, the electron Fermi energy (with the rest-mass subtracted off) must be larger than the mass difference between the initial  $(Z, A)$  and final  $(Z - 1, A)$  nucleus. We denote this threshold energy as  $\epsilon_Z^\beta$ . Usually it is satisfied  $\epsilon_{Z-1}^\beta < \epsilon_Z^\beta$  and therefore the initial nucleus undergoes two successive decays, i.e.  $(Z, A) \rightarrow (Z - 1, A) \rightarrow (Z - 2, A)$  (see e.g. Salpeter (1961a); Shapiro and Teukolsky (1983)). Some of the possible decay channels in WDs with the corresponding known experimental threshold energies  $\epsilon_Z^\beta$  are listed in Table B.5. The electrons in the WD may eventually reach the threshold energy to trigger a given decay at some critical density  $\rho_{\text{crit}}^\beta$ . Since the electrons are responsible for the internal pressure of the WD, configurations with  $\rho > \rho_{\text{crit}}^\beta$  become unstable due to the softening of the EOS as a result of the electron capture process (see e.g. Salpeter, 1961a). In Table B.5, correspondingly to each threshold energy  $\epsilon_Z^\beta$ , the critical density  $\rho_{\text{crit}}^\beta$  given by the RFMT EOS is shown; see Rotondo et al. (2011b) for details.

Decay	$\epsilon_Z^\beta$ (MeV)	$\rho_{\text{crit}}^\beta$ (g/cm <sup>3</sup> )
${}^4\text{He} \rightarrow {}^3\text{H} + n \rightarrow 4n$	20.596	$1.39 \times 10^{11}$
${}^{12}\text{C} \rightarrow {}^{12}\text{B} \rightarrow {}^{12}\text{Be}$	13.370	$3.97 \times 10^{10}$
${}^{16}\text{O} \rightarrow {}^{16}\text{N} \rightarrow {}^{16}\text{C}$	10.419	$1.94 \times 10^{10}$
${}^{56}\text{Fe} \rightarrow {}^{56}\text{Mn} \rightarrow {}^{56}\text{Cr}$	3.695	$1.18 \times 10^9$

**Table B.5.:** Onset for the inverse  $\beta$ -decay of  ${}^4\text{He}$ ,  ${}^{12}\text{C}$ ,  ${}^{16}\text{O}$  and  ${}^{56}\text{Fe}$ . The experimental values of the threshold energies  $\epsilon_Z^\beta$  have been taken from Table 1 of Audi et al. (2003b); see also (Shapiro and Teukolsky, 1983). The corresponding critical density  $\rho_{\text{crit}}^\beta$  are for the RFMT EOS (see Rotondo et al., 2011b)

### Pycnonuclear fusion reactions

In our WD model, we assume a unique nuclear composition  $(Z, A)$  throughout the star. We have just seen that inverse  $\beta$ -decay imposes a limit to the density of the WD over which the current nuclear composition changes from  $(Z, A)$  to  $(Z - 1, A)$ . There is an additional limit to the nuclear composition of a WD. Nuclear reactions proceed with the overcoming of the Coulomb barrier by the nuclei in the lattice. In the present case of zero temperatures  $T = 0$ , the Coulomb barrier can be overcome because the zero-point energy of the nuclei (see e.g. Shapiro and Teukolsky, 1983)

$$E_p = \hbar\omega_p, \quad \omega_p = \sqrt{\frac{4\pi e^2 Z^2 \rho}{A^2 M_u^2}}, \quad (\text{B.2.4})$$

where  $e$  is the fundamental charge and  $M_u = 1.6605 \times 10^{-24}$  g is the atomic mass unit.

Based on the pycnonuclear rates computed by Zel'Dovich (1958b) and Cameron (1959), Salpeter (1961a) estimated that in a time of 0.1 Myr,  ${}^1\text{H}$  is converted into  ${}^4\text{He}$  at  $\rho \sim 5 \times 10^4$  g cm<sup>-3</sup>,  ${}^4\text{He}$  into  ${}^{12}\text{C}$  at  $\rho \sim 8 \times 10^8$  g cm<sup>-3</sup>, and  ${}^{12}\text{C}$  into  ${}^{24}\text{Mg}$  at  $\rho \sim 6 \times 10^9$  g cm<sup>-3</sup>. The threshold density for the pycnonuclear fusion of  ${}^{16}\text{O}$  occurs, for the same reaction time 0.1 Myr, at  $\rho \sim 3 \times 10^{11}$  g cm<sup>-3</sup>, and for 10 Gyr at  $\sim 10^{11}$  g cm<sup>-3</sup>. These densities are much higher than the corresponding density for inverse  $\beta$ -decay of  ${}^{16}\text{O}$ ,  $\rho \sim 1.9 \times 10^{10}$  g cm<sup>-3</sup> (see Table B.5). The same argument applies to heavier compositions e.g.  ${}^{56}\text{Fe}$ ; so pycnonuclear reactions are not important for heavier than  ${}^{12}\text{C}$  in WDs.

It is important to analyze the case of  ${}^4\text{He}$  WDs in detail. At densities  $\rho_{\text{pyc}} \sim 8 \times 10^8$  g cm<sup>-3</sup> a  ${}^4\text{He}$  WD should have a mass  $M \sim 1.35M_\odot$  (see e.g. Fig. 3 in Rotondo et al., 2011b). However, the mass of  ${}^4\text{He}$  WDs is constrained to lower values from their previous thermonuclear evolution: a cold star with mass  $> 0.5M_\odot$  have already burned an appreciable part of its Helium content at earlier stages. Thus, WDs of  $M > 0.5M_\odot$  with  ${}^4\text{He}$  cores

are very unlikely (see Hamada and Salpeter, 1961, for details). It should be stressed that  ${}^4\text{He}$  WDs with  $M \lesssim 0.5M_{\odot}$  have central densities  $\rho \sim 10^6 \text{ g cm}^{-3}$  (Rotondo et al., 2011b) and at such densities pycnonuclear reaction times are longer than 10 Gyr, hence unimportant. However, we construct in this work  ${}^4\text{He}$  RWDs configurations all the way up to their inverse  $\beta$ -decay limiting density for the sake of completeness, keeping in mind that the theoretical  ${}^4\text{He}$  WDs configurations with  $M \gtrsim 0.5M_{\odot}$  could actually not be present in any astrophysical system.

From the above discussion we conclude that pycnonuclear reactions can be relevant only for  ${}^{12}\text{C}$  WDs. It is important to stress here that the reason for which the pycnonuclear reaction time,  $\tau_{pyc}^{\text{C}+\text{C}}$ , determines the lifetime of a  ${}^{12}\text{C}$  WD is that reaction times  $\tau_{pyc}^{\text{C}+\text{C}} < 10 \text{ Gyr}$  are achieved at densities  $\sim 10^{10} \text{ g cm}^{-3}$ , lower than the inverse  $\beta$  decay threshold density of  ${}^{24}\text{Mg}$ ,  ${}^{24}\text{Mg} \rightarrow {}^{24}\text{Na} \rightarrow {}^{24}\text{Ne}$ ,  $\rho \sim 3.2 \times 10^9 \text{ g cm}^{-3}$  (see e.g. Salpeter, 1961a; Shapiro and Teukolsky, 1983). Thus, the pycnonuclear  ${}^{12}\text{C}+{}^{12}\text{C}$  fusion produces unstable  ${}^{24}\text{Mg}$  that almost instantaneously decay owing to electron captures, and so the WD becomes unstable as we discussed in Subsec. B.2.3.

However, the pycnonuclear reaction rates are not known with precision due to theoretical and experimental uncertainties. Hamada and Salpeter (1961) had already pointed out in their work that the above pycnonuclear density thresholds are reliable only within a factor 3 or 4. The uncertainties are related to the precise knowledge of the Coulomb tunneling in the high density low temperature regime relevant to astrophysical systems, e.g. WDs and NSs, as well as with the precise structure of the lattice; impurities, crystal imperfections, as well as the inhomogeneities of the local electron distribution and finite temperature effects, also affect the reaction rates. The energies for which the so-called astrophysical  $S$ -factors are known from experiments are larger with respect to the energies found in WD and NS crusts, and therefore the value of the  $S$ -factors have to be obtained theoretically from the extrapolation of experimental values using appropriate nuclear models, which at the same time are poorly constrained. A detailed comparison between the different theoretical methods and approximations used for the computation of the pycnonuclear reaction rates can be found in (Gasques et al., 2005; Yakovlev et al., 2006).

The  $S$ -factors have been computed in (Gasques et al., 2005; Yakovlev et al., 2006) using up-to-date nuclear models. Following these works, we have computed the pycnonuclear reaction times for C+C fusion as a function of the density as given by Eq. (B.2.27),  $\tau_{pyc}^{\text{C}+\text{C}}$ , which we show in Fig. B.11; we refer to App. B.2.11 for details.

We obtain that for  $\tau_{pyc}^{\text{C}+\text{C}} = 10 \text{ Gyr}$ ,  $\rho_{pyc} \sim 9.26 \times 10^9 \text{ g cm}^{-3}$  while, for  $\tau_{pyc}^{\text{C}+\text{C}} = 0.1 \text{ Myr}$ ,  $\rho_{pyc} \sim 1.59 \times 10^{10} \text{ g cm}^{-3}$ , to be compared with the value  $\rho \sim 6 \times 10^9 \text{ g cm}^{-3}$  estimated by Salpeter (1961a). In order to compare the threshold densities for inverse  $\beta$ -decay and pycnonuclear fusion rates,

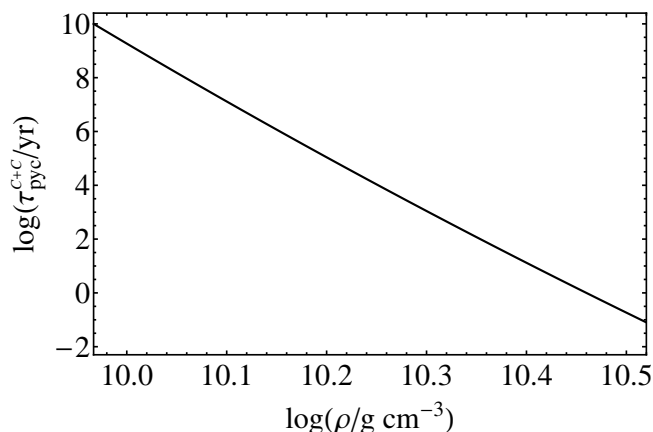


**Figure B.11.** Pycnonuclear reaction times at zero temperature for C+C fusion as a function of the density.

we shall indicate in our mass-density and mass-radius relations the above two density values corresponding to these two lifetimes. It is important to stress that the computation of the pycnonuclear reactions rates is subjected to theoretical and experimental uncertainties (see Gasques et al., 2005, for details). For instance, Hamada and Salpeter (1961) stated that these pycnonuclear critical densities are reliable within a factor 3 or 4. If three times larger, the above value of  $\rho_{\text{pyc}}$  for  $\tau_{\text{pyc}}^{\text{C+C}} = 0.1$  Myr becomes  $\rho_{\text{pyc}} \sim 4.8 \times 10^{10} \text{ g cm}^{-3}$ , larger than the inverse  $\beta$ -decay threshold density  $\rho_{\beta}^{\text{C}} \sim 3.97 \times 10^{10} \text{ g cm}^{-3}$  (see Table B.5). As we will see in Sec. B.2.7, the turning-point construction leads to an axisymmetric instability boundary in the density range  $\rho_{\text{crit}}^{\text{C},J=0} = 2.12 \times 10^{10} < \rho < \rho_{\beta}^{\text{C}} \text{ g cm}^{-3}$  in a specific range of angular velocities. This range of densities is particularly close to the above values of  $\rho_{\text{pyc}}$  which suggests a possible competition between different instabilities at high densities.

#### B.2.4. WD structure and stability boundaries

The structure of uniformly RWDs have been studied by several authors (see e.g. James, 1964; Anand, 1965; Roxburgh and Durney, 1966; Monaghan, 1966; Geroyannis and Hadjopoulos, 1989). The issue of the stability of both uniformly and differentially rotating WDs has been studied as well (see e.g. Ostriker and Bodenheimer, 1968; Ostriker and Tassoul, 1969; Tassoul and Ostriker, 1970; Durisen, 1975). All the above computations were carried out within Newtonian gravity or at the post-Newtonian approximation. The EOS of cold WD matter has been assumed to be either the one of a microscopically uniform degenerate electron fluid, which we refer hereafter as Chandrasekhar EOS (Chandrasekhar, 1931b), or assuming a polytropic EOS. However, microscopic screening caused by Coulomb interactions as well as the

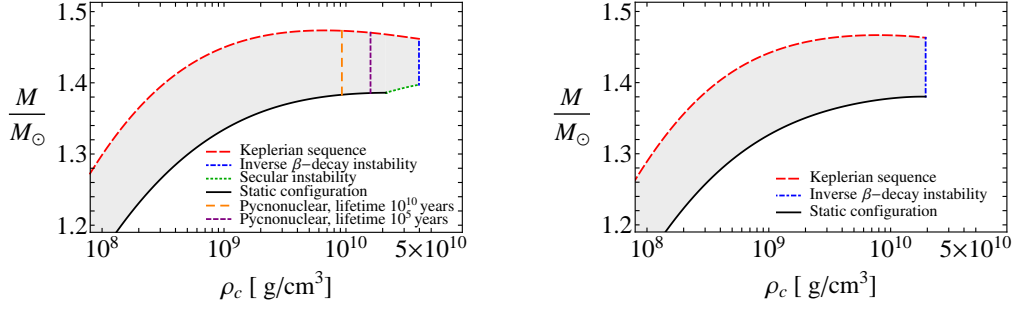


**Figure B.12.:** Mass in solar masses versus the central density for  $^{12}\text{C}$  (left panel) and for  $^{16}\text{O}$  (right panel) WDs. The solid curve corresponds to the mass of non-rotating WDs, the Keplerian sequence is the red thick dashed curve, the blue thick dotted-dashed curve is the inverse  $\beta$  instability boundary, and the green thick solid curve is the axisymmetric instability boundary. The orange and purple dashed boundaries correspond to the pycnonuclear densities for reaction times  $\tau_{pyc} = 10$  Gyr and 0.1 Myr, respectively. All rotating stable WDs are in the shaded region.

process of inverse  $\beta$ -decay of the composing nuclei cannot be properly studied within such EOS (see Rotondo et al., 2011c,b, for details).

The role of general relativistic effects, shown in Rotondo et al. (2011b), has been neglected in all the above precedent literature. The only exception to this rule is, up to our knowledge, the work of Arutyunyan et al. (1971), who investigated uniformly RWDs for the Chandrasekhar EOS within GR. They use an  $\Omega^2$  approximation following a method developed by Sedrakyan and Chubaryan (1968), independently of the work of Hartle (1967). A detailed comparison of our results with the ones of Arutyunyan et al. (1971) can be found in App. B.2.11.

In Figs. B.12–B.13 we show the mass-central density relation and the mass-radius relation of general relativistic rotating  $^{12}\text{C}$  and  $^{16}\text{O}$  WDs. We explicitly show the boundaries of mass-shedding, secular axisymmetric instability, inverse  $\beta$ -decay, and pycnonuclear reactions.

Turning now to the rotation properties, in Fig. B.14 we show the  $J$ - $M$  plane especially focusing on RWDs with masses larger than the maximum non-rotating mass, hereafter Super-Chandrasekhar WDs (SCWDs). It becomes clear from this diagram that SCWDs can be stable only by virtue of their non-zero angular momentum: the lower-half of the stability line of Fig. B.14, from  $J = 0$  at  $M/M_{max}^{J=0}$  all the way up to the value of  $J$  at  $M_{max}^{J \neq 0} \sim 1.06M_{max}^{J=0}$ , determines the critical(minimum) angular momentum under which a SCWDs becomes unstable. The upper half of the stability line determines, instead, the maximum angular momentum that SCWDs can have.

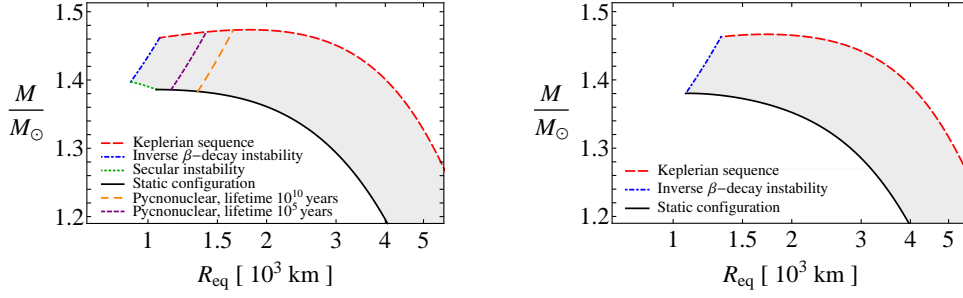


**Figure B.13.:** Mass in solar masses versus the equatorial radius in units of  $10^3$  km for  $^{12}\text{C}$  (left panel) and for  $^{16}\text{O}$  (right panel) WDs. The left and right panels show the configurations for the same range of central densities of the corresponding panels of Fig. B.12.

Composition	$\rho_{M_{max}^{J \neq 0}}$	$k$	$M_{max}^{J=0}/M_{\odot}$	$R_{M_{max}^{J=0}}$	$P_{min}$	$R_p^{P_{min}}$	$R_{eq}^{P_{min}}$	$(T/ W )^{P_{min}}$	$\epsilon^{P_{min}}$	$j^{P_{min}}$	$q^{P_{min}}$
$^4\text{He}$	$5.46 \times 10^9$	1.0646	1.40906	1163	0.284	564	736	0.0163	0.642	1.004	526
$^{12}\text{C}$	$6.95 \times 10^9$	1.0632	1.38603	1051	0.501	817	1071	0.0181	0.647	1.287	1330
$^{16}\text{O}$	$7.68 \times 10^9$	1.0626	1.38024	1076	0.687	1005	1323	0.0194	0.651	1.489	2263
$^{56}\text{Fe}$	$1.18 \times 10^9$	1.0864	1.10618	2181	2.195	2000	2686	0.0278	0.667	2.879	23702

**Table B.6.:** Properties of uniformly rotating general relativistic  $^4\text{He}$ ,  $^{12}\text{C}$ ,  $^{16}\text{O}$  and  $^{56}\text{Fe}$  WDs:  $\rho_{M_{max}^{J \neq 0}}$  is the central density in  $\text{g cm}^{-3}$  corresponding to the rotating maximum mass  $M_{max}^{J \neq 0}$ ;  $k$  is the dimensionless factor used to express the rotating maximum mass  $M_{max}^{J \neq 0}$  as a function of the non-rotating maximum mass  $M_{max}^{J=0}$  of WDs, in solar masses, obtained in Rotondo et al. (2011b), as defined in Eq. (B.2.5); the corresponding minimum radius is  $R_{M_{max}^{J=0}}$ , in km;  $P_{min}$  is the minimum rotation period in seconds. We recall that the configuration with  $P_{min}$  is obtained for a WD rotating at the mass-shedding limit and with central density equal to the critical density for inverse  $\beta$ -decay (see Table B.5 and the right panel of Fig. B.16). The polar  $R_p^{P_{min}}$  and equatorial  $R_{eq}^{P_{min}}$  radii of the configuration with  $P_{min}$  are also given in km. The quantity  $(T/|W|)^{P_{min}}$  is the ratio between the kinetic and binding energies, the parameter  $\epsilon^{P_{min}}$  is the eccentricity of the star, rotating at  $P_{min}$ . Finally,  $j^{P_{min}}$  and  $q^{P_{min}}$  are the dimensionless angular momentum and quadrupole moment of WDs, respectively.

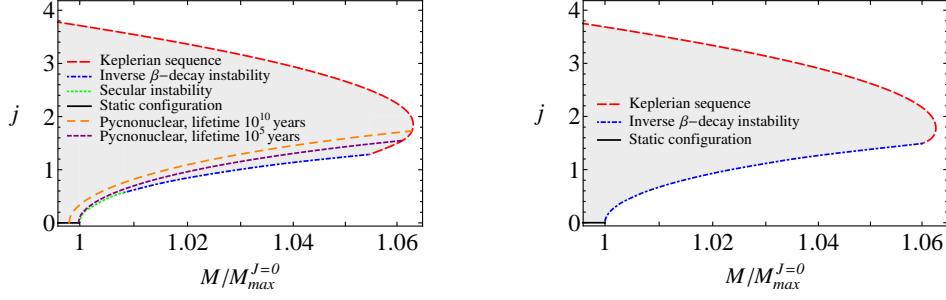


**Figure B.14.:** Dimensionless angular momentum  $j \equiv cJ/(GM^2)$  versus the mass of rotating  $^{12}\text{C}$  (left panel) and  $^{16}\text{O}$  (right panel) WDs, normalized to the maximum non-rotating mass. All rotating stable WDs are in the shaded region.

Nuclear Composition	EOS	$\rho_{M_{max}^{J \neq 0}}$ (g/cm <sup>3</sup> )	$R_p^{M_{max}^{J \neq 0}}$ (km)	$R_{eq}^{M_{max}^{J \neq 0}}$ (km)	$M_{max}^{J \neq 0}/M_\odot$	$P^{M_{max}^{J \neq 0}}$ (sec)
$\mu = 2$	Chandrasekhar	$1.07 \times 10^{10}$	1198.91	1583.47	1.5159	0.884
	Salpeter	$1.07 \times 10^{10}$	1193.08	1575.94	1.4996	0.883
$^4\text{He}$	RFMT	$5.46 \times 10^9$	1458.58	1932.59	1.5001	1.199
	Salpeter	$1.08 \times 10^{10}$	1183.99	1564.16	1.4833	0.878
$^{12}\text{C}$	RFMT	$6.95 \times 10^9$	1349.15	1785.98	1.4736	1.074
	Salpeter	$1.09 \times 10^{10}$	1178.88	1556.68	1.4773	0.875
$^{16}\text{O}$	RFMT	$7.68 \times 10^9$	1308.09	1730.65	1.4667	1.027
	Salpeter	$1.14 \times 10^9$	2002.43	2693.17	1.2050	2.202
$^{56}\text{Fe}$	RFMT	$1.18 \times 10^9$	2000.11	2686.06	1.2017	2.195

**Table B.7.:** The maximum rotating mass of general relativistic uniformly rotating  $^4\text{He}$ ,  $^{12}\text{C}$ ,  $^{16}\text{O}$  and  $^{56}\text{Fe}$  WDs for different EoS.  $\rho_{M_{max}^{J \neq 0}}$ ,  $R_p^{M_{max}^{J \neq 0}}$ ,  $R_{eq}^{M_{max}^{J \neq 0}}$ , and  $P^{M_{max}^{J \neq 0}}$  are central density, polar and equatorial radii, and rotation period of the configuration with the maximum mass,  $M_{max}^{J \neq 0}$ .

### B.2.5. The maximum mass

The maximum masses of rotating WDs belongs to the Keplerian sequence (see Figs. B.12–B.14) and it can be expressed as

$$M_{max}^{J \neq 0} = k M_{max}^{J=0}, \quad (\text{B.2.5})$$

where  $M_{max}^{J=0}$  is the maximum stable mass of non-rotating WDs and  $k$  is a numerical factor that depends on the chemical composition, see Table B.6 for details. For  $^4\text{He}$ ,  $^{12}\text{C}$ ,  $^{16}\text{O}$ , and  $^{56}\text{Fe}$  RWDs, we found  $M_{max}^{J \neq 0} \sim 1.500, 1.474, 1.467, 1.202 M_\odot$ , respectively.

In Table B.7 we compare the properties of the configuration with maximum mass using different EOS, namely Chandrasekhar  $\mu = 2$ , Salpeter, and RFMT EOS. A comparison with classical results obtained with different treatments and EOS can be found in App. B.2.11.

It is worth mentioning that the maximum mass of RWDs is not associated with a critical maximum density for gravitational collapse. This is in con-

Nuclear composition	EoS	$\rho_{\text{crit}}^{\beta}$ (g/cm <sup>3</sup> )	$R_p^{P_{\text{min}}}$ (km)	$R_{\text{eq}}^{P_{\text{min}}}$ (km)	$M_{P_{\text{min}}}^{J \neq 0} / M_{\odot}$	$P_{\text{min}}$ (sec)
$\mu = 2$	Chandra	$1.37 \times 10^{11}$	562.79	734.54	1.4963	0.281
	Salpeter	$1.37 \times 10^{11}$	560.41	731.51	1.4803	0.281
<sup>4</sup> He	RFMT	$1.39 \times 10^{11}$	563.71	735.55	1.4623	0.285
	Salpeter	$3.88 \times 10^{10}$	815.98	1070.87	1.4775	0.498
<sup>12</sup> C	RFMT	$3.97 \times 10^{10}$	816.55	1071.10	1.4618	0.501
	Salpeter	$1.89 \times 10^{10}$	1005.62	1324.43	1.4761	0.686
<sup>16</sup> O	RFMT	$1.94 \times 10^{10}$	1005.03	1323.04	1.4630	0.687
	Salpeter	$1.14 \times 10^9$	2002.43	2693.17	1.2050	2.202
<sup>56</sup> Fe	RFMT	$1.18 \times 10^9$	2000.11	2686.06	1.2018	2.195

**Table B.8.:** The minimum rotation period of general relativistic rotating <sup>4</sup>He, <sup>12</sup>C, <sup>16</sup>O and <sup>56</sup>Fe WDs.  $\rho_{\text{crit}}^{\beta}$  is the critical density for inverse  $\beta$  decay.  $M_{P_{\text{min}}}^{J \neq 0}$ ,  $R_p^{P_{\text{min}}}$ , and  $R_{\text{eq}}^{P_{\text{min}}}$  are the mass, polar, and equatorial radii corresponding to the configuration with minimum rotation period,  $P_{\text{min}}$ .

trast with the non-rotating case where the configuration of maximum mass (turning-point) corresponds to a critical maximum density over which the WD is unstable against gravitational collapse.

The angular momentum  $J$  along the mass-shedding sequence is not constant and thus the turning-point criterion (B.2.3) does not apply to this sequence. Therefore the configuration of maximum rotating mass (B.2.5) does not separate stable from secular axisymmetrically unstable WDs. We have also verified that none of the RWDs belonging to the mass-shedding sequence is a turning-point of some  $J = \text{constant}$  sequence, and therefore they are indeed secularly stable. We therefore extend the Keplerian sequence all the way up to the critical density for inverse  $\beta$  decay,  $\rho_{\text{crit}}^{\beta}$ , see Table B.5 and Fig. B.12.

### B.2.6. The minimum rotation period

The minimum rotation period  $P_{\text{min}}$  of WDs is obtained for a configuration rotating at Keplerian angular velocity, at the critical inverse  $\beta$ -decay density; i.e. is the configuration lying at the crossing point between the mass-shedding and inverse  $\beta$ -decay boundaries, see Figs. B.12 and B.14. For <sup>4</sup>He, <sup>12</sup>C, <sup>16</sup>O, and <sup>56</sup>Fe RWDs we found the minimum rotation periods  $\sim 0.28, 0.50, 0.69$  and 2.19 seconds, respectively (see Table B.6 for details). In Table B.7 we compare the properties of the configuration with minimum rotation period using different EOS, namely Chandrasekhar  $\mu = 2$ , Salpeter, and RFMT EOS.

In the case of <sup>12</sup>C WDs, the minimum period 0.50 seconds have to be compared with the value obtained assuming as critical density the threshold for pycnonuclear reactions. Assuming lifetimes  $\tau_{\text{pyc}}^{\text{C}+\text{C}} = 10$  Gyr and 0.1 Myr, corresponding to critical densities  $\rho_{\text{pyc}} \sim 9.26 \times 10^9$  g cm<sup>-3</sup> and  $\rho_{\text{pyc}} \sim 1.59 \times 10^{10}$  g cm<sup>-3</sup>, we obtain minimum periods  $P_{\text{min}}^{\text{pyc}} = 0.95$  and 0.75 seconds, respectively.

It is interesting to compare and contrast some classical results with the ones presented in this work. Using post-Newtonian approximation, Roxburgh and Durney (1966) analyzed the problem of dynamical stability of maximally

rotating RWDs, i.e. WDs rotating at the mass-shedding limit. The result was a minimum polar radius of 363 km, assuming the Chandrasekhar EOS with  $\mu = 2$ . The Roxburgh critical radius is rather small with respect to our minimum polar radii, see Table B.6. It is clear that such a small radius would lead to a configuration with the central density over the limit established by inverse  $\beta$ -decay: the average density obtained for the Roxburgh's critical configuration is  $\sim 1.47 \times 10^{10} \text{ g/cm}^3$ , assuming the maximum mass  $1.48M_{\odot}$  obtained in the same work (see Table B.9 in App. B.2.11). A configuration with this mean density will certainly have a central density larger than the inverse  $\beta$ -decay density of  $^{12}\text{C}$  and  $^{16}\text{O}$ ,  $3.97 \times 10^{10} \text{ g/cm}^3$  and  $1.94 \times 10^{10} \text{ g/cm}^3$ , respectively (see Table B.5). The rotation period of the WD at the point of dynamical instability of Roxburgh must be certainly shorter than the minimum values presented here.

The above comparison is in line with the fact that we did not find any turning-point that cross the mass-shedding sequence (see Figs. B.12–B.13). Presumably, ignoring the limits imposed by inverse  $\beta$ -decay and pycnonuclear reactions, the boundary determined by the turning-points could cross at some higher density the Keplerian sequence. Such a configuration should have a central density very similar to the one found by Roxburgh and Durney (1966).

In the work of Arutyunyan et al. (1971) the problem of the minimum rotation period of a WD was not considered. However, they showed their results for a range of central densities covering the range of interest of our analysis. Thus, we have interpolated their numerical values of the rotation period of WDs in the Keplerian sequence and calculated the precise values at the inverse  $\beta$ -decay threshold for  $^4\text{He}$ ,  $^{12}\text{C}$ , and  $^{16}\text{O}$  that have  $\mu = 2$  and therefore in principle comparable to the Chandrasekhar EOS results with the same mean molecular weight. We thus obtained minimum periods  $\sim 0.31, 0.55, 0.77$  seconds, in agreement with our results (see Table B.8).

It is important to stress that, although it is possible to compare the results using the Chandrasekhar EOS  $\mu = 2$  with the ones obtained for the RFMT EOS, both qualitative and quantitative differences exist between the two treatments. In the former a universal mass-density and mass-radius relation is obtained assuming  $\mu = 2$  while, in reality, the configurations of equilibrium depend on the specific values of  $Z$  and  $A$  in non-trivial way. For instance,  $^4\text{He}$ ,  $^{12}\text{C}$ , and  $^{16}\text{O}$  have  $\mu = 2$  but the configurations of equilibrium are rather different. This fact was emphasized by Hamada and Salpeter (1961) in the Newtonian case and further in GR by Rotondo et al. (2011b), for non-rotating configurations. In Fig. B.15 we present a comparison of the mass-density and mass-radius for the universal Chandrasekhar  $\mu = 2$  and the RFMT EOS for specific nuclear compositions.

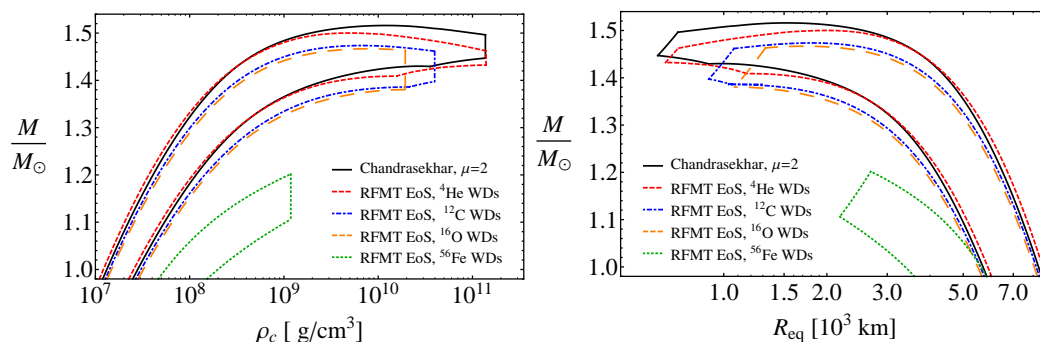


**Figure B.15.** Mass versus central density (left panel) and mass versus equatorial radius (right panel) for general relativistic WDs using the Chandrasekhar and the RFMT EOS.

### B.2.7. Occurrence of secular axisymmetric instability

Regarding the stability of rotating WDs, Ostriker and Bodenheimer (1968); Ostriker and Tassoul (1969); Durisen (1975) showed that uniformly rotating Newtonian polytropes and WDs described by the uniform degenerate electron fluid EOS are axisymmetrically stable at any rotation rate. In clear contrast with these results, we have shown here that uniformly RWDs can be indeed be secularly axisymmetric unstable as can be seen from Figs. B.12–B.14 (green boundary). We have constructed in App. B.2.11 Newtonian RWDs for the Chandrasekhar EOS and compare the differences with the general relativistic counterpart. Apart from the quantitative differences for the determination of the mass at high densities, it can be seen from Fig. B.17 (left panel) the absence of turning-points in the Newtonian mass-density relation. This can be understood from the fact that the maximum stable mass of non-rotating WDs is, in the Newtonian case, reached formally at infinite central density. We should then expect that turning-points will appear only from a post-Newtonian approximation, where the critical mass is shifted to finite densities (see e.g. Roxburgh and Durney, 1966, for the calculation of dynamical instability for post-Newtonian RWDs obeying the Chandrasekhar EOS).

In this respect the Fig. B.14 is of particular astrophysical relevance. Configurations lying in the filled region are stable against mass-shedding, inverse  $\beta$ -decay and secular axisymmetric instabilities. RWDs with masses smaller than the maximum non-rotating mass (Sub-Chandrasekhar WDs), i.e.  $M^{J \neq 0} < M_{max}^{J=0}$ , can have angular momenta ranging from a maximum at the mass-shedding limit all the way down to the non-rotating limit  $J = 0$ . SCWDs, however, are stabilized due to rotation and therefore there exist a minimum angular momentum,  $J_{min} > 0$ , to guarantee their stability. We have shown above that secular axisymmetric instability is relevant for the determination of this minimum angular momentum of SCWDs (see green boundary

in Fig. B.14). It is interesting to note in this respect that from our results it turns out that SCWDs with *light chemical compositions* such as  ${}^4\text{He}$  and  ${}^{12}\text{C}$ , are unstable against *axisymmetric*, inverse  $\beta$ -decay and mass-shedding instabilities. On the opposite, in SCWDs with *heavier chemical compositions*, such as  ${}^{16}\text{O}$  and  ${}^{56}\text{Fe}$ , the secular axisymmetric instability does not take place; see Fig. B.14. The existence of the new boundary due to secular axisymmetric instability is a critical issue for the evolution of SCWDs since their lifetime might be reduced depending on their initial mass and angular momentum.

From the quantitative point of view, we have found that axisymmetric instability sets in for  ${}^{12}\text{C}$  SCWDs in the range of masses  $M_{max}^{J=0} < M \lesssim 1.397M_{\odot}$ , for some specific range of rotation periods  $\gtrsim 1.24$  seconds. We can express the minimum rotation period that a SCWD with a mass  $M$  within the above mass range can have through the fitting formula

$$P_{axi} = 0.062 \left( \frac{M - M_{max}^{J=0}}{M_{\odot}} \right)^{-0.67} \text{ seconds}, \quad (\text{B.2.6})$$

where  $M_{max}^{J=0}$  is the maximum mass of general relativistic non-rotating  ${}^{12}\text{C}$  WDs,  $M_{max}^{J=0} \approx 1.386M_{\odot}$  (see Table B.4 and Rotondo et al. (2011b)). Thus, Eq. (B.2.6) describes the rotation periods of the configurations along the green-dotted boundary in Figs. B.12, B.13, and B.14. Correspondingly, the central density along this instability boundary varies from the critical density of static  ${}^{12}\text{C}$  WDs,  $\rho_{crit}^{C,J=0} = 2.12 \times 10^{10} \text{ g cm}^{-3}$  (see Table B.4), up to the inverse  $\beta$ -decay density,  $\rho_{\beta}^C = 3.97 \times 10^{10} \text{ g cm}^{-3}$  (see Table B.5).

It is important to note that at the lower edge of the density range for axisymmetric instability,  $\rho_{crit}^{C,J=0}$ , the timescale of C+C pycnonuclear reactions are  $\tau_{pyc}^{C+C} \approx 339 \text{ yr}$  (see Fig. B.11). It becomes then of interest to compare this timescale with the corresponding one of the secular axisymmetric instability that sets in at the same density.

The growing time of the secular instability is given by the dissipation time that can be driven either by gravitational radiation or viscosity (Chandrasekhar, 1970). However, gravitational radiation reaction is expected to drive secular instabilities for systems with rotational to gravitational energy ratio  $T/|W| \sim 0.14$ , the bifurcation point between McClaurin spheroids and Jacobi ellipsoids (see Chandrasekhar, 1970, for details). Therefore, we expect gravitational radiation to become important only for differentially rotating WDs, which can attain more mass and more angular momentum (Ostriker and Bodenheimer, 1968). In the present case of general relativistic uniformly RWDs, only the viscosity timescale  $\tau_v$  is relevant. A rotating star that becomes secularly unstable first evolve with a characteristic time  $\tau_v$  and eventually reach a point of dynamical instability, thus collapsing within a time  $\tau_{dyn} \approx \Omega_K^{-1} \sim \sqrt{R^3/GM} \lesssim 1 \text{ s}$ , where  $R$  is the radius of the star (see e.g.

Stergioulas, 2003).

The viscosity timescale can be estimated as  $\tau_v = R^2\rho/\eta$  (see e.g. Lindblom, 1987), where  $\rho$  and  $\eta$  are the density and viscosity of the star. The viscosity of a WD assuming degenerate relativistic electrons is given by (Durisen, 1973)

$$\eta_{fluid} = 4.74 \times 10^{-2} \frac{H_\Gamma(Z)}{Z} \rho^{5/3} \left[ \left( \frac{\rho}{2 \times 10^6} \right)^{2/3} + 1 \right]^{-1}, \quad (\text{B.2.7})$$

where  $H_\Gamma(Z)$  is a slowly varying dimensionless constant that depends on the atomic number  $Z$  and the Coulomb to thermal energy ratio

$$\Gamma = \frac{e^2 Z^2}{k_B T} \left( \frac{4\pi}{3} \frac{\rho}{2ZMu} \right)^{1/3}, \quad (\text{B.2.8})$$

where  $k_B$  is the Boltzmann constant and  $A \simeq 2Z$  has been used.

The expression (B.2.7) is valid for values of  $\Gamma$  smaller than the critical value for crystallization  $\Gamma_{cry}$ . The critical  $\Gamma_{cry}$  is not well constrained but its value should be of the order of  $\Gamma_{cry} \sim 100$  (see e.g. Durisen, 1973; Shapiro and Teukolsky, 1983). The critical value  $\Gamma_{cry}$  defines a crystallization temperature  $T_{cry}$  under which the system behaves as a solid. For  $\Gamma_{cry} \sim 100$ , we have  $T_{cry} \approx 8 \times 10^7 [\rho / (10^{10} \text{ g cm}^{-3})]^{1/3}$  K, for  $Z = 6$ . When  $\Gamma$  approaches  $\Gamma_{cry}$  the viscosity can increase drastically to values close to (van Horn, 1969; Durisen, 1973)

$$\eta_{cry} = 4.0 \times 10^{-2} \left( \frac{Z}{7} \right)^{2/3} \rho^{5/6} \exp[0.1(\Gamma - \Gamma_{cry})]. \quad (\text{B.2.9})$$

For instance, we find that at densities  $\rho_{crit}^{C,J=0}$  and assuming a central temperature  $T \gtrsim 0.5T_{cry}$  with  $T_{cry} \approx 10^8$  K, the viscous timescale is in the range  $10 \lesssim \tau_v \lesssim 1000$  Myr, where the upper limit is obtained using Eq. (B.2.7) and the lower limit with Eq. (B.2.9). These timescales are longer than the pycnonuclear reaction timescale  $\tau_{pyc}^{C+C} = 339$  yr at the same density. So, if the pycnonuclear reaction rates are accurate, it would imply that pycnonuclear reactions are more important to restrict the stability of RWDs with respect to the secular instability. However, we have to keep in mind that, as discussed in Sec. B.2.3, the pycnonuclear critical densities are subjected to theoretical and experimental uncertainties, which could in principle shift them to higher values. For instance, a possible shift of the density for pycnonuclear instability with timescales  $\tau_{pyc}^{C+C} \sim 1$  Myr to higher values  $\rho_{pyc}^{C+C} > \rho_{crit}^{C,J=0}$ , would suggest an interesting competition between secular and pycnonuclear instability in the density range  $\rho_{crit}^{C,J=0} < \rho < \rho_\beta^C$ .

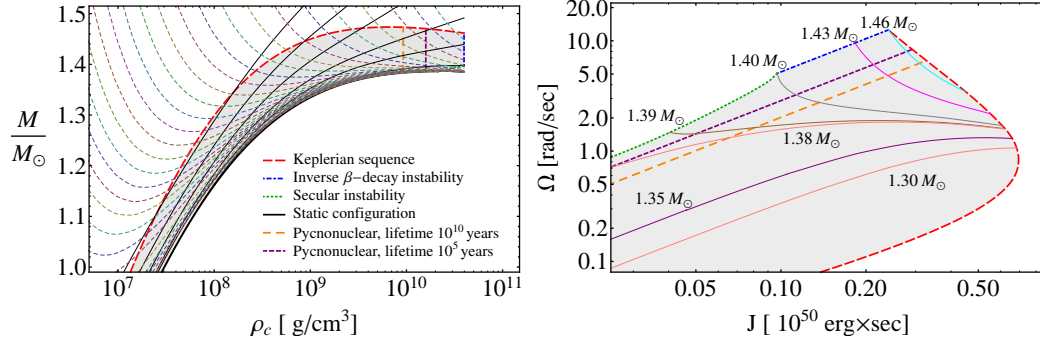


**Figure B.16.:** Left panel: mass versus the central density for  $^{12}\text{C}$  RWDs. The solid black curves correspond to  $J=\text{constant}$  sequences, where the static case  $J = 0$  the thickest one. The color thin-dashed curves correspond to  $\Omega=\text{constant}$  sequences. The Keplerian sequence is the red thick dashed curve, the blue thick dotted-dashed curve is the inverse  $\beta$ -decay instability boundary, and the green thick dotted curve is the axisymmetric secular instability boundary. Right panel: contours of constant rest-mass in the  $\Omega - J$  plane; RWDs that evolve along a track with  $\partial\Omega/\partial J > 0$  spin-down by losing angular momentum while, the ones with  $\partial\Omega/\partial J < 0$ , spin-up.

### B.2.8. Spin-up and spin-down evolution

It is known that at constant rest-mass  $M_0$ , entropy  $S$  and chemical composition  $(Z, A)$ , the spin evolution of a RWD is given by (see Shapiro et al., 1990, for details)

$$\dot{\Omega} = \frac{\dot{E}}{\Omega} \left( \frac{\partial\Omega}{\partial J} \right)_{M_0, S, Z, A}, \quad (\text{B.2.10})$$

where  $\dot{\Omega} \equiv d\Omega/dt$  and  $\dot{E} \equiv dE/dt$ , with  $E$  the energy of the star.

Thus, if a RWD is losing energy by some mechanism during its evolution, that is  $\dot{E} < 0$ , the change of the angular velocity  $\Omega$  in time depends on the sign of  $\partial\Omega/\partial J$ ; RWDs that evolve along a track with  $\partial\Omega/\partial J > 0$ , will spin-down ( $\dot{\Omega} < 0$ ) and the ones following tracks with  $\partial\Omega/\partial J < 0$  will spin-up ( $\dot{\Omega} > 0$ ).

In Fig. B.16 we show, in the left panel, the  $\Omega = \text{constant}$  and  $J = \text{constant}$  sequences in the mass-central density diagram and, in the right panel, contours of constant rest-mass in the  $\Omega - J$  plane.

The sign of  $\partial\Omega/\partial J$  can be analyzed from the left panel plot of Fig. B.16 by joining two consecutive  $J = \text{constant}$  sequences with an horizontal line and taking into account that  $J$  decreases from left to right and from up to down. The angular velocity  $\Omega$ , instead, decreases from right to left and from up to down for SCWDs and, for sub-Chandrasekhar WDs, from left to right and from up to down. We note that, in the SCWDs region  $\Omega = \text{constant}$  sequences satisfy  $\partial\Omega/\partial\rho_c < 0$  while, in the sub-Chandrasekhar region, both

$\partial\Omega/\partial\rho_c < 0$  and  $\partial\Omega/\partial\rho_c > 0$  appear (see minima). SCWDs can only either spin-up by angular momentum loss or spin-down by gaining angular momentum. In the latter case, the RWD becomes decompressed with time increasing its radius and moment of inertia, and then SCWDs following this evolution track will end at the mass-shedding limit (see Fig. B.16). Some evolutionary tracks of sub-Chandrasekhar WDs and SCWDs are shown in the right panel of Fig. B.16. It is appropriate to recall here that Shapiro et al. (1990) showed that spin-up behavior by angular momentum loss occurs for rapidly rotating Newtonian polytropes if the polytropic index is very close to  $n = 3$ , namely for an adiabatic index  $\Gamma \approx 4/3$ . It was shown explicitly by Geroyannis and Pappasotiropoulos (2000) that these conditions are achieved only by Super-Chandrasekhar polytropes.

Besides the confirmation of the above known result for SCWDs in the general relativistic case, we report here the presence of minima  $\partial\Omega/\partial\rho_c = 0$  for some sub-Chandrasekhar masses (see e.g. the evolution track of the RWD with  $M = 1.38M_\odot$  in the right panel of Fig. B.16) which raises the possibility that sub-Chandrasekhar WDs can experience, by angular momentum loss, not only the intuitively spin-down evolution, but also spin-up epochs.

### B.2.9. Astrophysical implications

It is appropriate to analyze the astrophysical consequences of the general relativistic RWDs presented in this work.

Most of the observed magnetic WDs are massive; for instance REJ 0317-853 with  $M \sim 1.35M_\odot$  and  $B \sim (1.7\text{--}6.6) \times 10^8$  G (see e.g. Barstow et al., 1995; Külebi et al., 2010b); PG 1658+441 with  $M \sim 1.31M_\odot$  and  $B \sim 2.3 \times 10^6$  G (see e.g. Liebert et al., 1983; Schmidt et al., 1992); and PG 1031+234 with the highest magnetic field  $\sim 10^9$  G (see e.g. Schmidt et al., 1986; Külebi et al., 2009). However, they are generally found to be slow rotators. It is worth mentioning that such a magnetic WDs can be indeed the result of the merger of double degenerate binaries; the misalignment of the final magnetic dipole moment of the newly born RWD with the rotation axis of the star depends on the difference of the masses of the WD components of the binary.

The precise computation of the evolution of the rotation period have to account for the actual value at each time of the moment of inertia and the equatorial and polar radii of the WD. Whether magnetic and gravitational radiation braking can explain or not the current relatively long rotation periods of some observed magnetic WDs is an important issue that deserves the appropriate attention and will be addressed elsewhere.

Magnetic braking of SCWDs has been recently invoked as a possible mechanism to explain the delayed time distribution of type Ia supernovae (SNe) (see Ilkov and Soker, 2012, for details): a type Ia SN explosion is delayed for a time typical of the spin-down time scale  $\tau_B$  due to magnetic braking, pro-

viding the result of the merging process of a WD binary system is a magnetic SCWD rather than a sub-Chandrasekhar one. The characteristic timescale  $\tau_B$  of SCWD has been estimated to be  $10^7 \lesssim \tau_B \lesssim 10^{10}$  yr for magnetic fields comprised in the range  $10^6 \lesssim B \lesssim 10^8$  G. A constant moment of inertia  $\sim 10^{49}$  g cm<sup>2</sup> and a fixed critical(maximum) rotation angular velocity

$$\Omega_{\text{crit}} \sim 0.7\Omega_K^{J=0} = 0.7\sqrt{\frac{GM^{J=0}}{R_{M^{J=0}}^3}}, \quad (\text{B.2.11})$$

have been adopted (Ilkov and Soker, 2012).

It is important to recall here that, as discussed in Sec. B.2.8, SCWDs spin-up by angular momentum loss, and therefore the reference to a “spin-down” time scale for them is just historical. SCWDs then evolve toward the mass-shedding limit, which determines in this case the critical angular velocity for rotational instability.

If we express  $\Omega_K^{J \neq 0}$  in terms of  $\Omega_K^{J=0}$  (see App. B.2.11), taking into account the values of  $j$  and  $q$  from the numerical integration, we find for RWDs that the Keplerian angular velocity can be written as

$$\Omega_K^{J \neq 0} = \sigma\Omega_K^{J=0}, \quad (\text{B.2.12})$$

**where the coefficient  $\sigma$  varies in the interval [0.78,0.75] in the range of central densities  $[10^5, 10^{11}]$  g cm<sup>-3</sup>.** It is important to mention that the above range of  $\sigma$  hold approximately the same independently on the chemical composition of the WD. However, the actual numerical value of the critical angular velocity,  $\Omega_K^{J \neq 0}$ , is different for different compositions owing to the dependence on  $(Z, A)$  of mass-radius relation of non-rotating WDs.

Furthermore, as we have shown, the evolution track followed by a SCWD depends strongly on the initial conditions of mass and angular momentum as well as on chemical composition, and evolution of the moment of inertia (see Fig. B.16 and Sec. B.2.8 for details). It is clear that the assumption of fixed moment of inertia  $I \sim 10^{49}$  g cm<sup>2</sup>, leads to a spin-down time scale depending only on the magnetic field strength. A detailed computation will lead to a strong dependence on the mass of the SCWD; resulting in a two-parameter family of delayed times  $\tau_B(M, B)$ . Detailed calculations of the lifetime of SCWDs braking-down due to magnetic dipole radiation are then needed to shed light on this important matter. Theoretical work along these lines is currently in progress and the results will be presented in a forthcoming publication.

Massive fast rotating and highly magnetized WDs have been proposed as an alternative scenario of Soft Gamma Ray Repeaters (SGRs) and Anomalous X-ray Pulsars (AXPs); see Malheiro et al. (2012) for details. Within such scenario, the range of minimum rotation periods of massive WDs found in this

work,  $0.3 \lesssim P_{min} \lesssim 2.2$  seconds, depending on the nuclear composition (see Table B.8), implies the rotational stability of SGRs and AXPs, which possess observed rotation periods  $2 \lesssim P \lesssim 12$  seconds. The relatively long minimum period of  $^{56}\text{Fe}$  RWDs  $\sim 2.2$  seconds, implies that RWDs describing SGRs and AXPs have to be composed of nuclear compositions lighter than  $^{56}\text{Fe}$ , e.g.  $^{12}\text{C}$  or  $^{16}\text{O}$ .

### B.2.10. Concluding remarks

We have calculated the properties of uniformly RWDs within the framework of GR using the Hartle formalism and our new EOS for cold WD matter based on the relativistic Feynman-Metropolis-Teller treatment (Rotondo et al., 2011c), which generalizes previous approaches including the EOS of Salpeter (1961a). A detailed comparison with RWDs described by the Chandrasekhar and the Salpeter EOS has been performed.

We constructed the region of stability of RWDs taking into account the mass-shedding limit, secular axisymmetric instability, inverse  $\beta$ -decay, and pycnonuclear reaction lifetimes. The latter have been computed using the updated theoretical models of Gasques et al. (2005); Yakovlev et al. (2006). We found that the minimum rotation periods for  $^4\text{He}$ ,  $^{12}\text{C}$ ,  $^{16}\text{O}$ , and  $^{56}\text{Fe}$  RWDs are  $\sim 0.3$ ,  $0.5$ ,  $0.7$  and  $2.2$  seconds, respectively (see Table B.8). For  $^{12}\text{C}$  WDs, the minimum period  $0.5$  seconds needs to be compared with the values  $P_{min}^{pyc} = 0.75$  and  $0.95$  seconds, obtained assuming as critical density the threshold for pycnonuclear reactions for lifetimes  $\tau_{pyc}^{C+C} = 0.1$  Myr and  $10$  Gyr, respectively. For the same chemical compositions, the maximum masses are  $\sim 1.500$ ,  $1.474$ ,  $1.467$ ,  $1.202 M_{\odot}$  (see Table B.7). These results and additional properties of RWDs can be found in Table B.6.

We have presented a new instability boundary of general relativistic SCWDs, over which they become axisymmetrically unstable. We have expressed the range of masses and rotation periods where this occurs through a fitting formula given by Eq. (B.2.6). A comparison with Newtonian RWDs in App. B.2.11 show to the conclusion that this new boundary of instability for uniformly rotating WDs is a general relativistic effect.

We showed that, by loosing angular momentum, sub-Chandrasekhar RWDs can experience both spin-up and spin-down epochs while, SCWDs, can only spin-up. These results are particularly important for the evolution of WDs whose masses approach, either from above or from below, the maximum non-rotating mass. The knowledge of the actual values of the mass, radii, and moment of inertia of massive RWDs are relevant for the computation of delay collapse times in the models of type Ia SN explosions. A careful analysis of all the possible instability boundaries as the one presented here have to be taken into account during the evolution of the WD at pre-SN stages.

We have indicated specific astrophysical systems where the results of this

work are relevant; for instance the long rotation periods of observed massive magnetic WDs; the delayed collapse of SCWDs as progenitors of type Ia SNe; and the alternative scenario for SGRs and AXPs based on massive RWDs.

### B.2.11. Supplementary information

#### The Hartle-Thorne solution and equatorial circular orbits

The HT metric given by Eq. (B.2.1) can be written in an analytic closed-form in the exterior vacuum case in terms of the total mass  $M$ , angular momentum  $J$ , and quadrupole moment  $Q$  of the rotating star. The angular velocity of local inertial frames  $\omega(r)$ , proportional to  $\Omega$ , and the functions  $h_0, h_2, m_0, m_2, k_2$ , proportional to  $\Omega^2$ , are derived from the Einstein equations (see Hartle, 1967; Hartle and Thorne, 1968, for details). Thus, the metric can be written as

$$\begin{aligned}
 ds^2 = & \left(1 - \frac{2M}{r}\right) \left[1 + 2k_1 P_2(\cos \theta) + 2 \left(1 - \frac{2M}{r}\right)^{-1} \frac{J^2}{r^4} (2 \cos^2 \theta - 1)\right] dt^2 \\
 & + \frac{4J}{r} \sin^2 \theta dt d\phi \\
 & - \left(1 - \frac{2M}{r}\right)^{-1} \left[1 - 2 \left(k_1 - \frac{6J^2}{r^4}\right) P_2(\cos \theta) - 2 \left(1 - \frac{2M}{r}\right)^{-1} \frac{J^2}{r^4}\right] dr^2 \\
 & - r^2 [1 - 2k_2 P_2(\cos \theta)] (d\theta^2 + \sin^2 \theta d\phi^2)
 \end{aligned} \tag{B.2.13}$$

where

$$\begin{aligned}
 k_1 &= \frac{J^2}{Mr^3} \left(1 + \frac{M}{r}\right) + \frac{5Q - J^2/M}{8M^3} Q_2^2 \left(\frac{r}{M} - 1\right), \\
 k_2 &= k_1 + \frac{J^2}{r^4} + \frac{5Q - J^2/M}{4M^2 r} \left(1 - \frac{2M}{r}\right)^{-1/2} Q_2^1 \left(\frac{r}{M} - 1\right),
 \end{aligned}$$

and

$$\begin{aligned}
 Q_2^1(x) &= (x^2 - 1)^{1/2} \left[ \frac{3x}{2} \ln \frac{x+1}{x-1} - \frac{3x^2 - 2}{x^2 - 1} \right], \\
 Q_2^2(x) &= (x^2 - 1) \left[ \frac{3}{2} \ln \frac{x+1}{x-1} - \frac{3x^3 - 5x}{(x^2 - 1)^2} \right],
 \end{aligned}$$

are the associated Legendre functions of the second kind, with  $x = r/M - 1$ , and  $P_2(\cos \theta) = (1/2)(3 \cos^2 \theta - 1)$  is the Legendre polynomial. The constants  $M, J$  and  $Q$  the total mass, angular momentum and mass quadrupole moment of the rotating object, respectively. This form of the metric corrects some misprints of the original paper by Hartle and Thorne (1968). The precise numerical values of  $M, J$  and  $Q$  are calculated from the matching procedure

of the exterior and interior metrics at the surface of the star.

The total mass of a rotating configuration is defined as  $M = M^{J \neq 0} = M^{J=0} + \delta M$ , where  $M^{J=0}$  is the mass of non-rotating configuration and  $\delta M$  is the change in mass of the rotating from the non-rotating configuration with the same central density. It should be stressed that in the terms involving  $J^2$  and  $Q$  the total mass  $M$  can be substituted by  $M^{J=0}$  since  $\delta M$  is already a second order term in the angular velocity.

The four-velocity  $u$  of a test particle on a circular orbit in equatorial plane of axisymmetric stationary spacetime can be parametrized by the constant angular velocity  $\Omega$  with respect to an observer at infinity

$$u = \Gamma[\partial_t + \Omega\partial_\phi], \quad (\text{B.2.14})$$

where  $\Gamma$  is a normalization factor which assures that  $u^\alpha u_\alpha = 1$ . From normalization and geodesics conditions we obtain the following expressions for  $\Gamma$  and  $\Omega = u^\phi/u^t$

$$\Gamma = \pm(g_{tt} + 2\Omega g_{t\phi} + \Omega^2 g_{\phi\phi})^{-1/2}, \quad (\text{B.2.15})$$

$$g_{tt,r} + 2\Omega g_{t\phi,r} + \Omega^2 g_{\phi\phi,r} = 0, \quad (\text{B.2.16})$$

hence,  $\Omega$ , the solution of (B.2.15), is given by

$$\Omega_{\pm orb}(r) = \frac{u^\phi}{u^t} = \frac{-g_{t\phi,r} \pm \sqrt{(g_{t\phi,r})^2 - g_{tt,r}g_{\phi\phi,r}}}{g_{\phi\phi,r}}, \quad (\text{B.2.17})$$

where  $(+/-)$  stands for co-rotating/counter-rotating orbits,  $u^\phi$  and  $u^t$  are the angular and time components of the four-velocity, and a colon stands for partial derivative with respect to the corresponding coordinate. In our case one needs to consider only co-rotating orbits (omitting the plus sign in  $\Omega_{+orb}(r) = \Omega_{orb}(r)$ ) to determine the mass shedding (Keplerian) angular velocity on the surface of the WD. For the Hartle-Thorne external solution Eq. (B.2.13) we have

$$\Omega_{orb}(r) = \sqrt{\frac{M}{r^3}} \left[ 1 - jF_1(r) + j^2F_2(r) + qF_3(r) \right], \quad (\text{B.2.18})$$

where  $j = J/M^2$  and  $q = Q/M^3$  are the dimensionless angular momentum

and quadrupole moment,

$$\begin{aligned}
 F_1 &= \left(\frac{M}{r}\right)^{3/2}, \\
 F_2 &= \frac{48M^7 - 80M^6r + 4M^5r^2 - 18M^4r^3 + 40M^3r^4 + 10M^2r^5 + 15Mr^6 - 15r^7}{16M^2r^4(r-2M)} + F, \\
 F_3 &= \frac{6M^4 - 8M^3r - 2M^2r^2 - 3Mr^3 + 3r^4}{16M^2r(r-2M)/5} - F, \\
 F &= \frac{15(r^3 - 2M^3)}{32M^3} \ln \frac{r}{r-2M}.
 \end{aligned}$$

The mass shedding limiting angular velocity of a rotating star is the Keplerian angular velocity evaluated at the equator ( $r = R_{eq}$ ), i.e.

$$\Omega_K^{J \neq 0} = \Omega_{orb}(r = R_{eq}). \quad (\text{B.2.19})$$

In the static case i.e. when  $j = 0$  hence  $q = 0$  and  $\delta M = 0$  we have the well-known Schwarzschild solution and the orbital angular velocity for a test particle  $\Omega_{ms}^{J=0}$  on the surface ( $r = R$ ) of the WD is given by

$$\Omega_K^{J=0} = \sqrt{\frac{MJ=0}{R_{MJ=0}^3}}. \quad (\text{B.2.20})$$

We turn now to the weak field limit. Let us estimate the values of  $j$  and  $q$  recovering physical units with  $c$  and  $G$ . The dimensionless angular momentum is

$$j = \frac{cJ}{GM^2} = \frac{c}{G} \frac{\alpha MR^2 \Omega}{M^2} = \alpha \left(\frac{\Omega R}{c}\right) \left(\frac{GM}{c^2 R}\right)^{-1}, \quad (\text{B.2.21})$$

where we have used the fact that  $J = I\Omega$ , with  $I = \alpha MR^2$ , and  $\alpha \sim 0.1$  from our numerical integrations. For massive and fast rotating WDs we have  $(\Omega R)/c \sim 10^{-2}$  and  $(GM)/(c^2 R) \sim 10^{-3}$ , so  $j \sim 1$ .

The dimensionless quadrupole moment  $q$  is

$$q = \frac{c^4}{G^2} \frac{Q}{M^3} = \frac{c^4}{G^2} \frac{\beta MR^2}{M^3} = \beta \left(\frac{GM}{c^2 R}\right)^{-2}, \quad (\text{B.2.22})$$

where we have expressed the mass quadrupole moment  $Q$  in terms of mass and radius of the WD,  $Q = \beta MR^2$ , where  $\beta \sim 10^{-2}$ , so we have  $q \sim 10^4$ .

The large values of  $j$  and  $q$  might arise some suspicion on the products  $jF_1$ ,  $j^2F_2$  and  $qF_3$  as real correction factors in Eq. (B.2.18). It is easy to check this in the weak field limit  $M/r \ll 1$ , where the functions  $F_i$  can be expanded as a

power-series

$$\begin{aligned}
 F_1 &= \left(\frac{M}{r}\right)^{3/2}, \\
 F_2 &\approx \frac{1}{2}\left(\frac{M}{r}\right)^3 - \frac{117}{28}\left(\frac{M}{r}\right)^4 - 6\left(\frac{M}{r}\right)^5 - \dots, \\
 F_3 &\approx \frac{3}{4}\left(\frac{M}{r}\right)^2 + \frac{5}{4}\left(\frac{M}{r}\right)^3 + \frac{75}{28}\left(\frac{M}{r}\right)^4 + 6\left(\frac{M}{r}\right)^5 + \dots
 \end{aligned}$$

so evaluating at  $r = R$

$$jF_1 = \alpha \left(\frac{\Omega R}{c}\right) \left(\frac{GM}{c^2 R}\right)^{1/2}, \quad j^2 F_2 = \frac{\alpha}{2} \left(\frac{\Omega R}{c}\right) \left(\frac{GM}{c^2 R}\right)^2, \quad (\text{B.2.23})$$

so we finally have  $jF_1 \sim 10^{-9/2}$ ,  $j^2 F_2 \sim 10^{-9}$ , and  $qF_3 \sim 10^{-2}$ . We can therefore see that the products are indeed correction factors and, in addition, that effect due to the quadrupole deformation is larger than the frame-dragging effect.

### Pycnonuclear fusion reaction rates

The theoretical framework for the determination of the pycnonuclear reaction rates was developed by Salpeter and van Horn (1969). The number of reactions per unit volume per unit time can be written as

$$R_{pyc} = Z^4 A \rho S(E_p) 3.90 \times 10^{46} \lambda^{7/4} \exp(-2.638/\sqrt{\lambda}) \text{ cm}^{-3} \text{ s}^{-1} \quad (\text{B.2.24})$$

$$\lambda = \frac{1}{Z^2 A^{4/3}} \left( \frac{\rho}{1.3574 \times 10^{11} \text{ g cm}^{-3}} \right)^{1/3}, \quad (\text{B.2.25})$$

where  $S$  are astrophysical factors in units of Mev barns ( $1 \text{ barn} = 10^{-24} \text{ cm}^2$ ) that have to be evaluated at the energy  $E_p$  given by Eq. (B.2.4).

For the  $S$ -factors we adopt the results of Gasques et al. (2005) calculated with the NL2 nuclear model parameterization. For center of mass energies  $E \geq 19.8 \text{ MeV}$ , the  $S$ -factors can be fitted by

$$S(E) = 5.15 \times 10^{16} \exp \left[ -0.428E - \frac{3E^{0.308}}{1 + e^{0.613(8-E)}} \right] \text{ MeV barn}, \quad (\text{B.2.26})$$

which is appropriate for the ranges of the zero-point energies at high densities. For instance,  $^{12}\text{C}$  nuclei at  $\rho = 10^{10} \text{ g cm}^{-3}$  have a zero-point oscillation energy  $E_p \sim 34 \text{ keV}$ .

All the nuclei  $(Z, A)$  at a given density  $\rho$  will fuse in a time  $\tau_{pyc}$  given by

$$\tau_{pyc} = \frac{n_N}{R_{pyc}} = \frac{\rho}{AM_u R_{pyc}}, \quad (\text{B.2.27})$$

where  $n_N = \rho/(AM_u)$  is the ion-density. Gasques et al. (2005) estimated that the  $S$ -factors (B.2.26) are uncertain within a factor  $\sim 3.5$ ; it is clear from the above equation that for a given lifetime  $\tau_{pyc}$  such uncertainties reflect also in the determination of the density threshold.

### Comparison with the Newtonian treatment and other works

We have constructed solutions of the Newtonian equilibrium equations for RWDs accurate up to order  $\Omega^2$ , following the procedure of Hartle (1967). In Fig. B.17 (left panel) we compare these Newtonian configurations with general relativistic RWDs for the Chandrasekhar EOS with  $\mu = 2$ . We can see clearly the differences between the two mass-density relations toward the high density region, as expected. A most remarkable difference is the existence of axisymmetric instability boundary in the general relativistic case, absent in its Newtonian counterpart.

Up to our knowledge, the only previous work on RWDs within GR is the one of Arutyunyan et al. (1971). A method to compute RWDs configurations accurate up to second order in  $\Omega$  was developed by two of the authors (see Sedrakyan and Chubaryan, 1968, for details), independently of the work of Hartle (1967). In (Arutyunyan et al., 1971), RWDs were computed for the Chandrasekhar EOS with  $\mu = 2$ .

In Fig. B.17 (right panel) we show the mass-central density relation obtained with their method with the ones constructed in this work for the same EOS. We note here that the results are different even at the level of static configurations, and since the methods are based on construction of rotating configurations from seed static ones, those differences extrapolate to the corresponding rotating objects. This fact is to be added to the possible additional difference arising from the different way of approaching the order  $\Omega^2$  in the approximation scheme. The differences between the two equilibrium configurations are evident.

Turning now to the problem of the maximum mass of a RWD, in Table B.9 we present the previous results obtained in Newtonian, Post-Newtonian approach and GR by several authors. Depending on their method, approach, treatment, theory and numerical code the authors showed different results. These maximum mass of RWDs are to be compared with the ones found in this work and presented in Table B.7 for the Chandrasekhar  $\mu = 2$ , Salpeter, and RFMT EOS.

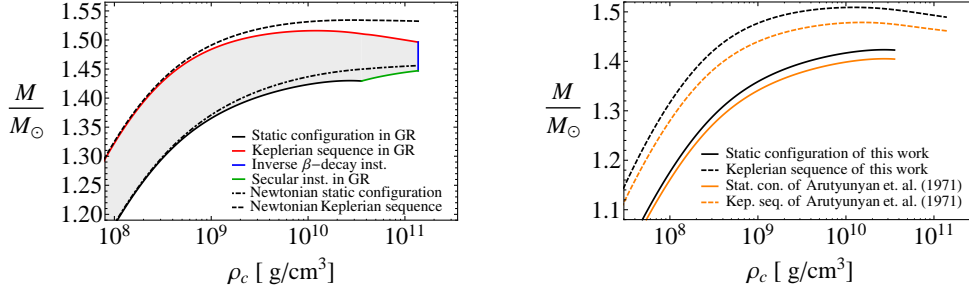


**Figure B.17.:** Left panel: Mass versus central density of Newtonian and general relativistic WDs for the Chandrasekhar EOS with  $\mu = 2$ . Both the non-rotating case and the Keplerian sequence are shown. We have stopped the density, just for sake of comparison, at the critical density for the onset of inverse  $\beta$ -decay of  ${}^4\text{He}$   $\rho = 1.39 \times 10^{11} \text{ g cm}^{-3}$ . Right panel: Mass versus central density relation for general relativistic WDs for the Chandrasekhar EOS with  $\mu = 2$  for the static and the Keplerian sequence in this work and the one of Arutyunyan et al. (1971).

Treatment/EOS	$M_{max}^{J \neq 0} / M_{\odot}$	References
Newtonian/Chandrasekhar $\mu = 2$	1.474	Anand (1965)
Newtonian/Polytrope $n = 3$	1.487	Roxburgh (1965)
Post-Newtonian/Chandrasekhar $\mu = 2$	1.482	Roxburgh and Durney (1966)
GR/Chandrasekhar $\mu = 2$	1.478	Arutyunyan et al. (1971)

**Table B.9.:** Maximum rotating mass of WDs in literature.

### Accuracy of the Hartle's approach

In his classic work, Hartle (1967) described the slow rotation regime by requesting that fractional changes in pressure, energy density, and gravitational field due to the rotation of the star are all much smaller with respect to a non-rotating star with the same central density. From a dimensional analysis, such a condition implies

$$\Omega^2 \ll \left(\frac{c}{R}\right)^2 \frac{GM^{J=0}}{c^2 R}, \quad (\text{B.2.28})$$

where  $M^{J=0}$  is the mass of the unperturbed configuration and  $R$  its radius. The expression on the right is the only multiplicative combination of  $M$ ,  $R$ ,  $G$ , and  $c$ , and in the Newtonian limit coincides with the critical Keplerian angular velocity  $\Omega_K^{J=0}$  given by Eq. (B.2.20). For unperturbed configurations with  $(GM)/(c^2 R) < 1$ , the condition (B.2.28) implies  $\Omega R/c \ll 1$ . Namely, every particle must move at non-relativistic velocities if the perturbation to the original geometry have to be small in terms of percentage. Eq. (B.2.28) can be also written as

$$\Omega \ll \Omega_K^{J=0}, \quad (\text{B.2.29})$$

which is the reason why it is often believed that the slow rotation approximation is not suitable for the description of stars rotating at their mass-shedding value.

Let us discuss this point more carefully. It is clear that the request that the contribution of rotation to pressure, energy density, and gravitational field to be small can be summarized in a single expression, Eq. (B.2.28), since all of them are quantitatively given by the ratio between the rotational and the gravitational energy of the star. The rotational energy is  $T \sim MR^2\Omega^2$  and the gravitational energy is  $|W| \sim GM^2/R = (GM/c^2 R)Mc^2$ , hence the condition  $T/|W| \ll 1$  leads to Eq. (B.2.28) or (B.2.29). Now we will discuss the above condition for realistic values of the rotational and gravitational energy of a rotating star, abandoning the assumption of either fiducial or order of magnitude calculations. We show below that the actual limiting angular velocity on the right-hand-side of the condition (B.2.29) has to be higher than the Keplerian value.

We can write the gravitational binding energy of the star as  $|W| = \gamma GM^2/R$  and the rotational kinetic energy as  $T = (1/2)I\Omega^2 = (1/2)\alpha MR^2\Omega^2$ , where the constants  $\gamma$  and  $\alpha$  are structure constants that depends on the density and pressure distribution inside the star. According to the slow rotation approximation,  $T/|W| \ll 1$ , namely

$$\frac{T}{|W|} = \frac{\alpha MR^2\Omega^2/2}{\gamma GM^2/R} = \left(\frac{\alpha}{2\gamma}\right) \left(\frac{GM}{R^3}\right)^{-1} \Omega^2 = \left(\frac{\alpha}{2\gamma}\right) \left(\frac{\Omega}{\Omega_K^{J=0}}\right)^2 \ll 1, \quad (\text{B.2.30})$$

which can be rewritten in analogous form to Eq. B.2.29 as

$$\Omega \ll \sqrt{\frac{2\gamma}{\alpha}} \Omega_K^{J=0}. \quad (\text{B.2.31})$$

Now we check that the ratio of the structural constants is larger than unity. Let us first consider the simplest example of a constant density sphere. In this case  $\alpha = 2/5$  and  $\gamma = 3/5$ , so  $\sqrt{2\gamma/\alpha} \approx 1.73$ , and the condition (B.2.31) is  $\Omega \ll 1.73\Omega_K^{J=0}$ . If we consider now a more realistic density profile, for instance, a polytrope of index  $n = 3$ , we have (see e.g. Shapiro and Teukolsky, 1983)

$$|W| = \frac{3}{5-n} \frac{GM^2}{R} = \frac{3}{2} \frac{GM^2}{R}, \quad T = \frac{1}{2} I \Omega^2 = \frac{1}{2} \frac{2}{3} M \langle r^2 \rangle \Omega^2 \quad (\text{B.2.32})$$

where  $\langle r^2 \rangle = 0.11303R^2$ . Therefore we have in this case  $\gamma = 3/2$  and  $\alpha = 0.075$ , and so Eq. (B.2.31) becomes  $\Omega \ll 6.32\Omega_K^{J=0}$ . This is not surprising since  $T/|W| \rightarrow 0.025$  when  $\Omega \rightarrow \Omega_K^{J=0}$ .

The above analysis has been done assuming spherical symmetry. When deviations from the spherical shape are taken into account, the ratio  $T/|W|$  turn to be even smaller than the previous estimates based on spherical polytropes. Since the equatorial radius satisfies  $R_{eq} > R$ , at mass-shedding we will have  $\Omega < \Omega_K^{J=0}$ . In fact, in the Roche model the mass-shedding angular velocity is  $\Omega_K^{J \neq 0} = (2/3)^{3/2} \Omega_K^{J=0} \approx 0.544\Omega_K^{J=0}$ , corresponding to a rotational to gravitational energy ratio  $T/|W| \approx 0.0074$  (see e.g. Shapiro and Teukolsky, 1983).

In our RWDs we have obtained that the mass-shedding angular velocity satisfies  $\Omega_K^{J \neq 0} \approx 0.75\Omega_K^{J=0}$  at any density; see Eq. (B.2.12). Accordingly to this, we show in the left panel of Fig. B.18 the ratio  $T/|W|$  for RWDs as a function of the central density for the Keplerian sequence. For an increasing central density  $T/|W|$  decreases. On the right panel we have plotted the eccentricity versus the central density. For increasing central density the eccentricity decreases, so RWDs become less oblate at higher densities.

Now we turn to evaluate more specifically the deviations from the spherical symmetry. The expansion of the radial coordinate of a rotating configuration  $r(R, \theta)$  in powers of the angular velocity is written as (Hartle, 1967)

$$r = R + \zeta(R, \theta) + O(\Omega^4), \quad (\text{B.2.33})$$

where  $\zeta$  is the difference in the radial coordinate,  $r$ , between a point located at the polar angle  $\theta$  on the surface of constant density  $\rho(R)$  in the rotating configuration, and the point located at the same polar angle on the same constant density surface in the non-rotating configuration. In the slow ro-

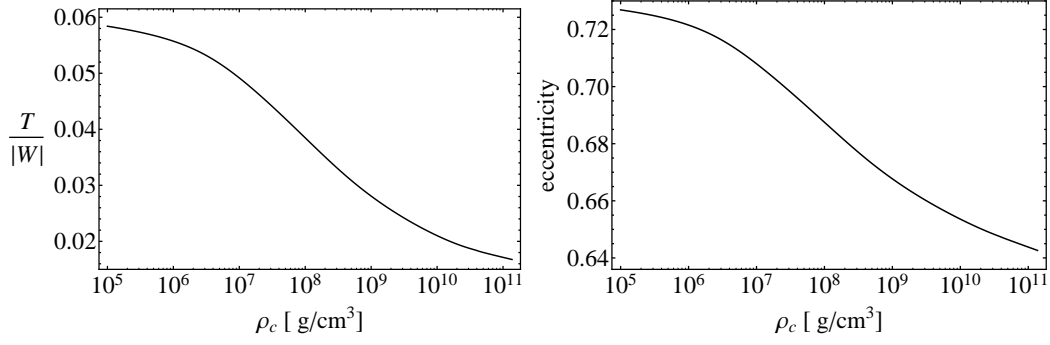


**Figure B.18.:** Left panel: rotational to gravitational energy ratio versus the central density for maximally rotating RWDs, calculated with the Chandrasekhar EOS  $\mu = 2$ . Right panel: the eccentricity versus the central density for the same sequence of RWDs.

tation regime, the fractional displacement of the surfaces of constant density due to the rotation have to be small, namely  $\xi(R, \theta)/R \ll 1$ , where  $\xi(R, \theta) = \xi_0(R) + \xi_2(R)P_2(\cos \theta)$  and  $\xi_0(R)$  and  $\xi_2(R)$  are function of  $R$  proportional to  $\Omega^2$ . On the right panel of Fig. B.19 the difference in the radial coordinate over static radius versus the central density is shown. Here we see the same tendency as in the case of the eccentricity, that these differences are decreasing with an increasing central density. On the left panel the rotation parameter  $\Omega R/c$  versus the central density is shown. Here, with an increasing central density the rotation parameter increases. Thus, for higher densities the system becomes less oblate, smaller in size with a larger rotation parameter i.e. higher angular velocity.

In order to estimate the accuracy of the slow rotation approximation for RWDs, based on the above results, it is useful to compare all the above numbers with the known results for NSs. For instance, we notice that in NSs  $\Omega R/c \sim 10^{-1}$ ,  $\xi(R, 0)/R \sim 10^{-2}$  and  $\xi(R, \pi/2)/R \sim 10^{-1}$  (see e.g. Berti et al., 2005), to be compared with the corresponding values of RWDs shown in Fig. B.19,  $\Omega R/c \lesssim 10^{-2}$ ,  $\xi(R, 0)/R \sim 10^{-2}$  and  $\xi(R, \pi/2)/R \sim 10^{-1}$ . Weber and Glendenning (1992) calculate the accuracy of the Hartle's second order approximation and found that the mass of maximally rotating NSs is accurate within an error  $\lesssim 4\%$ ; Benhar et al. (2005) found that the inclusion of third order expansion  $\Omega^3$  improved the mass-shedding limit numerical values in less than 1% for NSs obeying different EOS. On the other-hand, it is known that the ratio  $T/|W|$  in the case of NSs is as large as  $\sim 0.1$  in the Keplerian sequence (see e.g. Tables 1–5 of Berti and Stergioulas (2004)). Since RWDs have  $T/|W|$  and  $\Omega R/c$  smaller than NSs, and  $\delta R/R = \xi/R$  at least of the same order (see left panel of Fig. B.18), we expect that the description of the structure of RWDs up to the mass-shedding limit within the Hartle's approach to have at least the same accuracy as in the case of NSs.

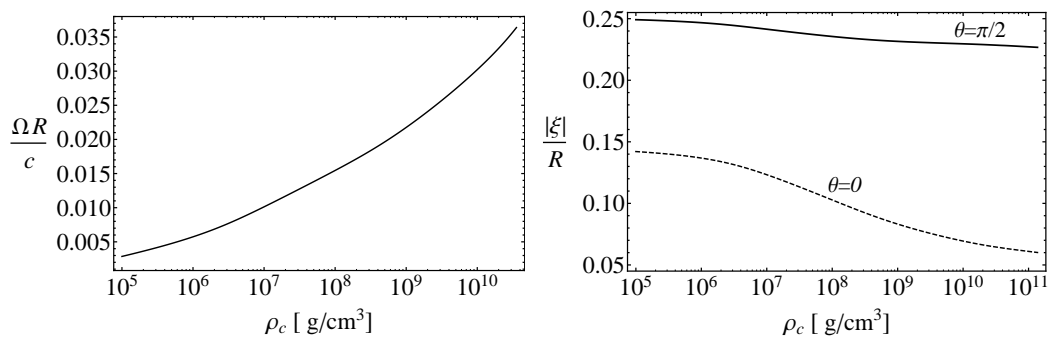


**Figure B.19.:** Left panel: the rotation parameter normalized to the speed of light versus the central density. Right panel: the difference in the radial coordinate over the static radius versus the central density. The solid curve corresponds to the difference between equatorial ( $\theta = \pi/2$ ) and static radii and the dashed curve corresponds to the difference between polar ( $\theta = 0$ ) and static radii.

## B.3. SGRs and AXPs as rotation powered massive white dwarfs

### B.3.1. Introduction

Soft Gamma Ray Repeaters (SGRs) and Anomalous X-ray Pulsars (AXPs) are a class of compact objects that show interesting observational properties (see e.g. Mereghetti, 2008): rotational periods in the range  $P \sim (2\text{--}12)$  s, a narrow range with respect to the wide range of ordinary pulsars  $P \sim (0.001\text{--}10)$  s; spin-down rates  $\dot{P} \sim (10^{-13}\text{--}10^{-10})$ , larger than ordinary pulsars  $\dot{P} \sim 10^{-15}$ ; strong outburst of energies  $\sim (10^{41}\text{--}10^{43})$  erg, and for the case of SGRs, giant flares of even large energies  $\sim (10^{44}\text{--}10^{47})$  erg, not observed in ordinary pulsars.

The recent observation of SGR 0418+5729 with a rotational period of  $P = 9.08$  s, an upper limit of the first time derivative of the rotational period  $\dot{P} < 6.0 \times 10^{-15}$  (Rea et al., 2010), and an X-ray luminosity of  $L_X = 6.2 \times 10^{31}$  erg/s promises to be an authentic Rosetta Stone, a powerful discriminant for alternative models of SGRs and AXPs.

If described as a neutron star of  $M = 1.4M_\odot$ ,  $R = 10$  km and a moment of inertia  $I \approx 10^{45}$  g cm<sup>2</sup>, which we adopt hereafter as fiducial parameters, the loss of rotational energy of the neutron star

$$\dot{E}_{\text{rot}}^{\text{NS}} = -4\pi^2 I \frac{\dot{P}}{P^3} = -3.95 \times 10^{46} \frac{\dot{P}}{P^3} \text{ erg/s}, \quad (\text{B.3.1})$$

associated to its spin-down rate  $\dot{P}$ , cannot explain the X-ray luminosity of SGR 0418+5729, i.e.  $\dot{E}_{\text{rot}}^{\text{NS}} < L_X$ , excluding the possibility of identifying this source as an ordinary spin-down powered pulsar.

The magnetar model of SGRs and AXPs, based on a neutron star of fiducial parameters, needs a magnetic field larger than the critical field for vacuum polarization  $B_c = m_e^2 c^3 / (e\hbar) = 4.4 \times 10^{13}$  G in order to explain the observed X-ray luminosity in terms of the release of magnetic energy (see Duncan and Thompson, 1992; Thompson and Duncan, 1995, for details). However, the inferred upper limit of the surface magnetic field of SGR 0418+5729  $B < 7.5 \times 10^{12}$  G describing it as a neutron star (see Rea et al., 2010, for details), is well below the critical field challenging the power mechanism based on magnetic field decay purported in the magnetar scenario.

We show that the observed upper limit on the spin-down rate of SGR 0418+5729 is, instead, perfectly in line with a model based on a massive fast rotating highly magnetized white dwarf (see e.g. Paczynski, 1990) of mass  $M = 1.4M_\odot$ , radius  $R = 10^3$  km, and moment of inertia  $I \approx 10^{49}$  g cm<sup>2</sup>, which we adopt hereafter as fiducial white dwarf parameters. Such a configuration leads for SGR 0418+5729 to a magnetic field  $B < 7.5 \times 10^8$  G. The X-ray luminosity can then be expressed as originating from the loss of rota-

tional energy of the white dwarf leading to a theoretical prediction for the first time derivative of the rotational period

$$\frac{L_X P^3}{4\pi^2 I} \leq \dot{P}_{\text{SGR0418+5729}} < 6.0 \times 10^{-15}, \quad (\text{B.3.2})$$

where the lower limit is established by assuming that the observed X-ray luminosity of SGR 0418+5729 coincides with the rotational energy loss of the white dwarf. For this specific source, the lower limit of  $\dot{P}$  given by Eq. (B.3.2) is  $\dot{P}_{\text{SGR0418+5729}} \geq 1.18 \times 10^{-16}$ . This prediction is left to be verified by the dedicated scientific missions.

The assumption of massive fast rotating highly magnetized white dwarfs appears to be very appropriate since their observation has been solidly confirmed in the last years thanks to observational campaigns carried out by the X-ray Japanese satellite Suzaku (see e.g. Terada et al., 2008c; Terada, 2008; Terada et al., 2008d,b,a). The magnetic fields observed in white dwarfs are larger than  $10^6$  G all the way up to  $10^9$  G (see e.g. Angel et al., 1981; Ferrario et al., 1997; Nalezyty and Madej, 2004; Ferrario and Wickramasinghe, 2005; Terada et al., 2008c; Külebi et al., 2009). These observed massive fast rotating highly magnetized white dwarfs share common properties with SGRs/AXPs. The specific comparison between SGR 0418+5729 and the white dwarf AE Aquarii (Terada et al., 2008c) is given in Sec. B.3.4.

The aim of this article is to investigate the implications of the above considerations to all observed SGRs and AXPs. The article is organized as follows. In Sec. B.3.2 we summarize the main features of a model for SGRs and AXPs based on rotation powered white dwarfs while, in Sec. B.3.3, we recall the magnetar model. In Sec. B.3.4 we present the observations of massive fast rotating highly magnetized white dwarfs. The constraints on the rotation rate imposed by the rotational instabilities of fast rotating white dwarfs are discussed in Sec. B.3.5 and in Sec. B.3.6 we analyze the glitch-outburst connection in SGRs and AXPs. The magnetospheric emission from the white dwarf is discussed in Sec. B.3.7 and the possible connection between SGRs and AXPs with supernova remnants is presented in Sec. B.3.8. In Sec. B.3.9 we address the problem of fiducial parameters of both white dwarfs and neutron stars and, in Sec. B.3.10, we summarize conclusions and remarks.

### B.3.2. SGRs and AXPs within the white dwarf model

We first recall the pioneering works of Morini et al. (1988) and Paczynski (1990) on 1E 2259+586. This source is pulsating in the X-rays with a period  $P = 6.98$  s (Fahlman and Gregory, 1981), a spin-down rate of  $\dot{P} = 4.8 \times 10^{-13}$  (Davies et al., 1990) and X-ray luminosity  $L_X = 1.8 \times 10^{34}$  erg/s (Gregory and Fahlman, 1980; Hughes et al., 1981; Morini et al., 1988). Specially relevant in the case of 1E 2259+586 is also its position within the supernova remnant

G109.1-1.0 with age estimated  $t - t_0 = (12-17)$  kyr (Gregory and Fahlman, 1980; Hughes et al., 1981).

Paczynski developed for 1E 2259+586 a model based on a massive fast rotating highly magnetized white dwarf. The upper limit on the magnetic field (see e.g. Ferrari and Ruffini, 1969) obtained by requesting that the rotational energy loss due to the dipole field be smaller than the electromagnetic emission of the dipole, is given by

$$B = \left( \frac{3c^3}{8\pi^2} \frac{I}{R^6} P\dot{P} \right)^{1/2}, \quad (\text{B.3.3})$$

where  $P$  and  $\dot{P}$  are observed properties and the moment of inertia  $I$  and the radius  $R$  of the object are model dependent properties. For the aforementioned fiducial parameters of a fast rotating magnetized white dwarf, Eq. (B.3.3) becomes

$$B = 3.2 \times 10^{15} (P\dot{P})^{1/2} \text{ G}. \quad (\text{B.3.4})$$

The loss of rotational energy within this model is given by

$$\dot{E}_{\text{rot}}^{\text{WD}} = -4\pi^2 I \frac{\dot{P}}{P^3} = -3.95 \times 10^{50} \frac{\dot{P}}{P^3} \text{ erg/s}, \quad (\text{B.3.5})$$

which amply justifies the steady X-ray emission of 1E 2259+586 (see Table B.12).

A further development for the source 1E 2259+586, came from Usov (1994), who introduced the possibility in a white dwarf close to the critical mass limit, to observe sudden changes in the period of rotation, namely glitches.

When the rotation of the white dwarf slows down, centrifugal forces of the core decrease and gravity pulls it to a less oblate shape thereby stressing it. The release of such stresses leads to a sudden decrease of moment of inertia and correspondingly, by conservation of angular momentum

$$J = I\Omega = (I + \Delta I)(\Omega + \Delta\Omega) = \text{constant}, \quad (\text{B.3.6})$$

to a shortening of the rotational period

$$\frac{\Delta I}{I} = \frac{\Delta P}{P} = -\frac{\Delta\Omega}{\Omega}, \quad (\text{B.3.7})$$

leading to a gain of rotational energy in the spin-up process of the glitch

$$\Delta E_{\text{rot}}^{\text{WD}} = -\frac{2\pi^2 I}{P^2} \frac{\Delta P}{P} = -1.98 \times 10^{50} \frac{\Delta P}{P^3} \text{ erg}, \quad (\text{B.3.8})$$

which is then released in the burst activity on the time scales from months to years (see e.g. Fig. B.20).

For the evolution of the period close to a glitch we follow the parameterization by Manchester and Taylor (1977). The angular velocity  $\Omega = 2\pi/P$ , since the glitch time  $t = t_g$ , until the complete or partial recovery, can be described as

$$\Omega = \Omega_0(t) + \Delta\Omega[1 - Q(1 - e^{-(t-t_g)/\tau_d})], \quad (\text{B.3.9})$$

where  $\Omega_0(t) = \Omega_0 + \dot{\Omega}(t - t_g)$  is the normal evolution of the frequency in absence of glitch, being  $\Omega_0$  the frequency prior to the glitch,  $\Delta\Omega = -2\pi\Delta P/P^2$  is the initial frequency jump, which can be decomposed in the persistent and decayed parts,  $\Delta\Omega_p$  and  $\Delta\Omega_d$  respectively,  $\tau_d$  is the timescale of the exponential decay of the frequency after the glitch and  $Q = \Delta\Omega_d/\Delta\Omega = 1 - \Delta\Omega_p/\Delta\Omega$  is the recovery fraction or ‘‘healing parameter’’. For full recovery we have  $Q = 1$ ,  $\Omega(t \gg \tau_d) = \Omega_0$ , and for zero recovery  $Q = 0$ ,  $\Omega(t \gg \tau_d) = \Omega_0(t) + \Delta\Omega$ . For simplicity we assume in the following and especially below in Sec. B.3.6, complete recovery  $Q = 1$ .

This mechanism in white dwarfs is similar, although simpler, than the one used to explain e.g. glitches in ordinary pulsars (see e.g. Baym and Pines, 1971; Shapiro and Teukolsky, 1983). The essential difference is that neutron stars are composed by a superfluid core and a solid crust, being the latter the place where starquakes can originate leading to glitches. A two-component description is then needed, see e.g. Shapiro and Teukolsky (1983). In the present case of a massive rotating white dwarf, such a two-component structure does not exist and the white dwarf behaves as a single solid system. What is important to stress is that the rotational energy released for  $Q \geq 1$  is largely sufficient for the explanation of the bursting phenomena, see Sec. B.3.6 for details.

The crystallization temperature of a white dwarf composed of nuclei ( $Z, A$ ) and mean density  $\bar{\rho}$  is given by (see e.g. Shapiro and Teukolsky, 1983; Usov, 1994)

$$T_{\text{cry}} \simeq 2.28 \times 10^5 \frac{Z^2}{A^{1/3}} \left( \frac{\bar{\rho}}{10^6 \text{g/cm}^3} \right)^{1/3} \text{ K}. \quad (\text{B.3.10})$$

Thus, assuming an internal white dwarf temperature  $\sim 10^7$  K we find that the mean density for the crystallization of the white dwarf should be  $\sim 2.2 \times 10^7 \text{ g/cm}^3$  for  $^{12}\text{C}$ ,  $\sim 5.2 \times 10^6 \text{ g/cm}^3$  for  $^{16}\text{O}$  and  $\sim 1.25 \times 10^6 \text{ g/cm}^3$  for  $^{56}\text{Fe}$ . Very massive white dwarfs as the ones we are considering here have mean densities  $\sim 10^9 \text{ g/cm}^3$  and therefore a considerable fraction of their size should be in principle solid at these high temperatures (see also Althaus et al., 2005, 2007). It is worth to mention that, the phase separation of the constituents of CO white dwarfs, theoretically expected to occur in the crystallization process (see Garcia-Berro et al., 1988, for details), has been recently observationally confirmed solving the puzzle of the age discrepancy of the open cluster NGC 6791 (García-Berro et al., 2010a).

Under these physical conditions, starquakes leading to glitches in the white

dwarf may occur with a recurrence time (see e.g. Baym and Pines, 1971; Usov, 1994)

$$\delta t_q = \frac{2D^2}{B} \frac{|\Delta P|/P}{|\dot{E}_{\text{rot}}|}, \quad (\text{B.3.11})$$

where  $\dot{E}_{\text{rot}}$  is the loss of rotational energy (B.3.5),  $D = (3/25) GM_c^2/R_c$ ,  $B = 0.33 (4\pi/3) R_c^3 e^2 Z^2 [\bar{\rho}_c / (Am_p)]^{4/3}$ ,  $M_c$ ,  $R_c$  and  $\bar{\rho}_c$  are the mass, the radius and the mean density of the solid core, and  $m_p$  is the proton mass.

For the specific case of 1E 2259+586, Usov predicted the possible existence of changes of period  $\Delta P/P \approx -(1-3) \times 10^{-6}$  with a recurrence time between cracks  $\delta t_q \approx 7 \times 10^6 |\Delta P|/P \text{ yr} \approx$  a few times (1–10) yr. It is impressive that in 2002 indeed changes of the order of  $\Delta P/P \approx -4 \times 10^{-6}$  were observed in 1E 2259+586 (Kaspi et al., 2003; Woods et al., 2004) (see Fig. B.20 for details).

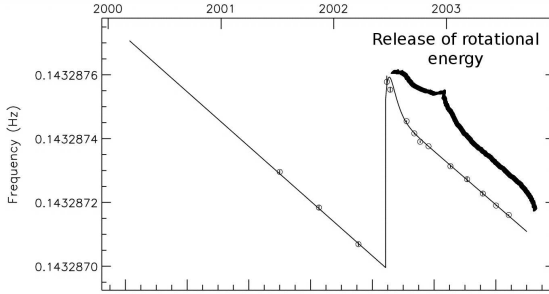


**Figure B.20.:** Timing analysis of the glitch of 1E 2259+586 on June 2002 (taken from Woods et al., 2004). The vertical axis shows the evolution of the spin frequency and the horizontal axis the date time. The observed fractional change of period is  $\Delta P/P = -\Delta\Omega/\Omega \sim -4 \times 10^{-6}$  and the observed energy released during the event is  $\sim 3 \times 10^{41}$  erg (Woods et al., 2004). Within the white dwarf model from such a  $\Delta P/P$  we obtain  $\Delta E_{\text{rot}}^{\text{WD}} \sim 1.7 \times 10^{43}$  erg as given by Eq. (B.3.8). We have modified the original figure (Woods et al., 2004) by indicating explicitly where the rotational energy is released after the spin-up, recovering its initial period prior to the glitch by the emission of a sequence of bursts on time scales from months to years (see e.g. Mereghetti, 2008).

Our aim in the following is to show that this model can be also applied to the other SGRs and AXPs. Their entire energetics is explained by the rotational energy loss of fast rotating magnetized white dwarfs: 1) the X-ray luminosity is well below the rotational energy loss of the white dwarf (see Fig. B.21); 2) in all cases the large magnetic field is well below the critical field for vacuum polarization (see Fig. B.22 and Table B.12); 3) the energetics of all

the bursts can be simply related to the change of rotational energy implied by the observed change of rotational period (see Fig. B.23, Sec. B.3.5 and Table B.11).

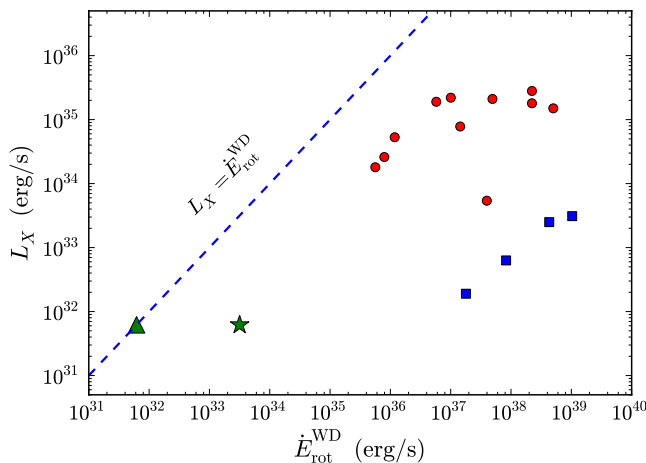


**Figure B.21.** X-ray luminosity  $L_X$  versus the loss of rotational energy  $\dot{E}_{rot}$  describing SGRs and AXPs by rotation powered white dwarfs. The green star and the green triangle correspond to SGR 0418+5729 using respectively the upper and the lower limit of  $\dot{P}$  given by Eq. (B.3.2). The blue squares are the only four sources that satisfy  $L_X < \dot{E}_{rot}$  when described as neutron stars (see Fig. B.25 for details).

### B.3.3. SGRs and AXPs within the magnetar model

Let us turn to the alternative model commonly addressed as “magnetar” (see e.g. Duncan and Thompson, 1992; Thompson and Duncan, 1995) based on an ultramagnetized neutron star of  $M = 1.4M_{\odot}$  and  $R = 10$  km and then  $I \approx 10^{45}$  g cm<sup>2</sup> as the source of SGRs and AXPs. The limit of the magnetic field obtained from Eq. (B.3.3) becomes

$$B = 3.2 \times 10^{19} (P\dot{P})^{1/2} \text{ G}, \quad (\text{B.3.12})$$

which is four orders of magnitude larger than the surface magnetic field within the fast rotating magnetized white dwarf model (see Fig. B.24).

There are innumerable papers dedicated to this model and for a review covering more than 250 references on the subject see Mereghetti (2008). The crucial point is that in this model there is no role of the rotational energy of the source: the X-ray luminosity is much bigger than the loss of rotational energy of the neutron star (see Fig. B.25).

Paradoxically, although the bursts appear to be correlated to the presence of glitches in the rotational period, the corresponding increase of change of

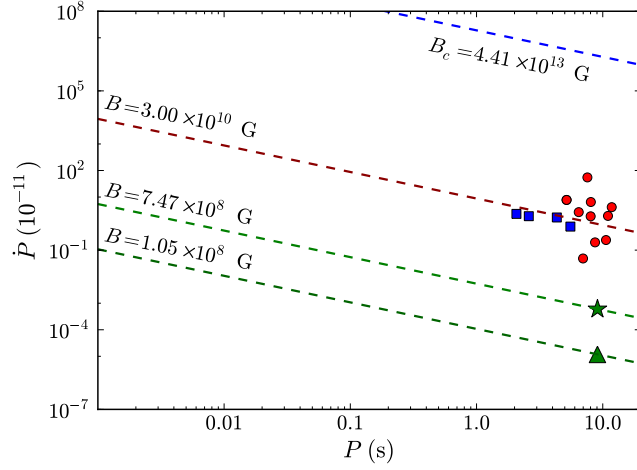


**Figure B.22.:**  $\dot{P}$ - $P$  diagram for all known SGRs and AXPs. The curves of constant magnetic field for white dwarfs given by Eq. (B.3.4) are shown. The blue dashed line corresponds to the critical magnetic field  $B_c = m_e^2 c^3 / (e\hbar)$ . The green star and the green triangle correspond to SGR 0418+5729 using respectively the upper and the lower limit of  $\dot{P}$  given by Eq. (B.3.2). The blue squares are the only four sources that satisfy  $L_X < \dot{E}_{\text{rot}}$  when described as rotation powered neutron stars (see Fig. B.25 for details).

rotational energy of the neutron star

$$\Delta E_{\text{rot}}^{\text{NS}} = -\frac{2\pi^2 I \Delta P}{p^2} \frac{\Delta P}{P} = -1.98 \times 10^{46} \frac{\Delta P}{P^3} \text{ erg}, \quad (\text{B.3.13})$$

cannot explain the burst energetic  $\sim (10^{44}-10^{47})$  erg. This is a clear major difference between the two models based respectively on neutron stars and white dwarfs (see Figs. B.23 and B.26 for details).

In magnetars, the value of the rotational period and its first time derivative are only used to establish an upper limit to the magnetic field of the neutron star. In view of the smallness of the moment of inertia of a neutron star with respect to the moment of inertia of a white dwarf, the magnetic field reaches in many cases outstandingly large values  $B \gg B_c \sim 4.4 \times 10^{13}$  G, from here the name magnetars (see Fig. B.24). The attempt has been proposed by Duncan and Thompson (1992) and Thompson and Duncan (1995) to assume a new energy source in physics and astrophysics: the magnetic energy in bulk. The role of thermonuclear energy has been well established by physics experiments on the ground as well as in astrophysics in the explanation of the energetics, life time, and build-up process of the nuclear elements in main sequence stars (see e.g. Bethe, 1968, and references therein); equally well established has been the role of rotational energy in pulsars (see e.g. Hewish, 1974; Bell and Hewish, 1967, and references therein); similarly well

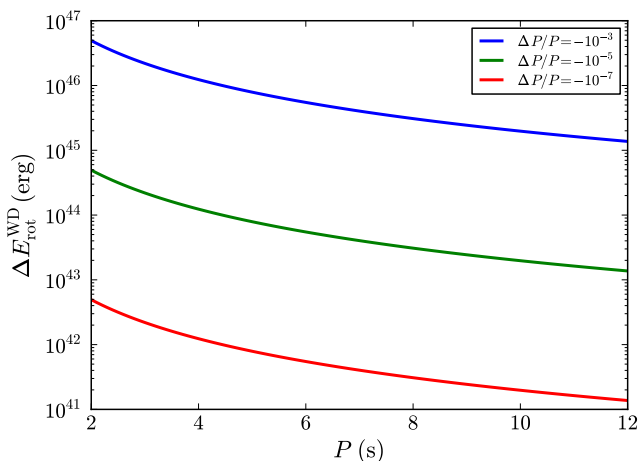


**Figure B.23.:** Change in the rotational energy of the white dwarf  $\Delta E_{\text{rot}}^{\text{WD}}$  given by Eq. (B.3.8) as a function of the rotational period  $P$  in seconds for selected fractional changes of period  $\Delta P/P$ .

established has been the role of gravitational energy in accretion process into neutron stars and black holes and binary X-ray sources (see e.g. Giacconi, 2002; Giacconi and Ruffini, 1978 Reprinted 2010, and references therein). In the magnetars instead, it is introduced an alternative primary energy source not yet tested neither in the laboratory (the case of magnetic monopoles) nor in astrophysics: a primary energy source due to overcritical magnetic fields.

The mostly qualitative considerations in the magnetar model can be summarized, see e.g. Ng et al. (2010): in the twisted magnetosphere model of magnetars (Thompson et al., 2002), the observed X-ray luminosity of a magnetar is determined both by its surface temperature and by magnetospheric currents, the latter due to the twisted dipolar field structure. The surface temperature in turn is determined by the energy output from within the star due to magnetic field decay, as well as on the nature of the atmosphere and the stellar magnetic field strength. This surface thermal emission is resonantly scattered by the current particles, thus resulting in an overall spectrum similar to a Comptonized blackbody (e.g. Lyutikov and Gavriil, 2006; Rea et al., 2008; Zane et al., 2009). In addition, the surface heating by return currents is believed to contribute substantially to  $L_X$ , at least at the same level as the thermal component induced from the interior field decay (Thompson et al., 2002). Magnetar outbursts in this picture occur with sudden increases in twist angle, consistent with the generic hardening of magnetar spectra during outbursts (e.g. Kaspi et al., 2003; Woods et al., 2004; Israel et al., 2007).

It is worth to recall that magnetic field configurations corresponding to a dipole twisted field have been routinely adopted in rotating neutron stars (see e.g. Cohen et al., 1973). Magnetic field annihilation and reconnection have been analogously adopted in solar physics (see e.g. Parker, 1957; Sweet,

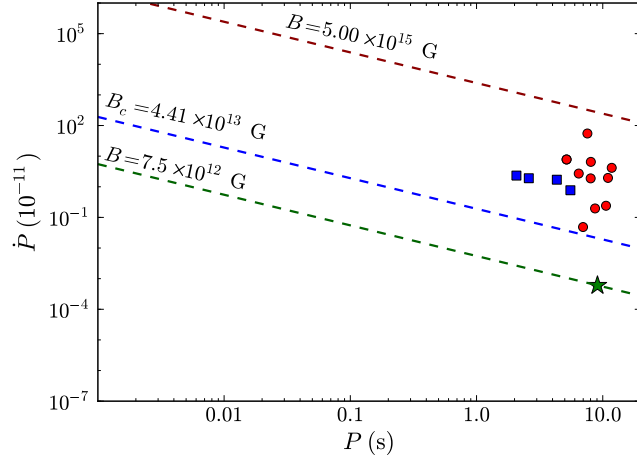


**Figure B.24.:**  $\dot{P}$ - $P$  diagram for all known SGRs and AXPs. The curves of constant magnetic field for neutron stars given by Eq. (B.3.12) are shown. The blue dashed line corresponds to the critical magnetic field  $B_c = m_e^2 c^3 / (e\hbar)$ . The green star corresponds to SGR 0418+5729 using the upper limit of  $\dot{P}$  given by Eq. (B.3.2). The blue squares are the only four sources that satisfy  $L_X < \dot{E}_{\text{rot}}$  when described as rotation powered neutron stars (see Fig. B.25 for details).

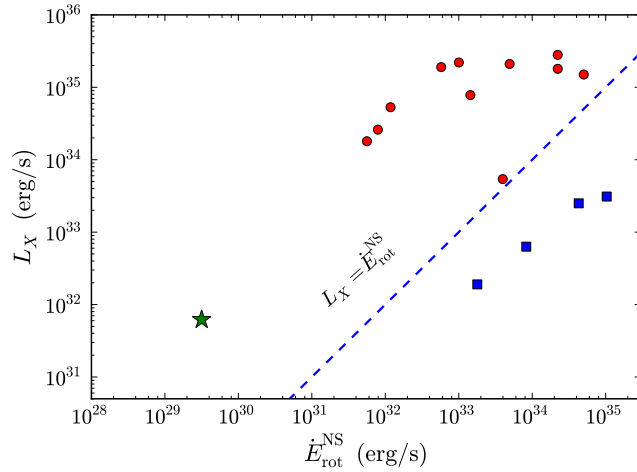


**Figure B.25.:** X-ray luminosity  $L_X$  versus the loss of rotational energy  $\dot{E}_{\text{rot}}$  describing SGRs and AXPs as neutron stars. The green star corresponds to SGR 0418+5729 using the upper limit of  $\dot{P}$  given by Eq. (B.3.2). The blue squares are the only four sources with  $L_X < \dot{E}_{\text{rot}}$ : 1E 1547.0-5408 with  $P = 2.07$  s and  $\dot{P} = 2.3 \times 10^{-11}$ ; SGR 1627-41 with  $P = 2.59$  s and  $\dot{P} = 1.9 \times 10^{-11}$ ; PSR J 1622-4950 with  $P = 4.33$  s and  $\dot{P} = 1.7 \times 10^{-11}$ ; and XTE J1810-197 with  $P = 5.54$  s and  $\dot{P} = 7.7 \times 10^{-12}$ .

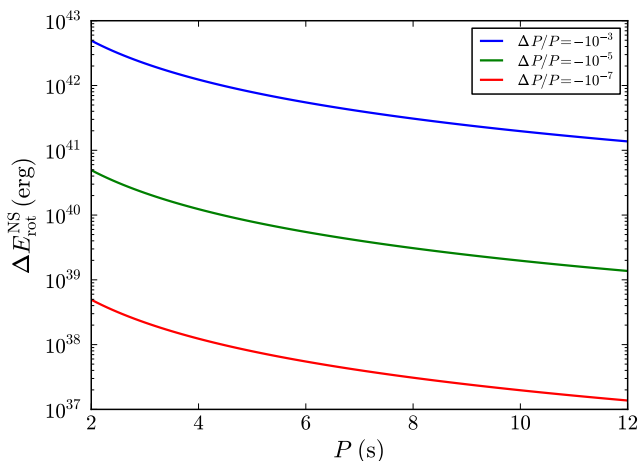


**Figure B.26.:** Change in the rotational energy of the neutron star  $\Delta E_{\text{rot}}^{\text{NS}}$  given by Eq. (B.3.13) as a function of the rotational period  $P$  in seconds for selected fractional changes of period  $\Delta P/P$ .

1958) and also magnetic instabilities have been routinely studied in Tokamak (see e.g. Coppi et al., 1976). These effects certainly occur in magnetized white dwarfs. What is important to stress here is that in none of these systems the magnetic field has been assumed to be the primary energy source of the phenomena, unlike in magnetars.

It is appropriate to recall just a few of the difficulties of the magnetar model in fitting observations, in addition to the main one of SGR 0418+5729 addressed in this article. In particular, e.g.: (1) as recalled by S. Mereghetti 2008, “up to now, attempts to estimate the magnetic field strength through the measurement of cyclotron resonance features, as successfully done for accreting pulsars, have been inconclusive”; (2) the prediction of the high-energy gamma ray emission expected in the magnetars has been found to be inconsistent with the recent observation of the Fermi satellite (see e.g. Tong et al., 2010, 2011); (3) finally, it has been shown to be not viable the attempt to relate magnetars to the energy of the supernova remnants (see e.g. Allen and Horvath, 2004; Ferrario and Wickramasinghe, 2006; Vink and Kuiper, 2006; Vink, 2008) or to the formation of black holes (see e.g. Kasen and Bildsten (2010); Woosley (2010), see however e.g. Patnaude et al. (2009)) and of Gamma Ray Bursts (see e.g. Levan et al. (2006); Castro-Tirado et al. (2008); Stefanescu et al. (2008); Bernardini et al. (2009), see however e.g. Goldstein et al. (2011); Rea et al. (2011)).

In Table B.12 we compare and contrast the parameters of selected SGRs and AXPs sources in the magnetar model and in the fast rotating highly magnetized white dwarf model: the larger radius of a white dwarf with respect to the radius of a neutron star of the same mass  $M = 1.4M_{\odot}$ , leads to the two models differing on the scale of mass density, moment of inertia, and ro-

tational energy which imply a different scale for the surface magnetic fields, leading to a very different physical interpretation of the observations of SGRs and AXPs.

### B.3.4. Observations of massive fast rotating highly magnetized white dwarfs

Some general considerations are appropriate. The white dwarf model appeals to standard and well tested aspects of physics and astrophysics. The observation of fast rotating white dwarfs with magnetic fields larger than  $10^6$  G all the way up to  $10^9$  G has been in the mean time solidly confirmed by observations (see e.g. Angel et al., 1981; Ferrario et al., 1997; Należyty and Madej, 2004; Ferrario and Wickramasinghe, 2005; Terada et al., 2008c). For a recent and extensive analysis of the magnetic field structure of highly magnetized white dwarfs see Külebi et al. (2009) and for a catalog of them see Külebi et al. (2010a) and also Kepler et al. (2010).

A specific example is the highly magnetized white dwarf AE Aquarii. The rotational period of this fast rotating magnetized white dwarf obtained from the sinusoidal pulsed flux in soft X-rays  $< 4$  keV (see e.g. Eracleous et al., 1991; Choi and Dotani, 2006) has been established to be  $P = 33$  s and it is spinning down at a rate  $\dot{P} = 5.64 \times 10^{-14}$ . The mass of the white dwarf is  $\sim M_{\odot}$  (de Jager et al., 1994) and the observed temperature is  $kT \sim 0.5$  keV. In addition to the soft X-ray component, hard X-ray pulsations were observed with the Japanese satellite Suzaku in October-November 2005 and October 2006. The luminosity of AE Aquarii  $\sim 10^{31}$  erg/s accounts for the 0.09% of the spin-down energy of the white dwarf (see Terada et al., 2008c, for details) and the inferred magnetic field of the source is  $B \sim 10^8$  G (Ikhsanov and Beskrovnaya, 2008).

This white dwarf is one of the most powerful particle accelerators: there is at least one event of detected TeV emission from this source during its optical flaring activity monitored between 1988 and 1992 (see e.g. Meintjes et al., 1992, 1993; de Jager et al., 1994; Ikhsanov and Biermann, 2006; Ikhsanov and Beskrovnaya, 2008; Kashiyama et al., 2011). In addition, it shows burst activity in X-rays (Terada et al., 2008c). Although AE Aquarii is a binary system with orbital period  $\sim 9.88$  hr (see de Jager et al., 1994, e.g.), very likely the power due to accretion of matter is inhibited by the fast rotation of the white dwarf (e.g. Itoh et al., 2006; Terada et al., 2008c).

Many of the observed physical properties of this white dwarf are very similar to the recently discovered SGR 0418+5729, as we explicitly show in Table B.10.

Although very fast, AE Aquarii is not the fastest white dwarf observed. The rotational period obtained from the pulsed X-ray emission of RXJ 0648.0-4418, the white dwarf in the binary system HD49798/RXJ 0648.0-4418, is  $P =$

	SGR 0418+5729	AE Aquarii
$P$ (s)	9.08	33.08
$\dot{P}$ ( $10^{-14}$ )	$< 0.6$	5.64
Age (Myr)	24	9.4
$L_X$ (erg/s)	$6.2 \times 10^{31}$	$\sim 10^{31}$
$kT$ (keV)	0.67	0.5
$B$ (G)	$< 7.45 \times 10^8$	$\sim 10^8$
Pulsed Fraction	0.3	$\sim 0.2-0.3$

**Table B.10.:** Comparison of the observational properties of SGR 0418+5729 and the white dwarf AE Aquarii. For SGR 0418+5729  $P$ ,  $\dot{P}$ , and  $L_X$  have been taken from Rea et al. (2010). The characteristic age is given by  $\text{Age} = P/(2\dot{P})$  and the surface magnetic field  $B$  is given by Eq. (B.3.4). The pulsed fraction of SGR 0418+5729 is taken from Esposito et al. (2010) and the one of the white dwarf AE Aquarii from Eracleous et al. (1991) and Choi and Dotani (2006).

13.2 s (Israel et al., 1997). This white dwarf is one of the most massive white dwarfs with  $M = 1.28 \pm 0.05M_\odot$  (see Mereghetti et al., 2009, for details). Other very massive and highly magnetized white dwarfs are: REJ 0317-853 with  $M \sim 1.35M_\odot$  and  $B \sim (1.7-6.6) \times 10^8$  G (see e.g. Barstow et al., 1995; Külebi et al., 2010b); PG 1658+441 with  $M \sim 1.31M_\odot$  and  $B \sim 2.3 \times 10^6$  G (see e.g. Liebert et al., 1983; Schmidt et al., 1992); and PG 1031+234 with the highest magnetic field  $\sim 10^9$  G (see e.g. Schmidt et al., 1986; Külebi et al., 2009). It is interesting to note that the most highly magnetized white dwarfs are massive as well as isolated (see e.g. Należyty and Madej, 2004, for details).

### B.3.5. Rotational instability of white dwarfs

In order to be stable against secular instability of the MacClaurin versus the Jacobi ellipsoid (Ferrari and Ruffini, 1969), the minimal period of a white dwarf with the parameters discussed here is  $P_{\text{crit}} \sim 0.94$  s. For  $P \lesssim P_{\text{crit}}$  we would expect very significant emission of gravitational waves due to the transition from the triaxial Jacobi ellipsoids to the axially symmetric MacClaurin ellipsoids. This is well in agreement and explains the observed long periods of SGRs and AXPs  $\gtrsim 2$  s (see Fig. B.27). In the specific case of the source 1E 2259+586, assuming that the supernova remnant G109.1-1.0 and 1E 2259+586 are coeval, we obtain the initial rotational period of the white dwarf in the range  $0.94 \text{ s} < P_0 < 6.8 \text{ s}$  where, the lower limit, is given by the bifurcation point between MacClaurin spheroids and Jacobi ellipsoids (see e.g. Ferrari and Ruffini, 1969) and, the upper limit, is obtained for a constant

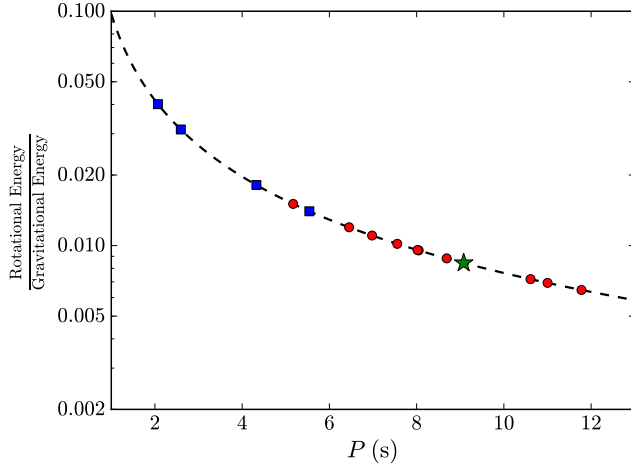


**Figure B.27.:** Ratio between the rotational energy and the gravitational energy of a MacClaurin spheroid of  $M = 1.4M_{\odot}$  and  $R = 10^3$  km as a function of its rotational period  $P$ . The rotational period between 2 and 12 s appears to be very appropriate for fast rotating white dwarfs. Fast rotating neutron stars present much shorter period in the millisecond region. We show on the curve the position of all known SGRs and AXPs. The green star corresponds to SGR 0418+5729. The blue squares are the only four sources that satisfy  $L_X < \dot{E}_{\text{rot}}$  when described as rotation powered neutron stars (see Fig. B.25 for details).

value of  $\dot{P}$ . Describing today 1E 2259+586 by a MacClaurin spheroid, we obtain the ratio between the rotational energy and the gravitational energy  $E_{\text{rot}}/|E_{\text{grav}}| \sim 0.011$  (see Fig. B.27), well below the secular instability  $\sim 0.14$  and the dynamical instability  $\sim 0.25$  (see Chandrasekhar, 1969; Shapiro and Teukolsky, 1983, for details).

The above considerations add interest in the recent theoretical analysis of white dwarfs taking into account nuclear, weak and electromagnetic interactions within a general relativistic treatment (Rotondo et al., 2011b). A specially relevant result has been recently obtained (Boshkayev et al., 2012) by analyzing a white dwarf endowed with mass, angular momentum, and quadrupole moment within the Hartle-Thorne formalism (Hartle, 1967; Hartle and Thorne, 1968). The rotating white dwarfs have been studied for the new equation of state given by Rotondo et al. (2011c) used for the construction of the non-rotating configurations by Rotondo et al. (2011b). The critical rotational periods for the onset of the axisymmetric, the mass-shedding and the inverse  $\beta$ -decay instabilities have been studied in detail. The exact value of the critical period of a white dwarf depends upon the central density of the configuration; rotationally stable white dwarfs exist for rotational periods  $P > P_{\text{min}}^{\text{WD}} \sim 0.3$  s. The shortest values for configurations supported by rotation with critical masses larger than the classical Chandrasekhar limit for non-rotating white dwarfs all the way up to  $M_{\text{max}} \sim 1.5M_{\odot}$  (see Boshkayev

et al., 2012, for details).

Consequently, also the fastest sources e.g. 1E 1547.0-5408 with  $P = 2.07$  s, SGR 1627-41 with  $P = 2.59$  s, and PSR J 1622-4950 with  $P = 4.33$  s, can be safely described as massive fast rotating white dwarfs as shown in Fig. B.21.

### B.3.6. Glitches and outbursts in SGRs and AXPs

The energetic of the observed bursts within the white dwarf model of SGRs and AXPs can be fully explained by the observed change of period  $\Delta P < 0$  (glitches). In the case of the famous event of 5th March 1979 in the SGR 0526-66 ( $P = 8.05$  s), a fractional change of period of the white dwarf  $\Delta P/P \sim -10^{-4}$  (see Fig. B.23) would be sufficient to explain the energetics  $\sim 3.6 \times 10^{44}$  erg (Mereghetti, 2008). Unfortunately, such a change of period could not be observed at the time (see e.g. Mazets et al., 1979), lacking the observations of the source prior to the event. Instead, in the case of the flares of 1E 2259+586 on June 2002 ( $P = 6.98$  s) and of 1E 1048.1-5937 ( $P = 6.45$  s) on March 2007, observational data are available. For 1E 2259+586, using the observed fractional change of period  $\Delta P/P \sim -4 \times 10^{-6}$  (Woods et al., 2004) (see also Fig. B.20), we obtain within the white dwarf model a change of rotational energy  $|\Delta E_{\text{rot}}^{\text{WD}}| \sim 1.7 \times 10^{43}$  erg, to be compared with the measured energy released during the event  $\sim 3 \times 10^{41}$  erg. For the glitch on the 26th March 2007 in 1E 1048.1-5937 with observed  $\Delta P/P \sim -1.63 \times 10^{-5}$ , we obtain  $|\Delta E_{\text{rot}}^{\text{WD}}| \sim 7.73 \times 10^{43}$  erg which is strikingly in agreement (and safely superior) with the observed energy released in the event  $4.3 \times 10^{42}$  erg (see e.g. Dib et al., 2009). In the case of super giant flares, there is no clear observational evidence of their association to glitches. However, changes in the moment of inertia of the white dwarf originating fractional changes of period of order  $\Delta P/P \sim -(10^{-5} - 10^{-3})$  (see Fig. B.23) could explain their large energetics ranging from  $10^{44}$  erg all the way up to  $10^{47}$  erg (see e.g. Mereghetti, 2008). For the giant flare of SGR 1806-20 on 27th December 2004 (see e.g. Borkowski et al., 2004; Hurley et al., 2005) with observed energy  $\sim 10^{46}$  erg there is a gap of timing data of the source between October 2004 and March 2005 (see Mereghetti et al., 2005; Tiengo et al., 2005). The observed rotational period of SGR 1806-20 after March 2005 is not consistent with the expected rotational period obtained from the spin-down rate  $\dot{P} = 5.5 \times 10^{-10}$ ; instead, this is consistent with  $\dot{P} = 1.8 \times 10^{-10}$ . The change of rotational period has been attributed to “global reconfigurations of the neutron star magnetosphere” (see e.g. Tiengo et al., 2005). Within the white dwarf model, such a burst activity is consistent with a glitch with fractional change of period  $\sim -3 \times 10^{-3}$ . All the above discussion is summarized in Table B.11 and Figs. B.20 and B.23.

In all the above cases the gain of rotational energy in the glitch is much larger than the energy observed in the flaring activities following the glitches. This means that there is ample room to explain these glitch-outburst events

	SGR 0526-66	1E 2259+586	1E 1048.1-5937	SGR 1806-20
Date	March 1979	June 2002	March 2007	December 2004
Observed Energy (erg)	$3.6 \times 10^{44}$	$3 \times 10^{41}$	$4.2 \times 10^{42}$	$\sim 10^{46}$
$ \Delta P /P$	$1.2 \times 10^{-4}$ (predicted)	$4.24 \times 10^{-6}$ (observed)	$1.63 \times 10^{-5}$ (observed)	$3 \times 10^{-3}$ (predicted)
Predicted Energy (erg)	$3.6 \times 10^{44}$	$1.7 \times 10^{43}$	$7.7 \times 10^{43}$	$\sim 10^{46}$

**Table B.11.:** Glitches and Outbursts of some SGRs and AXPs within the white dwarf model. The predicted values of  $|\Delta P|/P$  are calculated with Eq. (B.3.8) assuming  $|\Delta E_{\text{rot}}^{\text{WD}}|$  equals the observed energy of the burst event. The predicted values of the energy released in the burst event is calculated with Eq. (B.3.8) using the observed fractional change of rotational period  $|\Delta P|/P$ .

in a large range of recovery fractions  $Q$ . It appears to be appropriate to systematically monitor the  $Q$  factors for all the glitches in SGRs and AXPs.

It is interesting that PSR J1846-0258,  $P = 0.3$  s, experienced in June 2006 a radiative event with estimated isotropic energy  $\sim (3.8\text{--}4.8) \times 10^{41}$  erg (Kumar and Safi-Harb, 2008). Assuming that such an event was triggered by a glitch in the neutron star one obtains an associated fractional change of period  $\Delta P/P \sim -(1.73\text{--}2.2) \times 10^{-6}$ , as given by Eq. (B.3.13). Indeed, as shown by Kuiper and Hermsen (2009), the outburst emission was accompanied by a large glitch  $\Delta P/P \sim -(2.0\text{--}4.4) \times 10^{-6}$  in perfect agreement with the theoretical prediction given by the loss of rotational power after the spin-up of the neutron star without advocate any magnetar phenomena. This fact reinforces the idea that PSR J1846-0258 is not a magnetar but an ordinary rotationally powered neutron star, also in line with the recent suggestions by Kuiper and Hermsen (2009) and Rea et al. (2010).

### B.3.7. Magnetosphere emission from white dwarfs

We return now to the structure of the magnetosphere of the white dwarf model for SGRs and AXPs. In order to have an agreement between the observed X-ray luminosity and the X-ray spectral distribution, it is necessary that only a part of the surface of the white dwarf has to be X-ray emitter.

We can define the dimensionless filling factor

$$\mathcal{R} = \frac{L_X}{4\pi R^2 \sigma T^4}, \quad (\text{B.3.14})$$

where  $\sigma$  is the Stefan-Boltzmann constant and  $T$  the temperature of the source. This factor gives an estimate of the effective area of X-ray emission and consequently information about the structure of the magnetic field from the surface of the object. It is interesting that this factor for the white dwarf is in the range  $10^{-6}\text{--}10^{-5}$  (see Table B.12), quite similar to the one of the Sun  $\mathcal{R}_{\odot} = L_{\odot}^X / (4\pi R_{\odot}^2 \sigma T_{\odot}^4) \approx (7.03 \times 10^{-8}\text{--}1.2 \times 10^{-6})$  in the minimum  $L_{\odot}^X = 2.7 \times 10^{26}$  erg/s and in the maximum  $L_{\odot}^X = 4.7 \times 10^{27}$  erg/s of solar activity respectively (see e.g. Peres et al., 2000; Judge et al., 2003). This should be expected by the

general argument of the conservation of flux in the transition from a highly magnetized main sequence star to a white dwarf. The magnetic field of the order of  $\sim 10^9$  G on the surface of these white dwarfs must clearly have a filamentary structure in the range  $\mathcal{R} \sim 10^{-6}$ – $10^{-5}$ .

In the specific case of SGR 0418+572 such an  $\mathcal{R}$  factor is  $\sim 10^{-9}$ , which is of the same order as the one of the white dwarf AE Aquarii, as can be seen from Table B.10 by comparing the values of  $L_X$  and  $KT$ , which are the quantities involved in Eq. (B.3.14).

At times the presence of an  $\mathcal{R}$  factor has been interpreted as originating from a spot-like radial emission of the radiation from the surface of the white dwarf. If one were to assume that the radiation occurs radially beamed and occurring just from the surface either of the neutron star or the white dwarf, a spot radiation would lead to a pulsed fraction of the emission flux determined by  $\sqrt{1/n \sum_{i=1}^n (y_i - \bar{y})^2} / \bar{y} \sim 1$ , where  $n$  is the number of phase bins per cycle,  $y_i$  is the number of counts in the  $i$ th phase bin and  $\bar{y}$  is the mean number of counts in the cycle (see e.g. Esposito et al., 2010, for details about this definition). This problem, which seems to be in contradiction with the observations of pulsed fractions  $< 1$  in SGRs and AXPs (see e.g. Esposito et al., 2010), would be equally severe both for neutron stars and white dwarfs (see e.g. Table B.10).

It is appropriate to recall that all the SGRs and AXPs within a rotating white dwarf model have magnetic fields in the range  $10^8 \text{ G} \lesssim B \lesssim 10^{11} \text{ G}$  (see Table B.12). It is quite natural to assume that the X-ray emission be linked to the presence of the magnetic field. It is worth to note that the modeling of the physics and the geometrical structure of the magnetic field and of the magnetospheres is a most active field of current research. As shown by Romani and Watters (2010), the morphology of the pulses as well as of the light curves strongly depend on many model parameters, e.g. special and general relativistic effects, the viewing angle, the magnetic moment-spin axis angle, the spin axis-line of sight angle, the specific location of the emission zone, and the adopted magnetospheric model including possible corrections due to deviations from a pure dipolar structure.

From the broad sinusoidal pulsed flux of SGRs/AXPs (see e.g. Mereghetti, 2008), we know that the pulsed fraction is less than one and that the luminosity differs remarkably from a spiky one. We find then natural to assume that the emission comes from an area covering the white dwarf surface with a very marked filamentary structure. Similar considerations for neutron stars magnetospheres have been purported e.g. by Michel and Dessler (1981); Michel (1983) giving evidence of magnetospheric activity from the pole all the way up to the equator; see also the most interesting case of the pair production activities in the magnetosphere of a rotating white dwarf considered for the transient radio source GCRT J1745–3009 by Zhang and Gil (2005). Moreover, such structures are regularly observed in the Sun and in the Earth Aurora.

Explicit sinusoidal pulsed flux in soft X-rays ( $< 4$  keV) have been observed in AE Aquarii (see e.g. Eracleous et al., 1991; Choi and Dotani, 2006); and see also Fig. 6 in Mereghetti et al. (2011) for similar sinusoidal pulsed emission of the white dwarf RXJ 0648.0-4418 with rotational period  $P = 13.2$  s. For all the above sources, a filamentary structure of the magnetic field is clearly expected.

We do not discuss here the issue of the spectral features within the white dwarf model. The aim of this article is just to point out that all these problems can be address with merit starting from the rotational energy of a rotating white dwarf rather than the magnetic energy of a magnetar. The spectrum of the persistent emission of SGRs and AXPs for energies  $< 10$  keV is well fitted either by the superposition of a blackbody and a high energy tail or by a single blackbody or a double blackbody (see e.g. Mereghetti, 2008). Such a spectral feature is clearly already evidenced for rotating white dwarfs; following the work of Terada et al. (2008c): in addition to the thermal modulation in the softer X-ray band, spiky pulsations like the ones of pulsars have been observed by the Suzaku satellite in the hard X-ray band of over 4 keV in the white dwarf AE Aquarii. The X-ray spectrum requires an additional hard X-ray component on the well-known thermal emissions with temperatures of 0.5 and 2.9 keV. Combined with results from timing analyses, spectral shapes and flux, it was there concluded that the hard X-ray pulsations should have a non-thermal origin, for example, possible Synchrotron emission with sub MeV electrons. The claim of the first discovery of a white dwarf equivalent to a neutron star pulsar was there made. In view of the possible evidence of very high energy emission in the TeV region observed during the optical flares of AE Aquarii (see e.g. de Jager et al., 1994; Ikhsanov and Biermann, 2006; Ikhsanov and Beskrovnaya, 2008; Terada et al., 2008c,d; Kashiyama et al., 2011, and references therein), it would be important to have observations by INTEGRAL and Fermi of rotating magnetized white dwarf in the 20-200 keV band in order to establish further analogies between fast rotating highly magnetized white dwarfs and magnetar candidates.

More specifically, for the source SGR 0418+5729 and its interpretation as a white dwarf, a crucial result has been recently obtained by Durant et al. (2011). We first recall the observed range of temperatures of massive isolated white dwarfs  $1.14 \times 10^4 \text{ K} \leq T \leq 5.52 \times 10^4 \text{ K}$ ; see Table 1 in (Ferrario et al., 2005). From the broad band Hubble Space Telescope imaging of the field of SGR 0418+5729, the upper limits of the black body surface temperature,  $T < 3.14 \times 10^4 \text{ K}$  and  $T < 1.18 \times 10^4 \text{ K}$  in the F110W and F606W filters, can be established for a radius  $R = 10^8 \text{ cm}$ . In this respect is also worth to recall the optical observations of AXP 4U0142+61 of Hulleman et al. (2000). The photometric results of the field of 4U0142+61 at the 60-inch telescope on Palomar Mountain are in agreement with a  $1.3M_{\odot}$  white dwarf with a surface temperature  $\sim 4 \times 10^5 \text{ K}$  (see Hulleman et al., 2000, for details). These results are therefore fully consistent with the SGR/AXP white dwarf model, and

follow-on missions of Hubble and VLT are strongly recommended.

### **B.3.8. The connection with supernova remnants**

We would like to address the special issue of the supernova remnants energetics and their association with SGRs and AXPs. A firm association between SGRs/AXPs and supernovae have been purported by Gaensler et al. (2001) in the cases 1E 1841–045 (SNR G27.4+0.0, Kes 73), AX J1845.0–0258 (SNR G29.6+0.1), and 1E 2259+586 (SNR G109.1–1.0, CTB 109). See also Gelfand and Gaensler (2007) for the possible association 1E 1547.0–5408 (SNR G327.24–0.13). What is of interest for us here is the special issue of the energetics of the supernova remnant and the present of an SGR or an AXP.

Paczynski, in the case of AXP 1E 2259+586, attempted to explain the supernova remnant by assuming a merger of a binary system of ordinary white dwarf of mass  $\sim (0.7-1)M_{\odot}$  based on models by Iben and Tutukov (1984) and Paczynski (1985) leading both to the formation of a fast rotating white dwarf and to the supernova remnant. Recent simulations of white dwarf-white dwarf mergers (see e.g. Pakmor et al., 2010) point that mergers of  $(0.8-0.9M_{\odot})$  produce supernova events generally not very efficient energetically, well below the observed explosion energy  $\sim 7.4 \times 10^{50}$  erg of the supernova remnant G109.1-1.0 associated to 1E 2259+586 (see e.g. Sasaki et al., 2004).

In the intervening years much more has been understood on the process of gravitational collapse and on the composition of the material surrounding neutron stars and black holes both from pulsar observations and Gamma Ray Bursts. Fascinating evidence for the presence of planets around pulsars in supernova remnants has been established (see e.g. Konacki et al., 1999; Hansen, 2002; Konacki and Wolszczan, 2003). Similarly, the presence of many body process of gravitational collapse has been evidenced for Gamma Ray Bursts (see e.g. Ruffini, 2009).

In view of the above, we advance the possible scenario in which the SGRs/AXPs and the supernova remnant originate from a very close binary system composed of a white dwarf and a companion late evolved star, close to the process of gravitational collapse. The collapse of the companion star, either to a neutron star or to a black hole, leads to mass loss which can unbind the original binary system. Three possible cases can occur (see e.g. Ruffini, 1973): 1) if the loss of mass in the supernova explosion is  $M_{\text{loss}} < M/2$ , being  $M$  the total mass of the binary, the system holds bound; 2) if  $M_{\text{loss}} \sim M/2$  then the system becomes unbound and the white dwarf is expelled at nearly orbital motion velocity; and 3) if  $M_{\text{loss}} \gg M/2$  the white dwarf is kicked out with very high runaway velocities. Only in the first case the object will lie at the center of the supernova remnant. For a review on the evolution of binary systems see Stairs (2004) and for a detailed treatment of the problem of runaway velocities from supernova explosions see Tauris and Bailes (1996); Tauris and

Takens (1998). The white dwarf in this picture does not participate either to the gravitational collapse nor to the formation of the supernova remnant: it can have a period and a life time determine essentially by the prior evolution of the binary system. This explains the disagreement between the age of the supernova remnant and the characteristic age of the SGR/AXP when inferred by a neutron star model. In the case of large kick velocities the runaway white dwarf can collide with the surrounding material in the supernova remnant and very likely also with planets. Such collisions may well originate changes in the moment of inertia of the white dwarf, consequently in its rotational period, leading to glitches and burst activity.

In the above context it is appropriate to recall the pioneering work of Katz (1996) on explaining the super-Eddington luminosities in the flaring episodes of SGRs and AXPs as originating in accretion process of planetary fragments, in particular, the important role of magnetic confinement of an  $e^+e^-$  pair plasma. The model explains the observed self-absorbed thermal spectrum of flares and their nearly independence on their luminosity. Katz (1996) has shown that the infall of planetary fragments may lead to a continuous injection of energy to the magnetosphere which leads to magnetic confinement of the source if the magnetic field satisfies

$$B > \sqrt{\frac{2L}{cR^2}} = 2.6 \times 10^7 \sqrt{\frac{L_{41}}{R_8^2}} \text{ G}, \quad (\text{B.3.15})$$

where  $L_{41}$  is the luminosity in units of  $10^{41}$  erg/s and  $R_8$  is the radius of the source in units of  $10^8$  cm.

In the case when the radiation is not being continuously resupplied, but it is initially contained within the volume  $\sim 4\pi R^3/3$ , the minimum magnetic field for confinement is given by

$$B > \sqrt{\frac{6L\tau}{R^3}} = 2.45 \times 10^8 \sqrt{\frac{L_{41}\tau_{0.1}}{R_8^3}} \text{ G}, \quad (\text{B.3.16})$$

where  $\tau_{0.1}$  is the time  $\tau$  during which the source is radiating at a luminosity  $L$ , in units of 0.1 s. The fiducial values for  $L$  and for  $\tau$  has been chosen here to be typical of the bursting activity of SGRs/AXPs (see e.g. Mereghetti, 2008). The above two bounds for the magnetic field are indeed in line with the surface magnetic fields obtained in this paper; see Fig. B.22 for details. Thus, the super-Eddington luminosities observed in the outbursts can be well explained within the white dwarf model and there is no need of introducing the huge magnetic fields of the magnetar model (Paczynski, 1992; Thompson and Duncan, 1995).

### B.3.9. On the fiducial neutron star and white dwarf parameters in light of recent theoretical progress

Before concluding, we would like to introduce a word of caution on the fiducial values adopted both for the neutron star and the white dwarf in the above Sections. In the intervening years much more have been learned on the equation of state and on a more complex description of the structure parameters of both white dwarfs and neutron stars.

The equations of equilibrium of neutron stars, traditionally based on the Tolman-Oppenheimer-Volkoff equations, have been superseded by an alternative formulation based on the general relativistic Thomas-Fermi conditions of equilibrium within the Einstein-Maxwell equations Belvedere et al. (2012). Correspondingly, the above values of  $\sqrt{I/R^6}$  in Eq. (B.3.3) estimated into the fiducial parameters, leading to Eq. (B.3.12), can acquire in fact values in the range  $0.44 \lesssim \sqrt{I/R^6} / \sqrt{I_f/R_f^6} \lesssim 0.56$ , where the subscript ‘f’ stands for fiducial parameter. This range corresponds to the range of masses  $0.5 \lesssim M/M_\odot \lesssim 2.6$  (Belvedere et al., 2012). Correspondingly, the magnetic field is in the range  $0.44 \lesssim B/B_f^{\text{NS}} \lesssim 0.56$ , where  $B_f^{\text{NS}}$  is given by Eq. (B.3.12).

Similar considerations apply for the white dwarf case. General relativistic white dwarfs taking into account nuclear, weak and electromagnetic interactions have been recently constructed (Rotondo et al., 2011b) following the new equation of state for compressed nuclear matter given by Rotondo et al. (2011c). The case of rotating white dwarfs in general relativity has been studied by Boshkayev et al. (2012). It has been found that white dwarfs can be as fast as  $P_{\text{min}}^{\text{WD}} \sim 0.3$  s and as massive as  $M_{\text{max}} \sim 1.5M_\odot$ ; see Sec. B.3.5 for details. For example, a white dwarf of  $M = 1.44M_\odot$  rotating with period  $P = 3.2$  s, will have an equatorial radius  $R_{\text{eq}} \sim 3604$  km, polar radius  $R_p \sim 2664$  km, and moment of inertia  $I \sim 2.9 \times 10^{49}$  g cm<sup>2</sup>. In this case we will have  $\sqrt{I/R^6} / \sqrt{I_f/R_f^6} \sim 0.01$  and therefore  $B/B_f^{\text{WD}} \sim 0.01$  where  $B_f^{\text{WD}}$  is given by Eq. (B.3.4).

This issue is particularly relevant to the study of the four sources in Fig. B.25. These sources can be definitely explained within a unified framework of rotating white dwarfs with all the other SGRs and AXPs. In view of the parameters recently obtained they may be also interpreted as regular neutron stars with a barely critical magnetic field. For these sources an option remain open for their interpretation as white dwarfs or neutron stars. A more refined analysis will clarify the correctness of the two possible interpretations both, in any case, alternative to the magnetar model.

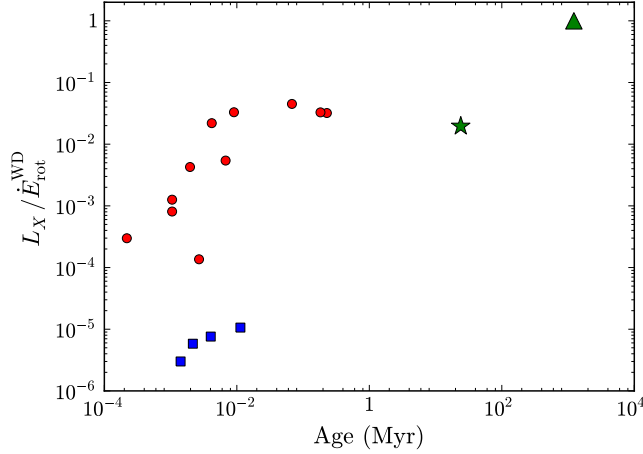


**Figure B.28.:** Ratio between the observed X-ray luminosity  $L_X$  and the loss of rotational energy  $\dot{E}_{rot}$  describing SGRs and AXPs by rotation powered white dwarfs. The green star and the green triangle correspond to SGR 0418+5729 using respectively the upper and the lower limit of  $\dot{P}$  given by Eq. (B.3.2). The blue squares are the only four sources that satisfy  $L_X < \dot{E}_{rot}$  when described as rotation powered neutron stars (see Fig. B.25 for details).

### B.3.10. Conclusions and remarks

The recent observations of the source SGR 0418+5729 cast a firm separatrix in comparing and contrasting the two models for SGRs and AXPs based respectively on an ultramagnetized neutron star and on a white dwarf. The limit on the magnetic field derived in the case of a neutron star  $B = 7.5 \times 10^{12}$  G makes it not viable as an explanation based on the magnetar model both from a global energetic point of view and from the undercritical value of the magnetic field. In the white dwarf model, the picture is fully consistent. It is interesting that the rotational energy loss appears to approach the value of the observed X-ray luminosity with time (see Fig. B.28) as the magnetospheric activity settles down.

The description of SGR 0418+5729 as a white dwarf predicts the lower limit of the spin-down rate  $\dot{P}$  given by Eq. (B.3.2), the surface magnetic field field is, accordingly to Eq. (B.3.4), constrained by  $1.05 \times 10^8 \text{ G} < B_{\text{SGR0418+5729}} < 7.47 \times 10^8 \text{ G}$  (see Fig. B.22). The campaign of observations launched by the Fermi and Agile satellites will address soon this issue and settle in the near future this theoretical prediction.

The characteristic changes of period  $\Delta P/P \sim -(10^{-7}-10^{-3})$  and the relating bursting activity  $\sim (10^{41}-10^{46}) \text{ erg}$  in SGRs and AXPs can be well explained in term of the rotational energy released after the glitch of the white dwarf. It is also appropriate to recall that fractional changes, on scales  $|\Delta P|/P \lesssim 10^{-6}$  are also observed in pulsars and routinely expressed in terms of the release of rotational energy of the neutron star, without appealing to

any magnetars phenomena; e.g. the glitch/outburst activity experienced in June 2006 by PSR J1846-0258 (see Sec. B.3.7) and the most recent event observed in the prototypical Crab pulsar B0531+21 in the Crab nebula (see e.g. Tavani, 2011; Fermi-LAT Collaboration, 2010).

The observation of massive fast rotating highly magnetized white dwarfs by dedicated missions as the one leaded by the X-ray Japanese satellite Suzaku (see e.g. Terada et al., 2008c) has led to the confirmation of the existence of white dwarfs sharing common properties with neutron star pulsars, hence their name white dwarf pulsars. The theoretical interpretation of the high-energy emission from white dwarf pulsars will certainly help to the understanding of the SGR and AXP phenomena (see e.g. Kashiyama et al., 2011).

We have given evidence that all SGRs and AXPs can be interpreted as rotating white dwarfs providing that the rotational period satisfies  $P > P_{\min}^{\text{WD}} \sim 0.3$  s. The white dwarf generate their energetics from the rotational energy and therefore there is no need to invoke the magnetic field decay of the magnetar model.

Concerning magnetized white dwarfs, the coupling between rotation and Rayleigh-Taylor instabilities arising from chemical separation upon crystallization may have an important role in the building of the magnetic field of the white dwarf.

	SGR 1806-20	SGR 0526-66	SGR 1900+14	SGR 0418+5729
$P$ (s)	7.56	8.05	5.17	9.08
$\dot{P}$ ( $10^{-11}$ )	54.9	6.5	7.78	$< 6.0 \times 10^{-4}$
Age (kyr)	2.22	1.97	1.05	$24.0 \times 10^3$
$L_X$ ( $10^{35}$ erg/s)	1.50	2.1	1.8	$6.2 \times 10^{-4}$
$kT$ (keV)	0.65	0.53	0.43	0.67
$\dot{E}_{\text{rot}}^{\text{WD}}$ ( $10^{37}$ erg/s)	50.24	4.92	22.24	$3.2 \times 10^{-4}$
$B_{\text{WD}}$ ( $10^9$ G)	206.10	73.18	64.16	0.75
$\mathcal{R}_{\text{WD}}$ ( $10^{-5}$ )	0.65	2.06	4.07	$2.4 \times 10^{-4}$
$\dot{E}_{\text{rot}}^{\text{NS}}$ ( $10^{35}$ erg/s)	0.502	0.05	0.22	$3.2 \times 10^{-6}$
$B_{\text{NS}}$ ( $10^{14}$ G)	20.61	7.32	6.42	0.075
$\mathcal{R}_{\text{NS}}$	0.065	0.21	0.41	$2.4 \times 10^{-5}$
	1E 1547-54	1E 1048-59	1E 1841-045	1E 2259+586
$P$ (s)	2.07	6.45	11.78	6.98
$\dot{P}$ ( $10^{-11}$ )	2.32	2.70	4.15	0.048
Age (kyr)	1.42	3.79	4.50	228.74
$L_X$ ( $10^{35}$ erg/s)	0.031	0.054	2.2	0.19
$kT$ (keV)	0.43	0.62	0.38	0.41
$\dot{E}_{\text{rot}}^{\text{WD}}$ ( $10^{37}$ erg/s)	103.29	3.97	1.01	0.056
$B_{\text{WD}}$ ( $10^9$ G)	22.17	42.22	70.71	5.88
$\mathcal{R}_{\text{WD}}$ ( $10^{-5}$ )	0.07	0.028	8.16	0.49
$\dot{E}_{\text{rot}}^{\text{NS}}$ ( $10^{35}$ erg/s)	1.03	0.040	0.010	$5.62 \times 10^{-4}$
$B_{\text{NS}}$ ( $10^{14}$ G)	2.22	4.22	7.07	0.59
$\mathcal{R}_{\text{NS}}$	0.007	0.0028	0.82	0.049

**Table B.12.:** SGRs and AXPs as white dwarfs and neutron stars. The rotational period  $P$ , the spin-down rate  $\dot{P}$ , the X-ray luminosity  $L_X$  and the temperature  $T$  have been taken from the McGill online catalog at [www.physics.mcgill.ca/~pulsar/magnetar/main.html](http://www.physics.mcgill.ca/~pulsar/magnetar/main.html). The characteristic age is given by  $\text{Age} = P/(2\dot{P})$ , the loss of rotational energy  $\dot{E}_{\text{rot}}$  is given by Eqs. (B.3.5) and Eq. (B.3.1) and the surface magnetic field is given by Eqs. (B.3.4) and (B.3.12) for white dwarfs and neutron stars respectively. The filling factor  $\mathcal{R}$  is given by Eq. (B.3.14).

## B.4. SGR 0418+5729 and Swift J1822.3-1606 as massive fast rotating highly magnetized white dwarfs

### B.4.1. Introduction

Following Malheiro et al. (2012) we describe the so-called *low magnetic field magnetars*, Swift J1822.3-1606 and SGR 0418+5729, as massive fast rotating highly magnetized white dwarfs. We give bounds for the mass, radius, moment of inertia, and magnetic field for these sources, by requesting the stability of realistic general relativistic uniformly rotating configurations. Based on these parameters, we improve the theoretical prediction of the lower limit of the spin-down rate of SGR 0418+5729. We also present the theoretical expectation of the infrared, optical and ultraviolet emission and show their consistency with the current available observational data. In addition, we compute the electron cyclotron frequencies corresponding to the predicted surface magnetic fields.

The observation of SGR 0418+5729 with a rotational period of  $P = 9.08$  s, an upper limit of the first time derivative of the rotational period  $\dot{P} < 6.0 \times 10^{-15}$  (Rea et al., 2010), and an X-ray luminosity of  $L_X = 6.2 \times 10^{31}$  erg s<sup>-1</sup> can be considered as the Rosetta Stone for alternative models of SGRs and AXPs.

The magnetar model, based on a neutron star of fiducial parameters  $M = 1.4M_\odot$ ,  $R = 10$  km and a moment of inertia  $I = 10^{45}$  g cm<sup>2</sup>, needs a magnetic field larger than the critical field for vacuum polarization  $B_c = m_e^2 c^3 / (e\hbar) = 4.4 \times 10^{13}$  G in order to explain the observed X-ray luminosity in terms of the release of magnetic energy (see Duncan and Thompson, 1992; Thompson and Duncan, 1995, for details). The inferred upper limit of the surface magnetic field of SGR 0418+5729  $B < 7.5 \times 10^{12}$  G describing it as a neutron star (see Rea et al., 2010, for details), is well below the critical field, which has challenged the power mechanism based on magnetic field decay in the magnetar scenario.

Alternatively, it has been recently pointed out how the pioneering works of Morini et al. (1988) and Paczynski (1990) on the description of 1E 2259+586 as a white dwarf (WD) can be indeed extended to all SGRs and AXPs. These WDs were assumed to have fiducial parameters  $M = 1.4M_\odot$ ,  $R = 10^3$  km,  $I = 10^{49}$  g cm<sup>2</sup>, and magnetic fields  $B \gtrsim 10^7$  G (see Malheiro et al., 2012, for details) inferred from the observed rotation periods and spin-down rates.

The energetics of SGRs and AXPs including their steady emission, glitches, and their subsequent outburst activities have been shown to be powered by the rotational energy of the WD (Malheiro et al., 2012). The occurrence of a glitch, the associated sudden shortening of the period, as well as the corresponding gain of rotational energy, can be explained by the release of gravitational energy associated with a sudden contraction and decrease of the

moment of inertia of the uniformly rotating WD, consistent with the conservation of their angular momentum.

By describing SGR 0418+5729 as a WD, Malheiro et al. (2012) calculated an upper limit for the magnetic field  $B < 7.5 \times 10^8$  G and show that the X-ray luminosity observed from SGR 0418+5729 can be well explained as originating from the loss of rotational energy of the WD leading to a theoretical prediction for the spin-down rate

$$\frac{L_X P^3}{4\pi^2 I} = 1.18 \times 10^{-16} \leq \dot{P}_{\text{SGR0418+5729}} < 6.0 \times 10^{-15}, \quad (\text{B.4.1})$$

where the lower limit was established by assuming that the observed X-ray luminosity of SGR 0418+5729 coincides with the rotational energy loss of the WD. As we will show below, these predictions can be still improved by considering realistic WD parameters instead of fiducial ones.

The situation has become even more striking considering the recent X-ray timing monitoring with Swift, RXTE, Suzaku, and XMM-Newton satellites of the recently discovered SGR Swift J1822.3–1606 (Rea et al., 2012). The rotation period  $P = 8.437$  s, and the spin-down rate  $\dot{P} = 9.1 \times 10^{-14}$  have been obtained. Assuming a NS of fiducial parameters, a magnetic field  $B = 2.8 \times 10^{13}$  G is inferred, which is again in contradiction with a magnetar explanation for this source.

We have recently computed in (Boshkayev et al., 2012) general relativistic configurations of uniformly rotating white dwarfs within Hartle’s formalism (Hartle, 1967). We have used the relativistic Feynman-Metropolis-Teller equation of state (Rotondo et al., 2011c) for WD matter, which we have shown generalizes the traditionally used equation of state of Salpeter (1961b). It has been there shown that rotating WDs can be stable up to rotation periods of  $\sim 0.28$  s (see Boshkayev et al. (2012) and Sec. B.4.3 for details). This range of stable rotation periods for WDs amply covers the observed rotation rates of SGRs and AXPs  $P \sim (2\text{--}12)$  s.

The aim of this article is to describe the so-called *low magnetic field magnetars*, SGR 0418+5729 and Swift J1822.3-1606, as massive fast rotating highly magnetized WDs. In doing so we extend the work of Malheiro et al. (2012) by using precise WD parameters recently obtained by Boshkayev et al. (2012) for general relativistic uniformly rotating WDs. It is also performed an analysis of the expected Optical and near-Infrared emission from these sources within the WD model and confront the results with the observational data.

### B.4.2. Rotation powered white dwarfs

The loss of rotational energy associated with the spin-down of the WD is given by

$$\dot{E}_{\text{rot}} = -4\pi^2 I \frac{\dot{P}}{P^3} = -3.95 \times 10^{50} I_{49} \frac{\dot{P}}{P^3} \text{ ergs}^{-1}, \quad (\text{B.4.2})$$

where  $I_{49}$  is the moment of inertia of the WD in units of  $10^{49} \text{ g cm}^2$ . This rotational energy loss amply justifies the steady X-ray emission of all SGRs and AXPs (see Malheiro et al., 2012, for details).

The upper limit on the magnetic field (see e.g. Ferrari and Ruffini, 1969) obtained by requesting that the rotational energy loss due to the dipole field be smaller than the electromagnetic emission of the magnetic dipole, is given by

$$B = \left( \frac{3c^3}{8\pi^2} \frac{I}{\bar{R}^6} P \dot{P} \right)^{1/2} = 3.2 \times 10^{15} \left( \frac{I_{49}}{\bar{R}_8^6} P \dot{P} \right)^{1/2} \text{ G}, \quad (\text{B.4.3})$$

where  $\bar{R}_8$  is the mean radius of the WD in units of  $10^8 \text{ cm}$ . The mean radius is given by  $\bar{R} = (2R_{eq} + R_p)/3$  (see e.g. Hartle and Thorne, 1968) with  $R_{eq}$  and  $R_p$  the equatorial and polar radius of the star.

It is clear that the specific values of the rotational energy loss and the magnetic field depend on observed parameters, such as  $P$  and  $\dot{P}$ , as well as on model parameters, such as the mass, moment of inertia, and mean radius of the rotating WD.

### B.4.3. Structure and stability of rotating white dwarfs

The rotational stability of fast rotating WDs was implicitly assumed by Malheiro et al. (2012). The crucial question of whether rotating WDs can or not attain rotation periods as short as the ones observed in SGRs and AXPs has been recently addressed by Boshkayev et al. (2012). The properties of uniformly rotating WDs were computed within the framework of general relativity through Hartle's formalism (Hartle, 1967). The equation of state for cold WD matter is based on the relativistic Feynman-Metropolis-Teller treatment Rotondo et al. (2011c), which generalizes the equation of state of Salpeter (1961b). The stability of rotating WDs was analyzed taking into account the mass-shedding limit, inverse  $\beta$ -decay instability, and secular axisymmetric instability, with the latter determined by the turning point method of Friedman et al. (1988); see Fig. B.29 and Boshkayev et al. (2012), for details.

The minimum rotation period  $P_{min}$  of WDs is obtained for a configuration rotating at Keplerian angular velocity, at the critical inverse  $\beta$ -decay density, namely this is the configuration lying at the crossing point between the mass-shedding and inverse  $\beta$ -decay boundaries. The numerical values of the minimum rotation period  $P_{min} \approx (0.3, 0.5, 0.7, 2.2) \text{ s}$  and the maximum

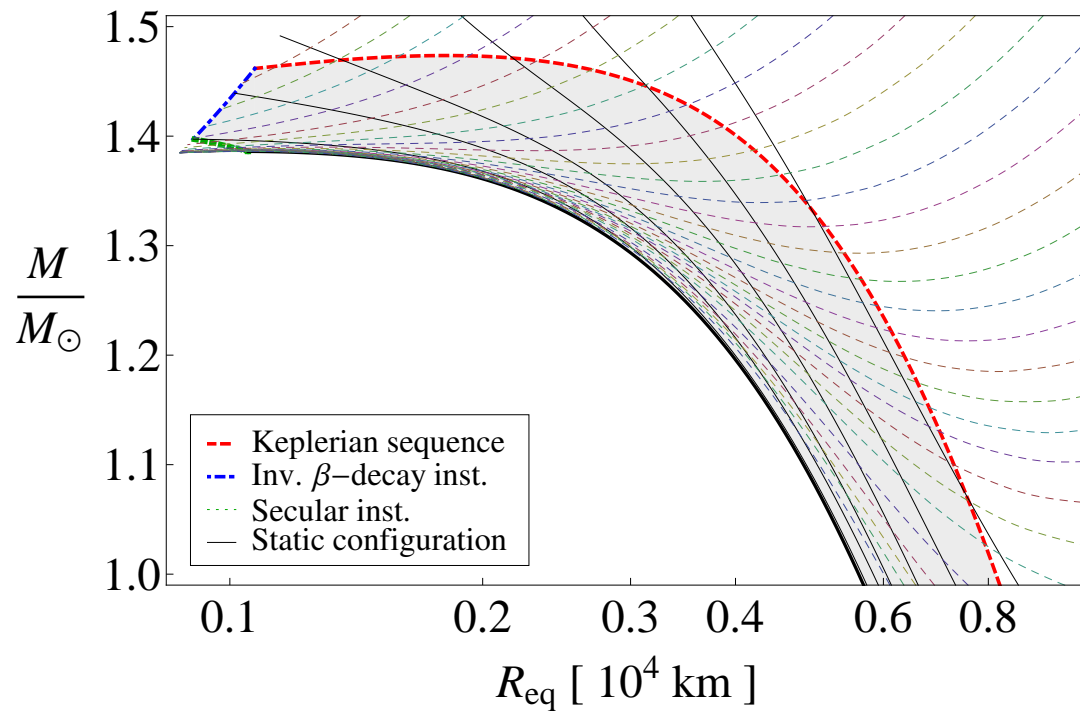


**Figure B.29.:** Mass versus equatorial radius of rotating Carbon WDs. The solid black curves correspond to  $J$ =constant sequences, where the static case  $J = 0$  the thickest one. The color thin-dashed curves correspond to  $\Omega$ =constant sequences. The Keplerian sequence is the red thick dashed curve, the blue thick dotted-dashed curve is the inverse  $\beta$  instability boundary, and the green thick dotted curve is the axisymmetric instability line. The gray-shaded region is the stability region of rotating white dwarfs (Boshkayev et al., 2012).

Composition	$P_{min}$ (s)	$M_{max}/M_{\odot}$
Helium	0.3	1.500
Carbon	0.5	1.474
Oxygen	0.7	1.467
Iron	2.2	1.202

**Table B.13.:** Minimum rotation period and maximum mass of general relativistic uniformly rotating WDs (see Boshkayev et al. (2012), for details).

masses were found for Helium (He), Carbon (C), Oxygen (O), and Iron (Fe) WDs, respectively (see Table B.13 and Boshkayev et al. (2012), for details). As a byproduct, these values show that indeed all SGRs and AXPs can be described as rotating WDs because their rotation periods are in the range  $2 \lesssim P \lesssim 12$  s.

The relatively long minimum period of rotating Fe WDs,  $\sim 2.2$  s, lying just at the lower edge of the observed range of rotation periods of SGRs and AXPs, reveals crucial information on the chemical composition of SGRs and AXPs, namely they are very likely made of elements lighter than Fe, such as C or O.

It can be seen from Fig. B.29 that every  $\Omega$ =constant sequence intersects the stability region of general relativistic uniformly rotating WDs ( $M$ - $R_{eq}$  curves inside the shaded region of Fig. B.29) in two points. These two points determine the minimum(maximum) and maximum(minimum)  $M_{min,max}(R_{eq}^{max,min})$ , respectively, for the stability of a WD with the given rotation angular velocity  $\Omega = 2\pi/P$ . Associated to the boundary values  $M_{min,max}$  and  $R_{eq}^{max,min}$ , we can obtain the corresponding bounds for the moment of inertia of the WD,  $I_{max,min}$ , respectively.

We turn now to a specific analysis to each of the two sources SGR 0418+5729 and SGR SGR 1822–1606.

#### B.4.4. SGR 0418+5729

##### Bounds on the WD parameters

SGR 0418+5729 has a rotational period of  $P = 9.08$  s, and the upper limit of the spin-down rate  $\dot{P} < 6.0 \times 10^{-15}$  was obtained by (Rea et al., 2010). The corresponding rotation angular velocity of the source is  $\Omega = 2\pi/P = 0.69$  rad s $^{-1}$ . We show in Table B.14 bounds for the mass, equatorial radius, mean radius, and moment of inertia of SGR 0418+5729 obtained by the request of the rotational stability of the rotating WD, as described in Section B.4.4, for selected chemical compositions. Hereafter we shall consider general relativistic rotating Carbon WDs.

Comp.	$M_{min}$	$M_{max}$	$R_{eq}^{min}$	$R_{eq}^{max}$	$\bar{R}_{min}$	$\bar{R}_{max}$	$I_{48}^{min}$	$I_{50}^{max}$	$B_{min}(10^7\text{G})$	$B_{max}(10^8\text{G})$
He	1.18	1.41	1.16	6.88	1.15	6.24	3.59	1.48	1.18	2.90
C	1.15	1.39	1.05	6.82	1.05	6.18	2.86	1.42	1.19	3.49
O	1.14	1.38	1.08	6.80	1.08	6.15	3.05	1.96	1.42	3.30
Fe	0.92	1.11	2.21	6.36	2.21	5.75	12.9	1.01	1.25	0.80

**Table B.14.:** Bounds for the mass  $M$  (in units of  $M_{\odot}$ ), equatorial  $R_{eq}$  and mean  $\bar{R}$  radius (in units of  $10^8$  cm), moment of inertia  $I$ , and surface magnetic field  $B$  of SGR 0418+5729.  $I_{48}$  and  $I_{50}$  is the moment of inertia in units of  $10^{48}$  and  $10^{50}$  g cm<sup>2</sup>, respectively.

### Solidification and glitches

It has been shown by Malheiro et al. (2012) that the massive WDs consistent with SGRs and AXPs possibly behave as solids since the internal temperature of the WD ( $\sim 10^7$ ) is very likely lower than the crystallization temperature (see e.g. Shapiro and Teukolsky, 1983; Usov, 1994)

$$T_{\text{cry}} \simeq 2.28 \times 10^5 \frac{Z^2}{A^{1/3}} \left( \frac{\bar{\rho}}{10^6 \text{g/cm}^3} \right)^{1/3} \text{ K}, \quad (\text{B.4.4})$$

where  $(Z, A)$  and  $\bar{\rho}$  denote the chemical composition and mean density, respectively.

This fact introduces the possibility in the WD to observe sudden changes in the period of rotation, namely glitches. The expected theoretical values of the fractional change of periods of massive WDs have been shown to be consistent with the values observed in many SGRs and AXPs (see Malheiro et al., 2012, for details).

From the bounds of  $M$  and  $R_{eq}$  we obtain that the mean density of SGR 0418+5729 must be in the range  $1.72 \times 10^6 \lesssim \bar{\rho} \lesssim 5.70 \times 10^8$  g cm<sup>3</sup>. Correspondingly, the crystallization temperature is comprised in the range  $4.3 \times 10^6 \text{ K} \lesssim T_{\text{cry}} \lesssim 2.97 \times 10^7$  K, where the lower and upper limits correspond to the configuration of minimum and maximum mass configurations, respectively.

The crystallization temperature obtained here indicates that SGR 0418+5729 should behave as a rigid solid body and therefore glitches during the rotational energy loss, accompanied by radiative events, are expected. Starquakes leading to glitches in the WD may occur with a recurrence time (see e.g. Baym and Pines, 1971; Usov, 1994; Malheiro et al., 2012)

$$\delta t_q = \frac{2D^2}{B} \frac{|\Delta P|/P}{|\dot{E}_{\text{rot}}|}, \quad (\text{B.4.5})$$

where  $\dot{E}_{\text{rot}}$  is the loss of rotational energy (B.4.2),  $D = (3/25) GM_c^2/R_c$ ,  $B = 0.33 (4\pi/3) R_c^3 e^2 Z^2 [\bar{\rho}_c / (Am_p)]^{4/3}$ ,  $M_c$ ,  $R_c$  and  $\bar{\rho}_c$  are the mass, the radius and

the mean density of the solid core, and  $m_p$  is the proton mass.

For the minimum and maximum mass configurations and the upper limit of the spin-down rate  $\dot{P} < 6 \times 10^{-15}$ , we obtain a lower limit for recurrence time of starquakes

$$\delta t_q > \begin{cases} 4 \times 10^9 (|\Delta P|/P) \text{ yr}, & M = M_{min} \\ 2 \times 10^{12} (|\Delta P|/P) \text{ yr}, & M = M_{max} \end{cases}, \quad (\text{B.4.6})$$

which for a typical fractional change of period  $|\Delta P|/P \sim 10^{-6}$  observed in SGRs and AXPs we obtain  $\delta t_q > 4 \times 10^3$  yr and  $\delta t_q > 2 \times 10^6$  yr, for  $M_{min}$  and  $M_{max}$  respectively. These very long starquake recurrent times are in agreement with the possibility that SGR 0418+5729 is an old WD whose magnetospheric activity is settling down, in agreement with its relatively low spin-down rate, magnetic field, and high efficiency parameter  $L_X/\dot{E}_{rot}$ , with respect to the values of other SGRs and AXPs (see e.g. Fig. 9 in Malheiro et al., 2012).

### Rotation power and magnetic field

Introducing the values of  $P$  and the upper limit  $\dot{P}$  into Eq. (B.4.2) we obtain an upper limit for the rotational energy loss

$$\dot{E}_{rot} < \begin{cases} -9.05 \times 10^{32} \text{ erg s}^{-1}, & M = M_{max} \\ -4.49 \times 10^{34} \text{ erg s}^{-1}, & M = M_{min} \end{cases}, \quad (\text{B.4.7})$$

which for any possible mass is larger than the observed X-ray luminosity of SGR 0418+5729,  $L_X = 6.2 \times 10^{31} \text{ erg s}^{-1}$ , assuming a distance of 2 kpc (Rea et al., 2010).

The corresponding upper limits on the surface magnetic field of SGR 0418+5729, obtained from Eq. (B.4.3) are (see also Table B.14)

$$B < \begin{cases} 1.19 \times 10^7 \text{ G}, & M = M_{min} \\ 3.49 \times 10^8 \text{ G}, & M = M_{max} \end{cases}. \quad (\text{B.4.8})$$

It is worth noting that the above maximum possible value of the surface magnetic field of SGR 0418+5729 obtained for the maximum possible mass of a WD with rotation period 9.08 s,  $B < 3.49 \times 10^8 \text{ G}$ , is even more stringent and improves the previously value given by Malheiro et al. (2012),  $B < 7.5 \times 10^8 \text{ G}$ , based on fiducial WD parameters.

The electron cyclotron frequency expected from such a magnetic field is

$$f_{cyc,e} = \frac{eB}{2\pi m_e c} = \begin{cases} 3.33 \times 10^{13} \text{ Hz}, & M = M_{min} \\ 9.76 \times 10^{14} \text{ Hz}, & M = M_{max} \end{cases}, \quad (\text{B.4.9})$$

corresponding to wavelengths 9.04 and 0.31  $\mu\text{m}$ , respectively.

### Prediction of the spin-down rate

Assuming that the observed X-ray luminosity of SGR 0418+5729 equals the rotational energy loss  $\dot{E}_{\text{rot}}$ , we obtain the lower limit for the spin-down rate

$$\dot{P} > \frac{L_X P^3}{4\pi^2 I} = \begin{cases} 8.28 \times 10^{-18}, & M = M_{\text{min}} \\ 4.11 \times 10^{-16}, & M = M_{\text{max}} \end{cases}, \quad (\text{B.4.10})$$

which in the case of the WD with the maximum possible mass is more stringent than the value reported by Malheiro et al. (2012),  $\dot{P} = 1.18 \times 10^{-16}$ , for a massive WD of fiducial parameters.

### Optical spectrum and luminosity

Durant et al. (2011) observed SGR 0418+5729 with the two wide filters F606W and F110W of the Hubble Space Telescope, and derive the upper limits of the apparent magnitudes,  $m_{F606W} > 28.6$  and  $m_{F110W} > 27.4$  (Vega system), within the positional error circle derived from Chandra observations of the field of SGR 0418+5729 (Rea et al., 2010). The approximate distance to the source is  $d = 2$  kpc (see Durant et al., 2011, for details). Assuming an interstellar extinction obtained from the  $N_H$  column absorption value observed in the X-ray data,  $A_V = 0.7$ , Durant et al. (2011) obtained the corresponding luminosity upper bounds  $L_{F606W} < 5 \times 10^{28}$  erg s $^{-1}$  and  $L_{F110W} < 6 \times 10^{28}$  erg s $^{-1}$ , respectively.

We use here a similar technique, i.e. computing the interstellar extinction values for the V band from the  $N_H$  column absorption value observed in the X-ray data,  $N_H = 1.5 \times 10^{21}$  cm $^{-2}$  (Rea et al., 2010), and then using the empirical formula described in (Predehl and Schmitt, 1995). Then we have extrapolated the extinction to the other filters by using the method delineated in (Cardelli et al., 1989). Since the F606W and the F110W are well approximated by the V and J band, we obtained for the extinction values  $A_{F606W} = 0.83$  and  $A_{F110W} = 0.235$  respectively. The corresponding luminosity upper bounds are, consequently,  $L_{F606W} < 6.82 \times 10^{28}$  erg s $^{-1}$  and  $L_{F110W} < 3.05 \times 10^{28}$  erg s $^{-1}$ .

An estimate of the effective surface temperature can be obtained by approximating the spectral luminosity in these bands by the black body luminosity

$$L = 4\pi R^2 \sigma T^4, \quad (\text{B.4.11})$$

where  $\sigma = 5.67 \times 10^{-5}$  erg cm $^{-2}$  s $^{-1}$  K $^{-4}$  is the Stefan-Boltzmann constant. For a WD of fiducial radius  $R = 10^8$  cm, the upper limits for the WD surface temperature,  $T < 9.58 \times 10^3$  K and  $T < 9.15 \times 10^3$  K, can be obtained for the

F110W and F606W filters, replacing the upper limits for  $L_{F110W}$  and  $L_{F606W}$  in Eq. (B.4.11).

The above bounds of the surface temperature of the WD can be improved by using the explicit dependence on the radius of the black body surface temperature for each filter. The black body flux at a given frequency  $\nu$ , in the source frame, is given by

$$\nu f_\nu = \pi \frac{2h}{c^2} \frac{\nu^4}{\exp[h\nu/(kT)] - 1}, \quad (\text{B.4.12})$$

where  $h$ ,  $k$ , and  $\nu$  are the Planck constant, the Boltzmann constant, and the spectral frequency respectively. From this expression we can obtain the temperature as a function of the frequency, the observed flux, the distance  $d$  and radius  $R$  of the black body source

$$T = \frac{h\nu}{k \ln \left( 1 + \frac{\pi 2h\nu^4 R^2}{c^2 d^2 F_{\nu,\text{obs}}} \right)}, \quad (\text{B.4.13})$$

where we have used the relation between the flux in the observed and source frames,  $F_{\nu,\text{obs}} = (R/d)^2 \nu f_\nu$ .

The observed fluxes, in units of  $\text{erg}, \text{cm}^{-2}, \text{s}^{-1}$ , corrected for the extinction are given by

$$F_{\nu,\text{obs}}^{F606W} = 3.6 \times 10^{-20} \nu_{F606W} \times 10^{0.4(m_{F606W} - A_{F606W})}, \quad (\text{B.4.14})$$

and

$$F_{\nu,\text{obs}}^{F110W} = 1.8 \times 10^{-20} \nu_{F110W} \times 10^{0.4(m_{F110W} - A_{F110W})}, \quad (\text{B.4.15})$$

where  $\nu_{F606W} = 5.07 \times 10^{14}$  Hz and  $\nu_{F110W} = 2.60 \times 10^{14}$  Hz.

Introducing the upper limits of the apparent magnitudes of Durant et al. (2011) with the extinction values computed in this work, Eq. (B.4.13) gives the upper bounds on the temperature

$$T < \begin{cases} \frac{1.25 \times 10^4}{\ln(1+0.44R_8^2)} & \text{K, F110W} \\ \frac{2.43 \times 10^4}{\ln(1+6.35R_8^2)} & \text{K, F606W} \end{cases}, \quad (\text{B.4.16})$$

where  $R_8^2$  is the radius of the WD in units of  $10^8$  cm and, following Durant et al. (2011), we have approximated the band integrated flux as  $\nu_c F_\nu$ , with  $\nu_c$  the pivot wavelength of the corresponding band filter.

In Fig. B.30, we show the constraints on the  $T$ - $R$  relation obtained from Eq. (B.4.16). We have used the range of radii defined by the minimum and maximum radius of SGR 0418+5729 inferred from the WD stability analysis and summarized in Table B.14. It is clear that the optical observational constraints are in agreement with a model based on a massive fast rotat-

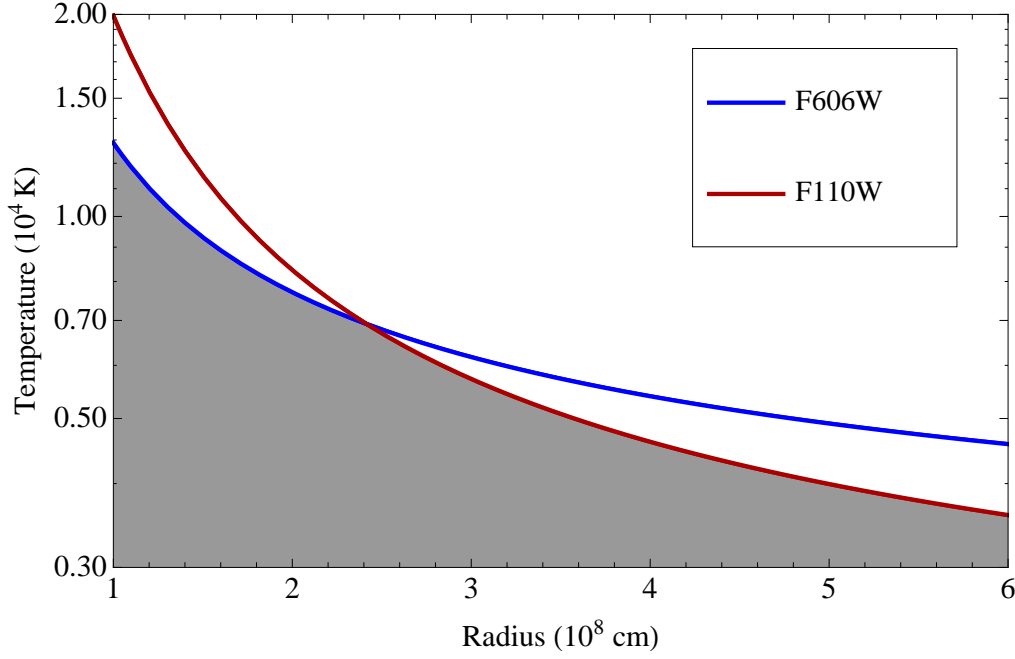


**Figure B.30.:** Temperature-Radius constraint given by Eq. (B.4.16). The gray region corresponds to the possible values for the temperature and the radius of the WD. The range of radii correspond to the one defined by the minimum and maximum radius of SGR 0418+5729 inferred from the WD stability analysis and summarized in Table B.14, namely  $R_{min} \leq R \leq R_{max}$ .

ing highly magnetic WD for SGR 0418+5729. It is appropriate to recall in this respect the observed range of temperatures of massive isolated WDs  $1.14 \times 10^4 \text{ K} \leq T \leq 5.52 \times 10^4 \text{ K}$ ; see Table 1 in (Ferrario et al., 2005).

Malheiro et al. (2012) obtained for a WD of fiducial parameters the upper limits for the WD surface temperature,  $T < 3.14 \times 10^4$ . We now improve these bounds on the surface temperature using realistic WD parameters. From the minimum and maximum values we have obtained for the equatorial radius of SGR 0418+5729 (see Table B.14) we obtain for the F110W filter

$$T_{F110W} < \begin{cases} 3.94 \times 10^3 \text{ K}, & M = M_{min} \\ 2.90 \times 10^4 \text{ K}, & M = M_{max} \end{cases}, \quad (\text{B.4.17})$$

and for the F606W filter

$$T_{F606W} < \begin{cases} 4.22 \times 10^3 \text{ K}, & M = M_{min} \\ 1.13 \times 10^4 \text{ K}, & M = M_{max} \end{cases}. \quad (\text{B.4.18})$$

These values are in agreement with a WD description of SGR 0418+5729. In this respect it is worth recalling the optical observations of 4U 0142+61

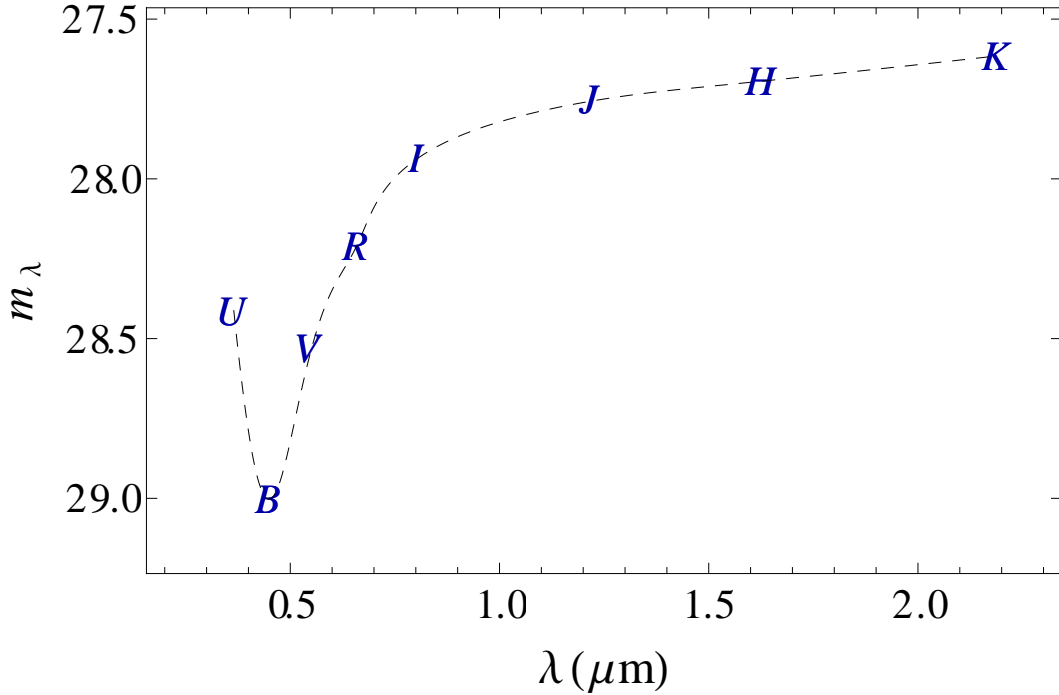


**Figure B.31.:** Expected optical magnitudes for the progenitor WD of SGR 0418+5729 obtained assuming a simple blackbody for the spectral emission from a WD with surface temperature  $T = 10^4$  K and a radius of  $1.5 \times 10^8$  cm, according to the constraints shown in Fig. B.30.

of Hulleman et al. (2000) where the photometric results of the field of 4U 0142+61 at the 60-inch telescope on Palomar Mountain were found to be in agreement with a  $1.3M_\odot$  WD with a surface temperature  $\sim 4 \times 10^5$  K (see Hulleman et al., 2000, for details).

We show in Fig. B.31 the expected optical magnitudes of a WD with surface temperature  $T = 10^4$  K and radius  $R = 1.5 \times 10^8$  cm, located at a distance of 2 kpc. This radius corresponds to the upper limit given by the gray region shown in Fig. B.30, for this specific value of the temperature.

### B.4.5. Swift J1822.3–1606

#### Bounds of the WD parameters

Swift J1822.3–1606 (or SGR 1822–1606) was recently discovered in July 2011 by Swift Burst Alert Telescope (BAT). A recent X-ray timing monitoring with Swift, RXTE, Suzaku, and XMM-Newton satellites found that SGR 1822-1606 rotates with a period of  $P = 8.44$  s and slows down at a rate  $\dot{P} = 9.1 \times 10^{-14}$  (see Rea et al., 2012, for details). The corresponding rotation angular velocity of the source is  $\Omega = 2\pi/P = 0.74$  rad s $^{-1}$ . Bounds for the mass, equatorial radius, and moment of inertia of SGR 0418+5729 obtained by the request of

Comp.	$M_{min}$	$M_{max}$	$R_{eq}^{min}$	$R_{eq}^{max}$	$\bar{R}_{min}$	$\bar{R}_{max}$	$I_{48}^{min}$	$I_{50}^{max}$	$B_{min}(10^7\text{G})$	$B_{max}(10^9\text{G})$
He	1.21	1.41	1.16	6.61	1.15	5.99	3.59	1.38	4.84	1.09
C	1.17	1.39	1.05	6.55	1.05	5.93	2.86	1.32	4.87	1.31
O	1.16	1.38	1.08	6.53	1.08	5.91	3.05	1.83	5.80	1.24
Fe	0.95	1.11	2.21	6.11	2.20	5.53	12.9	0.94	5.09	0.30

**Table B.15.:** Bounds for the mass  $M$  (in units of  $M_{\odot}$ ), equatorial  $R_{eq}$  and mean  $\bar{R}$  radius (in units of  $10^8$  cm), moment of inertia  $I$ , and surface magnetic field  $B$  of Swift J1822.3–1606.  $I_{48}$  and  $I_{50}$  is the moment of inertia in units of  $10^{48}$  and  $10^{50}$  g cm<sup>2</sup>, respectively.

the rotational stability of the rotating WD, as described in Section B.4.4, are shown in Table B.14.

### Solidification and glitches

The mean density of SGR 1822–1606 is in the range  $1.98 \times 10^6 \lesssim \bar{\rho} \lesssim 5.70 \times 10^8$  g cm<sup>3</sup>. The crystallization temperature for such a range following Eq. (B.4.4) is then in the range  $4.51 \times 10^6$  K  $\lesssim T_{\text{cry}} \lesssim 2.97 \times 10^7$  K, which indicates that SGR 1822-1606 will likely behave as a rigid solid body.

For the minimum and maximum mass configurations and the spin-down rate  $\dot{P} = 9.1 \times 10^{-14}$ , we obtain a lower limit for recurrence time of starquakes

$$\delta t_q > \begin{cases} 2 \times 10^8 (|\Delta P|/P) \text{ yr,} & M = M_{min} \\ 1 \times 10^{11} (|\Delta P|/P) \text{ yr,} & M = M_{max} \end{cases}, \quad (\text{B.4.19})$$

which for a typical fractional change of period  $|\Delta P|/P \sim 10^{-6}$  gives  $\delta t_q > 2 \times 10^2$  yr and  $\delta t_q > 1 \times 10^5$  yr, for  $M_{min}$  and  $M_{max}$  respectively. The long recurrence time for starquakes obtained in this case, confirms the similarities between SGR 1822–1606 and SGR 0418+5729 as old objects with a settling down magnetospheric activity.

### Rotation power and magnetic field

Using the observed values of  $P$  and  $\dot{P}$ , we obtain from Eq. (B.4.2) a rotational energy loss

$$\dot{E}_{\text{rot}} < \begin{cases} -1.71 \times 10^{34} \text{ erg s}^{-1}, & M = M_{max} \\ -7.89 \times 10^{35} \text{ erg s}^{-1}, & M = M_{min} \end{cases}, \quad (\text{B.4.20})$$

which amply justifies the observed X-ray luminosity of SGR 1822–1606,  $L_X = 4 \times 10^{32}$  erg s<sup>-1</sup>, obtained assuming a distance of 5 kpc (see Rea et al., 2012, for details).

The surface magnetic field of SGR 1822.3-1606, as given by Eq. (B.4.3), is

then between the values (see Table B.15)

$$B = \begin{cases} 3.63 \times 10^7 \text{ G}, & M = M_{min} \\ 1.30 \times 10^9 \text{ G}, & M = M_{max} \end{cases}. \quad (\text{B.4.21})$$

Corresponding to the above magnetic fields, the electron cyclotron frequencies are

$$f_{cyc,e} = \frac{eB}{2\pi m_e c} = \begin{cases} 1.01 \times 10^{14} \text{ Hz}, & M = M_{min} \\ 3.63 \times 10^{15} \text{ Hz}, & M = M_{max} \end{cases}, \quad (\text{B.4.22})$$

that correspond to wavelengths 2.96 and 0.08  $\mu\text{m}$ , respectively.

### Optical spectrum and luminosity

Rea et al. (2012) observed the field of SGR 1822–1606 with the Gran Telescopio Canarias (GranTeCan) within the Swift-XRT position (Pagani et al., 2011). Three sources (S1, S2, and S3) were detected with the Sloan  $z$  filter with corresponding  $z$ -band magnitudes  $m_{z,S1} = 18.13 \pm 0.16$ ,  $m_{z,S2} = 20.05 \pm 0.04$ , and  $m_{z,S3} = 19.94 \pm 0.04$  (see Rea et al., 2012, for details). No additional objects were found to be consistent with the Swift-XRT position up to a magnitude  $m_z = 22.2 \pm 0.2$  ( $3\sigma$ ).

In addition, data from the UK Infrared Deep Sky Survey (UKIDSS) for the field of SGR 1822–1606 were found to be available, giving the magnitudes of the three aforementioned sources in the  $J$ ,  $H$ , and  $K$  bands;  $m_{J,i} = (13.92, 16.62, 16.43)$ ,  $m_{H,i} = (12.37, 15.75, 15.40)$ , and  $m_{K,i} = (11.62, 15.20, 14.88)$ , where the index  $i$  indicates the values for the sources S1, S2, and S3. In addition to S1, S2, and S3, no sources were detected within the consistent position up to the limiting magnitudes  $m_J = 19.3$ ,  $m_H = 18.3$ , and  $m_K = 17.3$  ( $5\sigma$ ).

We repeat the same analysis for SGR 0418+5729 to the case of SGR 1822–1606. We consider only the upper limits, since the three sources reported in Rea et al. (2012), S1, S2 and S3, are very luminous to be a WD at the distance considered for the SGR,  $d \approx 5$  kpc. From the NH column density value,  $N_H = 7 \times 10^{21} \text{ cm}^{-2}$  we obtain an extinction in the  $V$ -band of  $A_V = 3.89$ . From the Cardelli et al. (1989) relation we obtain the extinction values for the four bands considered,  $A_z = 1.86$ ,  $A_J = 1.10$ ,  $A_H = 0.74$  and  $A_K = 0.44$ . The extinction corrected upper limits do not put very strong constraints to the temperature and the radius of the WD, due to the very large distance assumed for SRG 1822–1606. We show in Fig B.32 the expected extinction-corrected magnitudes for a WD with a temperature  $T = 10^4$  K and a radius  $R = 1.5 \times 10^8$  cm at a distance of 5 kpc. We obtain a very deep value for the  $K$ -band of  $\approx 30$ . We conclude that, if SGR 1822–1606 is at the distance of 5 kpc introduced by Rea et al. (2012), it will be hard to detect the WD. On the contrary, a possible detection would lead to a more precise determination of

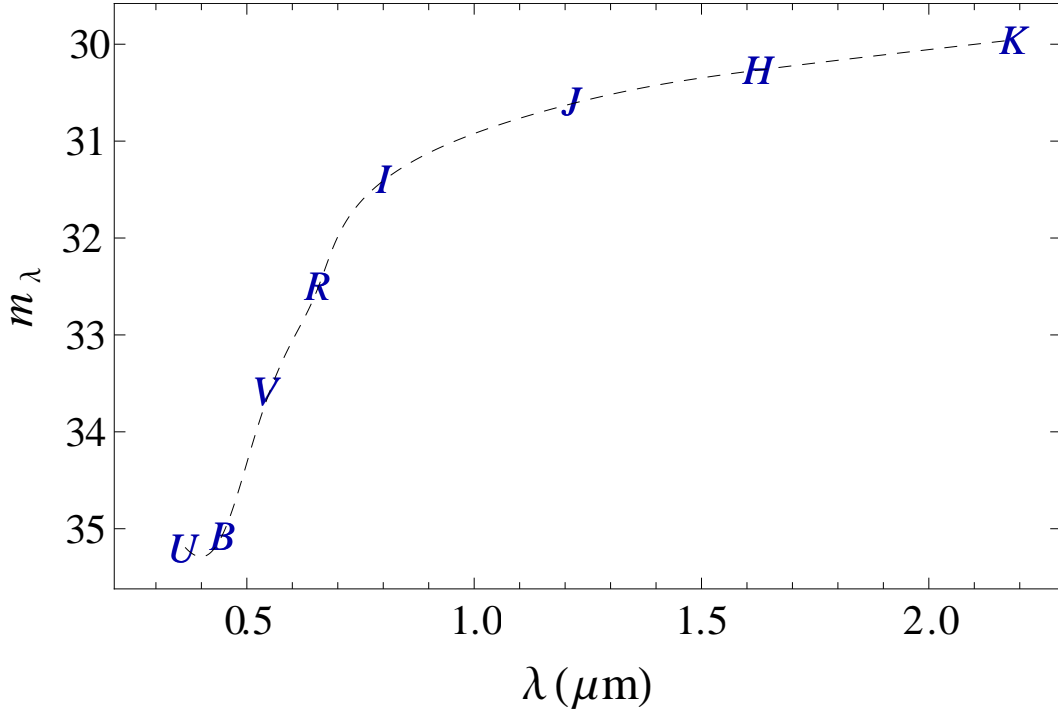


**Figure B.32.:** Expected optical magnitudes of SGR 1822–1606 assuming a blackbody spectral emission from a WD with surface temperature  $T = 10^4$  K and a radius of  $1.5 \times 10^8$  cm.

the distance.

#### B.4.6. Concluding Remarks

The recent observations of SGR 0418+5729 (Rea et al., 2010),  $P = 9.08$  and  $\dot{P} < 6.0 \times 10^{-15}$ , and Swift J1822.3-1606 (Rea et al., 2012),  $P = 8.44$  s and  $\dot{P} = 9.1 \times 10^{-14}$ , challenge the description of these sources as ultramagnetized NSs of the magnetar model of SGRs and AXPs. Based on the recent work of Malheiro et al. (2012), we have shown here that, instead, both SGR 0418+5729 and Swift J1822.3-1606 are in full agreement with a description based on massive fast rotating highly magnetic WDs.

From an analysis of the rotational stability of the WD using the results of Boshkayev et al. (2012), we have predicted the WD parameters. In particular, bounds for the mass, radius, moment of inertia, and magnetic field of SGR 0418+5729 and Swift J1822.3-1606 have been presented (see Tables B.14 and B.15, for details).

We have improved the theoretical prediction of the lower limit for the spin-down rate of SGR 048+5729, for which only the upper limit,  $\dot{P} < 6.0 \times 10^{-15}$  Rea et al. (2010), is currently known. Based on a WD of fiducial parameters, Malheiro et al. (2012) predicted for SGR 0418+5729 the lower limit

$\dot{P} > 1.18 \times 10^{-16}$ . Our present analysis based on realistic general relativistic rotating WDs allows us to improve such a prediction, see Eq. (B.4.10) for the new numerical values.

We have given in Eqs. (B.4.9) and (B.4.22) an additional prediction of the electron cyclotron frequencies of SGR 0418+5729 and Swift J1822.3-1606, respectively. The range we have obtained for such frequencies fall into the optical and infrared bands.

We have also presented the optical properties of SGR 0418+5729 and Swift J1822.3-1606 as expected from a model based on WDs. In particular, the surface temperature of the WD has been inferred and predictions for the emission fluxes in the UV, Optical, and Infrared bands have been given. Follow-on missions of Hubble and VLT are strongly recommended to establish the precise values of the luminosity in the Optical and in the near-Infrared bands, which will verify the WD nature of SGRs and AXPs.

We encourage future observational campaigns from space and ground to verify all the predictions presented in this work.

## B.5. White Dwarf Mergers as Progenitors of SGRs and AXPs: the case of 4U 0142+61

It has been recently pointed out by Malheiro et al. (2012) how the pioneering works of Morini et al. (1988) and Paczynski (1990) on the description of 1E 2259+586 as a white dwarf (WD) can be indeed extended to all SGRs and AXPs, as an alternative to the magnetar model (Duncan and Thompson, 1992; Thompson and Duncan, 1995). These WDs have been assumed to have fiducial parameters  $M = 1.4M_{\odot}$ ,  $R = 10^3$  km,  $I = 10^{49}$  g cm<sup>2</sup>, and magnetic fields  $B \gtrsim 10^7$  G, inferred from the observed rotation periods and spin-down rates. The energetics of SGRs and AXPs including their steady emission, glitches, and their subsequent outburst activities have been shown to be powered by the rotational energy of the WD. The occurrence of a glitch, the associated sudden shortening of the period, as well as the corresponding gain of rotational energy, can be explained by the release of gravitational energy associated with a sudden contraction and decrease of the moment of inertia of the uniformly rotating WD, consistent with the conservation of their angular momentum.

The rotational stability of fast rotating WDs was implicitly assumed by Malheiro et al. (2012). The crucial question of whether rotating WDs can or not attain rotation periods as short as the ones observed in SGRs and AXPs has been recently addressed by Boshkayev et al. (2012). The properties of uniformly rotating WDs were computed within the framework of general relativity using the Hartle's formalism (Hartle, 1967). The equation of state for cold WD matter is based on the relativistic Feynman-Metropolis-Teller treatment Rotondo et al. (2011c,b), which generalizes the equation of state of Salpeter (1961b). The stability of rotating WDs was analyzed taking into account the mass-shedding limit, inverse  $\beta$ -decay and pycnonuclear instability, as well as secular axisymmetric instability, with the latter determined by the turning point method of Friedman et al. (1988); see Boshkayev et al. (2012), for details. It was there found that the minimum rotation periods of WDs are  $\sim 0.3, 0.5, 0.7$  and  $2.2$  seconds <sup>4</sup>He, <sup>12</sup>C, <sup>16</sup>O, and <sup>56</sup>Fe WDs respectively, and the maximum masses for the same compositions are  $\sim 1.500, 1.474, 1.467, 1.202 M_{\odot}$ . Thus, this range of minimum rotation periods of massive WDs implies the rotational stability of SGRs and AXPs, which possess observed rotation periods  $2 \lesssim P \lesssim 12$  seconds. The relatively long minimum period of <sup>56</sup>Fe WDs,  $P_{min} \sim 2.2$  seconds, implies that the WDs describing SGRs and AXPs have to be composed of nuclei lighter than <sup>56</sup>Fe, e.g. <sup>12</sup>C or <sup>16</sup>O.

It is important to recall that the existence of fast rotating WDs with magnetic fields larger than  $10^6$  G all the way up to  $10^9$  G is solidly confirmed by observations; see e.g. Külebi et al. (2009), Külebi et al. (2010a) and Kepler et al. (2010). Even more strikingly is the fact that most of the observed magnetized WDs are massive; e.g. REJ 0317-853 with  $M \sim 1.35M_{\odot}$  and  $B \sim (1.7-$

$6.6) \times 10^8$  G (see e.g. Barstow et al., 1995; Külebi et al., 2010b); PG 1658+441 with  $M \sim 1.31M_{\odot}$  and  $B \sim 2.3 \times 10^6$  G (see e.g. Liebert et al., 1983; Schmidt et al., 1992); and PG 1031+234 with the highest magnetic field  $\sim 10^9$  G (see e.g. Schmidt et al., 1986; Külebi et al., 2009).

It has been recently shown by García-Berro et al. (2012) that massive magnetized WDs might be indeed the outcome of WD mergers. The merger as well as the subsequent evolution of the newly born massive magnetized WD are followed-up through Smoothed Particle Hydrodynamics (SPH) simulations. The result of the merging process is a WD that contains the mass of the undisrupted primary, with a hot corona made of about half of the mass of the disrupted secondary. In addition, a surrounding rapidly rotating Keplerian disk can be found. The mass of the disk is almost all the mass of the secondary that is not part of the hot corona because only a negligible part of the mass  $\sim 10^{-3}M_{\odot}$  is ejected during the merging. The strong magnetic field is the result of an efficient  $\alpha\omega$  dynamo mechanism. The efficiency of the dynamo is guaranteed by the high number of convective cycles before the energy of the hot corona is radiated away. The misalignment of the final magnetic dipole moment of the newly born WD with the rotation axis depends on the difference of the masses of the WD components of the binary (see García-Berro et al., 2012, for details).

We apply the above considerations to the specific case of 4U 0142+61 that is by far the best observed source in the near-Infrared (NIR), optical, and Ultra-Violet (UV) spectral bands. We first describe 4U 0142+61 as a general relativistic uniformly rotating  $^{12}\text{C}$  WD following the work of Boshkayev et al. (2012). From the request of equilibrium and using the observed values of the rotation period  $P$  and spin-down rate  $\dot{P}$ , we obtain theoretical bounds for the mass, polar and equatorial radii, moment of inertia, and magnetic field of 4U 0142+61. We then use this bounds to constrain the masses of the components of the WD binary progenitor. With the knowledge of the binary components, we perform the SPH simulations of the merger and follow the evolution of the resulting WD, based on (García-Berro et al., 2012). We show that the emission properties of this new massive fast rotating and highly magnetized WD fully agree with these observations, being the disk around the WD the responsible for the NIR emission while, the optical and UV emission, is due to the surface temperature of the WD. We give details of the WD and disk structure as well as the parameters of the binary progenitor.

We now turn to the stability of general relativistic uniformly rotating WDs. In Fig. B.33 we show the mass-equatorial radius relation of  $^{12}\text{C}$  WD for different values of the rotation period of the star, following (Boshkayev et al., 2012). All stable WDs are inside the filled region and dashed curves correspond sequences of constant rotation period. It can be seen that each  $P = 2\pi/\Omega = \text{constant}$  sequence intersects the stability region in two points. Here  $\Omega$  is the angular velocity of the WD. These two points determine the mini-

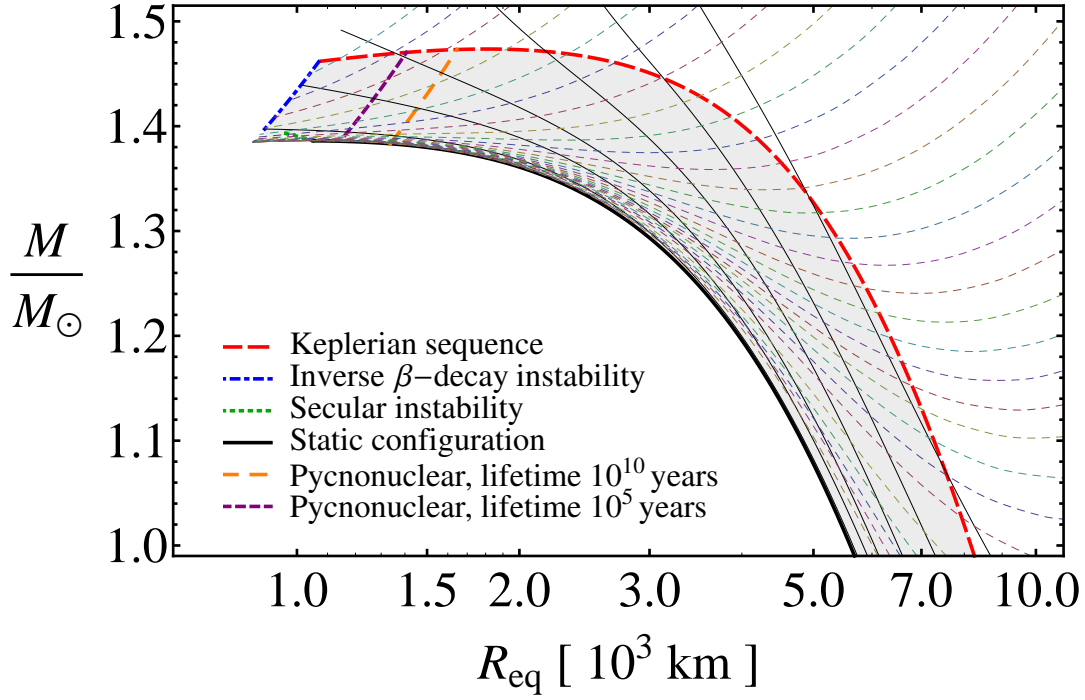


**Figure B.33.:** Mass versus equatorial radius of rotating  $^{12}\text{C}$  WDs (Boshkayev et al., 2012). The solid black curves correspond to  $J$ -constant sequences, where the static case  $J = 0$  the thickest one. The color thin-dashed curves correspond to  $P$ -constant sequences. The Keplerian sequence is the red thick dashed curve, the blue thick dotted-dashed curve is the inverse  $\beta$  instability boundary, and the green thick dotted curve is the axisymmetric instability line. The orange and purple dashed boundaries correspond to the pycnonuclear C+C fusion densities with reaction mean times  $\tau_{pyc} = 10 \text{ Gyr}$  and  $0.1 \text{ Myr}$ , respectively. The gray-shaded region is the stability region of rotating white dwarfs.

mum(maximum) and maximum(minimum)  $M_{min,max}(R_{eq}^{max,min})$ , respectively, for the stability of a WD with a given rotation period  $P$ . Associated to the boundary values  $M_{min,max}$  and  $R_{eq}^{max,min}$ , we can obtain the corresponding bounds for the moment of inertia of the WD,  $I_{max,min}$ , respectively.

The loss of rotational energy associated with the spin-down of the WD is given by

$$\dot{E}_{rot} = -4\pi^2 I \frac{\dot{P}}{P^3} = -3.95 \times 10^{50} I_{49} \frac{\dot{P}}{P^3} \text{ ergs}^{-1}, \quad (\text{B.5.1})$$

where  $I_{49}$  is the moment of inertia of the WD in units of  $10^{49} \text{ g cm}^2$ .

The upper limit on the magnetic field (see e.g. Ferrari and Ruffini, 1969) obtained by requesting that the rotational energy loss due to the dipole field

$M_{min}$ ( $M_{\odot}$ )	1.16
$M_{max}$ ( $M_{\odot}$ )	1.39
$R_{eq}^{min}$ ( $10^8$ cm)	1.05
$R_{eq}^{max}$ ( $10^8$ cm)	6.66
$\bar{R}_{min}$ ( $10^8$ cm)	1.05
$\bar{R}_{max}$ ( $10^8$ cm)	6.03
$I^{min}$ ( $10^{48}$ g cm <sup>2</sup> )	2.86
$I^{max}$ ( $10^{50}$ g cm <sup>2</sup> )	1.36
$B_{min}$ ( $10^8$ G)	2.26
$B_{max}$ ( $10^9$ G)	6.28

**Table B.16.:** Bounds for the mass  $M$ , equatorial  $R_{eq}$  and mean  $\bar{R}$  radius, moment of inertia  $I$ , and surface magnetic field  $B$  of 4U 0142+61.

be smaller than the electromagnetic emission of the magnetic dipole, is given by

$$B = \sqrt{\frac{3c^3}{8\pi^2} \frac{I}{\bar{R}^6} P\dot{P}} = 3.2 \times 10^{15} \sqrt{\frac{I_{49}}{\bar{R}_8^6} P\dot{P}} \text{ G}, \quad (\text{B.5.2})$$

where  $\bar{R}_8$  is the mean radius of the WD in units of  $10^8$  cm. The mean radius is given by  $\bar{R} = (2R_{eq} + R_p)/3$  (see e.g. Hartle and Thorne, 1968) with  $R_{eq}$  and  $R_p$  the equatorial and polar radius of the star.

4U 0142+61 rotates with a period  $P = 8.69$  s, and it is spinning down at a rate  $\dot{P} = 2.03 \times 10^{-12}$  (Hulleman et al., 2000). The corresponding rotation angular velocity of the source is  $\Omega = 2\pi/P = 0.72$  rad s<sup>-1</sup>. We show in Table B.16 bounds for the mass, equatorial radius, mean radius, and moment of inertia of SGR 0418+5729 obtained by the request of the rotational stability of the rotating WD, for selected chemical compositions.

Using the observed values of  $P$  and  $\dot{P}$ , we obtain from Eq. (B.5.1) a rotational energy loss  $|\dot{E}_{rot}| < 3.44 \times 10^{35}$ ,  $1.71 \times 10^{37}$  erg s<sup>-1</sup> and a magnetic field  $B = 3.49 \times 10^8$ ,  $1.19 \times 10^7$ , correspondingly to  $M = M_{max}$  and  $M_{min}$  respectively. Thus, the rotational energy loss amply covers the observed X-ray luminosity,  $L_X = 1.1 \times 10^{35}$  erg s<sup>-1</sup>, assuming a distance of 3.6 kpc (see Juett et al., 2002, for details). For the above magnetic field bounds, the electron cyclotron frequencies are  $\nu_{cyc,e} = eB/(2\pi m_e c) = 9.76 \times 10^{14}$  and  $3.33 \times 10^{13}$  Hz, that correspond to wavelengths that fall between the UV and the NIR, 0.31 and 9.01  $\mu\text{m}$ , respectively.

We turn to the observations of 4U 0142+61 in the IR, optical and UV bands. The observed magnitudes not corrected for the extinction are  $I = 23.84$ ,  $R = 24.89$ ,  $V = 25.62$ ,  $B = 28.1$  (Hulleman et al., 2004),  $J = 22.18$ ,  $H = 20.90$ ,  $K = 19.96$  (Durant and van Kerkwijk, 2006), and there is an upper limit in the  $U$ -band,  $U = 25.8$  (Dhillon et al., 2005). The absorptions in the  $V$ -band is  $A_V = 3.5 \pm 0.4$  for the distance  $d = 3.6$  kpc (Durant and van Kerkwijk,

2006). Using the relations in Table 3 of Cardelli et al. (1989), we compute the absorptions in the other bands as  $A_U = 1.569A_V$ ,  $A_B = 1.337A_V$ ,  $A_R = 0.751A_V$ ,  $A_I = 0.479A_V$ ,  $A_J = 1.569A_V$ ,  $A_H = 0.282A_V$ ,  $A_K = 0.114A_V$ .

We have fitted the spectrum of 4U 0142+61 as the sum of a black body component

$$F_{BB} = \pi \frac{2h}{c^2} \left( \frac{R_{wd}}{d} \right)^2 \frac{\nu^3}{e^{h\nu/(k_B T)} - 1}, \quad (\text{B.5.3})$$

where  $R_{wd}$  and  $T$  the radius and effective temperature of the WD, and a passive flat, opaque dust disk

$$F_{disk} = 12\pi^{1/3} \cos i \left( \frac{R_{wd}}{d} \right)^2 \left( \frac{2k_B T}{3h\nu} \right)^{8/3} \left( \frac{h\nu^3}{c^2} \right) \int_{x_{in}}^{x_{out}} \frac{x^{5/3}}{e^x - 1} dx, \quad (\text{B.5.4})$$

where  $i$  is the inclination angle of the disk, which we assume as zero degrees,  $x_{in} = h\nu/(k_B T_{in})$ ,  $x_{out} = h\nu/(k_B T_{out})$ , with  $T_{in}$  and  $T_{out}$  the temperatures of the disk at the inner and outer radii, respectively. These temperatures are related to the radii  $R_{in}$  and  $R_{out}$  of the disk through  $T_{in,out} = (2/3\pi)^{1/4} n (R_{wd}/R_{in,out})^{3/4} T$ .

The total flux is then given by  $F = F_{BB} + F_{disk}$ . We have fixed the values of  $R_{out} = 1.02R_\odot$  and find the best-fit of the rest of the parameters. The  $1\sigma$ - $3\sigma$  contour plot of the radius and temperature of the WD is shown in Fig. B.34; the best-fit is located at the center of the  $1\sigma$  red spot,  $R_{wd} = 0.0056R_\odot = 3.9 \times 10^8$  cm and  $T = 1.48 \times 10^5$  K.

The best-fit of the other parameters gives  $T_{in} = 2.37 \times 10^3$  K,  $T_{out} = 2.03 \times 10^3$  K, and  $R_{in} = 0.83R_\odot$ . We show in Fig. B.35 the observed spectrum of 4U 0142+61 in the IR, optical, and UV bands and the best-fit of the composite black body+disk model.

We turn now to the X-ray emission. Latest observations of 4U 0142+61 with the EPIC cameras on *XMM-Newton* indicate an unabsorbed X-ray flux  $f_X^{unabs} = 7.02 \times 10^{-11}$  erg s $^{-1}$  cm $^{-2}$  (Göhler et al., 2005). Assuming a distance  $d = 3.6$  kpc, this flux corresponds to an isotropic X-ray luminosity  $L_X = 4\pi d^2 f_X^{unabs} = 1.09 \times 10^{35}$  erg s $^{-1}$ , which is about twice the surface black body luminosity  $L_{BB} = 4\pi R_{wd}^2 \sigma T^4 = 5.2 \times 10^{34}$  erg s $^{-1}$ , where  $\sigma$  is the Stefan-Boltzmann constant. As we have shown, this contribution of the surface temperature explains the observations in the IR, optical, and UV bands. The time integrated X-ray spectrum of 4U 0142+61 is well described by a black body + power-law model with  $k_B T_{BB} = 0.4$  keV and photon index  $\Gamma = 3.62$  (see Göhler et al., 2005, for details). Such a black body component corresponds to a temperature  $T_{BB} \sim 4.6 \times 10^6$  K, higher than the surface temperature of the WD,  $T = 1.48 \times 10^5$  K. This is not surprising since we expect these systems to suffer the so-called *solar corona problem*; the temperature associated to the black body component of the solar corona spectrum,  $\sim 10^6$  K, is much higher

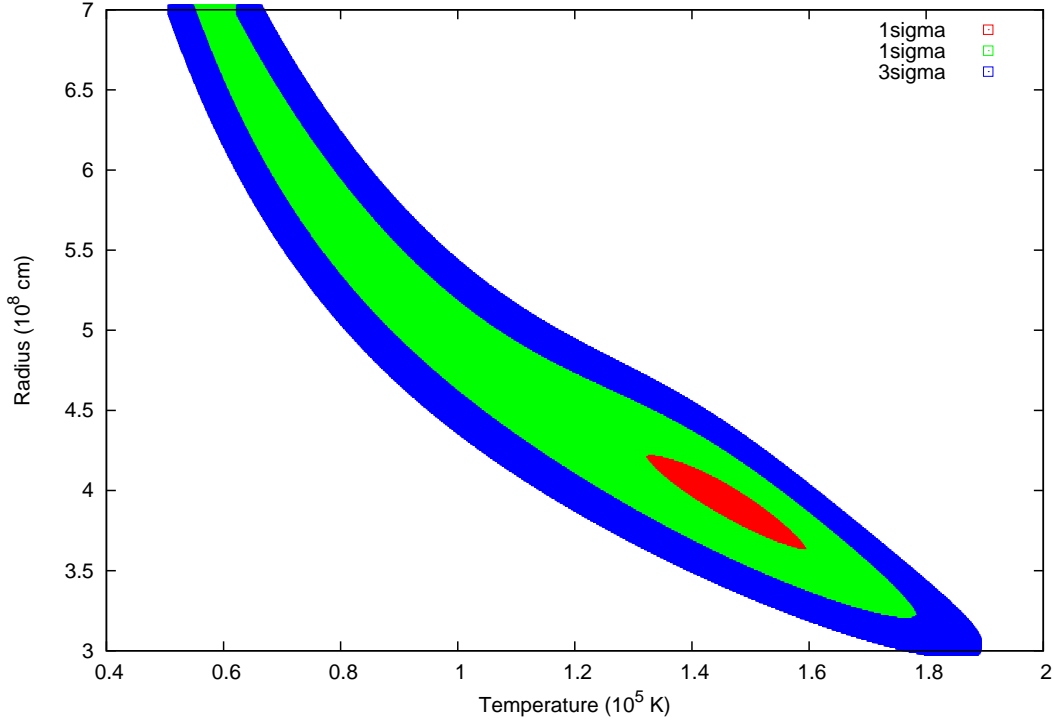


**Figure B.34.:**  $1\sigma$ - $3\sigma$  contours of the radius and temperature of the WD. The best-fit is at the center of the red spot,  $R_{wd} = 0.0056R_{\odot} = 3.9 \times 10^8$  cm and  $T = 1.48 \times 10^5$  K.

than the solar surface temperature  $\sim 6 \times 10^3$  K. This X-ray emission is thus very likely of magnetospheric origin. The solar X-ray luminosity is however million times smaller than the optical luminosity. We expect the  $L_X/L_{opt}$  ratio of rotation powered objects to be larger than in the case of slow not rotation powered objects. The extreme conditions in the magnetospheres of highly magnetized and fast rotating WDs certainly generate the conditions to produce a persistent high-energy (e.g. X-rays) radiation with similar mechanisms as the ones of pulsars.

Usov (1993) showed that indeed an X-ray luminosity  $\sim 10^{35}$  erg s $^{-1}$  can be generated by a fast rotating highly magnetized WD, and applied this idea to the specific case of the AXP 1E 2259+586. Following the Usov's idea, we calculate the theoretically expected X-ray luminosity of 4U 0142+61 and compare it with the observations. The most likely mechanism to produce X-rays in a magnetized WD is the reheating of the magnetosphere due to the bombardment of positrons moving backward toward the WD surface. Such positrons come from the electron-positron pair creation process occurring owing to the interaction of the high-energy photons with ultra-relativistic electrons. The cross-section for this process is  $\sigma_{\pm} \sim 10^{-26}$  cm $^2$ . Performing similar calculations we find that the polar caps reheating caused by the

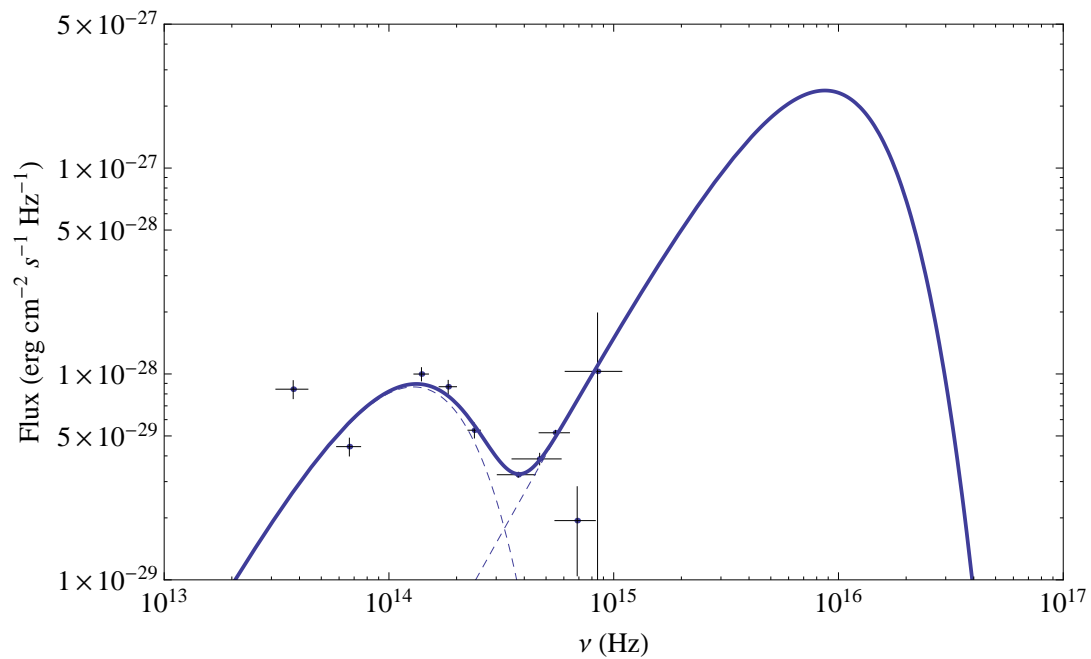


**Figure B.35.:** Observed and fitted spectrum of 4U 0142+61. The best-fit parameters of the black body+disk spectrum are  $R_{wd} = 0.0056R_{\odot} = 3.9 \times 10^8$  cm,  $T = 1.48 \times 10^5$  K,  $T_{in} = 2.37 \times 10^3$  K,  $T_{out} = 2.03 \times 10^3$  K, corresponding to  $R_{in} = 0.83R_{\odot}$  and  $R_{out} = 1.02R_{\odot}$ , respectively.

pair-created positrons could produce, using the parameters of 4U 0142+61m a persistent X-ray luminosity  $L_X \sim 2 \times 10^{35}$  erg s<sup>-1</sup>, in agreement with observations.

We performed SPH simulations of  $1 + 0.6 M_\odot$  WD mergers. The product of the merging process is a central WD with a hot corona surrounded by a hot disk. The results of the simulation are:  $R_{wd} = 0.006R_\odot$ ,  $R_{wd+cor} = 0.01R_\odot$ ,  $M_{wd} = 1.11M_\odot$ ,  $M_{disk} = 0.49M_\odot$ ,  $T_{in,disk} = 7.7 \times 10^8$  K,  $T_{out,disk} \approx 10^7$  K,  $I_{wd+cor} = 2 \times 10^{50}$  g cm<sup>2</sup>,  $\Omega = 0.38$  rad s<sup>-1</sup>,  $R_{in,disk} \approx R_{wd}$ ,  $R_{out,disk} \approx 0.1R_\odot$ . The properties of the central WD are in agreement with the ones we have inferred above from simple equilibrium requirements. It is important to recall that after the merging the system (WD+corona+disk) enters a braking and cooling process. We followed this subsequent cooling and find that both the WD and the disk cools to the values of our best-fit of 4U 0142+61 in a time of the order of kyr. The corona in this time is integrated into the central WD. The misalignment of the magnetic field as well as the magnetic dipole moment-disk coupling cause during this process the braking of the star. The braking rate will depend also on the accretion rate of the disk material onto the central WD. It implies that the initial angular velocity of the WD just after the merging must be higher than the currently observed value. The value of the magnetic field depends on the efficiency of the dynamo mechanism. García-Berro et al. (2012) showed that such an efficiency can be very high easily accommodating magnetic fields of up to  $10^{10}$  G.

We have seen that WD mergers leads to massive fast rotating highly magnetized WDs with similar properties to the ones required for the description of SGRs and AXPs. In particular, we showed that the WD that represents 4U 0142+61 can be the result of a  $1+0.6 M_\odot$  WD merger. We are currently performing additional merger simulations in order to obtain a better agreement of the angular velocity of the WD, which is the less accurate property we have obtained.

## B.6. Finite temperature effects on the mass-radius relation of white dwarfs

The extension of the relativistic Feynman-Metropolis-Teller equation of state to the case of finite temperatures has been discussed in App. A.3. The equation of state in the specific case of carbon is shown in Fig. B.36

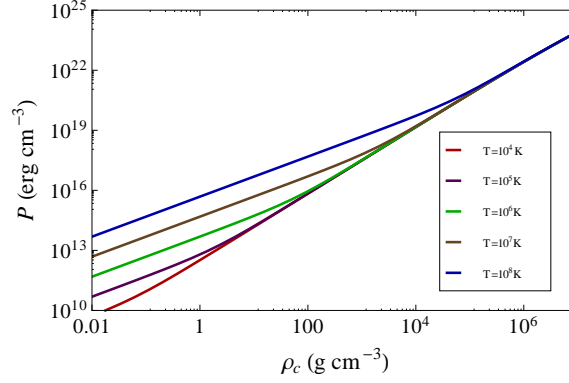


**Figure B.36.:** Total pressure as a function of the mass-density in the case of  $^{12}\text{C}$  for selected temperatures from  $T = 10^4\text{K}$  to  $T = 10^8\text{K}$ .

Now we use this new equation of state to construct equilibrium configurations of white dwarfs at finite temperatures. The equations of equilibrium to be integrated are the Einstein equations in the spherically symmetric case

$$\frac{dv(r)}{dr} = \frac{2G}{c^2} \frac{4\pi r^3 P(r)/c^2 + M(r)}{r^2 \left[1 - \frac{2GM(r)}{c^2 r}\right]}, \quad (\text{B.6.1})$$

$$\frac{dM(r)}{dr} = 4\pi r^2 \frac{\mathcal{E}(r)}{c^2}, \quad (\text{B.6.2})$$

$$\frac{dP(r)}{dr} = -\frac{1}{2} \frac{dv(r)}{dr} [\mathcal{E}(r) + P(r)], \quad (\text{B.6.3})$$

where  $v(r) = \ln(g_{00})$  and we have introduced the mass enclosed at the distance  $r$  through  $g_{11} = e^{\lambda(r)} = 1 - 2GM(r)/(c^2 r)$ ,  $\mathcal{E}(r)$  is the energy-density and  $P(r)$  is the total pressure.

We have integrated the Einstein equations for a wide range of central densities and temperatures, and chemical compositions. In Figs. B.37 and B.38 we show in particular our mass-radius and mass-density relation of  $^4\text{He}$  WDs.

It is clear that the effects of the temperature are particularly important at low densities, and hence for low-mass WDs. As an example, we analyze here the specific case of the WD companion of the pulsar PSR J1738+0333. This WD orbiting the pulsar is bright enough to allow an accurate optical spectroscopy and photometry, which has been recently presented by Antoniadis

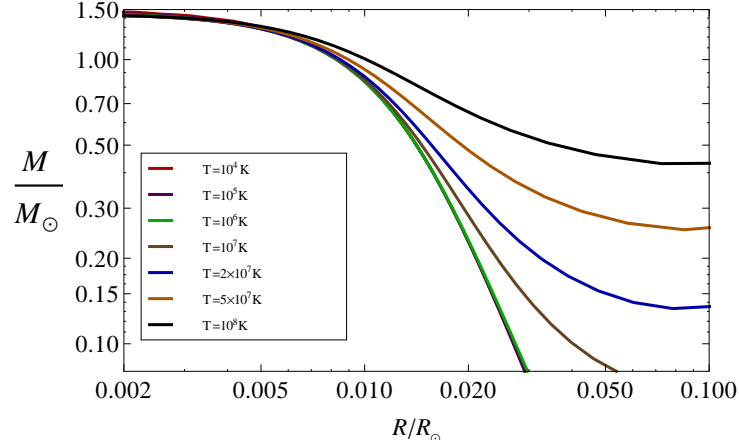


**Figure B.37.:** Total mass versus radius for  ${}^4\text{He}$  WDs for selected temperatures from  $T = 10^4$  K to  $T = 10^8$  K.

et al. (2012). From the spectroscopic and photometric study of the WD companion it has been possible to infer its radial-velocity curve, effective temperature, surface gravity and luminosity. The properties of WD are consistent with those of low-mass WDs with thick hydrogen envelopes.

The spectroscopy and photometry analysis leads to a surface temperature  $T_{eff} = 9130 \pm 150$  K, a logarithm of the surface gravity  $\log(g) = \log(GM_{wd}/R_{wd}^2) = 6.55 \pm 0.1$ , and a photometric WD radius  $R_{wd} = 0.042 \pm 0.004 R_{\odot}$ . In Fig. B.39 we show our theoretical  $\log(g)$  vs.  $M_{wd}$  for selected interior temperatures.

It is clear from Fig. B.39 that we identify the interior temperature of the WD in the range  $2 \times 10^7 \lesssim T \lesssim 5 \times 10^7$  K. The atmosphere analysis of Antoniadis et al. (2012) leads to a surface temperature of the WD  $T_{eff} \approx 9 \times 10^3$  K, so there is a large temperature gradient in the outer layers of the WD.

With the He cores mass-radius relations of Panei et al. (2000) at finite temperatures, Antoniadis et al. (2012) estimated, using the observed values of  $g$  and  $T_{eff}$ , the mass and radius of the WD  $M_{wd} = 0.181^{+0.007}_{-0.005} M_{\odot}$  and  $R_{wd} = 0.037^{+0.004}_{-0.003} R_{\odot}$ , respectively. It is simple to check that for these values of mass and radius, the internal temperature of the WD inferred from our mass-radius relation should be  $T \approx 2 \times 10^7$  K.

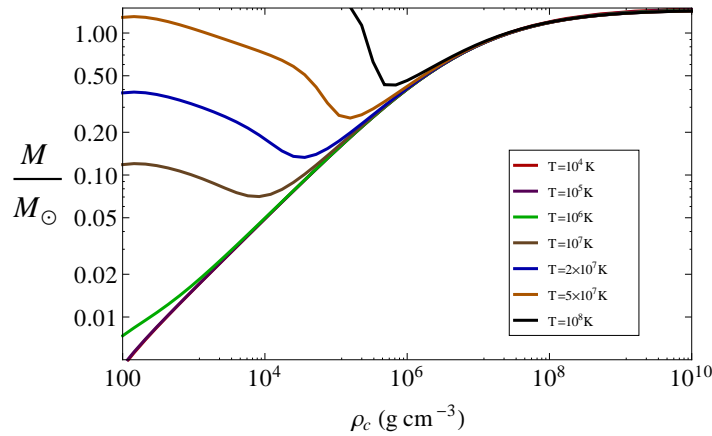


**Figure B.38.:** Total mass versus central density for  ${}^4\text{He}$  WDs for selected temperatures from  $T = 10^4$  K to  $T = 10^8$  K.

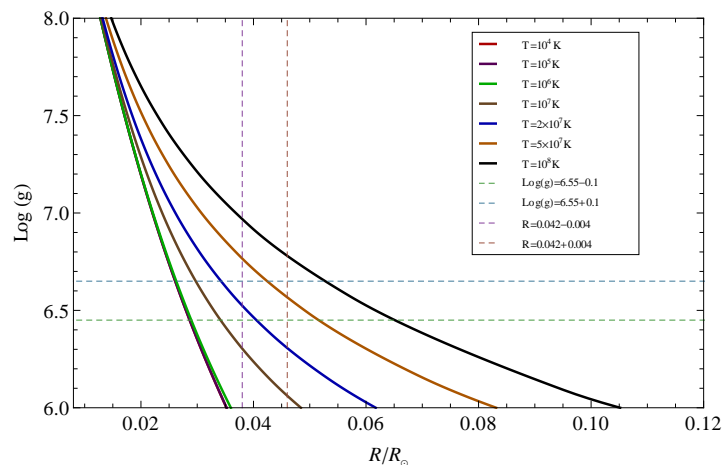


**Figure B.39.:** Logarithm of the surface gravity  $\log(g) = \log(GM_{wd}/R_{wd}^2)$  as a function of the mass-density for  ${}^4\text{He}$  WDs for selected temperatures from  $T = 10^4$  K to  $T = 10^8$  K. The horizontal dashed lines indicate the constant values  $\log(g) = 6.55 \pm 0.1$  and the vertical dashed curves indicate the constant radius values  $R_{wd} = 0.042 \pm 0.004 R_{\odot}$ .

# C. Neutron Stars Physics and Astrophysics

## C.1. The self-consistent general relativistic solution for a system of degenerate neutrons, protons and electrons in $\beta$ -equilibrium

### C.1.1. Introduction

The insurgence of critical electric fields in the process of gravitational collapse leading to vacuum polarization process (Ruffini et al., 2010b) has convinced us of the necessity of critically reexamining the gravitational and electro-dynamical properties in neutron stars. In this light we have recently generalized the Feynman, Metropolis and Teller treatment of compressed atoms to the relativistic regimes (Rotondo et al., 2011c). We have so enforced, self-consistently in a relativistic Thomas-Fermi equation, the condition of  $\beta$ -equilibrium extending the works of Popov (1971b), Zeldovich and Popov (1972), Migdal et al. (1976, 1977), Ferreira et al. (1980) and Ruffini and Stella (1981) for heavy nuclei. Thanks to the existence of scaling laws (see Rotondo et al. (2011c) and Ruffini (2008b)) this treatment has been extrapolated to compressed nuclear matter cores of stellar dimensions with mass numbers  $A \simeq (m_{\text{Planck}}/m_n)^3 \sim 10^{57}$  or  $M_{\text{core}} \sim M_{\odot}$ . Such configurations fulfill global but not local charge neutrality. They have electric fields on the core surface, increasing for decreasing values of the electron Fermi energy  $E_e^F$  reaching values much larger than the critical value  $E_c = m_e^2 c^3 / (e\hbar)$ , for  $E_e^F = 0$ . The assumption of constant distribution of protons at nuclear densities simulates, in such a treatment, the confinement due to the strong interactions in the case of nuclei and heavy nuclei and due to both the gravitational field and the strong interactions in the case of nuclear matter cores of stellar sizes.

In this work we introduce explicitly the effects of gravitation by considering a general relativistic system of degenerate fermions composed of neutrons, protons and electrons in  $\beta$ -equilibrium: this is the simplest nontrivial system in which new electro-dynamical and general relativistic properties of the equilibrium configuration can be clearly and rigorously illustrated. We first prove that the condition of local charge neutrality can never be implemented since it violates necessary conditions of equilibrium at the micro-

physical scale. We then prove the existence of a solution with global, but not local, charge neutrality by taking into account essential gravito-electrodynamical effects. First we recall the constancy of the general relativistic Fermi energy of each specie pioneered by Klein (1949). We subsequently introduce the general relativistic Thomas-Fermi equations for the three fermion species fulfilling relativistic quantum statistics, governed by the Einstein-Maxwell equations. The solution of this system of equations presents a formidable mathematical challenge in theoretical physics. The traditional difficulties encountered in proving the existence and unicity of the solution of the Thomas-Fermi equation are here enhanced by the necessity of solving the general relativistic Thomas-Fermi equation coupled with the Einstein-Maxwell system of equations. We present the general solution for the equilibrium configuration, from the center of the star all the way to the border, giving the details of the gravitational field, of the electro-dynamical field as well as of the conserved quantities.

We illustrate such a solution by selecting a central density  $\rho(0) = 3.94\rho_{\text{nuc}}$ , where  $\rho_{\text{nuc}} \simeq 2.7 \times 10^{14} \text{ g cm}^{-3}$  is the nuclear density. We point out the existence near the boundary of the core in the equilibrium configuration of three different radii, in decreasing order:  $R_e$  corresponding to the vanishing of the Fermi momentum of the electron component;  $P_e^F = 0$ ,  $R_p$  corresponding to the vanishing of the Fermi momentum of the proton component;  $P_p^F = 0$  and  $R_n$  corresponding to the radius at which the Fermi momentum of neutrons vanishes:  $P_n^F = 0$ . We then give explicit expressions for the proton versus electron density ratio and the proton versus neutron density ratio for any value of the radial coordinate as well as for the electric potential at the center of the configuration. A novel situation occurs: the description of the pressure and density is not anylonger a local one. Their determination needs prior knowledge of the global electro-dynamical and gravitational potentials on the entire system as well as of the radii  $R_n$ ,  $R_p$  and  $R_e$ . This is a necessary outcome of the self-consistent solution of the eigenfunction within general relativistic Thomas-Fermi equation in the Einstein-Maxwell background. As expected from the considerations in Rotondo et al. (2011c), the electric potential at the center of the configuration fulfills  $eV(0) \simeq m_\pi c^2$  and the gravitational potential  $1 - e^{v(0)/2} \simeq m_\pi/m_p$ . The implementation of the constancy of the general relativistic Fermi energy of each particle species and the consequent system of equations illustrated here is the simplest possible example admitting a rigorous nontrivial solution. It will necessarily apply in the case of additional particle species and of the inclusion of nuclear interactions: in this cases however it is not sufficient and the contribution of nuclear fields must be taken into due account.

### C.1.2. The impossibility of a solution with local charge neutrality

We consider the equilibrium configurations of a degenerate gas of neutrons, protons and electrons with total matter energy density and total matter pressure

$$\varepsilon = \sum_{i=n,p,e} \frac{2}{(2\pi\hbar)^3} \int_0^{P_i^F} \epsilon_i(p) 4\pi p^2 dp, \quad (\text{C.1.1})$$

$$P = \sum_{i=n,p,e} \frac{1}{3} \frac{2}{(2\pi\hbar)^3} \int_0^{P_i^F} \frac{p^2}{\epsilon_i(p)} 4\pi p^2 dp, \quad (\text{C.1.2})$$

where  $\epsilon_i(p) = \sqrt{c^2 p^2 + m_i^2 c^4}$  is the relativistic single particle energy. In addition, we require the condition of  $\beta$ -equilibrium between neutrons, protons and electrons

$$\mu_n = \mu_p + \mu_e, \quad (\text{C.1.3})$$

where  $P_i^F$  denotes the Fermi momentum and  $\mu_i = \partial\varepsilon/\partial n_i = \sqrt{c^2(P_i^F)^2 + m_i^2 c^4}$  is the free-chemical potential of particle-species with number density  $n_i = (P_i^F)^3/(3\pi^2\hbar^3)$ . We now introduce the extension to general relativity of the Thomas-Fermi equilibrium condition on the generalized Fermi energy  $E_e^F$  of the electron component

$$E_e^F = e^{\nu/2} \mu_e - m_e c^2 - eV = \text{constant}, \quad (\text{C.1.4})$$

where  $e$  is the fundamental charge,  $V$  is the Coulomb potential of the configuration and we have introduced the metric

$$ds^2 = e^{\nu(r)} c^2 dt^2 - e^{\lambda(r)} dr^2 - r^2 d\theta^2 - r^2 \sin^2 \theta d\varphi^2, \quad (\text{C.1.5})$$

for a spherically symmetric non-rotating neutron star. The metric function  $\lambda$  is related to the mass  $M(r)$  and the electric field  $E(r) = -e^{-(\nu+\lambda)/2} V'$  (a prime stands for radial derivative) through

$$e^{-\lambda} = 1 - \frac{2GM(r)}{c^2 r} + \frac{G}{c^4} r^2 E^2(r). \quad (\text{C.1.6})$$

Thus the equations for the neutron star equilibrium configuration consist of the following Einstein-Maxwell equations and general relativistic Thomas-

Fermi equation

$$M' = 4\pi r^2 \frac{\mathcal{E}}{c^2} - \frac{4\pi r^3}{c^2} e^{-\nu/2} \hat{V}' (n_p - n_e), \quad (\text{C.1.7})$$

$$\nu' = \frac{2G}{c^2} \frac{4\pi r^3 P/c^2 + M - r^3 E^2/c^2}{r^2 \left(1 - \frac{2GM}{c^2 r} + \frac{Gr^2 E^2}{c^4}\right)}, \quad (\text{C.1.8})$$

$$P' + \frac{\nu'}{2} (\mathcal{E} + P) = -(P^{\text{em}})' - \frac{4P^{\text{em}}}{r}, \quad (\text{C.1.9})$$

$$\hat{V}'' + \frac{2}{r} \hat{V}' \left[1 - \frac{r(\nu' + \lambda')}{4}\right] = -4\pi\alpha\hbar c e^{\nu/2} e^\lambda \left\{ n_p - \frac{e^{-3\nu/2}}{3\pi^2} [\hat{V}^2 + 2m_e c^2 \hat{V} - m_e^2 c^4 (e^\nu - 1)]^{3/2} \right\}, \quad (\text{C.1.10})$$

where  $\alpha$  denotes the fine structure constant,  $\hat{V} = E_e^F + eV$ ,  $P^{\text{em}} = -E^2/(8\pi)$  and we have used Eq. (C.1.4) to obtain Eq. (C.1.10).

It can be demonstrated that the assumption of the equilibrium condition (C.1.4) together with the  $\beta$ -equilibrium condition (C.1.3) and the hydrostatic equilibrium (C.1.9) is enough to guarantee the constancy of the generalized Fermi energy

$$E_i^F = e^{\nu/2} \mu_i - m_i c^2 + q_i V, \quad i = n, p, e, \quad (\text{C.1.11})$$

for all particle species separately. Here  $q_i$  denotes the particle unit charge of the  $i$ -species. Indeed, as shown by Olson and Bailyn (1975, 1978), when the fermion nature of the constituents and their degeneracy is taken into account, in the configuration of minimum energy the generalized Fermi energies  $E_i^F$  defined by (C.1.11) must be constant over the entire configuration. These minimum energy conditions generalize the equilibrium conditions of Klein (1949) and of Kodama and Yamada (1972) to the case of degenerate multi-component fluids with particle species with non-zero unit charge.

If one were to assume, as often done in literature, the local charge neutrality condition  $n_e(r) = n_p(r)$  instead of assuming the equilibrium condition (C.1.4), this would lead to  $V = 0$  identically (since there will be no electric fields generated by the neutral matter distribution) implying via Eqs. (C.1.3) and (C.1.9)

$$\begin{aligned} E_e^F + E_p^F &= e^{\nu/2} (\mu_e + \mu_p) - (m_e + m_p) c^2 = E_n^F \\ &+ (m_n - m_e - m_p) c^2 = \text{constant}. \end{aligned} \quad (\text{C.1.12})$$

Thus the neutron Fermi energy would be constant throughout the configuration as well as the sum of the proton and electron Fermi energies but not

the individual Fermi energies of each component. In Fig. C.1 we show the results of the Einstein equations for a selected value of the central density of a system of degenerate neutrons, protons, and electrons in  $\beta$ -equilibrium under the constraint of local charge neutrality. In particular, we have plotted the Fermi energy of the particle species in units of the pion rest-energy. It can be seen that indeed the Fermi energies of the protons and electrons are not constant throughout the configuration which would lead to microscopic instability. This proves the impossibility of having a self-consistent configuration fulfilling the condition of local charge neutrality for our system. This result is complementary to the conclusion of Eq. (4.6) of Olson and Bailyn (1975) who found that, at zero temperature, only a dust solution with zero particle kinetic energy can satisfy the condition of local charge neutrality and such a configuration is clearly unacceptable for an equilibrium state of a self-gravitating system.

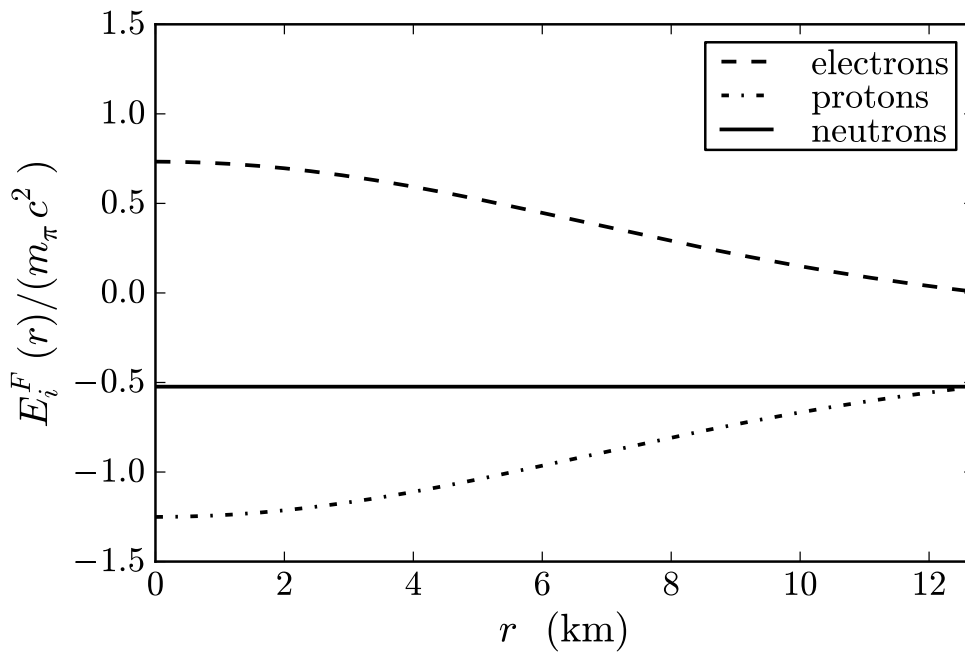


**Figure C.1.:** Fermi energies for neutrons, protons and electrons in units of the pion rest-energy for a locally neutral configuration with central density  $\rho(0) = 3.94\rho_{\text{nuc}}$ , where  $\rho_{\text{nuc}} = 2.7 \times 10^{14} \text{ g cm}^{-3}$  denotes the nuclear density.

### C.1.3. The solution with global charge neutrality

We turn now to describe the equilibrium configurations fulfilling only global charge neutrality. We solve self-consistently Eqs. (C.1.7) and (C.1.8) for the metric, Eq. (C.1.9) for the hydrostatic equilibrium of the three degenerate fermions and, in addition, we impose Eq. (C.1.3) for the  $\beta$ -equilibrium. The crucial equation relating the proton and the electron distributions is then given by the general relativistic Thomas-Fermi equation (C.1.10). The boundary conditions are: for Eq. (C.1.7) the regularity at the origin:  $M(0) = 0$ , for Eq. (C.1.9) a given value of the central density, and for Eq. (C.1.10) the regularity at the origin  $n_e(0) = n_p(0)$ , and a second condition at infinity which results in an eigenvalue problem determined by imposing the global charge neutrality conditions

$$\hat{V}(R_e) = E_e^F, \quad \hat{V}'(R_e) = 0, \quad (\text{C.1.13})$$

at the radius  $R_e$  of the electron distribution defined by

$$P_e^F(R_e) = 0, \quad (\text{C.1.14})$$

from which follows

$$\begin{aligned} E_e^F &= m_e c^2 e^{\nu(R_e)/2} - m_e c^2 \\ &= m_e c^2 \sqrt{1 - \frac{2GM(R_e)}{c^2 R_e}} - m_e c^2. \end{aligned} \quad (\text{C.1.15})$$

Then the eigenvalue problem consists in determining the gravitational potential and the Coulomb potential at the center of the configuration that satisfy the conditions (C.1.13)–(C.1.15) at the boundary.

### C.1.4. Numerical integration of the equilibrium equations

The solution for the particle densities, the gravitational potential, the Coulomb potential and the electric field are shown in Fig. (C.2) for a configuration with central density  $\rho(0) = 3.94\rho_{\text{nuc}}$ . In order to compare our results with those obtained in the case of nuclear matter cores of stellar dimensions Rotondo et al. (2011c) as well as to analyze the gravito-electrodynamical stability of the configuration we have plotted the electric potential in units of the pion rest-energy and the gravitational potential in units of the pion-to-proton mass ratio. One particular interesting new feature is the approach to the boundary of the configuration: three different radii are present corresponding to distinct radii at which the individual particle Fermi pressure vanishes. The radius  $R_e$  for the electron component corresponding to  $P_e^F(R_e) = 0$ , the radius  $R_p$  for the proton component corresponding to  $P_p^F(R_p) = 0$  and the radius  $R_n$  for

the neutron component corresponding to  $P_n^F(R_n) = 0$ .

The smallest radius  $R_n$  is due to the threshold energy for  $\beta$ -decay which occurs at a density  $\sim 10^7 \text{ g cm}^{-3}$ . The radius  $R_p$  is larger than  $R_n$  because the proton mass is slightly smaller than the neutron mass. Instead,  $R_e > R_p$  due to a combined effect of the difference between the proton and electron masses and the implementation of the global charge neutrality condition through the Thomas-Fermi equilibrium conditions.

For the configuration of Fig. C.2 we found  $R_n \simeq 12.735 \text{ km}$ ,  $R_p \simeq 12.863 \text{ km}$  and  $R_e \simeq R_p + 10^3 \lambda_e$  where  $\lambda_e = \hbar / (m_e c)$  denotes the electron Compton wavelength. We find that the electron component follows closely the proton component up to the radius  $R_p$  and neutralizes the configuration at  $R_e$  without having a net charge, contrary to the results e.g in Olson and Bailyn (1978).

It can be seen from Fig. C.2 that the negative proton gravitational potential energy is indeed always larger than the positive proton electric potential energy. Therefore the configuration is stable against Coulomb repulsion. This confirms the results in the simplified case analyzed by Rotondo et al. (2011c).

From Eq. (C.1.11) and the relation between Fermi momentum and the particle density  $P_i^F = (3\pi^2 \hbar^3 n_i)^{1/3}$ , we obtain the proton-to-electron and proton-to-neutron ratio for any value of the radial coordinate

$$\frac{n_p(r)}{n_e(r)} = \left[ \frac{f^2(r) \mu_e^2(r) - m_p^2 c^4}{\mu_e^2(r) - m_e^2 c^4} \right]^{3/2}, \quad (\text{C.1.16})$$

$$\frac{n_p(r)}{n_n(r)} = \left[ \frac{g^2(r) \mu_n^2(r) - m_p^2 c^4}{\mu_n^2(r) - m_n^2 c^4} \right]^{3/2}, \quad (\text{C.1.17})$$

where  $f(r) = (E_p^F + m_p c^2 - eV) / (E_e^F + m_e c^2 + eV)$ ,  $g(r) = (E_p^F + m_p c^2 - eV) / (E_n^F + m_n c^2)$  and the constant values of the generalized Fermi energies are given by

$$E_n^F = m_n c^2 e^{\nu(R_n)/2} - m_n c^2, \quad (\text{C.1.18})$$

$$E_p^F = m_p c^2 e^{\nu(R_p)/2} - m_p c^2 + eV(R_p), \quad (\text{C.1.19})$$

$$E_e^F = m_e c^2 e^{\nu(R_e)/2} - m_e c^2. \quad (\text{C.1.20})$$

A novel situation occurs: the determination of the quantities given in Eqs. (C.1.16) and (C.1.18) necessarily require the prior knowledge of the global electro-dynamical and gravitational potential from the center of the configuration all the way out to the boundary defined by the radii  $R_e$ ,  $R_p$  and  $R_n$ . This necessity is an outcome of the solution for the eigenfunction of the general relativistic Thomas-Fermi equation (C.1.10).

From the regularity condition at the center of the star  $n_e(0) = n_p(0)$  to-

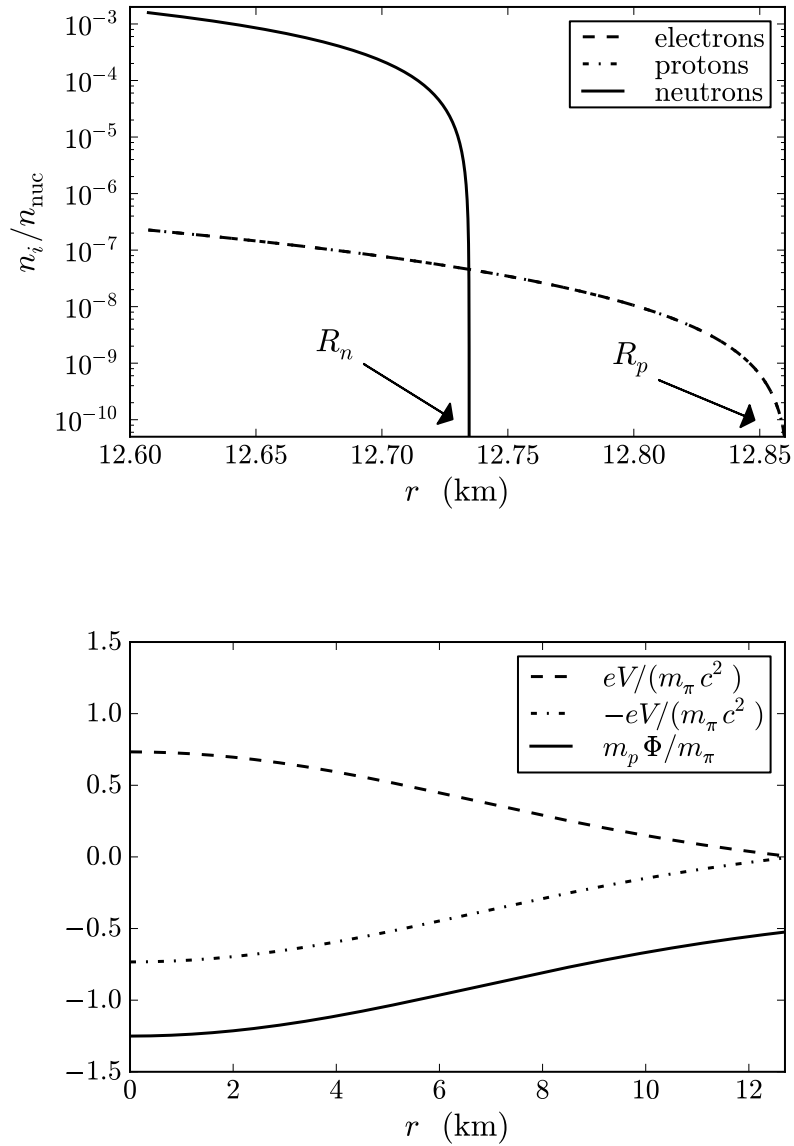


**Figure C.2.:** Top panel: particle number density of neutrons, protons, and electrons approaching the boundary of the configuration in units of the nuclear density  $n_{\text{nuc}} \simeq 1.6 \times 10^{38} \text{ cm}^{-3}$ . Bottom panel: proton and electron Coulomb potentials in units of the pion rest-energy  $eV/(m_\pi c^2)$  and  $-eV/(m_\pi c^2)$  respectively and the proton gravitational potential in units of the pion mass  $m_p \Phi / m_\pi$  where  $\Phi = (e^{\nu/2} - 1)$ .

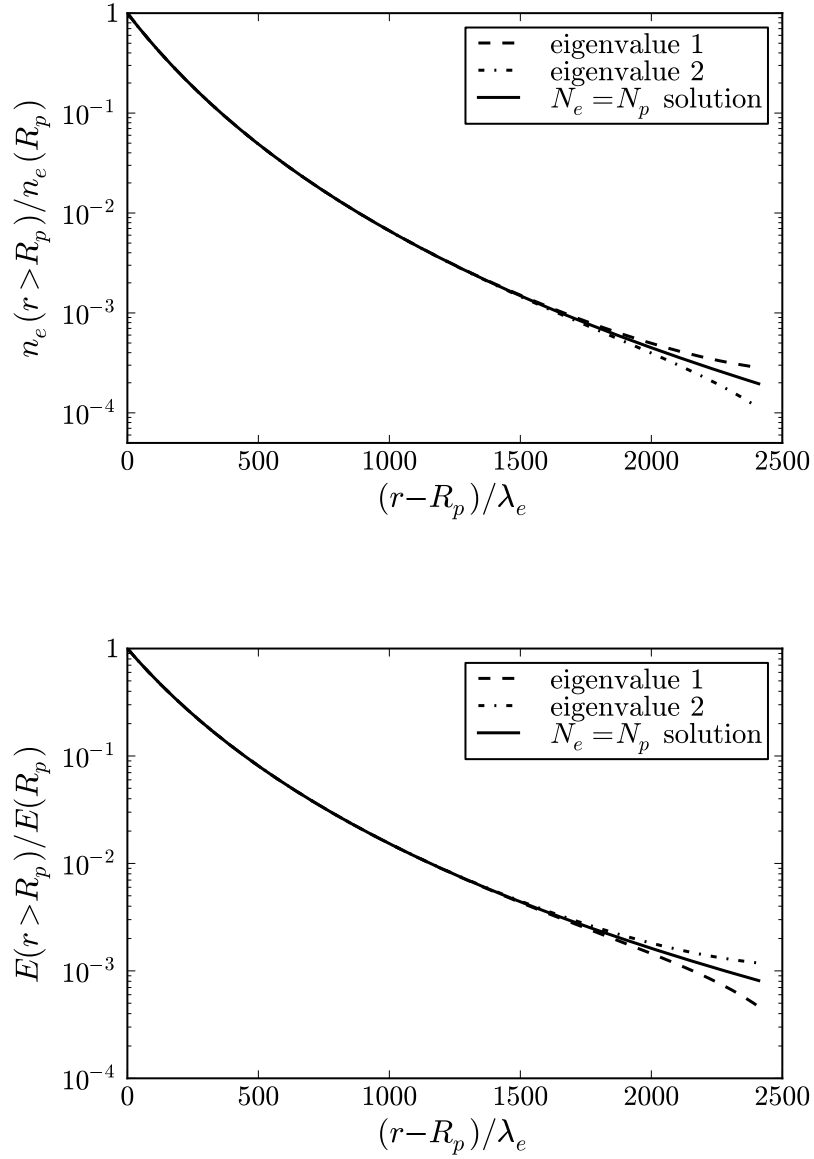


**Figure C.3.:** Top panel: electron number density for  $r \geq R_p$  normalized to its value at  $r = R_p$ . Bottom panel: electric field for  $r \geq R_p$  normalized to its value at  $r = R_p$ . We have shown also the behavior of the solution of the general relativistic Thomas-Fermi equation (C.1.10) for two different eigenvalues close to the one which gives the globally neutral configuration.

gether with Eq. (C.1.16) we obtain the Coulomb potential at the center of the configuration

$$eV(0) = \frac{(m_p - m_e)c^2}{2} \left[ 1 + \frac{E_p^F - E_e^F}{(m_p - m_e)c^2} - \frac{(m_p + m_e)c^2}{E_n^F + m_n c^2} e^{\nu(0)} \right], \quad (\text{C.1.21})$$

which after some algebraic manipulation and defining the central density in units of the nuclear density  $\eta = \rho(0)/\rho_{\text{nuc}}$  can be estimated as

$$eV(0) \simeq \frac{1}{2} \left[ m_p c^2 e^{\nu(R_p)/2} - m_e c^2 e^{\nu(R_e)/2} - \frac{m_n c^2 e^{\nu(R_n)/2}}{1 + [P_n^F(0)/(m_n c)]^2} \right] \simeq \frac{1}{2} \left[ \frac{(3\pi^2 \eta / 2)^{2/3} m_p}{(3\pi^2 \eta / 2)^{2/3} m_\pi + m_n^2 / m_\pi} \right] m_\pi c^2, \quad (\text{C.1.22})$$

where we have approximated the gravitational potential at the boundary as  $e^{\nu(R_e)/2} \simeq e^{\nu(R_p)/2} \simeq e^{\nu(R_n)/2} \simeq 1$ . Then for configurations with central densities larger than the nuclear density we necessarily have  $eV(0) \gtrsim 0.35 m_\pi c^2$ . In particular, for the configuration we have exemplified with  $\eta = 3.94$  in Fig. C.2, from the above expression (C.1.22) we obtain  $eV(0) \simeq 0.85 m_\pi c^2$ . This value of the central potential agrees with the one obtained in the simplified case of nuclear matter cores with constant proton density (Rotondo et al., 2011c).

### C.1.5. Conclusions

We have proved in the first part of this letter that the treatment generally used for the description of neutron stars adopting the condition of local charge neutrality, is not consistent with the Einstein-Maxwell equations and microphysical conditions of equilibrium consistent with quantum statistics (see Fig. C.1). We have shown how to construct a self-consistent solution for a general relativistic system of degenerate neutrons, protons and electrons in  $\beta$ -equilibrium fulfilling global but not local charge neutrality.

Although the mass-radius relation in the simple example considered here in our new treatment, differs slightly from the one of the traditional approaches, the differences in the electrodynamic structure are clearly very large. As is well-known these effects can lead to important astrophysical conse-

quences on the physics of the gravitational collapse of a neutron star to a black hole Ruffini et al. (2010b).

Having established in the simplest possible example the new set of Einstein-Maxwell and general relativistic Thomas-Fermi equations, we now proceed to extend this approach when strong interactions are present Rueda et al. (2011a). The contribution of the strong fields to the energy-momentum tensor, to the four-vector current and consequently to the Einstein-Maxwell equations have to be taken into account. Clearly in this more general case, the conditions introduced in this letter have to be still fulfilled: the  $r$ -independence of the generalized Fermi energy of electrons and the fulfillment of the general relativistic Thomas-Fermi equation Rueda et al. (2011a). In addition, the generalized Fermi energy of protons and neutrons will depend on the nuclear interaction fields. The fluid of neutrons, protons and electrons in this more general case does not extend all the way to the neutron star surface but is confined to the neutron star core endowed with overcritical electric fields, in precise analogy with the case of the compressed nuclear matter core of stellar dimension described in Rotondo et al. (2011c).

## C.2. The Klein first integrals in an equilibrium system with electromagnetic, weak, strong and gravitational interactions

### C.2.1. Introduction

The unsolved problems of supernovae theories as well as the necessity of processes leading to electrodynamical phenomena during the gravitational collapse to a black hole (Ruffini et al., 2010b) lead to the necessity of critically reexamining the current treatment of neutron stars. In a series of articles (see Rotondo et al. (2011c,d)), we have recently developed the first steps towards a new consistent treatment for the description of neutron stars, well beyond the traditional Tolman-Oppenheimer-Volkoff equations.

First we have generalized the treatment of compressed atoms of Feynman, Metropolis and Teller to the relativistic regimes (see Rotondo et al. (2011c) for details). There, it has been enforced self-consistently in a relativistic Thomas-Fermi equation, the condition of  $\beta$ -equilibrium extending the works of Popov (1971b), Zeldovich and Popov (1972), Migdal et al. (1976, 1977), Ferreira et al. (1980) and Ruffini and Stella (1981) for heavy nuclei. Then, through the using of scaling laws, following Ruffini (2008b); Popov (2010), this treatment was extrapolated to compressed nuclear matter cores at nuclear and supranuclear densities. Such cores have stellar dimensions and mass numbers  $A \simeq (m_{\text{Planck}}/m_n)^3 \sim 10^{57}$  or  $M_{\text{core}} \sim M_{\odot}$ . In addition, they fulfill global but not local charge neutrality having electric fields on the core surface, increasing for decreasing values of the electron Fermi energy  $E_e^F$  reaching values much larger than the critical value  $E_c = m_e^2 c^3 / (e\hbar)$ , for  $E_e^F = 0$ . The assumption of constant distribution of protons at nuclear densities simulates, in such a treatment, the confinement due to the strong interactions in the case of nuclei and heavy nuclei and due to both the gravitational field and strong interactions in the case of nuclear matter cores of stellar sizes at nuclear and supranuclear densities.

In a subsequent work Rotondo et al. (2011d), we have generalized the above approach explicitly including the effects of the gravitational field by considering the most simplified nontrivial but rigorous treatment of a general relativistic system of neutrons, protons and electrons in  $\beta$ -equilibrium. It has been there proved that the traditional treatment for the description of neutron stars adopting the condition of local charge neutrality is not consistent with the Einstein-Maxwell equations and with microphysical conditions of equilibrium within quantum statistics. The role of the constancy of the general relativistic Fermi energy of each particle species pioneered by Klein (1949) has been there emphasized and, the full system of equilibrium equations consisting of the Einstein-Maxwell and general relativistic Thomas-Fermi equations has been formulated. The corresponding solution of such a system of

equations has been there given in the simplest possible example of a configuration of neutrons, protons and electrons in  $\beta$ -equilibrium with electromagnetic, weak and gravitational interactions. New electrodynamic and general relativistic properties of the equilibrium configurations have been there illustrated.

The aim of this work is to make an essential new step: we further proceed to the description of a system of neutrons, protons and electrons fulfilling strong, electromagnetic, weak and gravitational interactions. The essential role of the Klein first integrals is evidenced and their theoretical formulation is presented in the Einstein-Maxwell background. For the sake of generality the treatment is performed in the most general case in which finite temperature effects are also taking into account. We adopt throughout the work natural units  $\hbar = c = 1$ .

### C.2.2. The Constitutive General Relativistic Equations

The densities in the core of a neutron star exceed the nuclear density  $\rho_{\text{nuc}} \sim 2.7 \times 10^{14} \text{ g/cm}^3$  and may reach densities of order  $\sim 10^{17} \text{ g/cm}^3$  at the verge of the gravitational collapse of the neutron star to a black hole. There is therefore the need of a consistent relativistic theory for the description of the interactions between the matter constituents. In particular, approaches for the nuclear interaction between nucleons based on phenomenological potentials and non-relativistic many-body theory become inapplicable (see Bowers et al. (1973b,a)).

A self-consistent relativistic and well-tested model for the nuclear interactions is the Walecka model (see Duerr (1956); Walecka (1974) for details). This model share common features with the model adopted by Bowers et al. in (Bowers et al., 1973b,a); in both of them the nucleons interact through a Yukawa coupling and the flat spacetime has been considered to construct the equation of state of nuclear matter. The technique of constructing the equation of state assuming flat spacetime has been generally used since, as pointed out in Bowers et al. (1973b,a), as long as  $\rho < 10^{14} \text{ g/cm}^3$  the gravitational contributions to interactions between particles are negligible. However, when we turn to neutron star configurations at nuclear and supranuclear densities, it has been shown in Rotondo et al. (2011d) how the solution of the Einstein-Maxwell system of equations is mandatory.

In the often called extended version of the Walecka model, the strong interaction between nucleons is described by the exchange of three virtual mesons:  $\sigma$  is an isoscalar meson field providing the attractive long-range part of the nuclear force;  $\omega$  is a massive vector field that models the repulsive short range and;  $\rho$  is the massive isovector field that takes account surface as well as isospin effects of nuclei (see also Boguta and Bodmer (1977); Ring (1996)).

The total Lagrangian density of the system is given by

$$\mathcal{L} = \mathcal{L}_g + \mathcal{L}_f + \mathcal{L}_\sigma + \mathcal{L}_\omega + \mathcal{L}_\rho + \mathcal{L}_\gamma + \mathcal{L}_{\text{int}}, \quad (\text{C.2.1})$$

where the Lagrangian densities for the free-fields are

$$\mathcal{L}_g = -\frac{R}{16\pi G}, \quad (\text{C.2.2})$$

$$\mathcal{L}_\gamma = -\frac{1}{4}F_{\mu\nu}F^{\mu\nu}, \quad (\text{C.2.3})$$

$$\mathcal{L}_\sigma = \frac{1}{2}\nabla_\mu\sigma\nabla^\mu\sigma - U(\sigma), \quad (\text{C.2.4})$$

$$\mathcal{L}_\omega = -\frac{1}{4}\Omega_{\mu\nu}\Omega^{\mu\nu} + \frac{1}{2}m_\omega^2\omega_\mu\omega^\mu, \quad (\text{C.2.5})$$

$$\mathcal{L}_\rho = -\frac{1}{4}\mathcal{R}_{\mu\nu}\mathcal{R}^{\mu\nu} + \frac{1}{2}m_\rho^2\rho_\mu\rho^\mu, \quad (\text{C.2.6})$$

where  $\Omega_{\mu\nu} \equiv \partial_\mu\omega_\nu - \partial_\nu\omega_\mu$ ,  $\mathcal{R}_{\mu\nu} \equiv \partial_\mu\rho_\nu - \partial_\nu\rho_\mu$ ,  $F_{\mu\nu} \equiv \partial_\mu A_\nu - \partial_\nu A_\mu$  are the field strength tensors for the  $\omega^\mu$ ,  $\rho$  and  $A^\mu$  fields respectively,  $\nabla_\mu$  stands for covariant derivative and  $R$  is the Ricci scalar. We adopt the Lorenz gauge for the fields  $A_\mu$ ,  $\omega_\mu$ , and  $\rho_\mu$ . The self-interaction scalar field potential  $U(\sigma)$  is a quartic-order polynom for a renormalizable theory (see e.g. Lee and Wick (1974)). The specific functional form of  $U(\sigma)$  is not relevant for the scope of this work, thus we will not adopt any particular form of it hereafter.

The Lagrangian density for the three fermion species is

$$\mathcal{L}_f = \sum_{i=e,N} \bar{\psi}_i (i\gamma^\mu D_\mu - m_i) \psi_i, \quad (\text{C.2.7})$$

where  $\psi_N$  is the nucleon isospin doublet,  $\psi_e$  is the electronic singlet,  $m_i$  states for the mass of each particle-specie and  $D_\mu = \partial_\mu + \Gamma_\mu$ , being  $\Gamma_\mu$  the Dirac spin connections that satisfy the commutation relation

$$[\gamma_\mu, \Gamma_\nu] = \partial_\nu\gamma_\mu - \Gamma_{\mu\nu}^\alpha\gamma_\alpha, \quad (\text{C.2.8})$$

where  $\Gamma_{\mu\nu}^\alpha$  denotes the Christoffel symbols.

The interacting part of the Lagrangian density is, in the minimal coupling assumption, given by

$$\mathcal{L}_{\text{int}} = -g_\sigma\sigma\bar{\psi}_N\psi_N - g_\omega\omega_\mu J_\omega^\mu - g_\rho\rho_\mu J_\rho^\mu + eA_\mu J_{\gamma,e}^\mu - eA_\mu J_{\gamma,N}^\mu, \quad (\text{C.2.9})$$

where the conserved currents are

$$J_\omega^\mu = \bar{\psi}_N \gamma^\mu \psi_N, \quad (\text{C.2.10})$$

$$J_\rho^\mu = \bar{\psi}_N \tau_3 \gamma^\mu \psi_N, \quad (\text{C.2.11})$$

$$J_{\gamma,e}^\mu = \bar{\psi}_e \gamma^\mu \psi_e, \quad (\text{C.2.12})$$

$$J_{\gamma,N}^\mu = \bar{\psi}_N \left( \frac{1 + \tau_3}{2} \right) \gamma^\mu \psi_N. \quad (\text{C.2.13})$$

The coupling constants of the  $\sigma$ ,  $\omega$  and  $\rho$ -fields are  $g_\sigma$ ,  $g_\omega$  and  $g_\rho$ , and  $e$  is the fundamental electric charge. The Dirac matrices  $\gamma^\mu$  and the isospin Pauli matrices satisfy the Dirac algebra in curved spacetime (see e.g. Lee and Pang (1987))

$$\{\gamma^\mu, \gamma^\nu\} = 2g^{\mu\nu}, \quad (\text{C.2.14})$$

$$\{\gamma_\mu, \gamma_\nu\} = 2g_{\mu\nu}, \quad (\text{C.2.15})$$

$$\{\gamma^\mu, \gamma_\nu\} = 2\delta_\nu^\mu, \quad (\text{C.2.16})$$

$$[\tau_i, \tau_j] = 2i\epsilon_{ijk}\tau^k. \quad (\text{C.2.17})$$

The Einstein-Maxwell-Dirac system of equations is then given by

$$G_{\mu\nu} + 8\pi G T_{\mu\nu} = 0, \quad (\text{C.2.18})$$

$$\nabla_\mu F^{\mu\nu} - e J_{ch}^\nu = 0, \quad (\text{C.2.19})$$

$$\nabla_\mu \Omega^{\mu\nu} + m_\omega^2 \omega^\nu - g_\omega J_\omega^\nu = 0, \quad (\text{C.2.20})$$

$$\nabla_\mu \mathcal{R}^{\mu\nu} + m_\rho^2 \rho^\nu - g_\rho J_\rho^\nu = 0, \quad (\text{C.2.21})$$

$$\nabla_\mu \nabla^\mu \sigma + \partial_\sigma U(\sigma) + g_s n_s = 0, \quad (\text{C.2.22})$$

$$[\gamma_\mu (iD^\mu - V_N^\mu) - \tilde{m}_N] \psi_N = 0, \quad (\text{C.2.23})$$

$$[\gamma_\mu (iD^\mu + eA^\mu) - m_e] \psi_e = 0, \quad (\text{C.2.24})$$

where the scalar density  $n_s = \bar{\psi}_N \psi_N$ , the nucleon effective mass  $\tilde{m}_N \equiv m_N + g_\sigma \sigma$ , and

$$V_N^\mu \equiv g_\omega \omega^\mu + g_\rho \tau \rho^\mu + e \left( \frac{1 + \tau_3}{2} \right) A^\mu, \quad (\text{C.2.25})$$

is the effective four potential of nucleons. The energy-momentum tensor of free-fields and free-fermions  $T^{\mu\nu}$  of the system (C.2.3)–(C.2.6) is

$$T^{\mu\nu} = T_f^{\mu\nu} + T_\gamma^{\mu\nu} + T_\sigma^{\mu\nu} + T_\omega^{\mu\nu} + T_\rho^{\mu\nu}, \quad (\text{C.2.26})$$

where

$$T_\gamma^{\mu\nu} = -F_\alpha^\mu F^{\alpha\nu} - \frac{1}{4}g^{\mu\nu}F_{\alpha\beta}F^{\alpha\beta}, \quad (\text{C.2.27})$$

$$T_\sigma^{\mu\nu} = \nabla^\mu \nabla^\nu \sigma - g^{\mu\nu} \left[ \frac{1}{2} \nabla_\sigma \sigma \nabla^\sigma \sigma - U(\sigma) \right], \quad (\text{C.2.28})$$

$$T_\omega^{\mu\nu} = -\Omega_\alpha^\mu \Omega^{\alpha\nu} - \frac{1}{4}g^{\mu\nu} \Omega_{\alpha\beta} \Omega^{\alpha\beta} + m_\omega^2 \left( \omega^\mu \omega^\nu - \frac{1}{2}g^{\mu\nu} \omega_\alpha \omega^\alpha \right) \quad (\text{C.2.29})$$

$$T_\rho^{\mu\nu} = -\mathcal{R}_\alpha^\mu \mathcal{R}^{\alpha\nu} - \frac{1}{4}g^{\mu\nu} \mathcal{R}_{\alpha\beta} \mathcal{R}^{\alpha\beta} + m_\rho^2 \left( \mathcal{R}^\mu \mathcal{R}^\nu - \frac{1}{2}g^{\mu\nu} \mathcal{R}_\alpha \omega^\alpha \right), \quad (\text{C.2.30})$$

are the contribution due to free-fields and  $T_f^{\mu\nu}$  is the contribution of free-fermions which we discuss below.

### C.2.3. The Thermodynamic Laws and the Field Equations in the Spherically Symmetric Case

We first introduce the non-rotating spherically symmetric spacetime metric

$$ds^2 = e^{\nu(r)} dt^2 - e^{\lambda(r)} dr^2 - r^2 d\theta^2 - r^2 \sin^2 \theta d\varphi^2, \quad (\text{C.2.31})$$

where the  $\nu(r)$  and  $\lambda(r)$  are only functions of the radial coordinate  $r$ .

For very large number of fermions, we can adopt the mean-field approximation in which fermion-field operators are replaced by their expectation values (see e.g. Walecka (1974) for details).

We write the nucleon doublet and the electronic spinor as  $\psi_i = \psi_i(k)e^{-ik_\mu x^\mu}$  in the phase-space. Suppose that neutrons, protons and electrons, and the corresponding antiparticles, are in thermodynamic equilibrium with a finite temperature  $T$ . The occupation fermion-number operators of the “ $k$ ”-state,  $N_i(k) = \psi_i^\dagger(k)\psi_i(k)$  with  $i = e, p, n$ , are replaced by their Fermi-distributions

$$f_i^\pm(k) = \langle \psi_i^\pm(k)^\dagger \psi_i^\pm(k) \rangle = \left[ \exp \left( \frac{\epsilon_i(k) \mp \mu_i}{k_B T} \right) + 1 \right]^{-1}, \quad (\text{C.2.32})$$

where  $k_B$  is the Boltzmann constant,  $\mu_i$  and  $\epsilon_i(k) = \sqrt{k^2 + \tilde{m}_i^2}$  denote the single-particle chemical potential and energy-spectrum (we recall that for electrons  $\tilde{m}_e = m_e$ ). The sign ‘+’ correspond to particles and ‘-’ to antiparticles. We do not consider “real” bosons to be present in the system; the only distribution functions involved in the computation are due to fermions and antifermions and therefore phenomena as Bose-Einstein condensation does not occur within this theory (see e.g. Bowers et al. (1973b) for details).

It is worth to recall that all the thermodynamic quantities, e.g.  $k, \epsilon, T \dots$ , are written here in the local frame which is related to the coordinate frame by the

Lorentz “boost”

$$\Lambda_\alpha^{(a)} = (u_\alpha, \chi_\alpha, \Theta_\alpha, \Phi_\alpha), \quad (\text{C.2.33})$$

where  $u_\alpha = e^{v/2}\delta_\alpha^0$ ,  $\chi_\alpha = e^{\lambda/2}\delta_\alpha^1$ ,  $\Theta_\alpha = r\delta_\alpha^2$ , and  $\Phi_\alpha = r \sin\theta\delta_\alpha^3$ , being  $\delta_\beta^\alpha$  the usual Kronecker delta symbol.

The number-density  $n_i$  of the  $i$ -specie, taking into account the antiparticle contribution is, within the mean-field approximation, given by

$$n_i = \frac{2}{(2\pi)^3} \int d^3k [f_i^+(k) - f_i^-(k)]. \quad (\text{C.2.34})$$

The contribution of free-fermions and antifermions to the energy-momentum tensor can be then written in the perfect fluid form (see e.g. Ruffini and Bonazzola (1969))

$$T_f^{\mu\nu} = (\mathcal{E} + \mathcal{P})u^\mu u^\nu - \mathcal{P}g^{\mu\nu}, \quad (\text{C.2.35})$$

where  $u^\mu$  is the four-velocity of the fluid which satisfies  $u^\mu u_\mu = 1$ , and the energy-density  $\mathcal{E}$  and the pressure  $\mathcal{P}$  are given by

$$\mathcal{E} = \sum_{i=n,p,e} \mathcal{E}_i, \quad \mathcal{P} = \sum_{i=n,p,e} \mathcal{P}_i, \quad (\text{C.2.36})$$

being  $\mathcal{E}_i$  and  $\mathcal{P}_i$  the single fermion-antifermion fluid contributions

$$\mathcal{E}_i = \frac{2}{(2\pi)^3} \int d^3k \epsilon_i(k) [f_i^+(k) + f_i^-(k)], \quad (\text{C.2.37})$$

$$\mathcal{P}_i = \frac{1}{3} \frac{2}{(2\pi)^3} \int d^3k \frac{k^2}{\epsilon_i(k)} [f_i^+(k) + f_i^-(k)]. \quad (\text{C.2.38})$$

The equation of state (C.2.36)–(C.2.38) satisfies the thermodynamic law

$$\mathcal{E} + \mathcal{P} - T\mathcal{S} = \sum_{i=n,p,e} n_i \mu_i, \quad (\text{C.2.39})$$

where  $\mathcal{S} = S/V$  is the entropy per unit volume (entropy density) and  $\mu_i = \partial\mathcal{E}/\partial n_i$  is the free-chemical potential of the  $i$ -specie. At zero-temperature  $T = 0$ ,  $\mu_i = \sqrt{(K_i^F)^2 + \tilde{m}_i^2}$  and  $n_i = (K_i^F)^3/(3\pi^2)$ , where  $K_i^F$  denotes the Fermi momentum of the  $i$ -specie.

The scalar density  $n_s$ , within the mean-field approximation, is given by the following expectation value

$$n_s = \langle \bar{\psi}_N \psi_N \rangle = \frac{2}{(2\pi)^3} \sum_{i=n,p} \int d^3k \frac{\tilde{m}_N}{\epsilon_i(k)} [f_i^+(k) + f_i^-(k)]. \quad (\text{C.2.40})$$

In the static case, only the temporal components of the covariant currents survive, i.e.  $\langle \bar{\psi}(x)\gamma^i\psi(x) \rangle = 0$ . Thus, by taking the expectation values of

Eqs. (C.2.10)–(C.2.13), we obtain the non-vanishing components of the currents

$$J_0^{ch} = n_{ch}u_0 = (n_p - n_e)u_0, \quad (\text{C.2.41})$$

$$J_0^\omega = n_b u_0 = (n_n + n_p)u_0, \quad (\text{C.2.42})$$

$$J_0^\rho = n_3 u_0 = (n_p - n_n)u_0, \quad (\text{C.2.43})$$

where  $n_b$ ,  $n_p$ ,  $n_n$  and  $n_e$  are the baryon, proton, neutron and electron number densities which are functions only of the spatial coordinates, and  $u_0 = \sqrt{g_{00}} = e^{v/2}$ .

Making a variation of Eq. (C.2.39) and using Eqs. (C.2.36)–(C.2.38) and (C.2.40), we obtain the generalized Gibbs-Duhem relation

$$d\mathcal{P} = \sum_{i=n,p,e} n_i d\mu_i - g_\sigma n_s d\sigma + \mathcal{S} dT, \quad (\text{C.2.44})$$

which can be rewritten as

$$d\mathcal{P} = \sum_{i=n,p,e} n_i d\mu_i - g_\sigma n_s d\sigma + \left( \mathcal{E} + \mathcal{P} - \sum_{i=n,p,e} n_i \mu_i \right) \frac{dT}{T}, \quad (\text{C.2.45})$$

where we have used Eq. (C.2.39) to eliminate  $\mathcal{S}$ , and we have used the relation between the scalar density and the fluid energy-density  $n_s = \partial\mathcal{E}/\partial\tilde{m}_N$ , which follows from Eqs. (C.2.36)–(C.2.38) and (C.2.40).

Therefore, the Einstein-Maxwell equations (C.2.18)–(C.2.22), within the mean-field approximation, become

$$e^{-\lambda(r)} \left( \frac{1}{r^2} - \frac{1}{r} \frac{d\lambda}{dr} \right) - \frac{1}{r^2} = -8\pi G T_0^0, \quad (\text{C.2.46})$$

$$e^{-\lambda(r)} \left( \frac{1}{r^2} + \frac{1}{r} \frac{dv}{dr} \right) - \frac{1}{r^2} = -8\pi G T_1^1, \quad (\text{C.2.47})$$

$$e^{-\lambda(r)} \left[ \frac{1}{2} \left( \frac{dv}{dr} - \frac{d\lambda}{dr} \right) \left( \frac{1}{r} + \frac{1}{2} \frac{dv}{dr} \right) + \frac{1}{2} \frac{d^2 v}{dr^2} \right] = -8\pi G T_3^3, \quad (\text{C.2.48})$$

$$\frac{d^2 V}{dr^2} + \frac{dV}{dr} \left[ \frac{2}{r} - \frac{1}{2} \left( \frac{dv}{dr} + \frac{d\lambda}{dr} \right) \right] = -e^\lambda e J_{ch}^0, \quad (\text{C.2.49})$$

$$\frac{d^2 \sigma}{dr^2} + \frac{d\sigma}{dr} \left[ \frac{2}{r} - \frac{1}{2} \left( \frac{dv}{dr} + \frac{d\lambda}{dr} \right) \right] = e^\lambda [\partial_\sigma U(\sigma) + g_s n_s], \quad (\text{C.2.50})$$

$$\frac{d^2 \omega}{dr^2} + \frac{d\omega}{dr} \left[ \frac{2}{r} - \frac{1}{2} \left( \frac{dv}{dr} + \frac{d\lambda}{dr} \right) \right] = -e^\lambda [g_\omega J_\omega^0 - m_\omega^2 \omega], \quad (\text{C.2.51})$$

$$\frac{d^2 \rho}{dr^2} + \frac{d\rho}{dr} \left[ \frac{2}{r} - \frac{1}{2} \left( \frac{dv}{dr} + \frac{d\lambda}{dr} \right) \right] = -e^\lambda [g_\rho J_\rho^0 - m_\rho^2 \rho], \quad (\text{C.2.52})$$

where we have introduced the notation  $\omega_0 = \omega$ ,  $\rho_0 = \rho$ , and  $A_0 = V$ . The metric function  $\lambda$  is related to the mass  $M(r)$  and the electric field  $E(r) = -e^{-(\nu+\lambda)/2}V'$  through

$$e^{-\lambda(r)} = 1 - \frac{2GM(r)}{r} + Gr^2E^2(r) = 1 - \frac{2GM(r)}{r} + \frac{GQ^2(r)}{r^2}, \quad (\text{C.2.53})$$

where we have introduced also the conserved charge  $Q(r) = r^2E(r)$ .

An important equation, although not independent of the Einstein-Maxwell equations (C.2.46)–(C.2.52), is given the energy-momentum conservation law

$$\nabla_\mu T^{\mu\nu} = -g_\omega J_\mu^\omega \Omega^{\mu\nu} - g_\rho J_\mu^\rho \mathcal{R}^{\mu\nu} + eJ_\mu^{ch} F^{\mu\nu}, \quad (\text{C.2.54})$$

from which we have

$$\frac{d\mathcal{P}}{dr} = -\frac{(\mathcal{E} + \mathcal{P})}{2} \frac{d\nu}{dr} - g_\sigma n_s \frac{d\sigma}{dr} - g_\omega J_\omega^0 \frac{d\omega}{dr} - g_\rho J_\rho^0 \frac{d\rho}{dr} - eJ_{ch}^0 \frac{dV}{dr}, \quad (\text{C.2.55})$$

where we have used the energy-momentum tensor  $T^{\mu\nu}$  given by Eq. (C.2.26).

#### C.2.4. Constancy of the Klein potentials and $\beta$ -equilibrium

Introducing the nucleon doublet and the electronic spinor in the wave-form  $\psi_i = \psi_i(k)e^{-ik_\mu x^\mu}$  in phase-space, the Dirac equations (C.2.24) become

$$(\gamma_\mu \mathcal{K}_i^\mu - \tilde{m}_i)\psi_i(k) = 0, \quad (\text{C.2.56})$$

where

$$\mathcal{K}_i^\mu \equiv k^\mu - V_i^\mu, \quad V_e^\mu = -eA^\mu. \quad (\text{C.2.57})$$

In the mean-field approximation, making the quadrature of Dirac operators in Eq. (C.2.56) and averaging over all states “ $k$ ”, we obtain the generalized chemical potentials or, for short Klein potentials for electrons  $E_e$ , neutrons  $E_n$  and protons  $E_p$

$$E_e = \sqrt{g_{00}}\mu_e - eV = e^{v/2}\mu_e - eV, \quad (\text{C.2.58})$$

$$E_p = \sqrt{g_{00}}\mu_p + g_\omega\omega + g_\rho\rho + eV = e^{v/2}\mu_p + g_\omega\omega + g_\rho\rho + eV \quad (\text{C.2.59})$$

$$E_n = \sqrt{g_{00}}\mu_n + g_\omega\omega - g_\rho\rho = e^{v/2}\mu_n + g_\omega\omega - g_\rho\rho, \quad (\text{C.2.60})$$

where we have used Eqs. (C.2.14)–(C.2.17) and Eqs. (C.2.32), (C.2.34), (C.2.36)–(C.2.38). In the zero-temperature case, they are generalized Fermi energies for electrons  $E_e = E_e^F$ , neutrons  $E_n = E_n^F$  and protons  $E_p = E_p^F$ .

Using the equations of motion for the fields  $\rho$ ,  $\omega$  and  $\sigma$ , and using the generalized Gibbs-Duhem relation (C.2.45), the energy-momentum conservation

equation (C.2.55) can be rewritten as

$$e^{\nu/2} \sum_{i=n,p,e} n_i \left( d\mu_i - \frac{dT}{T} \mu_i \right) + (\mathcal{E} + \mathcal{P}) e^{\nu/2} \left( \frac{dT}{T} + \frac{1}{2} d\nu \right) + g_\omega n_b d\omega + g_\rho n_3 d\rho + e n_{ch} dV = 0. \quad (\text{C.2.61})$$

The isothermal Tolman condition (Tolman, 1930) (see also Klein (1949)) demands the constancy of the gravitationally red-shifted temperature

$$\frac{dT}{T} + \frac{1}{2} d\nu = 0, \quad \text{or} \quad e^{\nu/2} T = \text{constant}. \quad (\text{C.2.62})$$

Such a condition can be used into Eq. (C.2.61) to obtain

$$\sum_{i=n,p,e} n_i d(e^{\nu/2} \mu_i) + g_\omega n_b d\omega + g_\rho n_3 d\rho + e n_{ch} dV = 0. \quad (\text{C.2.63})$$

Moreover, using the expressions (C.2.58)–(C.2.59) of the generalized chemical potentials, Eq. (C.2.63) can be rewritten as

$$\sum_{i=n,p,e} n_i dE_i = 0, \quad (\text{C.2.64})$$

which leads for independent and non-zero particle number densities  $n_i \neq 0$  to the constancy of the Klein potentials (C.2.58)–(C.2.60) for each particle-species, i.e.

$$E_e = e^{\nu/2} \mu_e - eV = \text{constant}, \quad (\text{C.2.65})$$

$$E_p = e^{\nu/2} \mu_p + \mathcal{V}_p = \text{constant}, \quad (\text{C.2.66})$$

$$E_n = e^{\nu/2} \mu_n + \mathcal{V}_n = \text{constant}, \quad (\text{C.2.67})$$

where

$$\mathcal{V}_p = g_\omega \omega + g_\rho \rho + eV, \quad (\text{C.2.68})$$

$$\mathcal{V}_n = g_\omega \omega - g_\rho \rho. \quad (\text{C.2.69})$$

In the case of nuclear matter in  $\beta$ -equilibrium (assuming not trapped neutrinos), the values of the constant Klein potentials (C.2.65)–(C.2.67) are linked by the condition

$$E_n = E_p + E_e, \quad (\text{C.2.70})$$

which can be rewritten explicitly in terms of the chemical potentials as

$$\mu_n = \mu_p + \mu_e + 2g_\rho \rho e^{-\nu/2}. \quad (\text{C.2.71})$$

### C.2.5. Concluding Remarks

We have presented the self-consistent equations of equilibrium at finite temperatures for a system of neutrons, protons and electrons in  $\beta$ -equilibrium within the framework of general relativity including quantum statistics, electro-weak, and strong interactions. In the mean-field approximation, we obtained the generalized particle chemical potentials from the Dirac equations for nucleons and electrons.

From the Einstein-Maxwell equations, the thermodynamic laws and energy-momentum conservation, we obtain the constancy of the Klein potential of each particle-specie and of the gravitationally red-shifted temperature throughout the configuration, i.e. the first Klein integrals and the Tolman isothermal condition respectively. In the non-interacting degenerate case, following a minimization energy procedure, it was demonstrated that the thermodynamic equilibrium condition of constancy of the generalized particle Fermi energy of all particle species holds (see Olson and Baily (1975)). Such a procedure can be straightforwardly applied to the present case, being the final result given by the equilibrium conditions (C.2.65) and (C.2.66).

The precise values of such constants are linked, in the case of nuclear matter in  $\beta$ -equilibrium, by Eq. (C.2.70), and their full determination needs the inclusion of additional constraints to the system, e.g. global charge neutrality (see e.g. Rotondo et al. (2011d)).

The correct implementation of such generalized Thomas-Fermi equilibrium conditions needs the self-consistent solution of the global problem of equilibrium of the configuration following from the solution of the Einstein-Maxwell equations (C.2.46), (C.2.47), (C.2.49)–(C.2.53), the general relativistic thermodynamic equilibrium conditions (C.2.62), (C.2.65) and (C.2.66), together with the constraints, e.g.  $\beta$ -equilibrium and global charge neutrality.

Thus, the full system of Einstein-Maxwell-Thomas-Fermi equations can be

rewritten in the form

$$e^{-\lambda(r)} \left( \frac{1}{r^2} - \frac{1}{r} \frac{d\lambda}{dr} \right) - \frac{1}{r^2} = -8\pi G T_0^0, \quad (\text{C.2.72})$$

$$e^{-\lambda(r)} \left( \frac{1}{r^2} + \frac{1}{r} \frac{dv}{dr} \right) - \frac{1}{r^2} = -8\pi G T_1^1, \quad (\text{C.2.73})$$

$$V'' + \frac{2}{r} V' \left[ 1 - \frac{r(v' + \lambda')}{4} \right] = -4\pi e e^{v/2} e^\lambda (n_p - n_e), \quad (\text{C.2.74})$$

$$\frac{d^2\sigma}{dr^2} + \frac{d\sigma}{dr} \left[ \frac{2}{r} - \frac{1}{2} \left( \frac{dv}{dr} + \frac{d\lambda}{dr} \right) \right] = e^\lambda [\partial_\sigma U(\sigma) + g_s n_s], \quad (\text{C.2.75})$$

$$\frac{d^2\omega}{dr^2} + \frac{d\omega}{dr} \left[ \frac{2}{r} - \frac{1}{2} \left( \frac{dv}{dr} + \frac{d\lambda}{dr} \right) \right] = -e^\lambda [g_\omega J_\omega^0 - m_\omega^2 \omega], \quad (\text{C.2.76})$$

$$\frac{d^2\rho}{dr^2} + \frac{d\rho}{dr} \left[ \frac{2}{r} - \frac{1}{2} \left( \frac{dv}{dr} + \frac{d\lambda}{dr} \right) \right] = -e^\lambda [g_\rho J_\rho^0 - m_\rho^2 \rho], \quad (\text{C.2.77})$$

$$E_e = e^{v/2} \mu_e - eV = \text{constant}, \quad (\text{C.2.78})$$

$$E_p = e^{v/2} \mu_p + \mathcal{V}_p = \text{constant}, \quad (\text{C.2.79})$$

$$E_n = e^{v/2} \mu_n + \mathcal{V}_n = \text{constant}, \quad (\text{C.2.80})$$

$$e^{v/2} T = \text{constant}, \quad (\text{C.2.81})$$

where the constants  $E_n$ ,  $E_p$  and  $E_e$  are linked by Eq. (C.2.70) and  $\mathcal{V}_{p,n}$  is given by Eq. (C.2.68). In particular, in the degenerate case  $T = 0$ , Eq. (C.2.74) becomes

$$\hat{V}'' + \frac{2}{r} \hat{V}' \left[ 1 - \frac{r(v' + \lambda')}{4} \right] = -4\pi\alpha e^{v/2} e^\lambda \left\{ n_p - \frac{e^{-3v/2}}{3\pi^2} [\hat{V}^2 + 2m_e \hat{V} - m_e^2 (e^v - 1)]^{3/2} \right\}, \quad (\text{C.2.82})$$

where  $\hat{V} \equiv eV + E_e$  and we have used Eq. (C.2.78) into Eq. (C.2.74). This equation is the general relativistic extension of the relativistic Thomas-Fermi equation recently introduced in Rotondo et al. (2011c) for the study of compressed atoms. In addition, Eq. (C.2.82) has been recently used to obtain the globally neutral configurations in the simpler case of degenerate neutrons, protons and electrons in  $\beta$ -equilibrium (Rotondo et al., 2011d).

### **C.3. On the constitutive equations of a self-gravitating system of neutrons, protons and electrons in $\beta$ -equilibrium at finite temperatures**

#### **C.3.1. Introduction**

We have recently introduced a new approach which thanks to the existence of scaling laws can apply to compressed atoms as well as to massive nuclear matter cores of stellar dimensions (Rotondo et al., 2011c). This approach concerning the compressed atom has already given a new contribution in the study of white dwarfs. It represents the first self-consistent calculation taking into due account the electromagnetic contribution in a relativistic treatment of the Thomas-Fermi equation, within global formulation of the equilibrium of white dwarfs in general relativity (Rotondo et al., 2011b).

The application of the above results (Rotondo et al., 2011c,b) to the case of neutron stars is much more complex and it has been approached stepwise. As a first step we have considered the application of this novel approach to the case of a system of neutrons, protons, and electrons in  $\beta$ -equilibrium at zero temperatures within general relativity (Rotondo et al., 2011d). These results are shortly recalled in Sec. C.3.2. The essential role of the generalized Fermi energy of particles (the Klein potentials) and their constancy on the entire equilibrium configuration has been outlined. The existence of an electric potential over the entire configuration has been evidenced.

We have there proved, for the case of this simplified example where strong interactions are neglected, that the traditional approach of describing the system imposing the condition of local charge neutrality and solving the corresponding TOV equations (see e.g. Shapiro and Teukolsky (1983)) is conceptually inconsistent. We have then substitute the condition of local charge neutrality with the condition of global charge neutrality and derived the correct system of equations within the Einstein-Maxwell-Thomas-Fermi system. The boundary conditions are also different from a traditional Cauchy data with the values of the functions and first derivatives at the center into a boundary condition at the center and delicate eigenvalue problem at the boundary determining the condition of charge neutrality at the border; see Sec. C.3.2. The conceptual differences and the alternative mathematical equations of the two approaches, the ones imposing local versus global charge neutrality, lead to the presence of additional electro-dynamical global structures. However, in the specific simple example considered in Rotondo et al. (2011d), they do not give significant quantitative differences in the mass-radius relation for the equilibrium configurations. A very different situation occurs when strong interactions are also taken into account.

Interestingly, these results should have been expected on the ground of some classical works dating back to Rosseland (1924) about the gravito-polarization in self-gravitating ideal Boltzmann electron-ion plasma. We indeed show that our general relativistic equations for the case of global charge neutrality in the Newtonian regime reproduce the Rosseland result. The work of Rosseland has attracted in time additional attention and has been generalized to the case of multicomponent systems; see e.g. Iosilevskiy (2009) and also in the case of general relativity the important results (Klein, 1949; Kodama and Yamada, 1972; Olson and Bailyn, 1975).

In order to transfer these results in the treatment of realistic neutron stars, the introduction of strong interactions is clearly necessary. We have recently generalized our treatment to the case of strong interactions in Rueda et al. (2011a). There the major aim has been to prove the constancy of the Klein potentials in the case in which the nuclear interactions are described by a Lagrangian including in addition to the gravitational, electromagnetic, and weak interactions, also the presence of  $\sigma$ ,  $\omega$ , and  $\rho$  virtual mesons that mediate the nuclear interactions. These results are shortly summarized for completeness in Sec. C.3.3.

It is clear that neutron stars are not at zero temperatures but have temperatures which in the case of the Crab pulsar are  $T \sim 10^6$  K, see e.g. Tennant et al. (2001); Weisskopf et al. (2004). It has been pointed out to us that the thermal energy expected in a neutron star is much larger than the Coulomb energy obtained e.g. in Rotondo et al. (2011d). Before proceeding further in this research we have to prove that these gravito-polarization effect do survive in the presence of a system at  $T \neq 0$ . In any way, the study of the equilibrium of a system of neutrons, protons, and electrons including all the interactions need to be generalized to the case of finite temperatures. This treatment is here presented in Sec. C.3.4. The constancy of the Klein potentials in this more general case is presented in Sec. C.3.5 where it is also explicitly shown how the thermal effects do not modify the existence of gravito-polarization. The generality of the formalism here introduced allows to approach as well the classical Boltzmann limit consistently.

we have finally outlined in the conclusions how this theoretical formulation is now sufficient to approach the problem of the possible existence of overcritical fields at the interface between the the core and the crust of the neutron star.

### C.3.2. Einstein-Maxwell-Thomas-Fermi equations in the degenerate case

Following Rotondo et al. (2011d), we consider the equilibrium configurations of a degenerate gas of neutrons, protons and electrons with total matter en-

ergy density and total matter pressure

$$\mathcal{E} = \sum_{i=n,p,e} \frac{2}{(2\pi\hbar)^3} \int_0^{P_i^F} \epsilon_i(p) 4\pi p^2 dp, \quad (\text{C.3.1})$$

$$P = \sum_{i=n,p,e} \frac{1}{3} \frac{2}{(2\pi\hbar)^3} \int_0^{P_i^F} \frac{p^2}{\epsilon_i(p)} 4\pi p^2 dp, \quad (\text{C.3.2})$$

where  $\epsilon_i(p) = \sqrt{c^2 p^2 + m_i^2 c^4}$  is the relativistic single particle energy and  $P_i^F$  denote the Fermi momentum, related to the particle number density  $n_i$  by  $n_i = (P_i^F)^3 / (3\pi^2 \hbar^3)$ .

Introducing the metric for a spherically symmetric non-rotating configuration

$$ds^2 = e^{\nu(r)} c^2 dt^2 - e^{\lambda(r)} dr^2 - r^2 d\theta^2 - r^2 \sin^2 \theta d\varphi^2, \quad (\text{C.3.3})$$

the full system of equations composed by the Einstein-Maxwell-Thomas-Fermi equations can be written as (see Rotondo et al. (2011d) for details)

$$M' = 4\pi r^2 \frac{\mathcal{E}}{c^2} - \frac{4\pi r^3}{c^2} e^{-\nu/2} \hat{V}' \left\{ n_p - \frac{e^{-3\nu/2}}{3\pi^2} [\hat{V}^2 + 2m_e c^2 \hat{V} - m_e^2 c^4 (e^\nu - 1)]^{3/2} \right\}, \quad (\text{C.3.4})$$

$$\nu' = \frac{2G}{c^2} \frac{4\pi r^3 P / c^2 + M - r^3 E^2 / c^2}{r^2 \left( 1 - \frac{2GM}{c^2 r} + \frac{Gr^2 E^2}{c^4} \right)}, \quad (\text{C.3.5})$$

$$E_e^F = e^{\nu/2} \mu_e - m_e c^2 - eV = \text{constant}, \quad (\text{C.3.6})$$

$$E_p^F = e^{\nu/2} \mu_p - m_p c^2 + eV = \text{constant}, \quad (\text{C.3.7})$$

$$E_n^F = E_e^F + E_p^F - (m_n - m_e - m_p) c^2, \quad (\text{C.3.8})$$

$$\hat{V}'' + \frac{2}{r} \hat{V}' \left[ 1 - \frac{r(\nu' + \lambda')}{4} \right] = -4\pi \alpha \hbar c e^{\nu/2} e^\lambda \left\{ n_p - \frac{e^{-3\nu/2}}{3\pi^2} [\hat{V}^2 + 2m_e c^2 \hat{V} - m_e^2 c^4 (e^\nu - 1)]^{3/2} \right\}, \quad (\text{C.3.9})$$

where a prime stands for radial derivative, Eqs. (C.3.6)–(C.3.7) are the extension to general relativity of the Thomas-Fermi equilibrium condition on the generalized Fermi energies of electrons and protons, Eq. (C.3.8) is the condition of  $\beta$ -equilibrium between neutrons, protons, and electrons. We recall that from Eqs. (C.3.6)–(C.3.8) it follows also the constancy of the generalized neutron Fermi energy. The Eq. (C.3.9) is the general relativistic extension of the relativistic Thomas-Fermi equation recently introduced in the rel-

ativistic Feynman-Metropolis-Teller treatment for the study of compressed atoms (Rotondo et al., 2011c). In the above equations  $e$  is the fundamental charge,  $\alpha$  is the fine structure constant,  $V$  is the Coulomb potential,  $\mu_i = \partial\mathcal{E}/\partial n_i = \sqrt{c^2(P_i^F)^2 + m_i^2 c^4}$  is the free-chemical potential of particle-species,  $\lambda(r)$  is the metric function related to the mass  $M(r)$  and the electric field  $E(r) = -e^{-(\nu+\lambda)/2}V'$  through

$$e^{-\lambda} = 1 - \frac{2GM(r)}{c^2 r} + \frac{G}{c^4} r^2 E^2(r). \quad (\text{C.3.10})$$

and  $\hat{V} = E_e^F + eV$ .

As shown in Rotondo et al. (2011d), the condition of local charge neutrality  $n_e(r) = n_p(r)$  often adopted in literature is not consistent with Eqs. (C.3.6) and (C.3.7), see Fig. 1 of Rotondo et al. (2011d) for details. Therefore, we consider equilibrium configurations fulfilling only global charge neutrality. We solve self-consistently Eq. (C.3.4) and (C.3.5) for the metric, Eqs. (C.3.6)–(C.3.8) for the equilibrium of the three degenerate fermion species and for the  $\beta$ -equilibrium. The crucial equation relating the proton and the electron distributions is then given by the general relativistic Thomas-Fermi equation (C.3.9). The boundary conditions are: for Eq. (C.3.4) the regularity at the origin:  $M(0) = 0$ , for Eqs. (C.3.6)–(C.3.8) a given value of the central density, and for Eq. (C.3.9) the regularity at the origin  $n_e(0) = n_p(0)$ , and a second condition at infinity which results in an eigenvalue problem determined by imposing the global charge neutrality conditions

$$\hat{V}(R_e) = E_e^F, \quad \hat{V}'(R_e) = 0, \quad (\text{C.3.11})$$

at the radius  $R_e$  of the electron distribution defined by

$$P_e^F(R_e) = 0, \quad (\text{C.3.12})$$

from which follows

$$\begin{aligned} E_e^F &= m_e c^2 e^{\nu(R_e)/2} - m_e c^2 \\ &= m_e c^2 \sqrt{1 - \frac{2GM(R_e)}{c^2 R_e}} - m_e c^2. \end{aligned} \quad (\text{C.3.13})$$

The eigenvalue problem consists in determining the gravitational potential and the Coulomb potential at the center of the configuration that satisfy the conditions (C.3.11)–(C.3.13) at the boundary. In Fig. 2 of Rotondo et al. (2011d) we have shown the solution for the density, the gravitational potential and electric potential for a configuration with central density  $\rho(0) = 3.94\rho_{\text{nuc}}$ , where  $\rho_{\text{nuc}} \sim 2.7 \times 10^{14} \text{ g/cm}^3$ .

A particular interesting new feature is the approach to the boundary of the

configuration where three different radii are present corresponding to distinct radii at which the individual particle Fermi pressures vanish. The radius  $R_e$  for the electron component corresponding to  $P_e^F(R_e) = 0$ , the radius  $R_p$  for the proton component corresponding to  $P_p^F(R_p) = 0$  and the radius  $R_n$  for the neutron component corresponding to  $P_n^F(R_n) = 0$ . For a configuration with the aforementioned central density we found, for instance,  $R_n \simeq 12.735$  km,  $R_p \simeq 12.863$  km and  $R_e \simeq R_p + 10^3 \lambda_e$  where  $\lambda_e = \hbar/(m_e c)$  denotes the electron Compton wavelength (see Figs. 2 and 3 of Rotondo et al. (2011d), for details). The occurrence of the radius  $R_n$  is due to the threshold energy for inverse  $\beta$ -decay equilibrium between free neutrons, protons, and electrons, at around  $\rho \sim 10^7$  (see e.g. Shapiro and Teukolsky (1983)). The electron component follows closely the proton component up to the radius  $R_p$  where the proton density drops to zero. The “proton skin”,  $R_p - R_n \sim 0.1$  km, can be understood as being due to the difference between the proton and the neutron mass. The charge difference leads to gravitational and Coulomb forces acting on protons and only gravitational force on neutrons. The electron component then fully neutralizes the positive charge at  $R_e$  leading to a global configuration without net charge, contrary to the results presented e.g. in Olson and Bailyn (1978).

It can be seen from Fig. 2 in Rotondo et al. (2011d) that the depth of the Coulomb potential is of the order of  $\lesssim m_\pi c^2$ . In Fig. C.4 we have plotted the Coulomb potential and the corresponding electric field of the configuration studied here and in Rotondo et al. (2011d). A Coulomb potential  $\sim m_\pi c^2/e$  decreasing in a typical macroscopic neutron star radius  $R \sim \lambda_\pi(m_{\text{Planck}}/m_p)$  creates an electric field  $\sim (m_p/m_{\text{Planck}})(m_\pi/m_e)^2 E_c \sim 10^{-14} E_c$ , being  $E_c = m_e^2 c^3/(e\hbar)$  the critical electric field for vacuum polarization.

### C.3.3. Newtonian limit

Despite the fact that the strong gravitational field of neutron stars requires a general relativistic treatment, it is interesting to explore the Newtonian limit of all the above considerations. This can help to elucidate if the gravito-electromagnetic effects we have found are of general relativistic nature or to prove their validity in a Newtonian regime.

The Newtonian limit of the equilibrium equations can be obtained by the weak-field non-relativistic limit. We expand the gravitational potential at first-order  $e^{v/2} \approx 1 + \Phi/c^2$ , where  $\Phi$  is the Newtonian gravitational potential. In the non-relativistic mechanics limit  $c \rightarrow \infty$ , the particle chemical potential becomes  $\mu_i \rightarrow \tilde{\mu}_i + m_i c^2$ , where  $\tilde{\mu}_i = (P_i^F)^2/(2m_i)$  denotes the non-relativistic free-chemical potential. Applying these considerations, the electron and pro-

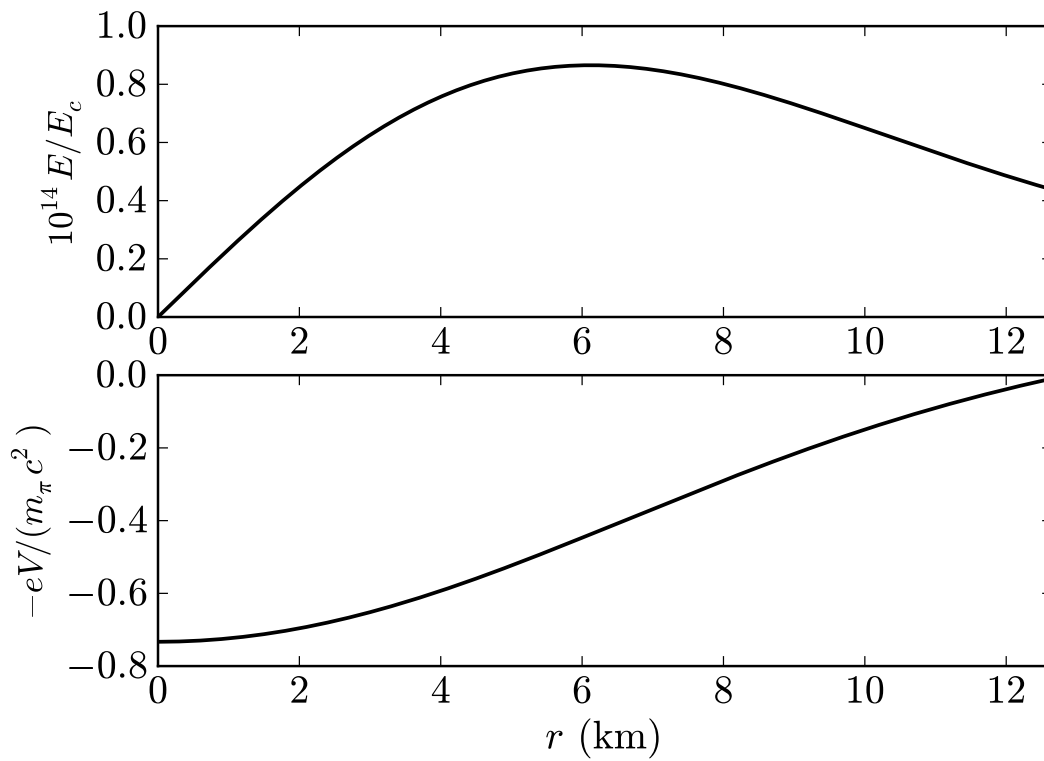


**Figure C.4.:** Electric field and electron Coulomb potential energy of the configuration of neutrons, protons, and electrons in  $\beta$ -equilibrium studied here and in Rotonondo et al. (2011d).

C.3. *On the constitutive equations of a self-gravitating system of neutrons, protons and electrons in  $\beta$ -equilibrium at finite temperatures*

---

ton equilibrium law (C.3.6) becomes

$$E_p^{F,\text{Newt}} = \tilde{\mu}_p + m_p\Phi + eV = \text{constant}, \quad (\text{C.3.14})$$

$$E_e^{F,\text{Newt}} = \tilde{\mu}_e + m_e\Phi - eV = \text{constant}, \quad (\text{C.3.15})$$

which is the classical condition of thermodynamic equilibrium of a fluid of charged particles in presence of external gravitational and electrostatic fields.

The condition of  $\beta$ -equilibrium is, in this case, given by

$$E_n^{F,\text{Newt}} = E_p^{F,\text{Newt}} + E_e^{F,\text{Newt}}, \quad (\text{C.3.16})$$

which links the constants  $E_p^{F,\text{Newt}}$  and  $E_e^{F,\text{Newt}}$  to the constant neutron Fermi energy  $E_n^{F,\text{Newt}}$ .

From the constancy of the proton and electron Fermi energies it follows the relation

$$\tilde{\mu}_p - \tilde{\mu}_e + (m_p - m_e)\Phi + 2eV = \text{constant}, \quad (\text{C.3.17})$$

which in the case of an ideal electron-ion gas becomes the Rosseland relation of equilibrium (see Eq. 7 in Rosseland (1924)). It is interesting to obtain from the above equation an estimate of the Coulomb potential well inside the configuration. Evaluating Eq. (C.3.17) at the radius of the configuration where the particle free chemical potentials go to zero, we obtain an estimate of the ratio of the Coulomb potential energy and the gravitational energy close to the surface of the configuration

$$\frac{eV(R)}{\Phi(R)} \sim -\frac{m_p - m_e}{2}. \quad (\text{C.3.18})$$

Assuming that the system is at nuclear density,  $\rho \sim m_p/\lambda_\pi^3$  where  $\lambda_\pi = \hbar/(m_\pi c)$  is the pion Compton wavelength, the mass and the radius of the configuration are roughly given by  $M \sim m_{\text{Planck}}^3/m_p^2$  and  $R \sim \lambda_\pi(m_{\text{Planck}}/m_p)$  and therefore the gravitational potential will be  $\Phi(R) = -GM/R \sim (m_\pi/m_p)c^2$ . Consequently, the Coulomb potential energy close to the border is approximately  $eV(R) \sim m_\pi c^2/2$ . Assuming a constant charge density approximation, the Coulomb potential energy at the center of the configuration is 3/2 times its value at the surface, thus we obtain approximately

$$eV(0) \sim \frac{3}{4}m_\pi c^2, \quad (\text{C.3.19})$$

which is in full agreement with both with the numerical results and with the general relativistic formulas given by Eqs. (21) and (22) of Rotondo et al. (2011d). This numerical value is also in line with the Coulomb potential well obtained from the idealized treatment presented in Ruffini (2008b); Popov

(2010); Rotondo et al. (2011e,c).

In the weak-field non-relativistic limit, the Einstein-Maxwell equations (C.3.4)–(C.3.9) become

$$M' = 4\pi r^2 \rho(r), \quad (\text{C.3.20})$$

$$\Phi' = \frac{GM}{r^2}, \quad (\text{C.3.21})$$

$$P' = -\frac{GM}{r^2} \rho - \left[ n_p - \frac{(2m_e)^{3/2}}{3\pi^2 \hbar^3} (\hat{V} - m_e \Phi)^{3/2} \right] \hat{V}', \quad (\text{C.3.22})$$

$$\hat{V}'' + \frac{2}{r} \hat{V}' = -4\pi e^2 \left[ n_p - \frac{(2m_e)^{3/2}}{3\pi^2 \hbar^3} (\hat{V} - m_e \Phi)^{3/2} \right], \quad (\text{C.3.23})$$

where  $\rho$  in this case is the rest-mass density

$$\rho = \sum_{i=n,p,e} m_i n_i. \quad (\text{C.3.24})$$

The solution of Eqs. (C.3.14), (C.3.20)–(C.3.23) together with the  $\beta$ -equilibrium condition (C.3.16) leads to qualitatively similar electrodynamical properties as the one obtained in the general relativistic case. In Fig. C.5 we show the electric field in the region  $r < R_n$  ( $R_n^{\text{Newt}} < R_n^{\text{GR}}$ ) both for the Newtonian as well as for the General Relativistic configuration for the given central density  $\rho(0) = 3.94\rho_{\text{nuc}}$ . From the quantitative point of view, the electric field of the Newtonian configuration is larger than the electric field of the general relativistic configuration.

### C.3.4. Introducing strong interactions

It is clear now that if one considers a fluid of only neutrons, protons, and electrons in  $\beta$ -equilibrium neglecting the effects of the strong interactions and the presence of a crust, then the electromagnetic structure is the one shown in Figs. C.4 and C.5.

The effect of having different radii  $R_n$ ,  $R_p$ , and  $R_e$  needs to be also studied in the more general case when strong interactions and the presence of the crust of the neutron star are included. The complete study of such a problem must to be necessarily done within a fully relativistic approach taking into account the strong, weak, electromagnetic, and gravitational interactions.

Indeed, in the mean time we have given an essential step forward in Rueda et al. (2011a) by formulating such a treatment. The nuclear interactions have been there included through the Walecka model (see Duerr (1956); Walecka (1974) for details, and Bowers et al. (1973b,a) for a similar theory) in which nucleons interact by Yukawa-like couplings. The strong interaction between nucleons is thus described by the exchange of three virtual mesons: an isoscalar

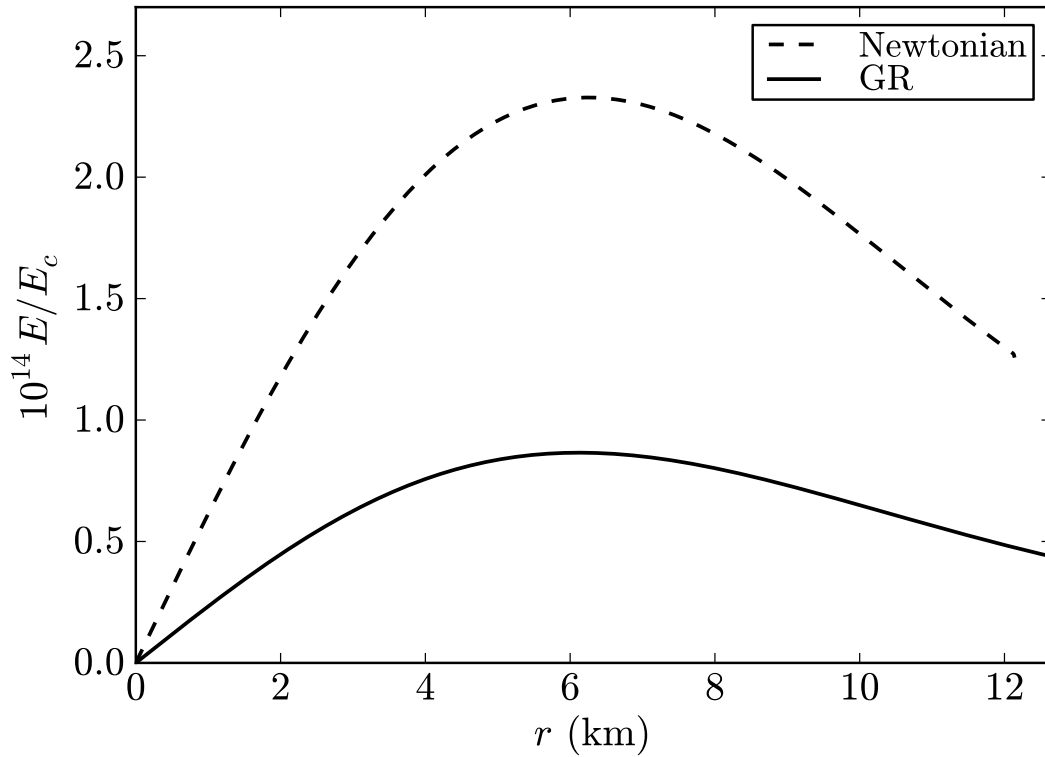


**Figure C.5.:** Electric field (multiplied by  $10^{14}$ ) in units of the critical field  $E_c = m_e^2 c^3 / (e\hbar) \sim 10^{16}$  Volt/cm in the region  $r < R_n$  both for the Newtonian and the General Relativistic configurations. The central density of both systems is  $\rho(0) = 3.94\rho_{\text{nuc}}$  where  $\rho_{\text{nuc}} = 2.7 \times 10^{14}$  g cm<sup>-3</sup> is the nuclear density.

meson field  $\sigma$  providing the attractive long-range part of the nuclear force; the massive vector field  $\omega_\mu$  that models the repulsive short range and; the massive isovector field  $\rho_\mu$  which takes account of the isospin effects of nuclei (see also Boguta and Bodmer (1977); Ring (1996)).

As shown in Rueda et al. (2011a), the more general Einstein-Maxwell-Thomas-Fermi equations including strong interactions which generalizes Eqs. (C.3.65)–(C.3.71) can be written as (in units with  $\hbar = c = 1$ )

$$e^{-\lambda(r)} \left( \frac{1}{r^2} - \frac{\lambda'}{r} \right) - \frac{1}{r^2} = -8\pi G T_0^0, \quad (\text{C.3.25})$$

$$e^{-\lambda(r)} \left( \frac{1}{r^2} + \frac{\nu'}{r} \right) - \frac{1}{r^2} = -8\pi G T_1^1, \quad (\text{C.3.26})$$

$$\nabla^\mu \nabla_\mu V = -4\pi e^\lambda e J_0^{ch}, \quad (\text{C.3.27})$$

$$\nabla^\mu \nabla_\mu \sigma = e^\lambda [\partial_\sigma U(\sigma) + g_\sigma n_s], \quad (\text{C.3.28})$$

$$\nabla^\mu \nabla_\mu \omega = -e^\lambda (g_\omega J_\omega^0 - m_\omega^2 \omega), \quad (\text{C.3.29})$$

$$\nabla^\mu \nabla_\mu \rho = -e^\lambda (g_\rho J_\rho^0 - m_\rho^2 \rho), \quad (\text{C.3.30})$$

$$E_e = e^{\nu/2} \mu_e - eV = \text{constant}, \quad (\text{C.3.31})$$

$$E_p = e^{\nu/2} \mu_p + \mathcal{V}_p = \text{constant}, \quad (\text{C.3.32})$$

$$E_n = e^{\nu/2} \mu_n + \mathcal{V}_n = \text{constant}, \quad (\text{C.3.33})$$

$$e^{\nu/2} T = \text{constant}, \quad (\text{C.3.34})$$

where  $\nabla^\mu \nabla_\mu = d^2/dr^2 + [2/r - (1/2)(\nu' + \lambda')]d/dr$ , being  $\nabla^\mu$  the covariant derivative and

$$\mathcal{V}_p = g_\omega \omega + g_\rho \rho + eV, \quad (\text{C.3.35})$$

$$\mathcal{V}_n = g_\omega \omega - g_\rho \rho, \quad (\text{C.3.36})$$

are the effective potentials of nucleons, being  $V \equiv A_0$ ,  $\omega \equiv \omega_0$ ,  $\rho \equiv \rho_0$  the time components of the electromagnetic and the meson potentials, and  $g_\sigma$ ,  $g_\omega$ ,  $g_\rho$  denote the coupling constants between the nucleons and the massive mesons. The self-interaction scalar field potential  $U(\sigma)$  can be in general a quartic-order polynom for a renormalizable theory (see e.g. Lee and Wick (1974)).

The scalar density is given by  $n_s = \partial \mathcal{E} / \partial \tilde{m}_N$  where  $\tilde{m}_N = m_N + g_\sigma \sigma$  is the effective nucleon mass. The only non-vanishing components of the currents are

$$J_0^{ch} = (n_p - n_e) u_0, \quad (\text{C.3.37})$$

$$J_0^\omega = (n_n + n_p) u_0, \quad (\text{C.3.38})$$

$$J_0^\rho = (n_p - n_n) u_0, \quad (\text{C.3.39})$$

*C.3. On the constitutive equations of a self-gravitating system of neutrons, protons and electrons in  $\beta$ -equilibrium at finite temperatures*

---

where  $u_0 = \sqrt{g_{00}} = e^{v/2}$  is the covariant time component of the four-velocity of the fluid.

The function  $\lambda(r)$  satisfies also in this case Eq. (C.3.10) and the energy-momentum tensor is

$$T^{\mu\nu} = T_f^{\mu\nu} + T_\gamma^{\mu\nu} + T_\sigma^{\mu\nu} + T_\omega^{\mu\nu} + T_\rho^{\mu\nu}, \quad (\text{C.3.40})$$

where

$$T_\gamma^{\mu\nu} = -\frac{1}{4\pi} \left( F_\alpha^\mu F^{\alpha\nu} + \frac{1}{4} g^{\mu\nu} F_{\alpha\beta} F^{\alpha\beta} \right), \quad (\text{C.3.41})$$

$$T_\sigma^{\mu\nu} = \nabla^\mu \nabla^\nu \sigma - g^{\mu\nu} \left[ \frac{1}{2} \nabla_\sigma \sigma \nabla^\sigma \sigma - U(\sigma) \right], \quad (\text{C.3.42})$$

$$\begin{aligned} T_\omega^{\mu\nu} &= -\Omega_\alpha^\mu \Omega^{\alpha\nu} - \frac{1}{4} g^{\mu\nu} \Omega_{\alpha\beta} \Omega^{\alpha\beta} \\ &+ m_\omega^2 \left( \omega^\mu \omega^\nu - \frac{1}{2} g^{\mu\nu} \omega_\alpha \omega^\alpha \right), \end{aligned} \quad (\text{C.3.43})$$

$$\begin{aligned} T_\rho^{\mu\nu} &= -\mathcal{R}_\alpha^\mu \mathcal{R}^{\alpha\nu} - \frac{1}{4} g^{\mu\nu} \mathcal{R}_{\alpha\beta} \mathcal{R}^{\alpha\beta} \\ &+ m_\rho^2 \left( \mathcal{R}^\mu \mathcal{R}^\nu - \frac{1}{2} g^{\mu\nu} \mathcal{R}_\alpha \mathcal{R}^\alpha \right), \end{aligned} \quad (\text{C.3.44})$$

$$T_f^{\mu\nu} = (\mathcal{E} + P) u^\mu u^\nu - P g^{\mu\nu}, \quad (\text{C.3.45})$$

where  $\Omega_{\mu\nu} \equiv \partial_\mu \omega_\nu - \partial_\nu \omega_\mu$ ,  $\mathcal{R}_{\mu\nu} \equiv \partial_\mu \rho_\nu - \partial_\nu \rho_\mu$ ,  $F_{\mu\nu} \equiv \partial_\mu A_\nu - \partial_\nu A_\mu$  are the field strength tensors for the  $\omega^\mu$ ,  $\rho^\mu$  and  $A^\mu$  fields respectively.

The equilibrium conditions of the constancy of the Klein potentials of the particles throughout the configuration is expressed by Eqs. (C.3.31)–(C.3.33) and Eq. (C.3.34) is the Tolman isothermality condition analogous to Eq. (C.3.71).

There are additional contributions of the strong interaction to the nuclear symmetry energy given within this theory mainly by the  $\rho$ -meson. Such contributions change the proton skin structure  $R_p > R_n$  shown in this work to a “neutron skin” effect  $R_n > R_p$  in the core-crust boundary layer at nuclear density Belvedere et al. (2012), in close analogy to the neutron skin observed in neutron rich nuclei, see e.g. Tamii et al. (2011).

### C.3.5. Finite temperature effects

The above results have been obtained within the zero temperature approximation. Temperatures of the order of  $\sim 10^6$  K are expected to exist at the surface of old neutron stars (Tennant et al., 2001; Weisskopf et al., 2004), or temperatures of  $10^8 - 10^9$  K could, in principle, exist in neutron star interiors. We are going to show that these thermal effects do not affect the considerations on gravito-polarization here introduced. For neutron stars, the Fermi

temperature

$$T_i^F = \frac{\mu_i - m_i c^2}{k}, \quad (\text{C.3.46})$$

where  $k$  is the Boltzmann constant, can be as large as  $\sim 10^{12}$  K for electrons,  $\sim 10^{11}$  K for protons and  $\sim 10^{13}$  K for neutrons for typical central densities of neutron stars. This means that neutron stars interiors are, at a high degree of accuracy, degenerate systems. However, the total thermal energy of a neutron star  $E_{\text{th}} \sim 10^{48} T_9^2$  erg (see e.g. Yakovlev and Pethick (2004)) where  $T_9$  is the temperature in units of  $10^9$  K, is much larger than the Coulomb energy  $E_C \sim (1/6)R^3 E^2 \sim 10^{16}$  erg, where  $E$  is the internal electric field here considered (see Figs. C.4 and C.5) and  $R$  is the radius of the configuration. It can be then of interest to ask the question if our electro-dynamical structure will still occur in presence of thermal effects.

In this more general case, the equation of state given by Eqs. (C.3.1) and (C.3.2), is replaced by

$$\mathcal{E} = \sum_{i=n,p,e} \frac{2}{(2\pi\hbar)^3} \int_0^\infty \tilde{\epsilon}_i(p) f_i(p) 4\pi p^2 dp, \quad (\text{C.3.47})$$

$$P = \sum_{i=n,p,e} \frac{1}{3} \frac{2}{(2\pi\hbar)^3} \int_0^\infty \frac{p^2 f_i(p)}{\tilde{\epsilon}_i(p) + m_i c^2} 4\pi p^2 dp, \quad (\text{C.3.48})$$

where

$$f_i(p) = \frac{1}{\exp[(\tilde{\epsilon}_i(p) - \tilde{\mu}_i)/(kT)] + 1}, \quad (\text{C.3.49})$$

is the Fermi-Dirac fermion distribution function which gives the particle number density  $n_i$

$$n_i = \frac{2}{(2\pi\hbar)^3} \int_0^\infty f_i(p) 4\pi p^2 dp, \quad (\text{C.3.50})$$

where  $\tilde{\epsilon}_i(p) = \epsilon_i(p) - m_i c^2 = \sqrt{c^2 p^2 + m_i^2 c^4} - m_i c^2$  and  $\tilde{\mu}_i$  are the free single particle energy and the free particle chemical potential with the particle rest mass-energy  $m_i c^2$  subtracted off.

### Tolman isothermality and conserved Klein potentials

We turn now to demonstrate the constancy of the Klein potentials and the constancy of the gravitationally red-shifted temperature throughout the configuration.

The equation of state (C.3.47)–(C.3.48) satisfies the thermodynamic law

$$\mathcal{E} + P - Ts = \sum_{i=n,p,e} n_i \mu_i, \quad (\text{C.3.51})$$

C.3. *On the constitutive equations of a self-gravitating system of neutrons, protons and electrons in  $\beta$ -equilibrium at finite temperatures*

---

where  $s = S/V$  is the entropy per unit volume and  $\mu_i = \partial\mathcal{E}/\partial n_i$  is the free-chemical potential of the  $i$ -specie. At zero-temperature  $T = 0$ ,  $\mu_i = \sqrt{(cP_i^F)^2 + \tilde{m}_i^2 c^4}$  and  $n_i = (P_i^F)^3 / (3\pi^2 \hbar^3)$ , where  $P_i^F$  denotes the Fermi momentum of the  $i$ -specie.

From Eq. (C.3.51) follows the Gibbs-Duhem relation

$$dP = \sum_{i=n,p,e} n_i d\mu_i + s dT, \quad (\text{C.3.52})$$

which can be rewritten as

$$dP = \sum_{i=n,p,e} n_i d\mu_i + \left( \mathcal{E} + P - \sum_{i=n,p,e} n_i \mu_i \right) \frac{dT}{T}. \quad (\text{C.3.53})$$

Using the Gibbs-Duhem relation (C.3.53) the energy-momentum conservation equation (see Rotondo et al. (2011d) for details)

$$e^{\nu/2} dP + e^{\nu/2} \frac{d\nu}{2} (\mathcal{E} + P) + e dV (n_p - n_e) = 0, \quad (\text{C.3.54})$$

can be rewritten as

$$e^{\nu/2} \sum_{i=n,p,e} n_i \left( d\mu_i - \frac{dT}{T} \mu_i \right) + (\mathcal{E} + P) e^{\nu/2} \left( \frac{dT}{T} + \frac{1}{2} d\nu \right) + e (n_p - n_e) dV = 0. \quad (\text{C.3.55})$$

The Tolman isothermal condition (Tolman, 1930) (see also Klein (1949)) demands the constancy of the gravitationally red-shifted temperature

$$\frac{dT}{T} + \frac{1}{2} d\nu = 0, \quad \text{or} \quad T_\infty = e^{\nu/2} T = \text{constant}, \quad (\text{C.3.56})$$

which can be used into Eq. (C.3.55) to obtain

$$\sum_{i=n,p,e} n_i d(e^{\nu/2} \mu_i) + e (n_p - n_e) dV = 0. \quad (\text{C.3.57})$$

We now introduce the generalized chemical potentials, or Klein potentials, for electrons  $E_e$ , protons  $E_p$  and neutrons  $E_n$

$$E_e = e^{\nu/2} \mu_e - m_e c^2 - eV, \quad (\text{C.3.58})$$

$$E_p = e^{\nu/2} \mu_p - m_p c^2 + eV, \quad (\text{C.3.59})$$

$$E_n = e^{\nu/2} \mu_n - m_n c^2, \quad (\text{C.3.60})$$

which in the zero temperature limit are the generalized Fermi energies for electrons  $E_e = E_e^F$ , neutrons  $E_n = E_n^F$  and protons  $E_p = E_p^F$  introduced in Sec. II (see Eq. (C.3.6)). Using Eqs. (C.3.58), (C.3.59) and (C.3.60), Eq. (C.3.57) becomes

$$\sum_{i=n,p,e} n_i dE_i = 0, \quad (\text{C.3.61})$$

which leads for independent and non-zero particle number densities  $n_i \neq 0$  to the constancy of the Klein potentials (C.3.58)–(C.3.60) for each particle-species, i.e.

$$E_e = e^{v/2} \mu_e - m_e c^2 - eV = \text{constant}, \quad (\text{C.3.62})$$

$$E_p = e^{v/2} \mu_p - m_p c^2 + eV = \text{constant}, \quad (\text{C.3.63})$$

$$E_n = e^{v/2} \mu_n - m_n c^2 = \text{constant}. \quad (\text{C.3.64})$$

In the zero temperature limit the constancy of the Klein potential of each particle-specie becomes the constancy of the generalized Fermi energies introduced in Sec. C.3.2 (see Eqs. (C.3.6)–(C.3.8)). This is a crucial point because, as discussed in Rotondo et al. (2011d), the constancy of the generalized Fermi energies proves the impossibility of having a self-consistent configuration fulfilling the condition of local charge neutrality and  $\beta$ -equilibrium (see e.g. Fig. 1 of Rotondo et al. (2011d)). Further, as shown in Rueda et al. (2011a), the constancy of the Klein potentials holds in the more general case when the strong interactions between nucleons are taken into account.

Therefore, introducing the new dimensionless variables  $\eta_i = \tilde{\mu}_i / (kT)$  and  $\beta_i = kT / (m_i c^2)$ , the new set of Einstein-Maxwell-Thomas-Fermi equations generalizing the system (C.3.4)–(C.3.9) to the case of finite temperatures is

$$M' = 4\pi r^2 \frac{\mathcal{E}}{c^2} - \frac{4\pi r^3}{c^2} e^{-v/2} \hat{V}' (n_p - n_e), \quad (\text{C.3.65})$$

$$v' = \frac{2G}{c^2} \frac{4\pi r^3 P / c^2 + M - r^3 E^2 / c^2}{r^2 \left( 1 - \frac{2GM}{c^2 r} + \frac{Gr^2}{c^4} E^2 \right)}, \quad (\text{C.3.66})$$

$$\begin{aligned} E_e &= m_e c^2 e^{v/2} (1 + \beta_e \eta_e) - m_e c^2 - eV \\ &= \text{constant}, \end{aligned} \quad (\text{C.3.67})$$

$$\begin{aligned} E_p &= m_p c^2 e^{v/2} (1 + \beta_p \eta_p) - m_p c^2 + eV \\ &= \text{constant}, \end{aligned} \quad (\text{C.3.68})$$

$$E_n = E_e + E_p - (m_n - m_e - m_p) c^2, \quad (\text{C.3.69})$$

$$\begin{aligned} \hat{V}'' + \frac{2}{r} \hat{V}' \left[ 1 - \frac{r(v' + \lambda')}{4} \right] &= -4\pi \alpha \hbar c e^{v/2} e^\lambda (n_p \\ &- n_e), \end{aligned} \quad (\text{C.3.70})$$

$$e^{v/2} \beta_i = \text{constant}, \quad i = n, p, e, \quad (\text{C.3.71})$$

where Eq. (C.3.69) is the condition of  $\beta$ -equilibrium between neutrons, protons and electrons, and the number density of the  $i$ -specie is given by

$$n_i = \frac{2^{1/2} m_i^3 c^3}{\pi^2 \hbar^3} \beta_i^{3/2} (F_{1/2}^i + \beta_i F_{3/2}^i), \quad (\text{C.3.72})$$

where we have introduced the relativistic Fermi-Dirac integrals of order  $j$

$$F_j^i = F_j(\eta_i, \beta_i) = \int_0^\infty \frac{x^j \left(1 + \frac{1}{2} \beta_i x\right)^{1/2}}{1 + e^{x - \eta_i}} dx. \quad (\text{C.3.73})$$

The above formulation generalizes to the case of finite temperatures the Einstein-Maxwell-Thomas-Fermi equations obtained in Rotondo et al. (2011d) and recalled here in Sec. C.3.2. This formulation can be also straightforwardly done in the presence of strong interactions generalizing the formulation of Sec. C.3.4 (see Rueda et al. (2011a) for details).

### Numerical results

We have integrated numerically the system of equations (C.3.65)–(C.3.71) for given temperatures  $T_\infty \neq 0$ . As expected, the results are both qualitatively and quantitatively similar to the ones obtained with the degenerate approximation. The largest difference we found is at the surface boundary of the configuration, where, due to the low density of the system, finite temperature effects are more effective. As an example, we compare in Fig. C.6 the electron density for  $r > R_p$  in the degenerate and in the non-degenerate case for  $T_\infty = 2.3 \times 10^5$  K. For distances  $r < R_p$  the results are essentially the same as in the degenerate case. In the region  $r \ll R_n$  at large densities  $> \rho_{\text{nuc}} = 2.7 \times 10^{14}$  g/cm<sup>3</sup>, the electro-dynamical properties of the configuration i.e. Coulomb potential and electric field remain unperturbed even for very large temperatures  $T_\infty \sim 10^{11}$  K. This is due to the fact that thermal effects are largely compensated by the gravitational potential as given by Eq. (C.3.56); the Coulomb interaction is not involved in this balance and is not affected by the thermal energy.

It is worth to mention that from general computations of the heating and cooling mechanisms it turns out that neutron star interiors are highly isothermal (in the sense of Tolman) due to the high thermal conductivity of degenerate particles (Yakovlev and Pethick, 2004). In real neutron stars, the fluid of neutrons, protons and electrons in  $\beta$ -equilibrium studied in this work does not extend all the way to the neutron star surface but is confined to the neutron star core surrounded by the neutron star crust. In this more general case, the surface structure shown in Fig. C.6 is replaced by the crust composed of nuclei and degenerate electrons. The condition of isothermality breaks down in the surface non-degenerate layers of the star due to existence of high tem-

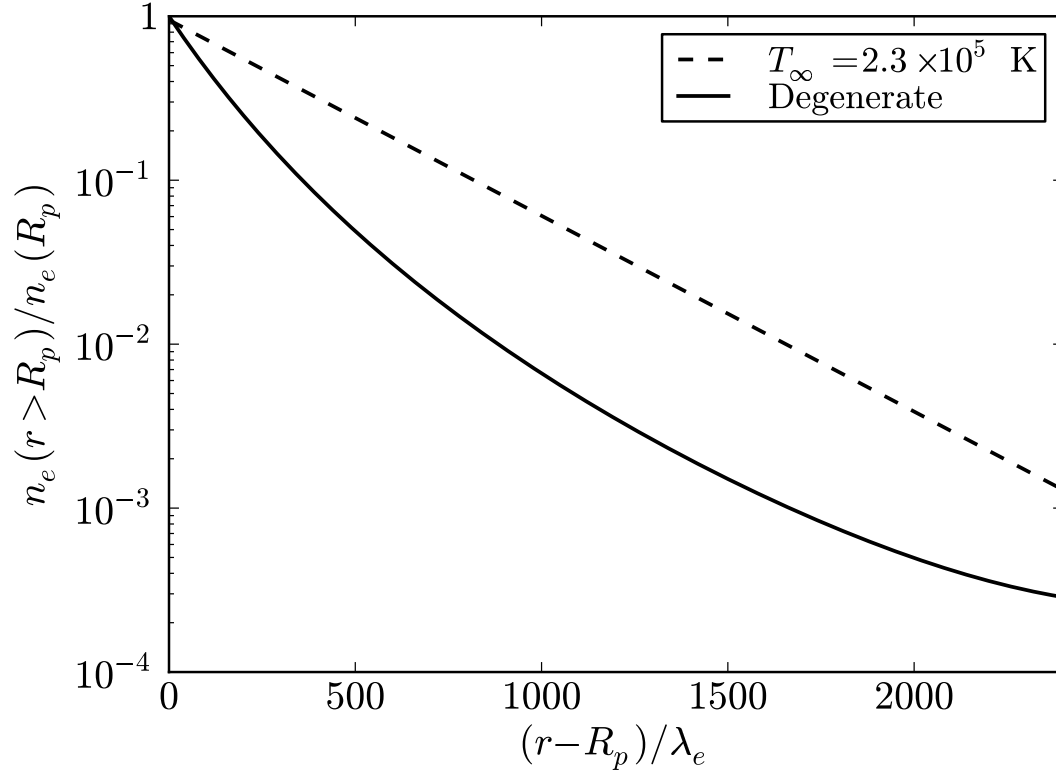


**Figure C.6.:** Electron number density for  $r \geq R_p$  normalized to its value at  $r = R_p$  both for  $T = 0$  K (degenerate case) and for a finite temperature of  $T_\infty = 2.3 \times 10^5$  K.

perature gradients (see e.g. Yakovlev and Pethick (2004), for details).

### C.3.6. Concluding Remarks

In this work we have addressed three additional aspects of the description of a self-gravitating system of neutrons, protons and electrons in  $\beta$ -equilibrium:

1) We have first recall the formulation of the constitutive Einstein-Maxwell-Thomas-Fermi equations and their solution in the simple case of self-gravitating neutrons, protons, and electrons in  $\beta$ -equilibrium. The properties of the electromagnetic structure of the configuration shown in Rotondo et al. (2011d) have been also recalled; the Coulomb potential energy inside the configuration is  $eV \sim m_\pi c^2$  and the corresponding electric field  $E \sim (m_p/m_{\text{Planck}})(m_\pi/m_e)^2 E_c$  and explicitly given in Fig. C.4.

2) We have presented the Newtonian limit of the treatment (Rotondo et al., 2011d) by taking the weak field approximation and the non-relativistic  $c \rightarrow \infty$  limit of the general relativistic Thomas-Fermi and Einstein-Maxwell equations (C.3.4)–(C.3.9). The numerical integration of the Newtonian equations shows that the gravito-electrodynamic structure evidenced in Rotondo et al.

(2011d) (see also Sec. C.3.2) is already present in the Newtonian regime. We have also shown how our equations fulfill the Rosseland relation of equilibrium (Rosseland, 1924) for an electron-ion ideal gas in the case of a Newtonian gravitational field, see Eqs. (C.3.17)–(C.3.18), Eqs. (C.3.20)–(C.3.23), and Eqs. (C.3.4)–(C.3.9). The differences in the electromagnetic structure between the Newtonian and the general relativistic treatments are very large (see Fig. C.5).

3) We have recalled in Sec. C.3.4 the extension of the Einstein-Maxwell-Thomas-Fermi equations (C.3.4)–(C.3.9) to the case when strong interactions between nucleons are taken into account by introducing the presence of  $\sigma$ ,  $\omega$  and  $\rho$  virtual mesons which mediate nuclear interactions in a Yukawa-like fashion, following our recent work (Rueda et al., 2011a), see Eqs. (C.3.25)–(C.3.34).

4) We have then extended all our previous works to the case of finite temperatures enforcing the Tolman “isothermal” condition in general relativity. We have reached a fundamental conclusion: although the thermal energy stored in old neutron stars with surface temperatures  $\sim 10^6$  K (Tennant et al., 2001; Weisskopf et al., 2004) is much larger than the internal Coulomb energy (see Sec. C.3.4), still the electromagnetic structure (see Fig. C.5) is unaffected by the presence of the thermal component. Physically this effect is due to the very large Fermi energy of the neutrons  $\sim 1$  GeV, of the protons  $\sim 10$  MeV and of the electrons  $\sim 0.1$  GeV, as can be seen from Eq. (C.3.46). In the general relativistic “isothermal” system there exists a temperature gradient, compensated by the variation of the gravitational potential as dictated by the Tolman condition given by Eq. (C.3.56). The Coulomb interaction is not involved in the balance between the thermal and the gravitational energies and is not affected by the presence of large thermal energies.

We recalled that a surface structure characterized by the presence of three different radii, one for each particle specie, emerges when global Coulomb effects are taken into due account. The radius  $R_e$  in the case  $T \neq 0$  is larger with respect to the one obtained in the degenerate approximation (see Fig. C.6). However, in realistic neutron stars the surface structure of Fig. C.6 is replaced by the surface layers composed of nuclei and non-degenerate electrons where isothermality breaks down due to existence of high temperature gradients (Yakovlev and Pethick, 2004).

As a by product, we have given the explicit demonstration of the constancy throughout the configuration of the Klein potentials of each species in the more general case of finite temperatures. This generalizes the condition of the constancy of the general relativistic Fermi energies derived in the special case  $T = 0$  in Rotondo et al. (2011d).

The above results are relevant to the extension to thermal effects of the relativistic Feynman-Metropolis-Teller treatment of compressed atoms (Rotondo et al., 2011c), recently applied to the construction of general relativistic white dwarf equilibrium configurations (Rotondo et al., 2011b). They are therefore

relevant for the description of the neutron star crust as well as of hot white dwarfs.

The study of the Thomas-Fermi equation within the Einstein-Maxwell system of equations responds to a precise request of consistency of a theoretical treatment. As evidenced in Rotondo et al. (2011d) it overcomes the conceptual difficulties of the Tolman-Oppenheimer-Volkoff treatment. Nevertheless, the two treatments when applied to the case of neutrons, protons, and electrons in  $\beta$ -equilibrium do not give quantitative appreciable differences in the masses and radii of the equilibrium configurations. It becomes therefore natural to ask under which physical conditions the gravito-polarization effects become quantitatively relevant.

When strong interactions are considered (Rueda et al., 2011a) a new situation occurs. The neutron star core necessarily presents a sharp boundary surrounded by a crust of nuclei and electrons described by the generalized Feynman-Metropolis-Teller treatment presented in Rotondo et al. (2011c). Under these conditions, the entire theoretical treatment presented in this work and in Rotondo et al. (2011d); Rueda et al. (2011a) are not optional and become a necessity.

The presence of a Coulomb potential affects the structure of the phase-transition leading to the occurrence of overcritical electric fields through core-crust boundary interface. Similar electrostatic effects are expected to occur at the interlayer boundaries within the crust of a neutron star where changes of the nucleus charge  $Z$  and mass number  $A$  of the composing nuclei occur (see e.g. Haensel and Pichon (1994)), as well as at the surface of quark stars (Alcock et al., 1986; Stejner and Madsen, 2005), at the transition from the hadronic phase to the color flavor locked phase in hybrid stars (Alford et al., 2001) and in liquid white dwarfs where it may cause sedimentation of heavy nuclei (Bildsten and Hall, 2001; Althaus et al., 2010; García-Berro et al., 2010b).

In Fig. C.7 we show the expected behavior of the Coulomb potential as modeled in the heuristic simplified approach (Ruffini, 2008b; Popov, 2010; Rotondo et al., 2011e). If the electron Coulomb potential  $-eV \sim m_\pi c^2$  suffers a sharp increasing in a scale typical of the electron screening length  $\sim \lambda_e = \hbar/(m_e c)$ , it will create an electric field of order  $\sim (m_\pi/m_e)^2 E_c \sim 10^3 E_c$ .

A key result in the present work is that the gravito-polarization effects survive at finite temperatures and we can therefore proceed to the study of neutron star configurations through the theoretical framework formulated in Rueda et al. (2011a) and recalled in Sec. C.3.4. It is now possible to confirm if the phase-transition at the boundary of the neutron star core follows the idealization advanced in Ruffini (2008b); Popov (2010); Rotondo et al. (2011e) and shown in Fig. C.7. It is clear that the formation of overcritical fields is of great astrophysical interest. The mass and thickness of the neutron star crust in the two alternative treatments are markedly different. The continuity of the generalized Klein potentials, at the boundary of the core, plays a crucial

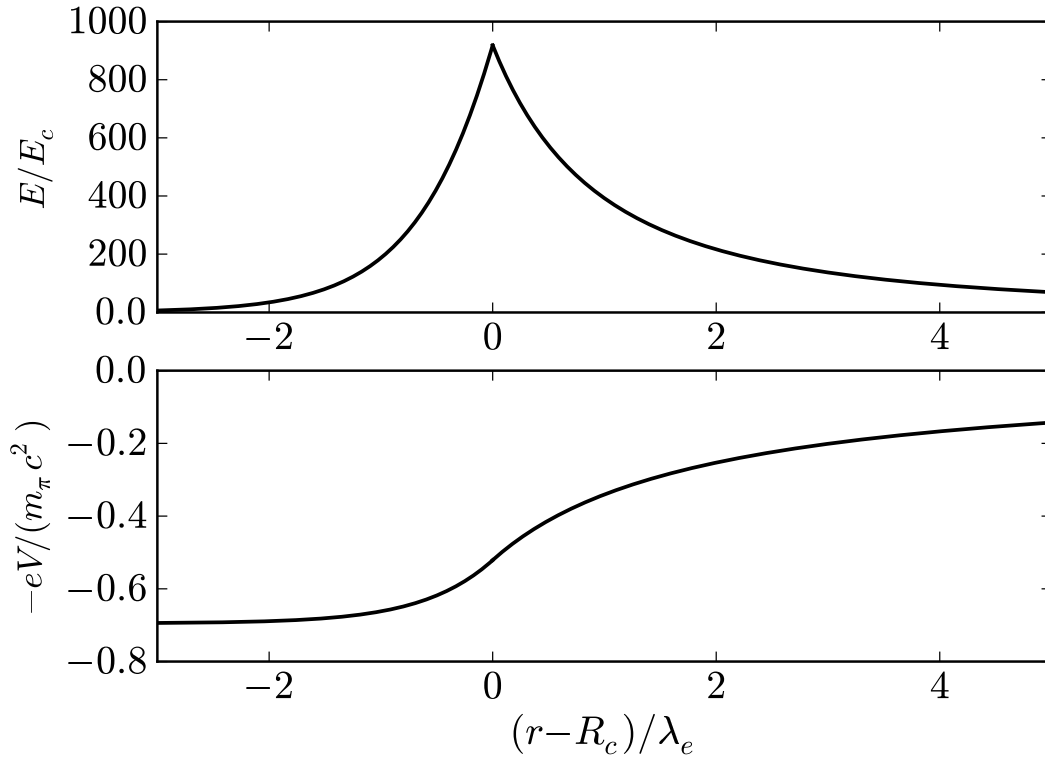


**Figure C.7.:** Expected enhancement of the electric field at a sharp increasing of the electron Coulomb potential  $-eV$  e.g. at a phase transition from the core to the crust in a neutron star as modeled in the simplified approach (Ruffini, 2008b; Popov, 2010; Rotondo et al., 2011e). Here  $R_c$  denotes the core radius.

role in the determination of the mass and thickness of the crust (Belvedere et al., 2012). The process of gravitational collapse of a core endowed with electromagnetic structure leads to signatures and energetics markedly different from the ones of a core endowed uniquely of gravitational interactions (Ruffini et al., 2003b,a; Ruffini and Xue, 2008; Ruffini et al., 2010b).

## **C.4. Neutron star equilibrium configurations within a fully relativistic theory with strong, weak, electromagnetic, and gravitational interactions**

### **C.4.1. Introduction**

It is well known that the classic works of Tolman (1939) and of Oppenheimer and Volkoff (1939), for short TOV, addresses the problem of neutron star equilibrium configurations composed only of neutrons. For the more general case when protons and electrons are also considered, in all of the scientific literature on neutron stars it is assumed that the condition of local charge neutrality applies identically to all points of the equilibrium configuration (see e.g. Haensel et al. (2007)). Consequently, the corresponding solutions in this more general case of a non-rotating neutron star, are systematically obtained also on the base of the TOV equations. We have recently shown the the condition of local charge neutrality is

In general, the formulation of the equilibrium of systems composed by different particle species must be established within the framework of statistical physics of multicomponent systems. Thermodynamic equilibrium of these systems is warranted by demanding the constancy throughout the configuration of the generalized chemical potentials, often called “electro-chemical”, of each of the components of the system; see e.g. Klein (1949); Kodama and Yamada (1972); Olson and Baily (1975). Such generalized potentials include not only the contribution due to kinetic energy but also the contribution due to the potential fields, e.g. gravitational and electromagnetic potential energies per particle, and in the case of rotating stars also the centrifugal potential. For such systems in presence of gravitational and Coulomb fields, global electric polarization effects at macroscopic scales occur. The balance of the gravitational and electric forces acting on ions and electrons in ideal electron plasma leading to the occurrence of gravito-polarization was pointed out in the classic work of Rosseland (1924).

If one turns to consider the gravito-polarization effects in neutron stars, the corresponding theoretical treatment acquires remarkable conceptual and theoretical complexity, since it must be necessarily formulated consistently within the Einstein-Maxwell system of equations. Klein (1949) first introduced the constancy of the general relativistic chemical potential of particles, hereafter “Klein potentials”, in the study of the thermodynamic equilibrium of a self-gravitating one-component fluid of neutral particles throughout the configuration within the framework of general relativity. The extension of the Klein’s work to the case of neutral multicomponent degenerate fluids can be found in Kodama and Yamada (1972) and to the case of multi-component

degenerate fluid of charged particles in Olson and Bailyn (1975).

Using the concept of Klein potentials, we have recently proved the impossibility of imposing the condition of local charge neutrality in the simplest case of a self-gravitating system of degenerate neutrons, protons and electrons in  $\beta$ -equilibrium Rotondo et al. (2011d): it has been shown that the consistent treatment of the above system implies the solution of the general relativistic Thomas-Fermi equations, coupled with the Einstein-Maxwell ones, being the TOV equations thus superseded.

We have recently formulated the theory of a system of neutrons, protons and electrons fulfilling strong, electromagnetic, weak and gravitational interactions (Rueda et al., 2011a). The role of the Klein first integrals has been again evidenced and their theoretical formulation in the Einstein-Maxwell background and in the most general case of finite temperature has been there presented, generalizing the previous results for the “non-interacting” case (Rotondo et al., 2011d). The strong interactions, modeled by a relativistic nuclear theory, are there described by the introduction of the  $\sigma$ ,  $\omega$  and  $\rho$  virtual mesons (Duerr, 1956; Walecka, 1974; Bowers et al., 1973b,a) (see Subsec. C.4.2 for details).

In this work we construct for the first time the equilibrium configurations of non-rotating neutron stars following the new approach (Rotondo et al., 2011d; Rueda et al., 2011a). The full set of the Einstein-Maxwell-Thomas-Fermi equations is solved numerically for zero temperatures and for selected parameterizations of the nuclear model.

## C.4.2. The Constitutive Relativistic Equations

### Core Equations

It has been clearly recognized that, since neutron stars cores may reach density of order  $\sim 10^{16}$ – $10^{17}$  g/cm<sup>3</sup>, much larger than the nuclear density  $\rho_{\text{nuc}} \sim 2.7 \times 10^{14}$  g/cm<sup>3</sup>, approaches for the nuclear interaction between nucleons based on phenomenological potentials and non-relativistic many-body theories become inapplicable (see Bowers et al. (1973b,a)). A self-consistent relativistic and well-tested model for the nuclear interactions has been formulated in Duerr (1956); Walecka (1974); Bowers et al. (1973b,a). Within this model the nucleons interact with  $\sigma$ ,  $\omega$  and  $\rho$  mesons through Yukawa-like couplings and assuming flat spacetime the equation of state of nuclear matter has been determined. However, it has been clearly stated in Rotondo et al. (2011d); Rueda et al. (2011a) that, when we turn into a neutron star configuration at nuclear and supranuclear, the global description of the Einstein-Maxwell-Thomas-Fermi equations is mandatory. Associated to this system of equations there is a sophisticated eigenvalue problem, especially the one for the general relativistic Thomas-Fermi equation is necessary in order to fulfill the global charge neutrality of the system and to consistently describe

the confinement of the ultrarelativistic electrons.

The strong interactions between nucleons are described by the exchange of three virtual mesons:  $\sigma$  is an isoscalar meson field providing the attractive long-range part of the nuclear force;  $\omega$  is a massive vector field that models the repulsive short range and;  $\rho$  is the massive isovector field that takes account surface as well as isospin effects of nuclei (see also Boguta and Bodmer (1977); Ring (1996)).

The total Lagrangian density of the system is given by

$$\mathcal{L} = \mathcal{L}_g + \mathcal{L}_f + \mathcal{L}_\sigma + \mathcal{L}_\omega + \mathcal{L}_\rho + \mathcal{L}_\gamma + \mathcal{L}_{\text{int}}, \quad (\text{C.4.1})$$

where the Lagrangian densities for the free-fields are

$$\mathcal{L}_g = -\frac{R}{16\pi G}, \quad (\text{C.4.2})$$

$$\mathcal{L}_\gamma = -\frac{1}{16\pi} F_{\mu\nu} F^{\mu\nu}, \quad (\text{C.4.3})$$

$$\mathcal{L}_\sigma = \frac{1}{2} \nabla_\mu \sigma \nabla^\mu \sigma - U(\sigma), \quad (\text{C.4.4})$$

$$\mathcal{L}_\omega = -\frac{1}{4} \Omega_{\mu\nu} \Omega^{\mu\nu} + \frac{1}{2} m_\omega^2 \omega_\mu \omega^\mu, \quad (\text{C.4.5})$$

$$\mathcal{L}_\rho = -\frac{1}{4} \mathcal{R}_{\mu\nu} \mathcal{R}^{\mu\nu} + \frac{1}{2} m_\rho^2 \rho_\mu \rho^\mu, \quad (\text{C.4.6})$$

where  $\Omega_{\mu\nu} \equiv \partial_\mu \omega_\nu - \partial_\nu \omega_\mu$ ,  $\mathcal{R}_{\mu\nu} \equiv \partial_\mu \rho_\nu - \partial_\nu \rho_\mu$ ,  $F_{\mu\nu} \equiv \partial_\mu A_\nu - \partial_\nu A_\mu$  are the field strength tensors for the  $\omega^\mu$ ,  $\rho$  and  $A^\mu$  fields respectively,  $\nabla_\mu$  stands for covariant derivative and  $R$  is the Ricci scalar. We adopt the Lorenz gauge for the fields  $A_\mu$ ,  $\omega_\mu$ , and  $\rho_\mu$ . The self-interaction scalar field potential  $U(\sigma)$  is a quartic-order polynom for a renormalizable theory (see e.g. Lee and Wick (1974)).

The Lagrangian density for the three fermion species is

$$\mathcal{L}_f = \sum_{i=e,N} \bar{\psi}_i (i\gamma^\mu D_\mu - m_i) \psi_i, \quad (\text{C.4.7})$$

where  $\psi_N$  is the nucleon isospin doublet,  $\psi_e$  is the electronic singlet,  $m_i$  states for the mass of each particle-specie and  $D_\mu = \partial_\mu + \Gamma_\mu$ , being  $\Gamma_\mu$  the Dirac spin connections.

The interacting part of the Lagrangian density is, in the minimal coupling assumption, given by

$$\begin{aligned} \mathcal{L}_{\text{int}} &= -g_\sigma \sigma \bar{\psi}_N \psi_N - g_\omega \omega_\mu J_\omega^\mu - g_\rho \rho_\mu J_\rho^\mu \\ &+ e A_\mu J_{\gamma,e}^\mu - e A_\mu J_{\gamma,N}^\mu, \end{aligned} \quad (\text{C.4.8})$$

where the conserved currents are

$$J_\omega^\mu = \bar{\psi}_N \gamma^\mu \psi_N, \quad (\text{C.4.9})$$

$$J_\rho^\mu = \bar{\psi}_N \tau_3 \gamma^\mu \psi_N, \quad (\text{C.4.10})$$

$$J_{\gamma,e}^\mu = \bar{\psi}_e \gamma^\mu \psi_e, \quad (\text{C.4.11})$$

$$J_{\gamma,N}^\mu = \bar{\psi}_N \left( \frac{1 + \tau_3}{2} \right) \gamma^\mu \psi_N. \quad (\text{C.4.12})$$

The coupling constants of the  $\sigma$ ,  $\omega$  and  $\rho$ -fields are  $g_\sigma$ ,  $g_\omega$  and  $g_\rho$ , and  $e$  is the fundamental electric charge. The Dirac matrices  $\gamma^\mu$  and the isospin Pauli matrices satisfy the Dirac algebra in curved spacetime (see e.g. Lee and Pang (1987) for details).

We first introduce the non-rotating spherically symmetric spacetime metric

$$ds^2 = e^{\nu(r)} dt^2 - e^{\lambda(r)} dr^2 - r^2 d\theta^2 - r^2 \sin^2 \theta d\varphi^2, \quad (\text{C.4.13})$$

where the  $\nu(r)$  and  $\lambda(r)$  are only functions of the radial coordinate  $r$ .

For very large number of fermions, we adopt the mean-field approximation in which fermion-field operators are replaced by their expectation values (see Ruffini and Bonazzola (1969) for details). Within this approximation, the full system of general relativistic equations can be written in the form

$$e^{-\lambda(r)} \left( \frac{1}{r^2} - \frac{1}{r} \frac{d\lambda}{dr} \right) - \frac{1}{r^2} = -8\pi G T_0^0, \quad (\text{C.4.14})$$

$$e^{-\lambda(r)} \left( \frac{1}{r^2} + \frac{1}{r} \frac{d\nu}{dr} \right) - \frac{1}{r^2} = -8\pi G T_1^1, \quad (\text{C.4.15})$$

$$V'' + \frac{2}{r} V' \left[ 1 - \frac{r(\nu' + \lambda')}{4} \right] = -4\pi e e^{\nu/2} e^\lambda (n_p - n_e), \quad (\text{C.4.16})$$

$$\frac{d^2\sigma}{dr^2} + \frac{d\sigma}{dr} \left[ \frac{2}{r} - \frac{1}{2} \left( \frac{d\nu}{dr} + \frac{d\lambda}{dr} \right) \right] = e^\lambda [\partial_\sigma U(\sigma) + g_s n_s], \quad (\text{C.4.17})$$

$$\frac{d^2\omega}{dr^2} + \frac{d\omega}{dr} \left[ \frac{2}{r} - \frac{1}{2} \left( \frac{d\nu}{dr} + \frac{d\lambda}{dr} \right) \right] = -e^\lambda (g_\omega J_\omega^0 - m_\omega^2 \omega), \quad (\text{C.4.18})$$

$$\frac{d^2\rho}{dr^2} + \frac{d\rho}{dr} \left[ \frac{2}{r} - \frac{1}{2} \left( \frac{d\nu}{dr} + \frac{d\lambda}{dr} \right) \right] = -e^\lambda (g_\rho J_\rho^0 - m_\rho^2 \rho), \quad (\text{C.4.19})$$

$$E_e^F = e^{\nu/2} \mu_e - eV = \text{constant}, \quad (\text{C.4.20})$$

$$E_p^F = e^{\nu/2} \mu_p + \mathcal{V}_p = \text{constant}, \quad (\text{C.4.21})$$

$$E_n^F = e^{\nu/2} \mu_n + \mathcal{V}_n = \text{constant}, \quad (\text{C.4.22})$$

where we have introduced the notation  $\omega_0 = \omega$ ,  $\rho_0 = \rho$ , and  $A_0 = V$  for the temporal components of the meson-fields. Here  $\mu_i = \partial\mathcal{E}/\partial n_i = \sqrt{(P_i^F)^2 + \tilde{m}_i^2}$

C.4. Neutron star equilibrium configurations within a fully relativistic theory with strong, weak, electromagnetic, and gravitational interactions

and  $n_i = (P_i^F)^3 / (3\pi^2)$  are the free-chemical potential and number density of the  $i$ -specie with Fermi momentum  $P_i^F$ . The particle effective mass is  $\tilde{m}_N = m_N + g_s\sigma$  and  $\tilde{m}_e = m_e$  and the effective potentials  $\mathcal{V}_{p,n}$  are given by

$$\mathcal{V}_p = g_\omega\omega + g_\rho\rho + eV, \quad (\text{C.4.23})$$

$$\mathcal{V}_n = g_\omega\omega - g_\rho\rho. \quad (\text{C.4.24})$$

The constancy of the generalized Fermi energies  $E_n^F$ ,  $E_p^F$  and  $E_e^F$ , the Klein potentials, derives from the thermodynamic equilibrium conditions given by the statistical physics of multicomponent systems, applied to a system of degenerate neutrons, protons, and electrons within the framework of general relativity (see Rueda et al. (2011a) for details). These constants are linked by the  $\beta$ -equilibrium between the matter constituents

$$E_n^F = E_p^F + E_e^F. \quad (\text{C.4.25})$$

The electron density  $n_e$  is, via Eq. (C.4.20), given by

$$n_e = \frac{e^{-3\nu/2}}{3\pi^2} [\hat{V}^2 + 2m_e\hat{V} - m_e^2(e^\nu - 1)]^{3/2}, \quad (\text{C.4.26})$$

where  $\hat{V} \equiv eV + E_e^F$ . Substituting Eq.( C.4.26) into Eq. (C.4.16) one obtains the general relativistic extension of the relativistic Thomas-Fermi equation recently introduced for the study of compressed atoms (Rotondo et al., 2011c,b). This system of equations has to be solved with the boundary condition of global neutrality; see Rotondo et al. (2011d); Rueda et al. (2011a) and below for details.

The scalar density  $n_s$ , within the mean-field approximation, is given by the following expectation value

$$n_s = \langle \bar{\psi}_N \psi_N \rangle = \frac{2}{(2\pi)^3} \sum_{i=n,p} \int d^3k \frac{\tilde{m}_N}{\epsilon_i(p)}, \quad (\text{C.4.27})$$

where  $\epsilon_i(p) = \sqrt{p^2 + \tilde{m}_i^2}$  is the single particle energy.

In the static case, only the temporal components of the covariant currents survive, i.e.  $\langle \bar{\psi}(x)\gamma^i\psi(x) \rangle = 0$ . Thus, by taking the expectation values of Eqs. (C.2.10)–(C.2.13), we obtain the non-vanishing components of the currents

$$J_0^{ch} = n_{ch}u_0 = (n_p - n_e)u_0, \quad (\text{C.4.28})$$

$$J_0^\omega = n_b u_0 = (n_n + n_p)u_0, \quad (\text{C.4.29})$$

$$J_0^\rho = n_3 u_0 = (n_p - n_n)u_0, \quad (\text{C.4.30})$$

where  $n_b = n_p + n_n$  is the baryon number density and  $u_0 = \sqrt{g_{00}} = e^{v/2}$  is the covariant temporal component of the four-velocity of the fluid, which satisfies  $u^\mu u_\mu = 1$ .

The metric function  $\lambda$  is related to the mass  $M(r)$  and the electric field  $E(r) = -e^{-(v+\lambda)/2} V'$  through

$$\begin{aligned} e^{-\lambda(r)} &= 1 - \frac{2GM(r)}{r} + Gr^2 E^2(r) \\ &= 1 - \frac{2GM(r)}{r} + \frac{GQ^2(r)}{r^2}, \end{aligned} \quad (\text{C.4.31})$$

being  $Q(r)$  the conserved charge, related to the electric field by  $Q(r) = r^2 E(r)$ .

The energy-momentum tensor of free-fields and free-fermions  $T^{\mu\nu}$  of the system is

$$T^{\mu\nu} = T_f^{\mu\nu} + T_\gamma^{\mu\nu} + T_\sigma^{\mu\nu} + T_\omega^{\mu\nu} + T_\rho^{\mu\nu}, \quad (\text{C.4.32})$$

where

$$T_\gamma^{\mu\nu} = -\frac{1}{4\pi} \left( F_\alpha^\mu F^{\alpha\nu} + \frac{1}{4} g^{\mu\nu} F_{\alpha\beta} F^{\alpha\beta} \right), \quad (\text{C.4.33})$$

$$T_\sigma^{\mu\nu} = \nabla^\mu \nabla^\nu \sigma - g^{\mu\nu} \left[ \frac{1}{2} \nabla_\sigma \sigma \nabla^\sigma \sigma - U(\sigma) \right], \quad (\text{C.4.34})$$

$$\begin{aligned} T_\omega^{\mu\nu} &= -\Omega_\alpha^\mu \Omega^{\alpha\nu} - \frac{1}{4} g^{\mu\nu} \Omega_{\alpha\beta} \Omega^{\alpha\beta} \\ &+ m_\omega^2 \left( \omega^\mu \omega^\nu - \frac{1}{2} g^{\mu\nu} \omega_\alpha \omega^\alpha \right), \end{aligned} \quad (\text{C.4.35})$$

$$\begin{aligned} T_\rho^{\mu\nu} &= -\mathcal{R}_\alpha^\mu \mathcal{R}^{\alpha\nu} - \frac{1}{4} g^{\mu\nu} \mathcal{R}_{\alpha\beta} \mathcal{R}^{\alpha\beta} \\ &+ m_\rho^2 \left( \mathcal{R}^\mu \mathcal{R}^\nu - \frac{1}{2} g^{\mu\nu} \mathcal{R}_\alpha \mathcal{R}^\alpha \right), \end{aligned} \quad (\text{C.4.36})$$

$$T_f^{\mu\nu} = (\mathcal{E} + \mathcal{P}) u^\mu u^\nu - \mathcal{P} g^{\mu\nu}, \quad (\text{C.4.37})$$

where the energy-density  $\mathcal{E}$  and the pressure  $\mathcal{P}$  are given by

$$\mathcal{E} = \sum_{i=n,p,e} \mathcal{E}_i, \quad \mathcal{P} = \sum_{i=n,p,e} \mathcal{P}_i, \quad (\text{C.4.38})$$

being  $\mathcal{E}_i$  and  $\mathcal{P}_i$  the single fermion fluid contributions

$$\mathcal{E}_i = \frac{2}{(2\pi)^3} \int_0^{P_i^F} \epsilon_i(p) 4\pi p^2 dp, \quad (\text{C.4.39})$$

$$\mathcal{P}_i = \frac{1}{3} \frac{2}{(2\pi)^3} \int_0^{P_i^F} \frac{p^2}{\epsilon_i(p)} 4\pi p^2 dp. \quad (\text{C.4.40})$$

*C.4. Neutron star equilibrium configurations within a fully relativistic theory with strong, weak, electromagnetic, and gravitational interactions*

---

It is worth to recall that the equation of state (C.4.38)–(C.4.40) satisfies the thermodynamic law

$$\mathcal{E} + \mathcal{P} = \sum_{i=n,p,e} n_i \mu_i. \quad (\text{C.4.41})$$

The parameters of the nuclear model, namely the coupling constants  $g_s$ ,  $g_\omega$  and  $g_\rho$ , and the meson masses  $m_\sigma$ ,  $m_\omega$  and  $m_\rho$  are usually fixed by fitting experimental properties of nuclei, e.g. saturation density, binding energy per nucleon (or experimental masses), symmetry energy, surface energy, and nuclear incompressibility. In Table C.1 we present selected fits of the nuclear parameters. In particular, we show the following parameter sets: NL3 (Lalazisis et al., 1997), NL-SH (Sharma et al., 1993), TM1 (Sugahara and Toki, 1994), and TM2 (Hirata et al., 1995).

	NL3	NL-SH	TM1	TM2
$m_\sigma$ (MeV)	508.194	526.059	511.198	526.443
$m_\omega$ (MeV)	782.501	783.000	783.000	783.000
$m_\rho$ (MeV)	763.000	763.000	770.000	770.000
$g_s$	10.2170	10.4440	10.0289	11.4694
$g_\omega$	12.8680	12.9450	12.6139	14.6377
$g_\rho$	4.4740	4.3830	4.6322	4.6783
$g_2$ (fm <sup>-1</sup> )	-10.4310	-6.9099	-7.2325	-4.4440
$g_3$	-28.8850	-15.8337	0.6183	4.6076
$c_3$	0.0000	0.0000	71.3075	84.5318

**Table C.1.:** Selected parameter sets of the  $\sigma$ - $\omega$ - $\rho$  model.

The constants  $g_2$  and  $g_3$  are the third and fourth order constants of the self-scalar interaction as given by the scalar self-interaction potential

$$U(\sigma) = \frac{1}{2}m_\sigma^2\sigma^2 + \frac{1}{3}g_2\sigma^3 + \frac{1}{4}g_3\sigma^4. \quad (\text{C.4.42})$$

The non-zero constant  $c_3$  that appears in the TM1 and TM2 models corresponds to the self-coupling constant of the non-linear vector self-coupling  $\frac{1}{4}c_3(\omega_\mu\omega^\mu)^2$ . We have not include such a self-coupling vector interaction in the general formulation presented above. However, we show also here the results of the integration when such a self-interaction is taken into account and we refer to Sugahara and Toki (1994); Hirata et al. (1995) for details about the motivations of including that contribution.

The numerical integration of the core equations can be started given a central density and the regularity conditions at the origin; see below Sec. C.4.3 for details. At nuclear density the phase-transition to the “solid” crust takes place. Thus, the radius of the core  $R_{\text{core}}$  is given by  $\mathcal{E}(r = R_{\text{core}})/c^2 = \rho_{\text{nuc}}$ . These equations must be solved with the boundary conditions given by the

fulfillment of the condition of global charge neutrality and the continuity of the Klein potentials of particles between the core and the crust.

### Core-crust transition layer equations

In the core-crust interface, the mean-field approximation for the meson-fields is not valid any longer and thus a full numerical integration of the meson-field equations of motion, taking into account all gradient terms, must be performed. We expect the core-crust transition boundary-layer to be a region with characteristic length scale of the order of the electron Compton wavelength  $\sim \lambda_e = \hbar/(m_e c) \sim 100$  fm corresponding to the electron screening scale. Then, in the core-crust transition layer, the system of equations (C.4.14)–(C.4.22) reduces to

$$V'' + \frac{2}{r}V' = -e^{\lambda_{\text{core}}} e J_{ch}^0, \quad (\text{C.4.43})$$

$$\sigma'' + \frac{2}{r}\sigma' = e^{\lambda_{\text{core}}} [\partial_\sigma U(\sigma) + g_s n_s], \quad (\text{C.4.44})$$

$$\omega'' + \frac{2}{r}\omega' = -e^{\lambda_{\text{core}}} [g_\omega J_\omega^0 - m_\omega^2 \omega], \quad (\text{C.4.45})$$

$$\rho'' + \frac{2}{r}\rho' = -e^{\lambda_{\text{core}}} [g_\rho J_\rho^0 - m_\rho^2 \rho], \quad (\text{C.4.46})$$

$$e^{\nu_{\text{core}}/2} \mu_e - eV = \text{constant}, \quad (\text{C.4.47})$$

$$e^{\nu_{\text{core}}/2} \mu_p + eV + g_\omega \omega + g_\rho \rho = \text{constant}, \quad (\text{C.4.48})$$

$$\mu_n = \mu_p + \mu_e + 2 g_\rho \rho e^{-\nu_{\text{core}}/2}, \quad (\text{C.4.49})$$

due to the fact that the metric functions are essentially constant on the core-crust transition layer and thus we can take their values at the core-radius  $e^{\nu_{\text{core}}} \equiv e^{\nu(R_{\text{core}})}$  and  $e^{\lambda_{\text{core}}} \equiv e^{\lambda(R_{\text{core}})}$ .

The system of equations of the transition layer has a stiff nature due to the existence of two different scale lengths. The first one is associated with the nuclear interactions  $\sim \lambda_\pi = \hbar/(m_\pi c) \sim 1.5$  fm and the second one is due to the aforementioned screening length  $\sim \lambda_e = \hbar/(m_e c) \sim 100$  fm. Thus, the numerical integration of Eqs. (C.4.43)–(C.4.49) has been performed subdividing the core-crust transition layer in the following three regions: (I) a mean-field-like region where all the fields vary slowly with length scale  $\sim \lambda_e$ , (II) a strongly interacting region of scale  $\sim \lambda_\pi$  where the surface tension due to nuclear interactions dominate producing a sudden decrease of the proton and the neutron densities and, (III) a Thomas-Fermi-like region of scale  $\sim \lambda_e$  where only a layer of opposite charge made of electrons is present producing the total screening of the positively charged core. The results of the numerical integration of the equilibrium equations are shown in Fig. C.8-C.9 for the NL3-model.

*C.4. Neutron star equilibrium configurations within a fully relativistic theory with strong, weak, electromagnetic, and gravitational interactions*

---

We have integrated numerically Eqs. (C.4.14)–(C.4.22) for the models listed in Table C.1. The boundary conditions for the numerical integration are fixed through the following procedure. We start assuming a value for the central baryon number density  $n_b(0) = n_n(0) + n_p(0)$ . From the regularity conditions at the origin we have  $e^{-\lambda(0)} = 1$  and  $n_e(0) = n_p(0)$ .

The metric function  $\nu$  at the origin can be chosen arbitrarily, e.g.  $\nu(0) = 0$ , due to the fact that the system of equations remain invariant under the shift  $\nu \rightarrow \nu + \text{constant}$ . The right value of  $\nu$  is obtained once the end of the integration of the core has been accomplished and duly matched to the crust, by fulfilling the following identity at the surface of the neutron star,

$$e^{\nu(R)} = e^{-\lambda(R)} = 1 - \frac{2GM(R)}{c^2R}, \quad (\text{C.4.50})$$

being  $M(R)$  and  $R$  the total mass and radius of the star. Then, taking into account the above conditions, we solve the system (C.4.17)–(C.4.22) at the origin for the other unknowns  $\sigma(0)$ ,  $\omega(0)$ ,  $\rho(0)$ ,  $n_n(0)$ ,  $n_p(0)$ ,  $n_e(0)$ .

The initial conditions for the numerical integration of the core-crust transition layer equations are determined by the final values given by the numerical integration of the core equations, i.e. we take the values of all the variables at the core-radius  $R_{\text{core}}$ .

In the region I the effect of the Coulomb interaction is clear: on the proton-profile we can see a bump due to Coulomb repulsion while the electron-profile decreases as expected. Such a Coulomb effect is indirectly felt also by the neutrons due to the coupled nature of the system of equations. However, the neutron-bump is much smaller than the one of protons and it is not appreciable in Fig. C.8-C.9 due to the plot-scale. In the region II we see clearly the effect of the surface tension due to nuclear interaction which produces a sharp decrease of the neutron and proton profiles in a characteristic scale  $\sim \lambda_\pi$ . In addition, it can be seen a neutron skin effect, analogous to the one observed in heavy nuclei, which makes the scale of the neutron density falloff slightly larger with respect to the proton one, in close analogy to the neutron skin effect observed in neutron rich nuclei, see e.g. Tamii et al. (2011). The region III is characterized by a smooth decreasing of the electron density which resembles the behavior of the electrons surrounding a nucleus in the Thomas-Fermi model.

The matching to the crust must be done at the radius  $R_{\text{core}} + \delta R$  where full charge neutrality is reached. The thickness of the core-crust transition boundary layer  $\delta R$  as well as the value of the electron density at the edge of the crust,  $R_{\text{core}} + \delta R$ , depends on the nuclear parameters, especially on the nuclear surface tension.

The equilibrium conditions given by the constancy of the Klein potentials (C.4.20)–(C.4.22) throughout the configuration, impose in the transition layer

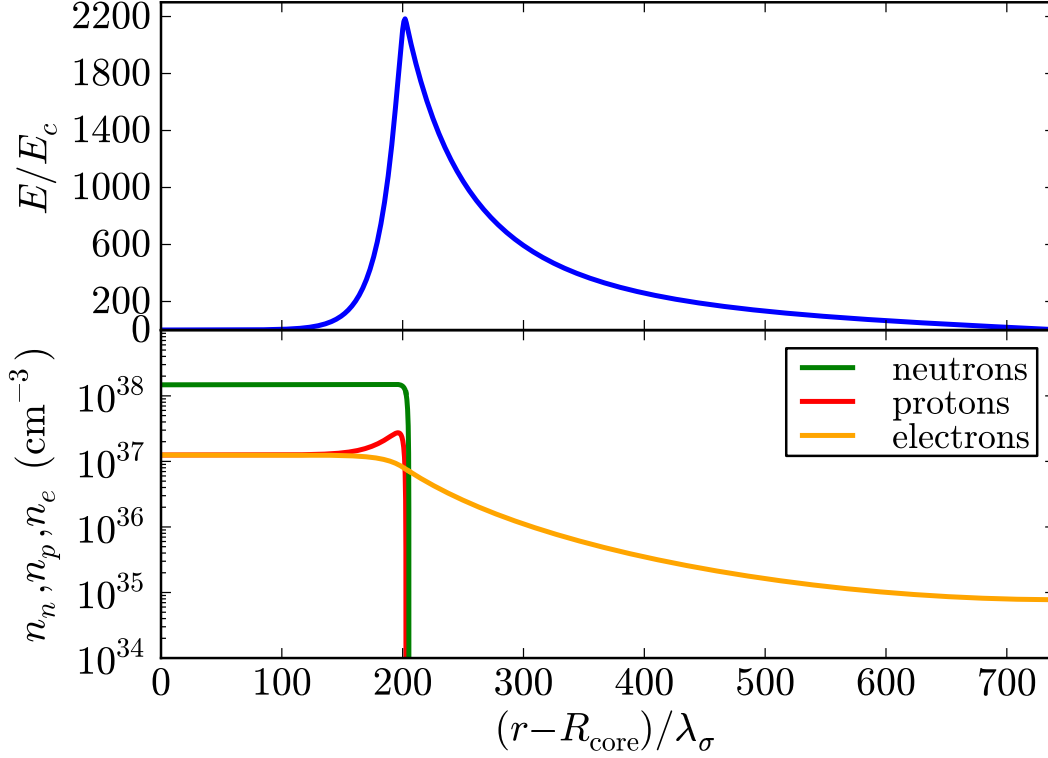


**Figure C.8.:** Upper panel: electric field in the core-crust transition layer in units of the critical field  $E_c$ . Lower panel: particle density profiles in the core-crust boundary interface in units of  $\text{cm}^{-3}$ . Here we use the NL3-model of Table C.1 and  $\lambda_\sigma = \hbar/(m_\sigma c) \sim 0.4$  fm denotes the sigma-meson Compton wavelength. The density at the edge of the crust in this example is  $\rho_{\text{crust}} = \rho_{\text{drip}} = 4.3 \times 10^{11}$  g/cm $^3$ .

the following continuity condition

$$e^{V_{\text{core}}/2} \mu_e^{\text{core}} - eV^{\text{core}} = e^{V_{\text{crust}}/2} \mu_e^{\text{crust}}. \quad (\text{C.4.51})$$

where  $\mu_e^{\text{core}} = \mu_e(R_{\text{core}})$ ,  $eV^{\text{core}} = eV(R_{\text{core}})$ , and  $\mu_e^{\text{crust}} = \mu_e(R_{\text{core}} + \delta R)$ , and  $e^{V_{\text{crust}}} \simeq e^{V_{\text{core}}}$ .

The electron chemical potential and the density decrease, in the boundary interface, until values  $\mu_e^{\text{crust}} < \mu_e^{\text{core}}$  and  $\rho_{\text{crust}} < \rho_{\text{core}}$ . For each central density, an entire family of core-crust interface boundaries and, correspondingly, an entire family of crusts with different mass and thickness, exist. The configuration with  $\rho_{\text{crust}} = \rho_{\text{drip}} \sim 4.3 \times 10^{11}$  g/cm $^3$  separates neutron stars with and without inner crust. In the so-called inner crust, the neutrons dripped from the nuclei in the crust form a fluid that coexist with the nuclei lattice and the degenerate electrons (Baym et al., 1971a). The presence of the neutron fluid in the crust changes the nuclear surface tension at the core radius, in

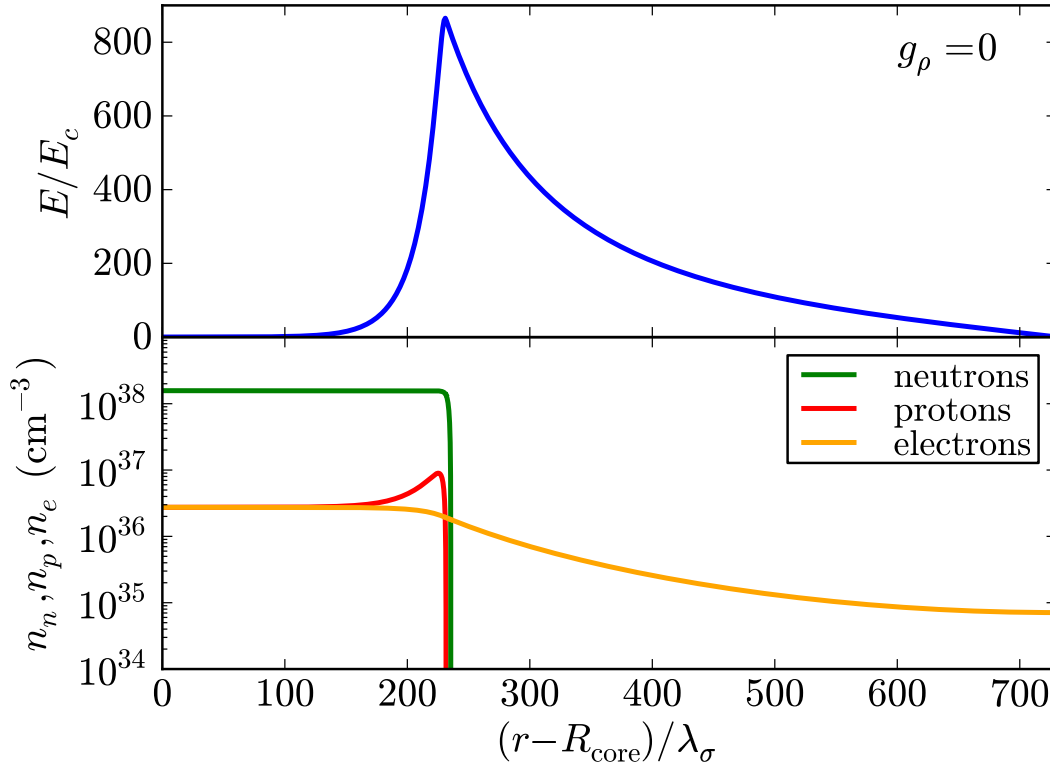


**Figure C.9.:** The same as Fig. C.8, but setting  $g_\rho = 0$  in order to see the effects of the  $\rho$ -meson with respect to the case  $g_\rho \neq 0$ .

close analogy to the reduction of the surface tension of the nuclei in the crust due to the presence of the dripped neutrons, see e.g. Baym et al. (1971a)) for details. This reduction of the nuclear tension is not taken into account in the nuclear parameters which are obtained to fit the properties of bare nuclei, see Table C.1. Thus we present here the results for configurations  $\rho_{\text{crust}} \leq \rho_{\text{drip}}$ , i.e. for neutron stars possessing only outer crust. The construction of configurations with  $\rho_{\text{crust}} > \rho_{\text{drip}}$  needs to be studied in more detail and will be the subject of a forthcoming work.

In Figs. C.8 and C.9, we show the core-crust transition layer for the NL3 model of Table C.1 with and without the presence of the  $\rho$ -meson respectively. The presence of the  $\rho$ -meson is responsible for the nuclear asymmetry within this nuclear model. The relevance of the nuclear symmetry energy on the structure of nuclei and neutron stars is continuously stressed in literature; see e.g. M  ther et al. (1987); Kubis (2007); Sharma and Pal (2009); Hebeler et al. (2010); Loan et al. (2011). The precise value of the nuclear symmetry energy plays here a crucial role in determining the precise value of the  $\rho$ -meson coupling which, in the present case, is essential in the determination of the intensity of the electric field in the core-crust boundary interface; as can be seen from the comparison of Figs. C.8 and C.9.

### Crust equations

Turning now to the crust, it is clear from our recent treatment of white dwarfs (Rotondo et al., 2011b) that also this problem can be solved by the adoption of Wigner-Seitz cells and from the relativistic Feynman-Metropolis-Teller (RFMT) approach (Rotondo et al., 2011c) it follows that the crust is clearly neutral. Thus, the structure equations to be integrated are the TOV equations

$$\frac{d\mathcal{P}}{dr} = -\frac{G(\mathcal{E} + \mathcal{P})(M + 4\pi r^3 \mathcal{P})}{r^2(1 - \frac{2GM}{r})}, \quad (\text{C.4.52})$$

$$\frac{dM}{dr} = 4\pi r^2 \mathcal{E}, \quad (\text{C.4.53})$$

where  $M = M(r)$  is the mass enclosed at the radius  $r$ .

The effects of the Coulomb interaction in “solid”-like electron-ion systems appears only at the microscopic level e.g. Debye-Hueckel screening in classical systems (Debye and Hueckerl, 1923) and Thomas-Fermi screening in the degenerate case (Mott, 1936). In order to analyze the effects of the microscopic screening on the structure of the configuration we will consider two equations of state for the crust: the locally neutral case or uniform approximation (see e.g. Chandrasekhar (1931b)) and, for simplicity, instead of using the RFMT EoS (Rotondo et al., 2011c), we use as second EoS the one due to Baym, Pethick and Sutherland (BPS) (Baym et al., 1971a), which is by far the most used equation of state in literature for the description of the neutron star crust (see e.g. Haensel et al. (2007)).

In the uniform approximation, both the degenerate electrons and the nucleons distribution are considered constant inside each cell of volume  $V_{\text{ws}}$ . This kind of configuration can be obtained only imposing microscopically the condition of local charge neutrality

$$n_e = \frac{Z}{V_{\text{ws}}}. \quad (\text{C.4.54})$$

The total pressure of the system is assumed to be entirely due to the electrons, i.e.

$$\mathcal{P} = \mathcal{P}_e = \frac{2}{3(2\pi\hbar)^3} \int_0^{p_e^F} \frac{c^2 p^2 4\pi p^2}{\sqrt{c^2 p^2 + m_e^2 c^4}} dp, \quad (\text{C.4.55})$$

while the total energy-density of the system is due to the nuclei, i.e.  $\mathcal{E} = (A/Z)m_N n_e$ , where  $m_N$  is the nucleon mass.

We turn now to the BPS equation of state. The first correction to the uniform model, corresponds to abandon the assumption of the electron-nucleon fluid through the so-called “lattice” model which introduces the concept of Wigner-Seitz cell: each cell of radius  $R_{\text{ws}}$  contains a point-like nucleus of charge  $+Ze$  with  $A$  nucleons surrounded by a uniformly distributed cloud

of  $Z$  fully-degenerate electrons.

The sequence of the equilibrium nuclides present at each density in the BPS equation of state is obtained by looking for the nuclear composition that minimizes the energy per nucleon for each fixed nuclear composition ( $Z, A$ ) (see Table C.2 and Baym et al. (1971a) for details). The pressure  $\mathcal{P}$  and the energy-density  $\mathcal{E}$  of the system are, within this model, given by

$$\mathcal{P} = \mathcal{P}_e + \frac{1}{3}W_L n_N, \quad (\text{C.4.56})$$

$$\frac{\mathcal{E}}{n_b} = \frac{W_N + W_L}{A} + \frac{\mathcal{E}_e(n_b Z/A)}{n_b}, \quad (\text{C.4.57})$$

where the electron energy-density is given by

$$\mathcal{E}_e = \frac{2}{(2\pi)^3} \int_0^{p_e^F} \sqrt{p^2 + m_e^2} 4\pi p^2 dp, \quad (\text{C.4.58})$$

and  $W_N(A, Z)$  is the total energy of an isolated nucleus given by the semi-empirical formula

$$W_N = m_n c^2 (A - Z) + m_p c^2 Z - bA, \quad (\text{C.4.59})$$

with  $b$  being the Myers and Swiatecki binding energy per nucleon (Myers, 1966). The lattice energy per nucleus  $W_L$  is given by

$$W_L = -\frac{1.819620Z^2 e^2}{a}, \quad (\text{C.4.60})$$

where the lattice constant  $a$  is related to the nucleon density  $n_N$  by  $n_N a^3 = 2$ .

### C.4.3. Neutron star structure

In the traditional TOV treatment the density and the pressure are a priori assumed to be continuous as well as the local charge neutrality of the system. The distinguishing feature of our new solution is that the Klein potentials are constant throughout the three regions; the core, the crust and the transition interface boundary. An overcritical electric field is formed and consequently a discontinuity in density is found with a continuous total pressure including the surface tension of the boundary. In Figs. C.10 and C.11, we compare and contrast the density profiles of configurations obtained from the traditional TOV treatment and with the treatment presented here.

In Figs. C.12–C.18 we show the results of the numerical integration of the system of the general relativistic constitutive equations of the configuration from the center all the way up to the surface with the appropriate boundary conditions between the involved phases. In particular, we have plotted the

mass-radius relation as well as the compactness of the neutron stars obtained with the models listed in Table C.1.

It is worth to note that the inclusion of the Coulomb interaction and in particular the presence of the negative lattice energy  $W_L$  results in a decreasing of the pressure of the cells. Such an effect, as shown in Fig. C.15–C.18, leads to a decreasing of the mass and the thickness of the crust with respect to the uniform-approximation case where no Coulomb interactions are taken into account.

Comparing the mass and the thickness of the crust obtained with these two different EoS, we obtain systematically crusts with smaller mass and larger thickness when Coulomb interactions are taken into account. This results are in line with the recent results in Rotondo et al. (2011b), where the mass-radius relation of white-dwarfs has been calculated using an EoS based on the relativistic Feynman-Metropolis-Teller model for compressed atoms (Rotondo et al., 2011c).

In the case of the BPS EoS, the average nuclear composition in the outer crust, namely the average charge to mass ratio of nuclei  $Z/A$ , is obtained by calculating the contribution of each nuclear composition present to the mass of the crust. We exemplified the analysis for two different cores:  $M_{\text{core}} = 2.56M_{\odot}$ ,  $R_{\text{core}} = 12.79$  km;  $M_{\text{core}} = 1.35M_{\odot}$ ,  $R_{\text{core}} = 11.76$  km. The relative abundance of each nuclide within the crust of the star can be obtained as

$$\text{R.A.} = \frac{1}{M_{\text{crust}}^{\text{BPS}}} \int_{\Delta r} 4\pi r^2 \varepsilon dr, \quad (\text{C.4.61})$$

where the integration is carried out in the layer of thickness  $\Delta r$  where the particular nuclide is present; see C.2 and Fig. C.19. Our results are in agreement with the analysis on the neutron star crust composition obtained in Goriely et al. (2011a,b). In both cases we obtain as average nuclear composition  $^{105}_{35}\text{Br}$ . The corresponding crusts with fixed nuclear composition  $^{105}_{35}\text{Br}$  for the two chosen cores are calculated neglecting Coulomb interactions (i.e. using the first EoS). The mass and the thickness of these crusts with fixed  $^{105}_{35}\text{Br}$  are different with respect to the ones obtained using the full BPS EoS, leading to such average nuclear composition. For the two selected examples we obtain that the mass and the thickness of the crust with average  $^{105}_{35}\text{Br}$  are, respectively, 18% larger and 5% smaller with respect to the ones obtained with the corresponding BPS EoS. This result shows how small microscopic effects due to the Coulomb interaction in the crust of the neutron star leads to quantitative not negligible effects on the macroscopic structure of the configuration.

*C.4. Neutron star equilibrium configurations within a fully relativistic theory with strong, weak, electromagnetic, and gravitational interactions*

Equilibrium Nuclei Below Neutron Drip						
Nucleus	Z	$\rho_{max}(\text{g cm}^{-3})$	$\Delta R_1$ (km)	R.A.1(%)	$\Delta R_2$ (km)	R.A.2(%)
<sup>56</sup> Fe	26	$8.1 \times 10^6$	0.0165	$7.56652 \times 10^{-7}$	0.0064	$6.96927 \times 10^{-7}$
<sup>62</sup> Ni	28	$2.7 \times 10^8$	0.0310	0.00010	0.0121	0.00009
<sup>64</sup> Ni	28	$1.2 \times 10^9$	0.0364	0.00057	0.0141	0.00054
<sup>84</sup> Se	34	$8.2 \times 10^9$	0.0046	0.00722	0.0017	0.00683
<sup>82</sup> Ge	32	$2.2 \times 10^{10}$	0.0100	0.02071	0.0039	0.01983
<sup>80</sup> Zn	38	$4.8 \times 10^{10}$	0.1085	0.04521	0.0416	0.04384
<sup>78</sup> Ni	28	$1.6 \times 10^{11}$	0.0531	0.25635	0.0203	0.25305
<sup>76</sup> Fe	26	$1.8 \times 10^{11}$	0.0569	0.04193	0.0215	0.04183
<sup>124</sup> Mo	42	$1.9 \times 10^{11}$	0.0715	0.02078	0.0268	0.02076
<sup>122</sup> Zr	40	$2.7 \times 10^{11}$	0.0341	0.20730	0.0127	0.20811
<sup>120</sup> Sr	38	$3.7 \times 10^{11}$	0.0389	0.23898	0.0145	0.24167
<sup>118</sup> Kr	36	$4.3 \times 10^{11}$	0.0101	0.16081	0.0038	0.16344

**Table C.2.:**  $\rho_{max}$  is the maximum density at which the nuclide is present;  $\Delta R_1$ ,  $\Delta R_2$  and R.A.1(%), R.A.2(%) are respectively the thickness of the layer where a given nuclide is present and their relative abundances in the outer crust for two different cases:  $M_{\text{core}} = 2.56M_{\odot}$ ,  $R_{\text{core}} = 12.79$  km;  $M_{\text{core}} = 1.35M_{\odot}$ ,  $R_{\text{core}} = 11.76$  km.

#### C.4.4. Observational constraints on the mass-radius relation

It has been recently pointed out that the most up-to-date stringent constraints to the mass-radius relation of neutron stars are provided by the largest mass, the largest radius, the highest rotational frequency, and the maximum surface gravity, observed for pulsars (Trümper, 2011).

So far, the highest neutron star mass measured with a high level of experimental confidence is the mass of the 3.15 millisecond pulsar PSR J1614-2230,  $M = 1.97 \pm 0.04M_{\odot}$ , obtained from the Shapiro time delay and the Keplerian orbital parameters of the binary system (Demorest et al., 2010a). The fitting of the thermonuclear burst oscillation light curves from the accreting millisecond pulsar XTE J1814-338 weakly constrain the mass-radius relation imposing an upper limit to the surface gravity of the neutron star,  $GM/(c^2R) < 0.24$  (Bhattacharyya et al., 2005). A lower limit of the radius of RX J1856-3754, as seen by an observer at infinity  $R_{\infty} = R[1 - 2GM/(c^2R)]^{-1/2} > 16.8$  km, has been obtained from the fit of the optical and X-ray spectra of the source (Trümper et al., 2004); it gives the constraint  $2GM/c^2 > R - R^3/(R_{\infty}^{\text{min}})^2$ , being  $R_{\infty}^{\text{min}} = 16.8$  km. Assuming a neutron star of  $M = 1.4M_{\odot}$  to fit the Chandra data of the low-mass X-ray binary X7, it turns out that the radius of the star satisfies  $R = 14.5_{-1.6}^{+1.8}$  km, at 90% confidence level, corresponding to  $R_{\infty} = [15.64, 18.86]$  km, respectively (see Heinke et al. (2006) for details). The maximum rotation rate of a neutron star taking into account both the effects of general relativity and deformations has been found to be  $\nu_{\text{max}} = 1045(M/M_{\odot})^{1/2}(10 \text{ km}/R)^{3/2}$  Hz, largely independent of the equation of

$M(M_{\odot})$	$R_{\text{NL3}}$	$R_{\text{NL-SH}}$	$R_{\text{TM1}}$	$R_{\text{TM2}}$
1.40	12.31	12.47	12.53	12.93
1.93	12.96	13.14	13.13	13.73
2.01	13.02	13.20	13.17	13.82

**Table C.3.:** Radii (in km) predicted by the nuclear parametrizations NL3, NL-Sh, TM1 and TM2 of Table C.1, for a canonical neutron star of  $M = 1.4M_{\odot}$  and for the millisecond pulsar PSR J1614-2230,  $M = 1.97 \pm 0.04M_{\odot}$ .

state (Lattimer and Prakash, 2004a). The fastest observed pulsar is PSR J1748-2246ad with a rotation frequency of 716 Hz (Hessels et al., 2006a), which results in the constraint  $M \geq 0.47(R/10 \text{ km})^3 M_{\odot}$ . In Fig. C.20 we show all these constraints and the mass-radius relation presented in this work.

As discussed by J. E. Trümper in Trümper (2011), the above constraints strongly favor stiff equations of state which provide high maximum masses for neutron stars. In addition, putting all of them together, the radius of a canonical neutron star of mass  $M = 1.4M_{\odot}$  is highly constrained to the range  $R \gtrsim 12 \text{ km}$  disfavoring, at the same time, the strange quark hypothesis for these specific objects. It is clear from Fig. C.20 that the mass-radius relation presented here is consistent with all the observation constraints, for all the nuclear parametrizations of Table C.1. We present in Table C.3, the radii predicted by our mass-radius relation for a canonical neutron star of  $M = 1.4M_{\odot}$  as well as for the millisecond pulsar PSR J1614-2230,  $M = 1.97 \pm 0.04M_{\odot}$ .

### C.4.5. Comparison with the traditional TOV treatment

In the traditional TOV treatment local charge neutrality as well as the continuity of the pressure and the density in the core-crust transition are assumed. This leads to explicit violation of the constancy of the Klein potentials throughout the configuration (see e.g. Rotonondo et al. (2011d)). In such a case there is a smooth transition from the core to the crust without any density discontinuity and therefore the density at the edge of the crust is  $\sim \rho_{\text{nuc}} \sim 2.7 \times 10^{14} \text{ g/cm}^3$ . The so-called inner crust in those configurations extends in the range of densities  $\rho_{\text{drip}} \lesssim \rho \lesssim \rho_{\text{nuc}}$  while, at densities  $\rho \lesssim \rho_{\text{drip}}$ , there is the so-called outer crust.

Due to the continuity of the Klein potentials in the transition from the core to the crust, there is a decrease of the Coulomb potential from  $\sim m_{\pi}c^2/e$  at the core radius  $R_{\text{core}}$  down to zero at the edge of the neutral crust. Correspondingly, the electron chemical potential decreases from its value at the core radius until a value approximately given by  $\mu_e^{\text{crust}} \sim \mu_e^{\text{drip}} \sim 26 \text{ MeV}$  (see Fig. C.8-C.9). Therefore, no crusts with densities larger than the neutron drip density  $\rho_{\text{drip}} \sim 4.3 \times 10^{11} \text{ g/cm}^3$  exist, leading to crusts made only of outer crust.

In Figs. C.21 and C.22 we compare and contrast the mass and the thickness

of the crust as obtained from the traditional TOV treatment with the new configurations presented here.

The markedly differences both in mass and thickness of the crusts (see Figs. C.21 and C.22) obtained from the traditional Tolman-Oppenheimer-Volkoff approach and the new equilibrium configurations presented here, leads to a very different mass-radius relations which we compare and contrast in Fig. C.23.

### C.4.6. Concluding Remarks

We have formulated the equations of equilibrium of neutron stars based on our recent works (Rueda et al., 2011a; Rotondo et al., 2011c,b,d). The strong, weak, electromagnetic, and gravitational interactions are taken into due account within the framework of general relativity. In particular, the strong interactions between nucleons is described by the exchange of the  $\sigma$ ,  $\omega$ , and  $\rho$  mesons. The equilibrium conditions are given by the set of Einstein-Maxwell-Thomas-Fermi equations and by the constancy of the general relativistic Fermi energies of particles, the Klein potentials, throughout the configuration.

We have solved these equilibrium equations numerically, in the case of zero temperatures, for the nuclear parameter sets NL3 (Lalazissis et al., 1997), NL-SH (Sharma et al., 1993), TM1 (Sugahara and Toki, 1994), and TM2 (Hirata et al., 1995); see Table C.1 for details.

A new structure of the star is found: the positively charged core at supranuclear densities is surrounded by an electronic distribution of thickness  $\gtrsim \hbar/(m_e c) \sim 10^2 \hbar/(m_\pi c)$  of opposite charge and, at lower densities, a neutral ordinary crust.

In the core interior the Coulomb potential well is  $\sim m_\pi c^2/e$  and correspondingly the electric field is  $\sim (m_p/m_{\text{Planck}})(m_\pi/m_e)^2 E_c \sim 10^{-14} E_c$ . Due to the equilibrium condition given by the constancy of the Klein potentials, there is a discontinuity in the density at the transition from the core to the crust, and correspondingly an overcritical electric field  $\sim (m_\pi/m_e)^2 E_c$  develops in the boundary interface; see Fig. C.8–C.9.

The continuity of the Klein potentials at the core-crust boundary interface leads to a decreasing of the electron chemical potential and density, until values  $\mu_e^{\text{crust}} < \mu_e^{\text{core}}$  and  $\rho_{\text{crust}} < \rho_{\text{core}}$  at the edge of the crust, where global charge neutrality is achieved. For each central density, an entire family of core-crust interface boundaries and, correspondingly, an entire family of crusts with different mass and thickness, exist. The larger  $\rho_{\text{crust}}$ , the smaller the thickness of the interface, the peak of the electric field, and the larger the mass and the thickness of the crust. The configuration with  $\rho_{\text{crust}} = \rho_{\text{drip}} \sim 4.3 \times 10^{11} \text{ g/cm}^3$  separates neutron stars with and without inner crust. The neutron stars with  $\rho_{\text{crust}} > \rho_{\text{drip}}$  deserve a further analysis in order to account for the reduction of the nuclear tension at the core-crust transition due to the

presence of dripped neutrons from the nuclei in the crust.

All the above new features lead to crusts with masses and thickness smaller than the ones obtained from the traditional TOV treatment, and we have shown specifically neutron stars with  $\rho_{\text{crust}} = \rho_{\text{drip}}$ ; see Figs. C.21–C.22. The mass-radius relation obtained in this case have been compared and contrasted with the one obtained from the locally neutral TOV approach; see Fig. C.23. We have shown that our mass-radius relation is in line with observations, based on the recent work by J. E. Trümper (Trümper, 2011); see Fig. C.20 for details.

The electromagnetic structure of the neutron star presented here is of clear astrophysical relevance. The process of gravitational collapse of a core endowed with electromagnetic structure leads to signatures and energetics markedly different from the ones of a core endowed uniquely of gravitational interactions; see e.g. Ruffini et al. (2003b,a); Ruffini and Xue (2008); Ruffini et al. (2010b).

It is clear that the release of gravitational energy in the process of gravitational collapse of the core, following the classic work of Gamow and Schoenberg (1941), is carried away by neutrinos. The additional nuclear and electromagnetic energy  $\sim 10^{51}$  erg of the collapsing core introduced in this work are expected to be carried away by electron-positron plasma created in the overcritical electromagnetic field in the collapsing core.

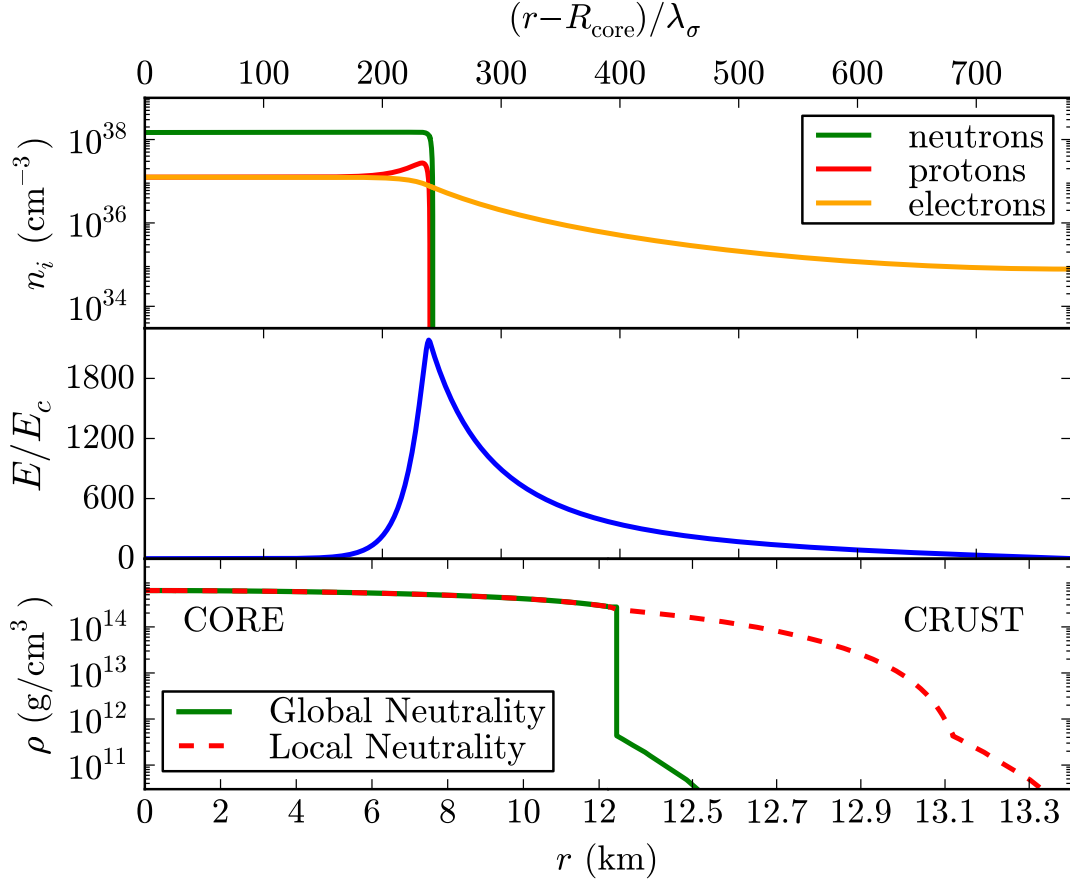


**Figure C.10.:** Upper panel: electric field in the core-crust transition layer, in units of the critical field  $E_c$ . Middle panel: particle density profiles in the core-crust boundary interface, in units of  $\text{cm}^{-3}$ . Lower panel: density profile inside a neutron star with central density  $\rho(0) \sim 5\rho_{\text{nuc}}$ . We compare and contrast the structural differences between the solution obtained from the traditional TOV equations (locally neutral case) and the globally neutral solution presented here. We use here the NL3 nuclear parametrization of Table C.1 and  $\lambda_\sigma = \hbar/(m_\sigma c) \sim 0.4$  fm, denotes the sigma-meson Compton wavelength. In this example the density at the edge of the crust is  $\rho_{\text{crust}} = \rho_{\text{drip}} = 4.3 \times 10^{11}$   $\text{g/cm}^3$ .

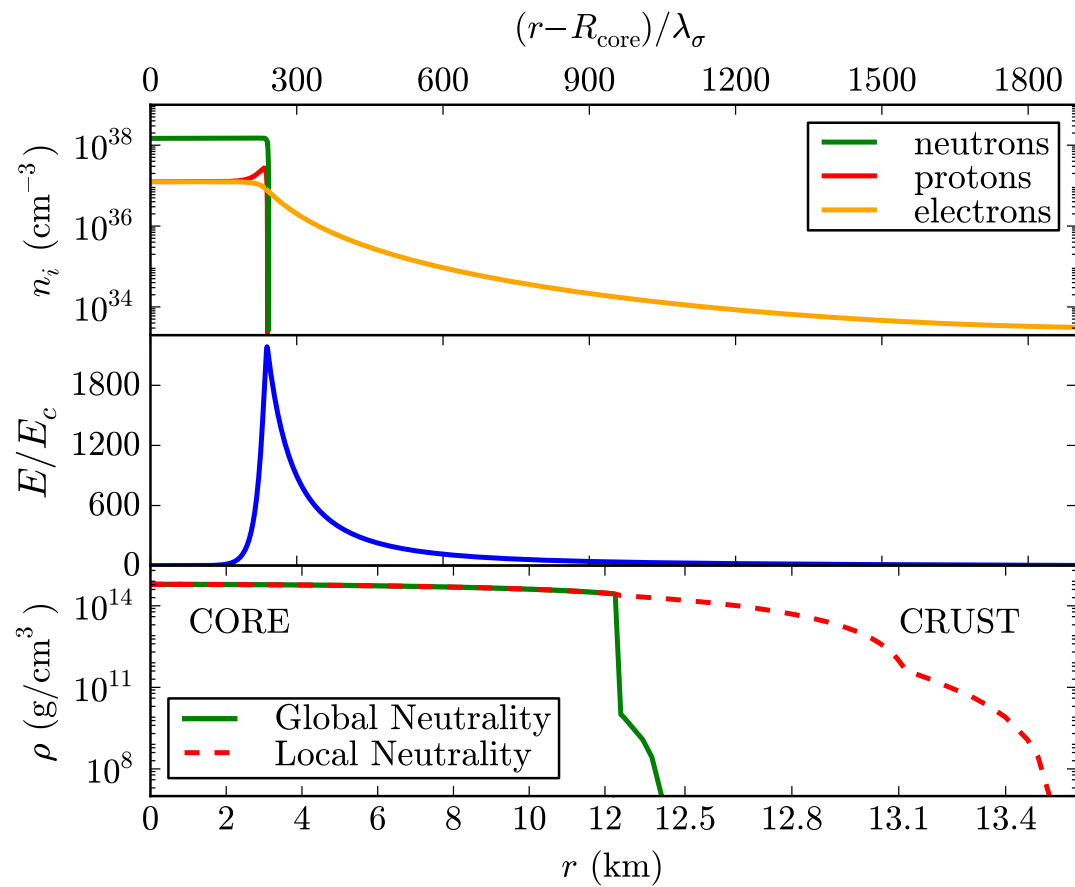


**Figure C.11.:** Same as Fig. C.10. In this example the density at the edge of the crust is  $\rho_{\text{crust}} = 10^{10} \text{ g/cm}^3$ .

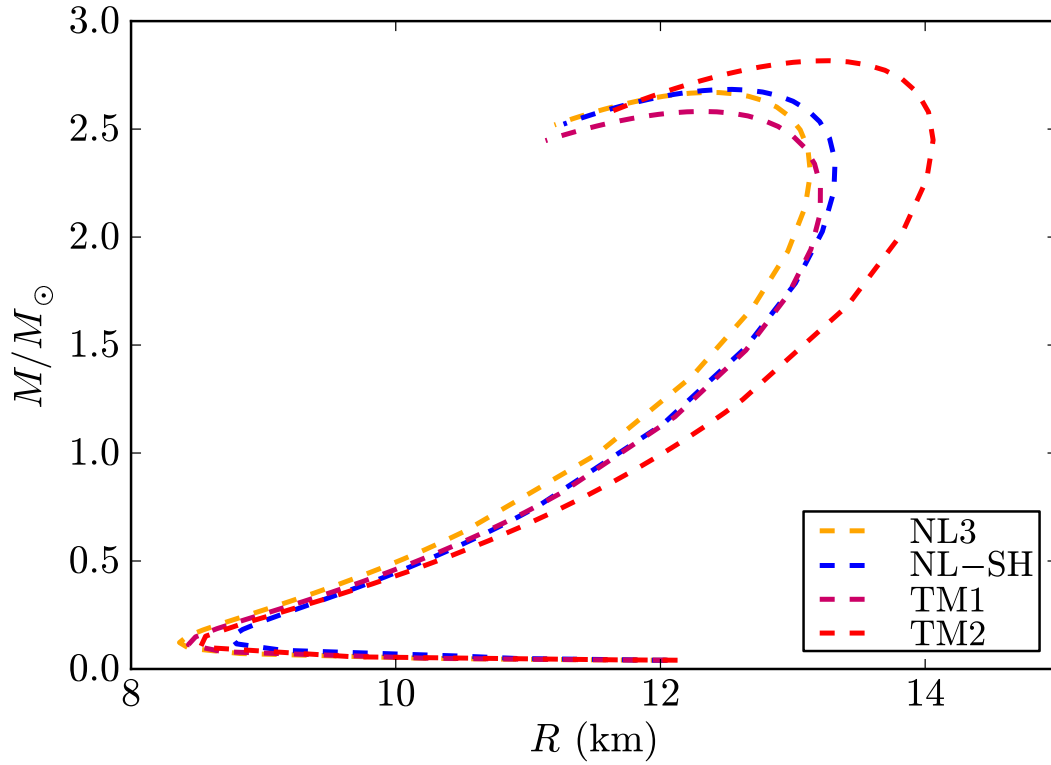


**Figure C.12.:** Mass-Radius relation for the neutron stars obtained with the nuclear models listed in Table C.1. In the crust we have used the BPS equation of state. The mass is given in solar masses and the radius in km.

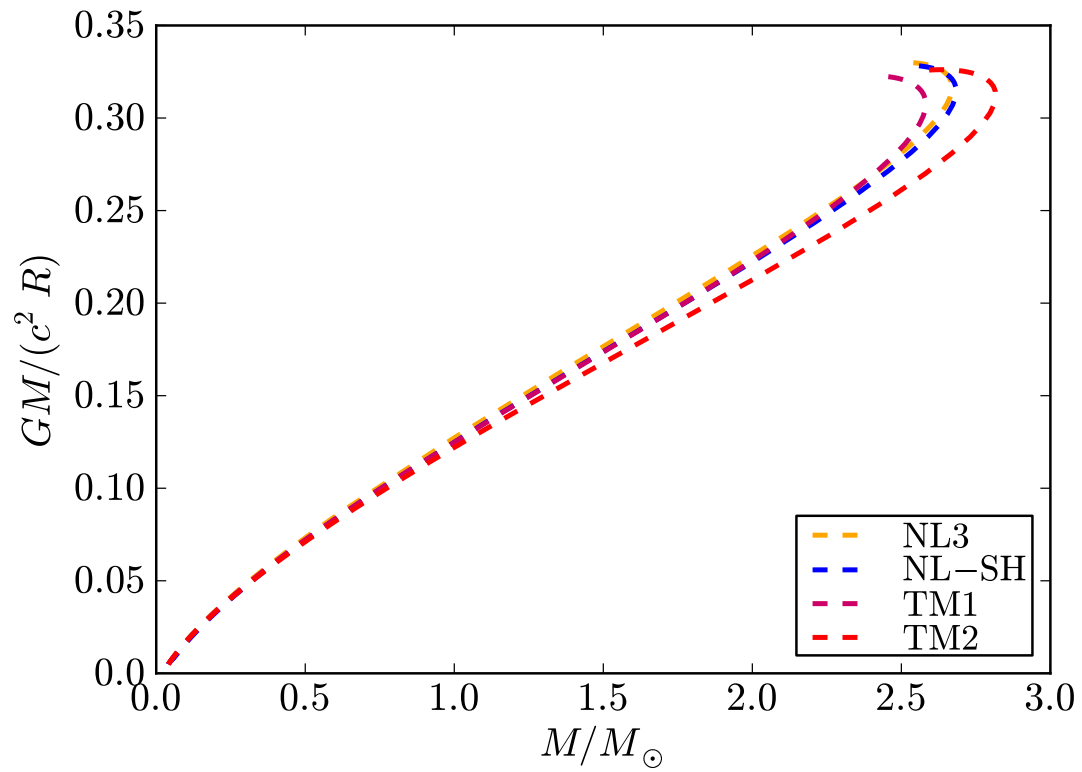


**Figure C.13.:** Compactness of the star  $GM/(c^2 R)$  as a function of the star mass  $M$ . In the crust we have used the BPS equation of state and the nuclear models are in Table C.1.

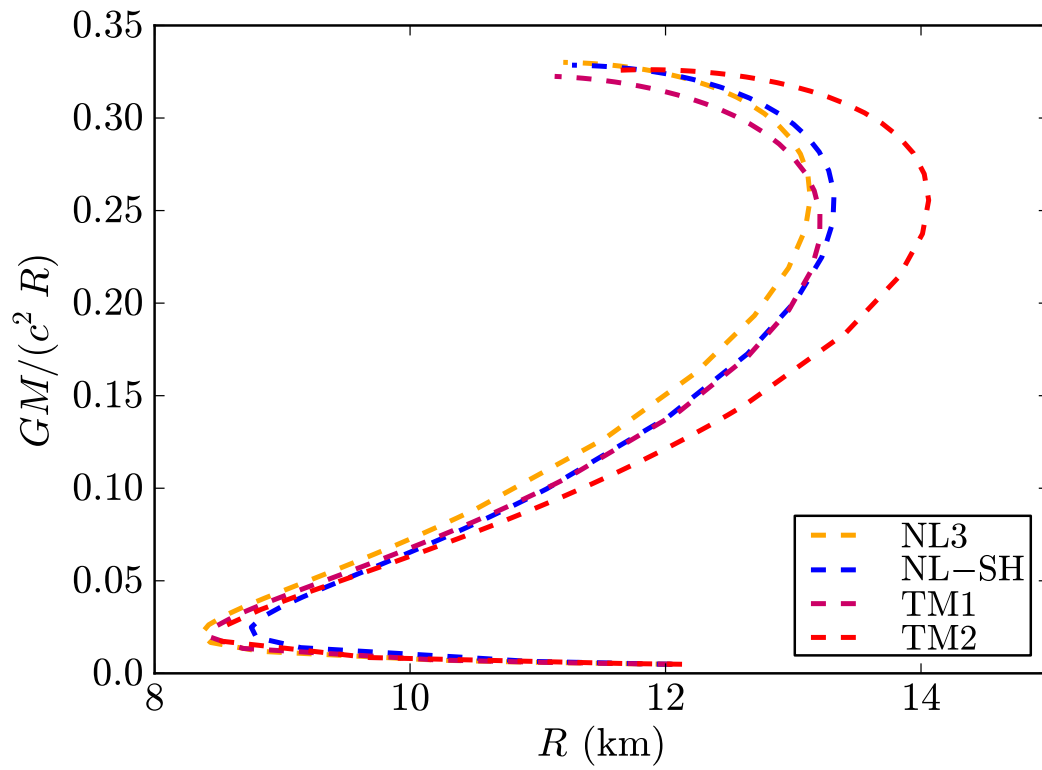


**Figure C.14.:** Compactness of the star  $GM/(c^2 R)$  as a function of the star radius  $R$ . In the crust we have used the BPS equation of state and the nuclear models are in Table C.1.

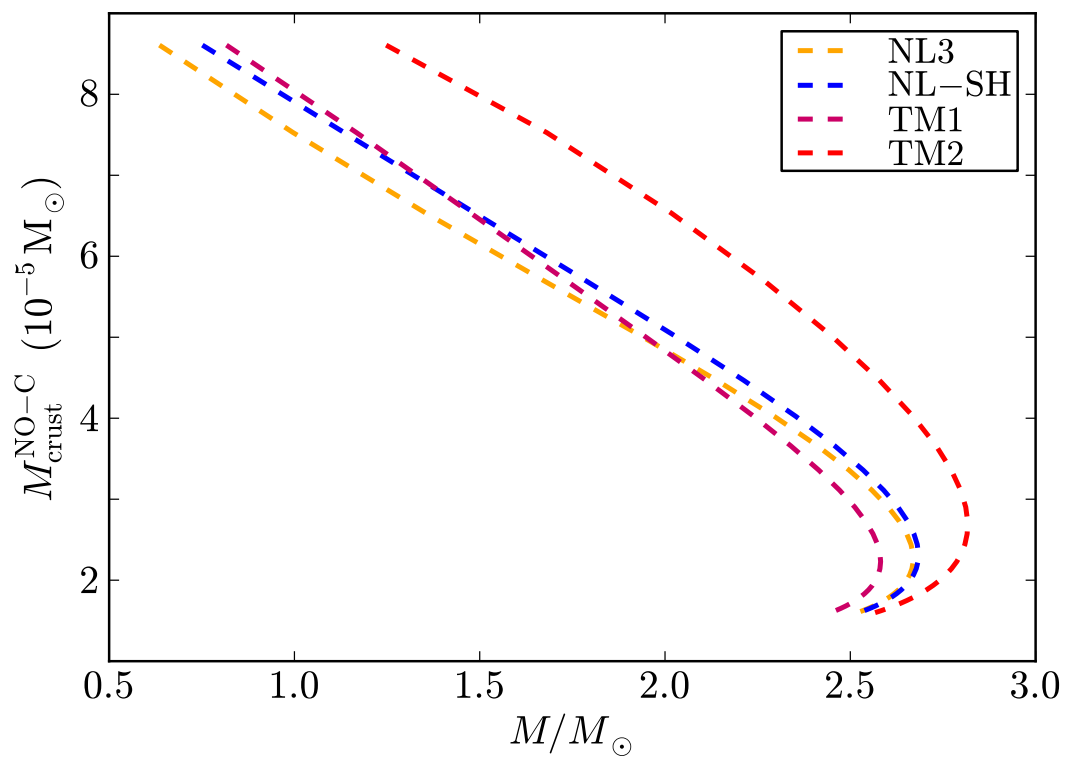


**Figure C.15.:** Mass of the crust as a function of the compactness for the crust EoS without Coulomb interactions.

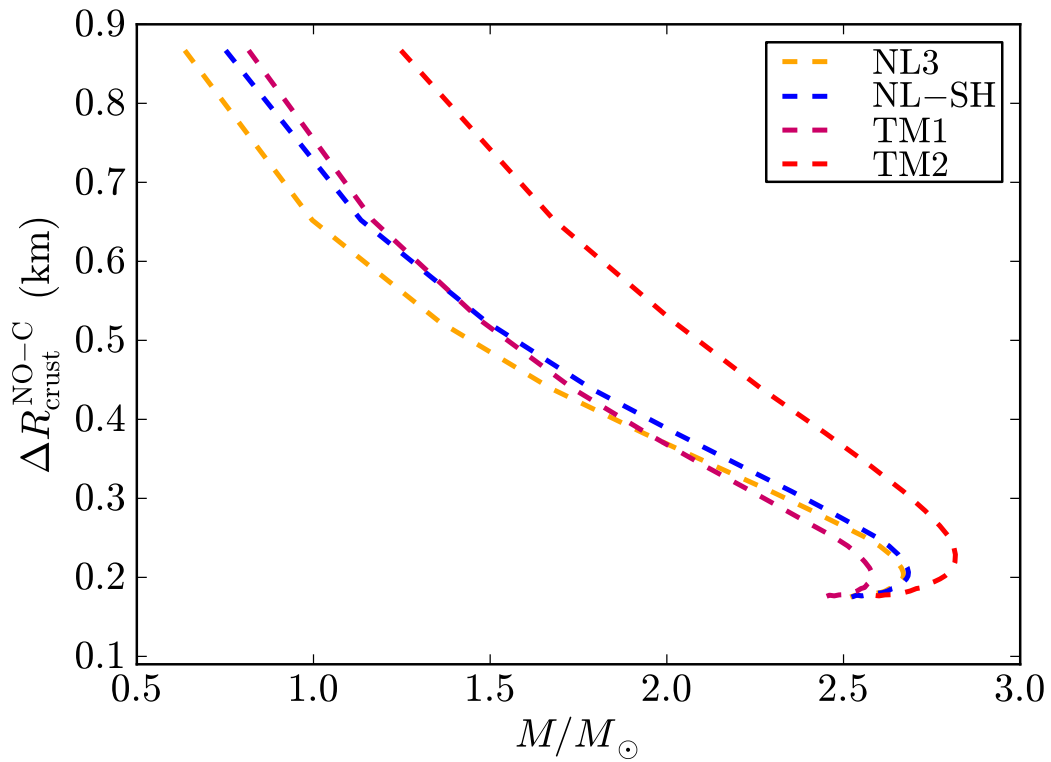


**Figure C.16.:** Crust-thickness as a function of the compactness for the crust EoS without Coulomb interactions.

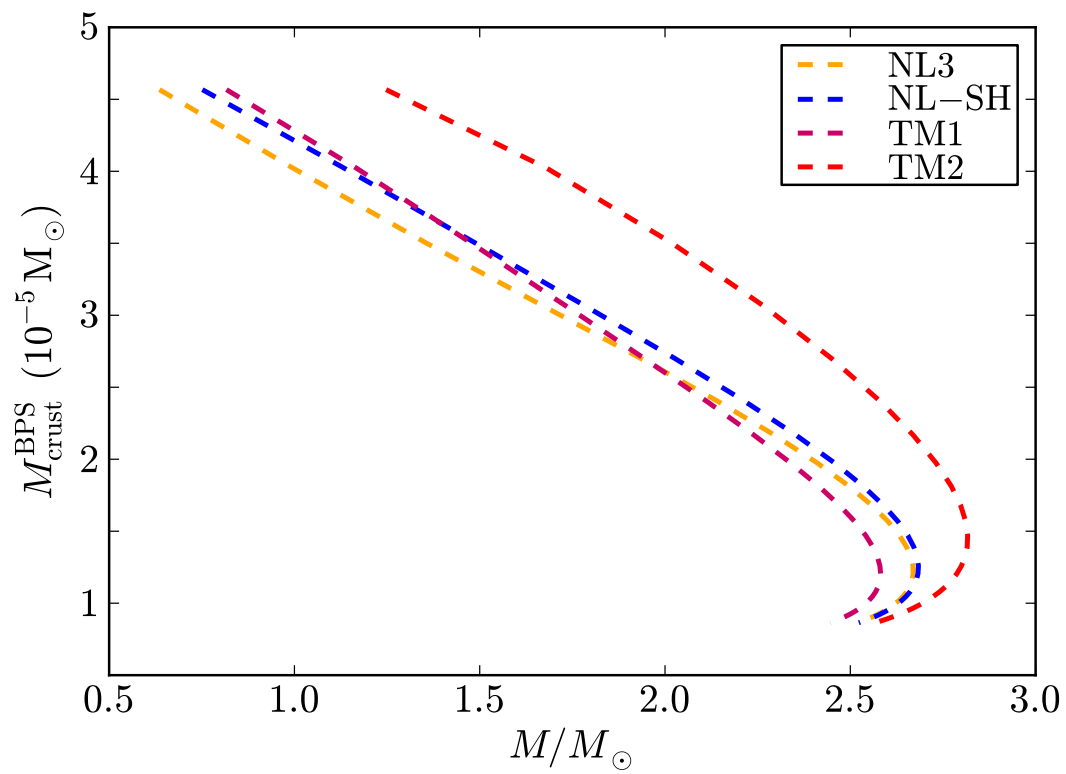


**Figure C.17.:** Crust mass as a function of the compactness for crust with the BPS EoS.

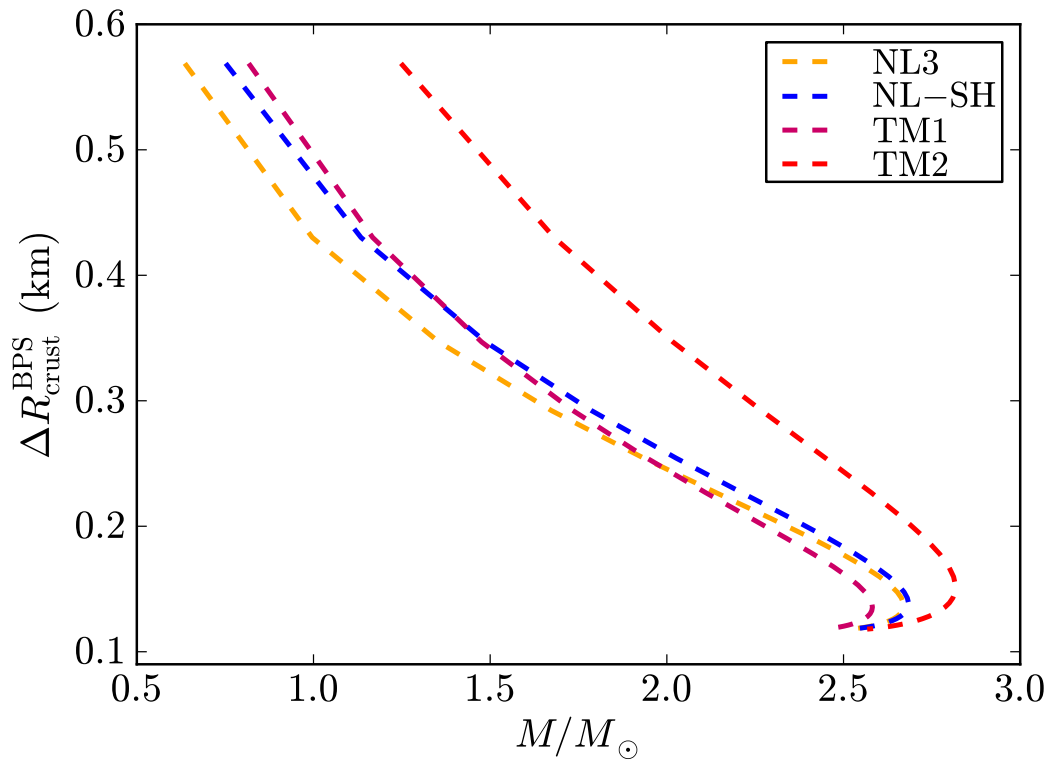


**Figure C.18.:** Crust thickness as a function of the compactness for crust with the BPS EoS.

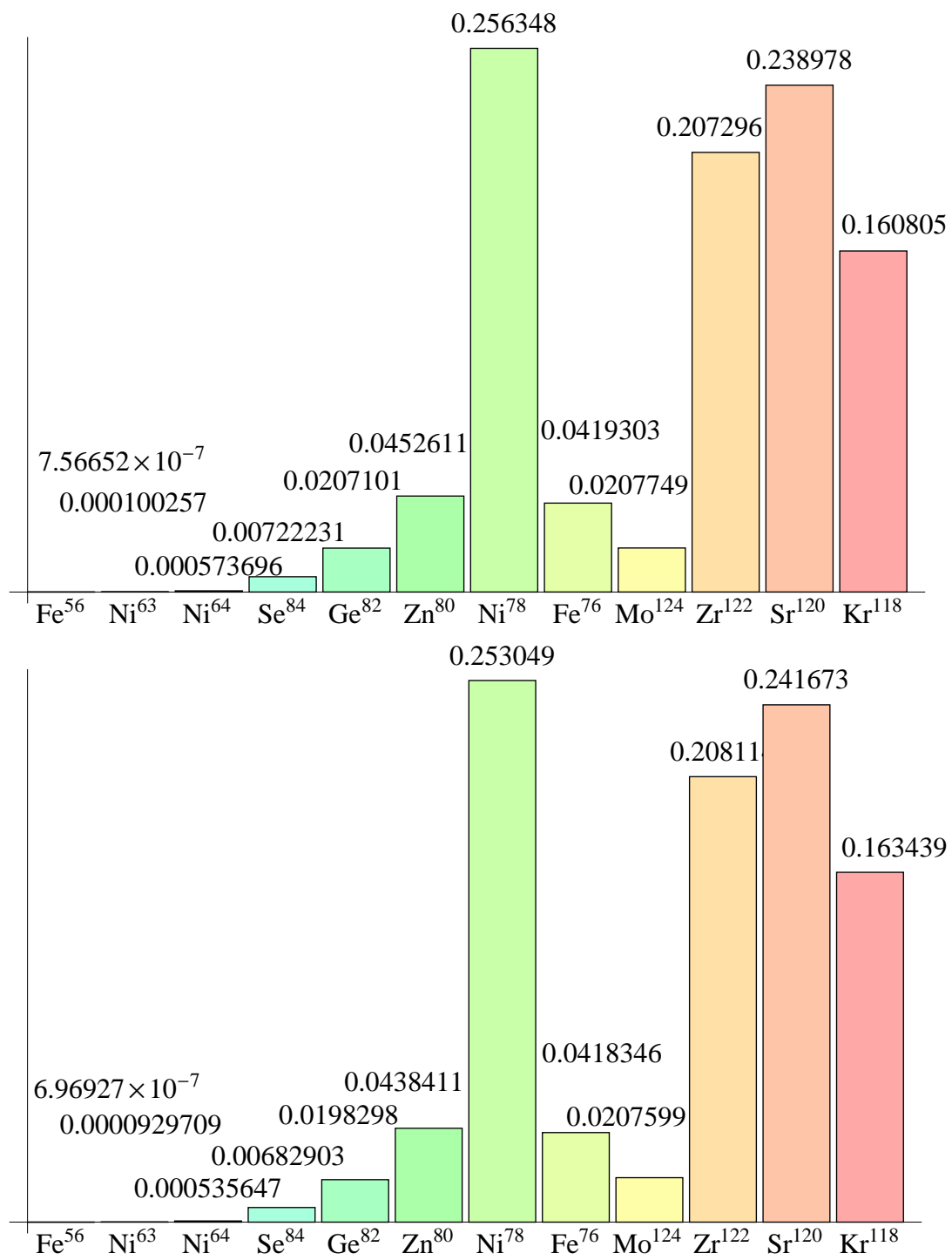


**Figure C.19.:** Relative abundances of chemical elements in the crust for the two cores analyzed in Table C.2

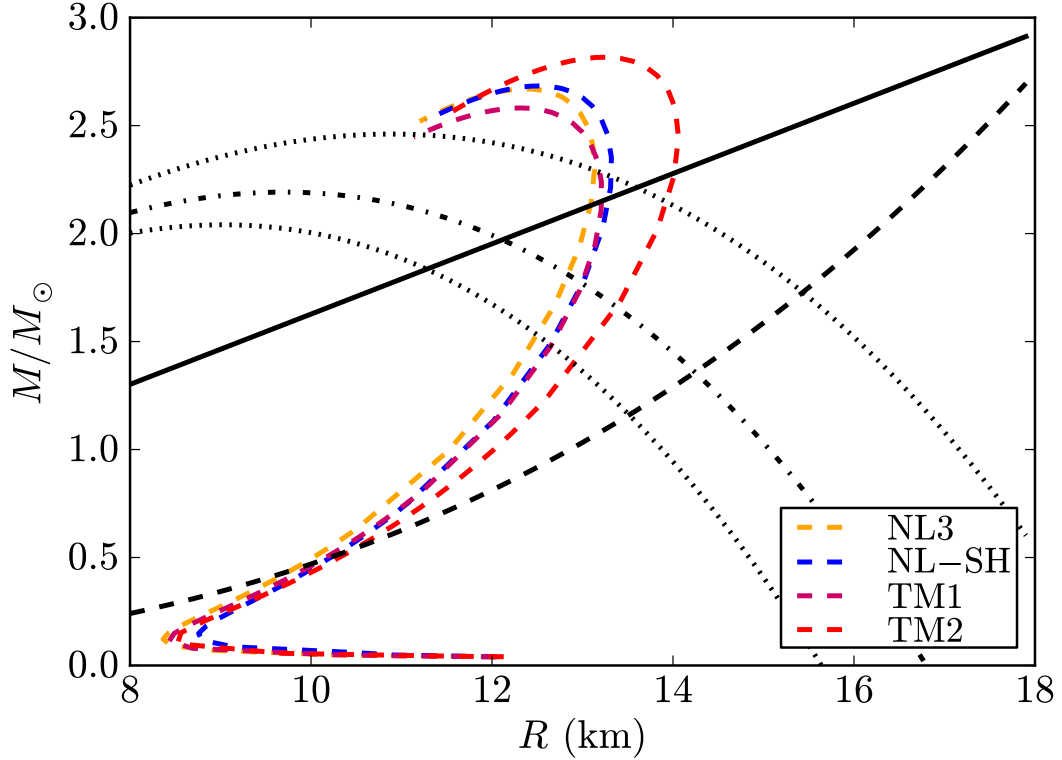


**Figure C.20.:** Constraints on the mass-radius relation given by J. E. Trümper in Trümper (2011) and the theoretical mass-radius relation presented in this work in Fig. C.12. The solid line is the upper limit of the surface gravity of XTE J1814-338, the dotted-dashed curve corresponds to the lower limit to the radius of RX J1856-3754, the dashed line is the constraint imposed by the fastest spinning pulsar PSR J1748-2246ad, and the dotted curves are the 90% confidence level contours of constant  $R_\infty$  of the neutron star in the low-mass X-ray binary X7. Any mass-radius relation should pass through the area delimited by the solid, the dashed and the dotted lines and, in addition, it must have a maximum mass larger than the mass of PSR J1614-2230,  $M = 1.97 \pm 0.04M_\odot$ .

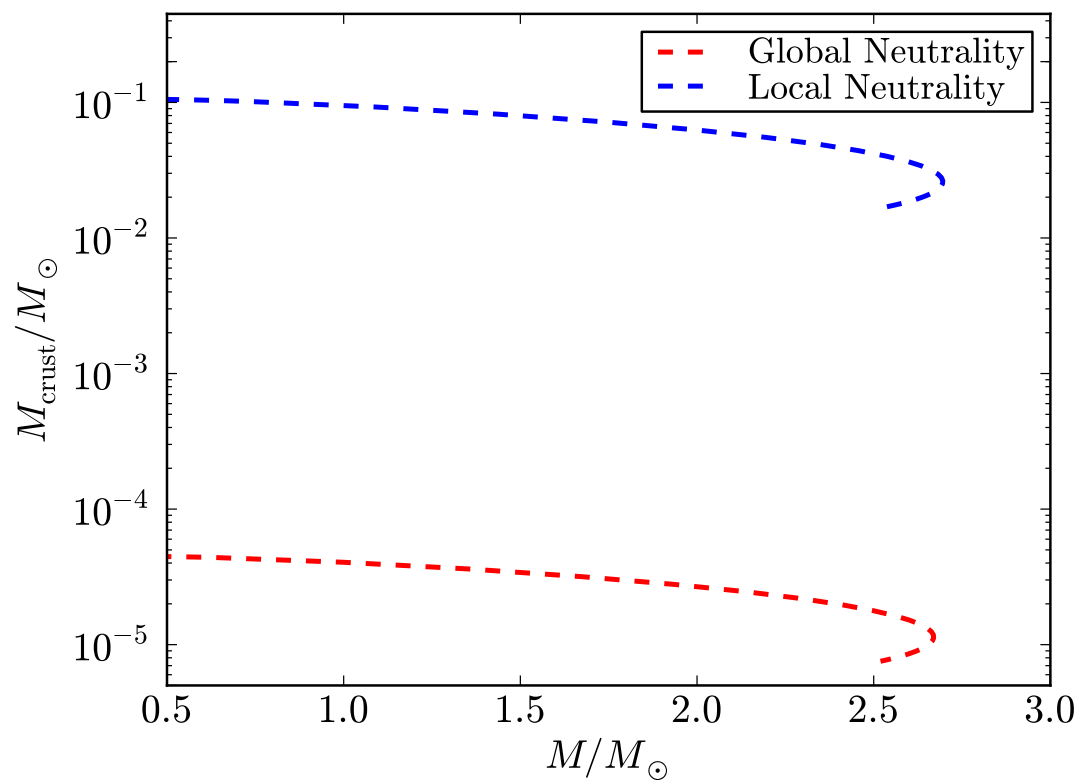


**Figure C.21.:** Mass of the crust given by the traditional locally neutral Tolman-Oppenheimer-Volkoff treatment and by the new globally neutral equilibrium configurations presented in this work. We use here the NL3 nuclear model, see Table C.1.

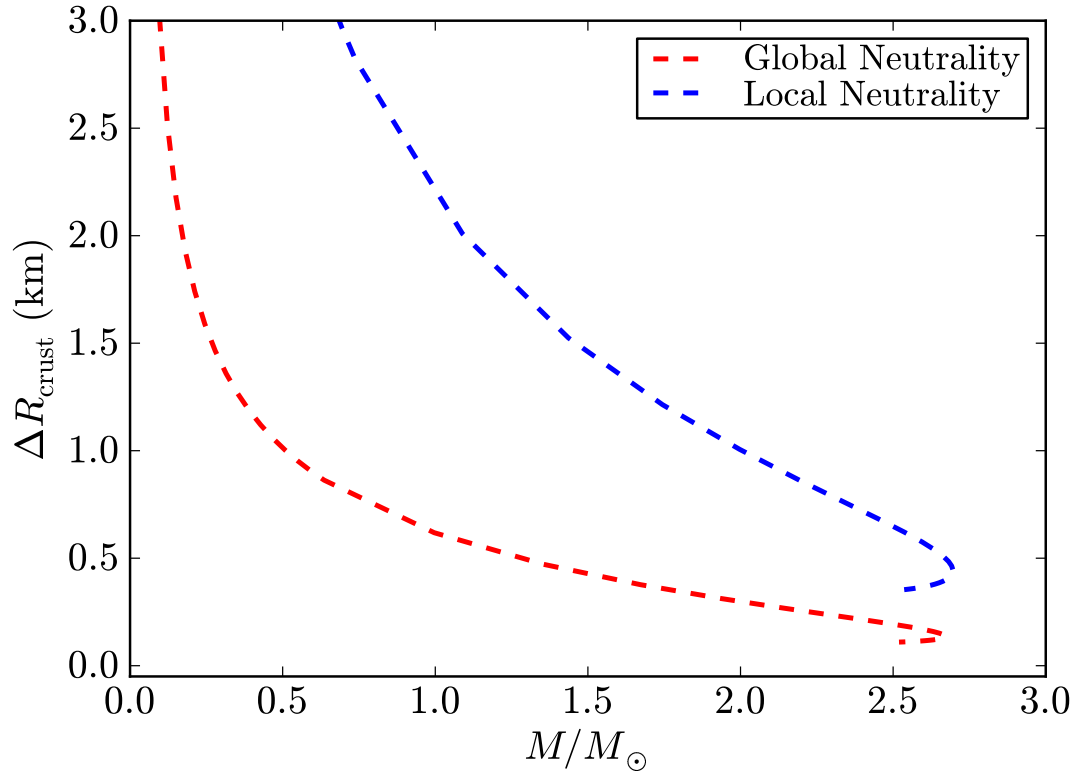


**Figure C.22.:** Thickness of the crust given by the traditional locally neutral Tolman-Oppenheimer-Volkoff treatment and by the new globally neutral equilibrium configurations presented in this work<sup>3</sup>. We use here the NL3 nuclear model, see Table C.1.

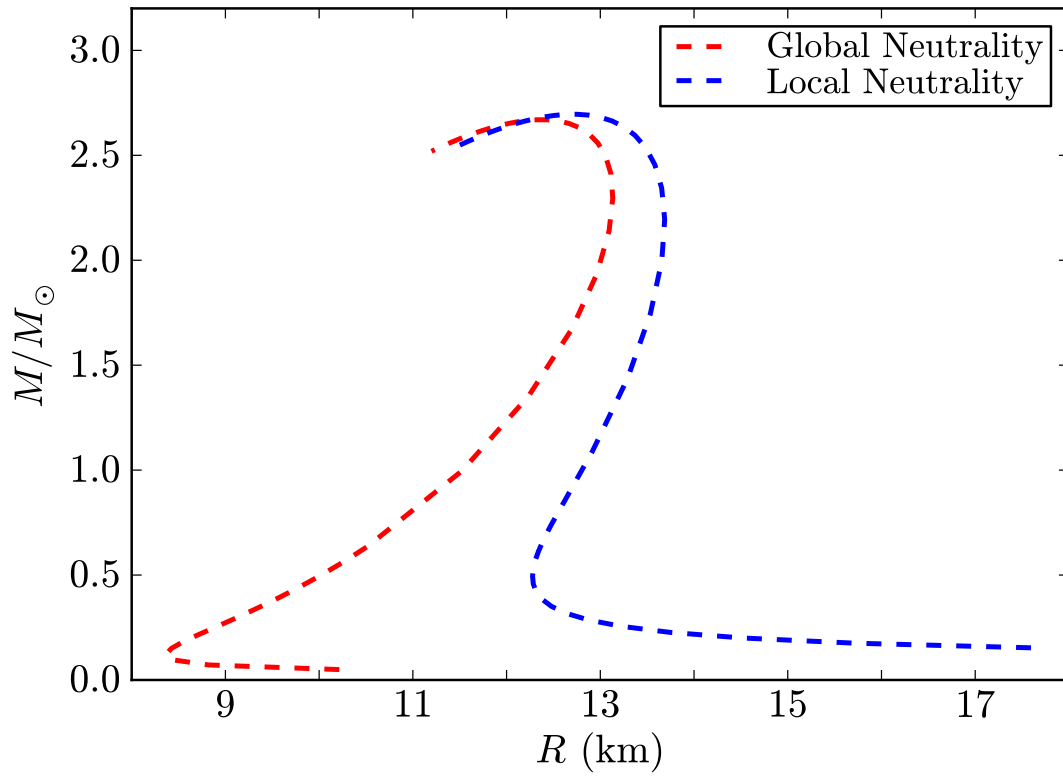


**Figure C.23.:** Mass-Radius relation obtained with the traditional locally neutral TOV treatment and with the new globally neutral equilibrium configurations presented here. We use here the NL3 nuclear model, see Table C.1.

## C.5. On uniformly rotating globally neutral neutron stars

We have recently computed in (Belvedere et al., 2012) equilibrium configurations of neutron stars including all fundamental interactions, i.e. strong, weak, electromagnetic, and gravitational within the framework of general relativity (see App. C.4, for details). The introduction of electromagnetic interactions has been done following a series of works (Rotondo et al., 2011d; Rueda et al., 2011b, see e.g.) in which a general formulation of the equations of equilibrium of neutron stars, the Einstein-Maxwell-Thomas-Fermi system of equations. The solution of these novel equations is subjected to the boundary condition of global charge neutrality, unlike the traditionally used condition of local charge neutrality. This latter condition reduces the equilibrium equations to the Tolman-Oppenheimer-Volkoff equations.

The nuclear interactions in (Belvedere et al., 2012) are described by the exchange of the  $\sigma$ ,  $\omega$ , and  $\rho$  virtual mesons. The equilibrium equations are then given by the Einstein-Maxwell-Thomas-Fermi equations along with the constancy of the general relativistic Fermi energies of particles, the “Klein potentials”, throughout the configuration. These equations have been solved numerically in the case of zero temperatures and for selected parameterizations of the nuclear models. The solutions lead to a new structure of the star: a positively charged core at supranuclear densities surrounded by an electronic distribution of thickness  $\sim \hbar/(m_e c) \sim 10^2 \hbar/(m_\pi c)$  of opposite charge, as well as a neutral crust at lower densities. Inside the core there is a Coulomb potential well of depth  $\sim m_\pi c^2/e$ . The constancy of the Klein potentials in the transition from the core to the crust, impose the presence of an overcritical electric field  $\sim (m_\pi/m_e)^2 E_c$ , the critical field being  $E_c = m_e^2 c^3/(e\hbar)$ . The electron chemical potential and the density decrease, in the boundary interface, until values  $\mu_e^{\text{crust}} < \mu_e^{\text{core}}$  and  $\rho_{\text{crust}} < \rho_{\text{core}}$ . For each central density, an entire family of core-crust interface boundaries and, correspondingly, an entire family of crusts with different mass and thickness, exist. The configuration with  $\rho_{\text{crust}} = \rho_{\text{drip}} \sim 4.3 \times 10^{11} \text{ g/cm}^3$  separates neutron stars with and without inner crust. Thus, these globally neutral neutron stars have crusts with smaller mass and thickness with respect to the ones constructed under the assumption of local charge neutrality following the Tolman-Oppenheimer-Volkoff treatment (see App. C.4).

Belvedere et al. (2012) considered however the neutron stars as non-rotating and therefore described by a Schwarzschild-like spacetime metric. We present here a natural extension of this previous work, that is to consider the uniformly rotating case. We follow the slowly rotating approximation of Hartle (1967), in a similar way as recently done for general relativistic white dwarfs by Boshkayev et al. (2012), and therefore we refer the reader to App. B.2 for details on the Hartle’s approach.

We show below uniformly rotating neutron stars constructed with the Hartle's formalism. The nuclear models are the same used in (Belvedere et al., 2012). We have compute the Keplerian sequence as well as sequences of constant angular momentum in order to construct the boundary of secular axisymmetric instability. The results are shown in Figs. C.24 and C.25.

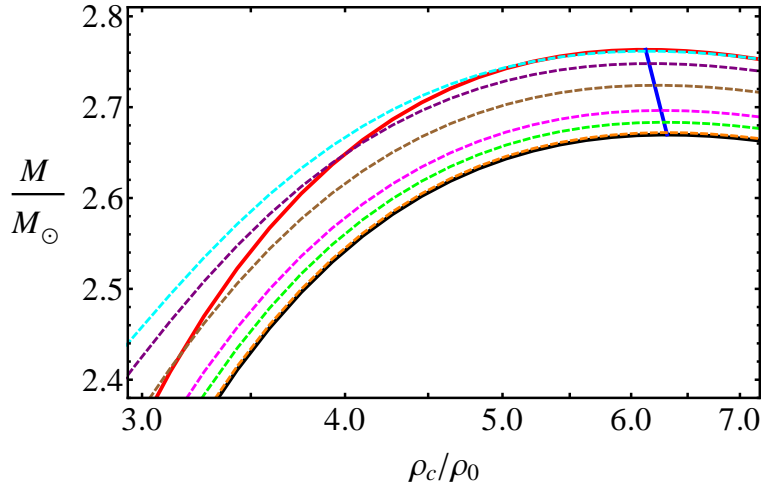


**Figure C.24.:** Mass versus central density of globally neutral neutron stars. The diagonal blue line corresponds to the secular axisymmetric instability boundary. The curve bounding the region of stable configurations from above (red curve) is formed by the Keplerian (mass-shedding) sequence. The dashed curves are sequences of constant angular momentum.

In Fig. C.26 we compare and contrast globally neutral and locally neutral neutron stars in the non-rotating and uniformly rotating cases. We have added the observational constraint boundaries used by Belvedere et al. (2012) (see App. C.4, for details).

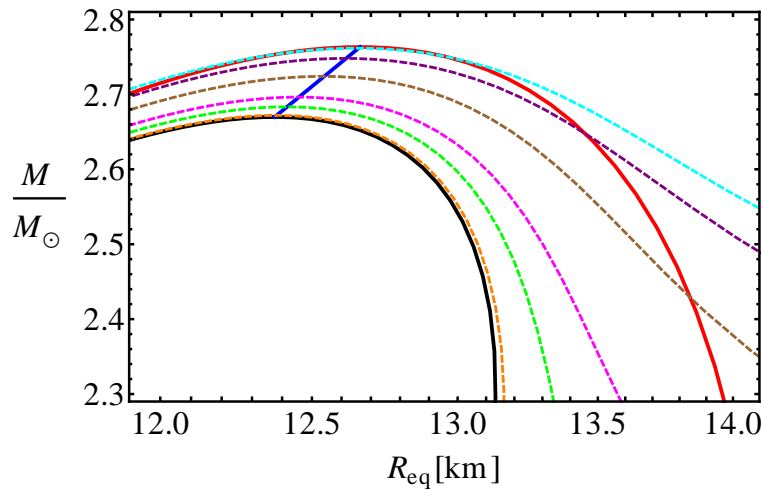


**Figure C.25.:** Mass versus equatorial radius of globally neutral neutron stars. The diagonal blue line corresponds to the secular axisymmetric instability boundary. The curve bounding the region of stable configurations from above (red curve) is formed by the Keplerian (mass-shedding) sequence. The dashed curves are sequences of constant angular momentum.

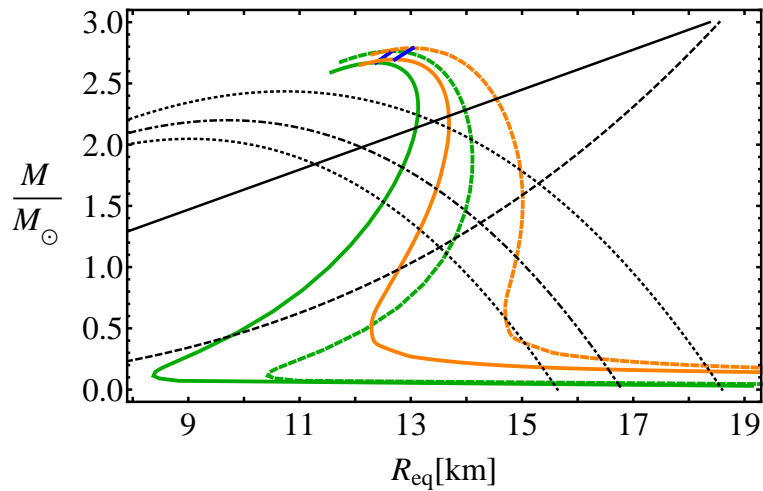


**Figure C.26.:** Comparison of globally (green) and locally (orange) neutral neutron star mass-radius relations. The solid curves are the non-rotating mass-radius relations while, the dashed curves, are the critically rotating (Keplerian sequences) configurations. The diagonal blue lines are the corresponding secular axisymmetric instability boundaries. The black dashed curves are the observational constraint boundaries used by Belvedere et al. (2012) (see App. C.4, for details).



# D. Neutron Stars Physics with Gamma-Ray Bursts

## D.1. Cooling of young neutron stars in GRB associated to Supernova

### D.1.1. Introduction

The investigation of the thermal evolution of neutron stars is a powerful tool to probe the inner composition of these objects. The cooling of neutron stars has been investigated by many authors, where many different microscopic models were assumed (see Schaab et al., 1996; Page et al., 2004, 2006, 2009; Blaschke et al., 2000; Grigorian et al., 2005; Blaschke et al., 2006; Negreiros et al., 2010). Most of the research on the thermal evolution of compact stars focus on objects with ages greater than 10-100 years, which is comprehensible if one consider that the thermal data, currently available to us, is for pulsars with estimated ages of or greater than 330 years (Page et al., 2004, 2009). In this letter we discuss the thermal evolution of young neutron stars, in the little explored time window that spans from ages greater than 1 minute (just after the proto-neutron star regime (Prakash et al., 2001)) to ages  $\leq 10$ -100 years, when the neutron star becomes isothermal (see Gnedin et al., 2001, for details).

We discuss the possibility that the late X-ray emission (URCA hereafter<sup>1</sup>) following a few GRBs associated with SNe; e.g. URCA-1 in GRB980425-SN1998bw (Ruffini et al., 2004; Frascchetti et al., 2005; Bernardini et al., 2008), URCA-2 in GRB030329-SN2003dh (Bernardini et al., 2004, 2005b), and URCA-3 in GRB031203-SN2003lw (Bernardini et al., 2005a; Ruffini et al., 2007a, 2008b) (see Fig. D.3 for details), might actually be originated by young ( $t \sim 1$  minute–(10–100) years), hot ( $T \sim 10^7$ – $10^8$  K) neutron stars, that are remnants of the SN (Ruffini et al., 2007a) and which we have here called neo-neutron stars. Relevant also are the observations of the isolated Type Ic Supernova SN 1994I

---

<sup>1</sup>The name URCA-1 and URCA-2 mentioned here were given to these sources when presented for the first time at the MG10 meeting held in Rio de Janeiro in the town of URCA. The location of the MG10 meeting was very close to the “Cassino da URCA” where George Gamow and Mario Schoenberg conceived the process of neutrino emission for the cooling process of neutron stars which also took the name from the town of URCA, the URCA process (see e.g detailed history in Ruffini et al., 2005; Gamow, 1970)

(Immler et al., 2002) and SN 2002ap (Soria et al., 2004) which present late emissions similar to the ones observed in URCA-1, URCA-2, and URCA-3.

In this letter we propose a revision of the boundary conditions usually employed in the thermal cooling theory of neutron stars, in order to match the proper conditions of the atmosphere at young ages. We also discuss the importance of the thermal processes taking place in the crust, which also have important effects on the initial stages of thermal evolution. We stress that we are not calling into question the validity of the current treatment of the atmosphere of compact stars but, instead, we point out the need of extending them to appropriately describe the conditions of neo-neutron stars.

### **D.1.2. Cooling of Young, Hot Neutron Stars**

There are three important ingredients that govern the thermal evolution of a compact star, these are: 1) the microscopic input, that accounts for the neutrino emissivities, specific heat and thermal conductivity; 2) the macroscopic structure of the star, namely its mass, radius, pressure profile, crust size, etc.; and 3) the boundary condition at the surface of the star, that provides a relationship between the mantle temperature and that of the atmosphere, the latter being what we ultimately observe. These ingredients have been extensively studied, and a comprehensive review can be found in Page et al. (2006). As discussed in Gnedin et al. (2001), during the initial stages of thermal evolution (ages  $\leq 10 - 100$  years), the core and the crust of the neutron star are thermally decoupled. This is due to the fact that the high density core is emitting neutrinos at a much higher rate than the crust, which causes it to cool down more quickly. This effectively means, that initially the neutron star is cooling “inside out”, with the core colder than the outer layers. This scenario is schematically depicted in Figure D.1.

The dominant neutrino emission processes in the crust are given by the Bremsstrahlung, plasmon decay, and electron-positron annihilation processes. Following the footsteps of Gnedin et al. (2001), we calculate the thermal evolution of neutron stars, by adding artificially a phenomenological source of heat (see details in Sec. D.1.4). This allow us to estimate how much heat is needed, so that the thermal evolution of a neo-neutron star matches the X-ray light curve of late emission of GRB-SN.

After this initial core-crust decoupled state, the “cooling wave” originated in the core reaches the crust, and the object becomes isothermal. The time scale of this process is between 10–100 years, depending on the properties of the crust (Gnedin et al., 2001). This means that during the initial stages of thermal evolution the crust shields the core, and all the information we might obtain at this stage, refers only to the crust and to the atmosphere of the star. This raises another issue, that concerns the atmosphere of the star. The thermal connection between the mantle and the atmosphere is what defines the

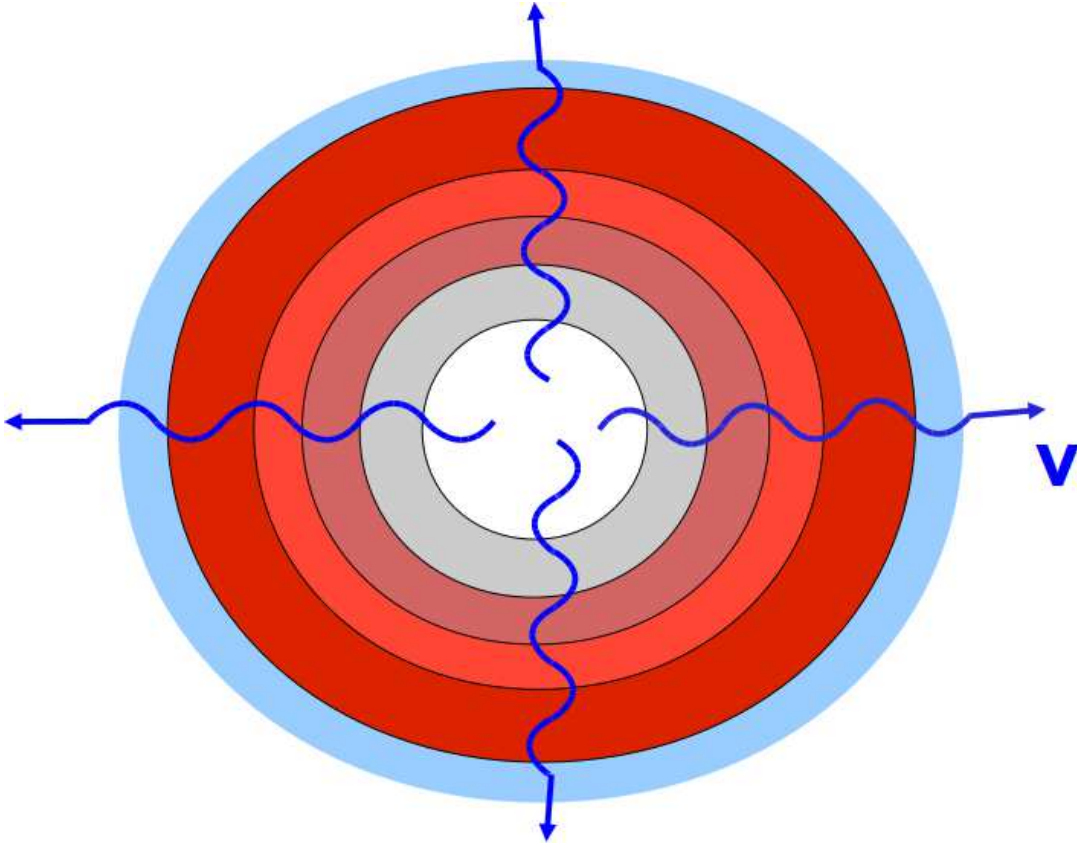


**Figure D.1.:** Schematic representation of the cooling of a young neutron star. Due to stronger neutrino emissivities, the core of the star cools down more quickly than the crust, causing the star to cool inside out. Darker and lighter areas represent higher and lower temperatures respectively.

photon luminosity, which is what we observe. Therefore, the appropriate description of the atmosphere is key to the correct understanding of the thermal evolution of neutron stars. In the usual approach, the thermal relaxation-time of the atmosphere is assumed to be much smaller than that of the neutron star, furthermore neutrino emissions from the atmosphere are also considered negligible (see Gudmundsson et al., 1983). Under these assumptions, and assuming a plane-parallel approximation (which is reasonable since the atmosphere is  $\sim 100$  m thick), one can get a relationship between the temperature of the mantle  $T_b$  and the temperature of atmosphere  $T_e$ , or equivalently the luminosity  $L_e$ . Gudmundsson et al. (1983) have originally found a  $T_b$ - $T_e$  relationship that depends on the surface gravity of the neutron star. This relationship was further developed by Potekhin et al. (1997), to account for the possibility of mass accreted in the initial stages, and of magnetic fields effects. As pointed out by Gudmundsson et al. (1983), such assumptions for the atmosphere of the star are only valid for objects older than a few 10 years, when the temperature, for densities below  $10^{10}$  g/cm<sup>3</sup>, has dropped below  $10^9$ K. In fact, we see that the current boundary conditions yields temperatures  $\sim 10^7$  K ( $L \sim 10^{37}$  erg/s, equivalently) for young neutron stars (age  $< 1$ –10 years). This should raise some suspicion since proto-neutron stars studies (see Prakash et al., 2001, and references therein), indicate that neutron stars just after this regime have temperatures  $\sim 10^{10}$ – $10^{11}$  K.

The properties of the atmosphere of a sufficiently hot, nascent neutron star should differ significantly from those considered in Gudmundsson et al. (1983) and Potekhin et al. (1997). Especially since at hot temperatures ( $T \gtrsim 10^9$  K) the atmosphere might not be transparent to neutrinos, and thus the neutrino transport equations have to be considered. The coupled equations of neutrino and photon transport, in the atmosphere of a neutron star, were solved by Salpeter and Shapiro (1981), and Duncan et al. (1986). In these works the authors have performed detailed calculations of the atmosphere properties of hot neutron stars. They have found the following photon luminosity, as observed at infinity,

$$L_\infty = 50 \times t^{-7/12} \times (T_{10})^{7/4} \times (R_{10})^{17/9} \times \left( \frac{M}{M_\odot} \right)^{-1} \times L_E, \quad (\text{D.1.1})$$

where  $t$  is time in seconds,  $T_{10}$  is the initial temperature in units of 10 MeV,  $R_{10}$  is the neutron star radius in units of 10 km,  $M$  is the neutron star mass, and  $L_E \sim 2.0 \times 10^{38}$  erg/s is the Eddington luminosity. Duncan et al. (1986) found that the above expression should be valid for at least the initial 100 s. In Fig. D.2 we can see how the luminosity of the star changes for the first 100 s, for stars with different initial temperatures.

According to these results, during the initial 100 s, the photon luminosity emerging from the atmosphere will be higher than the Eddington luminosity. This implies that there will be mass loss, due to neutrino-driven winds from

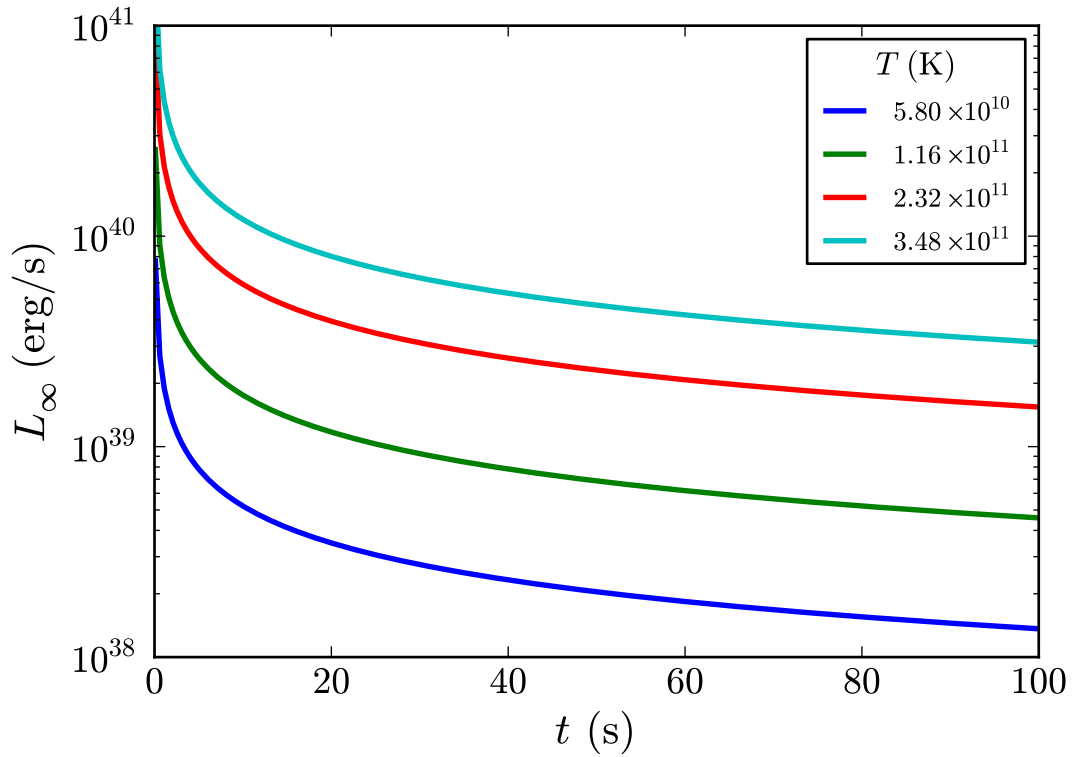


**Figure D.2.:** Luminosity of a hot nascent neutron star as observed at infinity given by Eq. (D.1.1) during the initial 100 s (Duncan et al., 1986), with the initial temperatures indicated. The neutron star is assumed to have a mass of  $1.4M_\odot$ , and a radius of 13 km.

the young atmosphere. As shown by Duncan et al. (1986), the total mass loss only becomes appreciable for neutron stars with large radii and high initial temperatures. For a typical neutron star with the canonical mass of  $1.4M_{\odot}$ , a radius of 13 km and initial temperature of  $\sim 10^{11}$  K, the total mass loss was estimated to be  $\sim 6.2 \times 10^{-6}M_{\odot}$ .

In addition to the high luminosities associated to the atmosphere of young neutron stars, one need also to consider fallback onto the surface of the neutron star. Potekhin et al. (1997) discussed how fallback, at earlier stages of evolution, would modify the properties of the atmosphere, and hence of the boundary conditions. Once more however, in this investigation, such a fallback is assumed to have happened at early times and the modified boundary conditions are only valid if the fallback has already ceased. Chevalier (1989) has studied the fallback onto young neutron stars, and found that while there is an envelope, a luminosity near the Eddington limit should be present. Furthermore, the authors have found that in this case the energy from the envelope can be radiated away in a time of  $\sim 1$  year. This timescale however, might be lengthened if effects of rotation are accounted during the fallback. In addition to that, Turolla et al. (1994) have discussed the possibility of “hot solutions” for the atmosphere of neutron stars undergoing spherical accretion. It was shown that for  $L \geq 10^{-2}L_E$  the temperature at the atmosphere of a neutron star might be  $\sim 10^9$ – $10^{11}$  K.

### **D.1.3. Late X-Ray Emission in GRBs associated to Supernovae: URCA**

It seems clear to us that, after the analysis of the scenario described above, we must extend the current model for the boundary conditions used in cooling calculations, to include the effects of a high temperature atmosphere, with possibly super-Eddington luminosity. Up until this point however, little attention has been given to the thermal evolution of young neutron stars, mainly due to the absence of observational data of neutron stars with ages  $< 330$  years. It has been recently proposed (see Ruffini et al., 2007a, for details) that the long lasting X-ray emission called there URCA (see Fig. D.3) of a few GRBs associated to SNe; URCA-1 in GRB980425-SN1998bw (Ruffini et al., 2004; Frascchetti et al., 2005; Bernardini et al., 2008), URCA-2 in GRB030329-SN2003dh (Bernardini et al., 2004, 2005b), and URCA-3 in GRB031203-SN2003lw (Bernardini et al., 2005a; Ruffini et al., 2007a, 2008b), might actually be originated in the compact star remnant of the SN: a neo-neutron star. In this scenario the GRB is described as the core collapse of a massive star, whose remnant is a black hole. This massive star is supposed to be in a binary system, whose companion is on the verge of going supernova. The GRB triggers the supernova explosion in the companion star, which in turns leaves behind a neutron star (Ruffini et al., 2001). An alternative scenario has been recently

**Table D.1.:** a) see Kaneko et al. (2007); b) Mazzali, P., private communication at MG11 meeting in Berlin, July 2006, Iwamoto et al. (1998); c) evaluated fitting the URCA with a power law followed by an exponentially decaying part; d) evaluated assuming a mass of the neutron star  $M = 1.5M_{\odot}$  and  $T \sim 5\text{--}7$  keV in the source rest frame; e) see Galama et al. (1998); Greiner et al. (2003); Prochaska et al. (2004); Mirabal et al. (2006). Here  $E_{e^{\pm}}^{\text{tot}}$  is the total energy of GRB,  $E_{SN}^{\text{bolom}}$  and  $E_{SN}^{\text{kin}}$  are the bolometric and the kinetic energy of the SN,  $E_{URCA}$  is the energy of the late X-ray emission URCA (see Fig. D.3),  $R_{NS}$  is the radius of the neutron star and  $z$  is the redshift of the event.

GRB	$E_{e^{\pm}}^{\text{tot}}$ (erg)	$E_{SN}^{\text{bolom}}$ (erg) <sup>a</sup>	$E_{SN}^{\text{kin}}$ (erg) <sup>b</sup>	$E_{URCA}$ (erg) <sup>c</sup>	$\frac{E_{e^{\pm}}^{\text{tot}}}{E_{URCA}}$	$\frac{E_{SN}^{\text{kin}}}{E_{URCA}}$	$R_{NS}$ (km) <sup>d</sup>	$z$ <sup>e</sup>
980425	$1.2 \times 10^{48}$	$2.3 \times 10^{49}$	$1.0 \times 10^{52}$	$3 \times 10^{48}$	0.4	$1.7 \times 10^4$	8	0.0085
030329	$2.1 \times 10^{52}$	$1.8 \times 10^{49}$	$8.0 \times 10^{51}$	$3 \times 10^{49}$	$6 \times 10^2$	$1.2 \times 10^3$	14	0.1685
031203	$1.8 \times 10^{50}$	$3.1 \times 10^{49}$	$1.5 \times 10^{52}$	$2 \times 10^{49}$	8.2	$3.0 \times 10^3$	20	0.105
060218	$1.8 \times 10^{50}$	$9.2 \times 10^{48}$	$2.0 \times 10^{51}$	?	?	?	?	0.033

suggested in which the so-called GRB is actually not a GRB but the observed X-ray emission originates from a collapsing core: a proto-neutron star leading directly to a SN explosion. This concept is very similar to the one of a proto-black hole introduced in Ruffini et al. (2011, 2010a); Izzo et al. (2011), where the emission from the collapsing core is clearly well distinguished from the GRB. In that case the collapsing core leads to the formation of the black hole while in the present case it leads to the formation of a neutron star.

Both scenarios lead to the formation of a neo-neutron star and they are supported by the observation of Supernova 1979C (Patnaude et al., 2011), where a similar X-ray light curve also followed the supernova. In Fig. D.3 we show the X-ray light curve associated with the URCA.

From Fig. D.3 we can see that the X-ray luminosities of these sources are of the same magnitude as that expected for neo-neutron stars, as discussed above. In Table D.1 we summarize the representative parameters of the four GRB-SN systems, including the very large kinetic energy observed in all SNe (Mazzali, 2006). We have also included the association GRB060218-SN2006aj (see Dainotti et al., 2007, 2010, for details). It must be noted that similar prolonged X-ray emission has been observed also in connection with other Type Ic SN not associated with GRBs, like e.g. SN1994I (Immler et al., 2002) and SN2002ap (Soria et al., 2004) (see Fig. D.4 for details).

#### D.1.4. Neo-Neutron Star Luminosity and the URCA

Another important ingredient for the cooling of young neutron stars are the crust properties. As illustrated in Fig. D.1, due to the stronger neutrino emission from the core, during the initial stages the core and crust are thermally decoupled. For that reason, the initial stages of the thermal evolution reflects the properties of the crust, while the core remains invisible. Thus the proper description of the crust structure and composition, is also fundamental for

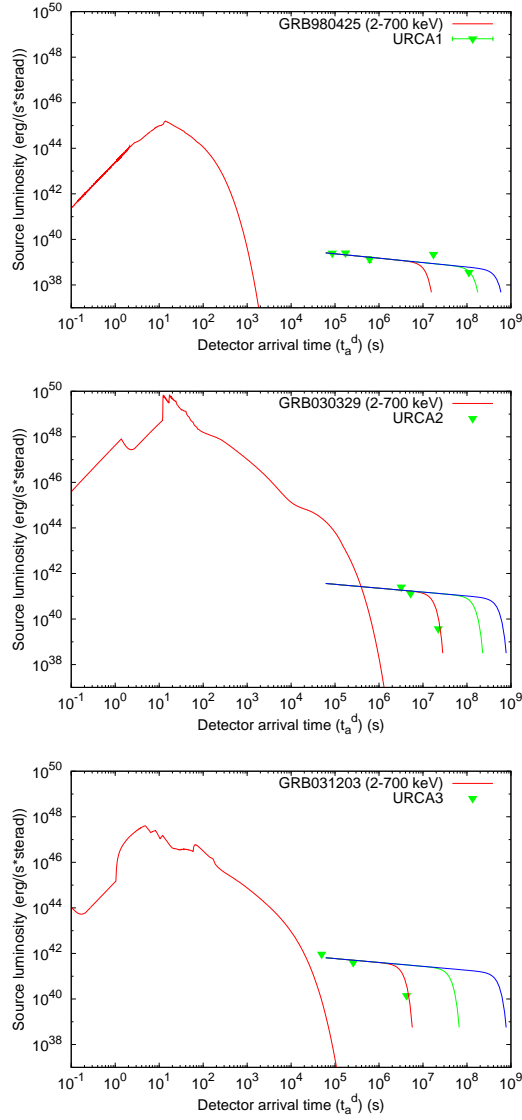


**Figure D.3.:** Synthetic light curves of GRB980425 (A) (Ruffini et al., 2004; Frascchetti et al., 2005; Bernardini et al., 2008) , GRB030329 (B) (Bernardini et al., 2004, 2005b) and GRB031203 (C) (Bernardini et al., 2005a; Ruffini et al., 2007a, 2008b) . The solid curves represent the hard X-ray emission (10-200 keV range) and the triangles are 2-10 keV flux points. The optical luminosities of the SNe accompanying these GRBs are also reported with crosses (see Ruffini et al., 2007a, for details). The curves fitting the late X-ray luminosity (URCAs) are qualitative cooling curves based on Canuto (1978); see also Ruffini et al. (2004, 2007a, 2008b); Bernardini et al. (2004, 2005a,b, 2008); Frascchetti et al. (2005), for details.

understanding the initial thermal evolution stages of a neutron star. We now briefly discuss the current understanding of the crustal processes and how

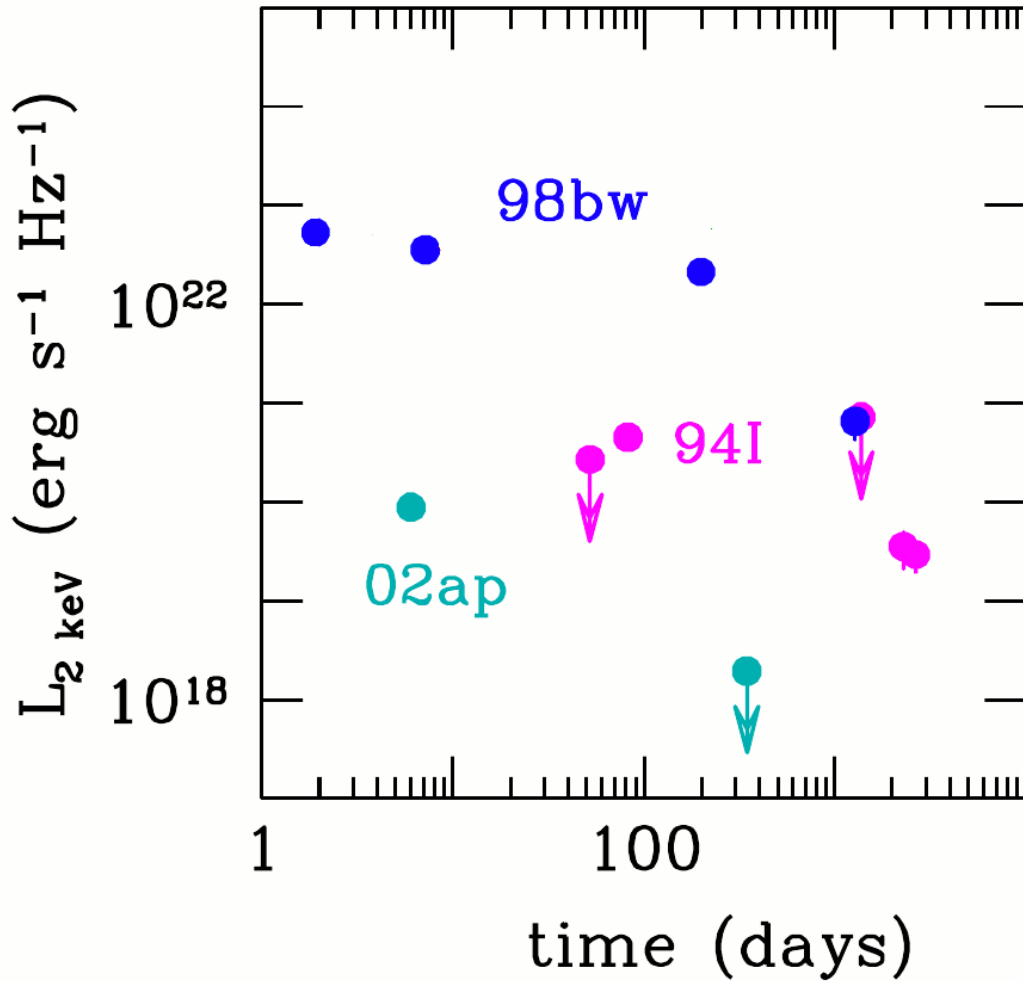


**Figure D.4.:** X-ray light curves of the counterparts of GRB980425-SN1998bw and of two Type Ic SNe not accompanied by GRBs: SN1994I (“normal”) and SN2002ap (broad-lined). The data are from Pian et al. (2000); Immler et al. (2002); Kouveliotou et al. (2004); Soria et al. (2004).

such might be related with the data available from the URCA's.

There are several active emission mechanisms in the neutron star crust, e.g.  $e$ -Ion Bremsstrahlung, plasmon decay,  $e^+e^-$  annihilation,  $e-e$  and  $n-n$  Bremsstrahlung, synchrotron emission, as well as Cooper pair processes for temperatures smaller than the critical temperature for superfluidity  $T_{\text{crit}}$ . However, as shown by Yakovlev et al. (2001), for temperatures above  $10^8$  K, which is the regime we are interested, the first three processes are the dominant ones. For instance, synchrotron emission channels might become slightly relevant, but only for  $T < 10^8$  K and for very high magnetic fields  $> 10^{14}$  G. The Cooper pair mechanism, possibly important for objects of a few hundred years old like Cas A (see e.g. Page et al., 2011; Shternin et al., 2011, for details), is irrelevant in the present case since we are dealing with neutron star ages  $< 10$  years and thus temperatures well above  $T_{\text{crit}}$ .

At temperatures  $T \sim 3 \times 10^9$  K, we can write for the most important emission processes in the crust

$$\epsilon_B \sim 10^{21} \text{erg s}^{-1} \text{cm}^{-3}, \quad (\text{D.1.2})$$

$$\epsilon_P \sim 10^{22} \text{erg s}^{-1} \text{cm}^{-3}, \quad (\text{D.1.3})$$

$$\epsilon_{ep} \sim 10^{19} \text{erg s}^{-1} \text{cm}^{-3}, \quad (\text{D.1.4})$$

where  $\epsilon_i$  denotes the emissivity and the indexes  $B, P, ep$  denote the Bremsstrahlung, plasmon decay, and pair annihilation processes, respectively.

In order to estimate the amount of heat needed to match the theoretical thermal evolution of a neo-neutron star to the light curve of the URCA's we have added a phenomenological source of heat parametrized by

$$H = H_0 e^{-t/\tau_s}, \quad (\text{D.1.5})$$

with  $H_0$  being the magnitude of the heat source, and  $\tau_s$  being the time scale in which it is active. For our calculations we set  $\tau_s = 1$  year.

In addition, we have introduced a phenomenological boundary condition for the early stages of evolution of the surface temperature  $T_s$  that follows the form  $T_s = T_x g_{s14}^{1/4} T_8^{0.55}$  K, where  $T_x = 0.87 \times 10^6 + (T_0 - 0.87 \times 10^6) e^{-t/\tau_s}$  K,  $T_8$  is the mantle temperature  $T_b$  in units of  $10^8$  K,  $T_0$  is the initial temperature of the atmosphere, and  $g_{s14}$  is the surface acceleration of gravity in units of  $10^{14}$  cm/s<sup>2</sup>. With this new boundary condition we can mimic the high temperature of the atmosphere for young neutron stars by setting the temperature at early times to a higher value and, for times greater than  $\tau_s$ , it asymptotically goes to its traditional value  $\sim 0.87 \times 10^6$  K.

In Fig. D.5 we show the cooling curves of neo-neutron stars resulting from the presence of the heating source given by Eq. (D.1.5), in addition to the traditional cooling processes of neutron stars. The cooling curves are obtained self-consistently by solving the full, general relativistic, energy trans-

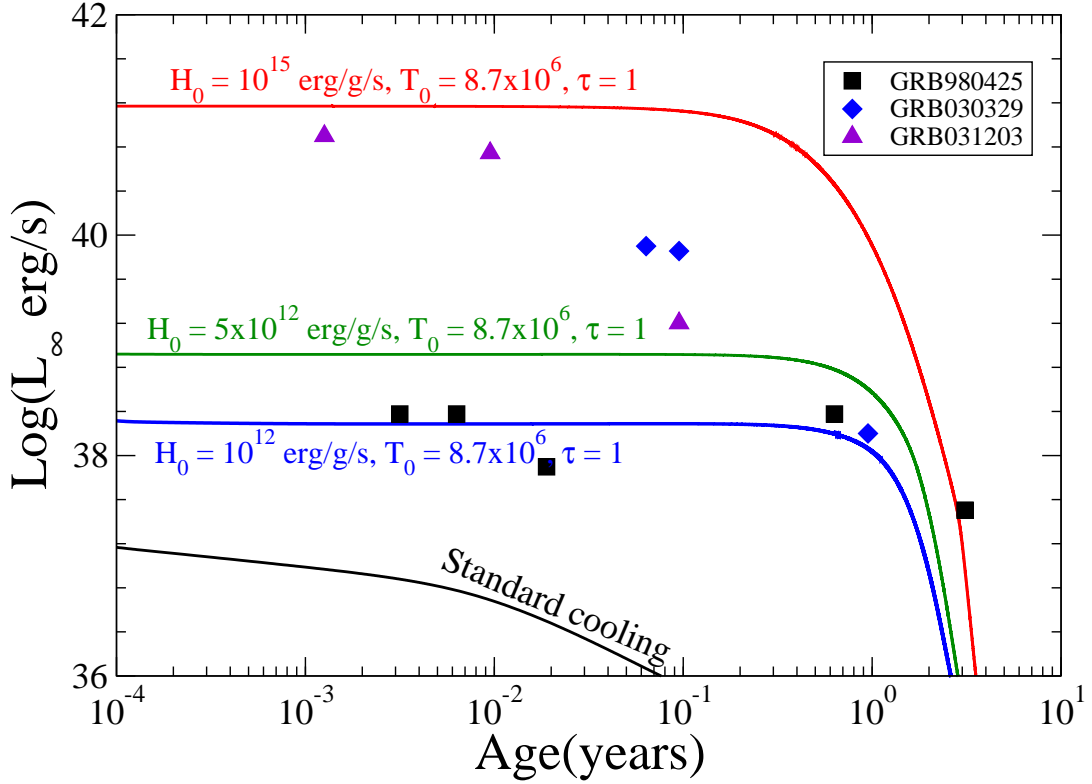


**Figure D.5.:** Thermal evolution of neo-neutron stars for selected values of the heating source  $H_0 = [10^{12}, 5 \times 10^{12}, 10^{15}]$  erg/g/s and for an initial temperature of the atmosphere  $T_0 = 8.7 \times 10^6$  K. The observed data represents the X-ray light curve associated with the URCAs.

port and balance equations with no approximations as described in Schaab et al. (1996); Page et al. (2006); Negreiros et al. (2010). We show also the observed data for the X-ray light curve associated with the URCAs. This allow us to identify the key factor leading to the matching of the neo-neutron star luminosity with the X-ray emission of the URCAs.

### D.1.5. Discussion and Conclusions

The major role played by the neutrino emissions from the crust of a neo-neutron star at the initial stages of the object is illustrated by Fig. D.5. In addition, by calibrating our additional heating source at early times to  $H_0 \sim 10^{12} - 10^{15}$  erg/g/s, we find a striking agreement of the luminosity obtained from the cooling of a neo-neutron stars with the prolonged ( $t = 10^8 - 10^9$  s) X-ray emission observed in GRB associated with Supernova (see Fig. D.5 for details). This could indicate that something might be missing in our current understanding of the crust of neutron stars. It might be that, as is the case for the atmosphere, we need to further develop our current models for the

crust, as to describe properly the properties of neo-neutron stars. The traditional thermal processes taking place in the crust might be enhanced by the extreme high temperature conditions of neo-neutron star and, additional heating processes not yet studied within this context could also take place under such conditions and deserve further analysis.

Particularly interesting in this respect are the processes of  $e^+e^-$  pair creation expected to occur in the interphase between the core and the crust during the neutron star formation leading to the appearance of critical fields (see Ruffini et al., 2007c; Ruffini, 2008a; Rueda et al., 2010a,b; Popov, 2010; Ruffini et al., 2010b; Rotondo et al., 2011c,d,e,a; Rueda et al., 2011a, for details)

It is also worth to mention that the additional heating source needed at early times,  $H_0 \sim 10^{12}-10^{15}$  erg/g/s (or  $H_0 \sim 10^{-6}-10^{-3}$  MeV/Nucleon/s), is in striking agreement with the heat released from nuclear fusion reactions, radiative neutron captures and photodisintegrations in the early stages of neutron star mergers found by Goriely et al. (2011a,b). Fission as well as  $\beta$ -decays have been also there included; i.e neutron-induced fission, spontaneous fission,  $\beta$ -delayed fission, photofission, as well as  $\beta$ -delayed neutron emission.

All this suggests the exciting possibility that we are, for the first time, observing a nascent hot neutron star. This possibility alone warrants further studies on this subject, so we might obtain a more concrete picture of the thermal evolution of neo-neutron stars. A proposal has been recently submitted by E. Pian et al. to the Chandra satellite to observe if a similar prolonged X-ray emission exists also in GRB100316D associated with SN2010bh (Pian et al., 2011). We encourage also dedicated observations of isolated SN in view of the similarities between URCA-1–URCA-3 and the Type Ic Supernova SN 1994I (Immler et al., 2002) and SN 2002ap (Soria et al., 2004).

## D.2. Gravitational Waves versus Electromagnetic Emission in Gamma-Ray Bursts

The recent progress in the understanding the physical nature of neutron star equilibrium configurations and the first observational evidence of a genuinely Short Gamma-Ray Burst, GRB 090227B, allows to give an estimate of the gravitational waves versus electromagnetic emission in a Gamma-Ray Burst.

We first recall that we have recently proved Belvedere et al. (2012); Rueda et al. (2011b); Rotondo et al. (2011d) how the consistent treatment of neutron star equilibrium configurations, taking into account the strong, weak, electromagnetic, and gravitational interactions, implies the solution of the general relativistic Thomas-Fermi equations, coupled with the Einstein-Maxwell system of equations. This new set of equations superseded the traditional Tolman-Oppenheimer-Volkoff (TOV) equations Tolman (1939); Oppenheimer and Volkoff (1939), which impose the condition of local charge neutrality throughout the configuration.

The solution of the Einstein-Maxwell-Thomas-Fermi coupled differential equations leads to a new structure of the star (Belvedere et al., 2012): the positively charged core at supranuclear densities,  $\rho > \rho_{\text{nuc}} \sim 2.7 \times 10^{14} \text{ g cm}^{-3}$ , is surrounded by an electron distribution of thickness  $\gtrsim \hbar/(m_e c)$  and, at lower densities  $\rho < \rho_{\text{nuc}}$ , a neutral ordinary crust. The equilibrium condition given by the constancy of the particle Klein potentials leads to a discontinuity in the density at the core-crust transition and, correspondingly, an overcritical electric field  $\sim (m_\pi/m_e)^2 E_c$ , where  $E_c = m_e^2 c^3/(e\hbar) \sim 1.3 \times 10^{16} \text{ Volt/cm}$ , develops in the boundary interface; see Fig. D.6. In particular, the continuity of the electron Klein potential leads to a decreasing of the electron chemical potential  $\mu_e$  and density at the core-crust boundary interface. They reach values  $\mu_e^{\text{crust}} < \mu_e^{\text{core}}$  and  $\rho_{\text{crust}} < \rho_{\text{core}}$  at the edge of the crust, where global charge neutrality is achieved (see Fig. D.6). We shall adopt some features of these neutron stars computed using the NL3 parameterization Lalazissis et al. (1997) of the phenomenological  $\sigma$ - $\omega$ - $\rho$  nuclear model; we refer to Belvedere et al. (2012) for details.

For each central density there exists an entire family of core-crust interface boundaries and, correspondingly, a family of crusts with different mass  $M_{\text{crust}}$  and thickness  $\Delta R_{\text{crust}}$ . The larger  $\rho_{\text{crust}}$ , the smaller the thickness of the core-crust interface, the peak of the electric field, and the larger the  $M_{\text{crust}}$  and  $\Delta R_{\text{crust}}$ . The configuration with  $\rho_{\text{crust}} = \rho_{\text{drip}} \sim 4.3 \times 10^{11} \text{ g/cm}^3$  separates neutron stars with and without inner crust. All the above new features lead to crusts with masses and thickness smaller than the ones obtained from the traditional TOV treatment. The mass-radius relation obtained in this case have been compared and contrasted with the one obtained from the locally neutral TOV approach; see Fig. D.7 and Belvedere et al. (2012) for details.

In Fig. D.7 we show how our new neutron star theory is in agreement with

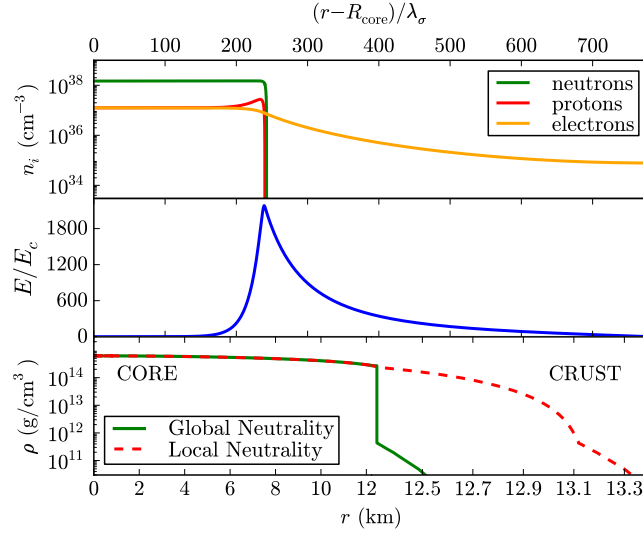


**Figure D.6.:** Upper panel: particle density profiles in the core-crust boundary interface, in units of  $\text{cm}^{-3}$ . Middle panel: electric field in the core-crust transition layer, in units of the critical field  $E_c$ . Lower panel: density profile inside a neutron star with central density  $\rho(0) \sim 5\rho_{\text{nuc}}$ . We compare and contrast the structural differences between the solution obtained from the traditional TOV equations (locally neutral case) and the globally neutral solution presented in Belvedere et al. (2012). In this example the density at the edge of the crust is  $\rho_{\text{crust}} = \rho_{\text{drip}} = 4.3 \times 10^{11} \text{ g/cm}^3$  and  $\lambda_\sigma = \hbar/(m_\sigma c) \sim 0.4 \text{ fm}$  denotes the  $\sigma$ -meson Compton wavelength.

the most up-to-date stringent observational constraints to the mass-radius relation of neutron stars, that are provided by the largest mass, the largest radius, the highest rotational frequency, and the maximum surface gravity, observed from pulsars Trümper (2011). They are imposed by the mass of PSR J1614-2230  $M = 1.97 \pm 0.04 M_\odot$  Demorest et al. (2010a), the lower limit to the radius of RX J1856-3754 Trümper et al. (2004) (dotted-dashed curve), the 716 Hz PSR J1748-2246ad Hessels et al. (2006a) (dashed curve), and the surface gravity of the neutron star in the Low Mass X-Ray Binary X7 from which 90% confidence level contours of constant  $R_\infty$  can be extracted Heinke et al. (2006) (dotted curves); see Belvedere et al. (2012) for further details.

The above constraints strongly favor stiff nuclear equations of state such as the ones obtained from relativistic mean field models, which provide high maximum masses for neutron stars Trümper (2011). In addition, the radius of a canonical neutron star of mass  $M = 1.4 M_\odot$  is highly constrained to the range  $R \gtrsim 12 \text{ km}$ , ruling out a strange quark hypothesis for these objects. Our new neutron star mass-radius relation fully agrees with all the above requirements, for instance, we find that a canonical neutron star with  $M = 1.40 M_\odot$  has a radius  $R = 12.31 \text{ km}$ , for the NL3 parameterization of the nuclear EoS

(see Belvedere et al., 2012, for details).

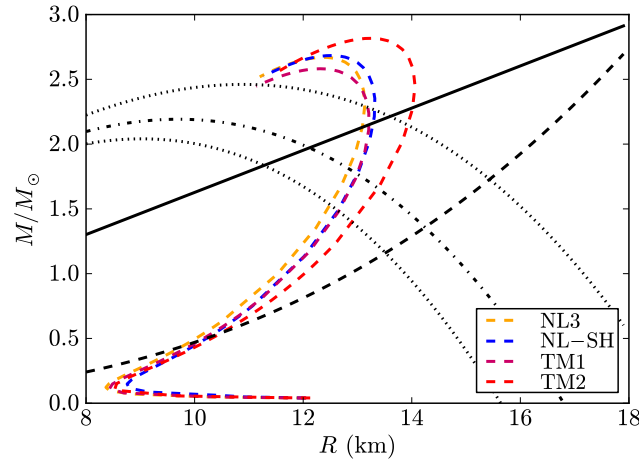


**Figure D.7.:** Constraints on the neutron star mass-radius relation (see Trümper, 2011, and references therein). We compare and contrast the theoretical  $M$ - $R$  relation of globally neutral neutron stars Belvedere et al. (2012) (blue curve) obtained from the solution of the Einstein-Maxwell-Thomas-Fermi equations and locally neutral neutron stars (red curve) obtained by solving the TOV equations. Any mass-radius relation have a maximum mass larger than  $M = 1.97 \pm 0.04M_{\odot}$  and should pass through the area delimited by the solid, dotted-dashed, dashed, and dotted curves.

We now turn to the observations of GRB 090227B (see Muccino et al., 2012, for details). The progress obtained from the Fermi-GBM and Konus-Wind satellites has been used to identify the new class of genuinely short GRBs: short bursts with the same inner engine of the long GRBs but endowed with a severely low value of the baryon load,  $B \equiv M_B c^2 / E_{tot}^{GRB} \lesssim 5 \times 10^{-5}$ , where  $M_B$  is the mass of the baryons engulfed by the expanding ultrarelativistic  $e^+e^-$  plasma of energy  $E_{tot}^{GRB}$ . The emission from these GRBs mainly consists in a first emission, the peak GRB (P-GRB), followed by a softer emission squeezed on the first one. The typical separation between the two components is expected to be shorter than 1–10 ms.

A special case is GRB 090227B. From the 16 ms time-binned light curves a significant thermal emission in the first 96 ms, which has been identified with the P-GRB, has been found Muccino et al. (2012). The subsequent emission is identified with the extended afterglow. The P-GRB of 090227B has the highest temperature ever observed,  $k_B T = 517$  keV, where  $k_B$  is the Boltzmann constant. The results of the fit of the light curve and spectrum of GRB 090227B are summarized in Table D.2. In particular we show the total energy emitted  $E_{tot}^{GRB}$ , Baryon load  $B$ , Lorentz factor at transparency  $\Gamma_{tr}$ , cosmological redshift  $z$ , intrinsic duration of the GRB emission  $\Delta t$ , and average density of the CircumBurst Medium (CBM)  $\langle n_{CBM} \rangle$ ; we refer to Muccino et al. (2012)

$E_{tot}^{GRB}$ (erg)	$2.83 \times 10^{53}$
$B$	$4.13 \times 10^{-5}$
$\Gamma_{tr}$	$1.44 \times 10^4$
$z$	1.61
$\Delta t$ (s)	0.35
$\langle n_{CBM} \rangle$ (cm $^{-3}$ )	$1.9 \times 10^{-5}$

**Table D.2.:** Properties of GRB 090227B:  $E_{tot}^{GRB}$  is the total energy emitted in the GRB,  $B$  is the Baryon load,  $\Gamma_{tr}$  is the Lorentz factor at transparency, the cosmological redshift is denoted by  $z$ , the intrinsic duration of the GRB is  $\Delta t$ , and the average density of the CBM is  $\langle n_{CBM} \rangle$ . We refer to Muccino et al. (2012) for additional details.

for further details.

The above quantitative results lead to the conclusion that the progenitor of GRB 090227B is a neutron star binary: (1) the natal kicks velocities imparted to a neutron star binary at birth can be even larger than  $200 \text{ km s}^{-1}$  and therefore a binary system can runaway to the halo of its host galaxy, clearly pointing to a very low average number density of the CBM; (2) the very large total energy, which we can indeed infer in view of the absence of beaming, and the very short time scale of emission point again to a neutron star binary; (3) as we shall show below the very small value of the baryon load is strikingly consistent with two neutron stars having small crusts, in line with the recent neutron star theory Belvedere et al. (2012).

We now infer the binary component parameters. It is clear that the merging of two neutron stars will lead to a GRB if the total mass of the binary satisfies

$$M_1 + M_2 \gtrsim M_{\text{crit}} = 2.67M_{\odot}, \quad (\text{D.2.1})$$

where  $M_{\text{crit}}$  is the critical mass over which a neutron star undergoes gravitational collapse to a black hole. The numerical value reported in Eq. (D.2.1) has been taken from Belvedere et al. (2012).

Assuming for simplicity a binary with twin components  $M_1 = M_2 = M$ , we obtain masses  $M = 1.335M_{\odot}$  and correspondingly radii  $R_1 = R_2 = 12.24 \text{ km}$  (see Fig. D.7 and Belvedere et al. (2012)). The mass of the corresponding crust of each component is  $M_{\text{crust}} \sim 3.6 \times 10^{-5}M_{\odot}$  and the thickness of the crust is  $\Delta R_{\text{crust}} \sim 0.47 \text{ km}$ .

The location of the binary in the very low interstellar density medium of galactic halos makes possible to probe the neutron star theory and equation of state through the knowledge of the baryon load  $B$  inferred from the fitting of the GRB light curve and spectrum. The baryonic matter which the GRB interact with is in these systems provided by the material of the neutron star crusts ejected during the binary coalescence. Thus, a theoretical expectation

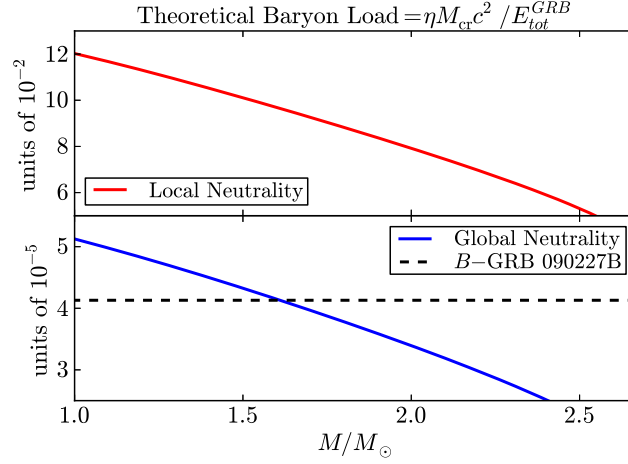


**Figure D.8.:** Baryon load expected to be left by a binary neutron star merger, given by Eq. (D.2.2) for  $\eta = 1$ , as a function of the total mass  $M$  of globally (lower panel, units  $10^{-5}$ ) and locally neutral (upper panel, units  $10^{-2}$ ) neutron stars, for the case of GRB 090227B. We have indicated the observed baryon load of GRB 090227B,  $B = 4.13 \times 10^{-5}$ ; see Table D.2 and Muccino et al. (2012).

of the baryon load  $B$  left in a binary neutron star merger is

$$B = \frac{\eta M_{\text{crust}} c^2}{E_{\text{tot}}^{\text{GRB}}}, \quad (\text{D.2.2})$$

where  $\eta$  is the fraction of the crustal mass ejected. Here we are assuming that the mass ejected during the merger comes from the outer layers of the neutron star, namely from the crust of the star.

In Fig. D.8 we have plotted the theoretical baryon load given by Eq. (D.2.2) for GRB 090227B, namely using  $E_{\text{tot}}^{\text{GRB}} = 2.83 \times 10^{53}$  erg, as a function of the mass  $M$  of the globally and locally neutral neutron stars shown in Fig. D.7.

The agreement of the observed baryon load of GRB 090227B (see Table D.2 and Muccino et al. (2012)) with the low mass of the crust obtained from the globally neutral neutron stars of Belvedere et al. (2012) is evident (see Fig. D.8). It can be compared and contrasted with the ones obtained enforcing the local charge neutrality condition. For the specific binary neutron star system studied here we obtain a theoretical prediction of the baryon load from Eq. (D.2.2) with  $\eta = 1$ ,  $B \sim 7.6 \times 10^{-5}$ , or a mass of the baryons  $M_B = E_{\text{crust}}^B / c^2 \sim 1.2 \times 10^{-5} M_{\odot}$ , to be confronted with the one obtained from the fitting procedure of GRB 090227B,  $B \sim 4.13 \times 10^{-5}$ , corresponding to  $M_B = B E_{\text{tot}}^{\text{GRB}} / c^2 \sim 0.7 \times 10^{-5} M_{\odot}$ . The above theoretical predictions of the neutron star crust mass  $M_{\text{crust}}$  and consequently the value of  $E_{\text{crust}}^B$  and  $B$  have been inferred for a crust with a density at its edge equal to the neutron

drip density  $\rho_{\text{drip}} \sim 4.3 \times 10^{11} \text{ g cm}^{-3}$ . Neutron star crusts with densities  $\rho < \rho_{\text{drip}}$  are predicted by the new neutron star theory Belvedere et al. (2012), there is still room for smaller values of the baryonic matter ejected in a binary process, and consequently to still shorter genuinely short GRBs.

The mass-energy of the baryon ejecta obtained from the estimate (D.2.2) gives for locally neutral neutron stars values  $10^2$ – $10^3$  bigger than the ones analyzed before (see Fig. D.8), due to the more massive crusts obtained from the TOV-like treatment (see Belvedere et al., 2012, for details). It implies that Eq. (D.2.2) gives in such a case  $M_B \sim 10^{-3}$ – $10^{-2}M_\odot$ , in line with previous results obtained from the numerical simulation of the dynamical evolution of neutron star binaries (see e.g. Ruffert and Janka, 2001; Goriely et al., 2011b), where locally neutral neutron stars are employed.

We are considering a neutron star binary with components  $(M_1, R_1)$  and  $(M_2, R_2)$  orbiting each other in a circular orbit of radius  $a$  (separation between the two neutron star centers), orbital angular velocity

$$\omega = \sqrt{\frac{G(M_1 + M_2)}{a^3}}, \quad (\text{D.2.3})$$

and total energy

$$E = -\frac{1}{2} \frac{GM_1M_2}{a}. \quad (\text{D.2.4})$$

The leading term driving the loss of energy via gravitational wave emission is given by

$$-\frac{dE}{dt} = \frac{32}{5} \frac{G^4}{c^5} \frac{(M_1 + M_2)(M_1M_2)^2}{a^5}, \quad (\text{D.2.5})$$

which leads to a decreasing of the separation  $a$  with time and consequently a shortening of the orbital period  $P = 2\pi/\omega$  dictated by

$$\frac{1}{P} \frac{dP}{dt} = (3/2) \frac{1}{a} \frac{da}{dt} = -(3/2) \frac{1}{E} \frac{dE}{dt} \quad (\text{D.2.6})$$

$P^{-1}dP/dt = (3/2)a^{-1}da/dt = -(3/2)E^{-1}dE/dt$  Landau and Lifshitz (1980). Additional contributions to the gravitational wave power due to higher multipole moments of the components such as angular momentum  $J$  and quadrupole moment  $Q$  (deformation) are conceptually relevant corrections to the above formula (see e.g. Ryan, 1995, and references therein) although quantitatively negligible. For instance, the first correction due to the spin angular momentum  $J$  of the neutron star components is given by  $-11/4 j\omega M$  in geometric units, where  $j = cJ/(GM^2)$  is the dimensionless angular momentum parameter. This correction is only of order  $10^{-2}$  for a binary orbit of very high angular frequency  $\sim$  kHz and for neutron stars with  $M = 1.335M_\odot$  and  $j = 0.4$ . We recall that the fastest observed pulsar, PSR J1748-2246ad, has a rotation frequency of 716 Hz Hessels et al. (2006a), which gives  $j \sim$

$0.51 I_{45}/(M_0/M_\odot)^2 = 0.26 I_{45}$  with the latter value for a canonical NS of  $M = 1.4M_\odot$ ,  $I_{45}$  is the moment of inertia in units of  $10^{45} \text{ g cm}^2$ . The first correction due to the quadrupole deformation multipole moment  $Q$  of the neutron star, given by  $-2 Q\omega^{4/3}M^{-5/3}$ , is of order  $10^{-3}$  for the same parameters with  $Q \sim 4 \times 10^{43} \text{ g cm}^2 \sim 3 \text{ km}^3$ , the latter value in geometric units.

The gravitational waves emission dominates the energy loss during the spiraling phase while the electromagnetic radiation dominates from the coalescence with the final emission of a short GRB if the total mass of the binary exceeds the critical mass for neutron star gravitational collapse  $\sim 2.67M_\odot$ , see Eq. (D.2.1). Thus, an upper limit for the gravitational wave emission radiated away can be obtained from the energy difference between the initial binary at time  $t_0 = 0$  with separation  $a_0$  and energy  $E_0$ , and the binary at time  $t_f$  and separation  $a_f = R_1 + R_2$ , with energy  $E_f$ , when the two components *touch* each other. An absolute upper limit for the gravitational wave energy emission,  $\Delta E_{GW}^{\max}$ , can be therefore determined by the assumption of an infinite initial separation  $a_0 \rightarrow \infty$ , i.e.

$$\Delta E_{GW}^{\max} = E(t_f) - E(t_0) = \frac{1}{2} \frac{GM_1M_2}{R_1 + R_2}. \quad (\text{D.2.7})$$

For the neutron star binary discussed in this work for GRB 090227B, we obtain the absolute upper bound

$$\Delta E_{GW}^{\max} = \frac{1}{4} \frac{GM^2}{R} \sim 9.6 \times 10^{52} \text{ erg} = 0.054M_\odot c^2, \quad (\text{D.2.8})$$

which in the case of the genuinely short GRB 090227B is one order of magnitude smaller than the emitted electromagnetic energy  $E_{tot}^{GRB} = 2.83 \times 10^{53} \text{ erg}$  (see Table D.2 and Muccino et al. (2012)). It is also worth mentioning that indeed this numerical value (D.2.8) limits from above the results of full numerical integrations of the gravitational wave radiation emitted in the neutron star binaries during the entire process of spiraling and merging (see Ruffert and Janka, 2001, e.g.).

We have shown that the observations of the genuinely short GRB 090227B lead to crucial information on the binary neutron star progenitor. The data obtained from the electromagnetic spectrum allows to probe crucial aspects of the correct theory of neutron stars and their equation of state. The baryon load parameter  $B$  obtained from the analysis of GRB 090227B, leads to a most remarkable agreement of the baryonic matter expected to be ejected in a neutron star binary merger and validate the choice of the parameters of the binary components,  $M_1 = M_2 = 1.34M_\odot$ , and  $R_1 = R_2 = 12.24 \text{ km}$ . This represents a test of the actual neutron star parameters described by the recent developed self-consistent theory of neutron stars Belvedere et al. (2012) that takes into account the strong, weak, electromagnetic and gravitational interactions within general relativity. In view of the above limits given in

Eq. (D.2.8), it is clear that the emission of electromagnetic radiation in a GRB by a binary neutron star system is at least one order of magnitude larger than the gravitational wave emission. We are currently estimating the detectability of these events by current and new generation gravitational waves detectors and the results will be presented shortly.

# E. Exact Solutions of the Einstein-Maxwell equations in Astrophysics

## E.1. On the relativistic precession and oscillation frequencies of test particles around rapidly rotating compact stars

### E.1.1. Introduction

One of the greatest challenges of the general theory of relativity has been the construction of solutions to the Einstein-Maxwell field equations representing the gravitational field of compact stars such as neutron stars (NSs). Stationary axially symmetric spacetimes satisfy basic properties one expects for rotating objects, namely time symmetry and reflection symmetry with respect to the rotation axis (see e.g. Pachón and Sanabria-Gómez, 2006). The simplest stationary axially symmetric exact exterior vacuum solution describing a rotating configuration is the well-known Kerr metric (Kerr, 1963). The Kerr metric is fully described by two free parameters: the mass  $M$  and the angular momentum  $J$  of the object. However, it is known from numerical models that the quadrupole moment of rotating NSs deviates considerably from the one given by the Kerr solution  $Q_{\text{Kerr}} = -J^2/(Mc^2)$  (see e.g. Laarakkers and Poisson, 1999, for details).

In the mean time, a considerable number of analytic exterior solutions with a more complex multipolar structure than the one of the Kerr solution have been developed (see e.g. Manko et al., 1995, 2000; Stephani et al., 2003). Whether analytic exterior solutions are accurate or not to describe the gravitational field of compact stars is an interesting and very active topic of research (see e.g. Stute and Camenzind, 2002; Berti and Stergioulas, 2004; Pachón et al., 2006, and references therein).

The accuracy of analytic solutions to describe the exterior geometry of a realistic rotating compact star has been tested by comparing physical properties, e.g. the radius of the Innermost Stable Circular Orbit (ISCO) on the equatorial plane and the gravitational redshift (see Sibgatullin and Sunyaev, 1998; Berti and Stergioulas, 2004; Pachón et al., 2006, for details). In order

to do such a comparison, the free parameters (i.e. the lowest multipole moments) of the analytic exterior spacetime, are fixed to the corresponding lowest multipole moments given by numerical interior solutions of the Einstein equations, for NS realistic models (see e.g. Berti and Stergioulas, 2004).

Following such a procedure, the solution of Manko et al. (2000) has been compared by Stute and Camenzind (2002) and by Berti and Stergioulas (2004) with the numerical solutions for NSs calculated by Cook et al. (1994) and with those derived by Berti and Stergioulas (2004), respectively. However, being a generalization of the solution of Tomimatsu and Sato (1972), it cannot describe slowly rotating compact stars (see e.g. Berti and Stergioulas, 2004), but the dynamics of astrophysical objects with anisotropic stresses (see Dubeibe et al., 2007, for details).

Following a similar procedure, based on tests of the ISCOs radii on the equatorial plane of the rotating neutron stars obtained by Berti and Stergioulas (2004), it has been shown that the six-parametric solution of Pachón et al. (2006) (hereafter PRS solution, see Sec. E.1.2 for details) is more accurate than the model of Manko et al. (2000). In addition, being a generalization of the Kerr solution, this solution can be used for arbitrary rotation rates.

Besides the ISCOs radii, there are additional physical properties that can be computed with analytic and numerical models and thus useful to compare and contrast the accuracy of analytic exact models. The aim of this work is to analyze the properties of orbital frequencies of neutral test particles in the PRS and in the Kerr geometries with especial focus on the Keplerian  $\nu_K$ , frame-dragging (Lense-Thirring)  $\nu_{LT}$ , as well as the precession(oscillation) frequencies of the radial and vertical motions,  $\nu_\rho^P(\nu_\rho^{OS})$  and  $\nu_z^P(\nu_z^{OS})$ , respectively.

The relevance of these frequencies relies on the fact that they are often invoked to explain the Quasi-Periodic Oscillations (QPOs) observed in some relativistic astrophysical systems such as Low Mass X-ray Binaries (LMXBs), binary systems harboring either a NS or a black hole (BH) accreting matter from a companion star. For instance, within the Relativistic Precession Model (RPM) introduced by Stella and Vietri (1998); Morsink and Stella (1999); Stella et al. (1999); Stella and Vietri (1999), the kHz QPOs are interpreted as a direct manifestation of the modes of relativistic epicyclic motion of blobs arising at various radii  $r$  in the inner parts of the accretion disk around the compact object (see Sec. E.1.6, for details).

In addition to the RPM, the Keplerian, precession and oscillation frequencies are used in other QPO theoretical models (see e.g. Lin et al., 2011, for a recent comparison of the existing models). Due to the influence of general relativistic effects in the determination of such frequencies, an observational confirmation of any of the models might lead to an outstanding test of general relativity in the strong field regime. In this line, it is of interest to compare and contrast the orbital frequencies given by the Kerr solution and by the PRS solution (see Sec. E.1.3), which help to establish the differences between pos-

sible BH and NS signatures. We emphasize in this work the major role of the quadrupole moment as well as of the octupole moment of the object, whose possible measurement can be used as a tool to test the no-hair theorem of BHs (see e.g. Johannsen and Psaltis, 2011). In the case of NSs, the interpretation of QPOs as the manifestation of orbital motion frequencies might lead to crucial information of the NS parameters such as mass, angular momentum (see e.g. Stella and Vietri, 1998; Török et al., 2010), and quadrupole moment (see e.g. Morsink and Stella, 1999). These parameters reveal, at the same time, invaluable information about the EoS of nuclear matter.

The work is organized as follows. In Sec. E.1.2 we recall the properties of the PRS solution. The computation of the orbital frequencies as well as the comparison of their features in the Kerr and in the PRS spacetimes, is shown in Sec. E.1.3. In Sec. E.1.4 we study the accuracy of the analytic formulas of the periastron and nodal frequencies derived by Ryan (1995) for stationary axially symmetric spacetimes. In Sections 5 and 6 we discuss the accuracy of the PRS solution in describing the frequencies of realistic NS models and its relevance in the Relativistic Precession Model, respectively. The conclusions of this work and a discussion on possible additional effects to be accounted for in the determination of the orbital frequencies, e.g. the effect of magnetic dipole moment, are outlined in Sec. E.1.7.

### **E.1.2. The PRS analytic exact solution**

We first recall the PRS analytic model (Pachón et al., 2006), for the exterior gravitational field of a compact object<sup>1</sup>. In the stationary axisymmetric case, the simplest form of the metric can be written as (Papapetrou, 1953)

$$ds^2 = -f(dt - \omega d\phi)^2 + f^{-1} \left[ e^{2\gamma} (d\rho^2 + dz^2) + \rho^2 d\phi^2 \right], \quad (\text{E.1.1})$$

where  $f$ ,  $\omega$  and  $\gamma$  are functions of the quasi-cylindrical Weyl coordinates  $(\rho, z)$ . Thus, the components of the metric tensor  $g_{\mu\nu}$  are

$$g_{\phi\phi} = \frac{\rho^2}{f(\rho, z)} - f(\rho, z)\omega(\rho, z)^2, \quad (\text{E.1.2})$$

$$g_{tt} = -f(\rho, z), \quad (\text{E.1.3})$$

$$g_{t\phi} = f(\rho, z)\omega(\rho, z), \quad (\text{E.1.4})$$

$$g_{zz} = g_{\rho\rho} = \frac{e^{2\gamma(\rho, z)}}{f(\rho, z)} = \frac{1}{g^{zz}} = \frac{1}{g^{\rho\rho}}. \quad (\text{E.1.5})$$

Using the above line element, the Einstein-Maxwell equations can be re-

---

<sup>1</sup>Mathematica 8.0 scripts with the solution, some limiting cases as well as the the calculations presented in this paper are available at <http://www.chem.utoronto.ca/~lpachon/scripts/nstars>

formulated, via Ernst's procedure in terms of two complex potentials  $\mathcal{E}(\rho, z)$  and  $\Phi(\rho, z)$  (Ernst, 1968a,b). By means of Sibgatullin's integral method (Sibgatullin, 1991; Manko and Sibgatullin, 1993) this system of equations can be solved via

$$\mathcal{E}(z, \rho) = \int_{-1}^1 \frac{d\sigma}{\pi} \frac{e(\xi)\mu(\sigma)}{\sqrt{1-\sigma^2}}, \quad (\text{E.1.6})$$

$$\Phi(z, \rho) = \int_{-1}^1 \frac{d\sigma}{\pi} \frac{f(\xi)\mu(\sigma)}{\sqrt{1-\sigma^2}}, \quad (\text{E.1.7})$$

where  $e(z) := \mathcal{E}(z, \rho = 0)$  and  $f(z) := \Phi(z, \rho = 0)$ . The unknown function  $\mu(\sigma)$  must satisfy the singular integral equation

$$\int_{-1}^1 \frac{\mu(\sigma)[e(\xi) + \bar{e}(\eta) + 2f(\xi)\bar{f}(\eta)]d\sigma}{(\sigma - \tau)\sqrt{1-\sigma^2}} = 0 \quad (\text{E.1.8})$$

and the normalizing condition

$$\int_{-1}^1 \frac{\mu(\sigma)d\sigma}{\sqrt{1-\sigma^2}} = \pi, \quad (\text{E.1.9})$$

where  $\xi = z + i\rho\sigma$ ,  $\eta = z + i\rho\tau$ ,  $\rho$  and  $z$  being the Weyl-Papapetrou quasi-cylindrical coordinates,  $\sigma, \tau \in [-1, 1]$ ,  $\bar{e}(\eta) := \overline{e(\bar{\eta})}$ ,  $\bar{f}(\eta) := \overline{f(\bar{\eta})}$  and the overbar stands for complex conjugation. In (Pachón et al., 2006), the Ernst potentials were chosen as

$$\begin{aligned} e(z) &= \frac{z^3 - z^2(m + ia) - kz + is}{z^3 + z^2(m - ia) - kz + is}, \\ f(z) &= \frac{qz^2 + i\mu z}{z^3 + z^2(m - ia) - kz + is}. \end{aligned} \quad (\text{E.1.10})$$

We calculate the multipole moments following the procedure of Hoense-laers and Perjés (1990). We denote the mass multipoles by  $M_i$  while, the current (rotation) multipoles, by  $S_i$ . The electric multipoles are denoted by  $Q_i$  and the magnetic ones by  $\mathcal{B}_i$ . Thus, for the PRS solution we have

$$\begin{aligned} M_0 &= m, & M_2 &= mk - ma^2, & \dots \\ S_1 &= ma, & S_3 &= -ma^3 + 2mak - ms, & \dots \end{aligned} \quad (\text{E.1.11})$$

$$\begin{aligned} Q_0 &= q, & Q_2 &= -a^2q - a\mu + kq, & \dots \\ \mathcal{B}_1 &= \mu + aq, & \mathcal{B}_3 &= -a^2\mu + \mu k - a^3q + 2akq - qs, & \dots \end{aligned} \quad (\text{E.1.12})$$

This allows us to identify  $m$  as the total mass,  $a$  as the total angular momentum per unit mass ( $a = J/m$ , being  $J$  the total angular momentum); while  $k$ ,  $s$ ,  $q$  and  $\mu$  are associated to the mass-quadrupole moment  $M_2$ , current octupole  $S_3$ , electric charge and magnetic dipole, respectively.

The potentials (E.1.10) can be written in an alternative way, we mean

$$e(z) = 1 + \sum_{i=3}^3 \frac{e_i}{z - \beta_i}, \quad f(z) = \sum_{i=3}^3 \frac{f_i}{z - \beta_i}, \quad (\text{E.1.13})$$

with

$$e_j = (-1)^j \frac{2m\beta_j^2}{(\beta_j - \beta_k)(\beta_j - \beta_i)}, \quad (\text{E.1.14})$$

$$f_j = (-1)^{j+1} \frac{i\mu + d\beta_j}{(\beta_j - \beta_k)(\beta_j - \beta_i)}, \quad i, k \neq j. \quad (\text{E.1.15})$$

Then, using Eqs. (E.1.6) and (E.1.10), we obtain the Ernst potentials

$$\varepsilon = \frac{A + B}{A - B}, \quad \Phi = \frac{C}{A - B}, \quad (\text{E.1.16})$$

and the metric functions in the whole spacetime

$$f = \frac{A\bar{A} - B\bar{B} + C\bar{C}}{(A - B)(\bar{A} - \bar{B})}, \quad e^{2\gamma} = \frac{A\bar{A} - B\bar{B} + C\bar{C}}{K\bar{K} \prod_{n=1}^6 r_n}, \quad (\text{E.1.17})$$

$$\omega = \frac{\text{Im}[(A + B)\bar{H} - (\bar{A} + \bar{B})G - C\bar{I}]}{A\bar{A} - B\bar{B} + C\bar{C}}, \quad (\text{E.1.18})$$

where the functions  $A$ ,  $B$ ,  $C$ ,  $H$ ,  $G$ ,  $K$ , and  $I$  can be found in the Appendix E.1.8.

The PRS electrovacuum exact solution belongs to the extended  $N$ -soliton solution of the Einstein-Maxwell equations derived by Ruiz et al. (1995), in the particular case  $N = 3$ . In addition, the functional form of the metric functions resembles the one derived previously by Bretón et al. (1999). Besides the limiting cases discussed in Pachón et al. (2006) it is worth mentioning that, in the vacuum case  $q = 0$  and  $\mu = 0$ , for  $s = 0$  this solution reduces to the solution of Manko et al. (1995) under the same physical conditions, namely  $q = 0$ ,  $c = 0$  and  $b = 0$  in Manko et al. (1995).

### E.1.3. Orbital Motion Frequencies on the Equatorial Plane

Although for the case of compact stars contributions from the magnetic field could be relevant (see e.g. Bakala et al., 2010; Sanabria-Gómez et al., 2010; Bakala et al., 2012), we focus in this work on the frequencies of neutral particles orbiting a neutral compact object. We calculate here the Keplerian  $\nu_K = \Omega_K/(2\pi)$ , frame-dragging (Lense-Thirring)  $\nu_{LT} = \Omega_{LT}/(2\pi)$ , radial oscillation and precession,  $\nu_\rho^{OS} = \Omega_\rho^{OS}/(2\pi)$  and  $\nu_\rho^P = \Omega_\rho^P/(2\pi)$ , and vertical oscillation and precession frequencies,  $\nu_z^{OS} = \Omega_z^{OS}/(2\pi)$  and  $\nu_\rho^P = \Omega_\rho^P/(2\pi)$ , respectively.

The geodesic motion of test particles along the radial coordinate, on the equatorial plane  $z = 0$ , is governed by the effective potential (see e.g. Ryan, 1995)

$$V(\rho) = 1 - \frac{E^2 g_{\phi\phi} + 2ELg_{t\phi} + L^2 g_{tt}}{g_{t\phi}^2 - g_{tt}g_{\phi\phi}}, \quad (\text{E.1.19})$$

where, for circular orbits, the energy  $E$  and angular momentum  $L$  are determined by the conditions  $V = 0$  and  $dV/d\rho = 0$  (see Eqs. E.1.22–E.1.23). The frequencies at the ISCO's location (determined by the additional condition  $d^2V/d\rho^2 = 0$ ) are of particular interest. Thus, before starting the discussion of the frequencies, it is important to explore the ISCO parametric dependence. We report here, as standard in the literature, the *physical* ISCO radius given by  $\sqrt{g_{\phi\phi}}$  evaluated at the root of Eq. (E.1.19) that gives the coordinate ISCO radius. In the upper panel of Fig. E.1 we plotted contours of constant ISCO radii as a function of the dimensionless angular momentum parameter  $j = J/M_0^2$  and the star quadrupole moment  $M_2$ , for the PRS solution. The use of the dimensionless parameter  $j$  in the horizontal axis allows to, qualitatively, relate deviations of the contour lines from vertical lines to the influence of the quadrupole moment. We can see that the ISCO radius decreases for increasing  $j$  and decreasing  $M_2$ . A quantitative measurement of this influence could be derived from the effective slope of the contour lines. We are interested in the comparison with the Kerr geometry, so in the lower panel, we plotted contours of constant ratio  $r_{\text{ISCO,PRS}}/r_{\text{ISCO,Kerr}}$  as a function of  $j$  and the difference between the quadrupole moment of the PRS solution  $M_{2,\text{PRS}}$  and the Kerr quadrupole  $M_{2,\text{Kerr}} = -ma^2$ , i.e.  $M_{2,\text{PRS}} - M_{2,\text{Kerr}} = M_{2,\text{PRS}} + ma^2 = mk$ , see Eq. (E.1.11). Deviations from the Kerr geometry are evident. Negative values of the angular momentum correspond to the radii of the counter-rotating orbits obtained here through the change  $g_{t\phi} \rightarrow -g_{t\phi}$  (see discussion below).

We stress that the accuracy of the PRS solution for describing the ISCO radius of *realistic* NSs was already shown to be higher with respect to other analytic models (see Pachón et al., 2006, for details). In Table E.1 we compare the ISCO radius for two rapidly rotating NS, models 20 and 26, of Table VI of Pappas and Apostolatos (2012) for the EoS L. The lowest multipole moments of the analytic models are fixed to the numerical values obtained by Pappas

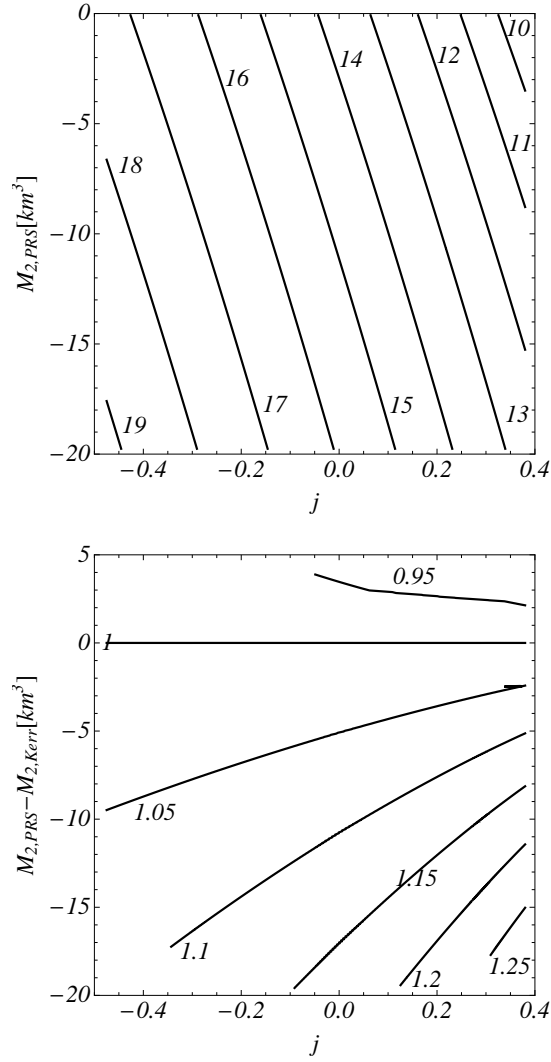


**Figure E.1.:** Upper panel: Contours of constant ISCO radius as a function of the dimensionless angular momentum parameter  $j = J/M_0^2$  and the quadrupole moment  $M_2$  for the PRS solution, for a compact object with mass  $M_0 = m = 1.88M_\odot = 2.78 \text{ km}$ . Contours are labeled by the corresponding the value of the ISCO radius in km. Negative values of  $j$  depict the counter-rotating case and negative values of the quadrupole moment  $M_2$  correspond to oblate configurations. The values of  $M_2$  are in the range  $0 \leq M_2 \leq 20 \text{ km}^3$  that corresponds in CGS units to  $0 \leq M_2 \leq -2.7 \times 10^{44} \text{ g cm}^2$ , which covers the typical range of fast rotating NSs. Lower panel: Contours of constant ratio  $r_{\text{ISCO,PRS}}/r_{\text{ISCO,Kerr}}$  as a function of  $j$  and the difference  $M_{2,\text{PRS}} - M_{2,\text{Kerr}}$ . The quadrupole moment difference is comprised in the range  $-2.7 \times 10^{44} \leq M_2 \leq 6.8 \times 10^{43} \text{ g cm}^2$ .

	$R_N$ [km]	$R_{SS}$ [km]	$R_{Kerr}$ [km]	$R_{PRS,s=0}$ [km]	$R_{PRS}$ [km]
M20	19.81	13.39	16.14	19.28	18.99
M26	19.87	17.16	15.94	19.65	19.54

**Table E.1.:** Comparison of the ISCO radius for the selected NS models 20 and 26 of Table VI of Pappas and Apostolatos (2012) for the EoS L. Model 20:  $M_0 = 4.167$  km ( $2.82M_\odot$ ),  $j = J/M_0^2 = 0.70$ ,  $M_2 = -79.8$  km<sup>3</sup> ( $-1.08 \times 10^{45}$  g cm<sup>2</sup>) and  $S_3 = -401.0$  km<sup>4</sup>. Model 26:  $M_0 = 4.36$  km ( $2.95M_\odot$ ),  $j = J/M_0^2 = 0.56$ ,  $M_2 = -45.2$  km<sup>3</sup> ( $-6.10 \times 10^{44}$  g cm<sup>2</sup>) and  $S_3 = -170.0$  km<sup>4</sup>. The subscript N stands for the numerical calculation of Pappas and Apostolatos (2012) and SS stands for the Shibata and Sasaki (1998) approximated ISCO radius expression.

and Apostolatos (2012). In the case of the Kerr solution, only  $M_0$  and  $J$  can be fixed, while  $M_2$ , and  $S_3$  have values that depend on  $M_0$  and  $J$  and therefore cannot be fixed. For the PRS solution with  $s = 0$ ,  $M_0$ ,  $J$  and  $M_2$  can be fixed while  $S_3$  remains induced by the lower moments. We present also the ISCO radius obtained by fixing  $M_0$ ,  $J$ ,  $M_2$ , as well as  $S_3$  in the PRS analytic exact model.

In Figs. E.1–E.6, we have fixed as an example  $M_0 = m = 1.88M_\odot = 2.78$  km, and  $s = 0$ . We recall that the quadrupole moment in the geometric units used here (km<sup>3</sup>) is related to the one in CGS units by  $M_2^{CGS} = (10^{15}c^2/G)M_2^{geo} = 1.35 \times 10^{43}(M_2^{geo}/\text{km}^3)$  g cm<sup>2</sup>, and the mass of the Sun is  $M_\odot^{geo} = 1.477$  km. The dimensionless angular momentum  $j$  is obtained from the CGS values of  $J$  and  $M_0$  as  $j = cJ/(GM_0^2)$ .

It is appropriate to compare the range of values of  $j = J/M_0^2$  and  $M_2$  used in Figs. E.1–E.6 with typical values of a NS. For the used mass  $M_0 = 1.88M_\odot$ , Morsink and Stella (1999) obtained a quadrupole moment  $M_2 = -5.3 \times 10^{43}$  g cm<sup>2</sup> =  $3.93$  km<sup>3</sup>, with the latter value in geometric units, for a NS of angular rotation frequency  $\nu_s = 290$  Hz (rotation period of 3.45 milliseconds), corresponding to a dimensionless angular momentum  $j = J/M_0^2 = 0.19$ , for the EoS L. For a fixed mass the quadrupole moment is an increasing function of  $j$  because an increasing of the angular momentum at fixed mass results in an increasing of the oblateness (eccentricity) of the star, and so the quadrupole moment. Based on this fact, it is clear that not all the pairs of quadrupole and angular momentum pairs depicted in, e.g., Fig. E.1 are physically realizable. The maximum rotation rate of a neutron star taking into account both the effects of general relativity and deformations has been found to be  $\nu_{s,max} = 1045(M_0/M_\odot)^{1/2}(10 \text{ km}/R)^{3/2}$  Hz, largely independent on the EoS (see Latimer and Prakash, 2004b, for details). Corresponding to this maximum rotation rate, the angular momentum is  $J_{max} = 2\pi\nu_{s,max}I \sim 6.56 \times 10^{48}I_{45}$  g cm<sup>2</sup> s<sup>-1</sup>, and  $j_{max} = GJ_{max}/(cM_0^2) \sim 0.74I_{45}/(M_0/M_\odot)^2$ , where  $I_{45}$  is the moment of inertia of the NS in units of  $10^{45}$  g cm<sup>2</sup>. The fastest observed pul-

star is PSR J1748-2246ad with a rotation frequency of 716 Hz (Hessels et al., 2006b), which constrains the mass of the NS to  $M_0 \geq 0.47(R/10 \text{ km})^3 M_\odot$ , and  $j \sim 0.51 I_{45} / (M_0 / M_\odot)^2$ , which becomes  $j \sim 0.26 I_{45}$  for a canonical NS of  $M_0 = 1.4 M_\odot$ .

### Keplerian Frequency

Now we turn into the frequencies analysis. For stationary axially symmetric spacetimes, the frequency of Keplerian orbits is given by (see e.g. Ryan, 1995)

$$\Omega_K = \frac{-g_{t\phi,\rho} \pm \sqrt{g_{t\phi,\rho}^2 - g_{\phi\phi,\rho} g_{tt,\rho}}}{g_{\phi\phi,\rho}}, \quad (\text{E.1.20})$$

where a colon stands for partial derivative with respect to the indicated coordinate and '+' and '-' stands for corotating and counter-rotating orbits, respectively.

For the case of static spacetimes, i.e. for  $\omega = 0$  and therefore  $g_{t\phi} = 0$ ,  $\Omega_K = \pm \sqrt{-g_{\phi\phi,\rho} g_{tt,\rho}} / g_{\phi\phi,\rho}$  and the energy  $E$  and angular momentum  $L$  per mass  $\mu$  of the test particle can be expressed in terms of the metric tensor components (see e.g. Ryan, 1995),

$$\frac{E}{\mu} = \frac{-g_{tt}}{\sqrt{-g_{tt} - g_{\phi\phi} \Omega_K^2}}, \quad \frac{L}{\mu} = \frac{g_{\phi\phi} \Omega_K}{\sqrt{-g_{tt} - g_{\phi\phi} \Omega_K^2}}. \quad (\text{E.1.21})$$

From here, it is clear that taking the negative branch of the root for  $\Omega_K$  in Eq. (E.1.20) is equivalent to studying a particle with opposite angular momentum, i.e.  $L_{\text{count-rot}} = -L_{\text{co-rot}}$ . Thus, in the static case the magnitude of the energy and angular momentum are invariant under the change  $\Omega_K \rightarrow -\Omega_K$ .

Now we consider the case of stationary space times,  $\omega \neq 0$ . The energy  $E$  and angular momentum  $L$  per mass  $\mu$  are, in this case, given by (see e.g. Ryan, 1995)

$$\frac{E}{\mu} = \frac{-g_{tt} - g_{t\phi} \Omega_K}{\sqrt{-g_{tt} - 2g_{t\phi} \Omega_K - g_{\phi\phi} \Omega_K^2}}, \quad (\text{E.1.22})$$

$$\frac{L}{\mu} = \frac{g_{t\phi} + g_{\phi\phi} \Omega_K}{\sqrt{-g_{tt} - 2g_{t\phi} \Omega_K - g_{\phi\phi} \Omega_K^2}}. \quad (\text{E.1.23})$$

The counter-rotating condition expressed by the negative branch of Eq. (E.1.20), can be generated by the change  $g_{t\phi} \rightarrow -g_{t\phi}$ , which seems to be a more physical and transparent condition. In contrast to the static case, the counter-rotating orbit has now different energy and different magnitude of the an-

gular momentum due the presence of the dragging of inertial frames, characterized by the metric component  $g_{t\phi}$  (cf. Eq. (E.1.26) below). In a nutshell, the dynamics of counter-rotating orbits of a test-particle can be derived, starting from the positive branch of Eq. (E.1.20), by considering a spacetime with  $g_{t\phi} \rightarrow -g_{t\phi}$ .

For the vacuum case, a similar analysis as the one developed by Herrera et al. (2006), clearly shows that the change in the global sign of  $g_{t\phi}$  is achieved by changing not only the angular momentum of the star,  $J \rightarrow -J$ , but *all the rotational multipolar moments*. For the Kerr metric this change is obtained by changing the sign of the parameter  $a$  (see Appendix E.1.8) while in the PRS solution we need additionally change the sign of the parameter  $s$  associated to *differential rotation*, i.e., by changing  $a \rightarrow -a$  and  $s \rightarrow -s^2$ .

Once we have clarified this important issue about the co-rotating and counter-rotating orbits, we proceed to analyze the functional dependence of the Keplerian frequency on the multipole moments. In the upper panel of Fig. E.2 we plotted contours of constant Keplerian frequency for the PRS solution,  $\nu_{K,PRS} = \Omega_{K,PRS}/(2\pi)$ , as a function of the dimensionless angular momentum parameter  $j$  and the quadrupole moment  $M_{2,PRS}$ , at the ISCO radius. It can be seen that the influence of the quadrupole moment is non-negligible, as evidenced from the departure of the contour lines from vertical lines. The Keplerian frequency grows for increasing  $J$  and  $M_2$ . In the lower panel, we plotted contours of constant ratio  $\nu_{K,PRS}/\nu_{K,Kerr}$  as a function of  $j$  and the difference between the quadrupole moment of the PRS solution,  $M_{2,PRS}$ , and the Kerr quadrupole,  $M_{2,Kerr}$ .

It is appropriate to recall here that because the Keplerian as well as the other frequencies calculated below are evaluated using formulas in the coordinate frame, see for instance Eq. (E.1.20), they must be evaluated at coordinate radii  $\rho$  and not at physical radii given by  $\sqrt{g_{\phi\phi}}$ . In the specific case of the ISCO the frequencies are evaluated at the radius that simultaneously solves the equations  $V = 0$ ,  $dV/d\rho = 0$ , and  $d^2V/d\rho^2 = 0$ , where  $V$  is the effective potential (E.1.19).

## Oscillation and Precession Frequencies

The radial and vertical oscillation (or epicyclic) frequencies are the frequencies at which the periastron and orbital plane of a circular orbit oscillates if we apply slightly radial and vertical perturbations to it, respectively. According to Ryan (1995), in stationary axially symmetric vacuum spacetimes described by the Weyl-Papapetrou metric (E.1.1), the radial and vertical epicyclic fre-

---

<sup>2</sup>For the vacuum case, in the solution by Manko et al. (2000), the sign change of  $g_{t\phi}$  is obtained after performing simultaneously the replacements  $a \rightarrow -a$  and  $b \rightarrow -b$ .

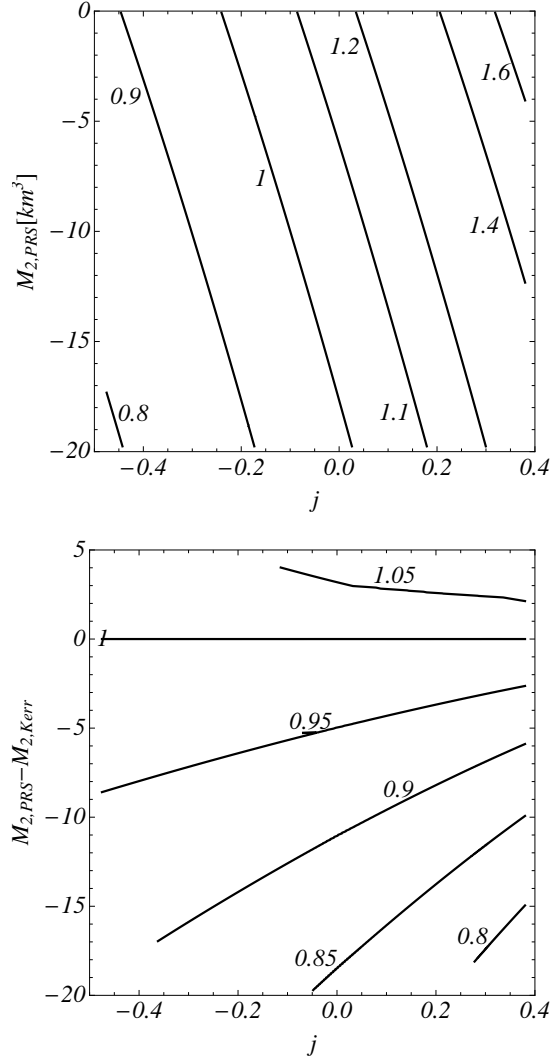


**Figure E.2.:** Upper panel: Contours of constant  $\nu_K$  (in kHz) as a function of the the dimensionless angular momentum parameter  $j = J/M_0^2$  and quadruple moment  $M_2$  for the PRS solution, at the ISCO radius, for a compact object with mass  $M_0 = m = 1.88M_\odot = 2.78$  km. Lower panel: Contours of constant ratio  $\nu_{K,PRS}/\nu_{K,Kerr}$  as a function of  $j$  and the difference  $M_{2,PRS} - M_{2,Kerr}$ , at the ISCO radius.

quencies can be obtained as

$$\begin{aligned} \nu_\alpha^{\text{OS}} = \frac{1}{2\pi} \left\{ -\frac{g^{\alpha\alpha}}{2} \left[ (g_{tt} + g_{t\phi}\Omega)^2 \left( \frac{g_{\phi\phi}}{\rho^2} \right)_{,\alpha\alpha} \right. \right. \\ - 2(g_{tt} + g_{t\phi}\Omega)(g_{t\phi} + g_{\phi\phi}\Omega) \left( \frac{g_{t\phi}}{\rho^2} \right)_{,\alpha\alpha} \\ \left. \left. + (g_{t\phi} + g_{\phi\phi}\Omega)^2 \left( \frac{g_{tt}}{\rho^2} \right)_{,\alpha\alpha} \right] \right\}^{1/2}, \end{aligned} \quad (\text{E.1.24})$$

and the corresponding periastron ( $\nu_\rho^{\text{P}}$ ) and nodal ( $\nu_z^{\text{P}}$ ) precession frequencies as

$$\nu_\alpha^{\text{P}} = \nu_{\text{K}} - \nu_\alpha^{\text{OS}}. \quad (\text{E.1.25})$$

where  $\alpha = \{\rho, z\}$ , respectively, and  $\nu_{\text{K}} = \Omega_{\text{K}}/(2\pi)$  is the Keplerian orbital frequency with  $\Omega_{\text{K}}$  given by Eq. (E.1.20).

In the upper panel of Fig. E.3, we plotted contours of constant nodal precession frequency  $\nu_z^{\text{P}}$  at the ISCO radius as a function of  $j = J/M_0^2$  and  $M_2$  for the PRS solution, at the ISCO radius. We can see now that the influence of the quadrupole moment is quite important. The nodal precession frequency increases for increasing  $J$  and decreasing  $M_2$ , at fixed  $M_0$ . In the lower panel we plotted contours of constant ratio  $\nu_{z,\text{PRS}}^{\text{P}}/\nu_{z,\text{Kerr}}^{\text{P}}$ , at the ISCO radius, as a function of  $j$  and the difference  $M_{2,\text{PRS}} - M_{2,\text{Kerr}}$ , in order to evidenciate deviations from the Kerr solution. The radial oscillation frequency  $\nu_\rho^{\text{OS}}$  vanishes at the ISCO radius and therefore at such location the radial precession frequency equals the Keplerian frequency, whose contours have been plotted in Fig. E.2.

In Figs. E.4 and E.5 we plotted the nodal precession frequency  $\nu_z^{\text{P}}$  and the radial oscillation frequency  $\nu_\rho^{\text{OS}}$  as a function of the Keplerian frequency  $\nu_{\text{K}}$ , respectively, for both the Kerr and PRS solutions. As an example, we have shown the results for rotating NS models 20 and 26 of Table VI of Pappas and Apostolatos (2012), for the EoS L. The lowest multipole moments of the PRS solution  $M_0, J, M_2$ , and  $S_3$  have been fixed to the numerical values obtained by Pappas and Apostolatos (2012). In the case of the Kerr solution, only  $M_0$  and  $J$  can be fixed, while  $M_2$ , and  $S_3$  have values induced by the lower moments  $M_0$  and  $J$ . For the PRS solution with  $s = 0$ ,  $M_0, J$  and  $M_2$  can be fixed while  $S_3$  cannot be fixed and depends on the lower moments. The results for the PRS analytic model obtained by fixing  $M_0, J, M_2$ , as well as  $S_3$  are also shown.

The deviations of the quadrupole and current octupole moments given by the Kerr solution from the numerical values of Pappas and Apostolatos (2012) can be used to show the low accuracy of the Kerr solution to describe fast rotating NSs. The accuracy of the PRS solution in describing the ISCO radii of these two models has been shown in Table E.1 of Section E.1.3.

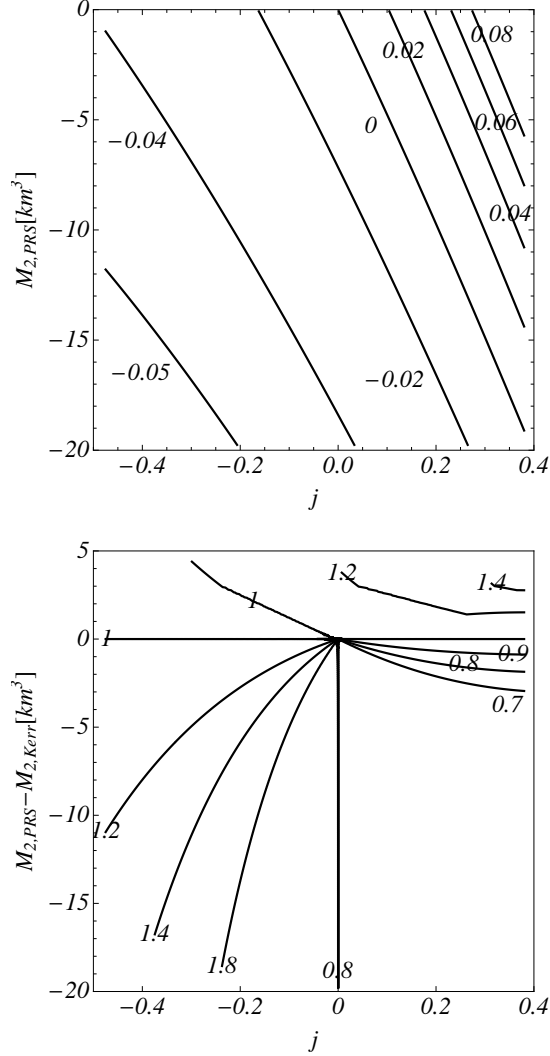


**Figure E.3.:** Upper panel:  $\nu_z^P$  (in kHz) as a function of the the dimensionless angular momentum parameter  $j = J/M_0^2$  and quadruple moment  $M_2$  for the PRS solution, at the ISCO radius, for a compact object with mass  $M_0 = m = 1.88M_\odot = 2.78 \text{ km}$ . Lower panel: Contours of constant ratio  $\nu_{z,PRS}^P / \nu_{z,Kerr}^P$  as a function of  $j$  and the difference  $M_{2,PRS} - M_{2,Kerr}$ , at the ISCO radius.

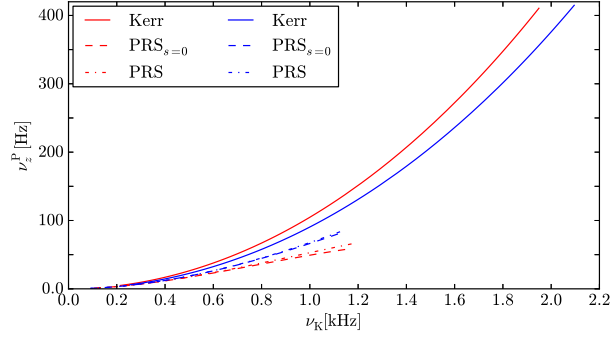


**Figure E.4.:** Nodal precession frequency  $\nu_z^P$  versus Keplerian frequency  $\nu_K$  given by the Kerr and PRS analytic solutions. The lowest multipole moments have been fixed from the rotating NS models 20 (red curves) and 26 (blue curves) of the Table VI of Pappas and Apostolatos (2012) for the EoS L. Model 20:  $M_0 = 4.167$  km ( $2.82M_\odot$ ),  $j = J/M_0^2 = 0.70$ ,  $M_2 = -79.8$  km<sup>3</sup> ( $-1.08 \times 10^{45}$  g cm<sup>2</sup>) and  $S_3 = -401.0$  km<sup>4</sup>. Model 26:  $M_0 = 4.36$  km ( $2.95M_\odot$ ),  $j = J/M_0^2 = 0.56$ ,  $M_2 = -45.2$  km<sup>3</sup> ( $-6.10 \times 10^{44}$  g cm<sup>2</sup>) and  $S_3 = -170.0$  km<sup>4</sup>.

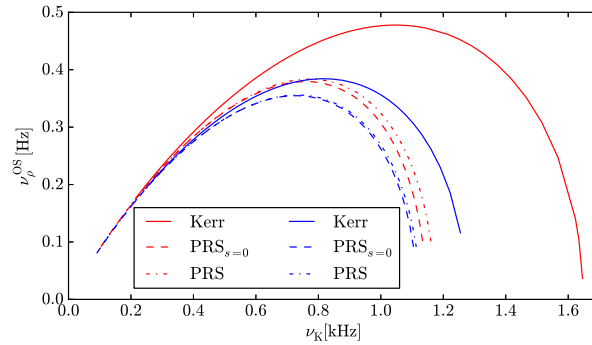


**Figure E.5.:** Radial oscillation frequency  $\nu_\rho^{\text{OS}}$  versus Keplerian frequency  $\nu_K$  given by the Kerr and PRS analytic solutions. The lowest multipole moments has been fixed from the rotating NS models 20 (red curves) and 26 (blue curves) of the Table VI of Pappas and Apostolatos (2012) for the EoS L. Model 20:  $M_0 = 4.167$  km ( $2.82M_\odot$ ),  $j = J/M_0^2 = 0.70$ ,  $M_2 = -79.8$  km<sup>3</sup> ( $-1.08 \times 10^{45}$  g cm<sup>2</sup>) and  $S_3 = -401.0$  km<sup>4</sup>. Model 26:  $M_0 = 4.36$  km ( $2.95M_\odot$ ),  $j = J/M_0^2 = 0.56$ ,  $M_2 = -45.2$  km<sup>3</sup> ( $-6.10 \times 10^{44}$  g cm<sup>2</sup>) and  $S_3 = -170.0$  km<sup>4</sup>.

In Figs. E.4 and E.5 we can see the differences of the  $\nu_z^P - \nu_K$  and  $\nu_\rho^{OS} - \nu_K$  relations between the Kerr and PRS solutions for *realistic NS models*. The deviations of the Kerr solution, especially at fast rotation rates, are evident because of the influence of the deformation (quadrupole  $M_2$ ) of the star as well as, although in less proportion, of the octupole current  $S_3$ . In general, we observe that the larger the angular momentum, the poorer the performance of the predictions of Kerr solution.

We have also shown in Figs. E.4–E.5 the influence of the current octupole  $S_3$  in the determination of the precession and oscillation frequencies. We found that the effect of  $S_3$  is only appreciable for the fastest models. The minor influence, in this case, of the current octupole  $S_3$  is expected from the small values of the parameter  $s$  needed to fit the numerical values of Pappas and Apostolatos (2012). Clearly, larger values of the parameter  $s$  needed to fit realistic values of  $S_3$  will enhance as well deviations from the Kerr spacetime.

The effects of a multipolar structure that deviates from the one of the Kerr geometry on the various quantities analyzed here are relevant for instance in the RPM of the QPOs observed in LMXBs (see e.g. Stella and Vietri (1998); Morsink and Stella (1999); Stella et al. (1999); Stella and Vietri (1999) and Section E.1.6, for details).

### Dragging of Inertial Frames

It is known that a prediction of general relativity is that a rotating object makes a zero angular momentum test particle to orbit around it, namely it *drags* the particle into the direction of its rotation angular velocity; such an effect is called dragging of inertial frames or Lense-Thirring effect. Consequently, oblique particle orbit planes with respect to the source equatorial plane will precess around the rotation axis of the object. In stationary axially symmetric spacetimes described by the metric (E.1.1) the frame dragging precession frequency is given by (see e.g. Ryan, 1995)

$$\nu_{LT} = -\frac{1}{2\pi} \frac{g_{t\phi}}{g_{\phi\phi}}. \quad (\text{E.1.26})$$

Many efforts have been done to test the predictions of general relativity around the Earth such as the analysis of the periastron precession of the orbits of the LASER GEODynamics Satellites, LAGEOS and LAGEOS II, (see e.g. Lucchesi and Peron, 2010) and the relativistic precession of the gyroscopes on-board the Gravity Probe B satellite (see Everitt et al., 2011, for details). The latter experiment measured a frame dragging effect within an accuracy of 19% with respect to the prediction of general relativity.

The smallness of this effect around the Earth makes such measurements quite difficult and has represented a multi year challenge for Astronomy. The frame dragging precession increases with the increasing of the angular mo-

mentum of the rotating object and therefore a major hypothetical arena for the searching of more appreciable Lense-Thirring precession is the spacetime around compact objects such as BHs and NSs. The much stronger gravitational field of these objects with respect to the Earth one allow them to attain much faster angular rotation rates and so larger angular momentum.

Stella and Vietri (1998) showed how, in the weak field slow rotation regime, the vertical precession frequency  $\nu_z^P$  (orbital plane precession frequency) can be divided into one contribution due to the Lense-Thirring precession and another one due to the deformation (non-zero quadrupole moment) of the rotating object, both of them comparable from the quantitative point of view. These frequencies could be in principle related to the motion of the matter in the accretion disks around BHs and NSs and thus particularly applicable to LMXBs. For fast rotating NSs and BHs the frequency at which the orbital plane, and so the frame dragging precession frequency, can reach values of the order of tens of Hz (see e.g. Stella and Vietri (1998) and Figs. E.3 and E.4).

Thus, it is clear that an observational confirmation of the relativistic precession of matter around either a NS or a BH will lead to an outstanding test of the general relativity in the strong field regime and, at the same time, an indirect check of the large effects of the frame dragging in the exterior spacetime of compact objects (see e.g. Morsink and Stella, 1999, for details).

Although making independent measurements of the frame dragging effect around BHs and NSs is a very complicate task, it is important to know the numerical values of the precession frequency due to the frame dragging with respect to other relativistic precession effects, e.g. geodetic precession. In addition, it is important to know the sensitivity of the precession frequency to the object parameters such as mass, angular momentum, quadrupole, and octupole moment.

In the upper panel of Fig. E.6 we plotted contours of constant frame dragging frequency  $\nu_{LT}$  for the PRS solution, at the ISCO radius, as a function of the the angular momentum per unit mass  $J/M_0$  and the quadruple moment  $M_2$ , for a compact object mass  $M_0 = m = 1.88M_\odot$ . Correspondingly, in the lower panel of Fig. E.6, we show the differences between the frame dragging precession frequency as predicted by the Kerr and PRS solutions, at the ISCO radius, as a function of  $j = J/M_0^2$  and the difference between the quadrupole moments,  $M_{2,PRS} - M_{2,Kerr}$ .

The influence of the quadrupole moment in the determination of the frame dragging frequency is evident; the frequency  $\nu_{LT}$  given by a NS is generally smaller than the one given by a BH as can be seen from the value of the ratio  $\nu_{LT,PRS}/\nu_{LT,Kerr} < 1$  obtained for configurations with a quadrupole moment that deviates with respect to the one given by the Kerr solution, namely for  $M_{2,PRS} - M_{2,Kerr} = M_{2,PRS} + ma^2 = mk \neq 0$ , see Eq. (E.1.11).

It is also worth mentioning that frame dragging precession can be affected as well by the presence of electromagnetic fields (Herrera et al., 2006, see) and further research in this respect deserves the due attention.

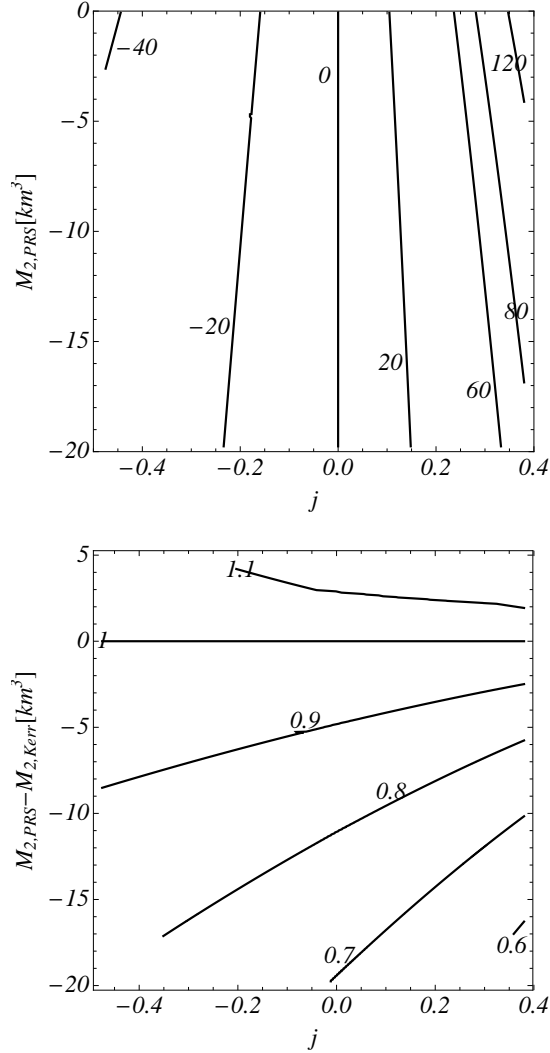


**Figure E.6.:** Upper panel: Contours of constant  $\nu_{LT}$  (in Hz) as a function of the the angular momentum per unit mass  $j = J/M_0^2$  and the quadrupole moment  $M_2$  for the PRS solution, at the ISCO radius, for a compact object with mass  $M_0 = m = 1.88M_\odot = 2.78$  km. Lower panel: Contours of constant ratio  $\nu_{LT,PRS}/\nu_{LT,Kerr}$  as a function of  $j$  and the difference  $M_{2,PRS} - M_{2,Kerr}$ , at the ISCO radius.

### E.1.4. Accuracy of Ryan's Analytic Formulas

Following a series expansion procedure in powers of  $1/\rho$ , Ryan (1995) found that the periastron (radial) and nodal (vertical) precession frequencies,  $\nu_\rho^P$  and  $\nu_z^P$  given by Eq. (E.1.24), can be written as a function of the Keplerian frequency  $\nu_K$  as

$$\begin{aligned} \frac{\nu_\rho^P}{\nu_K} = & 3\mathcal{V}^2 - 4\frac{S_1}{M_0^2}\mathcal{V}^3 + \left(\frac{9}{2} - \frac{3M_2}{2M_0^3}\right)\mathcal{V}^4 - 10\frac{S_1}{M_0^2}\mathcal{V}^5 \\ & + \left(\frac{27}{2} - 2\frac{S_1^2}{M_0^4} - \frac{21M_2}{2M_0^3}\right)\mathcal{V}^6 + \left(-48\frac{S_1}{M_0^2} - 5\frac{S_1M_2}{M_0^5}\right. \\ & \left.+ 9\frac{S_3}{M_0^4}\right)\mathcal{V}^7 + \left(\frac{405}{8} + \frac{2243}{84}\frac{S_1^2}{M_0^4} - \frac{661M_2}{14M_0^3}\right. \\ & \left.- \frac{21M_2^2}{8M_0^6} + \frac{15M_4}{4M_0^5}\right)\mathcal{V}^8 + \dots, \end{aligned} \quad (\text{E.1.27})$$

and

$$\begin{aligned} \frac{\nu_z^P}{\nu_K} = & 2\frac{S_1}{M_0^2}\mathcal{V}^3 + \frac{3M_2}{2M_0^3}\mathcal{V}^4 + \left(7\frac{S_1^2}{M_0^4} + 3\frac{M_2}{M_0^3}\right)\mathcal{V}^6 \\ & + \left(11\frac{S_1M_2}{M_0^5} - 6\frac{S_3}{M_0^4}\right)\mathcal{V}^7 + \left(\frac{153}{28}\frac{S_1^2}{M_0^4} + \frac{153M_2}{28M_0^3}\right. \\ & \left.+ \frac{39M_2^2}{8M_0^6} - \frac{15M_4}{4M_0^5}\right)\mathcal{V}^8 + \dots, \end{aligned} \quad (\text{E.1.28})$$

where  $\mathcal{V} = (2\pi M_0 \nu_K)^{1/3}$ ,  $[M_0, M_2, M_4]$  are the lowest three mass moments and,  $[S_1, S_3]$ , are the lowest two current moments. For the PRS solution in the vacuum case,  $M_4 = m(a^4 - 3a^2 + k^2 + 2as)$ .

The above formulas are approximate expressions of the periastron and nodal precession frequencies in the weak field (large distances from the source) and slow rotation regimes. We should therefore expect that they become less accurate at distances close to the central object, e.g. at the ISCO radius, and for fast rotating objects. However, such formulas are an important tool to understand the role of the lowest multipole moments on the values of the relativistic precession frequencies, such as the importance of the higher multipole moments at short distances and high frequencies as can be seen from Eqs. (E.1.27–E.1.28).

At high frequencies, for instance of the order of kHz, deviations from the above scaling laws are appreciable. In Figs. E.7 and E.8 we compare the radial precession and vertical oscillation frequencies,  $\nu_\rho^P$  and  $\nu_z^{\text{OS}}$ , as a function of the

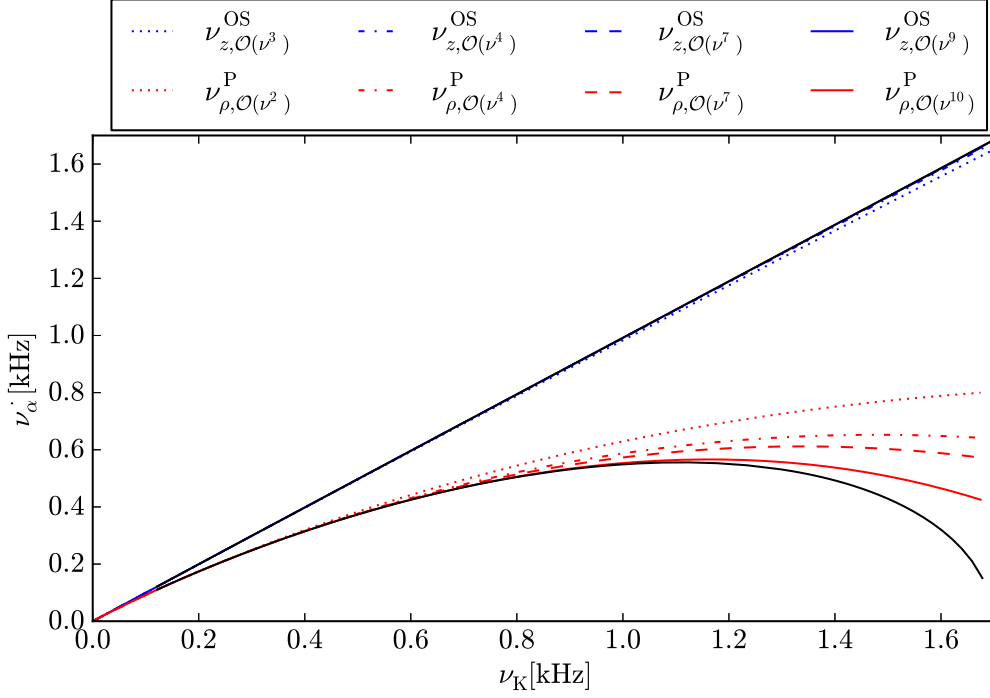


**Figure E.7.:** Comparison of the  $\nu_z^{\text{OS}}-\nu_K$  and  $\nu_\rho^{\text{P}}-\nu_K$  relations given by the PRS solution and the approximate expressions (E.1.27–E.1.28) derived by Ryan (1995). The lowest multipole moments  $M_0$ ,  $J$ ,  $M_2$ , and  $S_3$  have been fixed to the values of the Model 2 of the Table VI of Pappas and Apostolatos (2012):  $M_0 = 2.071$  km ( $1.402M_\odot$ ),  $j = 0.194$ ,  $M_2 = -2.76$  km<sup>3</sup> ( $3.73 \times 10^{43}$  g cm<sup>2</sup>), and  $S_3 = -2.28$  km<sup>4</sup>.

Keplerian frequency  $\nu_K$ , as given by the full expressions (E.1.24) for the PRS solution and by the approximate formulas (E.1.27) and (E.1.28), respectively.<sup>3</sup> The lowest multipole moments  $M_0$ ,  $J$ ,  $M_2$ , and  $S_3$  of the PRS solution have been fixed to the values of two models of the Table VI of Pappas and Apostolatos (2012); Model 2 with  $M_0 = 2.071$  km ( $1.402M_\odot$ ),  $j = 0.194$ ,  $M_2 = -2.76$  km<sup>3</sup> ( $3.73 \times 10^{43}$  g cm<sup>2</sup>),  $S_3 = -2.28$  km<sup>4</sup> and Model 20 with  $M_0 = 4.167$  km ( $2.82M_\odot$ ),  $j = J/M_0^2 = 0.70$ ,  $M_2 = -79.8$  km<sup>3</sup> ( $-1.08 \times 10^{45}$  g cm<sup>2</sup>) and  $S_3 = -401.0$  km<sup>4</sup>.

In the  $\nu_z^{\text{OS}}-\nu_K$  relation, the blue dotted curve depicts the contribution from the angular momentum (we plot the series (E.1.28) up to  $\mathcal{V}^3$ ), for the blue dot-dashed curve we added the first contribution from the quadrupole moment  $M_2$  (we cut the series at  $\mathcal{V}^4$ ), for the dashed blue line we added the first contribution from the octupole mass-current (series expansion up to  $\mathcal{V}^7$ ) and finally

<sup>3</sup>Because the scale of the  $\nu_\rho^{\text{P}}$  and  $\nu_z^{\text{P}}$  frequencies are very similar, we decided to plot in Fig. E.7  $\nu_\rho^{\text{P}}$  and  $\nu_z^{\text{OS}}$  whose scales are different allowing a more clear comparison with the PRS solution in a single figure.

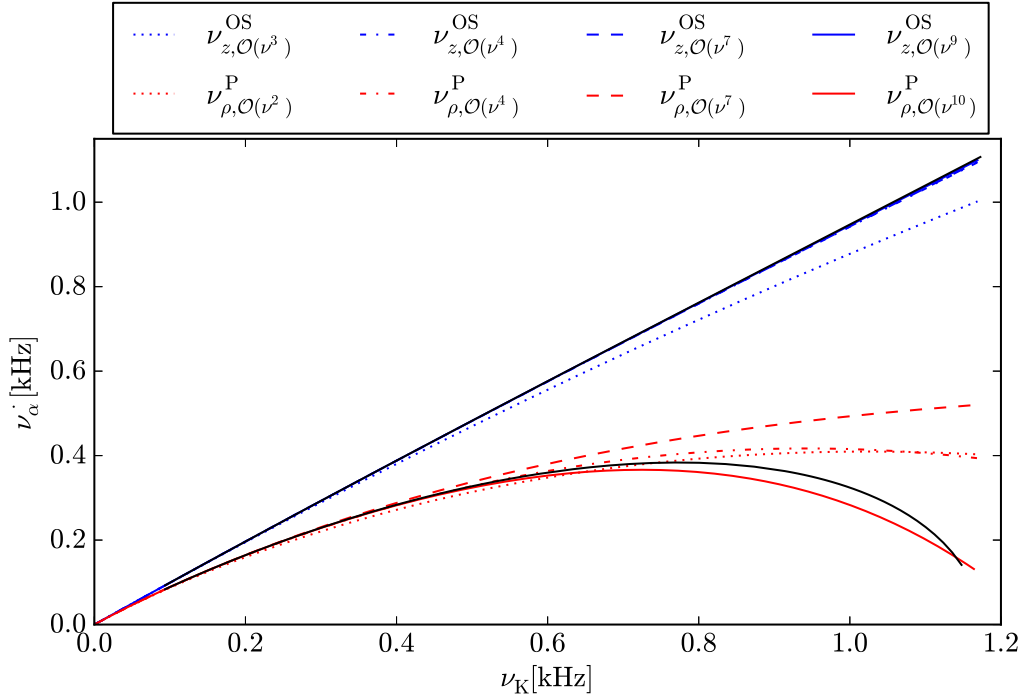


**Figure E.8.:** Comparison of the  $\nu_z^{\text{OS}}-\nu_K$  and  $\nu_\rho^{\text{P}}-\nu_K$  relations as given by the PRS solution and the approximate expressions (E.1.27-E.1.28) derived by Ryan (1995). The lowest multipole moments  $M_0$ ,  $J$ ,  $M_2$ , and  $S_3$  have been fixed to the values of the Model 20 of the Table VI of Pappas and Apostolatos (2012):  $M_0 = 4.167 \text{ km}$  ( $2.82M_\odot$ ),  $j = J/M_0^2 = 0.70$ ,  $M_2 = -79.8 \text{ km}^3$  ( $-1.08 \times 10^{45} \text{ g cm}^2$ ) and  $S_3 = -401.0 \text{ km}^4$

in the continuous blue line we consider contributions for higher multipole moments and stop the series at the order  $\mathcal{V}^9$ , not shown in Eqs. (E.1.28). For this case, we can see that Ryan's expressions clearly tend, from the bottom, to the exact result (continuous black curve) obtained by using the PRS solution.

For the analysis of the  $\nu_\rho^P - \nu_K$  relation we followed the same procedure as described above. In this case, the Ryan's expressions tend from the top to the exact result, the continuous black curve, represented by the PRS solution. It is interesting to see that the introduction of the octupole moment (dashed red line) makes the approximation to deviate from the exact result, however by including more terms the accuracy is enhanced. As can be seen from Figs. E.7 and E.8 the quantitative accuracy of the Ryan's approximate formulas in the periastron precession frequency  $\nu_\rho^P$  is less than the one obtained in the vertical oscillation frequency  $\nu_z^{\text{OS}}$ .

The importance of the high-order multipole moments such as the quadrupole and the octupole moments is evident in the high-frequency regime. This is in line with the results shown in Figs. E.2–E.3 and in Figs. E.4–E.5. We can see from Figs. E.7 and E.8 that the Ryan's approximate formulas describe more accurately the Model 2 than the Model 20. The reason is that, as we mentioned above, we should expect a better accuracy of the series expansions from low to moderate moderate rotation rates and consequently the same occur for the quadrupole deformations. It is clear that there are appreciable differences both in rotation and deformation between the two selected models; we recall also that the rotation frequency of the star can be expressed as a function of the dimensionless  $j$  parameter as  $\nu_s = GjM_0^2 / (2\pi cI) = 1.4(M/M_\odot)^2 / I_{45}$  kHz.

It is noteworthy that we have checked that the Ryan's series expansions, Eqs. (E.1.27) and (E.1.28), fit quite accurately the exact results if taken up to order  $\mathcal{V}^{10}$ . In particular the values of the vertical oscillation and precession frequencies are fit better than the corresponding radial ones. For the Model 2 the radial oscillation frequency is well fitted by the Ryan's expression up to Keplerian frequencies of order  $\sim 1.2$  kHz while, for the Model 20, the approximate formulas break down at a lower value  $\sim 0.7$  kHz. These results are of particular relevance because it makes possible the extraction of the object parameters (for instance the lowest multipoles up to  $S_3$ ) by the fitting of the observed QPO frequencies in LMXBs, providing they are indeed related to the precession and oscillation frequencies of matter in the accretion disk (see Section E.1.6, for details) and for Keplerian motion not exceeding a few kHz of frequency.

### **E.1.5. Accuracy of PRS solution**

We turn now to analyze the behavior of the Kerr and PRS solutions in predicting results for the Keplerian, frame dragging, and vertical oscillation fre-

quencies, for realistic NSs. In particular, we compare their predictions with the frequencies calculated by Morsink and Stella (1999). Since Morsink and Stella (1999) did not include the values of the octupole current moment  $S_3$ , here we set  $s = 0$  in Eq. (E.1.10) for the PRS solution. For the sake of comparison, we choose the results derived by Morsink and Stella (1999) for the EoS L, because for this EoS the highest rotating parameter  $j$  and quadrupole moment  $M_2$  were found. In addition, the stiffness of such an EoS allows the maximum mass of the NS to be larger than the highest observed NS mass,  $M_0 = 1.97 \pm 0.04 M_\odot$ , corresponding to the 317 Hz (3.15 milliseconds rotation period) pulsar J1614-2230 (see Demorest et al., 2010b, for details).

This regime of high  $j$  and  $M_2$  in realistic models is particularly interesting to test the deviations of the Kerr solution in the description of NS signatures as well as to explore the accuracy of the PRS solution. In Table E.2, we present the results for four different sets of the star spin frequency  $\nu_s$ , namely  $\nu_s = 290$  Hz (M1 and M2),  $\nu_s = 360$  Hz (M3 and M4),  $\nu_s = 580$  Hz (M5 and M6) and  $\nu_s = 720$  Hz (M7 and M8).

Model	$M_0/M_\odot$	$j$	$M_2/Q_0$	$r_+^{\text{MS}}[\text{km}]$	$r_+^{\text{Kerr}}$	$r_+^{\text{PRS}}$	$\nu_K^{\text{MS}}[\text{kHz}]$	$\nu_K^{\text{Kerr}}$	$\nu_K^{\text{PRS}}$	$\nu_{\text{LT}}^{\text{MS}}[\text{Hz}]$	$\nu_{\text{LT}}^{\text{Kerr}}$	$\nu_{\text{LT}}^{\text{PRS}}$	$\nu_z^{\text{PMS}}[\text{Hz}]$	$\nu_z^{\text{PKerr}}$	$\nu_z^{\text{PPRS}}$
M1	1.88	0.19	-5.3	15.4	14.90	15.42	1.31	1.363	1.304	39.7	42.248	38.476	18.6	39.697	22.040
M2	2.71	0.14	-3.0	22.2	22.16	22.23	0.90	0.906	0.902	19.6	19.676	19.493	17.2	18.809	17.629
M3	1.94	0.24	-8.2	15.6	14.89	15.63	1.29	1.380	1.296	49.8	57.001	49.804	17.5	52.608	26.197
M4	2.71	0.18	-4.8	21.8	21.62	21.74	0.93	0.937	0.931	26.1	27.245	26.833	21.9	25.670	23.635
M5	2.07	0.40	-23.1	16.3	14.18	16.06	1.26	1.514	1.289	84.3	125.75	88.905	-10.5	109.04	31.140
M6	2.72	0.30	-13.9	20.6	20.05	20.45	1.01	1.041	1.015	53.5	57.467	54.391	35.8	51.861	42.854
M7	2.17	0.51	-39.4	17.0	13.58	16.53	1.22	1.637	1.269	106.7	201.52	116.25	-51.8	166.55	29.804
M8	2.73	0.39	-24.4	19.8	18.85	19.65	1.06	1.136	1.077	78.8	90.821	80.895	38.4	79.079	57.187

**Table E.2.:** ISCO radius  $r_+$ , Keplerian frequency  $\nu_K$ , frame-dragging (Lense-Thirring) frequency  $\nu_{\text{LT}}$ , and vertical precession frequency  $\nu_z^{\text{P}}$  of the co-rotating orbits calculated numerically by Morsink and Stella (1999) (upper index MS) and comparison with the corresponding predicted values given by the Kerr (upper index Kerr) and the PRS $_{s=0}$  solution (upper index PRS). The quadrupole moment  $M_2$  have been normalized for convenience to the value  $Q_0 = 10^{43} \text{ g cm}^2$ .

In Table E.2, we clearly observe that the results predicted by the PRS $_{s=0}$  solution for the Keplerian and frame-dragging frequencies are in excellent agreement with those calculated by Morsink and Stella (1999) for even highly massive, rotating and deformed models such as the model M7 with  $M_0 = 2.17 M_\odot$ ,  $j = 0.51$  and  $M_2 = -39.4 Q_0$ . We notice that Morsink and Stella (1999) reported some configurations with negative values of  $\nu_z$  (see Table E.2). We advance the possibility that this is due to instabilities of the numerical code that occur when the ISCO radius is located very close or inside the surface of the object. Thus, the values of the frequencies given by the analytic solution in these cases are to be considered predictions to be tested for future numerical computations. This fact can be checked within the calculations of Morsink and Stella (1999) by exploring the properties of counter-rotating orbits which produce in general ISCO radii larger than the ones of the co-rotating ones. In Table E.3, we depicted the results in the counter-rotating case

where we can notice an improvement of the accuracy of the PRS solution with respect to the co-rotating case.

Model	$r^{\text{MS}}[\text{km}]$	$r^{\text{Kerr}}$	$r^{\text{PRS}}$	$\nu_{\text{K}}^{\text{MS}}[\text{kHz}]$	$\nu_{\text{K}}^{\text{Kerr}}$	$\nu_{\text{K}}^{\text{PRS}}$	$\nu_{\text{IT}}^{\text{MS}}[\text{Hz}]$	$\nu_{\text{IT}}^{\text{Kerr}}$	$\nu_{\text{IT}}^{\text{PRS}}$	$\nu_{\frac{1}{2}}^{\text{MS}}[\text{Hz}]$	$\nu_{\frac{1}{2}}^{\text{Kerr}}$	$\nu_{\frac{1}{2}}^{\text{PRS}}$
M1	18.8	18.35	18.73	0.99	1.023	0.997	21.7	22.61	21.39	29.0	23.88	29.70
M2	25.9	25.82	25.88	0.73	0.734	0.732	12.4	12.43	12.36	13.6	12.95	13.46
M3	19.9	19.39	19.89	0.93	0.960	0.928	24.0	25.79	24.04	32.9	27.61	34.20
M4	26.4	26.33	26.42	0.71	0.715	0.712	14.7	15.08	14.94	16.4	15.88	16.57
M5	23.3	22.22	23.24	0.77	0.816	0.768	28.2	32.59	28.78	41.3	36.31	44.65
M6	28.2	27.94	28.18	0.65	0.660	0.652	20.5	21.19	20.70	24.1	23.03	24.51
M7	25.9	24.37	25.78	0.67	0.731	0.678	28.9	34.62	29.64	43.4	39.56	47.90
M8	29.7	29.18	29.58	0.61	0.623	0.611	23.2	24.40	23.48	28.4	27.12	29.22

**Table E.3.:** Same as in Table E.2, but for the counter-rotating case.

In this line, we consider worth performing numerical computations of the precession and oscillation frequencies of particles around realistic NSs in a wider space of parameters and using up-to-date numerical techniques which will certainly help to establish and elucidate more clearly the accuracy of analytic models. It is also appropriate recalling the recent results of Pappas and Apostolatos (2012) on the computation of the general relativistic multipole moments in axially symmetric spacetimes.

### E.1.6. The Relativistic Precision Model

The X-ray light curves of LMXBs show a variability from which a wide variety of QPOs have been measured, expanding from relatively low  $\sim$  Hz frequencies all the way up to high  $\sim$  kHz frequencies (see e.g. van der Klis, 1995, for details). In particular, such frequencies usually come in pairs (often called twin peaks), the lower and upper frequencies,  $\nu_l$  and  $\nu_h$  respectively. BHs and NSs with similar masses can show similar signatures and therefore the identification of the compact object in a LMXB is not a simple task. If the QPO phenomena observed in these systems are indeed due to relativistic motion of accretion disk matter, the knowledge of the specific behavior of the particle frequencies (e.g. rotation, oscillation, precession) in the exterior geometry of NSs and BHs becomes essential as a tool for the identification of the nature of the compact object harbored by a LMXB.

It is not the scope of this work to test a particular model for the QPO phenomenon in LMXBs but instead to show the influence of the high multipole moments on the orbital motion of test particles especially the role of the quadrupole moment which is of particular interest to differentiate a NS from a BH. There are in the literature several models that describe the QPOs in LMXBs through the frequencies of particles around the compact object, and for a recent review and comparison of the different models we refer to the recent work of Lin et al. (2011). In order to show here the main features and differences between the Kerr and the PRS solutions we shall use the Relativistic Precession Model (RPM).

The RPM model identifies the lower and higher (often called twin-peaks) kHz QPO frequencies,  $\nu_l$  and  $\nu_h$ , with the periastron precession and Keple-

rian frequencies, namely  $\nu_l = \nu_\rho^P$  and  $\nu_h = \nu_K$ , respectively. The so-called horizontal branch oscillations (HBOs), which belong to the low frequency QPOs observed in high luminosity Z-sources (see e.g. van der Klis, 1995, for details), are related within the RPM model to the nodal precession frequency  $\nu_z^P$  of the same orbits (Morsink and Stella, 1999, see). We will use here in particular the realistic NS models of Morsink and Stella (1999) for the EoS L.

One of the salient features of the RPM model is that in the case of the HBO frequencies, the relations inferred from the first term of the expansions (E.1.27) and (E.1.28)

$$\nu_K = 3^{-3/5}(2\pi)^{-2/5}m^{-2/5}(\nu_\rho^P)^{3/5}, \quad (\text{E.1.29})$$

$$\nu_z^P = (2/3)^{6/5}\pi^{1/5}j m^{1/5}(\nu_\rho^P)^{6/5}, \quad (\text{E.1.30})$$

which implies a nodal precession frequency proportional to the square of the Keplerian frequency has been observed in some sources, for instance in the LMXB 4U 1728–34 (see Ford and van der Klis, 1998, for details). In addition, 6/5 power law relating the nodal and periastron precession frequencies can explain (see Stella et al., 1999) the correlation between two of the observed QPO frequencies found in the fluxes of NSs and BHs LMXBs (see Psaltis et al., 1999, for details). This fact provides, at the same time, a significant test of the Ryan’s analytic expressions.

It is interesting to analyze the level of predictability of the precession and oscillation frequencies on particular astrophysical sources. In Fig. E.9 we show the  $\nu_l$ – $\nu_h$  relation within the RPM model, namely  $\nu_\rho^P$  versus  $\nu_K$  for the models M1–M8 of Table E.2. In the upper panel we show the results for the PRS solution while, in the lower panel, we present the results for the Kerr solution. We have indicated the QPO frequencies observed in the sources GX 5–1 (see e.g. Wijnands et al., 1998; Jonker et al., 2002), 4U 1735–44 (see e.g. Ford et al., 1998), 4U 1636–53 (see e.g. Wijnands et al., 1997), Sco X1 (see e.g. van der Klis et al., 1996), GX 17–2 (see e.g. Homan et al., 2002), GX 340+0 (see e.g. Jonker et al., 2000), Cir X1 (see e.g. van der Klis et al., 1996), 4U 0614+091 (see e.g. Ford et al., 1997), and 4U 1728–34 (see e.g. Strohmayer et al., 1996).

Both the upper and lower panels of Fig. E.9 have been plotted using the same frequency scales in order to aid the identification of the differences between the Kerr and the PRS solutions. One can notice that all the solid curves in the Kerr solution (lower panel of Fig. E.9) are outside the range of the observed QPO frequencies exemplified, while all dashed and solid curves of the PRS are inside the QPO range. It is then clear that making a fit of the observed QPO frequencies of the selected LMXBs of Fig. E.9 will necessarily require a different choice of parameters in the Kerr and PRS solutions. Therefore, conclusions for instance on the NS parameters (e.g. mass, angular momentum, quadrupole deformation) based on fitting QPOs using the Kerr geometry will deviate from the actual parameters (see e.g. Laarakkers and Poisson, 1999, for

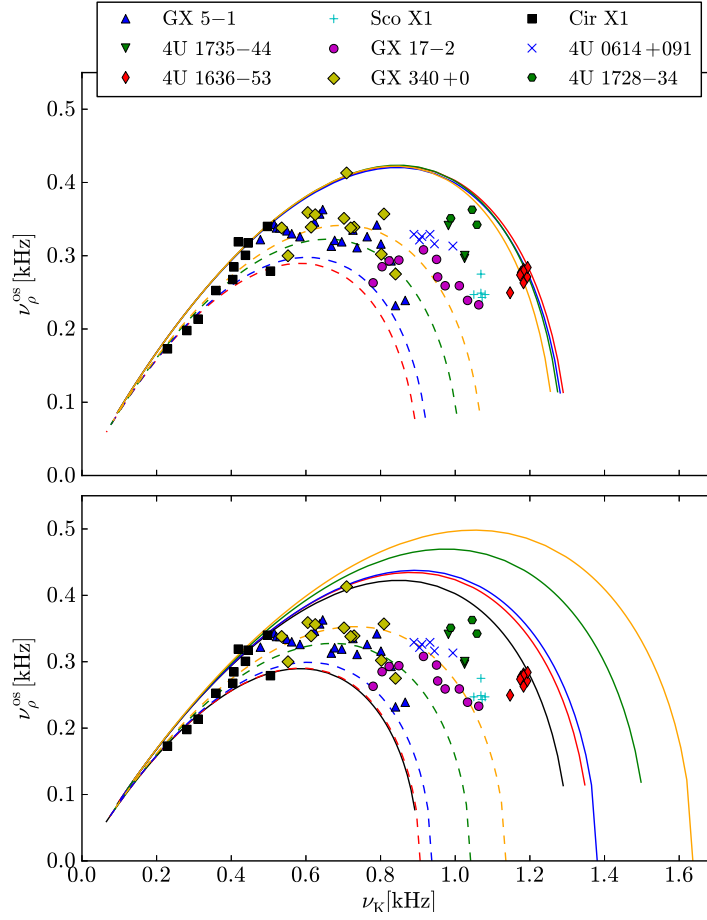


**Figure E.9.:** Periastron oscillation frequency,  $\nu_\rho^{\text{OS}}$ , as a function of the Keplerian frequency  $\nu_K$  for the NS realistic models in Table E.2. We indicate the QPO frequencies observed in the sources GX 5-1, 4U 1735-44, 4U 1636-53, Sco X1, GX 17-2, GX 340+0, Cir X1, 4U 0614+091, and 4U 1728-34. The solid curves depict the results for the models M1 (solid) and M2 (dashed) with red lines, for the models M3 (solid) and M4 (dashed) with blue lines, for the models M5 (solid) and M6 (dashed) with green lines while orange lines stands for the results from models M7 (solid) and M8 (dashed). In the upper panel we present the results derived from the  $\text{PRS}_{s=0}$  solution while in the lower panel we present the results for the Kerr solution. In the lower panel we have added, to guide the eye, the inner red dashed and outer red solid curves of the upper panel using black lines.

details), extractable more reliably from a more complex geometry, such as the PRS one, that allows a better estimate for instance of the quadrupole moment of a compact star.

In Fig. E.9 we show the relation  $\nu_z^P$  versus  $\nu_K$  for the models M1–M8 of Table E.2. For the sake of comparison we show the low frequency branch observed in the LMXB 4U 1728–34 (see Ford and van der Klis, 1998, for details). From the analysis of the pulsating X-ray flux it turns out that very likely the spin frequency of the NS in 4U 1728–34 is  $\sim 363$  Hz (see Strohmayer et al., 1996, for details). Thus, the models M3 ( $M_0 = 1.94M_\odot$ ,  $j = 0.24$ ) and M4 ( $M_0 = 2.71M_\odot$ ,  $j = 0.18$ ) in Table E.2 that correspond to a NS of spin frequency 360 Hz are of particular interest for the analysis of this source. It was suggested by Stella et al. (1999); Stella and Vietri (1999) that the low frequency observed in 4U 1728–34 are likely to be due to excitations of the second harmonic of the vertical motion and therefore a better fit of the lower-higher QPO frequencies of 4U 1728–34 (and of similar sources) will be obtained for the relation  $2\nu_z^P - \nu_K$ . The black curves in Fig. E.10 indicate the  $2\nu_z^P - \nu_K$  relation for the models M3 and M4 (solid and dashed) following the above suggestion. Although the improvement of the fit is evident, we notice that the NS parameters that correctly reproduce the features of 4U 1728–34 are likely in between the models M3 and M4.

### **E.1.7. Concluding Remarks**

We have done an extensive comparison of the orbital motion of neutral test particles in the PRS and Kerr spacetime geometries. In particular we have emphasized on the Keplerian and frame-dragging frequencies, as well as the precession and oscillation frequencies of the radial and vertical motions.

We have evidenced the differences in this respect between the Kerr and PRS solution, especially in the rapid  $\sim$ kHz rotation regime. Such differences are the manifestation of the influence of the high order multipole moments such as the quadrupole and octupole.

The analysis of the deviations between the Kerr and PRS features for given mass and angular momentum of a source studied in this work are useful to distinguish the signatures between BHs and NSs, which relevant to establish a separatrix for the identification of the compact objects harboring in X-Ray Binaries. In the case of BH candidates, these results might become important for testing the no-hair theorem of BHs (see e.g. Johannsen and Psaltis, 2011). Equally important, the application of the precession and oscillation frequencies to the explanation of QPOs in LMXBs possessing a NS, can unveil information on the NS parameters, leading to a possible identification of the behavior of the nuclear matter EoS at supranuclear densities. In this line, the identification of the rotation frequency of NSs in LMXBs from the pulsating X-ray flux  $\nu_{\text{burst}}$ , e.g. the case of 4U 1728–34 (Ford and van der

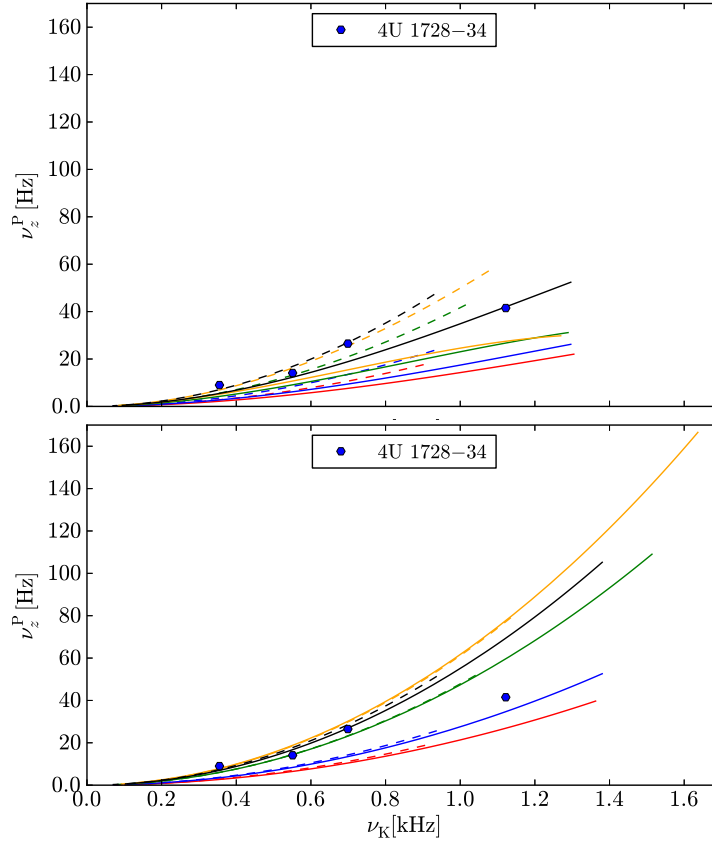


**Figure E.10.:** Nodal precession frequency,  $\nu_z^P$ , as a function of the Keplerian frequency  $\nu_K$  for the NS realistic models in Table E.2. The convention is as Fig. E.9. We indicate the QPO frequencies observed in the LMXB 4U 1728–34 (see Ford and van der Klis, 1998). The black curves indicate the  $2\nu_z^P - \nu_K$  relation for the models M3 and M4 (solid and dashed) following the suggestion of Stella et al. (1999); Stella and Vietri (1999).

Klis, 1998), 4U 1916–053 (Galloway et al., 2001) and more recently the case of IGR J17191–2821 (Altamirano et al., 2010), will certainly help to constrain QPO models as well as the NS parameters. Additional information coming from recent modeling of the photospheric radius expansion phenomena observed in these systems (see e.g. Munro et al., 2001, for details) during their transient activity with Super-Eddington emission can become of paramount importance if combined with the QPO information.

The generalization of the present work to the electrovacuum case is important to establish the influence of the magnetic dipole and quadrupole moments on the orbital motion of particles around compact objects (see e.g. Bakala et al., 2010; Sanabria-Gómez et al., 2010; Bakala et al., 2012).

Interesting effects on the epicyclic frequencies due to the presence of the magnetic dipole have been already pointed out recently by Bakala et al. (2010) and Bakala et al. (2012). These effects were predicted after neglecting the contribution of the electromagnetic field to the curvature, for  $j = 0$  Bakala et al. (2010) and for  $j \neq 0$  Bakala et al. (2012). In Bakala et al. (2010) the authors assume the model of the star as a dipole magnetic field superimposed on a Schwarzschild black hole. In the second work, they studied the case of a magnetized slowly rotating neutron stars; to build the model they superimpose an dipolar magnetic field on the Lense-Thirring geometry. The effects of the magnetic dipole on the location of the ISCO, within the PRS solution, has been investigated by Sanabria-Gómez et al. (2010).

A complete analysis of the effects due to the emergence of electromagnetic structure on the orbital motion of charged particles is therefore of interest and deserve the appropriate attention. Recent observations have shown that for stars with strong magnetic fields the quadrupole and octupole magnetic terms make significant contributions to the magnetic field (Donati et al., 2006), which indicates that arbitrary higher order multipole components might be required in a realistic model. The presence of a magnetic quadrupole demands the breaking of the reflection symmetry (see Pachón and Sanabria-Gómez, 2006, for details), by means of a slightly change to the Ernst electric potential over the symmetry axis

$$f(z) = \frac{qz^2 + i\mu z + i\zeta}{z^3 + z^2(m - ia) - kz + is}, \quad (\text{E.1.31})$$

a quadrupolar magnetic component  $\mathcal{B}_2 = \zeta$  can be introduced to the PRS solution. Such a change generates just a redefinition of the coefficients  $f_i$  in Eq. (E.1.15). In this way the PRS solution can be readily use to explore the effect of strong magnetic fields with non-dipolar structure.

### E.1.8. Supplementary information

#### Metric Functions

The functions  $A$ ,  $B$ ,  $C$ ,  $H$ ,  $G$ ,  $K$ , and  $I$  used to express the metric functions (E.1.17) are given by

$$A = \sum_{1 \leq i < j < k \leq 6} a_{ijk} r_i r_j r_k, \quad B = \sum_{1 \leq i < j \leq 6} b_{ij} r_i r_j, \quad (\text{E.1.32})$$

$$C = \sum_{1 \leq i < j \leq 6} c_{ij} r_i r_j, \quad K = \sum_{1 \leq i < j < k \leq 6} a_{ijk}, \quad (\text{E.1.33})$$

$$H = z A - (\beta_1 + \beta_2 + \beta_3) B + \sum_{1 \leq i < j < k \leq 6} h_{ijk} r_i r_j r_k + \sum_{1 \leq i < j \leq 6} (\alpha_i + \alpha_j) b_{ij} r_i r_j, \quad (\text{E.1.34})$$

$$G = -(\beta_1 + \beta_2 + \beta_3) A + z B + \sum_{1 \leq i < j \leq 6} g_{ij} r_i r_j + \sum_{1 \leq i < j < k \leq 6} (\alpha_i + \alpha_j + \alpha_k) a_{ijk} r_i r_j r_k, \quad (\text{E.1.35})$$

$$I = (f_1 + f_2 + f_3)(A - B) + (\beta_1 + \beta_2 + \beta_3 - z) C + \sum_{1 \leq i < j < k \leq 6} p_{ijk} r_i r_j r_k + \sum_{i=1}^6 p_i r_i + \sum_{1 \leq i < j \leq 6} [p_{ij} - (\alpha_i + \alpha_j) c_{ij}] r_i r_j, \quad (\text{E.1.36})$$

with

$$\begin{aligned} r_i &= \sqrt{\rho^2 + (z - \alpha_i)^2}, \quad a_{ijk} = (-1)^{i+j+1} \Lambda_{ijk} \Gamma_{l|mn}, \quad b_{ij} = (-1)^{i+j} \lambda_{ij} H_{l|mnp}, \\ c_{ij} &= (-1)^{i+j} \lambda_{ij} [f(\alpha_l) \Gamma_{m|np} - f(\alpha_m) \Gamma_{n|pl} + f(\alpha_n) \Gamma_{p|lm} - f(\alpha_p) \Gamma_{l|mn}], \\ h_{ijk} &= (-1)^{i+j+k} \Lambda_{ijk} (e_1^* \delta_{23|lmn} + e_2^* \delta_{31|lmn} + e_3^* \delta_{12|lmn}), \\ g_{ij} &= (-1)^{i+j} \lambda_{ij} (\alpha_l \Gamma_{m|np} - \alpha_m \Gamma_{n|pl} + \alpha_n \Gamma_{p|lm} - \alpha_p \Gamma_{l|mn}), \\ p_i &= (-1)^i D_i [f(\alpha_l) H_{m|nps} - f(\alpha_m) H_{n|psl} + f(\alpha_n) H_{p|slm} - f(\alpha_p) H_{s|lmn} + f(\alpha_s) H_{l|mnp}], \\ p_{ij} &= (-1)^{i+j} \lambda_{ij} (e_1^* Y_{23|lmnp} + e_2^* Y_{31|lmnp} + e_3^* Y_{12|lmnp}), \\ p_{ijk} &= (-1)^{i+j+1} \Lambda_{ijk} (e_1^* \Psi_{23|lmn} + e_2^* \Psi_{31|lmn} + e_3^* \Psi_{12|lmn}), \\ \lambda_{ij} &= (\alpha_i - \alpha_j) D_i D_j, \quad \Lambda_{ijk} = (\alpha_i - \alpha_j)(\alpha_i - \alpha_k)(\alpha_j - \alpha_k) D_i D_j D_k, \\ D_i &= \frac{1}{(\alpha_i - \beta_1)(\alpha_i - \beta_2)(\alpha_i - \beta_3)}, \\ \Gamma_{l|mn} &= H_3(\alpha_l) \Delta_{12|mn} + H_3(\alpha_m) \Delta_{12|nl} + H_3(\alpha_n) \Delta_{12|lm}, \end{aligned}$$

and

$$\begin{aligned} \Delta_{lm|np} &= H_l(\alpha_n) H_m(\alpha_p) - H_l(\alpha_p) H_m(\alpha_n), \\ H_l(\alpha_n) &= \frac{2 \prod_{p \neq n} (\alpha_p - \beta_l^*)}{\prod_{k \neq l} (\beta_l^* - \beta_k^*) \prod_{k=1}^3 (\beta_l^* - \beta_k)} - \sum_{k=1}^3 \frac{2 f_l^* f_k}{(\beta_l^* - \beta_k)(\alpha_n - \beta_k)}, \\ \delta_{lm|nps} &= \Delta_{lm|np} + \Delta_{lm|ps} + \Delta_{lm|sn}, \quad h_{l|mnp} = H_3(\alpha_l) \delta_{12|mnp}, \\ H_{l|mnp} &= h_{l|mnp} + h_{m|npl} + h_{n|plm} + h_{p|lmn}, \\ \Psi_{lm|nps} &= f(\alpha_n) \Delta_{lm|ps} + f(\alpha_p) \Delta_{lm|sn} + f(\alpha_s) \Delta_{lm|np}, \\ Y_{lm|nprs} &= f(\alpha_n) \delta_{lm|prs} - f(\alpha_p) \delta_{lm|rsn} + f(\alpha_r) \delta_{lm|snp} - f(\alpha_s) \delta_{lm|npr}, \end{aligned}$$

being  $\alpha$ 's the roots of the Sibgatullin equation Sibgatullin (1991); Manko and Sibgatullin (1993)

$$e(z) + \tilde{e}(z) + 2\tilde{f}(z)f(z) = 0. \quad (\text{E.1.37})$$

### Kerr's metric in Weyl-Papapetrou quasi-cylindrical coordinates

In order to keep comparisons in the save place, we consider useful to display the Kerr solution in the Weyl-Papapetrou quasi-cylindrical coordinates. For this case,

$$f = \frac{A\bar{A} - B\bar{B}}{(A - B)(\bar{A} - \bar{B})}, \quad e^{2\gamma} = \frac{A\bar{A} - B\bar{B}}{K\bar{K} \prod_{n=1}^2 r_n}, \quad \omega = \frac{\text{Im}[(A + B)\bar{H} - (\bar{A} + \bar{B})G]}{A\bar{A} - B\bar{B}}, \quad (\text{E.1.38})$$

where for our own convenience we do not present the definition of each term, but present the final combination of them, i.e.,

$$\begin{aligned} A\bar{A} - B\bar{B} &= -8 (a^2 - m^2)^3 (\rho^2 + z^2) \left( m^2 \sqrt{-2z\sqrt{m^2 - a^2} - a^2 + m^2 + \rho^2 + z^2} \right. \\ &\quad \left. \sqrt{(\sqrt{m^2 - a^2} + z)^2 + \rho^2} - 2a^2 \sqrt{-2z\sqrt{m^2 - a^2} - a^2 + m^2 + \rho^2 + z^2} \right. \\ &\quad \left. \sqrt{(\sqrt{m^2 - a^2} + z)^2 + \rho^2 + a^2 m^2 - m^4 + m^2 \rho^2 + m^2 z^2} \right), \end{aligned} \quad (\text{E.1.39})$$

$$\begin{aligned}
 (A - B)(\bar{A} - \bar{B}) &= -8 (m^2 - a^2)^3 (\rho^2 + z^2) \\
 &\left( a^2 \left( 2m \left( \sqrt{-2z\sqrt{m^2 - a^2} - a^2 + m^2 + \rho^2 + z^2} + \sqrt{2z\sqrt{m^2 - a^2} - a^2 + m^2 + \rho^2 + z^2} \right) \right. \right. \\
 &+ 2\sqrt{-2z\sqrt{m^2 - a^2} - a^2 + m^2 + \rho^2 + z^2} \sqrt{2z\sqrt{m^2 - a^2} - a^2 + m^2 + \rho^2 + z^2} + 3m^2 \\
 &- m^2 \left( 2m \left( \sqrt{-2z\sqrt{m^2 - a^2} - a^2 + m^2 + \rho^2 + z^2} + \sqrt{2z\sqrt{m^2 - a^2} - a^2 + m^2 + \rho^2 + z^2} \right) \right. \\
 &+ \sqrt{-2z\sqrt{m^2 - a^2} - a^2 + m^2 + \rho^2 + z^2} \sqrt{2z\sqrt{m^2 - a^2} - a^2 + m^2 + \rho^2 + z^2} \\
 &\left. \left. + 3m^2 + \rho^2 + z^2 \right) \right), \tag{E.1.40}
 \end{aligned}$$

$$K\bar{K} \prod_{n=1}^2 r_n = 16 (m^2 - a^2)^4 (\rho^2 + z^2) \sqrt{(z - \sqrt{m^2 - a^2})^2 + \rho^2} \sqrt{(\sqrt{m^2 - a^2} + z)^2 + \rho^2} \tag{E.1.41}$$

$$\begin{aligned}
 \text{Im}[(A + B)\bar{H} - (\bar{A} + \bar{B})G] &= 16am (m^2 - a^2)^3 (\rho^2 + z^2) \\
 &\left( -m^2 \sqrt{-2z\sqrt{m^2 - a^2} - a^2 + m^2 + \rho^2 + z^2} - m \sqrt{-2z\sqrt{m^2 - a^2} - a^2 + m^2 + \rho^2 + z^2} \right. \\
 &\sqrt{(\sqrt{m^2 - a^2} + z)^2 + \rho^2} + a^2 \sqrt{-2z\sqrt{m^2 - a^2} - a^2 + m^2 + \rho^2 + z^2} \\
 &- z \sqrt{m^2 - a^2} \sqrt{-2z\sqrt{m^2 - a^2} - a^2 + m^2 + \rho^2 + z^2} - m^2 \sqrt{(\sqrt{m^2 - a^2} + z)^2 + \rho^2} \\
 &+ a^2 \sqrt{(\sqrt{m^2 - a^2} + z)^2 + \rho^2} + z \sqrt{m^2 - a^2} \sqrt{(\sqrt{m^2 - a^2} + z)^2 + \rho^2} \\
 &\left. + a^2 m - m^3 + m\rho^2 + mz^2 \right). \tag{E.1.42}
 \end{aligned}$$

From here, it is clear how changing  $a \rightarrow -a$  will cause only a global change in the sign of the metric function  $\omega$  and therefore only a change in the  $g_{t\phi}$  metric component.



# Bibliography

«On the critical mass: the case of white dwarfs».

In H. Gursky, R. Ruffini, & L. Stella (ed.), *Exploring the universe: a Festschrift in honor of Riccardo Giacconi "Dedicated to Riccardo Giacconi for his sixty-fifth birthday, on the occasion of his being awarded a "Laurea Honoris Causa" in physics at the University of Rome "La Sapienza". Rome, Italy, October 1997* Singapore: World Scientific, 2000, xii, 383 p., *Advanced series in astrophysics and cosmology*, v.13. Edited by H. Gursky, R. Ruffini, and L. Stella. ISBN 9810244231 (2000).

AKSENOV, A.G., RUFFINI, R. AND VERESHCHAGIN, G.V.

«Thermalization of Nonequilibrium Electron-Positron-Photon Plasmas».  
*Physical Review Letters*, **99(12)**, pp. 125003–+ (2007).

ALCOCK, C., FARHI, E. AND OLINTO, A.

«Strange stars».  
*Astrophysical Journal*, **310**, pp. 261–272 (1986).

ALFORD, M., RAJAGOPAL, K., REDDY, S. AND WILCZEK, F.

«Minimal color-flavor-locked-nuclear interface».  
*Physical Review D*, **64(7)**, pp. 074017–+ (2001).

ALLEN, M.P. AND HORVATH, J.E.

«Influence of an Internal Magnetar on Supernova Remnant Expansion».  
*Astrophysical Journal*, **616**, pp. 346–356 (2004).

ALTAMIRANO, D., WATTS, A., LINARES, M., MARKWARDT, C.B., STROHMAYER, T. AND PATRUNO, A.

«Type I X-ray bursts and burst oscillations in the accreting millisecond X-ray pulsar IGR J17511-3057».  
*Monthly Notices of the Royal Astronomical Society*, **409**, pp. 1136–1145 (2010).

ALTHAUS, L.G., GARCÍA-BERRO, E., ISERN, J. AND CÓRSICO, A.H.

«Mass-radius relations for massive white dwarf stars».  
*Astronomy & Astrophysics*, **441**, pp. 689–694 (2005).

ALTHAUS, L.G., GARCÍA-BERRO, E., ISERN, J., CÓRSICO, A.H. AND ROHRMANN, R.D.

«The age and colors of massive white dwarf stars».  
*Astronomy & Astrophysics*, **465**, pp. 249–255 (2007).

- ALTHAUS, L.G., GARCÍA-BERRO, E., RENEDO, I., ISERN, J., CÓRSICO, A.H. AND ROHRMANN, R.D.  
«Evolution of White Dwarf Stars with High-metallicity Progenitors: The Role of  $^{22}\text{Ne}$  Diffusion».  
*Astrophysical Journal*, **719**, pp. 612–621 (2010).
- ANAND, S.P.S.  
«On Chandrasekhar’s Limiting Mass for Rotating White Dwarf Stars».  
*Proceedings of the National Academy of Science*, **54**, pp. 23–26 (1965).
- ANGEL, J.R.P., BORRA, E.F. AND LANDSTREET, J.D.  
«The magnetic fields of white dwarfs».  
*Astrophysical Journal Supplement Series*, **45**, pp. 457–474 (1981).
- ANTONIADIS, J., VAN KERKWIJK, M.H., KOESTER, D., FREIRE, P.C.C., WEX, N., TAURIS, T.M., KRAMER, M. AND BASSA, C.G.  
«The relativistic pulsar-white dwarf binary PSR J1738+0333 - I. Mass determination and evolutionary history».  
*Monthly Notices of the Royal Astronomical Society*, **423**, pp. 3316–3327 (2012).
- ARUTYUNYAN, G.G., SEDRAKYAN, D.M. AND CHUBARYAN, É.V.  
«Rotating white dwarfs in the general relativity theory».  
*Astrophysics*, **7**, pp. 274–280 (1971).
- AUDI, G., WAPSTRA, A.H. AND THIBAUT, C.  
«The Ame2003 atomic mass evaluation (II). Tables, graphs and references».  
*Nuclear Physics A*, **729**, pp. 337–676 (2003a).
- AUDI, G., WAPSTRA, A.H. AND THIBAUT, C.  
«The Ame2003 atomic mass evaluation (II). Tables, graphs and references».  
*Nuclear Physics A*, **729**, pp. 337–676 (2003b).
- BAKALA, P., URBANEC, M., ŠRÁMKOVÁ, E., STUHLÍK, Z. AND TÖRÖK, G.  
«On magnetic-field-induced corrections to the orbital and epicyclic frequencies: paper II. Slowly rotating magnetized neutron stars».  
*Classical and Quantum Gravity*, **29(6)**, p. 065012 (2012).
- BAKALA, P., ŠRÁMKOVÁ, E., STUHLÍK, Z. AND TÖRÖK, G.  
«On magnetic-field-induced non-geodesic corrections to relativistic orbital and epicyclic frequencies».  
*Classical and Quantum Gravity*, **27(4)**, p. 045001 (2010).
- BARSTOW, M.A., JORDAN, S., O’DONOGHUE, D., BURLEIGH, M.R., NAPIWOTZKI, R. AND HARROP-ALLIN, M.K.  
«RE J0317-853: the hottest known highly magnetic DA white dwarf».  
*Monthly Notices of the Royal Astronomical Society*, **277**, pp. 971–985 (1995).

- BAYM, G., BETHE, H.A. AND PETHICK, C.J.  
«Neutron star matter».  
*Nuclear Physics A*, **175**, pp. 225–271 (1971a).
- BAYM, G., PETHICK, C. AND SUTHERLAND, P.  
«The Ground State of Matter at High Densities: Equation of State and Stellar Models».  
*Astrophysical Journal*, **170**, pp. 299–+ (1971b).
- BAYM, G. AND PINES, D.  
«Neutron starquakes and pulsar speedup.»  
*Annals of Physics*, **66**, pp. 816–835 (1971).
- BELL, S.J. AND HEWISH, A.  
«Angular Size and Flux Density of the Small Source in the Crab Nebula at 81.5 Mc/s».  
*Nature*, **213**, pp. 1214–1216 (1967).
- BELVEDERE, R., PUGLIESE, D., RUEDA, J.A., RUFFINI, R. AND XUE, S.S.  
«Neutron star equilibrium configurations within a fully relativistic theory with strong, weak, electromagnetic, and gravitational interactions».  
*Nuclear Physics A*, **883**, pp. 1–24 (2012).
- BENHAR, O., FERRARI, V., GUALTIERI, L. AND MARASSI, S.  
«Perturbative approach to the structure of rapidly rotating neutron stars».  
*Physical Review D*, **72(4)**, pp. 044028–+ (2005).
- BERNARDINI, F., ISRAEL, G.L., DALL’OSSO, S., STELLA, L., REA, N., ZANE, S., TUROLLA, R., PERNA, R., FALANGA, M., CAMPANA, S. ET AL.  
«From outburst to quiescence: the decay of the transient AXP XTE J1810-197».  
*Astronomy & Astrophysics*, **498**, pp. 195–207 (2009).
- BERNARDINI, M.G., BIANCO, C.L., CAITO, L., DAINOTTI, M.G., GUIDA, R. AND RUFFINI, R.  
«Grb980425 and the puzzling urca1 emission».  
In R.T. Jantzen, H. Kleinert and R. Ruffini (eds.), *The Eleventh Marcel Grossmann Meeting* (Singapore: World Scientific, 2008).
- BERNARDINI, M.G., BIANCO, C.L., CHARDONNET, P., FRASCHETTI, F., RUFFINI, R. AND XUE, S.S.  
«A new astrophysical "trilogy": Grb030329/sn2003dh/urca-2».  
In E. Fenimore and M. Galassi (eds.), *Gamma-Ray Bursts: 30 Years of Discovery*, volume 727 of *American Institute of Physics Conference Series*, pp. 312–315 (2004).

- BERNARDINI, M.G., BIANCO, C.L., CHARDONNET, P., FRASCHETTI, F., RUFFINI, R. AND XUE, S.S.  
«Theoretical interpretation of the luminosity and spectral properties of grb 031203».  
*ApJ*, **634**, pp. L29–L32 (2005a).
- BERNARDINI, M.G., BIANCO, C.L., RUFFINI, R., XUE, S.S., CHARDONNET, P. AND FRASCHETTI, F.  
«General features of grb 030329 in the embh model».  
In M. Novello, S. Perez Bergliaffa and R. Ruffini (eds.), *The Tenth Marcel Grossmann Meeting. On recent developments in theoretical and experimental general relativity, gravitation and relativistic field theories*, p. 2459 (Singapore: World Scientific, 2005b).
- BERTI, E. AND STERGIIOULAS, N.  
«Approximate matching of analytic and numerical solutions for rapidly rotating neutron stars».  
*Monthly Notices of the Royal Astronomical Society*, **350**, pp. 1416–1430 (2004).
- BERTI, E., WHITE, F., MANIOPOULOU, A. AND BRUNI, M.  
«Rotating neutron stars: an invariant comparison of approximate and numerical space-time models».  
*Monthly Notices of the Royal Astronomical Society*, **358**, pp. 923–938 (2005).
- BERTONE, G. AND RUFFINI, R.  
«Equilibrium configurations of relativistic white dwarfs».  
*Nuovo Cimento B Serie*, **115**, pp. 935–+ (2000).
- BETHE, H.A.  
*Energy production in stars. Nobel lecture.* (1968).
- BHATTACHARYYA, S., STROHMAYER, T.E., MILLER, M.C. AND MARKWARDT, C.B.  
«Constraints on Neutron Star Parameters from Burst Oscillation Light Curves of the Accreting Millisecond Pulsar XTE J1814-338».  
*Astrophysical Journal*, **619**, pp. 483–491 (2005).
- BILDSTEN, L. AND HALL, D.M.  
«Gravitational Settling of  $^{22}\text{Ne}$  in Liquid White Dwarf Interiors».  
*Astrophysical Journal*, **549**, pp. L219–L223 (2001).
- BLASCHKE, D., KLAHN, T. AND VOSKRESENSKY, D.  
«Diquark condensates and compact star cooling».  
*ApJ*, **533**, p. 406412 (2000).
- BLASCHKE, D., VOSKRESENSKY, D. AND GRIGORIAN, H.  
«Cooling of Neutron Stars with Color Superconducting Quark Cores».

- Nuclear Physics A*, **774**, pp. 815–818 (2006).  
ISSN 03759474.
- BOCCALETTI, D. AND RUFFINI, R.  
*Fermi and Astrophysics* (World Scientific, Singapore, 2010).
- BOGUTA, J. AND BODMER, A.R.  
«Relativistic calculation of nuclear matter and the nuclear surface».  
*Nuclear Physics A*, **292**, pp. 413–428 (1977).
- BORKOWSKI, J., GOTZ, D., MEREGHETTI, S., MOWLAVI, N., SHAW, S. AND  
TURLER, M.  
«Giant flare from Sgr 1806-20 detected by INTEGRAL.»  
*GRB Coordinates Network*, **2920**, pp. 1–+ (2004).
- BOSHKAYEV, K., RUEDA, J.A., RUFFINI, R. AND SIUTSOU, I.  
«On general relativistic uniformly rotating white dwarfs».  
*Astrophysical Journal*, *in press* (2012).
- BOWERS, R.L., CAMPBELL, J.A. AND ZIMMERMAN, R.L.  
«Relativistic Baryon Effective Masses and Thresholds for Strongly Interact-  
ing Superdense Matter».  
*Physical Review D*, **8**, pp. 1077–1087 (1973a).
- BOWERS, R.L., CAMPBELL, J.A. AND ZIMMERMAN, R.L.  
«Relativistic Many-Body Theory for Strongly Interacting Matter».  
*Physical Review D*, **7**, pp. 2278–2288 (1973b).
- BRETÓN, N., MANKO, V.S. AND AGUILAR SÁNCHEZ, J.  
«On the equilibrium of charged masses in general relativity: II. The sta-  
tionary electrovacuum case».  
*Classical and Quantum Gravity*, **16**, pp. 3725–3734 (1999).
- BÜRVENICH, T.J., MISHUSTIN, I.N. AND GREINER, W.  
«Nuclei embedded in an electron gas».  
*Physical Review C*, **76(3)**, pp. 034310–+ (2007).
- CAMERON, A.G.W.  
«Pycnonuclear Reactions and Nova Explosions.»  
*Astrophysical Journal*, **130**, p. 916 (1959).
- CAMERON, A.G.W.  
«Neutron Stars».  
*Annual Review of Astronomy and Astrophysics*, **8**, pp. 179–+ (1970).
- CANUTO, V.  
«Neutron stars».

- In R. Giacconi and R. Ruffini (eds.), *Physics and Astrophysics of Neutron Stars and Black Holes*, pp. 448–527 (1978).
- CARDELLI, J.A., CLAYTON, G.C. AND MATHIS, J.S.  
«The relationship between infrared, optical, and ultraviolet extinction».  
*Astrophysical Journal*, **345**, pp. 245–256 (1989).
- CASTRO-TIRADO, A.J., DE UGARTE POSTIGO, A., GOROSABEL, J., JELÍNEK, M., FATKHULLIN, T.A., SOKOLOV, V.V., FERRERO, P., KANN, D.A., KLOSE, S., SLUSE, D. ET AL.  
«Flares from a candidate Galactic magnetar suggest a missing link to dim isolated neutron stars».  
*Nature*, **455**, pp. 506–509 (2008).
- CHABRIER, G. AND POTEKHIN, A.Y.  
«Equation of state of fully ionized electron-ion plasmas».  
*Physical Review E*, **58**, pp. 4941–4949 (1998).
- CHANDRASEKHAR, S.  
«The highly collapsed configurations of a stellar mass».  
*Monthly Notices of the Royal Astronomical Society*, **91**, pp. 456–466 (1931a).
- CHANDRASEKHAR, S.  
«The Maximum Mass of Ideal White Dwarfs».  
*Astrophysical Journal*, **74**, pp. 81–+ (1931b).
- CHANDRASEKHAR, S.  
«The highly collapsed configurations of a stellar mass (Second paper)».  
*Monthly Notices of the Royal Astronomical Society*, **95**, pp. 207–225 (1935).
- CHANDRASEKHAR, S.  
*An introduction to the study of stellar structure* (1939).
- CHANDRASEKHAR, S.  
*Ellipsoidal figures of equilibrium* (1969).
- CHANDRASEKHAR, S.  
«The Effect of Gravitational Radiation on the Secular Stability of the Maclaurin Spheroid».  
*Astrophysical Journal*, **161**, p. 561 (1970).
- CHANDRASEKHAR, S.  
*The mathematical theory of black holes* (1992).
- CHERUBINI, C., GERALICO, A., J. A. RUEDA, H. AND RUFFINI, R.  
« $e^- - e^+$  pair creation by vacuum polarization around electromagnetic black holes».  
*Physical Review D*, **79(12)**, pp. 124002–+ (2009).

- CHEVALIER, R.A.  
«Neutron star accretion in a supernova».  
*ApJ*, **346**, p. 847 (1989).  
ISSN 0004-637X.
- CHOI, C.S. AND DOTANI, T.  
«A Flare of AE Aquarii Observed with XMM-Newton».  
*Astrophysical Journal*, **646**, pp. 1149–1159 (2006).
- CHRISTIANSEN, M.B. AND GLENDENNING, N.K.  
«Finite size effects and the mixed quark-hadron phase in neutron stars».  
*Physical Review C*, **56**, pp. 2858–2864 (1997).
- CHRISTIANSEN, M.B., GLENDENNING, N.K. AND SCHAFFNER-BIELICH, J.  
«Surface tension between a kaon condensate and the normal nuclear matter phase».  
*Physical Review C*, **62(2)**, pp. 025804–+ (2000).
- CIUFOLINI, I. AND RUFFINI, R.  
«Equilibrium configurations of neutron stars and the parametrized post-Newtonian metric theories of gravitation».  
*Astrophysical Journal*, **275**, pp. 867–877 (1983).
- COHEN, R.H., COPPI, B. AND TREVES, A.  
«Magnetic Configuration in the Neighborhood of a Collapsed Star».  
*Astrophysical Journal*, **179**, pp. 269–276 (1973).
- COOK, G.B., SHAPIRO, S.L. AND TEUKOLSKY, S.A.  
«Rapidly rotating neutron stars in general relativity: Realistic equations of state».  
*Astrophysical Journal*, **424**, pp. 823–845 (1994).
- COPPI, B., PELLAT, R., ROSENBLUTH, M., RUTHERFORD, P. AND GALVAO, R.  
«Resistive internal kink modes».  
*Soviet Journal of Plasma Physics*, **2**, pp. 961–966 (1976).
- DAINOTTI, M.G., BERNARDINI, M.G., BIANCO, C.L., CAITO, L., GUIDA, R. AND RUFFINI, R.  
«Grb 060218 and grbs associated with supernovae ib/c».  
*A&A*, **471**, pp. L29–L32 (2007).
- DAINOTTI, M., BERNARDINI, M.G., BIANCO, C.L., CAITO, L., GUIDA, R. AND RUFFINI, R.  
«The astrophysical triptych: Grb, sn and urca can be extended to grb060218?»  
*J. Kor. Phys. Soc.*, **56**, p. 1588 (2010).

- DAVIES, S.R., COE, M.J. AND WOOD, K.S.  
«HEAO-1 observations of the X-ray pulsar 1E2259 + 586».  
*Monthly Notices of the Royal Astronomical Society*, **245**, pp. 268–274 (1990).
- DE JAGER, O.C., MEINTJES, P.J., O'DONOGHUE, D. AND ROBINSON, E.L.  
«The Discovery of a Brake on the White Dwarf in Ae-Aquarii».  
*Monthly Notices of the Royal Astronomical Society*, **267**, pp. 577–+ (1994).
- DEBYE, P. AND HUECKERL, E.  
*Phyz. Zeitschr.*, **24**, p. 185 (1923).
- DEMOREST, P.B., PENNUCCI, T., RANSOM, S.M., ROBERTS, M.S.E. AND HESSELS, J.W.T.  
«A two-solar-mass neutron star measured using Shapiro delay».  
*Nature*, **467**, pp. 1081–1083 (2010a).
- DEMOREST, P.B., PENNUCCI, T., RANSOM, S.M., ROBERTS, M.S.E. AND HESSELS, J.W.T.  
«A two-solar-mass neutron star measured using Shapiro delay».  
*Nature*, **467**, pp. 1081–1083 (2010b).
- DHILLON, V.S., MARSH, T.R., HULLEMAN, F., VAN KERKWIJK, M.H., SHEARER, A., LITTLEFAIR, S.P., GAVRIIL, F.P. AND KASPI, V.M.  
«High-speed, multicolour optical photometry of the anomalous X-ray pulsar 4U 0142+61 with ULTRACAM».  
*Monthly Notices of the Royal Astronomical Society*, **363**, pp. 609–614 (2005).
- DIB, R., KASPI, V.M. AND GAVRIIL, F.P.  
«Rossi X-Ray Timing Explorer Monitoring of the Anomalous X-ray Pulsar 1E 1048.1 - 5937: Long-term Variability and the 2007 March Event».  
*Astrophysical Journal*, **702**, pp. 614–630 (2009).
- DIRAC, P.A.M.  
*Proc. Cambridge Phil. Soc.*, **26**, pp. 376–+ (1930).
- DONATI, J.F., HOWARTH, I.D., JARDINE, M.M., PETIT, P., CATALA, C., LANDSTREET, J.D., BOURET, J.C., ALECIAN, E., BARNES, J.R., FORVEILLE, T. ET AL.  
«The surprising magnetic topology of  $\tau$  Sco: fossil remnant or dynamo output?»  
*Monthly Notices of the Royal Astronomical Society*, **370**, pp. 629–644 (2006).
- DOUCHIN, F. AND HAENSEL, P.  
«A unified equation of state of dense matter and neutron star structure».  
*Astronomy & Astrophysics*, **380**, pp. 151–167 (2001).

- DUBEIBE, F.L., PACHÓN, L.A. AND SANABRIA-GÓMEZ, J.D.  
«Chaotic dynamics around astrophysical objects with nonisotropic stresses».  
*Physical Review D*, **75**(2), pp. 023008–+ (2007).
- DUERR, H.  
«Relativistic Effects in Nuclear Forces».  
*Physical Review*, **103**, pp. 469–480 (1956).
- DUNCAN, R.C. AND THOMPSON, C.  
«Formation of very strongly magnetized neutron stars - Implications for gamma-ray bursts».  
*Astrophysical Journal*, **392**, pp. L9–L13 (1992).
- DUNCAN, R.C., SHAPIRO, S.L. AND WASSERMAN, I.  
«Neutrino-driven winds from young, hot neutron stars».  
*ApJ*, **309**, p. 141 (1986).  
ISSN 0004-637X.
- DURANT, M., KARGALTSEV, O. AND PAVLOV, G.G.  
*Astrophysical Journal*, in press; *arXiv:1108.3340* (2011).
- DURANT, M. AND VAN KERKWIJK, M.H.  
«Multiwavelength Variability of the Magnetar 4U 0142+61».  
*Astrophysical Journal*, **652**, pp. 576–583 (2006).
- DURISEN, R.H.  
«Viscous Effects in Rapidly Rotating Stars with Application to White-Dwarf Models. Theory and Techniques».  
*Astrophysical Journal*, **183**, pp. 205–214 (1973).
- DURISEN, R.H.  
«Upper mass limits for stable rotating white dwarfs».  
*Astrophysical Journal*, **199**, pp. 179–183 (1975).
- EDDINGTON, SIR, A.S.  
«On "relativistic degeneracy,"».  
*Monthly Notices of the Royal Astronomical Society*, **95**, pp. 194–206 (1935).
- EMDEN, R.  
*Gaskugeln Anwendungen der Mechanischen Wärmetheorie auf Kosmologische und Meteorologische Probleme* (Leipzig, Teubner, Berlin, 1907).
- ERACLEOUS, M., PATTERSON, J. AND HALPERN, J.  
«A search for periodicities in the X-ray emission from cataclysmic variables».  
*Astrophysical Journal*, **370**, pp. 330–340 (1991).

- ERNST, F.J.  
«New Formulation of the Axially Symmetric Gravitational Field Problem».  
*Physical Review*, **167**, pp. 1175–1177 (1968a).
- ERNST, F.J.  
«New Formulation of the Axially Symmetric Gravitational Field Problem.  
II».  
*Physical Review*, **172**, pp. 1850–1850 (1968b).
- ESPOSITO, P., ISRAEL, G.L., TUROLLA, R., TIENGO, A., GÖTZ, D., DE LUCA,  
A., MIGNANI, R.P., ZANE, S., REA, N., TESTA, V. ET AL.  
«Early X-ray and optical observations of the soft gamma-ray repeater  
SGR0418+5729».  
*Monthly Notices of the Royal Astronomical Society*, **405**, pp. 1787–1795 (2010).
- EVERITT, C.W.F., DEBRA, D.B., PARKINSON, B.W., TURNEAURE, J.P., CON-  
KLIN, J.W., HEIFETZ, M.I., KEISER, G.M., SILBERGLEIT, A.S., HOLMES,  
T., KOLODZIEJCZAK, J. ET AL.  
«Gravity Probe B: Final Results of a Space Experiment to Test General Rel-  
ativity».  
*Physical Review Letters*, **106(22)**, 221101 (2011).
- FAHLMAN, G.G. AND GREGORY, P.C.  
«An X-ray pulsar in SNR G109.1-1.0».  
*Nature*, **293**, pp. 202–204 (1981).
- FERMI, E. (ed.).  
*Nuclear physics* (1950).
- FERMI-LAT COLLABORATION.  
«Gamma-ray flares from the Crab Nebula».  
*arXiv:1011.3855* (2010).
- FERRARI, A. AND RUFFINI, R.  
«Theoretical Implications of the Second Time Derivative of the Period of  
the Pulsar NP 0532».  
*Astrophysical Journal*, **158**, pp. L71+ (1969).
- FERRARIO, L., VENNES, S., WICKRAMASINGHE, D.T., BAILEY, J.A. AND  
CHRISTIAN, D.J.  
«EUVE J0317-855 A rapidly rotating, high-field magnetic white dwarf».  
*Monthly Notices of the Royal Astronomical Society*, **292**, pp. 205–+ (1997).
- FERRARIO, L. AND WICKRAMASINGHE, D.  
«Modelling of isolated radio pulsars and magnetars on the fossil field hy-  
pothesis».  
*Monthly Notices of the Royal Astronomical Society*, **367**, pp. 1323–1328 (2006).

- FERRARIO, L., WICKRAMASINGHE, D., LIEBERT, J. AND WILLIAMS, K.A.  
«The open-cluster initial-final mass relationship and the high-mass tail of the white dwarf distribution».  
*Monthly Notices of the Royal Astronomical Society*, **361**, pp. 1131–1135 (2005).
- FERRARIO, L. AND WICKRAMASINGHE, D.T.  
«Magnetic fields and rotation in white dwarfs and neutron stars».  
*Monthly Notices of the Royal Astronomical Society*, **356**, pp. 615–620 (2005).
- FERREIRINHO, J., RUFFINI, R. AND STELLA, L.  
«On the relativistic Thomas-Fermi model».  
*Physics Letters B*, **91**, pp. 314–316 (1980).
- FEYNMAN, R.P., METROPOLIS, N. AND TELLER, E.  
«Equations of State of Elements Based on the Generalized Fermi-Thomas Theory».  
*Physical Review*, **75**, pp. 1561–1573 (1949).
- FORD, E.C., KAARET, P., CHEN, K., TAVANI, M., BARRET, D., BLOSER, P., GRINDLAY, J., HARMON, B.A., PACIASAS, W.S. AND ZHANG, S.N.  
«Energy Spectra and High-Frequency Oscillations in 4U 0614+091».  
*Astrophysical Journal*, **486**, p. L47 (1997).
- FORD, E.C. AND VAN DER KLIS, M.  
«Strong Correlation between Noise Features at Low Frequency and the Kilohertz Quasi-Periodic Oscillations in the X-Ray Binary 4U 1728-34».  
*Astrophysical Journal*, **506**, pp. L39–L42 (1998).
- FORD, E.C., VAN DER KLIS, M., VAN PARADIJS, J., MÉNDEZ, M., WIJNANDS, R. AND KAARET, P.  
«Discovery of a Second Kilohertz QPO in the X-Ray Binary 4U 1735-44».  
*Astrophysical Journal*, **508**, pp. L155–L158 (1998).
- FOWLER, R.H.  
«On dense matter».  
*Monthly Notices of the Royal Astronomical Society*, **87**, pp. 114–122 (1926).
- FRASCHETTI, F., BERNARDINI, M.G., BIANCO, C.L., RUFFINI, R., XUE, S.S. AND CHARDONNET, P.  
«Inferences on the ism structure around grb 980425 and grb 980425-sn1998bw association in the embh model».  
In M. Novello, S. Perez Bergliaffa and R. Ruffini (eds.), *The Tenth Marcel Grossmann Meeting. On recent developments in theoretical and experimental general relativity, gravitation and relativistic field theories*, p. 2451 (Singapore: World Scientific, 2005).

FRENKEL, Y.I.

*Zeit. fur Phys.*, **50**, p. 234 (1928).

FRIEDMAN, J.L., IPSER, J.R. AND SORKIN, R.D.

«Turning-point method for axisymmetric stability of rotating relativistic stars».

*Astrophysical Journal*, **325**, pp. 722–724 (1988).

FRIEDMAN, J.L., PARKER, L. AND IPSER, J.R.

«Rapidly rotating neutron star models».

*Astrophysical Journal*, **304**, pp. 115–139 (1986).

GAENSLER, B.M., SLANE, P.O., GOTTHELF, E.V. AND VASISHT, G.

«Anomalous X-Ray Pulsars and Soft Gamma-Ray Repeaters in Supernova Remnants».

*Astrophysical Journal*, **559**, pp. 963–972 (2001).

GALAMA, T.J., VREESWIJK, P.M., VAN PARADIJS, J., KOUVELIOTOU, C., AUGUSTEIJN, T., BÖHNHARDT, H., BREWER, J.P., DOUBLIER, V., GONZALEZ, J.F., LEIBUNDGUT, B. ET AL.

«An unusual supernova in the error box of the  $\gamma$ -ray burst of 25 april 1998».

*Nature*, **395**, pp. 670–672 (1998).

GALLOWAY, D.K., CHAKRABARTY, D., MUNO, M.P. AND SAVOV, P.

«Discovery of a 270 Hertz X-Ray Burst Oscillation in the X-Ray Dipper 4U 1916-053».

*Astrophysical Journal*, **549**, pp. L85–L88 (2001).

GAMOW, G.

*My world line: An informal autobiography.* (1970).

GAMOW, G. AND SCHOENBERG, M.

«Neutrino Theory of Stellar Collapse».

*Physical Review*, **59**, pp. 539–547 (1941).

GARCIA-BERRO, E., HERNANZ, M., ISERN, J. AND MOCHKOVITCH, R.

«Properties of high-density binary mixtures and the age of the universe from white dwarf stars».

*Nature*, **333**, pp. 642–644 (1988).

GARCÍA-BERRO, E., LORÉN-AGUILAR, P., AZNAR-SIGUÁN, G., TORRES, S., CAMACHO, J., ALTHAUS, L.G., CÓRSICO, A.H., KÜLEBI, B. AND ISERN, J.

«Double Degenerate Mergers as Progenitors of High-field Magnetic White Dwarfs».

*Astrophysical Journal*, **749**, 25 (2012).

- GARCÍA-BERRO, E., TORRES, S., ALTHAUS, L.G., RENEDO, I., LORÉN-AGUILAR, P., CÓRSICO, A.H., ROHRMANN, R.D., SALARIS, M. AND ISERN, J.  
«A white dwarf cooling age of 8Gyr for NGC 6791 from physical separation processes».  
*Nature*, **465**, pp. 194–196 (2010a).
- GARCÍA-BERRO, E., TORRES, S., ALTHAUS, L.G., RENEDO, I., LORÉN-AGUILAR, P., CÓRSICO, A.H., ROHRMANN, R.D., SALARIS, M. AND ISERN, J.  
«A white dwarf cooling age of 8Gyr for NGC 6791 from physical separation processes».  
*Nature*, **465**, pp. 194–196 (2010b).
- GASQUES, L.R., AFANASJEV, A.V., AGUILERA, E.F., BEARD, M., CHAMON, L.C., RING, P., WIESCHER, M. AND YAKOVLEV, D.G.  
«Nuclear fusion in dense matter: Reaction rate and carbon burning».  
*Physical Review C*, **72(2)**, 025806 (2005).
- GELFAND, J.D. AND GAENSLER, B.M.  
«The Compact X-Ray Source 1E 1547.0-5408 and the Radio Shell G327.24-0.13: A New Proposed Association between a Candidate Magnetar and a Candidate Supernova Remnant».  
*Astrophysical Journal*, **667**, pp. 1111–1118 (2007).
- GEROYANNIS, V.S. AND HADJOPOULOS, A.A.  
«Models of white dwarfs under rapid uniform or differential rotation - Numerical results».  
*Astrophysical Journal Supplement Series*, **70**, pp. 661–677 (1989).
- GEROYANNIS, V.S. AND PAPANOTIRIOU, P.J.  
«Spin-up and Spin-down of Rotating Magnetic White Dwarfs: A Straight-forward Numerical Approach».  
*Astrophysical Journal*, **534**, pp. 359–366 (2000).
- GIACCONI, R.  
*The dawn of x-ray astronomy. Nobel lecture.* (2002).
- GIACCONI, R. AND RUFFINI, R. (eds.).  
*Physics and astrophysics of neutron stars and black holes* (1978 Reprinted 2010).
- GINZBURG, V.L.  
«The Magnetic Fields of Collapsing Masses and the Nature of Superstars».  
*Soviet Physics Doklady*, **9**, pp. 329–+ (1964).
- GLENDENNING, N.K.

- «First-order phase transitions with more than one conserved charge: Consequences for neutron stars».  
*Physical Review D*, **46**, pp. 1274–1287 (1992).
- GLENDENNING, N.K.  
«Phase transitions and crystalline structures in neutron star cores».  
*Physics Reports*, **342**, pp. 393–447 (2001).
- GLENDENNING, N.K. AND PEI, S.  
«Crystalline structure of the mixed confined-deconfined phase in neutron stars».  
*Physical Review C*, **52**, pp. 2250–2253 (1995).
- GLENDENNING, N.K. AND SCHAFFNER-BIELICH, J.  
«First order kaon condensate».  
*Physical Review C*, **60(2)**, pp. 025803–+ (1999).
- GNEDIN, O.Y., YAKOVLEV, D.G. AND POTEKHIN, A.Y.  
«Thermal relaxation in young neutron stars».  
*MNRAS*, **324(3)**, pp. 725–736 (2001).  
ISSN 0035-8711.
- GÖHLER, E., WILMS, J. AND STAUBERT, R.  
«XMM-Newton observation of the anomalous X-ray pulsar 4U 0142+61».  
*Astronomy & Astrophysics*, **433**, pp. 1079–1083 (2005).
- GOLDSTEIN, A., PREECE, R.D., BRIGGS, M.S., VAN DER HORST, A.J., MCBREEN, S., KOUVELIOTOU, C., CONNAUGHTON, V., PACIESAS, W.S., MEEGAN, C.A., BHAT, P.N. ET AL.  
«A New Derivation of GRB Jet Opening Angles from the Prompt Gamma-Ray Emission».  
*arXiv:1101.2458* (2011).
- GOMBÁS, P.  
*Die Statistische Theorie des Atoms und Ihre Anwendungen* (1949).
- GORIELY, S., BAUSWEIN, A. AND JANKA, H.T.  
«r-process Nucleosynthesis in Dynamically Ejected Matter of Neutron Star Mergers».  
*Astrophysical Journal*, **738**, pp. L32+ (2011a).
- GORIELY, S., CHAMEL, N., JANKA, H.T. AND PEARSON, J.M.  
«The decompression of the outer neutron star crust and r-process nucleosynthesis».  
*Astronomy & Astrophysics*, **531**, A78 (2011b).

- GREENBERG, J.S. AND GREINER, W.  
«Search for the sparking of the vacuum».  
*Physics Today*, **35**, pp. 24–35 (1982).
- GREGORY, P.C. AND FAHLMAN, G.G.  
«An extraordinary new celestial X-ray source».  
*Nature*, **287**, pp. 805–+ (1980).
- GREINER, J., PEIMBERT, M., ESTABAN, C., KAUFER, A., JAUNSEN, A.,  
SMOKE, J., KLOSE, S. AND REIMER, O.  
«Redshift of GRB 030329.»  
*GCN Circ.*, **2020** (2003).
- GRIGORIAN, H., BLASCHKE, D. AND VOSKRESENSKY, D.  
«Cooling of neutron stars with color superconducting quark cores».  
*Phys. Rev. C*, **71(4)**, pp. 1–8 (2005).  
ISSN 0556-2813.
- GUDMUNDSSON, E.H., PETHICK, C.J. AND EPSTEIN, R.I.  
«Structure of neutron star envelopes».  
*ApJ*, **272**, p. 286 (1983).  
ISSN 0004-637X.
- HAENSEL, P. AND PICHON, B.  
«Experimental nuclear masses and the ground state of cold dense matter».  
*Astronomy & Astrophysics*, **283**, pp. 313–318 (1994).
- HAENSEL, P., POTEKHIN, A.Y. AND YAKOVLEV, D.G. (eds.).  
*Neutron Stars 1 : Equation of State and Structure*, volume 326 of *Astrophysics  
and Space Science Library* (2007).
- HAENSEL, P. AND ZDUNIK, J.L.  
«Equation of state and structure of the crust of an accreting neutron star».  
*Astronomy & Astrophysics*, **229**, pp. 117–122 (1990a).
- HAENSEL, P. AND ZDUNIK, J.L.  
«Non-equilibrium processes in the crust of an accreting neutron star».  
*Astronomy & Astrophysics*, **227**, pp. 431–436 (1990b).
- HAMADA, T. AND SALPETER, E.E.  
«Models for Zero-Temperature Stars.»  
*Astrophysical Journal*, **134**, pp. 683–+ (1961).
- HANSEN, B.M.S.  
«Stellar Collisions and Pulsar Planets».  
In M. M. Shara (ed.), *Stellar Collisions, Mergers and their Consequences*, vol-  
ume 263 of *Astronomical Society of the Pacific Conference Series*, p. 221 (2002).

- HARRISON, B.K., THORNE, K.S., WAKANO, M. AND WHEELER, J.A.  
*Gravitation Theory and Gravitational Collapse* (1965).
- HARRISON, B.K., WAKANO, M. AND WHEELER, J.A.  
*Onzieme Conseil de Physique de Solvay* (1958).
- HARTLE, J.B.  
«Slowly Rotating Relativistic Stars. I. Equations of Structure».  
*Astrophysical Journal*, **150**, p. 1005 (1967).
- HARTLE, J.B. AND THORNE, K.S.  
«Slowly Rotating Relativistic Stars. II. Models for Neutron Stars and Supermassive Stars».  
*Astrophysical Journal*, **153**, p. 807 (1968).
- HEBELER, K., LATTIMER, J.M., PETHICK, C.J. AND SCHWENK, A.  
«Constraints on Neutron Star Radii Based on Chiral Effective Field Theory Interactions».  
*Physical Review Letters*, **105(16)**, 161102 (2010).
- HEINKE, C.O., RYBICKI, G.B., NARAYAN, R. AND GRINDLAY, J.E.  
«A Hydrogen Atmosphere Spectral Model Applied to the Neutron Star X7 in the Globular Cluster 47 Tucanae».  
*Astrophysical Journal*, **644**, pp. 1090–1103 (2006).
- HERRERA, L., GONZÁLEZ, G.A., PACHÓN, L.A. AND RUEDA, J.A.  
*Classical and Quantum Gravity*, **23**, pp. 2395–2408 (2006).
- HESSELS, J.W.T., RANSOM, S.M., STAIRS, I.H., FREIRE, P.C.C., KASPI, V.M. AND CAMILO, F.  
«A Radio Pulsar Spinning at 716 Hz».  
*Science*, **311**, pp. 1901–1904 (2006a).
- HESSELS, J.W.T., RANSOM, S.M., STAIRS, I.H., FREIRE, P.C.C., KASPI, V.M. AND CAMILO, F.  
«A Radio Pulsar Spinning at 716 Hz».  
*Science*, **311**, pp. 1901–1904 (2006b).
- HEWISH, A.  
*Pulsars and High Density Physics. Nobel lecture.* (1974).
- HIRATA, D., TOKI, H. AND TANIHATA, I.  
«Relativistic mean-field theory on the xenon, cesium and barium isotopes».  
*Nuclear Physics A*, **589**, pp. 239–248 (1995).

- HOENSELAERS, C. AND PERJES, Z.  
«Multipole moments of axisymmetric electrovacuum spacetimes».  
*Classical and Quantum Gravity*, **7**, pp. 1819–1825 (1990).
- HOMAN, J., VAN DER KLIS, M., JONKER, P.G., WIJNANDS, R., KUULKERS, E., MÉNDEZ, M. AND LEWIN, W.H.G.  
«RXTE Observations of the Neutron Star Low-Mass X-Ray Binary GX 17+2: Correlated X-Ray Spectral and Timing Behavior».  
*Astrophysical Journal*, **568**, pp. 878–900 (2002).
- HOYLE, F. AND FOWLER, W.A.  
«Nucleosynthesis in Supernovae.»  
*Astrophysical Journal*, **132**, pp. 565–+ (1960).
- HUGHES, V.A., HARTEN, R.H. AND VAN DEN BERGH, S.  
«A new supernova remnant G109.2-1.0».  
*Astrophysical Journal*, **246**, pp. L127–L131 (1981).
- HULLEMAN, F., VAN KERKWIJK, M.H. AND KULKARNI, S.R.  
«An optical counterpart to the anomalous X-ray pulsar 4U0142+61».  
*Nature*, **408**, pp. 689–692 (2000).
- HULLEMAN, F., VAN KERKWIJK, M.H. AND KULKARNI, S.R.  
«The Anomalous X-ray Pulsar 4U 0142+61: Variability in the infrared and a spectral break in the optical».  
*Astronomy & Astrophysics*, **416**, pp. 1037–1045 (2004).
- HUND, F.  
*Erg. d. exacten Natwis.*, **15**, p. 189 (1936).
- HURLEY, K., BOGGS, S.E., SMITH, D.M., DUNCAN, R.C., LIN, R., ZOGLAUER, A., KRUCKER, S., HURFORD, G., HUDSON, H., WIGGER, C. ET AL.  
«An exceptionally bright flare from SGR 1806-20 and the origins of short-duration  $\gamma$ -ray bursts».  
*Nature*, **434**, pp. 1098–1103 (2005).
- IBEN, JR., I. AND TUTUKOV, A.V.  
«Supernovae of type I as end products of the evolution of binaries with components of moderate initial mass (M not greater than about 9 solar masses)».  
*Astrophysical Journal Supplement Series*, **54**, pp. 335–372 (1984).
- IKHSANOV, N.R. AND BESKROVNAYA, N.G.  
«AE Aquarii: The first white dwarf in the family of spin-powered pulsars».  
*arXiv:0809.1169* (2008).

- IKHSANOV, N.R. AND BIERMANN, P.L.  
«High-energy emission of fast rotating white dwarfs».  
*Astronomy & Astrophysics*, **445**, pp. 305–312 (2006).
- ILKOV, M. AND SOKER, N.  
«Type Ia supernovae from very long delayed explosion of core-white dwarf merger».  
*Monthly Notices of the Royal Astronomical Society*, **419**, pp. 1695–1700 (2012).
- IMMLER, S., WILSON, A.S. AND TERASHIMA, Y.  
«X-Ray Emission from the Type Ic Supernova 1994I Observed with Chandra».  
*ApJ*, **573**, pp. L27–L30 (2002).
- IOSILEVSKIY, I.L.  
«Plasma polarization in massive astrophysical objects».  
*Journal of Physics A Mathematical General*, **42(21)**, p. 214008 (2009).
- ISRAEL, G.L., CAMPANA, S., DALL’OSSO, S., MUNO, M.P., CUMMINGS, J., PERNA, R. AND STELLA, L.  
«The Post-Burst Awakening of the Anomalous X-Ray Pulsar in Westerlund 1».  
*Astrophysical Journal*, **664**, pp. 448–457 (2007).
- ISRAEL, G.L., STELLA, L., ANGELINI, L., WHITE, N.E., KALLMAN, T.R., GIOMMI, P. AND TREVES, A.  
«The Discovery of 13 Second X-Ray Pulsations from the Hydrogen-depleted Subdwarf O6 Star Binary HD 49798».  
*Astrophysical Journal*, **474**, pp. L53+ (1997).
- ITOH, K., OKADA, S., ISHIDA, M. AND KUNIEDA, H.  
«Density Diagnostics of the Hot Plasma in AE Aquarii with XMM-Newton».  
*Astrophysical Journal*, **639**, pp. 397–404 (2006).
- ITOH, N.  
«Hydrostatic Equilibrium of Hypothetical Quark Stars».  
*Progress of Theoretical Physics*, **44**, pp. 291–292 (1970).
- IWAMOTO, K., MAZZALI, P.A., NOMOTO, K., UMEDA, H., NAKAMURA, T., PATAT, F., DANZIGER, I.J., YOUNG, T.R., SUZUKI, T., SHIGEYAMA, T. ET AL.  
«A hypernova model for the supernova associated with the  $\gamma$ -ray burst of 25 april 1998».  
*Nature*, **395**, pp. 672–674 (1998).

- IZZO, L., RUEDA, J.A. AND RUFFINI, R.  
«GRB 090618: The First Example of a Neutron Star Gravitational Collapse to a Black Hole Induced by a Type Ib/c Supernova».  
*Astronomy & Astrophysics, in press* (2012a).
- IZZO, L., RUFFINI, R., PENACCHIONI, A.V., BIANCO, C.L., CAITO, L., CHAKRABARTI, S.K., RUEDA, J.A., NANDI, A. AND PATRICELLI, B.  
*Astronomy & Astrophysics, submitted* (2011).
- IZZO, L., RUFFINI, R., PENACCHIONI, A.V., BIANCO, C.L., CAITO, L., CHAKRABARTI, S.K., RUEDA, J.A., NANDI, A. AND PATRICELLI, B.  
«A double component in GRB 090618: a proto-black hole and a genuinely long gamma-ray burst».  
*Astronomy & Astrophysics*, **543**, A10 (2012b).
- JAMES, R.A.  
«The Structure and Stability of Rotating Gas Masses.»  
*Astrophysical Journal*, **140**, p. 552 (1964).
- JOHANNSEN, T. AND PSALTIS, D.  
«Testing the No-hair Theorem with Observations in the Electromagnetic Spectrum. III. Quasi-periodic Variability».  
*Astrophysical Journal*, **726**, 11 (2011).
- JONKER, P.G., VAN DER KLIS, M., HOMAN, J., MÉNDEZ, M., LEWIN, W.H.G., WIJNANDS, R. AND ZHANG, W.  
«Low- and high-frequency variability as a function of spectral properties in the bright X-ray binary GX 5-1».  
*Monthly Notices of the Royal Astronomical Society*, **333**, pp. 665–678 (2002).
- JONKER, P.G., VAN DER KLIS, M., WIJNANDS, R., HOMAN, J., VAN PARADIJS, J., MÉNDEZ, M., FORD, E.C., KUULKERS, E. AND LAMB, F.K.  
«The Power Spectral Properties of the Z Source GX 340+0».  
*Astrophysical Journal*, **537**, pp. 374–386 (2000).
- JUDGE, P.G., SOLOMON, S.C. AND AYRES, T.R.  
«An Estimate of the Sun's ROSAT-PSPC X-Ray Luminosities Using SNOE-SXP Measurements».  
*Astrophysical Journal*, **593**, pp. 534–548 (2003).
- JUETT, A.M., MARSHALL, H.L., CHAKRABARTY, D. AND SCHULZ, N.S.  
«Chandra High-Resolution Spectrum of the Anomalous X-Ray Pulsar 4U 0142+61».  
*Astrophysical Journal*, **568**, pp. L31–L34 (2002).

- KANEKO, Y., RAMIREZ-RUIZ, E., GRANOT, J., KOUVELIOTOU, C., WOOSLEY, S.E., PATEL, S.K., ROL, E., ZAND, J.J.M.I., VAN DER HORST, A.J., WIJERS, R.A.M.J. ET AL.  
«Prompt and afterglow emission properties of gamma-ray bursts with spectroscopically identified supernovae».  
*ApJ*, **654**, pp. 385–402 (2007).
- KASEN, D. AND BILDSTEN, L.  
«Supernova Light Curves Powered by Young Magnetars».  
*Astrophysical Journal*, **717**, pp. 245–249 (2010).
- KASHIYAMA, K., IOKA, K. AND KAWANAKA, N.  
«White dwarf pulsars as possible cosmic ray electron-positron factories».  
*Physical Review D*, **83(2)**, pp. 023002–+ (2011).
- KASPI, V.M., GAVRIIL, F.P., WOODS, P.M., JENSEN, J.B., ROBERTS, M.S.E. AND CHAKRABARTY, D.  
«A Major Soft Gamma Repeater-like Outburst and Rotation Glitch in the No-longer-so-anomalous X-Ray Pulsar 1E 2259+586».  
*Astrophysical Journal*, **588**, pp. L93–L96 (2003).
- KATZ, J.I.  
«The Eddington Limit and Soft Gamma Repeaters».  
*Astrophysical Journal*, **463**, p. 305 (1996).
- KEPLER, S.O., KLEINMAN, S.J., PELISOLI, I., PEÇANHA, V., DIAZ, M., KOESTER, D., CASTANHEIRA, B.G. AND NITTA, A.  
«Magnetic White Dwarfs in the SDSS and Estimating the Mean Mass of Normal DA and DB WDs».  
In K. Werner & T. Rauch (ed.), *American Institute of Physics Conference Series*, volume 1273 of *American Institute of Physics Conference Series*, pp. 19–24 (2010).
- KERR, R.P.  
«Gravitational field of a spinning mass as an example of algebraically special metrics».  
*Phys. Rev. Lett.*, **11**, pp. 237–238 (1963).
- KETTNER, C., WEBER, F., WEIGEL, M.K. AND GLENDENNING, N.K.  
«Structure and stability of strange and charm stars at finite temperatures».  
*Physical Review D*, **51**, pp. 1440–1457 (1995).
- KLEIN, O.  
«On the Thermodynamical Equilibrium of Fluids in Gravitational Fields».  
*Reviews of Modern Physics*, **21**, pp. 531–533 (1949).

- KODAMA, T. AND YAMADA, M.  
«Theory of Superdense Stars».  
*Progress of Theoretical Physics*, **47**, pp. 444–459 (1972).
- KONACKI, M., LEWANDOWSKI, W., WOLSZCZAN, A., DOROSHENKO, O.  
AND KRAMER, M.  
«Are There Planets around the Pulsar PSR B0329+54?»  
*Astrophysical Journal*, **519**, pp. L81–L84 (1999).
- KONACKI, M. AND WOLSZCZAN, A.  
«Masses and Orbital Inclinations of Planets in the PSR B1257+12 System».  
*Astrophysical Journal*, **591**, pp. L147–L150 (2003).
- KOUVELIOTOU, C., WOOSLEY, S.E., PATEL, S.K., LEVAN, A., BLANDFORD,  
R., RAMIREZ-RUIZ, E., WIJERS, R.A.M.J., WEISSKOPF, M.C., TENNANT,  
A., PIAN, E. ET AL.  
«Chandra observations of the x-ray environs of sn 1998bw / grb 980425».  
*ApJ*, **608**, pp. 872–882 (2004).
- KRAMER, M.  
private communication (2010).
- KUBIS, S.  
«Nuclear symmetry energy and stability of matter in neutron stars».  
*Physical Review C*, **76(2)**, 025801 (2007).
- KUIPER, L. AND HERMSEN, W.  
«High-energy characteristics of the schizophrenic pulsar PSR J1846-0258  
in Kes 75. Multi-year RXTE and INTEGRAL observations crossing the  
magnetar-like outburst».  
*Astronomy & Astrophysics*, **501**, pp. 1031–1046 (2009).
- KÜLEBI, B., JORDAN, S., EUCHNER, F., GAENSICKE, B.T. AND HIRSCH, H.  
«Magnetic fields in white dwarfs (Kuelebi+, 2009)».  
*VizieR Online Data Catalog*, **350**, pp. 61341–+ (2010a).
- KÜLEBI, B., JORDAN, S., EUCHNER, F., GÄNSICKE, B.T. AND HIRSCH, H.  
«Analysis of hydrogen-rich magnetic white dwarfs detected in the Sloan  
Digital Sky Survey».  
*Astronomy & Astrophysics*, **506**, pp. 1341–1350 (2009).
- KÜLEBI, B., JORDAN, S., NELAN, E., BASTIAN, U. AND ALTMANN, M.  
«Constraints on the origin of the massive, hot, and rapidly rotating mag-  
netic white dwarf RE J 0317-853 from an HST parallax measurement».  
*Astronomy & Astrophysics*, **524**, pp. A36+ (2010b).

- KUMAR, H.S. AND SAFI-HARB, S.  
«Variability of the High Magnetic Field X-Ray Pulsar PSR J1846-0258 Associated with the Supernova Remnant Kes 75 as Revealed by the Chandra X-Ray Observatory».  
*Astrophysical Journal*, **678**, pp. L43–L46 (2008).
- LAARAKKERS, W.G. AND POISSON, E.  
«Quadrupole Moments of Rotating Neutron Stars».  
*Astrophysical Journal*, **512**, pp. 282–287 (1999).
- LALAZISSIS, G.A., KÖNIG, J. AND RING, P.  
«New parametrization for the Lagrangian density of relativistic mean field theory».  
*Physical Review C*, **55**, pp. 540–543 (1997).
- LANDAU, L.D.  
«On the theory of stars».  
*Phys. Z. Sowjetunion*, **1**, pp. 285–288 (1932).
- LANDAU, L.D.  
*Nature*, **19**, p. 333 (1938).
- LANDAU, L.D. AND LIFSHITZ, E.M.  
*Statistical physics. Part 1* (Pergamon Press, Oxford, 1980).
- LATTIMER, J.M. AND PRAKASH, M.  
«The Physics of Neutron Stars».  
*Science*, **304**, pp. 536–542 (2004a).
- LATTIMER, J.M. AND PRAKASH, M.  
«The Physics of Neutron Stars».  
*Science*, **304**, pp. 536–542 (2004b).
- LEE, T.D. AND PANG, Y.  
«Fermion soliton stars and black holes».  
*Physical Review D*, **35**, pp. 3678–3694 (1987).
- LEE, T.D. AND WICK, G.C.  
«Vacuum stability and vacuum excitation in a spin-0 field theory».  
*Physical Review D*, **9**, pp. 2291–2316 (1974).
- LEVAN, A.J., WYNN, G.A., CHAPMAN, R., DAVIES, M.B., KING, A.R., PRIDDEY, R.S. AND TANVIR, N.R.  
«Short gamma-ray bursts in old populations: magnetars from white dwarf-white dwarf mergers».  
*Monthly Notices of the Royal Astronomical Society*, **368**, pp. L1–L5 (2006).

- LIEB, E.H. AND SIMON, B.  
«Thomas-Fermi Theory Revisited».  
*Physical Review Letters*, **31**, pp. 681–683 (1973).
- LIEBERT, J., SCHMIDT, G.D., GREEN, R.F., STOCKMAN, H.S. AND MCGRAW, J.T.  
«Two hot, low-field magnetic DA white dwarfs».  
*Astrophysical Journal*, **264**, pp. 262–272 (1983).
- LIN, Y.F., BOUTELIER, M., BARRET, D. AND ZHANG, S.N.  
«Studying Frequency Relationships of KiloHertz Quasi-periodic Oscillations for 4U 1636-53 and Sco X-1: Observations Confront Theories».  
*Astrophysical Journal*, **726**, pp. 74–+ (2011).
- LINDBLOM, L.  
«The role of the viscous secular instability in rotating neutron stars».  
*Astrophysical Journal*, **317**, pp. 325–332 (1987).
- LOAN, D.T., TAN, N.H., KHOA, D.T. AND MARGUERON, J.  
«Equation of state of neutron star matter, and the nuclear symmetry energy».  
*Physical Review C*, **83(6)**, 065809 (2011).
- LUCCHESI, D.M. AND PERON, R.  
«Accurate Measurement in the Field of the Earth of the General-Relativistic Precession of the LAGEOS II Pericenter and New Constraints on Non-Newtonian Gravity».  
*Physical Review Letters*, **105(23)**, pp. 231103–+ (2010).
- LUNDQVIST, S. AND MARCH, N.H.  
*Theory of the Inhomogeneous Electro Gas* (1983).
- LYUTIKOV, M. AND GAVRIIL, F.P.  
«Resonant cyclotron scattering and Comptonization in neutron star magnetospheres».  
*Monthly Notices of the Royal Astronomical Society*, **368**, pp. 690–706 (2006).
- MALHEIRO, M., RUEDA, J.A. AND RUFFINI, R.  
«SGRs and AXPs as Rotation-Powered Massive White Dwarfs».  
*Publications of the Astronomical Society of Japan*, **64**, p. 56 (2012).
- MANCHESTER, R.N. AND TAYLOR, J.H.  
*Pulsars* (1977).
- MANKO, V.S., MARTÍN, J. AND RUIZ, E.  
«Six-parameter solution of the Einstein-Maxwell equations possessing equatorial symmetry».  
*Journal of Mathematical Physics*, **36**, pp. 3063–3073 (1995).

- MANKO, V.S., SANABRIA-GÓMEZ, J.D. AND MANKO, O.V.  
«Nine-parameter electrovac metric involving rational functions».  
*Physical Review D*, **62(4)**, pp. 044048–+ (2000).
- MANKO, V.S. AND SIBGATULLIN, N.R.  
«Construction of exact solutions of the Einstein-Maxwell equations corresponding to a given behaviour of the Ernst potentials on the symmetry axis».  
*Classical and Quantum Gravity*, **10**, pp. 1383–1404 (1993).
- MARCH, N.H.  
«The Thomas-Fermi approximation in quantum mechanics».  
*Advances in Physics*, **6**, pp. 1–101 (1957).
- MARSH, J.S.  
«Magnetic and electric fields of rotating charge distributions».  
*American Journal of Physics*, **50**, pp. 51–53 (1982).
- MAZETS, E.P., GOLENTSKII, S.V., ILINSKII, V.N., APTEKAR, R.L. AND GURYAN, I.A.  
«Observations of a flaring X-ray pulsar in Dorado».  
*Nature*, **282**, pp. 587–589 (1979).
- MAZZALI, P.  
talk presented at the congress “Swift and GRBs: unveiling the relativistic universe”, Venice, Italy, June 5-9 (2006).
- MEINTJES, P.J., DE JAGER, C.O. AND ET AL.  
«Persistent Optical-like Pulsed TeV  $\gamma$ -Ray Emission from AE Aquarii».  
In *International Cosmic Ray Conference*, volume 1 of *International Cosmic Ray Conference*, pp. 338–+ (1993).
- MEINTJES, P.J., RAUBENHEIMER, B.C., DE JAGER, O.C., BRINK, C., NEL, H.I., NORTH, A.R., VAN URK, G. AND VISSER, B.  
«AE Aquarii - an emitter of pulsed TeV gamma rays resembling optical emission during flares».  
*Astrophysical Journal*, **401**, pp. 325–336 (1992).
- MEREGHETTI, S.  
«The strongest cosmic magnets: soft gamma-ray repeaters and anomalous X-ray pulsars».  
*Astronomy & Astrophysics Review*, **15**, pp. 225–287 (2008).
- MEREGHETTI, S., LA PALOMBARA, N., TIENGO, A., PIZZOLATO, F., ESPOSITO, P., WOUTD, P.A., ISRAEL, G.L. AND STELLA, L.  
«X-Ray and Optical Observations of the Unique Binary System HD 49798/RX J0648.0-4418».

- Astrophysical Journal*, **737**, 51 (2011).
- MEREGHETTI, S., TIENGO, A., ESPOSITO, P., GÖTZ, D., STELLA, L., ISRAEL, G.L., REA, N., FEROCI, M., TUROLLA, R. AND ZANE, S.  
«An XMM-Newton View of the Soft Gamma Repeater SGR 1806-20: Long-Term Variability in the Pre-Giant Flare Epoch».  
*Astrophysical Journal*, **628**, pp. 938–945 (2005).
- MEREGHETTI, S., TIENGO, A., ESPOSITO, P., LA PALOMBARA, N., ISRAEL, G.L. AND STELLA, L.  
«An Ultramassive, Fast-Spinning White Dwarf in a Peculiar Binary System».  
*Science*, **325**, pp. 1222– (2009).
- MICHEL, F.C.  
«Radio pulsar disk electrodynamics».  
*Astrophysical Journal*, **266**, pp. 188–200 (1983).
- MICHEL, F.C. AND DESSLER, A.J.  
«Pulsar disk systems».  
*Astrophysical Journal*, **251**, pp. 654–664 (1981).
- MIGDAL, A.B., POPOV, V.S. AND VOSKRESENSKIÏ, D.N.  
«The vacuum charge distribution near super-charged nuclei».  
*Soviet Journal of Experimental and Theoretical Physics*, **45**, pp. 436–+ (1977).
- MIGDAL, A.B., VOSKRESENSKIÏ, D.N. AND POPOV, V.S.  
«Distribution of vacuum charge near supercharged nuclei».  
*Soviet Journal of Experimental and Theoretical Physics Letters*, **24**, pp. 163–+ (1976).
- MILNE, E.A.  
«The analysis of stellar structure».  
*Monthly Notices of the Royal Astronomical Society*, **91**, pp. 4–55 (1930).
- MIRABAL, N., HALPERN, J.P., AN, D., THORSTENSEN, J.R. AND TERNDRUP, D.M.  
«Grb 060218/sn 2006aj: A gamma-ray burst and prompt supernova at  $z = 0.0335$ ».  
*ApJ*, **643**, pp. L99–L102 (2006).
- MONAGHAN, J.J.  
«The structure of rapidly rotating white dwarfs».  
*Monthly Notices of the Royal Astronomical Society*, **132**, p. 305 (1966).
- MORINI, M., ROBBA, N.R., SMITH, A. AND VAN DER KLIS, M.

- «EXOSAT observations of the supernova remnant G109.1-1.0 and the X-ray pulsar 1E 2259+586».  
*Astrophysical Journal*, **333**, pp. 777–787 (1988).
- MORSINK, S.M. AND STELLA, L.  
«Relativistic Precession around Rotating Neutron Stars: Effects Due to Frame Dragging and Stellar Oblateness».  
*Astrophysical Journal*, **513**, pp. 827–844 (1999).
- MOTT, N.F.  
«The Electrical Resistance of Dilute Solid Solutions».  
*Proceedings of the Cambridge Philosophical Society*, **32**, p. 281 (1936).
- MUCCINO, M., RUFFINI, R., BIANCO, C.L., IZZO, L. AND PENACCHIONI, A.V.  
«GRB 090227B: the missing link between the genuine short and long GRBs».  
*Astrophysical Journal*, *accepted; arXiv:1205.6600* (2012).
- MÜLLER, B., PEITZ, H., RAFELSKI, J. AND GREINER, W.  
«Solution of the Dirac Equation for Strong External Fields».  
*Physical Review Letters*, **28**, pp. 1235–1238 (1972).
- MUNO, M.P., CHAKRABARTY, D., GALLOWAY, D.K. AND SAVOV, P.  
«Millisecond Oscillations and Photospheric Radius Expansion in Thermonuclear X-Ray Bursts».  
*Astrophysical Journal*, **553**, pp. L157–L160 (2001).
- MÜTHER, H., PRAKASH, M. AND AINSWORTH, T.L.  
«The nuclear symmetry energy in relativistic Brueckner-Hartree-Fock calculations».  
*Physics Letters B*, **199**, pp. 469–474 (1987).
- MYERS, W.  
«Nuclear masses and deformations».  
*Nuclear Physics A*, **81**, pp. 1–60 (1966).
- NALEŻYTY, M. AND MADEJ, J.  
«A catalogue of isolated massive white dwarfs. Mass distribution of massive star».  
*Astronomy & Astrophysics*, **420**, pp. 507–513 (2004).
- NEGREIROS, R., RUFFINI, R., BIANCO, C.L. AND RUEDA, J.A.  
«Cooling of young neutron stars in GRB associated to supernovae».  
*Astronomy & Astrophysics*, **540**, A12 (2012).

- NEGREIROS, R., DEXHEIMER, V. AND SCHRAMM, S.  
«Modeling hybrid stars with an SU(3) nonlinear  $\sigma$  model».  
*Phys. Rev. C*, **82(3)**, pp. 1–9 (2010).  
ISSN 0556-2813.
- NG, C., KASPI, V.M., DIB, R., OLAUSEN, S.A., SCHOLZ, P., GEVER, T.,  
OZEL, F., GAVRIIL, F.P. AND WOODS, P.M.  
«Chandra and RXTE Observations of 1E 1547.0-5408: Comparing the 2008  
and 2009 Outbursts».  
*arXiv:1008.1165* (2010).
- OLSON, E. AND BAILYN, M.  
«Internal structure of multicomponent static spherical gravitating fluids».  
*Physical Review D*, **12**, pp. 3030–3036 (1975).
- OLSON, E. AND BAILYN, M.  
«Charge effects in a static, spherically symmetric, gravitating fluid».  
*Physical Review D*, **13**, pp. 2204–2211 (1976).
- OLSON, E. AND BAILYN, M.  
«Internal structure of multicomponent fluids».  
*Physical Review D*, **18**, pp. 2175–2179 (1978).
- OPPENHEIMER, J.R. AND VOLKOFF, G.M.  
«On Massive Neutron Cores».  
*Physical Review*, **55**, pp. 374–381 (1939).
- Ostriker, J.P. AND Bodenheimer, P.  
«Rapidly Rotating Stars. II. Massive White Dwarfs».  
*Astrophysical Journal*, **151**, p. 1089 (1968).
- Ostriker, J.P. AND TassoUL, J.L.  
«On the Oscillations and Stability of Rotating Stellar Models. II. Rapidly  
Rotating White Dwarfs».  
*Astrophysical Journal*, **155**, p. 987 (1969).
- PACHÓN, L.A., RUEDA, J.A. AND SANABRIA-GÓMEZ, J.D.  
«Realistic exact solution for the exterior field of a rotating neutron star».  
*Physical Review D*, **73(10)**, pp. 104038–+ (2006).
- PACHÓN, L.A., RUEDA, J.A. AND VALENZUELA-TOLEDO, C.A.  
«On the Relativistic Precession and Oscillation Frequencies of Test Particles  
around Rapidly Rotating Compact Stars».  
*Astrophysical Journal*, **756**, 82 (2012).
- PACHÓN, L.A. AND SANABRIA-GÓMEZ, J.D.

«COMMENTS, REPLIES AND NOTES: Note on reflection symmetry in stationary axisymmetric electrovacuum spacetimes».  
*Classical and Quantum Gravity*, **23**, pp. 3251–3254 (2006).

PACZYNSKI, B.

«Evolution of cataclysmic binaries».  
In D. Q. Lamb & J. Patterson (ed.), *Cataclysmic Variables and Low-Mass X-ray Binaries*, volume 113 of *Astrophysics and Space Science Library*, pp. 1–12 (1985).

PACZYNSKI, B.

«X-ray pulsar 1E 2259 + 586 - A merged white dwarf with a 7 second rotation period?»  
*Astrophysical Journal*, **365**, pp. L9–L12 (1990).

PACZYNSKI, B.

«GB 790305 as a very strongly magnetized neutron star».  
*Acta Astronomica*, **42**, pp. 145–153 (1992).

PAGANI, C., BEARDMORE, A.P. AND KENNEA, J.A.

«Swift J1822.3-1606: Enhanced Swift-XRT position».  
*The Astronomer's Telegram*, **3493**, p. 1 (2011).

PAGE, D., GEPPERT, U. AND WEBER, F.

«The cooling of compact stars».  
*Nuclear Physics A*, **777**, pp. 497–530 (2006).  
ISSN 03759474.

PAGE, D., LATTIMER, J., PRAKASH, M. AND STEINER, A.W.

«Minimal Cooling of Neutron Stars: A New Paradigm».  
*ApJSS*, **155(2)**, pp. 623–650 (2004).  
ISSN 0067-0049.

PAGE, D., LATTIMER, J., PRAKASH, M. AND STEINER, A.W.

«Neutrino Emission From Cooper Pairs and Minimal Cooling of Neutron Stars».  
*ApJ*, **707(2)**, pp. 1131–1140 (2009).  
ISSN 0004-637X.

PAGE, D., PRAKASH, M., LATTIMER, J.M. AND STEINER, A.W.

«Rapid Cooling of the Neutron Star in Cassiopeia A Triggered by Neutron Superfluidity in Dense Matter».  
*Physical Review Letters*, **106(8)**, pp. 081101–+ (2011).

PAKMOR, R., KROMER, M., RÖPKE, F.K., SIM, S.A., RUITER, A.J. AND HILLEBRANDT, W.

- «Sub-luminous type Ia supernovae from the mergers of equal-mass white dwarfs with mass  $0.9M_{\odot}$ ».  
*Nature*, **463**, pp. 61–64 (2010).
- PANEI, J.A., ALTHAUS, L.G. AND BENVENUTO, O.G.  
«Mass-radius relations for white dwarf stars of different internal compositions».  
*Astronomy & Astrophysics*, **353**, pp. 970–977 (2000).
- PAPAPETROU, A.  
«Eine rotationssymmetrische Lösung in der allgemeinen Relativitätstheorie».  
*Annalen der Physik*, **447**, pp. 309–315 (1953).
- PAPPAS, G. AND APOSTOLATOS, T.A.  
«Revising the Multipole Moments of Numerical Spacetimes and its Consequences».  
*Physical Review Letters*, **108(23)**, 231104 (2012).
- PARKER, E.N.  
«Acceleration of Cosmic Rays in Solar Flares».  
*Physical Review*, **107**, pp. 830–836 (1957).
- PATNAUDE, D.J., LOEB, A. AND JONES, C.  
«Evidence for a Black Hole Remnant in the Type III Supernova 1979C».  
*arXiv:0912.1571* (2009).
- PATNAUDE, D., LOEB, A. AND JONES, C.  
«Evidence for a possible black hole remnant in the Type III Supernova 1979C».  
*New Astronomy*, **16(3)**, pp. 187–190 (2011).  
ISSN 13841076.
- PENACCHIONI, A.V., RUFFINI, R., IZZO, L., MUCCINO, M., BIANCO, C.L., CAITO, L., PATRICELLI, B. AND AMATI, L.  
«Evidence for a proto-black hole and a double astrophysical component in GRB 101023».  
*Astronomy & Astrophysics*, **538**, A58 (2012).
- PERES, G., ORLANDO, S., REALE, F., ROSNER, R. AND HUDSON, H.  
«The Sun as an X-Ray Star. II. Using the Yohkoh/Soft X-Ray Telescope-derived Solar Emission Measure versus Temperature to Interpret Stellar X-Ray Observations».  
*Astrophysical Journal*, **528**, pp. 537–551 (2000).

PERLMUTTER, S., ALDERING, G., GOLDHABER, G., KNOP, R.A., NUGENT, P., CASTRO, P.G., DEUSTUA, S., FABBRO, S., GOOBAR, A., GROOM, D.E. ET AL.

«Measurements of Omega and Lambda from 42 High-Redshift Supernovae».

*Astrophysical Journal*, **517**, pp. 565–586 (1999).

PHILLIPS, M.M.

«The absolute magnitudes of Type IA supernovae».

*Astrophys. J. Lett.*, **413**, pp. L105–L108 (1993).

PIAN, E., AMATI, L., ANTONELLI, L.A., BUTLER, R.C., COSTA, E., CUSUMANO, G., DANZIGER, J., FEROCI, M., FIORE, F., FRONTERA, F. ET AL.

«BeppoSax observations of grb 980425: Detection of the prompt event and monitoring of the error box».

*ApJ*, **536**, pp. 778–787 (2000).

PIAN, E. ET AL.

Proposal for Chandra Observations: The X-Ray Remnant of XRF100316D/SN2010BH (2011).

PIEPER, W. AND GREINER, W.

«Interior electron shells in superheavy nuclei».

*Zeitschrift fur Physik*, **218**, pp. 327–340 (1969).

POPOV, V.

«From super-charged nuclei to massive nuclear density cores».

In R. Ruffini & G. Vereshchagin (ed.), *American Institute of Physics Conference Series*, volume 1205 of *American Institute of Physics Conference Series*, pp. 127–131 (2010).

POPOV, V.S.

«On the Properties of the Discrete Spectrum for  $Z$  Close to 137».

*Soviet Journal of Experimental and Theoretical Physics*, **33**, pp. 665–+ (1971a).

POPOV, V.S.

«Position Production in a Coulomb Field with  $Z \gtrsim 137$ ».

*Soviet Journal of Experimental and Theoretical Physics*, **32**, pp. 526–+ (1971b).

POTEKHIN, A.Y., CHABRIER, G. AND ROGERS, F.J.

«Equation of state of classical Coulomb plasma mixtures».

*Physical Review E*, **79(1)**, pp. 016411–+ (2009).

POTEKHIN, A.Y., CHABRIER, G. AND YAKOVLEV, D.G.

«Internal temperatures and cooling of neutron stars with accreted envelopes».

- A&A*, **323**, pp. 415–428 (1997).
- PRAKASH, M., LATTIMER, J., PONS, J., STEINER, A. AND REDDY, S.  
«Evolution of a neutron star from its birth to old age».  
*Physics of Neutron Star Interiors*, pp. 364–423 (2001).
- PREDEHL, P. AND SCHMITT, J.H.M.M.  
«X-raying the interstellar medium: ROSAT observations of dust scattering halos.»  
*Astronomy & Astrophysics*, **293**, pp. 889–905 (1995).
- PROCHASKA, J.X., BLOOM, J.S., CHEN, H.W., HURLEY, K.C., MELBOURNE, J., DRESSLER, A., GRAHAM, J.R., OSIP, D.J. AND VACCA, W.D.  
«The host galaxy of grb 031203: Implications of its low metallicity, low redshift, and starburst nature».  
*ApJ*, **611**, pp. 200–207 (2004).
- PSALTIS, D., BELLONI, T. AND VAN DER KLIS, M.  
«Correlations in Quasi-periodic Oscillation and Noise Frequencies among Neutron Star and Black Hole X-Ray Binaries».  
*Astrophysical Journal*, **520**, pp. 262–270 (1999).
- REA, N., ESPOSITO, P., TUROLLA, R., ISRAEL, G.L., ZANE, S., STELLA, L., MEREGHETTI, S., TIENGO, A., GÖTZ, D., GÖĞÜŞ, E. ET AL.  
«A Low-Magnetic-Field Soft Gamma Repeater».  
*Science*, **330**, pp. 944– (2010).
- REA, N., ISRAEL, G.L., ESPOSITO, P., PONS, J.A., CAMERO-ARRANZ, A., MIGNANI, R.P., TUROLLA, R., ZANE, S., BURGAY, M., POSSENTI, A. ET AL.  
«A New Low Magnetic Field Magnetar: The 2011 Outburst of Swift J1822.3-1606».  
*Astrophysical Journal*, **754**, 27 (2012).
- REA, N., JONKER, P.G., NELEMANS, G., PONS, J.A., KASLIWAL, M.M., KULKARNI, S.R. AND WIJNANDS, R.  
«The X-ray quiescence of Swift J195509.6+261406 (GRB 070610): an optical bursting X-ray binary?»  
*arXiv:1101.3483* (2011).
- REA, N., ZANE, S., TUROLLA, R., LYUTIKOV, M. AND GÖTZ, D.  
«Resonant Cyclotron Scattering in Magnetars' Emission».  
*Astrophysical Journal*, **686**, pp. 1245–1260 (2008).
- REISENEGGER, A.  
«Chemical Equilibrium and Stable Stratification of a Multicomponent Fluid: Thermodynamics and Application to Neutron Stars».

- Astrophysical Journal*, **550**, pp. 860–862 (2001).
- REISENEGGER, A.  
«Magnetic field evolution in neutron stars».  
*Astronomische Nachrichten*, **328**, pp. 1173–+ (2007).
- REISENEGGER, A., BENGURIA, R., PRIETO, J.P., ARAYA, P.A. AND LAI, D.  
«Hall drift of axisymmetric magnetic fields in solid neutron-star matter».  
*Astronomy & Astrophysics*, **472**, pp. 233–240 (2007).
- RIESS, A.G., FILIPPENKO, A.V., CHALLIS, P., CLOCCHIATTI, A., DIERCKS, A., GARNAVICH, P.M., GILLILAND, R.L., HOGAN, C.J., JHA, S., KIRSHNER, R.P. ET AL.  
«Observational Evidence from Supernovae for an Accelerating Universe and a Cosmological Constant».  
*Astronomical Journal*, **116**, pp. 1009–1038 (1998).
- RIESS, A.G., STROLGER, L., TONRY, J., CASERTANO, S., FERGUSON, H.C., MOBASHER, B., CHALLIS, P., FILIPPENKO, A.V., JHA, S., LI, W. ET AL.  
«Type Ia Supernova Discoveries at  $z \lesssim 1$  from the Hubble Space Telescope: Evidence for Past Deceleration and Constraints on Dark Energy Evolution».  
*Astrophysical Journal*, **607**, pp. 665–687 (2004).
- RING, P.  
«Relativistic mean field theory in finite nuclei».  
*Progress in Particle and Nuclear Physics*, **37**, pp. 193–263 (1996).
- ROMANI, R.W. AND WATTERS, K.P.  
«Constraining Pulsar Magnetosphere Geometry with  $\gamma$ -ray Light Curves».  
*Astrophysical Journal*, **714**, pp. 810–824 (2010).
- ROSSELAND, S.  
«Electrical state of a star».  
*Monthly Notices of the Royal Astronomical Society*, **84**, pp. 720–728 (1924).
- ROTONDO, M., RUEDA, J.A., RUFFINI, R. AND XUE, S.S.  
«On the equilibrium of self-gravitating neutrons, protons and electrons in  $\beta$ -equilibrium».  
*ArXiv: 1107.2777* (2011a).
- ROTONDO, M., RUEDA, J.A., RUFFINI, R. AND XUE, S.S.  
«Relativistic Feynman-Metropolis-Teller theory for white dwarfs in general relativity».  
*Physical Review D*, **84(8)**, 084007 (2011b).

- ROTONDO, M., RUEDA, J.A., RUFFINI, R. AND XUE, S.S.  
«Relativistic Thomas-Fermi treatment of compressed atoms and compressed nuclear matter cores of stellar dimensions».  
*Physical Review C*, **83(4)**, 045805 (2011c).
- ROTONDO, M., RUEDA, J.A., RUFFINI, R. AND XUE, S.S.  
«The self-consistent general relativistic solution for a system of degenerate neutrons, protons and electrons in  $\beta$ -equilibrium».  
*Physics Letters B*, **701**, pp. 667–671 (2011d).
- ROTONDO, M., RUFFINI, R., XUE, S.S. AND POPOV, V.  
«On Gravitationally and Electrodynamically Bound Nuclear Matter Cores of Stellar Dimensions».  
*International Journal of Modern Physics D*, **20**, pp. 1995–2002 (2011e).
- ROXBURGH, I.W.  
«On Models of Non Spherical Stars. II. Rotating White Dwarfs. With 2 Figures in the Text».  
*Zeitschrift fur Astrophysik*, **62**, p. 134 (1965).
- ROXBURGH, I.W. AND DURNEY, B.R.  
«Structure, Oscillations and Stability of Rotating White Dwarfs».  
*Zeitschrift fur Astrophysik*, **64**, p. 504 (1966).
- RUDERMAN, M.  
«Pulsars: Structure and Dynamics».  
*Annual Review of Astronomy and Astrophysics*, **10**, pp. 427–+ (1972).
- RUDERMAN, M.  
«Spin-Driven Changes in Neutron Star Magnetic Fields».  
*Journal of Astrophysics and Astronomy*, **16**, pp. 207–+ (1995).
- RUEDA, J.A., ROTONDO, M., RUFFINI, R. AND XUE, S.S.  
«A self-consistent approach to neutron stars».  
*Journal of Korean Physical Society*, **57**, pp. 560–+ (2010a).
- RUEDA, J.A. AND RUFFINI, R.  
«Gravitational Waves versus Electromagnetic Emission in Gamma-Ray Bursts».  
*arXiv:1205.6915* (2012a).
- RUEDA, J.A. AND RUFFINI, R.  
«On the Induced Gravitational Collapse of a Neutron Star to a Black Hole by a Type Ib/c Supernova».  
*Astrophysical Journal*, **758**, L7 (2012b).

- RUEDA, J.A., RUFFINI, R. AND XUE, S..  
«The Klein first integrals in an equilibrium system with electromagnetic, weak, strong and gravitational interactions».  
*Nuclear Physics A*, in press; *arXiv:1104.4062* (2011a).
- RUEDA, J.A., RUFFINI, R. AND XUE, S.S.  
«On the electrostatic structure of neutron stars».  
In R. Ruffini & G. Vereshchagin (ed.), *American Institute of Physics Conference Series*, volume 1205 of *American Institute of Physics Conference Series*, pp. 143–147 (2010b).
- RUEDA, J.A., RUFFINI, R. AND XUE, S.S.  
«The Klein first integrals in an equilibrium system with electromagnetic, weak, strong and gravitational interactions».  
*Nuclear Physics A*, **872**, pp. 286–295 (2011b).
- RUFFERT, M. AND JANKA, H.T.  
«Coalescing neutron stars - A step towards physical models. III. Improved numerics and different neutron star masses and spins».  
*Astronomy & Astrophysics*, **380**, pp. 544–577 (2001).
- RUFFINI, R.  
«On the energetics of black holes.»  
In A. Giannaras (ed.), *Black Holes (Les Astres Occlus)*, pp. 451–546 (1973).
- RUFFINI, R.  
«The Role of Thomas-Fermi Approach in Neutron Star Matter».  
In *Path Integrals - New Trends and Perspectives*, pp. 207–218 (2008a).
- RUFFINI, R.  
«The Role of Thomas-Fermi Approach in Neutron Star Matter».  
In *Path Integrals - New Trends and Perspectives*, pp. 207–218 (2008b).
- RUFFINI, R.  
«Title of the Talk».  
In T. Damour and R. Ruffini (ed.), *Proceedings of the 12th Marcel Grossmann Meeting on General Relativity*, World Scientific, Singapore (2009).
- RUFFINI, R., BERNARDINI, M.G., BIANCO, C.L., CAITO, L., CHARDONNET, P., CHERUBINI, C., DAINOTTI, M.G., FRASCHETTI, F., GERALICO, A., GUIDA, R. ET AL.  
«On Gamma-Ray Bursts».  
In H. Kleinert, R.T. Jantzen and R. Ruffini (eds.), *The Eleventh Marcel Grossmann Meeting On Recent Developments in Theoretical and Experimental General Relativity, Gravitation and Relativistic Field Theories*, pp. 368–505 (2008a).

- RUFFINI, R., BERNARDINI, M.G., BIANCO, C.L., CAITO, L., CHARDONNET, P., DAINOTTI, M.G., FRASCHETTI, F., GUIDA, R., VERESHCHAGIN, G. AND XUE, S.S.  
«The role of grb 031203 in clarifying the astrophysical grb scenario».  
In S. Grebenev, R. Sunyaev, C. Winkler, A. Parmar and L. Ouwehand (eds.), *The 6<sup>th</sup> Integral Workshop - The Obscured Universe*, volume SP-622 of *ESA Special Publication*, p. 561 (2007a).
- RUFFINI, R., BERNARDINI, M.G., BIANCO, C.L., CHARDONNET, P., FRASCHETTI, F. AND XUE, S.S.  
«Grb 980425, sn1998bw and the embh model».  
*Advances in Space Research*, **34**, pp. 2715–2722 (2004).
- RUFFINI, R., BERNARDINI, M.G., BIANCO, C.L., CHARDONNET, P., FRASCHETTI, F. AND XUE, S.  
«Theoretical Interpretation of GRB 031203 and URCA-3».  
In B. Aschenbach, V. Burwitz, G. Hasinger and B. Leibundgut (eds.), *Relativistic Astrophysics Legacy and Cosmology - Einstein's Legacy*, p. 399 (2008b).
- RUFFINI, R., BERNARDINI, M.G., BIANCO, C.L., VITAGLIANO, L., XUE, S.S., CHARDONNET, P., FRASCHETTI, F. AND GURZADYAN, V.  
«Black hole physics and astrophysics: The grb-supernova connection and urca-1 - urca-2».  
In M. Novello, S. Perez Bergliaffa and R. Ruffini (eds.), *The Tenth Marcel Grossmann Meeting. On recent developments in theoretical and experimental general relativity, gravitation and relativistic field theories*, p. 369 (Singapore: World Scientific, 2005).
- RUFFINI, R., BIANCO, C.L., CHARDONNET, P., FRASCHETTI, F. AND XUE, S.S.  
«On a possible gamma-ray burst-supernova time sequence».  
*ApJ*, **555**, pp. L117–L120 (2001).
- RUFFINI, R. AND BONAZZOLA, S.  
«Systems of Self-Gravitating Particles in General Relativity and the Concept of an Equation of State».  
*Physical Review*, **187**, pp. 1767–1783 (1969).
- RUFFINI, R., CHAKRABARTI, S.K. AND IZZO, L.  
«Possible multiple components in a GRB: the case of GRB 090618».  
*Submitted to Adv. Sp. Res.* (2010a).
- RUFFINI, R., IZZO, L., PENACCHIONI, A.V., BIANCO, C.L., CAITO, L., CHAKRABARTI, S.K. AND NANDI, A.  
«GRB 090618: a possible case of multiple GRB?»  
*PoS(Texas2010)*, p. 101 (2011).

- RUFFINI, R., ROTONDO, M. AND XUE, S.  
«Electrodynamics for Nuclear Matter in Bulk».  
*International Journal of Modern Physics D*, **16**, pp. 1–9 (2007b).
- RUFFINI, R., ROTONDO, M. AND XUE, S.S.  
«Electrodynamics for nuclear matter in bulk».  
*IJMPD*, **16**, pp. 1–9 (2007c).
- RUFFINI, R. AND STELLA, L.  
«Some comments on the relativistic Thomas-Fermi model and the Vallarta-Rosen equation».  
*Physics Letters B*, **102**, pp. 442–444 (1981).
- RUFFINI, R., VERESHCHAGIN, G. AND XUE, S.  
«Electron-positron pairs in physics and astrophysics: From heavy nuclei to black holes».  
*Physics Reports*, **487**, pp. 1–140 (2010b).
- RUFFINI, R., VITAGLIANO, L. AND XUE, S.S.  
«On a separatrix in the gravitational collapse to an overcritical electromagnetic black hole».  
*Physics Letters B*, **573**, pp. 33–38 (2003a).
- RUFFINI, R., VITAGLIANO, L. AND XUE, S.S.  
«On plasma oscillations in strong electric fields».  
*Physics Letters B*, **559**, pp. 12–19 (2003b).
- RUFFINI, R. AND XUE, S.S.  
«Effective Dyadosphere».  
In Y.-F. Huang, Z.-G. Dai, & B. Zhang (ed.), *American Institute of Physics Conference Series*, volume 1065 of *American Institute of Physics Conference Series*, pp. 289–293 (2008).
- RUIZ, E., MANKO, V.S. AND MARTÍN, J.  
«Extended N-soliton solution of the Einstein-Maxwell equations».  
*Physical Review D*, **51**, pp. 4192–4197 (1995).
- RYAN, F.D.  
«Gravitational waves from the inspiral of a compact object into a massive, axisymmetric body with arbitrary multipole moments».  
*Physical Review D*, **52**, pp. 5707–5718 (1995).
- SALPETER, E.E.  
«Energy and Pressure of a Zero-Temperature Plasma.»  
*Astrophysical Journal*, **134**, pp. 669–+ (1961a).

- SALPETER, E.E.  
«Energy and Pressure of a Zero-Temperature Plasma».  
*ApJ*, **134**, p. 669 (1961b).
- SALPETER, E.E. AND SHAPIRO, S.L.  
«Neutrino and photon emission from a dense, high temperature atmosphere».  
*ApJ*, **251**, p. 311 (1981).  
ISSN 0004-637X.
- SALPETER, E.E. AND VAN HORN, H.M.  
«Nuclear Reaction Rates at High Densities».  
*Astrophysical Journal*, **155**, p. 183 (1969).
- SANABRIA-GÓMEZ, J.D., HERNÁNDEZ-PASTORA, J.L. AND DUBEIBE, F.L.  
«Innermost stable circular orbits around magnetized rotating massive stars».  
*Physical Review D*, **82(12)**, 124014 (2010).
- SASAKI, M., PLUCINSKY, P.P., GAETZ, T.J., SMITH, R.K., EDGAR, R.J. AND SLANE, P.O.  
«XMM-Newton Observations of the Galactic Supernova Remnant CTB 109 (G109.1-1.0)».  
*Astrophysical Journal*, **617**, pp. 322–338 (2004).
- SCHAAB, C., WEBER, F., WEIGEL, M. AND GLENDENNING, N.K.  
«Thermal evolution of compact stars».  
*Nuclear Phys A*, **605**, p. 531 (1996).
- SCHMIDT, G.D., BERGERON, P., LIEBERT, J. AND SAFFER, R.A.  
«Two ultramassive white dwarfs found among candidates for magnetic fields».  
*Astrophysical Journal*, **394**, pp. 603–608 (1992).
- SCHMIDT, G.D., WEST, S.C., LIEBERT, J., GREEN, R.F. AND STOCKMAN, H.S.  
«The new magnetic white dwarf PG 1031 + 234 - Polarization and field structure at more than 500 million Gauss».  
*Astrophysical Journal*, **309**, pp. 218–229 (1986).
- SEDRAKYAN, D.M. AND CHUBARYAN, E.V.  
«Internal solution for stationary axially symmetric gravitational fields».  
*Astrophysics*, **4**, pp. 227–233 (1968).
- SEGRÉ, E.  
*Nuclei and Particles* (1977).

- SHAPIRO, S.L. AND TEUKOLSKY, S.A.  
*Black holes, white dwarfs, and neutron stars: The physics of compact objects* (1983).
- SHAPIRO, S.L., TEUKOLSKY, S.A. AND NAKAMURA, T.  
«Spin-up of a rapidly rotating star by angular momentum loss».  
*Astrophysical Journal*, **357**, pp. L17–L20 (1990).
- SHARMA, B.K. AND PAL, S.  
«Nuclear symmetry energy effects in finite nuclei and neutron star».  
*Physics Letters B*, **682**, pp. 23–26 (2009).
- SHARMA, M.M., NAGARAJAN, M.A. AND RING, P.  
«Rho meson coupling in the relativistic mean field theory and description of exotic nuclei».  
*Physics Letters B*, **312**, pp. 377–381 (1993).
- SHIBATA, M. AND SASAKI, M.  
«Innermost stable circular orbits around relativistic rotating stars».  
*Phys. Rev. D*, **58**, p. 104011 (1998).
- SHTERNIN, P.S., YAKOVLEV, D.G., HEINKE, C.O., HO, W.C.G. AND PATNAUDE, D.J.  
«Cooling neutron star in the Cassiopeia A supernova remnant: evidence for superfluidity in the core».  
*Monthly Notices of the Royal Astronomical Society*, **412**, pp. L108–L112 (2011).
- SIBGATULLIN, N.R.  
*Oscillations and Waves in Strong Gravitational and Electromagnetic Fields*. (1991).
- SIBGATULLIN, N.R. AND SUNYAEV, R.A.  
«Disk accretion in the gravitational field of a rapidly rotating neutron star with a rotationally induced quadrupole mass distribution».  
*Astronomy Letters*, **24**, pp. 774–787 (1998).
- SLATER, J.C. AND KRUTTER, H.M.  
«The Thomas-Fermi Method for Metals».  
*Phys. Rev.*, **47**, pp. 559–+ (1935).
- SORIA, R., PIAN, E. AND MAZZALI, P.A.  
«A second glance at SN 2002ap and the M 74 field with XMM-Newton».  
*A&A*, **413**, pp. 107–119 (2004).
- SORKIN, R.  
«A Criterion for the Onset of Instability at a Turning Point».  
*Astrophysical Journal*, **249**, p. 254 (1981).

- SORKIN, R.D.  
«A Stability Criterion for Many Parameter Equilibrium Families».  
*Astrophysical Journal*, **257**, p. 847 (1982).
- SPRUIT, H.C.  
«Dynamo action by differential rotation in a stably stratified stellar interior».  
*Astronomy & Astrophysics*, **381**, pp. 923–932 (2002).
- STAIRS, I.H.  
«Pulsars in Binary Systems: Probing Binary Stellar Evolution and General Relativity».  
*Science*, **304**, pp. 547–552 (2004).
- STEFANESCU, A., KANBACH, G., SŁOWIKOWSKA, A., GREINER, J., MCBREEN, S. AND SALA, G.  
«Very fast optical flaring from a possible new Galactic magnetar».  
*Nature*, **455**, pp. 503–505 (2008).
- STEJNER, M. AND MADSEN, J.  
«Gaps below strange star crusts».  
*Physical Review D*, **72(12)**, 123005 (2005).
- STELLA, L. AND VIETRI, M.  
«Lense-Thirring Precession and Quasi-periodic Oscillations in Low-Mass X-Ray Binaries».  
*Astrophysical Journal*, **492**, pp. L59+ (1998).
- STELLA, L. AND VIETRI, M.  
«kHz Quasiperiodic Oscillations in Low-Mass X-Ray Binaries as Probes of General Relativity in the Strong-Field Regime».  
*Physical Review Letters*, **82**, pp. 17–20 (1999).
- STELLA, L., VIETRI, M. AND MORSINK, S.M.  
«Correlations in the Quasi-periodic Oscillation Frequencies of Low-Mass X-Ray Binaries and the Relativistic Precession Model».  
*Astrophysical Journal*, **524**, pp. L63–L66 (1999).
- STEPHANI, H., KRAMER, D., MACCALLUM, M., HOENSELAERS, C. AND HERLT, E.  
*Exact solutions of Einstein's field equations* (2003).
- STERGIOULAS, N.  
«Rotating Stars in Relativity».  
*Living Reviews in Relativity*, **6**, p. 3 (2003).

STONER, E.C.

«The limiting density of White Dwarfs».  
*Philosophical Magazine (Series 7)*, **7**, pp. 63–70 (1929).

STROHMAYER, T.E., ZHANG, W., SWANK, J.H., SMALE, A., TITARCHUK, L.,  
DAY, C. AND LEE, U.

«Millisecond X-Ray Variability from an Accreting Neutron Star System».  
*Astrophysical Journal*, **469**, p. L9 (1996).

STUTE, M. AND CAMENZIND, M.

«Towards a self-consistent relativistic model of the exterior gravitational  
field of rapidly rotating neutron stars».

*Monthly Notices of the Royal Astronomical Society*, **336**, pp. 831–840 (2002).

SUGAHARA, Y. AND TOKI, H.

«Relativistic mean-field theory for unstable nuclei with non-linear  $\sigma$  and  $\omega$   
terms».

*Nuclear Physics A*, **579**, pp. 557–572 (1994).

SWEET, P.A.

«The Neutral Point Theory of Solar Flares».

In B. Lehnert (ed.), *Electromagnetic Phenomena in Cosmical Physics*, volume 6  
of *IAU Symposium*, pp. 123–+ (1958).

TAKAMI, K., REZZOLLA, L. AND YOSHIDA, S.

«A quasi-radial stability criterion for rotating relativistic stars».

*Monthly Notices of the Royal Astronomical Society*, **416**, pp. L1–L5 (2011).

TAMII, A., POLTORATSKA, I., VON NEUMANN-COSEL, P., FUJITA, Y.,  
ADACHI, T., BERTULANI, C.A., CARTER, J., DOZONO, M., FUJITA, H.,  
FUJITA, K. ET AL.

«Complete Electric Dipole Response and the Neutron Skin in Pb208».

*Physical Review Letters*, **107(6)**, 062502 (2011).

TASSOUL, J.L. AND OSTRICKER, J.P.

«Secular Stability of Uniformly Rotating Polytropes».

*Astronomy & Astrophysics*, **4**, p. 423 (1970).

TAURIS, T.M. AND BAILES, M.

«The origin of millisecond pulsar velocities.»

*Astronomy & Astrophysics*, **315**, pp. 432–444 (1996).

TAURIS, T.M. AND TAKENS, R.J.

«Runaway velocities of stellar components originating from disrupted bi-  
naries via asymmetric supernova explosions».

*Astronomy & Astrophysics*, **330**, pp. 1047–1059 (1998).

- TAVANI, M.  
«AGILE Discovery of Gamma-ray Flares from the Crab Nebula».  
In *American Astronomical Society Meeting Abstracts*, volume 217 of *American Astronomical Society Meeting Abstracts*, pp. 434.06–+ (2011).
- TAYLER, R.J.  
«The adiabatic stability of stars containing magnetic fields-I.Toroidal fields».  
*Monthly Notices of the Royal Astronomical Society*, **161**, pp. 365–+ (1973).
- TENNANT, A.F., BECKER, W., JUDA, M., ELSNER, R.F., KOLODZIEJCZAK, J.J., MURRAY, S.S., O'DELL, S.L., PAERELS, F., SWARTZ, D.A., SHIBAZAKI, N. ET AL.  
«Discovery of X-Ray Emission from the Crab Pulsar at Pulse Minimum».  
*Astrophysical Journal*, **554**, pp. L173–L176 (2001).
- TERADA, Y.  
«White Dwarf Equivalent of Pulsars, Discovered with Suzaku».  
*Astronomical Herald*, **101**, pp. 526–534 (2008).
- TERADA, Y., HAYASHI, T., ISHIDA, M., MAKISHIMA, K., MUKAI, K., DOTANI, T., OKADA, S., NAKAMURA, R., NAIK, S., BAMBA, A. ET AL.  
«Suzaku Discovery of Hard X-ray Pulsations from the Rotating Magnetized White Dwarf, AE Aquarii».  
In *AAS/High Energy Astrophysics Division #10*, volume 10 of *AAS/High Energy Astrophysics Division*, pp. 10.03–+ (2008a).
- TERADA, Y., HAYASHI, T., ISHIDA, M., MUKAI, K., DOTANI, T., BAMBA, A., OKADA, S., NAKAMURA, R., MAKISHIMA, K., MORIGAMI, K. ET AL.  
«Suzaku Observation of a White Dwarf as a new Candidate of Cosmic-ray Origin».  
In F. A. Aharonian, W. Hofmann, & F. Rieger (ed.), *American Institute of Physics Conference Series*, volume 1085 of *American Institute of Physics Conference Series*, pp. 689–692 (2008b).
- TERADA, Y., HAYASHI, T., ISHIDA, M., MUKAI, K., DOTANI, T., OKADA, S., NAKAMURA, R., NAIK, S., BAMBA, A. AND MAKISHIMA, K.  
«Suzaku Discovery of Hard X-Ray Pulsations from a Rotating Magnetized White Dwarf, AEAquarii».  
*Publ. Astron. Soc. Japan*, **60**, pp. 387– (2008c).
- TERADA, Y., ISHIDA, M., MUKAI, K., DOTANI, T., MAKISHIMA, K., NAIK, S., HAYASHI, T., OKADA, S., NAKAMURA, R. AND ENOTO, T.  
«Possible Suzaku detection of non-thermal X-ray signals from a rotating magnetized white dwarf».  
*Advances in Space Research*, **41**, pp. 512–517 (2008d).

- THOMPSON, C. AND DUNCAN, R.C.  
«Neutron star dynamos and the origins of pulsar magnetism».  
*Astrophysical Journal*, **408**, pp. 194–217 (1993).
- THOMPSON, C. AND DUNCAN, R.C.  
«The soft gamma repeaters as very strongly magnetized neutron stars - I. Radiative mechanism for outbursts».  
*Monthly Notices of the Royal Astronomical Society*, **275**, pp. 255–300 (1995).
- THOMPSON, C. AND DUNCAN, R.C.  
«The Soft Gamma Repeater as Very Strongly Magnetized Neutron Stars. II. Quiescent Neutrino, X-Ray, and Alfvén Wave Emission».  
*Astrophysical Journal*, **473**, pp. 322–+ (1996).
- THOMPSON, C., LYUTIKOV, M. AND KULKARNI, S.R.  
«Electrodynamics of Magnetars: Implications for the Persistent X-Ray Emission and Spin-down of the Soft Gamma Repeater and Anomalous X-Ray Pulsars».  
*Astrophysical Journal*, **574**, pp. 332–355 (2002).
- TIENGO, A., ESPOSITO, P., MEREGHETTI, S., REA, N., STELLA, L., ISRAEL, G.L., TUROLLA, R. AND ZANE, S.  
«The calm after the storm: XMM-Newton observation of SGR 1806-20 two months after the Giant Flare of 2004 December 27».  
*Astronomy & Astrophysics*, **440**, pp. L63–L66 (2005).
- TOLMAN, R.C.  
«On the Weight of Heat and Thermal Equilibrium in General Relativity».  
*Physical Review*, **35**, pp. 904–924 (1930).
- TOLMAN, R.C.  
«Static Solutions of Einstein’s Field Equations for Spheres of Fluid».  
*Physical Review*, **55**, pp. 364–373 (1939).
- TOLMAN, R.C. AND EHRENFEST, P.  
«Temperature Equilibrium in a Static Gravitational Field».  
*Physical Review*, **36**, pp. 1791–1798 (1930).
- TOMIMATSU, A. AND SATO, H.  
«New Exact Solution for the Gravitational Field of a Spinning Mass».  
*Physical Review Letters*, **29**, pp. 1344–1345 (1972).
- TONG, H., SONG, L.M. AND XU, R.X.  
«Non-detection in a Fermi/LAT Observation of AXP 4U 0142+61: Magnetars?»  
*Astrophysical Journal*, **725**, pp. L196–L199 (2010).

- TONG, H., SONG, L.M. AND XU, R.X.  
«AXPs and SGRs in the outer gap model: confronting Fermi observations».  
*arXiv:1101.2289* (2011).
- TOROK, G., BAKALA, P., STUCHLIK, Z. AND CECH, P.  
«Modeling the Twin Peak QPO Distribution in the Atoll Source 4U 1636-53».  
*Acta Astronomica*, **58**, pp. 1–14 (2008).
- TÖRÖK, G., BAKALA, P., ŠRÁMKOVÁ, E., STUHLÍK, Z. AND URBANEC, M.  
«On Mass Constraints Implied by the Relativistic Precession Model of Twin-peak Quasi-periodic Oscillations in Circinus X-1».  
*Astrophysical Journal*, **714**, pp. 748–757 (2010).
- TRÜMPER, J.E.  
«Observations of neutron stars and the equation of state of matter at high densities».  
*Progress in Particle and Nuclear Physics*, **66**, pp. 674–680 (2011).
- TRÜMPER, J.E., BURWITZ, V., HABERL, F. AND ZAVLIN, V.E.  
«The puzzles of RX J1856.5-3754: neutron star or quark star?»  
*Nuclear Physics B Proceedings Supplements*, **132**, pp. 560–565 (2004).
- TUROLLA, R., ZAMPIERI, L., COLPI, M. AND TREVES, A.  
«Spherical accretion onto neutron stars revisited: Are hot solutions possible?»  
*ApJ*, **426**, p. L35 (1994).  
ISSN 0004-637X.
- USOV, V.V.  
«High-frequency emission of X-ray pulsar 1E 2259+586».  
*Astrophysical Journal*, **410**, pp. 761–763 (1993).
- USOV, V.V.  
«Glitches in the X-ray pulsar 1E 2259+586».  
*Astrophysical Journal*, **427**, pp. 984–986 (1994).
- USOV, V.V.  
«Bare Quark Matter Surfaces of Strange Stars and  $e^+e^-$  Emission».  
*Physical Review Letters*, **80**, pp. 230–233 (1998).
- VAN DER KLIS, M.  
«Quasi-periodic Oscillations and Noise in Accreting Black Holes and Low-Magnetic Field Neutron Stars».  
In J. Greiner, H.W. Duerbeck and R.E. Gershberg (eds.), *IAU Colloq. 151: Flares and Flashes*, volume 454 of *Lecture Notes in Physics*, Berlin Springer Verlag, p. 321 (1995).

- VAN DER KLIS, M., SWANK, J.H., ZHANG, W., JAHODA, K., MORGAN, E.H., LEWIN, W.H.G., VAUGHAN, B. AND VAN PARADIJS, J.  
«Discovery of Submillisecond Quasi-periodic Oscillations in the X-Ray Flux of Scorpius X-1».  
*Astrophysical Journal*, **469**, p. L1 (1996).
- VAN HORN, H.M.  
«Physical processes in white dwarfs».  
In S.S. Kumar (ed.), *Low-Luminosity Stars*, p. 297 (1969).
- VINK, J.  
«Supernova remnants with magnetars: Clues to magnetar formation».  
*Advances in Space Research*, **41**, pp. 503–511 (2008).
- VINK, J. AND KUIPER, L.  
«Supernova remnant energetics and magnetars: no evidence in favour of millisecond proto-neutron stars».  
*Monthly Notices of the Royal Astronomical Society*, **370**, pp. L14–L18 (2006).
- WALECKA, J.D.  
«A theory of highly condensed matter.»  
*Annals of Physics*, **83**, pp. 491–529 (1974).
- WEBER, F. AND GLENDENNING, N.K.  
«Application of the improved Hartle method for the construction of general relativistic rotating neutron star models».  
*Astrophysical Journal*, **390**, pp. 541–549 (1992).
- WEISSKOPF, M.C., O'DELL, S.L., PAERELS, F., ELSNER, R.F., BECKER, W., TENNANT, A.F. AND SWARTZ, D.A.  
«Chandra Phase-Resolved X-Ray Spectroscopy of the Crab Pulsar».  
*Astrophysical Journal*, **601**, pp. 1050–1057 (2004).
- WIJNANDS, R., MENDEZ, M., VAN DER KLIS, M., PSALTIS, D., KUULKERS, E. AND LAMB, F.K.  
«Discovery of Kilohertz Quasi-periodic Oscillations in the Z Source GX 5-1».  
*Astrophysical Journal*, **504**, p. L35 (1998).
- WIJNANDS, R.A.D., VAN DER KLIS, M., VAN PARADIJS, J., LEWIN, W.H.G., LAMB, F.K., VAUGHAN, B. AND KUULKERS, E.  
«Discovery in 4U 1636-53 of Two Simultaneous Quasi-periodic Oscillations near 900 HZ and 1176 HZ».  
*Astrophysical Journal*, **479**, p. L141 (1997).
- WITTEN, E.  
«Cosmic separation of phases».

- Physical Review D*, **30**, pp. 272–285 (1984).
- WOLTJER, L.  
«X-Rays and Type i Supernova Remnants.»  
*Astrophysical Journal*, **140**, pp. 1309–1313 (1964).
- WOODS, P.M., KASPI, V.M., THOMPSON, C., GAVRIIL, F.P., MARSHALL, H.L., CHAKRABARTY, D., FLANAGAN, K., HEYL, J. AND HERNQUIST, L.  
«Changes in the X-Ray Emission from the Magnetar Candidate 1E 2259+586 during Its 2002 Outburst».  
*Astrophysical Journal*, **605**, pp. 378–399 (2004).
- WOOSLEY, S.E.  
«Bright Supernovae from Magnetar Birth».  
*Astrophysical Journal*, **719**, pp. L204–L207 (2010).
- YAKOVLEV, D.G., GASQUES, L.R., AFANASJEV, A.V., BEARD, M. AND WIESCHER, M.  
«Fusion reactions in multicomponent dense matter».  
*Physical Review C*, **74(3)**, 035803 (2006).
- YAKOVLEV, D.G., KAMINKER, A.D., GNEDIN, O.Y. AND HAENSEL, P.  
«Neutrino emission from neutron stars».  
*Physics Reports*, **354(1-2)**, pp. 1–155 (2001).  
ISSN 03701573.
- YAKOVLEV, D.G. AND PETHICK, C.J.  
«Neutron Star Cooling».  
*Annual Review of Astronomy & Astrophysics*, **42**, pp. 169–210 (2004).
- ZANE, S., REA, N., TUROLLA, R. AND NOBILI, L.  
«X-ray spectra from magnetar candidates - III. Fitting SGR/AXP soft X-ray emission with non-relativistic Monte Carlo models».  
*Monthly Notices of the Royal Astronomical Society*, **398**, pp. 1403–1413 (2009).
- ZEL'DOVICH, I.B.  
«Nuclear Reactions in Super-Dense Cold Hydrogen».  
*Soviet Journal of Experimental and Theoretical Physics*, **6**, pp. 760–+ (1958a).
- ZEL'DOVICH, I.B.  
«Nuclear Reactions in Super-Dense Cold Hydrogen».  
*Soviet Journal of Experimental and Theoretical Physics*, **6**, p. 760 (1958b).
- ZELDOVICH, Y.B. AND POPOV, V.S.  
«Reviews of Topical Problems: Electronic Structure of Superheavy Atoms».  
*Soviet Physics Uspekhi*, **14**, pp. 673–694 (1972).

ZHANG, B. AND GIL, J.

«GCRT J1745-3009 as a Transient White Dwarf Pulsar».  
*Astrophysical Journal*, **631**, pp. L143–L146 (2005).